The Pennsylvania State University

The Graduate School

GEODETIC EXPLORATION OF THE KINEMATICS AND FAULT SLIP RATES OF THE SOUTHEASTERN AND WESTERN CARIBBEAN PLATE BOUNDARIES AND THE CALDERA DYNAMICS OF THE SIERRA NEGRA VOLCANO

A Dissertation in

Geosciences

by

Machel Higgins

Submitted in Partial Fulfillment
of the Requirements
for the Degree of

Doctor of Philosophy

August 2021

The dissertation of Machel Higgins was reviewed and approved by the following:

Peter La Femina
Professor of Geosciences
Dissertation Advisor
Chair of Committee

Charles J. Ammon
Professor of Geosciences

Derek Elsworth
Professor of Geosciences

Douglas Miller
Research Professor of Landscape Science

Mark Patzkowsky
Professor of Geosciences
Associate Head for Graduate Programs in Geosciences

ABSTRACT

Determining plate boundary kinematics and fault slip rates is critical to gaining an understanding of the seismogenic nature of the faults. The kinematics of plate boundaries vary widely and are a reflection of plate boundaries history, current tectonic regime, geology, and crustal properties. Geodesy is a useful tool for probing the kinematics of plate boundaries, active fault identification, slip rates, and stress accumulation.

This dissertation presents research on the faulting and kinematics of the western and southern Caribbean plate boundaries. Specifically, this research focuses on the 900 km long Caribbean-South American transform plate boundary and the Caribbean-Cocos plate convergent margin in Nicaragua. This dissertation is composed of four main chapters: (1) the interseismic strain accumulation and slip partitioning at the CA-SA transform boundary, (2) exploring bookshelf faulting in Nicaragua using upper-plate earthquakes, (3) modeling bookshelf faulting in Nicaragua using geodetic data, and (4) investigating the faulting of intra-caldera earthquakes during the 2018 eruption of the Sierra Negra volcano.

We combined Global Positioning System (GPS) and Interferometric Synthetic Aperture Radar (InSAR) data to characterize the interseismic behavior (i.e., locked or creeping), and strain partitioning for the faults along the Caribbean – South American transform plate boundary. Interseismic strain is distributed mainly on three faults, the San Sebastian, El Pilar, and Central Range faults, but partitioning occurs across multiple faults in the west (San Sebastian and La Victoria faults) and east (Sub-Tobago Terrane, Central Range, and South Coast faults). In northern Venezuela, slip is partitioned on the San Sebastian (16.4 ± 1.7 mm/yr) and La Victoria (4.3 ± 0.9 mm/yr) faults. In north-eastern Venezuela, the El Pilar fault accommodates slip at a rate of 18.6 ± 1.8 mm/yr. In Trinidad and Tobago, slip is partitioned between the Sub-Tobago Terrane (3.0 ± 0.1 mm/yr), Central Range (14.5 ± 2.0 mm/yr), and South Coast (3.0 ± 0.1 mm/yr) faults. The La Victoria, San Sebastian, the western El Pilar segment, and Sub-Tobago Terrane faults are locked to depths of 16 ± 4 km, 7 ± 5 km, 6 ± 2 km, and 8 ± 1 km, respectively. The eastern segment of

the El Pilar, the Central Range, and the South Coast faults all creep. Our new InSAR results indicate that the entire Central Range Fault is creeping. The locked western segment of this transform plate boundary is capable of producing a M_w 8 earthquake, which is a significant finding regarding seismic hazard and risk.

Oblique convergence and strong mechanical coupling along subduction zones result in strain partitioning and the development of translating forearc terranes. Translation of the fore-arc relative to the over-riding plate is typically accommodated by strike-slip fault systems; for example, the Great Sumatran Fault, Indonesia. The Central American Fore-Arc (CAFA) is a northwestward translating (8 mm/yr to 14 mm/yr) fore-arc sliver, the result of oblique Cocos - Caribbean convergence, and Cocos Ridge collision. However, the CAFA in Nicaragua does not have the expected trench-parallel, strike-slip fault system to accommodate its relative motion with the Caribbean Plate. It has been proposed that CAFA-Caribbean dextral shear is accommodated by clockwise rotating tectonic blocks (bookshelf faulting), where faulting is characterized by NE-trending left-lateral faulting. Using Global Positioning System data, and a Bayesian inversion approach, the kinematics and geometries of three moderate-magnitude upper-plate earthquakes in Nicaragua were determined. The April 10th, 2014 Mw 6.1, September 15th, 2016 Mw 5.7, and September 28th, 2016 Mw 5.5 earthquakes were investigated. It was found that the April 10th, 2014 earthquake occurred on a NW-SE (313°) striking fault with right-lateral coseismic slip. This is the first well-documented historical earthquake with this geometry and kinematics. The September 15th and September 28th, 2016 earthquakes were located on faults with strikes of N55° & N22°, respectively, with left-lateral and dip-slip coseismic slip. Coulomb failure stress analysis suggests that the 2016 earthquakes were promoted by the 2014 earthquake and that the September 28th, 2016 earthquake was triggered by the September 15th, 2016 earthquake. It was also found that the April 15th earthquake occurred in the vicinity of the Momotombo volcano and would have dilated the volcano magmatic system, allowing magma ascent and the subsequent December 1st, 2015 eruption. The determination of the geometry and kinematics of these upper-plate earthquakes provides support for CAFA-Caribbean dextral shear via bookshelf faulting and important implications for seismic hazard estimates.

In Nicaragua, the CAFA-CA relative motion is accommodated primarily by bookshelf faulting. This project models Global Position System (GPS) data to explore bookshelf faulting. First, elastic and hetero-elastic models were investigated for arc-parallel fault systems. A two-fault elastic dislocation model fits the geodetic data but does not honor the real-world fault configuration. Second, the boundary element method (BEM) was used to investigate the arc-normal and arc-oblique faults of bookshelf faulting. BEM models show that an array of arc-normal faults, with lengths of 15 km to 20 km and spaced by 5 km or less, fits the geodetic signature seen across-strike the CAFA. These faults also have an average slip rate of 3 mm/yr. The CAFA-CA interface produces destructive shallow M_w 5.5 earthquakes. These earthquakes would have a reoccurrence interval of ~50 years.

The Sierra Negra volcano is the largest of the basaltic shield volcanos on the western volcanic province of the Galapagos Islands, Ecuador. Prior to the June 26^{th,} 2018 Sierra Negra eruption there was 6.5 m of inflation of the caldera. A M_w 5.3 earthquake occurred on the intra-caldera trapdoor fault ~8 hours before the eruption began. This project determines the coseismic faulting and kinematics of the earthquakes that occurred during the eruption. These are the Mw 5.3 June 26th, Ml 4.9 July 5th, and Ml 4.8 July 22nd earthquakes. It was found that these earthquakes occurred on the southern limb of the trapdoor fault system. It was also found that the June 26th had coseismic slip of 1.8 m right-lateral slip and 4.5 m of dip-slip (reverse motion). While the July 5th earthquake had coseismic slip of 0.4 m left-lateral and -3.2 m of dip-slip (normal faulting) and the July 22nd earthquake coseismic slip was pure dip-slip of -1.2 m (normal faulting). These earthquakes are events of rapid inflation and subsidence of the caldera floor. Over the course of the eruption net uplift of the caldera floor, with a maximum of 1.5 m, was observed. The net coseismic reverse dip-slip over the three earthquakes was of 0.2 m, which is sufficient enough to produce the observed net uplift over the eruption, leading to building the resurgent caldera. Similar earthquakes over many eruptive cycles are responsible for caldera resurgence and some of the features within the caldera.

TABLE OF CONTENTS

LIST OF FIGURES

LIST OF TABLES

ACKNOWLEDGEMENTS

I would like to thank my advisor, Peter LaFemina, who gave me the opportunity to pursue a Ph.D. and molded me into a geoscientist. I benefitted greatly from his knowledge and our many discussions from which I gained the skill of rigorously approaching problem-solving in geoscience. I may have tested his patience with my many mistakes but he ultimately turned those mistakes into learning experiences. His wisdom, guidance, and insight were invaluable. I would also like to thank my committee members, Chuck Ammon, Derek Elsworth, and Douglas Miller. They always made themselves available to help solve problems I thought were intractable, offered wisdom, and in many ways were instrumental in the completion of the research projects in this dissertation.

The coursework offered by the faculty of the Department of Geoscience and the knowledge of Pete and my committee members served to make me a competent geoscientist but I would be remiss to not acknowledge my other teachers. Gorki Ruiz was not only my lab mate but he was also was my geology teacher. I am very appreciative of the discussions we had and the friendship that I hope will endure. Halldor Geirsson, without obligation, accepted my harassing emails and offered excellent advice. His invaluable input into some of my research projects is greatly appreciated. I consider him my second advisor. I would not have been at Penn State if were not for John Weber. I am grateful for his willingness to have me undertake a Ph.D., his knowledge about the geology of Venezuela and Trinidad and Tobago, and the mud he made me smear unto my face in Moruga whilst collecting GPS data. I am indebted to him for his sage wisdom and willingness to offer help. Finally, I would like to thank Sasha P. James. She was my cheerleader and my support while earning my Ph.D. degree. Though we were in separate countries, she rarely complained about the distance, the flights, and the nights I simply could not talk because I was busy.

This work was financially supported by the NSF: EAR-1826508 (Collaborative Research: Deciphering upper plate deformation and faulting processes in Central America with integrated geodetic and seismic) awarded to Peter LaFemina. Journal submission of the work presented in

Chapter 2 of this dissertation and travel to conferences were supported by funds from the Barry Voight Endowment and the Krynine travel fund. ALOS-2 SAR data were made available by the Japanese Aerospace Exploration Agency (JAXA) for the sixth RA proposal (PI no. 3153). The findings and conclusions within this dissertation do not necessarily reflect the view of the NSF nor JAXA.

Chapter 1
Introduction

1.1 Fault Slip Rates, Strain Partitioning, and Earthquake Geodesy

A comprehensive understanding of fault slip rates, strain partitioning, and seismogenic potential at plate boundaries is important in determining the seismic hazard exposure of populations living in these regions. Identifying and characterizing interseismic strain accumulation near active faults can be accomplished with ground deformation measurements. The use of geodetic techniques in measuring ground deformation has shed light on the complex tectonics surrounding the Caribbean plate (La Femina et al., 2009; Symithe et al., 2015; Pérez et al., 2018; Weber et al., 2020). In this dissertation, I use space-borne geodetic data to investigate interseismic elastic strain partitioning and accumulation along-strike the Caribbean-South American transform plate boundary and the Central American Forearc-Caribbean boundary in the Caribbean-Cocos plate convergent margin. I also investigate the seismogenic nature of these plate boundaries. I present findings that the western segments of the Caribbean-South America transform boundary is locked and capable of producing a Mw 8 earthquake and the Nicaraguan segment of Central American Forearc-Caribbean produces M 5 to 6 earthquakes with a reoccurrence interval of ~50 years. I also determined the faulting and kinematics of three upper-plate earthquakes, using geodetic data. The faulting of the three earthquakes supports the bookshelf faulting model being the mechanism that accommodates the relative motion between the forearc and the Caribbean plate. Finally, I present a study in Chapter 5 investigating three earthquakes and the kinematics of the trapdoor fault in the caldera of the Sierra Negra volcano, Galapagos, during the 2018 eruption.

1.2 Strain Partitioning and Interseismic Fault Behavior Along the Caribbean-South American Transform Plate Boundary

The 900 km long Caribbean-South America transform boundary runs through northern Venezuela and the islands of Trinidad and Tobago and accommodates ~22 mm/yr of relative plate motion (Symithe et al., 2015; Pérez et al., 2018; Weber et al., 2020). Using Global Positioning System (GPS) and Interferometric Synthetic Aperture Radar (InSAR) data, I modeled the slip partitioning, and interseismic fault locking along the plate boundary. The work presented in this dissertation has found that slip is partitioned on three fault systems: (1) the San Sebastian and La Victoria fault system, (2) the El Pilar fault, and (3) the Sub-Tobago Terrane, Central Range, and South Coast fault system. The slip rates for the San Sebastian and La Victoria faults are both locked and take up 16 mm/yr and 4.3 mm/yr of relative motion, respectively. The El Pilar fault accommodates ~18.4 mm/yr of relative plate motion and its western segment is locked while the eastern segment creeps. The Sub-Tobago Terrane takes up 3 mm/yr of relative motion and is locked. The Central Range and South coast faults both creep at rates of 14.5 mm/yr and 3.1 mm/yr, respectively. There have been many damaging earthquakes on the plate boundary; for example, the 1967 M 6.5 Caracas earthquake (Pérez 1998a) and the 1900 M 7.6 to M 8.0 earthquake (Pacheco & Sykes, 1992). The San Sebastian fault and the western segment of the El Pilar fault are connected (Escalona & Mann, 2011) and if both segments rupture together they would produce a M 8.0 earthquake.

1.3 Central American Forearc-Caribbean Plate Shear Mechanism and Magmatic-Tectonic Interaction in Nicaragua

Strain partitioning in the Central American Forearc (CAFA) in the Caribbean-Cocos plate convergent margin, is due to oblique convergence and the collision of the Cocos Ridge with the western Caribbean plate. The CAFA translates to the northwest at rates of 8-14 mm/yr (Ellis et al., 2018 and references therein). There are varying types of faulting that accommodate the CAFA-Caribbean plate relative motion (La Femina et al., 2002; Corti et al., 2005; Montero et al., 2013). The dextral shear in the Nicaraguan segment of the CAFA-CA boundary is accommodated by bookshelf faulting where rotating tectonic units approximate the motion of a transform fault (La Femina et al., 2002). Using geodetic data and numerical modeling, Chapter 3 investigates the co-seismic displacements for three upper plate, arc earthquakes. We then discuss these earthquakes in the context of the bookshelf faulting model.

1.4 The Across-Strike Geodetic Signature of the Central American Forearc-Caribbean Boundary in Nicaragua

Following the results of Chapter 3, the bookshelf faulting model was explored in an attempt to replicate the across-strike geodetic signal that is observed at the CAFA-CA boundary. The GPS velocity field in the Nicaraguan segment of the CAFA suggests that a locked throughgoing transform fault accommodates the CAFA-CA relative motion. However, this is not the kinematics of the faulting for the seismicity in the CAFA (Algermissen et al., 1974; La Femina et al., 2002; French et al., 2010). Faults that are arc-normal or arc-oblique of the bookshelf faulting model appear to be active. I explore the resulting surface displacements due to bookshelf faulting using the boundary element method. Modeling results presented in Chapter 4 indicate that bookshelf faulting can produce the observed GPS-derived horizontal velocity field.

1.5 The Dynamics of Trapdoor Faulting During the 2018 Sierra Negra Eruption

The June 26th, 2018 eruption of Sierra Negra volcano, Isabela Island in the Galapagos Islands, Ecuador, was accompanied by many earthquakes on the intra-caldera trapdoor fault system. Eight hours before the eruption, there was a Mw 5.4 earthquake (USGS) on the trapdoor fault that caused a maximum of ~2 m of vertical displacement of the caldera floor. The earthquake on the trapdoor fault triggered magma migration from 2 km depth via a dike and a sill and governed the fissure location (Bell et al. 2021). Following the eruption, there was a net 1.5 m vertical displacement recorded near the southern limb of the trapdoor fault, which indicates that the caldera grew through resurgence during this eruptive and intrusive episode (Bell et al. 2021). Understanding the faulting and kinematics of the trapdoor fault is beneficial in forecasting eruption and eruptive fissure location. In Chapter 5, I present the analysis of co-seismic displacements for three earthquakes on the trapdoor fault system and find that the magnitudes of coseismic strike-slip and dip-slip are responsible for developing some of the features of the Sierra Negra caldera.

1.6 References

Bell, Andrew F., Peter C. La Femina, Mario Ruiz, Falk Amelung, Marco Bagnardi, Christopher J. Bean, Benjamin Bernard, et al. 2021. "Caldera Resurgence during the 2018 Eruption of Sierra Negra Volcano, Galápagos Islands." *Nature Communications* 12 (1): 1–9. https://doi.org/10.1038/s41467-021-21596-4.

Corti, Giacomo, Eugenio Carminati, Francesco Mazzarini, and Marvyn Oziel Garcia. 2005. "Active Strike-Slip Faulting in El Salvador, Central America." *Geology* 33 (12): 989–92. https://doi.org/10.1130/G21992.1.

Ellis, A., C. DeMets, P. Briole, B. Cosenza, O. Flores, S.E. Graham, M. Guzmán-Speziale, et al. 2018. "GPS Constraints on Deformation in Northern Central America from 1999 to 2017, Part 1 – Time-Dependent Modelling of Large Regional Earthquakes and Their Post-Seismic Effects." *Geophysical Journal International* 214 (3): 2177–94. https://doi.org/10.1093/gji/ggy249.

Femina, P. C. La, T. H. Dixon, and W. Strauch. 2002. "Bookshelf Faulting in Nicaragua." *Geology* 30 (8): 751–54. https://doi.org/10.1130/0091-7613(2002)030<0751:BFIN>2.0.CO;2.

French, S. W., L. M. Warren, K. M. Fischer, G. A. Abers, W. Strauch, J. M. Protti, and V. Gonzalez. 2010. "Constraints on Upper Plate Deformation in the Nicaraguan Subduction Zone from Earthquake Relocation and Directivity Analysis." *Geochemistry, Geophysics, Geosystems* 11 (3): 1–17. https://doi.org/10.1029/2009GC002841.

Montero, P.W., J.C. Lewis, J.S. Marshall, S. Kruse, and P. Wetmore. 2013. "Neotectonic Faulting and Forearc Sliver Motion along the Atirro-Río Sucio Fault System, Costa Rica, Central America." *Bulletin of the Geological Society of America* 125 (5–6): 857–76. https://doi.org/10.1130/B30471.1.

Pacheco, Javier F, and Lynn R Sykes. 1992. "Seismic Moment Catalog of Large Shallow Earthquakes, 1900 to 1989." *Bulletin of the Seismological Society of America* 82 (3): 1306–49.

Pérez, O. J. 1998. "Seismological Report on the Mw = 6.8 Strong Shock of 9 July 1997 in Cariaco, Northeastern Venezuela." *Bulletin of the Seismological Society of America* 88 (3): 874–79.

Pérez, O. J., Steven G. Wesnousky, Roberto De La Rosa, Julio Márquez, Redescal Uzcátegui, Christian Quintero, Luis Liberal, Héctor Mora-Páez, and Walter Szeliga. 2018. "On the Interaction of the North Andes Plate with the Caribbean and South American Plates in Northwestern South America from GPS Geodesy and Seismic Data." *Geophysical Journal International* 214 (3): 1986–2001. https://doi.org/10.1093/GJI/GGY230.

Symithe, S., E. Calais, J. B. De Chabalier, R. Robertson, and M. Higgins. 2015. "Current Block Motions and Strain Accumulation on Active Faults in the Caribbean." *Journal of Geophysical Research B: Solid Earth* 120 (5): 3748–74. https://doi.org/10.1002/2014JB011779.

Weber, John, Halldor Geirsson, Peter La Femina, Richard Robertson, Chris Churches, Kenton Shaw, Joan Latchman, Machel Higgins, and Keith Miller. 2020. "Fault Creep and Strain Partitioning in Trinidad-Tobago: Geodetic Measurements, Models, and Origin of Creep." *Tectonics* 39 (1). https://doi.org/10.1029/2019TC005530.

Chapter 2
Strain Partitioning and Interseismic Fault Behavior Along the Caribbean-South American Transform Plate Boundary

2.1 Introduction

Continental transform plate boundaries can be complex deformation zones with multiple faults accommodating relative plate motion. The Pacific – North American plate boundary is a complex continental transform system dominated by the San Andreas fault, but with at least five major overlapping faults in the south, and three faults in the north (e.g., Lisowski et al., 1991). The North Anatolian fault system also displays along-strike complexities (Bohnhoff et al., 2006; Şengör et al., 2005). The faults that comprise continental transform fault systems can also have variable interseismic behavior, varying from completely locked to creeping at full relative plate motion rate.

Fault systems such as the San Andreas (Savage and Burford 1973; Titus, DeMets, and Tikoff 2006; Maurer and Johnson 2014), the North Anatolian (Bilham et al., 2016; Cetin et al., 2014), and the Haiyuan (Cavalié et al. 2008; Jolivet et al. 2012) each have segments that together display this full spectrum of interseismic behavior, with earthquakes occurring in not only the locked segments but also in the creeping segments or in transition zones between locked and creeping segments (Bakun et al., 2005; Gans et al., 2003; Wallace, 1970; WGCEP, 2003).

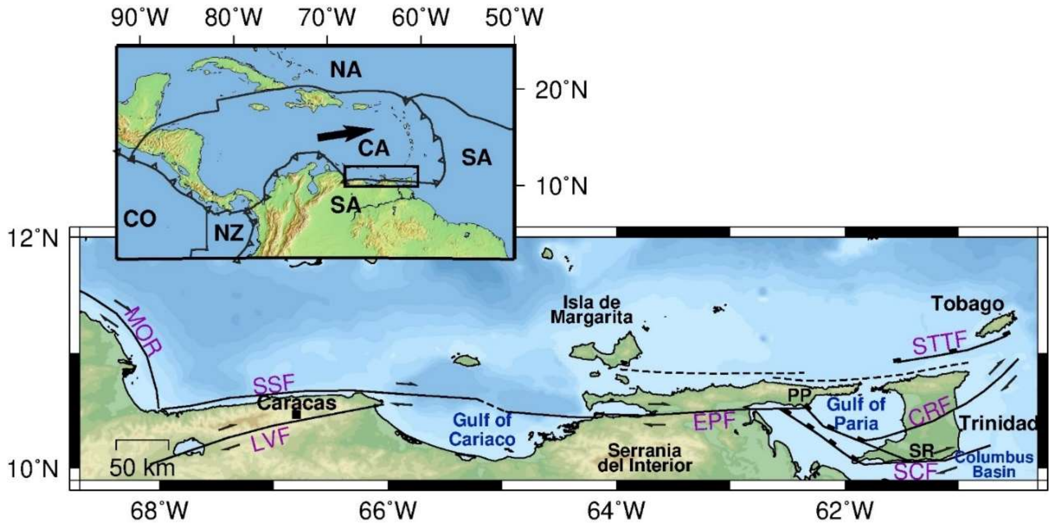

Figure **2-1**: Active faults of the southeastern Caribbean – South American transform plate boundary. MOR – Morrocoy Fault, SSF – San Sabastian Fault, LVF – La Victoria Fault (Pérez et al., 1997), EPF - El Pilar Fault, CRF - Central Range Fault Zone, SC – South Coast Fault, and STTF – Sub-Tobago Terrane Fault (Robertson and Burke 1989; Soto et al., 2007; Weber et al., 2020). Region names: SDI - Serrania del Interior, PP - Paria Peninsula, and SR - Southern Range. Bathymetry and topography are from ETOPO1 (Amante and Eakins, 2009). Inset shows tectonic setting around the Caribbean plate (CA – Caribbean plate, CO – Cocos plate, NZ – Nazca plate, NA – North American plate and, SA – South American plate) with black box identifying the region of study and black arrow showing the direction of CA motion relative to SA at the region of study.

The Caribbean (CA) – South American (SA) transform plate boundary zone demonstrates the characteristics of variable along-strike strain partitioning and the complete spectrum of interseismic fault behavior (Pérez et al., 1997, 2001, 2018; Reinoza et al, 2015; Weber et al., 2011, 2020). The dextral transform boundary is comprised of three main fault systems: 1) the San Sebastian (SSF) and La Victoria (LVF) faults (Schubert, 1981; Schubert & Krause, 1984); 2) the El Pilar fault (EPF) (Molnar & Sykes, 1969; Pérez et al., 2001; Russo & Speed, 1992; Russo et al., 1993; Speed, 1985); and 3) the Central Range (CRF), South Coast (SCF) and Sub-Tobago Terrane (STTF) faults (Figure **2-1**) (Weber et al., 2001, 2010, 2020). These fault systems accommodate the ~21 mm/yr of CA-SA relative motion (DeMets et al., 2010; Symithe et al., 2015), and display variable historical seismicity along strike (e.g., Audemard, 2007; Baumbach et al., 2004; Pérez et al., 1997). To determine its seismic potential, it is essential to resolve how strain is partitioned and how interseismic strain accumulates near faults along this boundary.

This project combines Global Positioning System (GPS) and Interferometric Synthetic Aperture Radar (InSAR) data, to evaluate for the first time, interseismic fault behavior (i.e., the magnitude and location of interseismic strain and locking depth) along the entire CA-SA transform plate boundary. This project comprehensively quantifies the modes of interseismic behavior, including elastic strain accumulation and partitioning along strike, compare this project's geodetic model results to the pattern and magnitude of historical seismic moment release, and attempt to correlate fault behavior to geology.

2.2 Active Faults and Geology of the CA-SA Transform Plate Boundary

The CA-SA transform plate boundary is composed of three faults systems with six faults that accommodate the ~21 mm/yr of relative CA-SA dextral shear (Figure **2-1**). In the following sections, a detailed description of these faults and their historical seismicity will be presented, results of previous geodetic studies, and describe how the geology changes along the plate boundary.

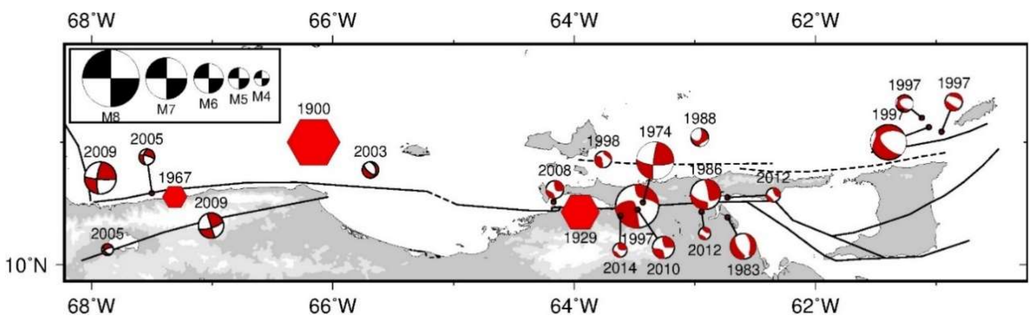

Figure **2-2**: Shallow seismicity (<30 km) with magnitude 3.5 or greater labeled with the year of occurrence above or below the symbol (see Tables 2-1 & 2-2). Focal mechanisms are from the GCMT (Dziewonski et al., 1981; Ekström et al., 2012) and ISC (Lentas, 2017; Lentas et al., 2019) catalogs with locations from the ISC published catalog (Storchak et al., 2015). Focal mechanism for 1974 (M6.1) earthquake from Russo and Speed (1994). Hexagons are earthquakes from the ISC catalog and the Centennial Earthquake Catalogue (Engdahl et al., 2013) except for the 1929 Cumana earthquake (Mocquet et al., 1996). Black lines are major faults of the region of study.

2.2.1 San Sebastian and La Victoria Faults

The E-W trending SSF and the WSW-ENE trending LVF accommodate ~90% of the CA-SA motion (i.e., ~19 mm/yr) in the western segment of the plate boundary in north-central Venezuela (Figure **2-1**) (Schubert 1981; Pérez et al., 2018). The SSF has a fairly simple 280 km long fault trace (Colón et al., 2015; Escalona et al., 2011; Schubert & Krause, 1984), and connects to the western EPF across the Gulf of Cariaco pull-apart basin (Schubert, 1985; Escalona et al., 2011). The LVF has a 230 km long trace and terminates in the Gulf of Cariaco (Schubert and Krause 1984).

The SSF and LVF have produced intermediate to large magnitude earthquakes (Table **2-1**). The SSF ruptured during the September 12th, 2009 M_w 6.1, the damaging 1967 M 6.5 Caracas (Pérez, 1998a; Suárez & Nábělek, 1990), and the 1900 M 7.6 to M 8.0 earthquakes, where the latter ruptured the eastern SSF segment (Figure **2-2**; Colón et al., 2015; Pacheco & Sykes, 1992). Microseismicity (M ≤ 4) has been detected on the SSF, with a greater number of events on its eastern segment than on its central and western segments (Pérez, Sanz, and Lagos 1997). The LVF has had several moderate magnitude earthquakes, including several earthquakes with magnitudes greater than M 6 (e.g., 1641 and 1878) (Pérez et al., 1997; Pérez, 1998b).

Table **2-1**: Strong earthquakes on the SSF and LVF compiled from the ISC Focal Mechanism catalogue (Lentas, 2017; Lentas et al., 2019) and the Centennial Earthquake Catalogue (Engdahl et al., 2013).

Earthquake	**Longitude**	**Latitude**	**M**
1900	-66.16	11.00	8.0
1967	-67.31	10.56	5.5
2003	-65.69	10.78	4.2
2005	-67.50	10.59	4.1
2005	-67.87	10.12	3.2
2009	-67.01	10.20	5.5
2009	-67.93	10.71	6.4

There has been only one geodetic study of the interseismic behavior of the SSF and LVF. Pérez et al. (2018) inverted episodic GPS-derived horizontal velocities and found that the SSF and LVF accommodate 17.0 ± 0.8 mm/yr and 2.1 ± 0.8 mm/yr, respectively, and are locked to a depth of 14 km.

2.2.2 El Pilar Fault

The E-W trending EPF accommodates ~85% of the CA-SA motion (i.e., ~18 mm/yr) in the central section of the plate boundary (Beltran et al., 2016; Jouanne et al., 2011; Pérez et al., 2001; Reinoza et al., 2015), and four along-strike segments have been mapped. From west to east these are: 1) a 100 km-long segment from the Gulf of Cariaco pull-apart to a restraining bend at the city of Cumana (Lidz et al., 1968; Escalona et al., 2011); 2) an 80 km long linear segment from Cumana to the Casanay restraining bend (Beltran et al., 1996); 3) a 45 km long linear segment from the Casanay restraining bend to the town of El Pilar (Beltran et al., 1996); and 4) the easternmost 65 km-long segment that terminates in the Gulf of Paria pull-apart basin (Beltran et al., 1996; Flinch et al., 1999; Speed, 1985). EPF segmentation was further highlighted by analysis of aftershocks from the 1997 Cariaco earthquake (Figure **2-2**). Baumbach et al. (2004) found six micro-segments, corresponding to previously described segments 2, 3, and 4, and surface ruptures were observed that correspond to segments 2 and 3 (Audemard, 2006).

Table **2-2**: Major earthquakes on the EPF compiled from the Global CMT catalogue (Ekström et al., 2012) with the exception of the 1929 (Mocquet et al. Singer 1996) and 1974 (Russo and Speed 1994) earthquakes.

Earthquake	Longitude	Latitude	M
1929	-63.95	10.43	6.7
1974	-63.47	10.61	6.1
1986	-62.93	10.60	6.2
1997	-63.49	10.53	6.9
2008	-64.17	10.51	5.2
2010	-63.48	10.45	5.6
2012	-62.94	10.43	4.2
2014	-63.62	10.40	4.6

The EPF is historically the most seismically active of all the faults in the plate boundary (Figure **2-2**; Table **2-2**). It has experienced multiple intermediate to large magnitude earthquakes in modern times, with the largest being the 1997 M_w 6.8 Cariaco (Mendoza 2000; Pérez 1998a) and the 1929 M 6.5 Cumana earthquakes (Figure **2-2**; Mocquet et al., 1996). The western segment of the EPF had an intermediate magnitude, possibly >M 6.5, earthquake in 1797 (Audemard 2007); however, there are no earthquakes recorded on this segment during instrumented times (Figure **2-2**). The eastern segment of the EPF has ~M 5 earthquakes regularly (i.e., approximately every 2 years), as well as larger magnitude earthquakes (ISC catalog; Storchak et al., 2015, 2017).

Damaging historical earthquakes (e.g., 1684) have also been associated with this segment (Audemard, 2007).

Given the record of frequent seismicity and the disparate geology across the fault (Jordan 1975; Schubert 1979), the EPF was one of the first transform faults identified and therefore much work has focused on this segment of the plate boundary. Previous geodetic studies characterized the interseismic slip rate and locking depth of the EPF. Pérez, et al. (2001) used local and regional episodic GPS data (1994, 1999, and 2000) to model an interseismic locking depth of 14 km for the entire EPF. Reinoza, et al. (2015) used a more expansive GPS network and inverted continuous and episodic GPS data (from observations taken in 2003, 2005, and 2013) along the EPF using a suite of modeling methods. First, the authors projected GPS velocity data from the entire 240 km length of the fault system and width of their geodetic network onto one fault-normal profile. They then inverted those data using the method of Savage and Burford (1973) and found a locking depth of 1.6 km. Second, the authors used a distributed-slip model (Wang et al., 2013) to determine the interseismic slip deficit and locking on discretized fault patches (patch sizes of 4 km^2) along the strike of the EPF. The results of this model indicated that there is an EPF fault patch west of Cumana with partial slip (10 mm/yr to 12 mm/yr relative to plate motion) and that all other segments creep at the plate motion rate. Finally, Beltran et al. (2016) used InSAR time-series analysis of 18 ALOS-1 synthetic aperture radar data to study aseismic creep on the eastern EPF between 2007 and 2011. These authors found that the rate of creep decreased from ~25 ± 9.5 mm/yr (i.e., 4 mm/yr faster than the relative plate rate) in the west (63.7°W) to ~13 ± 6.9 mm/yr in the east (63.3°W).

2.2.3 Sub-Tobago Terrane, Central Range, and South Coast Faults

CA-SA relative motion is partitioned between three faults at the longitude of Trinidad-Tobago. From north to south these are: the Sub-Tobago Terrane (STTF), Central Range (CRF), and South Coast (SCF) (Figure **2-1**; Weber et al., 2020). The STTF is seismically active and has ruptured during several moderate magnitude earthquakes, including the 1997 M_w 6.7 Tobago, which was a dextral oblique-slip earthquake (J. C. Weber et al. 2015). The CRF cuts through central Trinidad with a strike of ~070°, roughly aligned with CA-SA relative plate motion (Flinch et al., 1999; Weber et al., 2020 and references therein). The western onshore portion of the CRF is aseismically creeping and separates rocks with a thermogenic petroleum charge to its south, from those with only dry biogenic gas to the north (Weber et al., 2020 and references therein). Weber et al. (2020) suggested that overpressured hydrocarbons and weak fault gouge result in aseismic creep on the western CRF. Before this study, slip on the eastern segment of the CRF had not been previously quantified.

The E-W trending SCF spans the entire length of the south coast of Trinidad and separates the onshore Southern Range from the Columbus Basin, an active extensional province (Erlich & Barrett, 1990; Garciacaro et al., 2011; Pindell & Kennan, 2001). The seismic behavior on the SCF is not well known; no historical earthquakes have been associated with this fault. However, the fault is thought to be creeping at ~3 mm/yr based on analysis of geodetic data (Weber et al., 2020), and abundant evidence for overpressured fluids, including the presence of fault-aligned and deeply rooted mud volcanoes (Deville & Guerlais, 2009; Heppard et al., 1998; Henry et al., 2010; Higgins & Saunders, 1967).

Previous work using geodesy to investigate the earthquake hazard of the CRF and partitioning of plate boundary strain across Trinidad – Tobago has mainly been carried out by Weber, et al. (2001, 2010, 2011, 2020). This body of work demonstrates that the CRF accommodates ~70% of the CA-SA motion (13 to 14 mm/yr) and is creeping, while the STTF and SCF each accommodates ~3 mm/yr. Weber, et al. (2020) found this slip partitioning using a GPS network that formed a fault normal profile across the western CRF. The network lacked the spatial resolution to determine variation in locking along strike. We improve upon these studies here with expanded spatial resolution by combining GPS and InSAR data sets.

2.2.4 Geology of CA-SA Transform Boundary

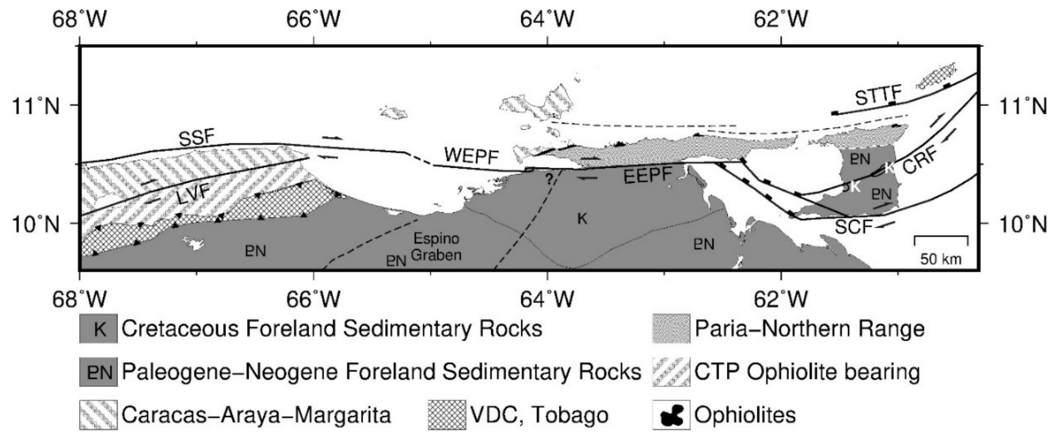

Figure **2-3**: Bedrock geological map showing principal tectonostratigraphic units in the CA-SA transform boundary (Modified from Avé Lallemant & Sisson, 2005; French & Schenk, 2004). Quaternary deposits are omitted. PN and K – foreland and passive margin sedimentary units of Paleogene-Neogene and Cretaceous age, respectively. Espino Graben – Jurassic subsurface structure. CTP – ophiolite-bearing rocks of Caucagua-El Tinaco and Paracotos belts. VDC – Villa de Cura Nappe. Fault names in large fonts are: SSF – San Sabastian Fault, LVF – La Victoria Fault, WEPF – western El Pilar Fault segment, EEPF – eastern El Pilar Fault segment, CRF - Central Range Fault Zone, SCF – South Coast Fault, and STTF – Sub-Tobago Terrane Fault.

The CA-SA boundary is geologically complex, owing to several phases of tectonic development. The current crustal geology is associated with rifting during the Cretaceous breakup of Pangea (Stockhert 1995), Paleogene oblique convergence between CA and SA (Speed 1985; Pindell and Barrett 1990), and Pliocene to present eastward translation of the CA plate (Boschman et al., 2014; Burke, 1988). The geology is divided into five principal tectonostratigraphic units (Figure **2-3**). The SSF and LVF together bound the Caracas-Araya-Margarita unit which is comprised of high-grade, blueschist-bearing metamorphic rocks that experienced Cretaceous metamorphism, likely in a subduction zone (Sisson et al., 2005; Sisson et al., 1997; Sorensen et al., 2005). The Caucauga-El Tinaco-Paracotos (CTP) unit, south of the LVF, is an ophiolite-bearing metamorphic complex with variable protolith and metamorphic ages and a wide variety of metamorphic rock types (Ostos & Sisson, 2005; Ysaccis, 1998). The Villa de Cura unit, located south of the CTP, is a thrust-bounded (klippe) accreted Cretaceous arc, part of Burke (1988) Great Arc of the Caribbean, the geology of which correlates with units in Tobago and the Leeward

Antilles (Ostos and Sisson 2005; Ysaccis 1998; Maresch 1974). Low-grade metasedimentary rocks (e.g. schist, marble, quartzite), that were metamorphosed and exhumed in the Cenozoic, crop out in the Paria Peninsula in northeastern Venezuela and Trinidad's Northern Range (Avé Lallemant, 1997; Cruz et al., 2007; Weber et al., 2001). South of the metamorphic units, the South American passive margin, and foreland sedimentary fill sequence consists of and exposes both Cretaceous (e.g., the Serrania del Interior and central Trinidad), and younger Paleogene-Neogene rocks (Figure **2-3**). The Espino Graben is a Jurassic-aged subsurface feature related to Pangea breakup that is known primarily from oil and gas drilling and exploration (Garcia-Abdeslem et al., 2013).

2.3 Data

To explore the interseismic behavior of the southern CA-SA transform plate boundary, this project uses both geodetic and earthquake data. The project unifies published GPS velocity vectors, newly analyzed continuous GPS (cGPS), and ALOS-2 Synthetic Aperture Radar (SAR) data to characterize interseismic strain accumulation along the entire ~900 km length of the plate boundary. To determine the seismic moment released along the plate boundary this project uses the reviewed International Seismological Centre (ISC) catalog (Storchak et al., 2015; 2017).

2.3.1 Global Positioning System Data

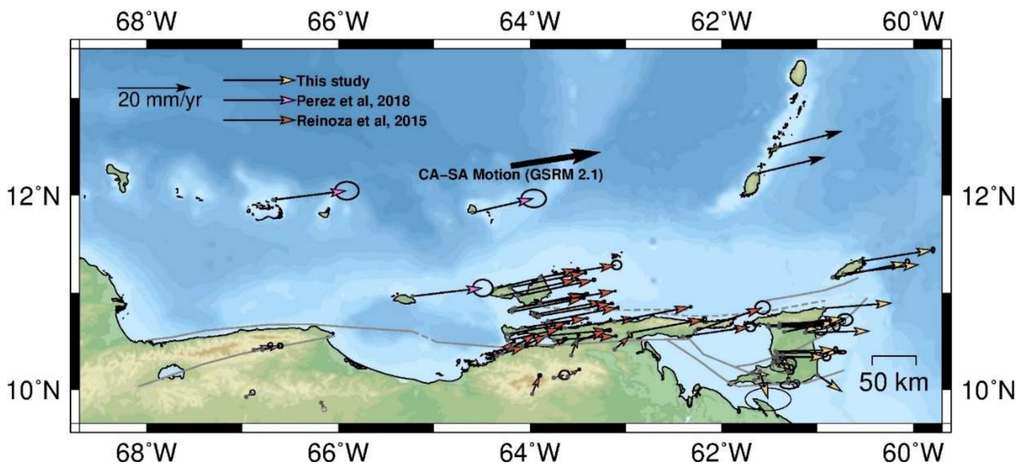

Figure **2-4**: GPS velocities in the ITRF2008 South America-fixed reference frame (Kreemer et al. 2014). Violet- and red-tipped velocity vectors are from Pérez et al, (2018) and Reinoza et al., (2015), respectively. Only seven of the eight GPS velocities from Pérez et al, (2018) are plotted, the eight are off the map. Yellow-tipped velocity vectors are updated GPS data from Weber et al., (2020). Black velocity vectors are GPS velocities from this study but not used in modeling. Large black vector shows the relative motion (~21 mm/yr) of CA with respect to SA (Kreemer et al., 2014). Major faults are shown as thin grey lines.

This study uses GPS velocities in the ITRF2008 reference frame to study: 1) SSF and LVF (8 GPS stations; Pérez et al., (2018), EPF (33 GPS stations; Reinoza et al., 2015), and STTF, CRF, and SCF (19 GPS stations; Weber et al., 2020) (Figure 2-4; Table A-1); and 2) new data from 11 cGPS stations, which extends time series, improving precision and accuracy, for stations presented in Weber, et al. (2020) (Figure 2-4; Tables A-1 & A-2). New cGPS data were processed using GIPSY-OASIS 6.3 software with satellite ephemerides from the Jet Propulsion Laboratory (JPL). Daily positions were estimated using the precise point positioning method (Zumberge et al., 1997). Phase ambiguity resolution was performed using the single receiver algorithm (Bertiger et al., 2010). Ocean loading corrections were applied using FES2004 (Lyard et al., 2006). Wet and dry tropospheric zenith delays were modeled with VMF1 mapping functions (Boehm et al., 2006). Final solutions were transformed into the IGb08 reference frame (Rebischung et al., 2012), a geodetic realization of the ITRF2008 reference frame (Altamimi et al., 2012). Analysis of the daily position time series, including the estimation of seasonal signals and GPS velocities and uncertainties, was performed using the HECTOR software (Bos et al., 2013). Analysis of the cGPS daily position time series, including the estimation of seasonal signals, velocities, and uncertainties, was performed using the HECTOR software (Bos et al., 2013).

The new horizontal GPS velocity field (60 stations; Table **A-1**; Figure **2-4**) was then transformed from ITRF2008 into a SA reference frame (Kreemer et al., 2014). The velocity field clearly shows a transition from SA to CA motion across the SSF, EPF, and CRF, with most vectors aligned with the azimuth of CA relative motion (Figure **2-4**). Velocities south of the LVF tend to SA motion (i.e., ~0.0 mm/yr). Residual velocities of up to 3 mm/yr, south of the EPF have no clear agreement in azimuth. This project uses this new horizontal velocity field to investigate the interseismic nature of the CA-SA plate boundary, including interseismic strain accumulation, creep, and locking depths on the main active faults in this region in Section 4.

2.3.2 Interferometric Synthetic Aperture Radar Data

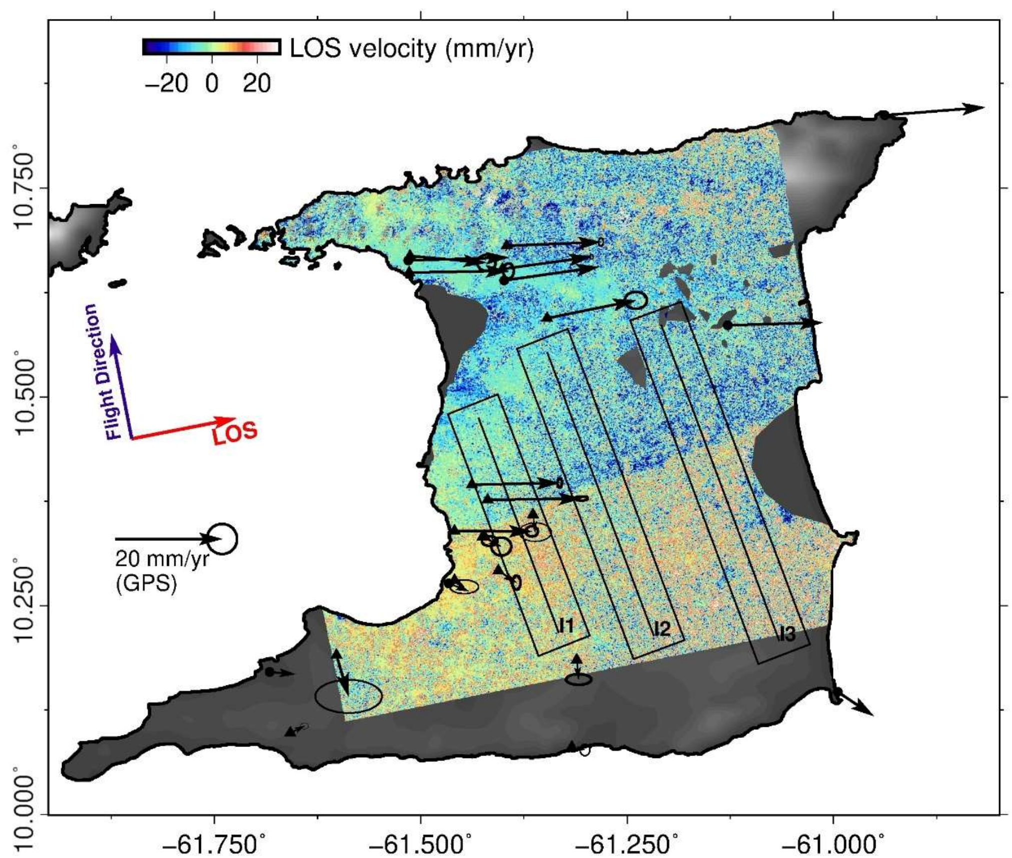

Figure **2-5**: ALOS-2 line-of-sight velocity field in mm/yr calculated using the small-baseline subset algorithm method. Horizontal GPS velocity vectors as in Figure 2-4, where circle icons are cGPS stations and triangle icons are episodic GPS stations.

This project uses Interferometric Synthetic Aperture Radar (InSAR) to investigate tectonic displacement on the island of Trinidad, by utilizing Synthetic Aperture Radar (SAR) scenes from the PALSAR-2 sensor (wavelength of 23 cm) onboard the ALOS-2 satellite. L-Band SAR (wavelength of 15 to 30 cm) has the ability to penetrate the tropical broadleaf vegetation found in this region (Wei and Sandwell 2010). The SAR scenes from the L-band ALOS-1, the predecessor of the ALOS-2 mission, were not used because of large perpendicular baselines (>300 m) between scenes and the resulting poor coherence interferograms for this region. Nine ALOS-2 SAR scenes (path 36, frame 200) were used, with acquisition dates from 2015-02-04 to 2019-03-27 (4.14 years).

ALOS-2 SAR scenes were processed and co-registered to a primary scene using the GMTSAR software package (Sandwell et al. 2016). Nineteen interferometric pairs with perpendicular baselines less than 300 m and temporal baselines less than 600 days were created. The 19 interferometric pairs were unwrapped by first masking out water bodies and low coherence pixels and interpolating the remaining phases with the nearest-neighbor approach, and using the minimum spanning tree algorithm implemented in the SNAPHU software (Chen and Zebker, 2000, 2002). Interferograms with orbital error trends were detrended by identifying the planar trend by least-squares fitting and removing the resulting trend. The coherence-based small-baseline subset algorithm (SBAS) was then used in calculating the time series of the scenes and the velocities of pixels in the scenes (Berardino et al., 2002; Schmidt & Bürgmann, 2003; Tong & Schmidt, 2016; Xu et al., 2017). SBAS derived velocities were further detrended to remove long-wavelength planar trends (see Figure **2-5**). There is a long-wavelength trend in the final SBAS-calculated velocities with across-strike velocity increasing eastwards (Figure S-6). This is correlated with an increase in topographic elevation (0 – 300 m) eastward across Trinidad that may be caused by atmospheric turbulence, which introduces atmospheric errors (e.g., Webley et al., 2004), and is present in most of the interferograms (See Section A.2 in Appendix A).

The resulting LOS velocities corroborate well with the GPS velocities (Figures **2-6**)

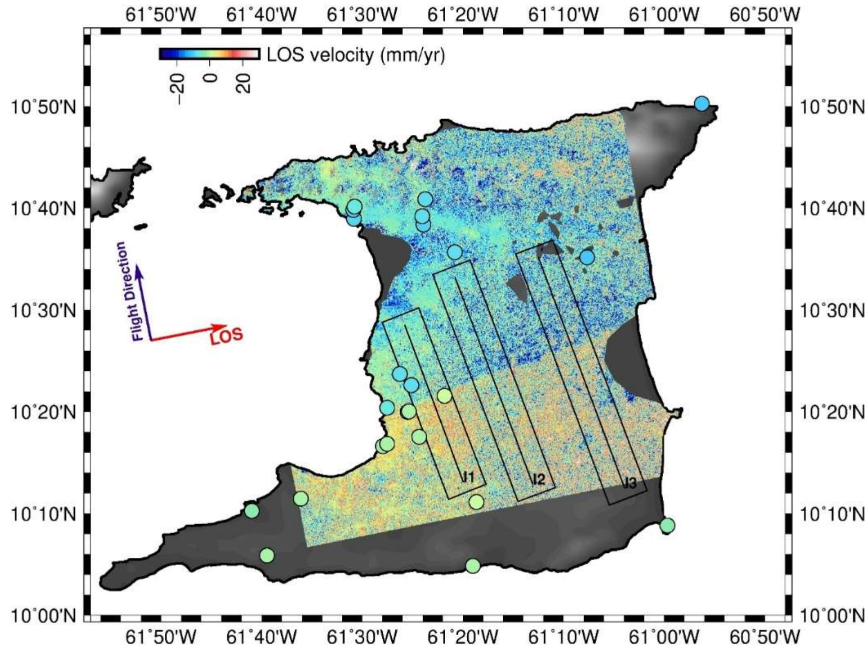

Figure **2-6**: SBAS calculated displacements with all planar trends removed and GPS velocities (circles), which were projected into LOS.

2.3.3 Earthquake Data

The epicenter location and magnitude data from the International Seismological Centre (ISC) reviewed catalog (Storchak et al., 2015, 2017) was used to determine the seismic moment released on the plate boundary. The catalog incorporates data from local seismic observatories (i.e., Fundación Venezolana de Investigaciones Sismológicas and the University of the West Indies, Seismic Research Centre), as well as that from global seismic networks. Therefore this catalog is more complete at a regional scale for low- to moderate-magnitude earthquakes than other global catalogs (Willemann and Storchak 2001). The catalog includes 1,881 earthquakes from 1927 to 2017 with hypocenter depths of 20 km or less, in the region from latitude 8.5°N to 12°N and longitude 60.0°W to 68.0°W.

2.4 Modeling Methods

This project used the elastic dislocation model of Savage & Burford, (1973) to investigate interseismic fault behavior (locked and accumulating strain versus creeping), locking depth, and strain partitioning along the entire ~900 km CA-SA transform plate boundary for the very first time. The GPS and InSAR (CRF only) derived fault-parallel velocities were modeled for each of the three fault systems: (1) SSF and LVF; (2) EPF; and (3) STTF, CRF, and SCF, by projecting horizontal velocities onto the strike of one fault in each fault system. For the SSF and LVF and the STTF, CRF, and SCF fault systems, the modeling strategy treats these faults as subparallel, even though their strikes differ by a maximum of 11°. The difference in strikes is equivalent to no greater than a 6% change in projected velocities, which is within the uncertainty (~1.5 mm/yr) of the observed GPS velocities. To estimate parameter uncertainties and to avoid local minima, a Monte Carlo (MC) inversion scheme was implemented. The MC method perturbed the datasets by randomly sampling within the $\pm 1\sigma$ error of the original velocities. Uncertainties were 1σ of the resulting probability density function after inversion. Goodness of fit of a model to the data was calculated using the reduced chi-square. The modeling treatment of each fault system is described in the following sections.

2.4.1 San Sebastian and La Victoria Faults

For modeling the interseismic slip deficits and locking depths of the SSF and LVF, it was assumed the faults were parallel and used SSF fault-parallel velocities. The across-strike distance of the SSF and LVF assumed to be 0 km and -47 km, respectively, following Pérez, et al. (2018). To test the effect of low velocity uncertainties for stations south of the SSF (Figure **2-4**), a hybrid bootstrap method was incorporated, randomly selecting and removing one station before inversion. A full bootstrapping method could not be employed given the small number (8) of data points.

2.4.2 El Pilar Fault

To investigate along-strike changes in interseismic slip deficit and locking depth on the previously described segments of the EPF, the velocity profiles that were normal to the fault were modeled. First, evenly spaced velocity profiles (profiles 1 through 7; Figure **2-7**) along the length of the fault zone were modeled, which guided the choice to model three profiles (i.e., profiles A, B, and C; Figure **2-8**) selected to capture the separate segments of the EPF and its important transition from locking to creeping.

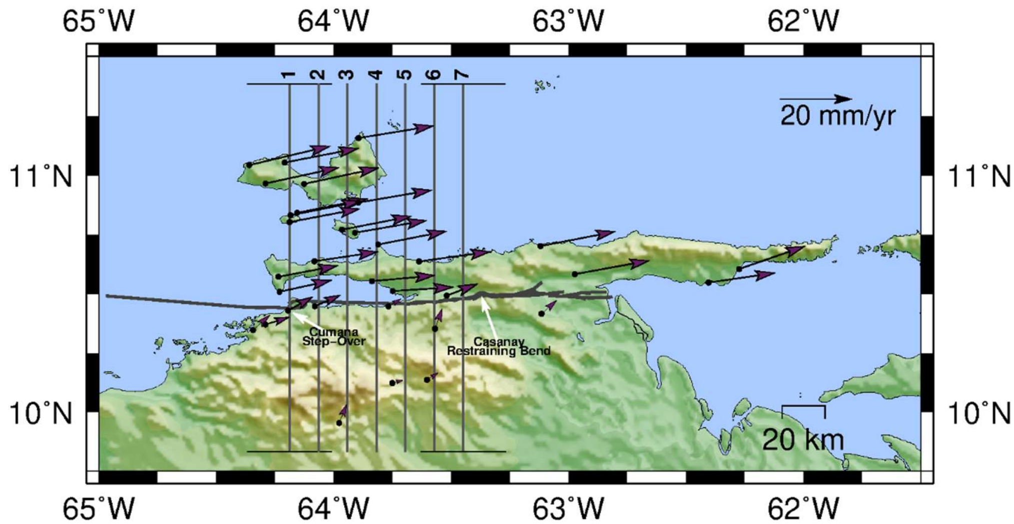

Figure **2-7**: Location of GPS velocity profiles number 1 through 7. Horizontal bars on profiles 1 and 7 show the 20 km horizontal extent for which GPS station velocities were incorporated into each profile's modeling.

Seven evenly spaced velocity profiles along-strike (profiles 1 – 7; Figure **2-7**) were modeled to determine if there is any transition in locking depth or slip and to reveal the segments of the fault that may be locked (locking depth >2 km) or creeping segments (locking depth <2 km). The profiles were equally spaced at 14 km from longitude 63.55°W to 64.28°W. Each profile captured GPS station velocities in the extent 20 km parallel to the fault strike (i.e., 10 km on either side of the profile). This ensured that profiles overlapped. A bootstrapping strategy was also used to ensure some velocities would not bias the results.

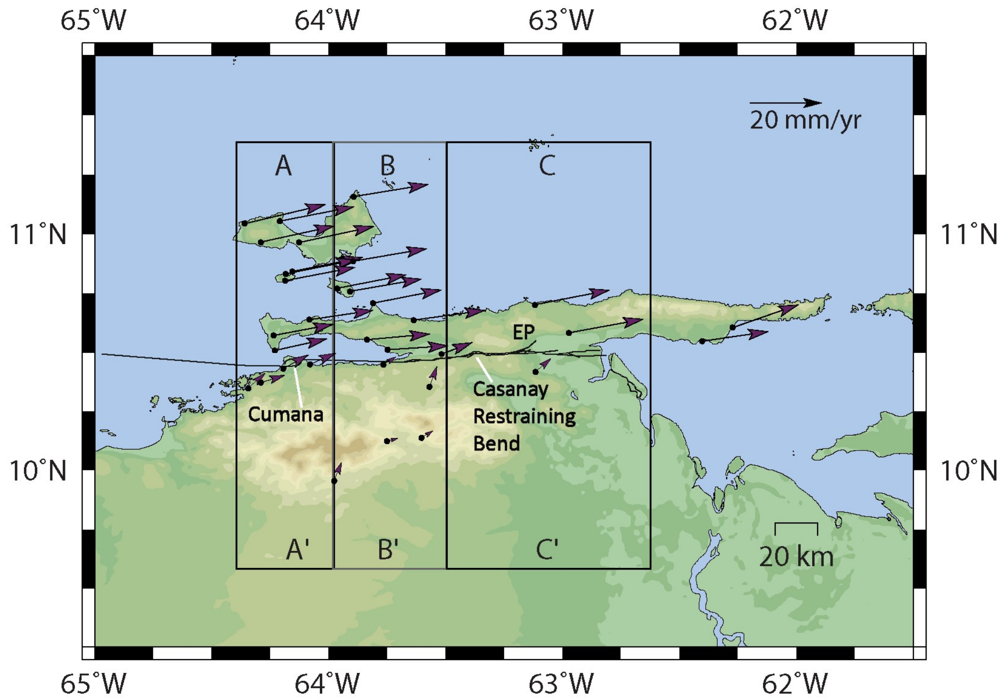

Figure **2-8**: GPS velocity profile locations A, B, and C for the EPF. EP – the town of El Pilar, which corresponds to the easternmost extent of EPF segment 4.

From the results of the seven velocity profiles, profiles A, B, and C were created and model (Figure **2-8**). Profile A captures the western 55 km of the EPF (previously described segment 1), which has a significant locking depth. Profile B (eastern 50 km of segment 2 described in Section 2.2.2) constitutes a transitional segment, which hosts moderate magnitude earthquakes (Figure **2-2**), and has a shallower locking depth compared to profile A. Profile C captures the 45 km long creeping segment (segment 3) of the EPF.

2.4.3 STTF, CRF, and SCF

Interseismic behavior was next modeled for the major faults accommodating CA-SA relative plate motion in the vicinity of Trinidad and Tobago; the STTF, CRF, and SCF. The analysis was carried out using both GPS velocities and velocities from InSAR time series analysis. First, GPS-derived horizontal velocities were inverted for interseismic slip deficit and locking depth on the three known faults, with velocities projected parallel to the strike of the CRF (Figure **2-5**). The inter-fault spacing values of Weber et al. (2020) were used for the STTF (50 km), CRF (0 km), and SCF (-40 km). Due to the lack of nearfield GPS data for the STTF and lack of GPS data south of the SCF, for slip rates for both the STTF and SCF, a variety of models with fixed locking depths (i.e., 2 km, 5 km, 10 km, and 15 km) was also inverted.

Secondly, the InSAR line-of-sight (LOS) velocities over an area that covers most of Trinidad and the entire onshore trace of the CRF was modeled. Three velocity profiles normal to the CRF (i.e., I1, I2, and I3) (Figure **2-5**), extracted from the SBAS-derived velocity field, were modeled. InSAR LOS velocities were inverted with the MC scheme, where random sampling was done within ± 5 mm/yr of the LOS velocities. Modeled LOS velocities were then projected to fault-parallel horizontal velocities. The look vector of ALOS-2 is [north = -0.5035, east = -0.0998, vertical = 0.8582] and, assuming the relative motion across the CRF has no vertical component, the horizontal velocity was recovered using the following equation,

$$|\boldsymbol{CRF}| = \frac{|\boldsymbol{LS}|}{\widehat{\boldsymbol{LS}} \cdot \widehat{\boldsymbol{CRF}}} \quad \text{2-1}$$

where $\boldsymbol{LS}$ is the look vector and $\boldsymbol{CRF}$ is the vector of the strike of the CRF.

2.4.4 Geodetic & Seismic Moment Analyses

One of the principal aims of this study was to compare variations in historic seismic moment release and current interseismic strain accumulation along the plate boundary. To do this, for each segment of the plate boundary the geometric moment deficit from our modeled slip rates and locking depths was estimated using the following relationship:

$$\boldsymbol{M} = \boldsymbol{G\Delta wDL} \quad \text{2-2}$$

where G is the crustal shear modulus, which was assumed to be 30 GPa (e.g., Smith-Konter et al., 2011), Δw (m) is the magnitude of the slip deficit for a given period of time, L (m) is the fault length, and D (m) is the inversion-derived locking depth.

To determine the seismic moment released along the plate boundary, location-magnitude data from the ISC catalog was used (Storchak et al., 2015, 2017). The catalog was found to be complete from 1970 to 2017 for earthquake magnitudes 3.5 to 7 and for shallow (<20 km) depths. The catalog was first declustered (Reasenberg 1985) to remove the numerous triggered earthquakes and aftershocks (45% of complete catalog) that are associated with deep intra-slab or STEP-related earthquakes (i.e., Paria Cluster earthquakes; see Govers & Wortel, 2005; Russo & Speed, 1992), whose low-accuracy hypolocation depths were approximately 20 ± ~5 km. Reported non-moment magnitudes (e.g., M_l or mb) were then converted to moment magnitude (M_w) following Gutenberg & Richter (1956), Katsuyuki (1981), and Scordilis (2006). Finally, using the revised magnitude-uniform catalog, and following Kanamori, (1977), the total seismic moment released between 1970 and 2017 was calculated for the main fault segments of the plate boundary.

2.5 Results

The model results span the entire ~900 km long CA-SA transform plate boundary for the first time, highlighting the variable nature and complexity of strain accumulation and partitioning along the full length of this transform boundary. The results for each fault system are summarized below and in Table **2-3**.

Table **2-3**: Model results.

	This Project		Other Studies	
	D (km)	V_{FF} (mm/yr)	D (km)	V_{FF} (mm/yr)
SSF	7.7 ± 5.1	16.4 ± 1.6	14 ± 3*	17.0 ± 0.5*
LVF	16.2 ± 4.0	4.3 ± 1.0	14 ± 3*	2.6 ± 0.4*
EPF			1.6†	20†
Profile A	6.7 ± 2.2	18.6 ± 1.8		
Profile B	1.0 ± 0.6	17.6 ± 1.0		
Profile C	1.0 ± 2.0	15.8 ± 3.6		
SCF	0.0 ± 0.1	3.1 ± 0.1		
CRF-GPS	0.6 ± 0.1	14.8 ± 0.1	0.2 ± 0.2 ††	13.4 ± 0.3 ††
STTF	8.0 ± 0.2	3.0 ± 0.1		
CRF-InSAR				
Profile I1	0.1 ± 0.2	14.5 ± 2.0		
Profile I2	0.2 ± 0.3	15.1 ± 2.0		
Profile I3	0.9 ± 1.5	19.2 ± 2.7		

*Pérez et al. (2018), †Reinoza et al. (2015), ††Weber et al. (2020)

2.5.1 San Sebastian and La Victoria Faults

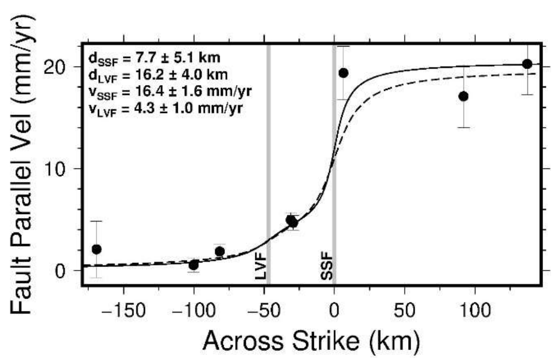

Figure **2-9**: GPS-derived fault parallel, horizontal velocity profile for the LVF and SSF faults. This study's elastic dislocation model with locking depths of 16.2 ± 4.0 km and 7.7 ± 5.1 km for the LVF and SSF, respectively, and slip distributed on the LVF and SSF at 4.3 ± 1.0 mm/yr and 16.4 ± 1.6 mm/yr, respectively (black line). Dashed line: elastic dislocation model of Pérez et al. (2018) with locking depths on both faults at 14 km, and slip on the LVF and SSF are 2.6 mm/yr and 17 mm/yr, respectively. d – locking depth. v – relative motion across fault.

Inversion of the GPS velocities from Pérez et al. (2018) yielded slip deficits of 16.4 ± 1.6 mm/yr and 4.3 ± 1.0 mm/yr and locking depths of 7.7 ± 5.2 km and 16.2 ± 4.0 km, for the SSF and

LVF, respectively (Figure **2-9**; Table **2-3**). The estimated locking depths have large uncertainties (≥4 km) and log-normal distributions (Figure **A-8**).

2.5.2 El Pilar Fault

Results for the seven evenly spaced profiles (profiles 1 – 7; Figure **2-10** & Table **2-4**) show that the western segment of the EPF (east of 64° W) is locked from the surface to depths of 6 km to 5.5 km, and there is a sharp transition creep at 64° W. Profiles A, B, and C (Figure **2-11** and Table **2-3**) demonstrate a clear transition from locking and elastic strain accumulation to creep along-strike on the El Pilar fault. This provides a significant improvement and refinement as previous studies averaged motion on the five disparate segments into one single "average" profile (e.g., Reinoza et al., 2015). Profile A has a slip deficit of 18.6 ± 1.8 mm/yr and a locking depth of 6.7 ± 2.2 km. Traversing eastward, at longitude ~64° W, the locking depth decreases sharply to 1 km in Profile B where this segment creeps at a rate of 17.6 ± 1.0 mm/yr. An equivalent slip rate of 15.8 ± 3.6 mm/yr and a locking depth of 1.0 ± 2.0 km was obtained for profile C, which indicates that the entire 200 km long eastern segment (segments 2, 3, & 4 and east of 64° W) of the EPF was creeping during the observation period.

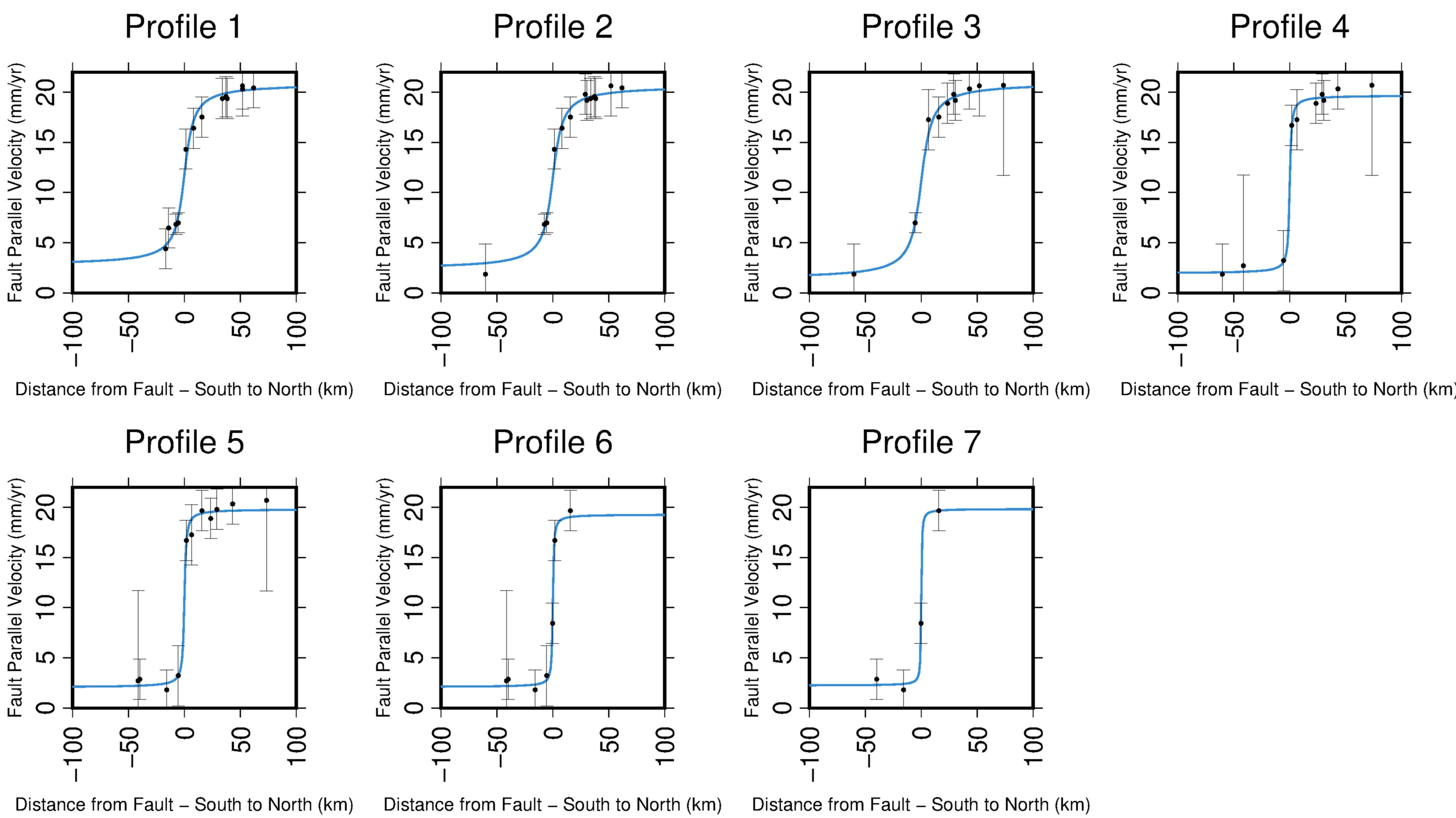

Figure **2-10**: Results from evenly spaced profiles, 1 through 7, along EPZ. See Figure 2-8 for locations.

Table **2-4**: Results for profiles 1 through 7.

	V_{FF} (mm/yr)	D (km)	χ^2
Profile 1	18.10	6.07	3.13
Profile 2	18.54	6.58	1.63
Profile 3	19.32	6.15	1.92
Profile 4	17.74	1.14	0.54
Profile 5	16.90	0.70	0.61
Profile 6	17.28	0.70	0.41
Profile 7	17.62	0.47	0.17

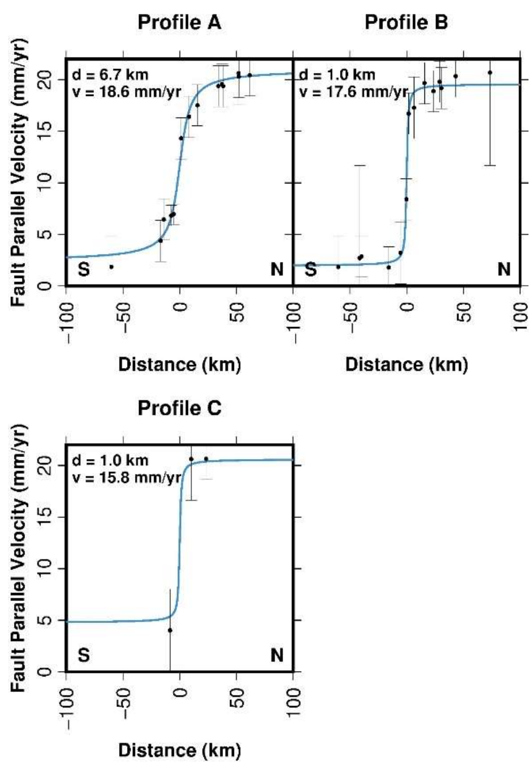

Figure **2-11**: GPS fault velocity profiles and best-fit elastic dislocation models for EPF profiles A, B, and C (see Figure 2-9 for locations). Best-fit model parameters for locking depth (d) and slip deficit (v) are given on each plot.

2.5.3 STTF, CRF and SCF

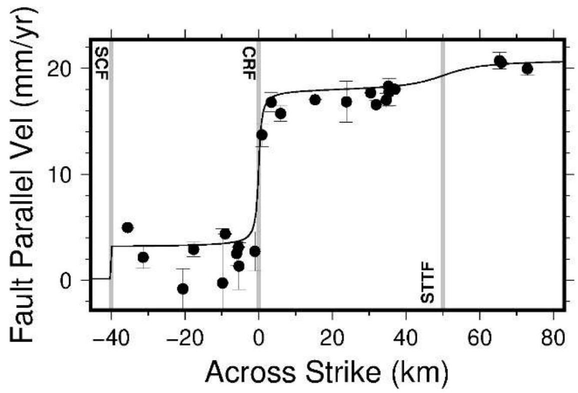

Figure **2-12**: GPS-derived fault-parallel horizontal velocity profile across the SCF, CRF, and STTF, Trinidad-Tobago. Black line is the best fit elastic dislocation model with locking depths on the SCF, CRFZ, and STTF of 0.0 ± 0.1 km, 0.6 ± 0.1 km, and 8.0 ± 0.2 km, respectively. Best fit model slip rates for the SCF, CRF, and STFF are 3.1 ± 0.1 mm/yr, 14.8 ± 0.1 mm/yr, and 3.0 ± 0.1 mm/yr.

Results from inversion of GPS data for the western CRF and the remaining onshore segment of the CRF using InSAR-derived velocities demonstrate for the first time that the entire onshore CRF in Trinidad is creeping over the examined observation period (Figures **2-12** & **2-13**). Inversion of the GPS dataset for the STTF, CRF, and SCF demonstrates that the CRF accommodates ~14.5 mm/yr or ~70% of relative plate motion (Table **2-4**; Figure **2-12**). The best-fit model (i.e., lowest reduced chi-square; Table **2-4**), where the locking depths for all faults were estimated, produced a shallow CRF locking depth (0.5 km), and slip deficit rates for the STTF and SCF of 3.0 ± 0.1 mm/yr each. Of note, the best-fit model produced a locking depth of 8.0 ± 0.2 km for the STTF and 0.0 ± 0.1 km for the SCF. All other models, with locking depths of the STTF and SCF held fixed from 2 km to 15 km, produced $\overline{\chi^2}$ values that were an order of magnitude larger than that of the best-fit model, which is, therefore, the preferred solution. While there is no geodetic data south of the SCF the model estimated slip rate and locking depth on this fault is most likely correct. The modeling assumption requires the geodetic signature to be symmetric across the fault and that the fault-parallel velocity tends to zero south of the SCF because of the fixed stable South America reference frame. A maximum locking depth of 3 km is required to fit velocities within 10 km of the SCF.

Table **2-4**: CRF, STTF, and SCF simple elastic dislocation inversion results.

Solving Locking Depths on all Faults			
	Slip (mm/yr)	**Locking Depth (km)**	$\overline{\chi^2}$
SCF	3.1 ± 0.1	0.0 ± 0.1	0.9299
CRF	14.8 ± 0.1	0.6 ± 0.1	
STTF	3.0 ± 0.1	8.0 ± 0.2	
Fixed Locking Depth for SCF and STTF Fault (2 km)			
SCF	4.0 ± 0.1	2	14.2715
CRF	13.8 ± 0.1	0.0 ± 0.0	
STTF	2.9 ± 0.1	2	
Fixed Locking Depth for SCF and STTF Fault (5 km)			
SCF	4.2 ± 0.1	5	14.6923
CRF	13.5 ± 0.1	0.0 ± 0.1	
STTF	3.6 ± 0.1	5	
Fixed Locking Depth for SCF and STTF Fault (10 km)			
SCF	4.2 ± 0.1	10	14.4155
CRF	13.3 ± 0.1	0.0 ± 0.1	
STTF	3.9 ± 0.1	10	
Fixed Locking Depth for SCF and STTF Fault (15 km)			
SCF	4.2 ± 0.1	15	14.3197
CRF	13.0 ± 0.1	0.0 ± 0.1	
STTF	4.6 ± 0.1	15	

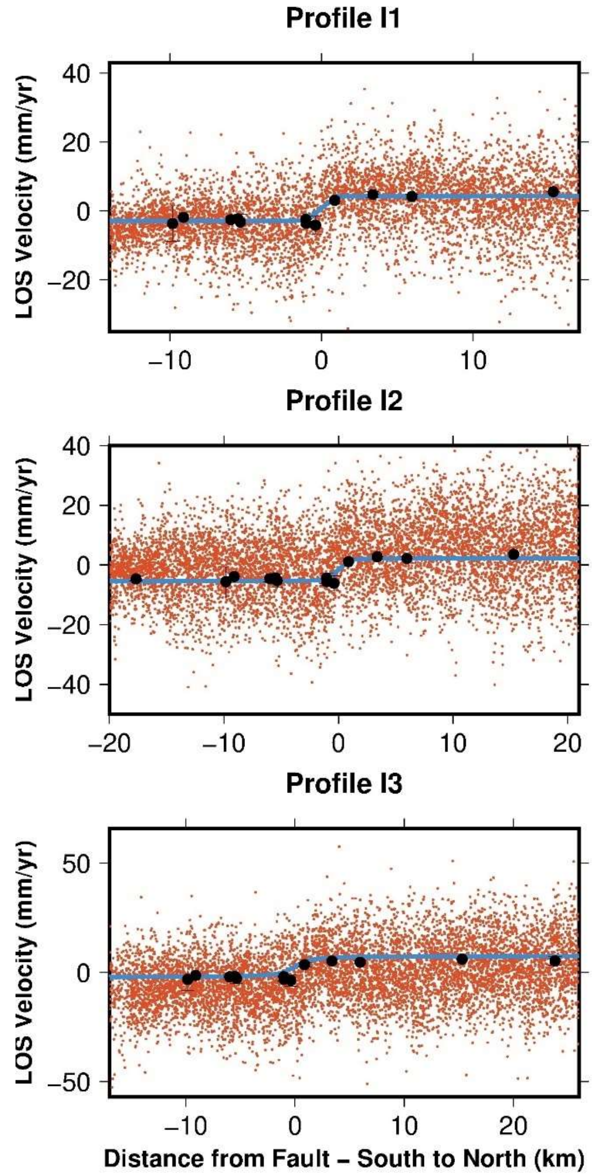

Figure **2-13**: InSAR LOS velocities across the CRF and model fit (blue line) for Profiles I1 (top), I2, (middle), and I3 (bottom). Profile locations are shown in Figure 2-5. Black circles are Trinidad GPS velocities projected into LOS for comparison.

The InSAR velocity field confirms and expands on the results of Weber et al., (2020), which showed that no additional faults in Trinidad are currently active nor accumulating strain. Inversion results from the InSAR data also confirm that the CRF is creeping: all profiles (I1, I2, and I3) produced extremely shallow locking depths of less than 1 ± ~0.8 km (Table **2-3**; Figure **2-13**). InSAR profile I1 (Figure **2-13**) produced a creeping rate of 14.5 ± 2.0 mm/yr, in agreement with the GPS model results.

Model results for profiles I2 and I3 yielded creeping rates of 15.1 ± 2.0 mm/yr and 19.2 ± 2.7 mm/yr, respectively, which are equivalent to profile I1 within uncertainty.

2.5.4 Geodetic & Seismic Moment Analyses

Analysis of the geodetically derived moment deficit and the total seismic moment released from 1970 to 2017 shows that a key along-strike transition is present in the plate boundary (Figure **2-14**). The transition for both the geodetic moment deficit and the total seismic moment is located at ~64°W longitude. West of this longitude, the total seismic moment is roughly an order of magnitude lower than that in the eastern segments, whereas the geodetic moment deficit is an order of magnitude larger than that of the eastern segments. The STTF is the single exception, where the seismic moment and moment deficit are equivalent (Figure **2-14**).

2.6 Discussion

Continental transform plate boundaries are complex zones of deformation that typically exhibit significant along-strike variations in interseismic fault behavior and strain partitioning (Harris, 2017, and references therein). These are parameters that in turn correlate with seismogenesis. Prior to this study, no unified study of the entire ~900 km long CA-SA transform plate boundary existed. This project found that systematic and significant transitions in interseismic fault behavior (i.e., locked to creeping), strain partitioning, and moment release exist along the CA-SA transform plate boundary (Figure **2-14**).

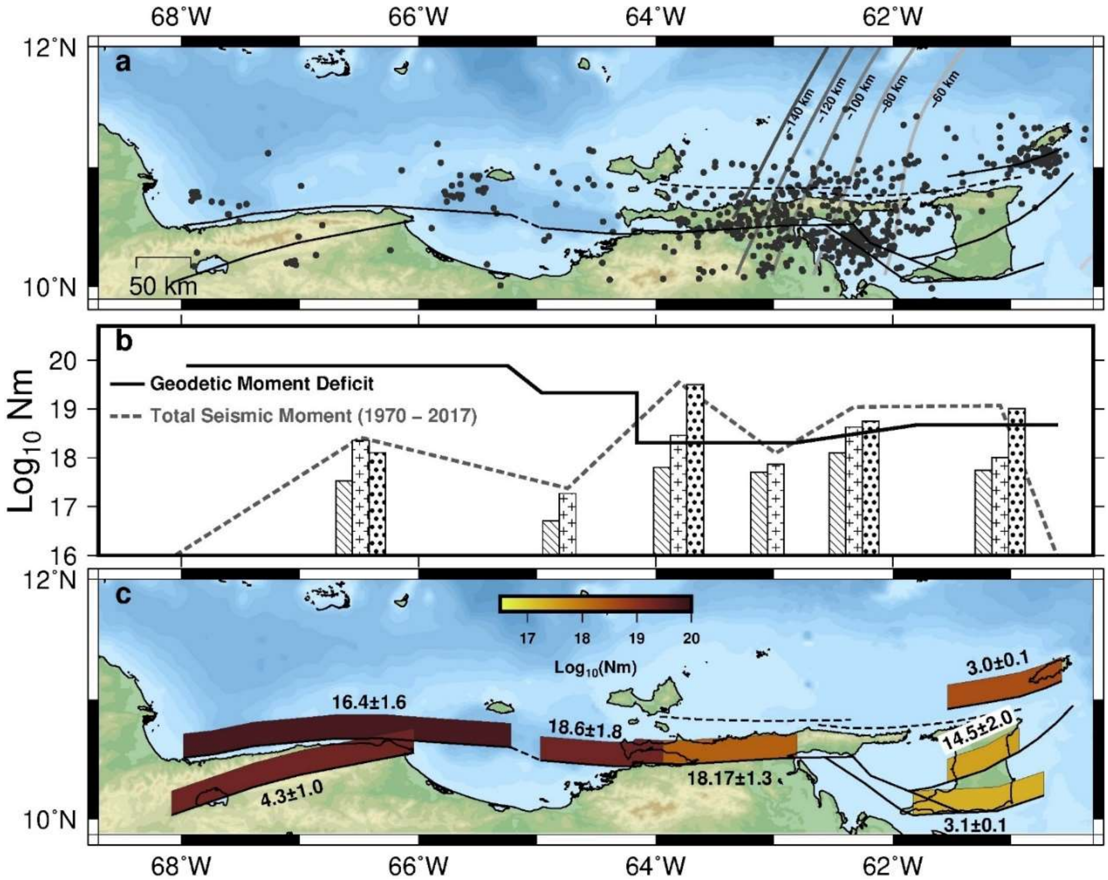

Figure **2-14**: a) Shallow earthquakes (<20 km) and magnitudes greater than M4 from the ISC catalog (1970 – 2017). Grey-scale lines show the depth of the subducted SA slab (Hayes et al., 2018). b) Total seismic moment released (dashed line) along the plate boundary from 1970 - 2017, including total moment contributions for magnitude bins M4 to M5 (diagonal striped bar), M5 to M6 (cross hatched bar), and M6 to M7 (circle hatched bar). Estimated accumulated geodetic moment deficit (solid black line) from inversion-derived locking depths and slip deficits for each segment for the same period (1970 – 2017, 47 years), which was calculated, per segment, with a shear modulus of 30 GPa, the inversion derived slip deficit, the period of the complete ISC catalog (47 years), and fault area from the segment's length and inversion derived locking depths. For creeping segments, a nominal value of 500 m was used as the locking depth. c) The calculated accumulated geodetic moment deficit along the plate boundary, except for the STTF (20 years, 1997 to 2017) taking into account the Mw 6.7 1997 Tobago earthquake. Estimated slip deficits and creeping rates (mm/yr) for each fault are provided.

2.6.1 Interseismic Strain Accumulation & Partitioning

The faults in the western segment (west of 64°W) of this plate boundary are locked, whereas those in the east (east of 64°W), with one exception (i.e., the STTF), are creeping. In the west, the inversion results show that both the SSF and LVF are locked to seismogenic depths (i.e., ~7 km and

~16 km depth, respectively) (Figure **2-10**; Table **2-3**). The results also indicate that the ~21 mm/yr of CA-SA relative plate motion (Kreemer et al., 2014) is partitioned across these two faults, with the SSF accommodating ~16 mm/yr and the LVF ~4 mm/yr.

Seismic segmentation of the EPF has previously been recognized based on; for example, aftershock locations and observed surface ruptures from the 1997 M_w 6.8 Cariaco earthquake (Baumbach et al. 2004; Audemard 2007). The modeling results confirm that the EPF is indeed segmented, with its western and eastern segments exhibiting significantly different interseismic behaviors. The western EPF (i.e., EPF segment 1; profile A in Figure **2-8**) has a locking depth of 6.7 ± 2.2 km (Figures **2-11**), similar to that of the SSF, and a slip deficit of 18.6 ± 1.8 mm/yr. The EPF transitions to shallower locking at segment 2 (i.e., profile B in Figure **2-8**), which continues along the entire eastern segment (i.e., segments 3 and 4; profile C in Figure **2-8**). The locking depth along these segments (2, 3, & 4) is shallow at ~1 km (Figure **2-11**; Table **2-3**) and accommodates 17.6 ± 1.0 mm/yr. Because of the shallow locking depth result, it is most likely that the entire eastern segment of the EPF to be creeping at close to the full relative plate rate from ~64° W longitude to the Gulf of Paria pull-apart basin. As noted in section 2.3.1, there is ~3 mm/yr residual shear deficit between the model results and the CA-SA relative plate motion rate along the EPF. This residual deficit might be accommodated by shear within the Serrania del Interior, south of the EPF. However, there is insufficient data to place this shear deformation onto any individual structures.

In the easternmost section of the plate boundary (i.e., islands of Trinidad and Tobago) the results indicate variable interseismic behavior and partitioning between three active faults. The STTF is locked to a depth of 8.0 ± 0.2 km and the CRF and SCF are both creeping (i.e., interseismic locking at <1 km depth). These results are consistent with those of Weber et al. (2020). The InSAR analysis, however, provides two important new findings: 1) the CRF has a visually identifiable consistent strike of ~70° (i.e., aligned parallel with CA-SA plate motion) across all of Trinidad (Figure **2-5**), and 2) the

CRF is creeping along its entire onshore length. The former is an important result, as the eastern CRF trace has proven difficult to map (see e.g., Crosby et al., 2009). The latter result is important as paleoseismic studies have shown that the western segment of the CRF ruptured between 2710 yr BP and 550 yr BP (Prentice et al., 2010), suggesting the possibility of both temporally and/or spatially variable interseismic strain accumulation. This project's results indicate that interseismic strain is partitioned across these three main faults, with 3.1 mm/yr on the STTF, ~14.5 mm/yr on the CRF, and 3.0 mm/yr on the SCF, in general agreement with the results of Weber et al. (2020). There are several well-studied analogs to the CA-SA transform plate boundary that also display along-strike variations in interseismic behavior and strain partitioning. Geodetic studies of the North Anatolian fault zone have revealed locked and creeping segments with clear transition zones (Cetin et al., 2014). The San Andreas fault (SAF) also demonstrates locked and creeping segmentation, along with variable seismic moment release rates along its various segments (Smith-Konter et al., 2011), and strain partitioning at its ends. Various proportions of creep occur between the locked NW and SE segments of the SAF, which produced the 1906 and 1857 ruptures, respectively (Wallace, 1970). The Parkfield segment is a ~40 km-long transitional segment at the SE end of the 140 km long creeping segment of the SAF (Bakun et al., 2005; Murray et al., 2001; Titus et al., 2006). Finally, ~75% of PA-NA plate motion is accommodated on three transform faults systems in the north, the single San Andreas fault in the central segment, and then up to five transform faults in the south (Lisowski et al., 1991), analogous to the two-fault (SSF and LVF) one-fault (EPF) three-fault (STTF, CRF, and SCF) system of the CA-SA transform plate boundary described here.

2.6.2 Geodetic and Seismic Moment

The modeling results and analyses indicate a spatial correlation between interseismic behavior and seismic moment release along the CA-SA plate boundary. Figure **2-14** (B & C) shows the geodetically derived moment deficit and the total seismic moment for the plate boundary from 1970 to 2017 for shallow (<20 km) and M >3.5 earthquakes. This project's earthquake data analysis shows that the seismic moment release rates are significantly higher on the eastern (creeping) segment than on the western (locked) segment of the plate boundary. The transition from locked to creeping (profile B) correlates well with the change in the pattern of moderate magnitude seismicity (Figure **2-2**), and therefore the seismic moment release (Figure **2-14b**), and occurs over a ~20 km wide segment of the EPF (see Section S4). There is a large and significant deficit in seismic moment release (~10^{20} Nm) along the western plate boundary segment, with interseismic strain accumulating on the SSF, LVF, and western EPF at close to the full plate motion rate. This is expected as these segments are currently locked and accumulating interseismic strain. Moderate to large earthquakes are known to have occurred on the SSF, LVF, and western EPF with the largest historical event being the 1900 M 7.6 to M 8.0 on the eastern segment of the SSF (Pérez et al., 1997, 1998a, 2018; Colón et al., 2015). There has not been a large magnitude (M ≥ 6.5) earthquake on the western segment of the EPF since 1929. The largest instrumentally observed earthquake on the LVF was the May 4th, 2009 M_w 5.4 (Storchak et al., 2015). Previous to this event were the M ≥6.5 earthquakes in 1641 and 1878. These earthquakes suggest that moderate magnitude earthquakes on the LVF have a reoccurrence interval between ~130 years and ~200 years. The estimated slip deficit and locking depth for the LVF requires a future M_w 5.5 earthquake with a repeat time of 200 years.

If it can be considered that the SSF and western EPF could behave as one single fault (total length of ~400 km) and that an earthquake with a repeat time of 100 years nucleates at the estimated locking depth of ~7 km for the SSF and EPF, then it is possible to produce another M_w ~8.0 earthquake, similar to that which occurred in 1900. One M_w 8.0 earthquake on the western segment of the plate boundary would recover the moment deficit of this region (Figure **2-14**). While continental strike-slip faults rarely produce such large magnitude earthquakes (Harris 2017), this scenario could be quite possible. Analogous earthquakes include the 1872 M_w 7.8 – 7.9 Owens Valley, California (Hough and

Hutton, 2008), and the 2002 M_w 7.9 Denali, Alaska earthquakes (Eberhart-Phillips et al., 2003). A M_w 8.0 is likely the maximum magnitude for an earthquake on the CA-SA transform plate boundary. Considering that earthquakes on continental strike-slip faults do not generally propagate through creeping segments (e.g., Jolivet et al., 2013; Murray & Langbein, 2006) the rupture strike length for the western CA-SA transform plate boundary is likely limited to that discussed above.

The earthquake catalog used (ISC reviewed catalog; Storchak et al., 2015, 2017) is temporally aliased, as it does not include historical earthquakes; for example, the 1929 M6.5 Cumana earthquake. However, including historical seismicity for the last 400 years on the SSF and LVF (e.g., M >6 1641 and 1878 LVF; Pérez, 1998b; and M 7.7 1900 SSF earthquakes; Pacheco & Sykes, 1992), the total seismic moment release is essentially the same for all segments of the plate boundary.

In contrast to the western segment of the CA-SA plate boundary, the central and eastern segments of the EPF have a much higher frequency of low to moderate magnitude earthquakes (Figures **2-2 & 14**). The central EPF (segment 2; profile B), a transition zone between the locked western EPF and the creeping eastern segment, has produced at least two M_w 6 – M_w 7 earthquakes in the last 50 years (Figure **2-2**). The 100 km long eastern segment of the EPF accommodates ~95% of the seismic moment via creep and low magnitude earthquakes ($M \leq 5$) (Figure **2-14**). This is similar to the creeping segment of the SAF northwest of Parkfield, along which aseismic creep takes up a significant part of its slip budget, while still producing moderate magnitude earthquakes; for example, the 2004 M_w 6.0 Parkfield earthquake (Bakun et al., 2005; Gans et al., 2003; WGCEP, 2003). The SCF and CRF creep aseismically while the STTF is locked and is seismically active, having ruptured during the 1997 M_w 6.7 earthquake. A similar magnitude earthquake on the STTF will have a reoccurrence interval of ~200 years.

2.6.3 Correlation between Interseismic Behavior and Geology

Geodetic studies of continental transform faults have stimulated studies that correlate interseismic fault behavior (i.e., locked to creeping) with the geology of the fault zones, in particular emphasizing possible geologic causes for fault creep. Cetin et al., (2014) determined that creep on the North Anatolian fault is spatially associated with serpentinite and carbonate bedrock lithologies. The creeping segment of the Longitudinal Valley Fault, Taiwan is associated with the Lichi mélange, whereas the locked segment cuts through more competent forearc sedimentary and volcaniclastic units (Thomas et al., 2014). Thomas et al. (2014) suggest that the composition of the mélange helps to facilitate pressure-solution creep, which in turn allows for aseismic slip and creep. The Parkfield segment of the SAF is thought to creep due to the presence of talc-lubricated fault gouge (D. E. Moore and Rymer 2007). This section explores whether the interseismic behavior and seismogenic nature of the faults in the CA-SA transform plate boundary could be a function of geology.

The western segment of the plate boundary defined by the active SSF, LVF, and western EPF cut predominantly high-grade (blueschist-bearing) metamorphic rocks in the coastal mountains (Caracas-Araya-Margarita belt), and further inboard cut ophiolite-bearing rocks of the Caucagua-El Tinaco and Paracotos belt (Figure **2-3**). The central plate boundary segment of the EPF separates low-grade metamorphic rocks of the coastal Paria-Northern Range belt from the sedimentary cover rocks of the passive margin and foreland. According to the modeling results, the transition from western EPF locking to eastern EPF creep occurs at ~64°W. While CRF creep has been suggested to be due to elevated pore fluid pressures related to thermogenic oil and gas and mud volcanoes on the south side of the CRF (J. C. Weber et al. 2020), that same mechanism cannot be inferred for creep on the eastern EPF. The oil fields of eastern Venezuela are ~100 km south of the EPF (C. D. French and Schenk 2004). Eastern EPF creep might therefore be due to the geology observed across the fault and/or in the subsurface. On the north side of the ~64°W transition, rocks in the coastal mountains change from

Paria-Northern Range to Caracas-Araya-Margarita metamorphics. In addition, gypsum, which is known to be a weak mineral phase, occurs in the Cariaquito/Laventille unit along the southern flanks of the Paria-Northern Range belt (Cruz et al. 2007). Old (Cretaceous) and topographically high passive margin sedimentary rocks south of the eastern EPF transition to younger (Paleogene-Neogene) and topographically lower foreland basin fill to the southwest. The subsurface position of the Jurassic Espino graben is also somewhat coincident with the observed ~64° W transition. The geology may therefore play a role in creep on the eastern EPF, but more detailed investigations are still needed.

7.0 Conclusions

The ~900 km long CA-SA transform plate boundary from 68°W to 60°W is characterized by significant along-strike strain partitioning and variability in interseismic behavior. The plate boundary faults west of 64°W are locked, while faults east of this longitude, except for one (STTF), are creeping. Despite displaying predominantly active creep, many of the faults in the eastern plate boundary are currently or have been seismogenic. These spatial and temporal variations in seismic moment release are most likely governed by geology and/or changes in pore fluid pressures. The CRF is the only active fault on the island of Trinidad; it is creeping along its entire ~50 km length, and it accommodates 70% of the CA-SA relative motion. The remaining 30% of plate motion at this longitude is partitioned onto the STTF and SCF. Future work, including establishing borehole seismometers, strain and creepmeters, and a denser cGPS network, is needed to better characterize time-varying strain and the seismogenic potential of the CRF. Further work is needed to determine the mechanism that allows for creep on the eastern EPF. From these findings, it can be inferred that the entire western segment of the CA-SA transform plate boundary may be capable of rupturing a M_w 8 earthquake, an inference that should help guide future seismic hazard and risk zonation for this populated region.

2.7 References

Altamimi, Z., Métivier, L., & Collilieux, X. (2012). ITRF2008 plate motion model. *Journal of Geophysical Research: Solid Earth*, *117*(7), 1–14. doi: 10.1029/2011JB008930

Amante, C., & Eakins, B. W. (2009). *ETOPO1 1 arc-minute global relief model: procedures, data sources and analysis*. Boulder, Colorado.

Audemard, F. A. (2006). Surface rupture of the Cariaco July 09, 1997 earthquake on the El Pilar fault, northeastern Venezuela. *Tectonophysics*, *424*(1–2), 19–39. doi: 10.1016/j.tecto.2006.04.018

Audemard, F. A. (2007). Revised seismic history of the El Pilar fault, Northeastern Venezuela, from the Cariaco 1997 earthquake and recent preliminary paleoseismic results. *Journal of Seismology*, *11*(3), 311–326. doi: 10.1007/s10950-007-9054-2

Avé Lallemant, H. G. (1997). Transpression, displacement partitioning, and exhumation in the eastern Caribbean / South American plate boundary zone. *Tectonics*, *16*(2), 272–289. doi: 10.1029/96TC03725

Avé Lallemant, H. G., & Sisson, V. B. (2005). Exhumation of eclogites and blueschists in northern Venezuela: Constraints from kinematic analysis of deformation structures. *Geological Society of America Special Paper*, *394*, 193–206. doi: 10.1130/2005.2394(07).

Bakun, W. H., Aagaard, B., Dost, B., Ellsworth, W. L., Hardebeck, J. L., Harris, R. A., … Waldhauser, F. (2005). Implications for prediction and hazard assessment from the 2004 Parkfield earthquake. *Nature*, *437*(7061), 969–974. doi: 10.1038/nature04067

Baumbach, M., Grosser, H., Torres, G., Rojas Gonzales, J. L., Sobiesiak, M., & Welle, W. (2004). Aftershock pattern of the July 9, 1997 Mw=6.9 Cariaco earthquake in Northeastern Venezuela. *Tectonophysics*, *379*(1–4), 1–23. doi: 10.1016/j.tecto.2003.10.018

Beltran, C., Singer, A., & Rodriguez, A. (1996). the El Pilar Fault Active Trace (Northeastern Venezuela): Neotectonic Evidences and Paleoseismic Data . *Third International Symposium on Andean Geodynamics, Saint Malo (France)*, 153–156.

Beltran, P. L., Pathier, E., François, J., Vassallo, R., Reinoza, C., Audemard, F., … Volat, M. (2016). Spatial and temporal variations in creep rate along the El Pilar fault at the Caribbean-South American plate boundary (Venezuela), from InSAR. *Journal of Geophysical Research: Solid Earth*, (Figure 1), 8276–8296. doi: 10.1002/2016JB013121

Berardino, P., Fornaro, G., Lanari, R., & Sansosti, E. (2002). A new algorithm for surface deformation monitoring based on small baseline differential SAR interferograms. *IEEE Transactions on Geoscience and Remote Sensing*, *40*(11), 2375–2383. doi: 10.1109/TGRS.2002.803792

Bilham, R., Ozener, H., Mencin, D., Dogru, A., Ergintav, S., Cakir, Z., … Mattioli, G. (2016). Surface creep on the North Anatolian Fault at Ismetpasa, Turkey, Turkey, 1944–2016. *Journal of Geophysical Research : Solid Earth*, *121*(10), 7409–7431. doi: 10.1002/2016JB012928

Bohnhoff, M., Grosser, H., & Dresen, G. (2006). Strain partitioning and stress rotation at the North Anatolian fault zone from aftershock focal mechanisms of the 1999 Izmit MW = 7.4 earthquake. *Geophysical Journal International*, *166*(1), 373–385. doi: 10.1111/j.1365-246X.2006.03027.x

Bos, M. S., Fernandes, R. M. S., Williams, S. D. P., & Bastos, L. (2013). Fast error analysis of continuous GNSS observations with missing data. *Journal of Geodesy*, *87*(4), 351–360. doi: 10.1007/s00190-012-0605-0

Boschman, L. M., van Hinsbergen, D. J. J., Torsvik, T. H., Spakman, W., & Pindell, J. L. (2014). Kinematic reconstruction of the Caribbean region since the early Jurassic. *Earth-Science Reviews*, *138*, 102–136. doi: 10.1016/j.earscirev.2014.08.007

Burke, K. (1988). Tectonic evolution of the Caribbean. *Annual Review of Earth and Planetary Sciences*, *16*(1), 201–230.

Cavalié, O., Lasserre, C., Doin, M. P., Peltzer, G., Sun, J., Xu, X., & Shen, Z. K. (2008). Measurement of interseismic strain across the Haiyuan fault (Gansu, China), by InSAR. *Earth and Planetary Science Letters*, *275*(3–4), 246–257. doi: 10.1016/j.epsl.2008.07.057

Cetin, E., Cakir, Z., Meghraoui, M., Ergintav, S., & Akoglu, A. M. (2014). Extent and distribution of aseismic slip on the Ismetpaşa segment of the North Anatolian Fault (Turkey) from Persistent Scatterer InSAR. *Geochemistry, Geophysics, Geosystems*, *15*(7), 2883–2894. doi: 10.1002/2014GC005307.Received

Chen, C. W., & Zebker, H. A. (2000). Network approaches to two-dimensional phase unwrapping: intractability and two new algorithms. *Journal of the Optical Society of America. A, Optics, Image Science, and Vision*, *17*(3), 401–414. Retrieved from http://www.ncbi.nlm.nih.gov/pubmed/10708020

Chen, C. W., & Zebker, H. A. (2002). Phase unwrapping for large SAR interferograms: Statistical segmentation and generalized network models. *IEEE Transactions on Geoscience and Remote Sensing*, *40*(8), 1709–1719. doi: 10.1109/TGRS.2002.802453

Colón, S., Audemard, F. A., Beck, C., Avila, J., Padrón, C., De Batist, M., … Van Welden, A. (2015). The 1900 Mw 7.6 earthquake offshore north-central Venezuela: Is La Tortuga or San Sebastián the source fault? *Marine and Petroleum Geology*, *67*, 498–511. doi: 10.1016/j.marpetgeo.2015.06.005

Crosby, C. J., Prentice, C. S., Weber, J., & Ragona, D. (2009). *Logs of paleoseismic excavations across the Central Range fault, Trinidad*.

Cruz, L., Fayon, A. K., Teyssier, C., & Weber, J. (2007). Exhumation and deformation processes in transpressional orogens: The Venezuelan Paria Península, SE Caribbean – South American plate boundary. *Geological Society of America Special Papers*, *434*(08), 149–165. doi: 10.1130/2007.2434(08).

DeMets, C., Gordon, R. G., & Argus, D. F. (2010). Geologically current plate motions. *Geophysical Journal International*, *181*(1), 1–80. doi: 10.1111/j.1365-246X.2009.04491.x

Deville, E., & Guerlais, S. H. (2009). Cyclic activity of mud volcanoes: Evidences from Trinidad (SE Caribbean). *Marine and Petroleum Geology*, *26*(9), 1681–1691. doi: 10.1016/j.marpetgeo.2009.03.002

Dziewonski, A. M., Chou, T. A., & Woodhouse, J. H. (1981). Determination of earthquake source parameters from waveform data for studies of global and regional seismicity. *Journal of Geophysical Research: Solid Earth*, *86*(B4), 2825–2852.

Eberhart-Phillips, D., Haeussler, P. J., Freymueller, J. T., Frankel, A. D., Rubin, C. M., Craw, P., … Wallace, W. K. (2003). The 2002 Denali fault earthquake, Alaska: A large magnitude, slip-partitioned event. *Science*, *300*(5622), 1113–1118. doi: 10.1126/science.1082703

Ekström, G., Nettles, M., & Dziewoński, A. M. (2012). The global CMT project 2004-2010: Centroid-moment tensors for 13,017 earthquakes. *Physics of the Earth and Planetary Interiors*, *200–201*, 1–9. doi: 10.1016/j.pepi.2012.04.002

Engdahl, E. R., Storchak, D. A., Di Giacomo, D., Bondár, I., Harris, J., Lee, W. H. K., … Bormann, P. (2013). Public release of the ISC--GEM global instrumental earthquake catalogue (1900--2009). *Seismological Research Letters*, *84*(5), 810–815.

Erlich, R., & Barrett, S. F. (1990). Cenozoic Plate tectonic history of the northern Venezuela-Trinidad Area. *Tectonics*, *9*(1), 161–184.

Escalona, A., Mann, P., & Jaimes Martha, M. (2011). Miocene to recent Cariaco basin, offshore Venezuela: Structure, tectonosequences, and basin-forming mechanisms. *Marine and Petroleum Geology*, *28*(1), 177–199. doi: 10.1016/j.marpetgeo.2009.04.001

Flinch, J. F., Rambaran, V., Ali, W., Lisa, V. De, Hernandez, G., Rodrigues, K., & Sams, R. (1999). Chapter 17 Structure of the Gulf of Paria pull-apart basin (Eastern Venezuela-Trinidad). *Sedimentary Basins of the World*, *4*(C), 477–494. doi: 10.1016/S1874-5997(99)80051-3

French, C. D., & Schenk, C. J. (2004). *Map showing geology, oil and gas fields, and geologic provinces of the Caribbean region*.

Gans, C. R., Furlong, K. P., & Malservisi, R. (2003). Fault creep and microseismicity on the Hayward fault, California: Implications for asperity size. *Geophysical Research Letters*, *30*(19), 8–11. doi: 10.1029/2003GL017904

Garcia-Abdeslem, J., Regalado-Sosa, J. J., & Cerquone-Ravelo, H. R. (2013). Un modelo 3D de la densidad del subsuelo en el graben de Espino: un aulacógeno Jurásico en el oriente de Venezuela. *Revista Mexicana de Ciencias Geológicas*, *30*(1), 110–120.

Garciacaro, E., Mann, P., & Escalona, A. (2011). Regional structure and tectonic history of the obliquely colliding Columbus foreland basin, offshore Trinidad and Venezuela. *Marine and Petroleum Geology*, *28*(1), 126–148. doi: 10.1016/j.marpetgeo.2009.08.016

Govers, R., & Wortel, M. J. R. (2005). Lithosphere tearing at STEP faults: Response to edges of subduction zones. *Earth and Planetary Science Letters*, *236*(1–2), 505–523. doi: 10.1016/j.epsl.2005.03.022

Gutenberg, B., & Richter, C. F. (1956). Earthquake magnitude, intensity, energy, and acceleration: (Second paper). *Bulletin of the Seismological Society of America*, *46*(2), 105–145.

Harris, R. A. (2017). Large earthquakes and creeping faults. *Reviews of Geophysics*, *55*(1), 169–198. doi: 10.1002/2016RG000539

Hayes, G. P., Moore, G. L., Portner, D. E., Hearne, M., Flamme, H., Furtney, M., & Smoczyk, G. M. (2018). *Zone Geometry Model*. *61*(October), 58–61.

Heppard, P. D., Cander, H. S., & Eggertson, E. B. (1998). Abnormal pressure and the occurrence of hydrocarbons in offshore eastern Trinidad, West Indies. *AAPG Memoir*, *1902*(70), 215–246.

Hough, S. E., & Hutton, K. (2008). Revisiting the 1872 Owens Valley, California, Earthquake. *Bulletin of the Seismological Society of America*, *98*(2), 931–949. doi: 10.1785/0120070186

Jolivet, R., Lasserre, C., Doin, M. P., Guillaso, S., Peltzer, G., Dailu, R., … Xu, X. (2012). Shallow creep on the Haiyuan fault (Gansu, China) revealed by SAR interferometry. *Journal of Geophysical Research: Solid Earth*, *117*(6), 1–18. doi: 10.1029/2011JB008732

Jolivet, R., Lasserre, C., Doin, M. P., Peltzer, G., Avouac, J. P., Sun, J., & Dailu, R. (2013). Spatio-temporal evolution of aseismic slip along the Haiyuan fault, China: Implications for fault frictional properties. *Earth and Planetary Science Letters*, *377*, 23–33.

Jordan, T. H. (1975). The present-day motions of the Caribbean Plate. *Journal of Geophysical Research*, *80*(32), 4433–4439. doi: 10.1029/JB080i032p04433

Jouanne, F., Audemard, F. A., Beck, C., Van Welden, A., Ollarves, R., & Reinoza, C. (2011). Present-day deformation along the El Pilar Fault in eastern Venezuela: Evidence of creep along a major transform boundary. *Journal of Geodynamics*, *51*(5), 398–410. doi: 10.1016/j.jog.2010.11.003

Kanamori, H. (1977). The energy release in great earthquakes. *Journal of Geophysical Research*, *82*(20), 2981–2987.

Katsuyuki, A. (1981). Magnitudes of large shallow earthquakes from 1904 to 1980. *Physics of the Earth and Planetary Interiors*, *27*(1), 72–92.

Kreemer, C., Klein, E., Shen, Z. K., Wang, M., Estey, L., Wier, S., & Boler, F. (2014). A geodetic plate motion and Global Strain Rate Model. *Geochemistry, Geophysics, Geosystems*, 130. doi: 10.1002/2014GC005407.Received

Lentas, K. (2017). Towards routine determination of focal mechanisms obtained from first motion P-wave arrivals. *Geophysical Journal International*, *212*(3), 1665–1686.

Lentas, K., Di Giacomo, D., Harris, J., & Storchak, D. A. (2019). The ISC Bulletin as a comprehensive source of earthquake source mechanisms. *Earth System Science Data*, *11*(2), 565–578.

Lidz, L., Ball, M., & Charm, W. (1968). Geophysical Measurements Bearing on the Problem of the El Pilar Fault in the Northern Venezuelan Offshore. *Bulletin of Marine Science*, *18*(3), 545–560. Retrieved from http://www.ingentaconnect.com/content/umrsmas/bullmar/1968/00000018/00000003/art00001

Lisowski, M., Savage, J. C., & Prescott, W. H. (1991). The velocity field along the San Andreas fault in central and southern California. *Journal of Geophysical Research: Solid Earth*, *96*(B5), 8369–8389.

Magnani, M. B., Zelt, C. A., Levander, A., & Schmitz, M. (2009). Crustal structure of the South American-Caribbean plate boundary at 67°W from controlled source seismic data. *Journal of Geophysical Research: Solid Earth*, *114*(2), 1–23. doi: 10.1029/2008JB005817

Maresch, W. V. (1974). Plate tectonics origin of the Caribbean mountain system of Northern South America: Discussion and proposal. *Bulletin of the Geological Society of America*, *85*(5), 669–682. doi: 10.1130/0016-7606(1974)85<669:PTOOTC>2.0.CO;2

Maurer, J., & Johnson, K. (2014). Fault coupling and potential for earthquakes on the creeping section of the central San Andreas Fault. *Journal of Geophysical Research: Solid Earth*, *119*(5), 4414–4428.

Mendoza, C. (2000). Rupture history of the 1997 Cariaco, Venezuela, earthquake from teleseismic P waves. *Geophysical Research Letters*, *27*(10), 1555–1558. doi: 10.1029/1999GL011278

Mocquet, A., Beltran, C., Lugo, M., Rodriguez, J. A., & Singer, A. (1996). Seismological Interpretation of the Historical Data Related to the 1929 Cumana Earthquake, Venezuela. *Third International Symposium on Andean Geodynamics, Saint Malo (France)*, 203–206.

Molnar, P., & Sykes, L. R. (1969). Tectonics of the Caribbean and Middle America Regions from Focal Mechanisms and Seismicity. *Geological Society of America Bulletin*, *80*(September), 1639–1684. doi: 10.1130/0016-7606(1969)80

Moore, D. E., & Rymer, M. J. (2007). Talc-bearing serpentinite and the creeping section of the San Andreas fault. *Nature*, *448*(7155), 795–797. doi: 10.1038/nature06064

Murray, J. R., & Langbein, J. (2006). Slip on the San Andreas fault at Parkfield, California, over two earthquake cycles, and the implications for seismic hazard. *Bulletin of the Seismological Society of America*, *96*(4 B), 283–303. doi: 10.1785/0120050820

Murray, J. R., Segall, P., Cervelli, P., Prescott, W., & Svarc, J. (2001). Inversion of GPS data for spatially variable slip-rate on the San Andreas Fault near Parkfield, CA. *Geophysical Research Letters*, *28*(2), 359–362. doi: 10.1029/2000GL011933

Ostos, M., & Sisson, V. B. (2005). Geochemistry and tectonic setting of igneous and metaigneous rocks of northern Venezuela. *Caribbean-South American Plate Interactions, Venezuela*, *394*(04), 119–155. doi: 10.1130/0-8137-2394-9.119

Pacheco, J. F., & Sykes, L. R. (1992). Seismic moment catalog of large shallow earthquakes, 1900 to 1989. *Bulletin of the Seismological Society of America*, *82*(3), 1306–1349.

Pérez, O. J. (1998a). Seismological report on the Mw = 6.8 strong shock of 9 July 1997 in Cariaco, Northeastern Venezuela. *Bulletin of the Seismological Society of America*, *88*(3), 874–879.

Pérez, O. J. (1998b). Sismicidad y tectónica en Venezuela y áreas vecinas. *Física de La Tierra*, *1998*(10), 87–110.

Pérez, O. J., Bilham, R., Bendick, R., Velandia, J. R., Hernández, N., Moncayo, C., … Kozuch, M. (2001). Velocity field across the southern Caribbean plate boundary and estimates of Caribbean/South-American plate motion using GPS geodesy 1994--2000. *Geophysical Research Letters*, *28*(15), 2987–2990.

Pérez, O. J., Sanz, C., & Lagos, G. (1997). Microseismicity, tectonics and seismic potential in southern Caribbean and northern Venezuela. *Journal of Seismology*, *1*(1), 15–28. Retrieved from http://www.scopus.com/inward/record.url?eid=2-s2.0-0346435794&partnerID=40&md5=f848c9cfc83cd775cba97f27f96032a0

Pérez, O. J., Wesnousky, S. G., De La Rosa, R., Márquez, J., Uzcátegui, R., Quintero, C., … Szeliga, W. (2018). On the interaction of the North Andes plate with the Caribbean and South American plates in northwestern South America from GPS geodesy and seismic data. *Geophysical Journal International*, *214*(3), 1986–2001. doi: 10.1093/GJI/GGY230

Pindell, J. L., & Barrett, S. F. (1990). Geological evolution of the Caribbean region; A Plate tectonic perspective. *The Geology of North America*, pp. 405–432. doi: n/a

Pindell, J. L., & Kennan, L. (2001). Processes and Events in the Terrane Assembly of Trinidad and Eastern Venezuela. *Petroleum Systems of Deep-Water Basins: Global and Gulf of Mexico Experience*, *21*, 159–192. doi: 10.5724/gcs.01.21.0129

Prentice, C. S., Weber, J. C., Crosby, C. J., & Ragona, D. (2010). Prehistoric earthquakes on the Caribbean-South American plate boundary, central range fault, Trinidad. *Geology*, *38*(8), 675–678. doi: 10.1130/G30927.1

Reasenberg, P. (1985). Second-order moment of central California seismicity, 1969--1982. *Journal of Geophysical Research: Solid Earth*, *90*(B7), 5479–5495.

Reinoza, C., Jouanne, F., Audemard, F. A., Schmitz, M., & Beck, C. (2015). Geodetic exploration of strain along the El Pilar Fault in northeastern Venezuela. *Journal of Geophysical Research: Solid Earth*, *120*(3 (2015)), 1993–2013. doi: 10.1002/2014JB011483

Robertson, P., & Burke, K. (1989). Evolution of southern Caribbean Plate boundary, vicinity of Trinidad and Tobago. *AAPG Bulletin*, *73*(4), 490–509.

Russo, R. M., Speed, R. C. (1994). Spectral analysis of gravity anomalies and the architecture of tectonic wedging, NE Venezuela and Trinidad. *Tectonics*, *13*(3), 613–622. doi: 10.1029/94TC00052

Russo, R. M., & Speed, R. C. (1992). Oblique collision and tectonic wedging of the South American continent and Caribbean terranes. *Geology*, *20*(5), 447–450. doi: 10.1130/0091-7613(1992)020<0447:OCATWO>2.3.CO;2

Russo, R. M., Speed, R. C., Okal, E. a., Shepherd, J. B., & Rowley, K. C. (1993). Seismicity and tectonics of the southeastern Caribbean. *Journal of Geophysical Research*, *98*, 299–319. doi: 10.1029/93JB00507

Sandwell, D. T., Xu, X., Mellors, R., Wei, M., Tong, X., & Wessel, P. (2016). *GMTSAR: An InSAR Processing System Based on Generic Mapping Tools (Second Edition)*. Retrieved from http://topex.ucsd.edu/gmtsar/tar/GMTSAR_2ND_TEX.pdf

Savage, J. C., & Burford, R. O. (1973). Geodetic determination of relative plate motion in central California. *Journal of Geophysical Research*, *78*(5), 832–845.

Schmidt, D. A., & Bürgmann, R. (2003). Time-dependent land uplift and subsidence in the Santa Clara valley, California, from a large interferometric synthetic aperture radar data set. *Journal of Geophysical Research: Solid Earth*, *108*(B9).

Schubert, C. (1979). El Pilar fault zone, northeastern Venezuela: brief review. *Tectonophysics*, *52*(1–4), 447–455.

Schubert, C. (1981). Are the Venezuelan fault systems part of the southern Caribbean plate boundary? *Geologische Rundschau*, *70*(2), 542–551. doi: 10.1007/BF01822134

Schubert, C. (1985). Neotectonic aspects of the southern Caribbean plate boundary. *First Geological Conference of the Geological Society of Trinidad & Tobago*, 265–268. Geological Society of Trinidad & Tobago.

Schubert, C., & Krause, F. F. (1984). Móron fault zone, north-central Venezuelan borderland:

Identification, definition, and neotectonic character. *Marine Geophysical Researches*, *6*(3), 257–273.

Scordilis, E. M. (2006). Empirical global relations converting MS and mb to moment magnitude. *Journal of Seismology*, *10*(2), 225–236. doi: 10.1007/s10950-006-9012-4

Şengör, A. M. ., Tüysüz, O., İmren, C., Sakınç, M., Eyidoğan, H., Görür, N., … Rangin, C. (2005). the North Anatolian Fault: a New Look. *Annual Review of Earth and Planetary Sciences*, *33*(1), 37–112. doi: 10.1146/annurev.earth.32.101802.120415

Sisson, V. B., Avé Lallemant, H. G., Ostos, M., Blythe, A. E., Snee, L. W., Copeland, P., … Guth, L. R. (2005). Overview of radiometric ages in three allochthonous belts of northern Venezuela: Old ones, new ones, and their impact on regional geology. *Caribbean-South American Plate Interactions, Venezuela*, *394*(03), 91–118. doi: 10.1130/0-8137-2394-9.91

Sisson, V. B., Ertan, I. . E., & Avé Lallemant, H. G. (1997). High-pressure (~2000 MPa) kyanite- and glaucophane-bearing pelitic schist and eclogite from Cordillera de la Costa belt, Venezuela. *Journal of Petrology*, *38*(1), 65–83. doi: 10.1093/petroj/38.1.65

Smith-Konter, B. R., Sandwell, D. T., & Shearer, P. (2011). Locking depths estimated from geodesy and seismology along the San Andreas Fault System: Implications for seismic moment release. *Journal of Geophysical Research: Solid Earth*, *116*(6), 1–13. doi: 10.1029/2010JB008117

Sorensen, S. S., Sisson, V. B., & Avé Lallemant, H. G. (2005). Geochemical evidence for possible trench provenance and fl uid-rock histories, Cordillera de la Costa eclogite belt, Venezuela. *Geological Society of America Special Paper*, *394*(06), 173–192. doi: 10.1130/2005.SPE394(06).

Soto, M. D., Mann, P., Escalona, A., & Wood, L. J. (2007). Late Holocene strike-slip offset of a subsurface channel interpreted from three-dimensional seismic data, eastern offshore Trinidad. *Geology*, *35*(9), 859–862. doi: 10.1130/G23738A.1

Speed, R. C. (1985). Cenozoic collision of the Lesser Antilles Arc and continental South America and the origin of the El Pilar Fault. *Tectonics*, *4*(1), 41–69. doi: 10.1029/TC004i001p00041

Stockhert, B. (1995). Crustal history of Margarita Island (Venezuela) in detail: constraint on the Caribbean plate-tectonic scenario. *Geology*, *23*(9), 787–790. doi: 10.1130/0091-7613(1995)023<0787:CHOMIV>2.3.CO;2

Storchak, D. A., Di Giacomo, D., Engdahl, E. R., Harris, J., Bondár, I., Lee, W. H. K., … Villaseñor, A. (2015). The ISC-GEM global instrumental earthquake catalogue (1900--2009): introduction. *Physics of the Earth and Planetary Interiors*, *239*, 48–63.

Storchak, D. A., Harris, J., Brown, L., Lieser, K., Shumba, B., Verney, R., … Korger, E. I. M. (2017). Rebuild of the Bulletin of the International Seismological Centre (ISC), part 1: 1964–1979. *Geoscience Letters*, *4*(1). doi: 10.1186/s40562-017-0098-z

Suárez, G., & Nábělek, J. (1990). The 1967 Caracas earthquake: Fault geometry, direction of rupture propagation and seismotectonic implications. *Journal of Geophysical Research: Solid Earth*, *95*(B11), 17459–17474.

Symithe, S., Calais, E., De Chabalier, J. B., Robertson, R., & Higgins, M. (2015). Current block motions and strain accumulation on active faults in the Caribbean. *Journal of Geophysical Research: Solid Earth*, *120*(5). doi: 10.1002/2014JB011779

Thomas, M. Y., Avouac, J. P., Gratier, J. P., & Lee, J. C. (2014). Lithological control on the deformation mechanism and the mode of fault slip on the Longitudinal Valley Fault, Taiwan. *Tectonophysics*, *632*(C), 48–63. doi: 10.1016/j.tecto.2014.05.038

Titus, S. J., DeMets, C., & Tikoff, B. (2006). Thirty-five-year creep rates for the creeping segment of the San Andreas fault and the effects of the 2004 Parkfield earthquake: Constraints from alignment arrays, continuous global positioning system, and creepmeters. *Bulletin of the Seismological Society of America*, *96*(4 B), 250–268. doi: 10.1785/0120050811

Tong, X., & Schmidt, D. (2016). Active movement of the Cascade landslide complex in Washington from a coherence-based InSAR time series method. *Remote Sensing of Environment*, *186*, 405–415.

Wallace, R. E. (1970). Earthquake recurrence intervals on the San Andreas fault. *Geological Society of America Bulletin*, *81*(10), 2875–2890.

Wang, C., Shan, X., Wang, C., Ding, X., Zhang, G., & Masterlark, T. (2013). Using finite element and Okada models to invert coseismic slip of the 2008 Mw 7.2 Yutian earthquake, China, from InSAR data. *Journal of Seismology*, *17*(2), 347–360. doi: 10.1007/s10950-012-9324-5

Weber, J. C. (2010). Neotectonics in the Trinidad and Tobago, West Indies segment of the Caribbean-South American plate boundary. *Occasional Papers of the Geological Institute of Hungary*, *204*, 21–29.

Weber, J. C., Dixon, T. H., DeMets, C., Ambeh, W. B., Jansma, P., Mattioli, G., … Peŕez, O. (2001). GPS estimate of relative motion between the Caribbean and South American plates, and geologic implications for Trinidad and Venezuela. *Geology*, *29*(1), 75–78. doi: 10.1130/0091-7613(2001)029<0075:GEORMB>2.0.CO;2

Weber, J. C., Ferrill, D. A., & Roden-Tice, M. K. (2001). Calcite and quartz microstructural geothermometry of low-grade metasedimentary rocks, Northern Range, Trinidad. *Journal of Structural Geology*, *23*(1), 93–112. doi: 10.1016/S0191-8141(00)00066-3

Weber, J. C., Geirsson, H., La Femina, P., Robertson, R., Churches, C., Shaw, K., … Miller, K. (2020). Fault Creep and Strain Partitioning in Trinidad-Tobago: Geodetic Measurements, Models, and Origin of Creep. *Tectonics*, *39*(1), 1–15. doi: 10.1029/2019TC005530

Weber, J. C., Geirsson, H., Latchman, J. L., Shaw, K., La Femina, P., Wdowinski, S., … Norabuena, E. (2015). Tectonic inversion in the Caribbean-South American plate boundary: GPS geodesy, seismology, and tectonics of the Mw 6.7 22 April 1997 Tobago earthquake. *Tectonics*, *34*(6), 1181–1194. doi: 10.1002/2014TC003665.Received

Weber, J. C., Saleh, J., Balkaransingh, S., Dixon, T., Ambeh, W., Leong, T., … Miller, K. (2011). Triangulation-to-GPS and GPS-to-GPS geodesy in Trinidad, West Indies: Neotectonics, seismic risk, and geologic implications. *Marine and Petroleum Geology*, *28*(1), 200–211. doi: 10.1016/j.marpetgeo.2009.07.010

Wei, M., & Sandwell, D. T. (2010). Decorrelation of L-band and C-band interferometry over vegetated areas in California. *IEEE Transactions on Geoscience and Remote Sensing*, *48*(7), 2942–2952. doi: 10.1109/TGRS.2010.2043442

WGCEP. (2003). Earthquake probabilities in the San Francisco Bay region: 2002–2031. *US Geol. Surv. Open-File Rep.*, *2003*(214), 1–-340.

Willemann, R. J., & Storchak, D. A. (2001). Data collection at the International Seismological Centre. *Seismological Research Letters*, *72*(4), 440–453. doi: 10.1785/gssrl.72.4.440

Xu, X., Sandwell, D. T., Tymofyeyeva, E., González-Ortega, A., & Tong, X. (2017). Tectonic and anthropogenic deformation at the Cerro Prieto geothermal step-over revealed by Sentinel-1A InSAR. *IEEE Transactions on Geoscience and Remote Sensing*, *55*(9), 5284–5292.

Ysaccis, B. R. (1998). *Tertiary evolution of the northeastern Venezuela offshore.* (Rice University). Retrieved from https://scholarship.rice.edu/handle/1911/19330

Chapter 3
Central American Forearc-Caribbean Plate Shear Mechanism and Magmatic-Tectonic Interaction in Nicaragua

3.1 Introduction

At oblique convergent margins with strong mechanical coupling at the subduction interface, strain is partitioned between the megathrust and the overriding plate (Jarrard 1986a; Fitch 1972). Strain in the overriding plate is accommodated by margin-parallel shear, often by margin-parallel strike-slip faults (McCaffrey 1992). This is the case for the Indo-Australian – Eurasian plate boundary in Sumatra where strain partition occurs in the forearc and ~25 mm/yr of relative motion between the forearc and back-arc (i.e., Eurasian Plate) is accommodated by the margin-parallel Great Sumatran fault that runs through the volcanic arc (Genrich et al., 2000; Sieh and Natawidjaja 2000). However, the margin parallel shear in the overriding plate may not necessarily be accommodated by margin parallel strike-slip fault systems. Another mode of accommodating forearc motion is by bookshelf faulting where rotating tectonic blocks approximate the motion of a transform fault (La Femina et al., 2002). The forearc of the Pacific-North American plate margin in the Aleutian archipelago exhibits this mode of shear (Geist et al., 1988). High convergence obliquity (~90°) and relatively fast convergence rates (87-91 mm/yr)(DeMets et al., 2010) results in arc-parallel strain within the forearc (Avé Lallemant & Oldow 2000).

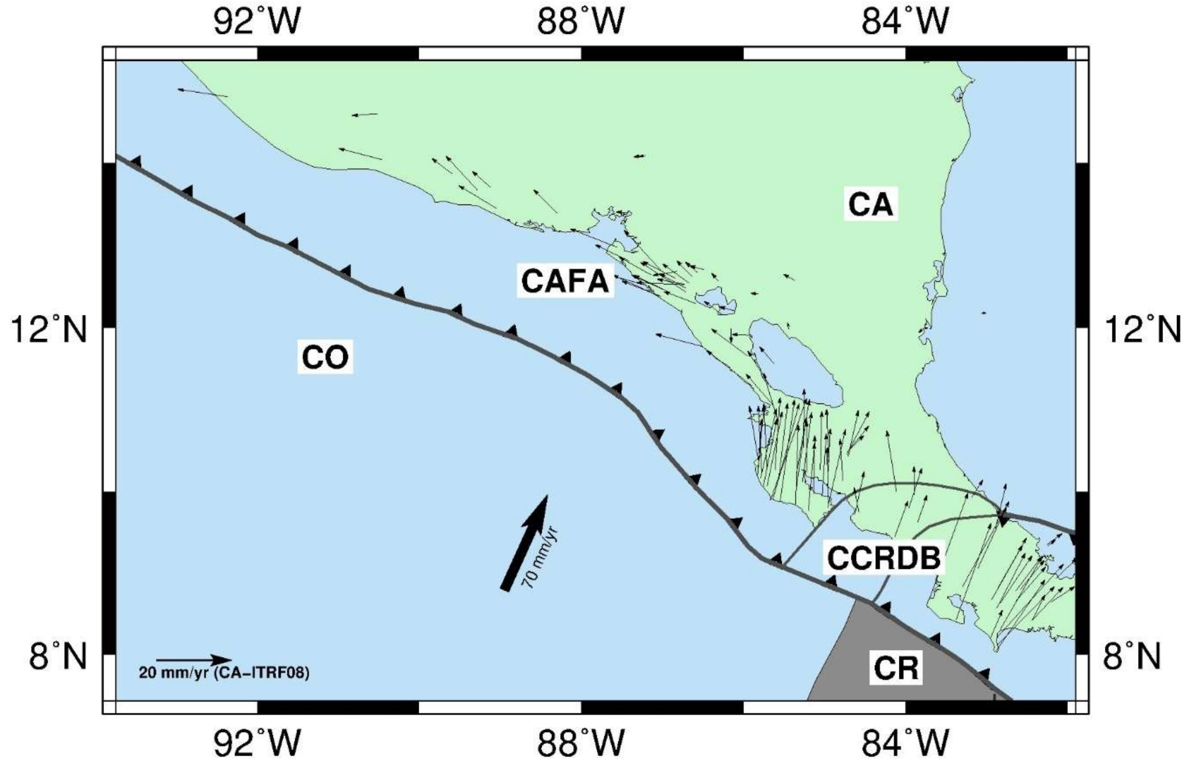

Figure **3-1**: Major tectonic units, general convergence rate and azimuth (large black arrow), and GPS velocities (small black arrows). Major tectonic units are CO – Cocos plate, CR – Cocos Ridge, CAFA – Central American Forearc, CCRDB – Central-Costa Rican Deformed Belt. GPS velocities for Guatemala, El Salvador and Costa Rica are from Kobayashi et al. (2014). GPS velocities for Panama are from Ruiz et al. (in prep). GPS velocities in Nicaragua are from this study.

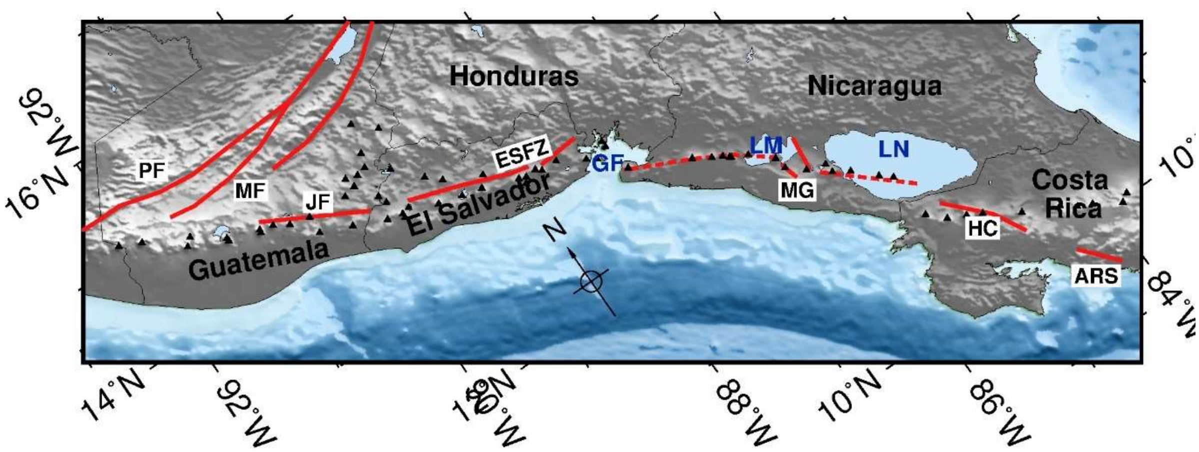

Figure **3-2:** Major tectonic faults of the western Caribbean and North American plate boundaries (red lines): PF Polochic – fault, MF – Motagua fault, JF – Jalpatagua fault (Authemayou et al., 2011), ESFZ – El Salvador fault zone (Corti et al., 2005), MG – Managua graben (Cowan et al., 2000), HC – Haciendas-Chirapas fault system (Montero et al., 2017), ARS – San Miguel-Atirro-Rio Sucio fault. Water bodies (Montero et al., 2013): GF – Gulf of Fonseco, LM – Lake Managua, and LN – Lake Nicaragua. Black triangles are Holocene volcanoes.

The CO-CA is an oblique convergent margin with the Central American Forearc (CAFA), which is an escaping tectonic unit driven by the collision of the Cocos Ridge with the CA plate (Figure **3-1**). The forearc sliver translates to the NW at a rate of ~14 mm/yr (Turner et al., 2007; Correa-Mora et al., 2009; LaFemina et al., 2009; Kobayashi et al., 2014) and most of the forearc-back-arc dextral shear is accommodated within the volcanic arc, evidenced by a 25 km-wide band of upper-plate earthquakes centered on the volcanic arc (White and Harlow 1993; Syracuse et al. 2008; Carr and Stoiber 1977; Dewey and Algermissen 1974; LaFemina et al., 2009; Kobayashi et al., 2014) and geodetic studies (Ellis et al., 2019; Staller et al., 2016; LaFemina et al., 2009; Kobayashi et al., 2014). The mechanism of shear accommodation throughout the arc varies, with well-expressed right-lateral fault systems and geomorphic structures indicating extension along the arc. The CAFA-CA shear in Nicaragua is thought to be accommodated mostly by bookshelf faulting on NE trending left-lateral inter-volcano faulting (La Femina et al., 2002; Cailleau et al., 2007). Identified structures and mapped faults indicate that this fault trend is pervasive in Nicaragua (LaFemina et al., 2002). Upper-plate earthquakes in Nicaragua and their sense of motion can be interpreted as ruptures on N-S or NE-SW trending left-lateral faults or NW-SE trending right-lateral faults. These moderate magnitude upper-plate earthquakes (Ms ≤6.5; White & Harlow, 1993) are more destructive than the megathrust events on the subduction interface due to their frequency, shallow hypocenters, and proximity to population centers.

The destructive Ms 6.2 1972 Managua earthquake occurred on a NNE-trending (arc-oblique) fault with left-lateral motion (Algermissen et al., 1974). There is evidence that many of the observed upper-plate earthquakes were due to left-lateral faulting (LaFemina et al., 2002; White & Harlow, 1993). These left-lateral faults, or bookshelf faults, accommodate the CAFA-CA shear. This project will explore the coseismic characteristics of three moderate magnitude upper-plate earthquakes (April 10th, 2014 (M_w 6.1), September 15th, 2016 (M_w 5.7), and September 28th, 2016 (M_w 5.5)) to shed light on bookshelf faulting in Nicaragua. This project will use Global Positioning System (GPS) data to investigate the co-seismic displacements of these upper-plate earthquakes to determine the kinematics of forearc-arc faulting and shed light on the primary mechanism accommodating CAFA- CA shear. The April 10th, 2014 earthquake occurred in the vicinity of the Momotombo volcano (INETER 2014; Suárez et al. 2016), which had a VEI eruption on December 1st, 2015. This project will also investigate the possible role of the April 2014 earthquake in the subsequent eruption of Momotombo and whether the three earthquakes were a triggered sequence.

3.2 Background

The CAFA extends from the Central Costa Rican Deformed Belt (CCRDB) to the CAFA-CA-NA triple junction in Guatemala and has, not only varying degrees of convergence at the trench, from 0° in Costa Rica to ~20° in Guatemala (Figure **3-1**), but also varying rates of its northwest translation from 8 mm/yr in Costa Rica (Norabuena et al., 2004; Kobayashi et al., 2014), ~14 mm/yr in Nicaragua (Kobayashi et al. 2014; Ellis et al. 2019), and ~12 mm/yr in El Salvador (Alvarado et al., 2010; Ellis et al., 2019; Staller et al., 2016; Kobayashi et al., 2014). The trench-parallel motion of the CAFA is driven by Cocos Ridge collision with the CA plate (LaFemina et al., 2009) and coupling along the obliquely convergent segments. Geodetic studies have shown that offshore Nicaragua and El Salvador, there is little evidence of significant locking on the megathrust, with coupling possibly occurring up-dip of the interface (< 20 km) (Correa-Mora et al., 2009; La Femina et al., 2009). However, the Cocos Ridge, which is young buoyant oceanic crust that is thickened by passage over the Galapagos hotspot (Werner et al. 1999), is indenting the CA in Costa Rica (Protti et al., 1994), providing the mechanism for displacing the CAFA (La Femina et al., 2009). The onset of the Coco Ridge-CA plate collision is between 0.5 Ma to 3.5 Ma (Gardner et al., 1992; MacMillan et al., 2004; Morell et al., 2012; Zeumann & Hampel 2017) making the CAFA sliver a relatively young tectonic feature.

CAFA-CA relative motion is partly accommodated by shallow moderate magnitude ($M_s \leq 6.5$) earthquakes that occur predominantly in the volcanic arc (Corti et al., 2005; La Femina et al., 2002; White & Harlow, 1993). These upper-plate earthquakes, being close to volcanic centers, may induce magmatism but there has only been one case of magmatic-tectonic interaction (La Femina et al., 2004) and anecdotal evidence of temporally correlated historical earthquakes and eruptions (White et al., 1987).

3.2.1 Accommodating Central American Forearc - Caribbean Plate Dextral Shear

The faulting and structures of the CAFA-CA are complex and variable. CAFA-CA shear in Costa Rica, Nicaragua, and El Salvador is accommodated by margin-normal left-lateral bookshelf faulting, margin parallel right-lateral strike-slip fault systems, and pull-apart basins at right-steps in the dextral shear system (e.g., Managua Graben; Figure **3-2**). In the southernmost extent of the CAFA in Costa Rica, geomorphic and seismic evidence suggests that CAFA-CA dextral displacement occurs on two NW-striking fault systems: 1) the San Miguel-Atirro-Rio Sucio fault (ARSF) system, a broad zone of deformation that begins on the northern flank of the Cordillera de Talamanca and ends in Cordillera Volcanic Central (Montero et al., 2013) in the CCRDB (Marshall et al., 2000; Lewis et al., 2008); and 2) the Haciendas-Chirapas fault system (HCFS) that parallels the Guanacaste volcanic arc (Araya & Biggs, 2020; Montero et al., 2017). The ARSF, on the northern flanks of the Cordillera, is a broad zone of displacement with complex right-lateral and conjugate faulting that becomes less anastomosing beyond the Irazú-Turrialba volcanic fields, while the HCFS is a less complex right-lateral fault system.

In El Salvador, the CAFA-CA shear is transferred from the Gulf of Fonseco pull-apart to the El Salvador Fault Zone (ESFZ) (Funk et al. 2009; Turner et al. 2007; Ellis et al. 2019; Correa-Mora et al. 2009; Alvarado et al. 2010), a 20 km wide shear zone (Alvarado et al. 2010). West of the Gulf, seismic, paleomagnetic, and geodetic studies indicate that shear is diffused through the Eastern El Salvador Deformation area, a pull-apart with possible bookshelf faulting expressed by N-S trending normal faults (Alvarado et al. 2010; Staller et al. 2016), and is bound to the north by the right-lateral San Miguel fault segment (Corti et al., 2005). Shear in the central and western ESFZ is accommodated via bookshelf faulting within the volcanic arc, where faulting is characterized as arc-normal or arc-oblique normal (bookshelf faults), and well-expressed right-lateral strike-slip faults (Alvarado et al., 2010; Corti et al., 2005; Garibaldi et al., 2016; Legrand et al., 2020; Martínez-Díaz et al., 2004; Ambraseys et al., 2001; Canora et al., 2014; Agostini et al., 2006). Further NW, along the ESFZ and near the El Salvador-Guatemala border, the CAFA-CA shear is accommodated by the right-lateral Jalpatagua fault (Carr 1976; Wunderman and Rose 1984; Duffield et al., 1992) that ultimately can be traced to the Motagua-Polochic fault system (Figure **3-2**) that is the North American-CA plate boundary (Authemayou et al., 2011).

In Nicaragua, there is a transition of terrane from the high relief of the Cordillera Volcanic Central, Costa Rica to the Nicaragua Depression (McBirney and Williams 1964), where faults that take up CAFA-CA displacement are not apparent (La Femina et al., 2002 and references therein). The Nicaragua Depression, the result of Miocene to Pliocene fore-arc extension, possibly due to slab retreat (Weinberg 1992), is a NW trending structure, with both Lakes Nicaragua and Managua, and terminates in the Gulf of Fonseca. The depression is a half-graben bounded by the Nicaragua Highlands to the northeast and the Pacific plains to the southwest, where normal faults are present, and hosts the Holocene volcanic arc (Figure **3-3**). In the Nicaragua segment of the CAFA, the predominant fault trends are (1) arc-transverse (N10°E - N10°W); (2) arc-normal (N30° - 40°E); and (3) arc-parallel (N50° - 60°W) (McBirney & Williams 1964; Weinberg 1992; Carr & Stoiber 1977; LaFemina et al., 2002). The Managua Graben is a seismically active structure that indicates that E-W extension is ongoing and is a right step in the volcanic arc (McBirney and Williams 1964). Within the graben, active north-striking (arc-oblique and arc-normal) left-lateral and normal faults have been identified (Algermissen et al., 1974; Cowan et al., 2000; Frischbutter, 2002; White & Harlow, 1993). Arc-transverse faults at the southwest boundary of the Nicaragua Depression are readily apparent but are inactive as seismicity, which represents the CAFA-CA shear, is confined to the volcanic arc. Focal mechanisms within the volcanic arc (Figure **3-3**) support northwest-striking faults possibly being active and will be detailed in the following section (Central American Forearc Seismicity). These fault trends are possibly responsible for the CAFA-CA shear in Nicaragua.

LaFemina, et al., (2002) proposed that in Nicaragua, bookshelf faulting accommodates the dextral shear via NE-SW-trending (N30°E) left-lateral faults based on earthquake focal mechanisms and mapped structures. French et al., (2010) determined the motion and fault planes of the August 3rd, 2005 M_w 6.3 and 5.3 Ometepe earthquakes in Lake Nicaragua using relocated aftershocks and directivity analysis. The authors found the first and larger shock occurred on a N60°E-striking, nearly vertical, left-lateral fault. The subsequent shock occurred on a right-lateral fault that is almost normal to the mainshock, with a strike of N~350°E. This earthquake sequence supports that bookshelf faulting is ongoing in Nicaragua. Funk et al. (2009), using seismic profiles in both Lakes Nicaragua and Managua, suggests that reactivated northwest-trending arc-parallel normal faults, related to forearc extension and the resulting Nicaragua Depression, now accommodate the motion of the forearc. The authors interpreted the faulting of Lake Managua and the Managua graben to be restraining bends, where reactivated normal faults accommodate right-lateral motion resulting in SW-NE extension and NW translation of the forearc.

3.2.2 Central American Forearc Seismicity

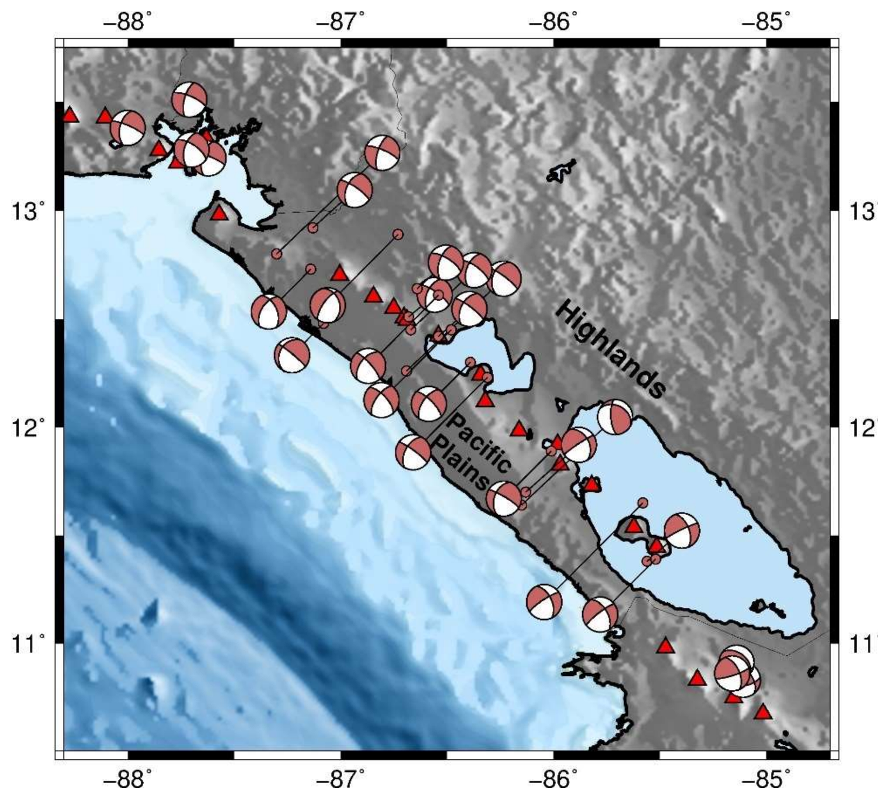

Figure **3-3:** Focal mechanisms of earthquakes for the Nicaraguan CAFA segment, with a maximum depth of 20 km and a minimum magnitude of M_w 5 from GCMT o(Dziewonski et al., 1981; Ekström et al., 2012).

Upper-plate seismicity, concentrated within the volcanic arc, has an upper magnitude limit of M_s 6.5 (White & Harlow 1993). The earthquake magnitude has been found to be modulated by the spacing of volcanic centers, where larger magnitude earthquakes occur between farther spaced volcanic centers (Cailleau et al., 2007; White & Harlow, 1993). While White & Harlow (1993) had noted the correlation, Cailleau et al. (2007), using finite element Coulomb failure stress analysis, demonstrated that shearing of the thermally weakened lithosphere of volcanic centers increases the stress in the stronger inter-volcano lithosphere, thereby promoting seismicity. The strike of historical seismicity within the CAFA is predominantly right-lateral (arc-parallel) (Alvarado et al., 2010; Martínez-Díaz et al., 2004; White et al., 1987) or left-lateral (arc-normal) (Algermissen et al., 1974;

Ambraseys et al., 2001; Brown et al., 1974; Harlow et al., 1993; Legrand et al., 2020; White & Harlow, 1993). In Nicaragua, either fault trend may be responsible for the CAFA-CA shear due to the ambiguity of the fault plane of focal mechanisms from instrument observed seismicity (LaFemina et al., 2002; Figure **3-3**).

Aftershock seismicity and co-seismic surface ruptures in Nicaragua have revealed that NE-trending left-lateral faults are predominantly active (LaFemina et al., 2002). The 1972 Ms 6.2 Managua earthquake occurred on the NNE-trending left-lateral Tiascapa fault, located within the active Managua Graben (Algermissen et al., 1974; Brown et al., 1974; Langer et al., 1974). The 1931 M 6 Managua occurred on the NNE-trending left-lateral Estadio fault, sub-parallel to the Tiscapa fault (White and Harlow 1993). Beyond the Managua Graben, the 1982 Ms 6.0 Gulf of Fonseco and 1985 M_w 6.1 Lake Nicaragua earthquakes were ruptures of NE-striking left-lateral faults (White and Harlow 1993; LaFemina et al., 2002). The well-instrumented August 3rd, 2005 M_w 5.3 and M_w 6.3 Ometepe Island/Lake Nicaragua earthquakes were ruptures on a NNW-striking (355°) right-lateral fault and a NE-striking (60°) left-lateral fault, respectively. Instrumented seismicity in Nicaragua indicates that primarily NE- and NNE-strike faults are active.

The April 10th, 2014 (M_w 6.1), September 15th, 2016 (M_w 5.7), and September 28th, 2016 (M_w 5.5) earthquakes represent the CAFA-CA shear in Nicaragua. The April 10th, 2014 earthquake occurred in Lake Managua and was preceded by a M_l 4.1 foreshock that was located east of the Momotombo volcano (INETER Bulletin, April 2014). Relocated aftershocks, the largest being M_w 5.3, and the focal mechanism of the mainshock indicate that the ruptured fault plane is 15 km long and trending to the northwest (Suárez et al., 2016). Four days later, a M_w 5.2 earthquake occurred ~20 km southeast from the mainshock in the vicinity of the Apoyoque volcano and appears to have its aftershocks (Suárez et al., 2016). The M_w 5.7 September 15th, 2016 earthquake was located on the eastern flanks of the El Hoyo volcano with a focal mechanism that implies faulting on a NE trending left-lateral fault (INETER Bulletin, September 2016; Alvarez et al., 2018). The focal mechanism for the 5.5 September 28th, 2016 also implies left-lateral motion on a northeast-trending fault (Alvarez et al., 2018). This earthquake was located on the western flanks of Momotombo (INETER Bulletin, September 2016).

3.2.3 Magma-Tectonic Interactions

Although rare, there have been instances where earthquakes within the volcanic arc are spatiotemporally correlated with or have been shown to promote volcanic eruptions. The 1917 San Salvador volcanic eruption was preceded by a Ms 6.4 earthquake that occurred 30 minutes before the eruption and 20 to 30 km west of the volcano (White et al., 1987). The August 1999 Maribios Range, Nicaragua earthquake swarm, with the largest being three M_w ~5.2, occurred in the vicinity of the Cerro La Mula-Cerro Negro volcanic center. Eleven hours after the three moderate magnitude (M ~5) earthquakes, a VEI 1, small volume (0.001 km^3) eruption occurred at the Cerro Negro volcano (La Femina et al., 2004). It was found that the earthquake sequence increased the static stress state around the volcano (Díez et al., 2005), which was optimally aligned to the volcano's lineament, thereby dilatating the magmatic plumbing system, allowing dike injection and the subsequent small and short-lived (2 days) eruption (La Femina et al., 2004). The VEI 2 2015 Momotombo eruption occurred after the M_w 6.1 April 10th, 2014 (INETER Bulletin, December 2015). The earthquake had an epicenter that was within 20 km of Momotombo (INETER Bulletin, April 2014).

3.3 Data

3.3.1 GPS

The faulting and coseismic slip of the three upper-plate earthquakes (i.e., the M_w 6.1 April 10th, 2014, M_w 5.7 September 15th, 2016, and M_w 5.5 September 28th, 2016) was determined using coseismic displacements estimated using campaign-style episodic GPS (eGPS) and continuous GPS (cGPS) time series. Daily static positions were produced by processing GPS data using the GIPSY-

OASIS 6.4 software with satellite ephemerides from the Jet Propulsion Laboratory (JPL). Phase ambiguity resolution was performed using the single receiver algorithm (Bertiger et al., 2010). Ocean loading corrections were applied using FES2004 (Lyard et al., 2006). Wet and dry tropospheric zenith delays are modeled with VMF1 mapping functions (Boehm et al., 2006). Final solutions were transformed into the IGb08 reference frame (Rebischung et al., 2012).

GPS coseismic displacements for cGPS stations were estimated by least-squares fitting Heaviside functions (Equation **3-1)** to the 20 days (centered on the earthquake day of occurrence) of daily static positions. For example, the September 15th and September 28th, 2016 earthquakes occurred temporally close together, which required the following function to determine the coseismic offsets at each GPS station. The Heaviside functions were

$$A_i H_{eq1}(t_i - t_{eq1}) + B_i H_{eq2}(t_i - t_{eq2}) \tag{3-3}$$

where $H_{eq1}(t)$ is the Heaviside function for coseismic displacement after the September 15th earthquake, A_i is the amplitude of the Heaviside function, and B_i is the amplitude of $H_{eq}\ (t)$, which is the Heaviside function for coseismic displacement after the September 28th earthquake. Afterslip was not observed after the earthquakes and therefore not estimated. The uncertainties for the displacements were estimated by the RMS of the residuals of the fitted function to positions ten days before and after each earthquake. For episodic GPS (eGPS) stations, earthquake displacements were calculated by determining the pre-event interseismic velocity and the difference of positions after the event compared to the expected positions predicted by the interseismic velocity. The differences of these epochs represent the permanent offset due to an earthquake. The coseismic displacements and uncertainties for the three earthquakes are detailed in Tables **3-1**, **3-2**, and **3-3** and Figures **3-4** to **3-9**.

Table **3-1**: GPS coseismic displacements for April 10, 2014 M_w 6.1 earthquake. Asterisks denote eGPS stations.

Station	**Longitude**	**Latitude**	**E (mm)**	**N (mm)**	**V (mm)**	**σE (mm)**	**σN (mm)**	**σV (mm)**
CALV	-86.8456	12.5724	-6	-1	1	6	5	250
CN22	-87.0447	12.3841	-5	-1	0	1	2	26
CNG2	-86.6993	12.5012	-5	0	3	5	3	8
HERH	-86.8310	12.6093	-2	-1	3	4	3	256
HOYN	-86.8281	12.5987	-3	-1	4	3	2	16
JCFI	-86.8283	12.6837	-1	-1	3	2	2	17
LEME	-86.9095	12.4274	-7	0	-3	2	2	7
MANA	-86.2490	12.1489	1	2	-1	2	2	123
MASN	-86.1576	11.9889	0	2	1	2	2	750
MOM0	-86.5409	12.4061	10	-59	-24	7	3	15
SCW2	-87.0209	12.6966	-3	-2	2	6	5	14
TECF	-86.8383	12.6031	-4	0	2	3	3	16
TELN	-86.8348	12.6064	-3	0	2	2	3	47
LAGA*	-86.3132	12.5663	-6	-11	-21	1	2	5
MMAR*	-86.7193	12.4375	-17	0	49	4	3	38
PAZC*	-86.5921	12.2948	-41	-11	-12	4	4	16
ROSA*	-86.3727	12.7524	-7	6	542	2	3	16
VIST*	-86.4869	12.7052	-9	-13	-11	4	4	3

Table **3-2**: GPS coseismic displacements for September 15th, 2016 M_w 5.7 earthquake.

Station	**Longitude**	**Latitude**	**E (mm)**	**N (mm)**	**V (mm)**	**σE (mm)**	**σN (mm)**	**σV (mm)**
CNG2	-86.6993	12.5012	10	-17	-5	3	3	11
ELMA	-86.6748	12.4658	-13	-42	-20	4	3	42
KIOS	-86.7017	12.4943	7	-13	-15	4	4	725
LEME	-86.9095	12.4274	-3	1	-3	3	3	7
MANA	-86.2490	12.1489	-1	1	5	2	2	150
MOGA	-86.5700	12.4412	36	0	4	6	3	85
MOM0	-86.5409	12.4061	12	-1	-1	4	4	23
MOM2	-86.5382	12.3922	8	2	-4	4	4	9
MOMC	-86.4845	12.4372	12	1	-3	3	2	226
MONE	-86.5187	12.4771	18	3	-3	4	3	39
POLS	-86.8129	12.6493	10	-9	-20	0	1	46
SCW2	-87.0209	12.6966	1	1	8	5	3	18
TECF	-86.8383	12.6031	-1	-2	-7	3	2	19
TELN	-86.8348	12.6064	-1	-2	-6	7	4	73

Table **3-3**: GPS coseismic displacements for September 28th, 2016 M_w 5.5 earthquake.

Station	**Longitude**	**Latitude**	**E (mm)**	**N (mm)**	**V (mm)**	**σE (mm)**	**σN (mm)**	**σV (mm)**
CN22	-87.0447	12.3841	-2	0	-4	3	2	26
CNG2	-86.6993	12.5012	3	-2	4	3	3	18
ELMA	-86.6748	12.4658	7	-7	-7	3	3	48
KIOS	-86.7017	12.4943	5	0	9	4	4	739
LEME	-86.9095	12.4274	0	1	5	4	3	10
MANA	-86.2490	12.1489	-1	2	0	2	2	141
MOGA	-86.5700	12.4412	6	3	13	6	3	114
MOM0	-86.5409	12.4061	13	1	9	3	3	33
MOM2	-86.5382	12.3922	10	-3	8	2	3	13
MOMC	-86.4845	12.4372	6	1	4	2	2	210
MONE	-86.5187	12.4771	6	4	3	3	2	60
POLS	-86.8129	12.6493	-6	10	8	0	1	105
SCW2	-87.0209	12.6966	-2	-1	-1	5	3	13
TECF	-86.8383	12.6031	-2	1	5	4	2	24
TELN	-86.8348	12.6064	-1	1	7	5	6	79

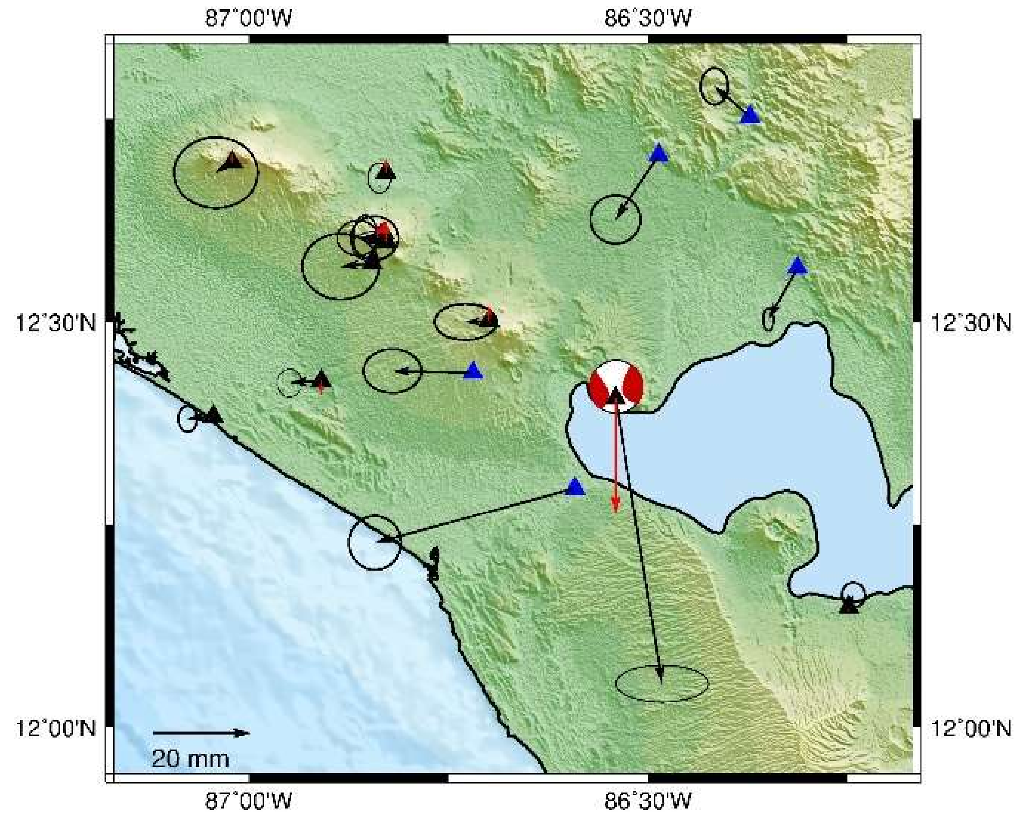

Figure **3-4**: GPS displacements for April 10, 2014 M_w 6.1 earthquake. Black vectors are horizontal displacements. Red vectors are vertical displacements. Blue triangles are eGPS stations. Black triangles are cGPS stations. Focal mechanisms from GCMT (Dziewonski et al., 1981; Ekström et al., 2012).

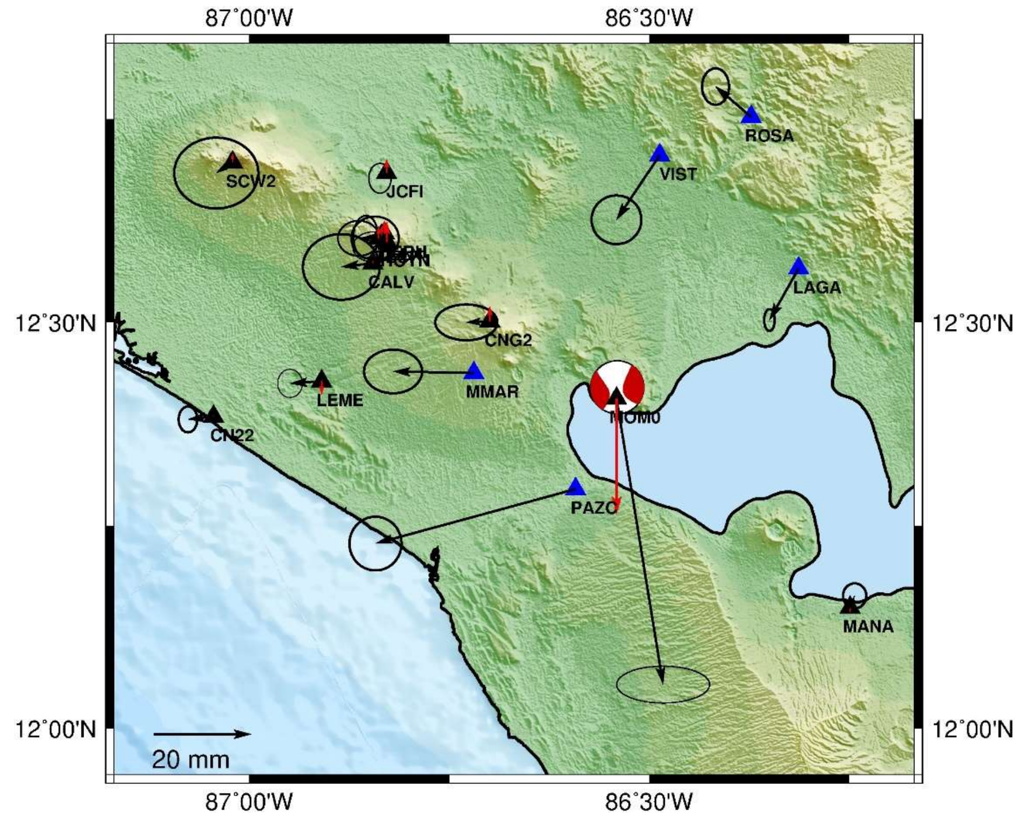

Figure **3-5**: Same as Figure **3-4** with GPS station names included.

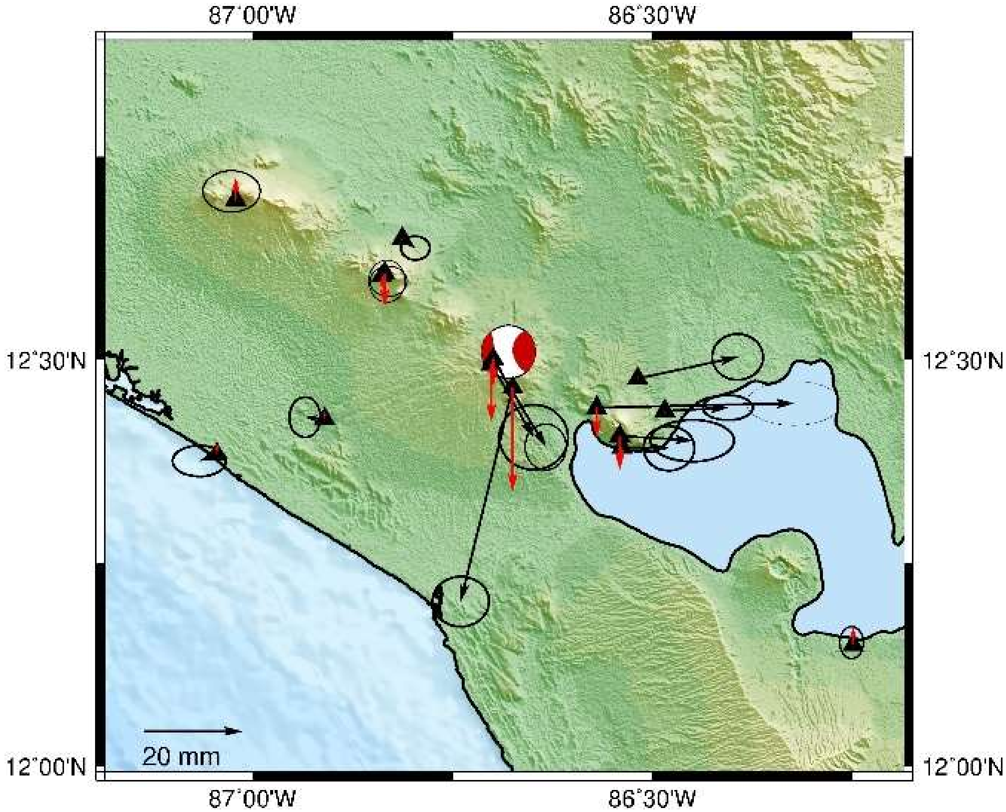

Figure **3-6**: GPS displacements for September 15th, 2016 M_w 5.7 earthquake. Black vectors are horizontal displacements. Red vectors are vertical displacements. Black triangles are cGPS stations. Focal mechanisms from GCMT (Dziewonski et al., 1981; Ekström et al., 2012).

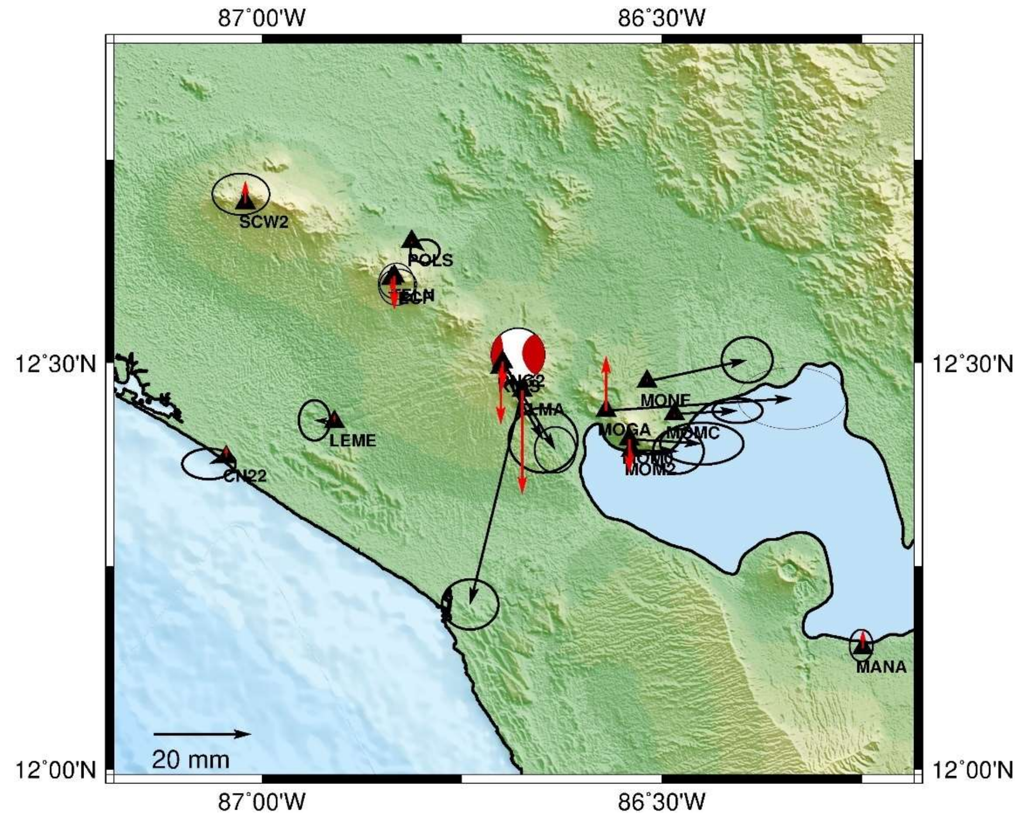

Figure **3-7**: Same as Figure **3-6** with GPS station names included.

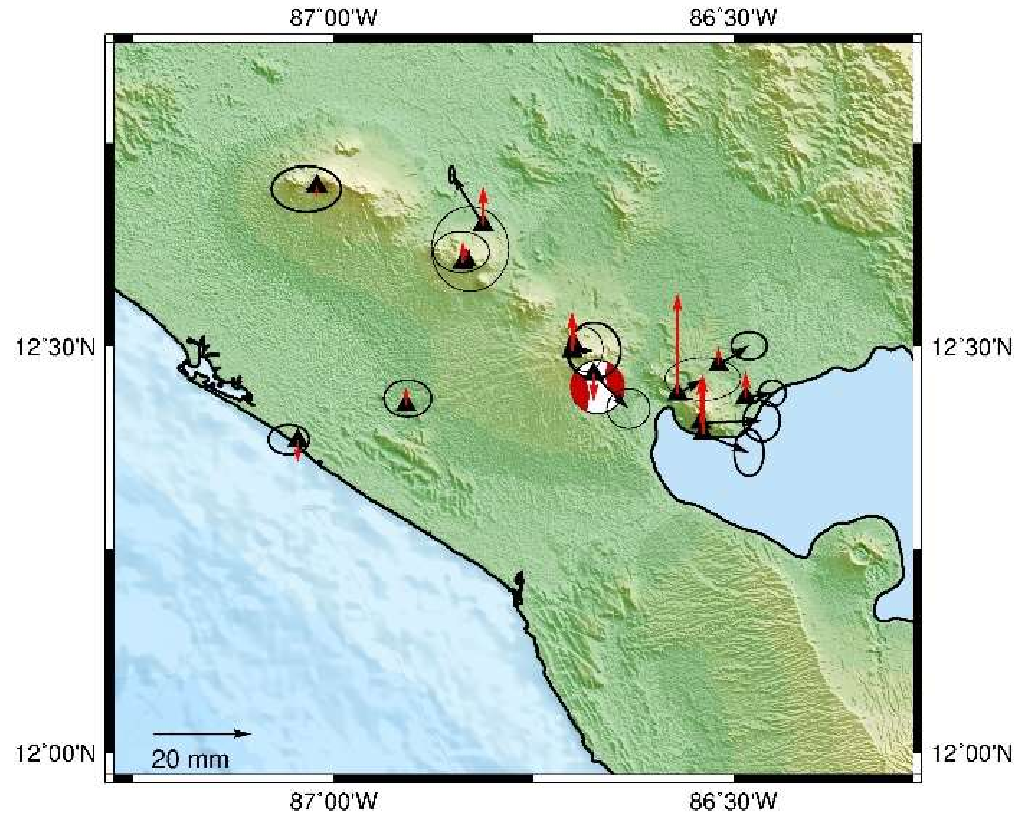

Figure **3-8**: GPS displacements for September 15th, 2016 M_w 5.7 earthquake. Black vectors are horizontal displacements. Red vectors are vertical displacements. Black triangles are cGPS stations. Focal mechanisms from GCMT (Dziewonski et al., 1981; Ekström et al., 2012).

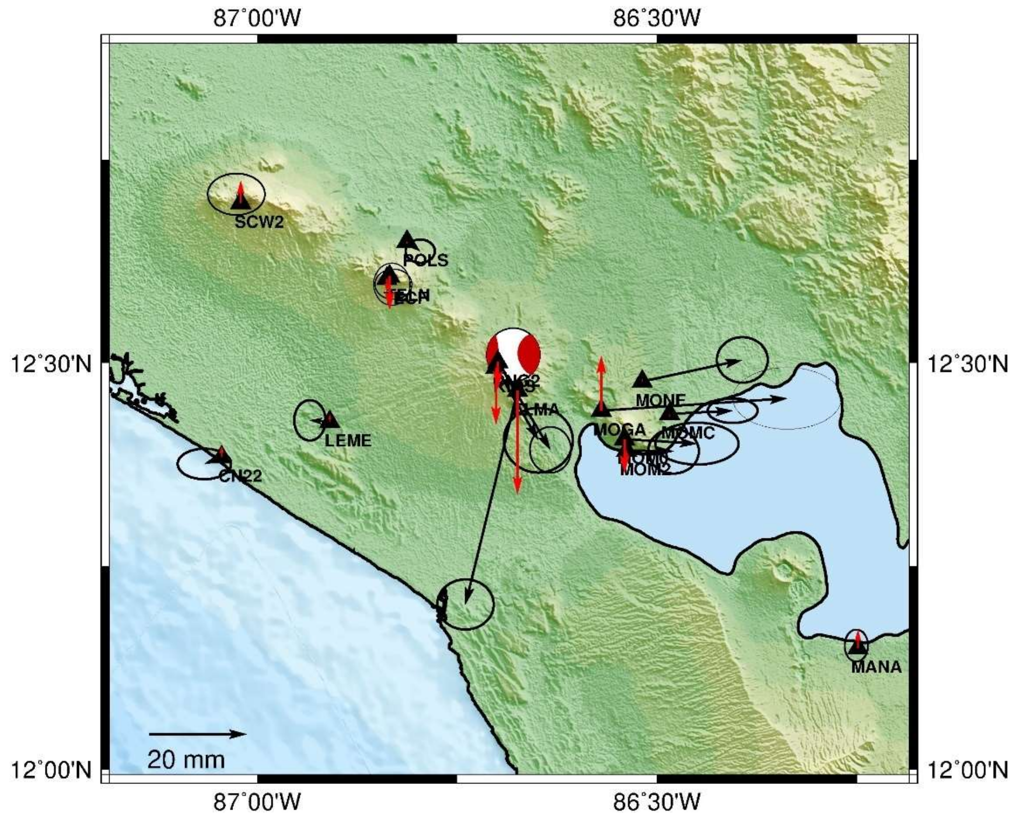

Figure **3-9**: Same as Figure **3-8** with GPS station names included.

3.3.2 Earthquake Data

GCMT focal mechanisms (Dziewonski et al., 1981; Ekström et al., 2012) for all three earthquakes will be used to constrain fault dimensions, depth, strike, and dip during inversion. The GCMT fault planes and double couple component for these earthquakes are detailed in Table **3-4** and Figure **3-10**.

Table **3-4**: GCMT fault planes for all three earthquakes.

		Fault Plane 1			**Fault Plane 2**		
Earthquake	**M_w**	**Strike**	**Dip**	**Slip**	**Strike**	**Dip**	**Slip**
2014-04-10	6.1	127	75	-173	35	84	-15
2016-09-15	5.7	212	85	-3	303	87	-175
2016-09-28	5.4	301	80	-171	210	82	-10

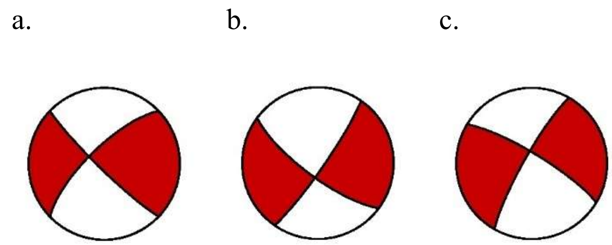

Figure **3-10**: Double couple component of (a) April 10th, 2014 (b), September 15th, (c) 2016, and September 28th, 2016 earthquakes. Focal mechanisms from GCMT (Dziewonski et al., 1981; Ekström et al., 2012).

3.4 Methods

This study aims to determine the kinematics and geometry of the three upper-plate earthquakes and ultimately shed light on the accommodation of CAFA-CA relative motion in Nicaragua. Inversion of these moderate magnitude earthquakes in western Nicaragua presents a problem that may have non-unique solutions due to data spatial coverage and signal-to-noise ratio. For this reason, a Bayesian approach was adopted for the inversion of the geodetic data. Bayesian optimization is usually employed for adjoint inversions or high-dimensional problems (e.g., Minson et al., 2014; Bagnardi and Hooper 2018) but is suited for this problem, where the region is not data-rich and inversion is being attempted on moderate-size earthquakes that produce sub-centimeter coseismic offsets for most GPS stations.

The upper-plate earthquakes may be a triggered sequence and, for this reason, static stress changes for these earthquakes will be explored. This study also investigates the possible role of the April 10th, 2014 earthquake in promoting the December 2015 Momotombo eruption. Normal stress changes will be analyzed from the resulting inversion yielding fault plane and coseismic slip to determine if the magmatic plumbing system was dilated to allow magma intrusion and ascent.

3.4.1 Earthquake Faulting and Slip Inversion

The Bayesian global optimization uses the Bayes Theorem (Bayes 1763), which can be summarized as the posterior probability of a model, given data, is proportional to the likelihood of data given the model and the prior probability of the model.

In applying a Bayesian framework to inversion, the problem has $\boldsymbol{D}$ data, $\boldsymbol{D} = \{d_1, .., d_n\}$, which corresponds to a model function $\boldsymbol{G}(\boldsymbol{\theta})$ with $\boldsymbol{\theta}$ vector of model parameters,

$$\boldsymbol{D} = \boldsymbol{G}(\boldsymbol{\theta}) + \boldsymbol{\epsilon}, \tag{3-4}$$

where the non-linear model, $\boldsymbol{G}$**,** is the modeled displacements computed by the Okada (1985) functions for the surface response to a planar motion in half-space, and $\boldsymbol{\epsilon}$ is noise present when evaluating $\boldsymbol{G}(\boldsymbol{\theta})$ that we assume to be Gaussian and zero mean. The Bayesian formulation for this inversion is

$$P(\boldsymbol{\theta}|\boldsymbol{D}) = \frac{P(\boldsymbol{D}|\boldsymbol{\theta})P(\boldsymbol{\theta})}{P(\boldsymbol{D})} \tag{3-5}$$

where $P(\boldsymbol{\theta}|\boldsymbol{D})$ is the posterior conditional probability distribution, $P(\boldsymbol{D}|\boldsymbol{\theta})$ is the likelihood, $P(\boldsymbol{\theta})$ is the prior distribution, and $P(\boldsymbol{D})$ is the probability distribution of $\boldsymbol{D}$. For the posterior distribution only the following is only considered

$$P(\boldsymbol{\theta}|\boldsymbol{D}) \propto P(\boldsymbol{D}|\boldsymbol{\theta})P(\boldsymbol{\theta}) \tag{3-6}$$

This function is updated during the inversion as more model parameters, $\boldsymbol{\theta}_i$, are sampled. This work takes the machine learning approach by modeling the likelihood as a Gaussian process (implemented in the GPML code, Williams and Rasmussen, 2006) since the model parameters are independent, joint probability distributions can be created. This procedure attempts to fit a Gaussian distribution to each parameter $\boldsymbol{\theta}_i$. The likelihood has the form

$$P(\boldsymbol{D}|\boldsymbol{\theta}) = \prod_{i}^{n} \frac{1}{2\pi} \exp\left(\frac{-\left\|\boldsymbol{D}_i - \boldsymbol{\theta}_i^T \boldsymbol{w}\right\|^2}{2}\right) \quad \textbf{3-7}$$

$$P(\boldsymbol{D}|\boldsymbol{\theta}) = \frac{1}{(2\pi)^{-n/2}} \exp\left(\frac{-\|\boldsymbol{D} - \boldsymbol{\Theta w}\|^2}{2}\right) \quad \textbf{3-8}$$

where n is the number of samples for a parameter, $\boldsymbol{\Theta}$ is the m x n matrix of evaluated parameters values of the model, and $\boldsymbol{w}$ is the weighting in the linear Gaussian process regression $f(\boldsymbol{\theta}) = \boldsymbol{\theta w}$. The weights are a zero-mean Gaussian with covariance matrix Σ_p, which is the noise introduced during sampling.

The advantage of using this framework is that the sampling strategy is directly informed by the posterior probability of the model. In this work, the Gaussian process regression is used to govern sampling. The sampling strategy use the mean function ($\mu(\boldsymbol{\theta})$) of the Gaussian process and covariance function that is the Matérn 5/2 order kernel. The mean function is

$$\mu(\boldsymbol{\theta}) = \mathbb{E}[f(\boldsymbol{\theta})] \quad \textbf{3-9}$$

and the Matérn 5/2 order kernel is (see Snoek et al., 2012)

$$k(\theta_p, \theta_q) = \left(1 + r\sqrt{5} + \frac{5r^2}{3}\right) \exp\left(-r\sqrt{5}\right) \quad \textbf{3-10}$$

where

$$r^2(\theta_p, \theta_q) = \sum_{p,q} (\theta_p - \theta_q)^2 \quad \textbf{3-11}$$

for each model parameter. Model parameters are not correlated and are assumed to be independent. The variable θ_p and θ_q are values of a parameter that were previously evaluated and selected to update the posterior.

Using the mean and covariance functions, the selection criterion was implemented as the Expected Improvement method (Schonlau et al., 1998; Jones et al., 1998), which determines which model parameters values should update the posterior. Consider that the probability of improvement for a set of parameter samples is

$$\gamma(\widehat{\boldsymbol{\theta}}) = \frac{f^*(\boldsymbol{\theta}_{best}) - \mu(\boldsymbol{\theta})}{k(\boldsymbol{\theta}, \widehat{\boldsymbol{\theta}})} \qquad \textbf{3-12}$$

where $\widehat{\boldsymbol{\theta}}$ is the set of sample parameter values that are chosen at random from $\pm\sigma$ of the probability density function of $\boldsymbol{\theta}$, $\boldsymbol{\theta}_{best}$ is the parameter sample from the previous selected model parameters, and f^* is the Gaussian process predicted value. Denoting the cumulative distribution function and the probability density function $\widehat{\boldsymbol{\theta}}$ respectively as $\Phi(\widehat{\boldsymbol{\theta}})$ and $\phi(\widehat{\boldsymbol{\theta}})$, the Expected Improvement is

$$EI(\widehat{\boldsymbol{\theta}}) = \begin{cases} ((\mu(\boldsymbol{\theta}) - G(\boldsymbol{\theta}_{best}) - \xi)\Phi(\gamma) + k(\boldsymbol{\theta}, \widehat{\boldsymbol{\theta}})\phi(\gamma), & k(\boldsymbol{\theta}, \widehat{\boldsymbol{\theta}}) < 0 \\ 0, & k(\boldsymbol{\theta}, \widehat{\boldsymbol{\theta}}) = 0 \end{cases} \qquad \textbf{3-11}$$

The ξ term is considered the exploration-exploitation or greedy term. A value of 0.005 was found to yield quick solution convergence using 13 synthetic GPS displacement data for a M_w 5.7 earthquake with added normal noise of $\sigma = 3\ mm$, equivalent to the uncertainties in the observed displacements (Figure **3-11**). The inversion of the synthetic data used model parameter constraints that are described at the end of this section. During sampling, if, after a predetermined number of iterations, the new best scoring samples are the comparable within a predefined threshold (10^{-3}) of the selected samples from the previous iteration, a random jump is done. This inversion strategy employs maximum ignorance for the priors. Before inversion, priors are built with 100 random samples for each parameter within specified constraint ranges. Uncertainties were estimated from the resulting probability distribution of $\boldsymbol{\theta}$.

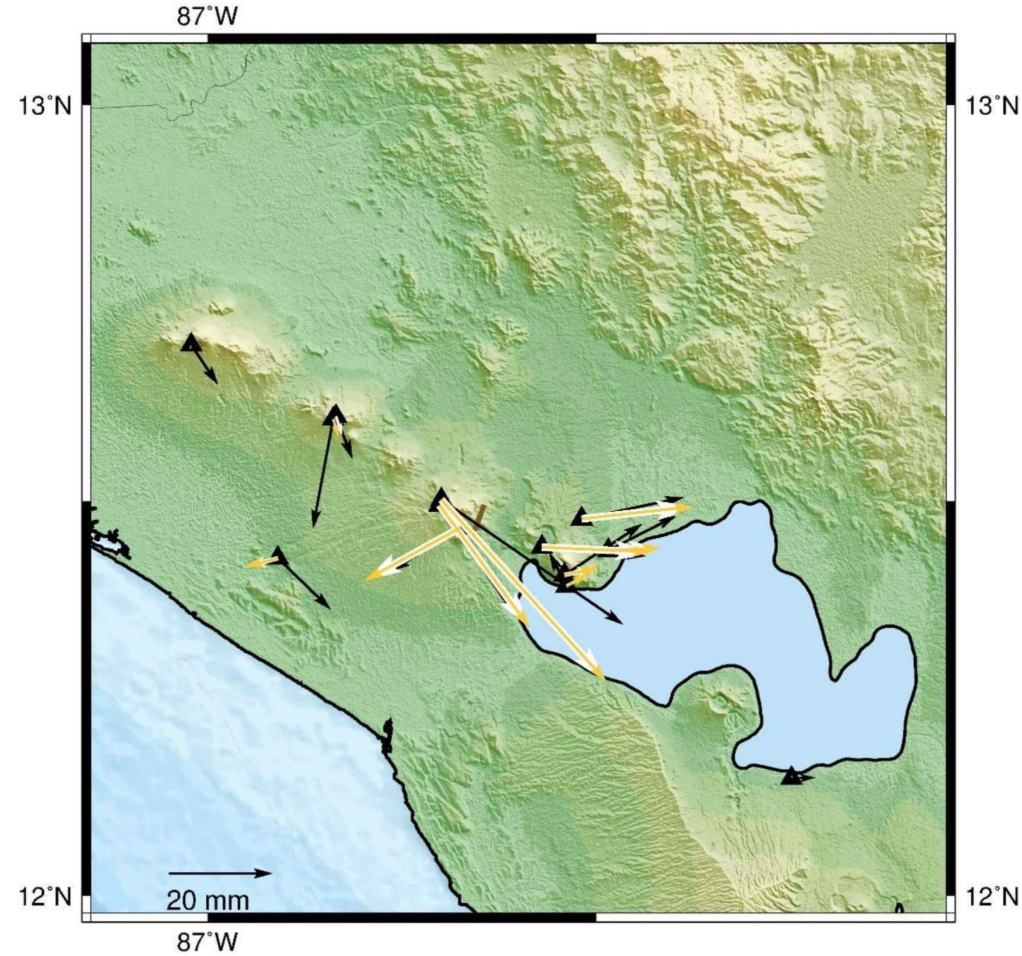

Figure **3-11**: Inversion of a synthetic model with random normal noise ($\sigma = 3\ mm$) introduced to displacements. Misfit for noiseless data is 0.00001 mm, while the misfit for displacements with normal noise is 0.003 mm. White vectors are noise-less synthetic displacements, black vectors are synthetic displacements with normal noise added, and gold vectors are modeled displacements. Brown line is the fault trace of the synthetic model.

The inversion sought the best model fit using the 10 parameters detailed in Table **3-5**.

Table **3-5**: Inversion model parameters.

Inversion Model Parameters
Fault surface trace start (x_i, y_i)
Fault surface trace end (x_f, y_f)
Fault top depth
Fault width down-dip
Fault dip
Strike-slip displacement of the fault
Dip-Slip displacement of the fault
Poisson Ratio

The constraints on these parameters during the inversion of each earthquake are detailed below. For all inversions, strike-slip and dip-slip components of displacements were constrained based on the moment magnitude of the earthquake, and the fault dip was allowed to exceed 90° in case the fault trace was reversed.

During inversion, eGPS measured displacements were downweighted. Likewise, the vertical displacements observed at all GPS stations were also downweighted. The inversion was further constrained by applying a penalty (WRMS +50) for a model that yields a moment magnitude larger than the GCMT reported moment magnitude. Model uncertainties were calculated from the parameter probability density distribution.

3.4.1.1 April 10th, 2014 Mw 6.1 Model Constraints

Coseismic displacements were inverted for two models for the April 10th, 2014 (M_w 6.1) earthquake. A through-going right-lateral fault is the simplest mode to accommodate CAFA-CA shear. For this reason, the first model allowed right-lateral coseismic slip with the fault dip fixed to be vertical (Table **4-6**). A second inversion also only allowed right-lateral coseismic slip but the fault dip was also estimated (Table **3-7**). A third inversion was also conducted that inverted for both dip- and strike-slip (oblique-slip) motion (Table **3-8**). The initial fault trace for all three models was guided by relocated aftershocks that were provided by Karen Fischer at Brown University.

Table **3-6**: Constraints for right-lateral-slip-only with fixed vertical dip inversion for April 2014 earthquake coseismic displacements.

Initial Fault Trace	86.40°W, 12.24°N
	86.55°W, 12.40°N
Initial Fault Length	24 km
Initial Fault Strike	135°
Fault Trace Constraints	± 10 km
Fault Top Depth	0 km to 15 km
Fault Width	2 km to 8 km
Right-Lateral Slip	0.2 m to 0.9 m
Poisson Ration	0.3 to 0.4

Table **3-7**: Constraints for right-lateral-slip-only inversion for April 2014 earthquake coseismic displacements.

Initial Fault Trace	86.40°W, 12.24°N
	86.55°W, 12.40°N
Initial Fault Length	24 km
Initial Fault Strike	135°
Fault Trace Constraints	± 10 km
Fault Top Depth	0 km to 15 km
Fault Width	2 km to 8 km
Fault Dip	70° to 90°
Right-Lateral Slip	0.2 m to 0.9 m
Poisson Ration	0.3 to 0.4

Table **3-8**: Constraints of inversion for April 2014 earthquake coseismic displacements, allowing oblique slip.

Initial Fault Trace	86.40°W, 12.24°N
	86.55°W, 12.40°N
Initial Fault Length	24 km
Initial Fault Strike	135°
Fault Trace Constraints	± 10 km
Fault Top Depth	0 km to 15 km
Fault Width	2 km to 8 km
Fault Dip	70° to 90°
Right-Lateral Slip	0.2 m to 0.9 m
Dip-Slip Slip	-1.0 to 0 m
Poisson Ration	0.3 to 0.4

3.4.1.2 September 15th, 2016 Mw 5.7 Model Constraints

Constraints for inversion of the M_w 5.7 September 15th, 2016 earthquake are detailed in Table **3-9**. The initial fault trace is guided by the epicenter reported by INETER (INETER Bulletin, September 2016). A second inversion was performed where the fault plane and coseismic slip of the mainshock and a possibly triggered event were jointly inverted. The second event is the shallow (<2 km) mb 4.7 earthquake that occurred 5 minutes after the mainshock (Figure **3-12**). Constraints for the two-earthquake joint inversion are detailed in Table **3-10**. Right-lateral slip was allowed for the inversion of the triggered earthquake because slip on a NW trending right-lateral fault could represent the residuals observed from the first model.

Table **3-9**: Constraints of inversion for the September 15th, 2016 earthquake.

Initial Fault Trace	86.60°W, 12.50°N 86.66°W, 12.45°N
Initial Fault Length	8.5 km
Initial Fault Strike	50°
Fault Trace Constraints	± 8 km
Fault Top Depth	0.5 km to 9 km
Fault Width	2 km to 6 km
Fault Dip	70° to 90°
Right-Lateral Slip	-0.9 m to 0.6 m
Dip-Slip	-0.9 m to 0 m
Poisson Ration	0.3 to 0.4

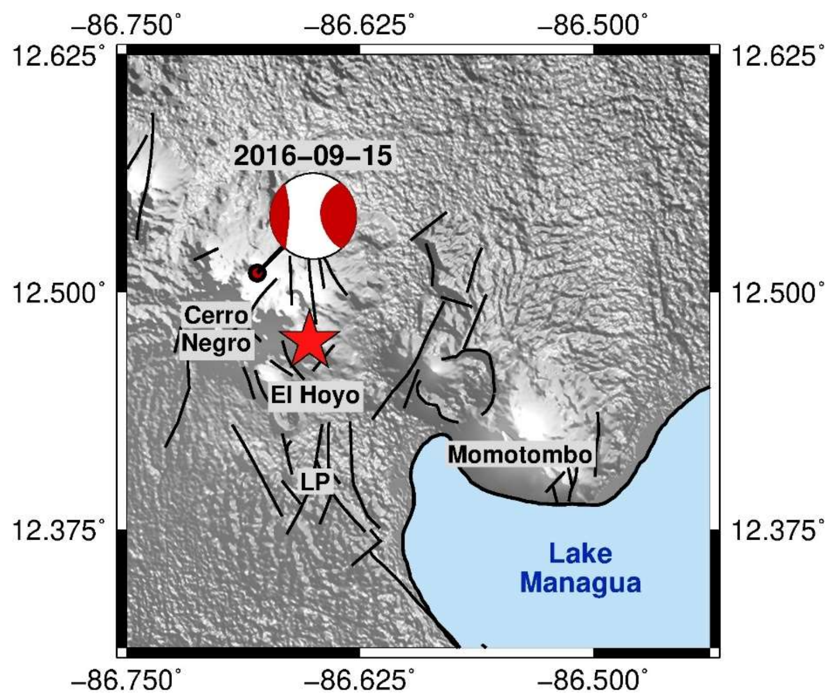

Figure **3-12**: GCMT epicenter of September 15th, 2016 earthquake and subsequent INETER reported epicenter of triggered mb 4.7 earthquake (star) that occurred five minutes after the mainshock. LP – La Paz Centro fault zone. Faults modified from La Femina et al., (2004).

Table **3-10**: Constraints of inversion for September 15th, 2016 earthquake for both the mainshock and a triggered earthquake.

	Mainshock	**Triggered Earthquake**
Initial Fault Trace	86.66°W, 12.45°N	-86.71°W, 12.46°N
	86.60°W, 12.50°N	-86.67°W, 12.50°N
Initial Faul Length	8.5 km	6 km
Initial Fault Strike	50°	50°
Fault Trace Constraints	± 8 km	± 8 km
Fault Top Depth	0.5 km to 9 km	0.5 km to 9 km
Fault Width	2 km to 6 km	2 km to 6 km
Fault Dip	70° to 90°	70° to 90°
Right-Lateral Slip	-0.9 m to 0.6 m	-0.1 m to 0.0 m
Dip-Slip	-0.9 m to 0 m	-0.1 m to 1.0 m
Poisson Ration	0.3 to 0.4	0.3 to 0.4

3.4.1.3 September 28th, 2016 Mw 5.5 Model Constraints

Most GPS stations observed sub-centimeter displacement for the M_w 5.5 September 28th, 2016 earthquake. To address the paucity of data and associated uncertainty (σ = ~3 mm), two inversions were carried out with fault traces constrained to known geomorphic structures. The first model was highly spatially constrained (± 5 km) on a NE-SW trending structure on the western flank of Momotombo (Figure **3-12** & Table **3-11**). The second model was, to a lesser degree, spatially constrained (± 20 km) to the La Paz Centro fault zone (Figure **3-12**; Table **3-12**).

Table **3-11**: Constraints of inversion for September 28th, 2016 earthquake, spatially constrained to the western flank of Momotombo.

Initial Fault Trace	86.58°W, 12.43°N
	86.56°W, 12.48°N
Fault Trace Constraints	± 5 km
Fault Depth*	0.5 km to 9 km
Fault Width	2 km to 6 km
Fault Dip	70° to 90°
Right-Lateral Slip	-0.7 m to 0.7 m
Dip-Slip	-0.6 m to 0.1 m
Poisson Ration	0.3 to 0.4

Table **3-12**: Constraints of inversion for September 28th, 2016 earthquake, spatially constrained to La Paz Centro fault zone.

Initial Fault Trace	86.64°W, 12.39°N
	86.61°W, 12.35°N
Fault Trace Constraints	± 20 km
Fault Depth*	0.5 km to 9 km
Fault Width	2 km to 6 km
Fault Dip	70° to 90°
Right-Lateral Slip	-0.7 m to 0.7 m
Dip-Slip	-0.6 m to 0.1 m
Poisson Ration	0.3 to 0.4

3.4.2 Static Stress Change

Following the inversion of the three upper-plate earthquakes in Nicaragua, the static stress changes induced by these earthquakes were determined. The three (or possibly four) earthquakes may have been a triggered sequence. Coulomb failure stress analysis (ΔCFS) was performed on the four previously described models of the April 10th, 2014 and September 15th, 2016 earthquakes. This analysis was also extended to determine if the stress change from the April 10th, 2014 earthquake is correlated with the December 1st, 2015 Momotombo eruption.

Several ΔCFS calculations were carried out to determine if these earthquakes were a triggered sequence. The ΔCFS induced by the April 10th, 2014 earthquake was determined for a left-lateral receiver fault with the strikes of 40° that is the average strike of the fault planes of the besting fitting models for the September 2016 earthquakes. To investigate if the April 10th earthquake may have pushed the seismically active faults of the Managua graben closer to failure, a ΔCFS analysis was performed for a left-lateral receiver fault, which is north-striking (N0°S) and a vertical dip. The ΔCFS of the September 15th, 2016 earthquake was determined for several receiver faults. First, the ΔCFS was calculated for the left-lateral receiver fault of the September 28th earthquake which had a strike of 55° and dip of 85°. Then the ΔCFS was calculated for the receiver fault of the triggered earthquake of the September 15th mainshock-triggered earthquake model. The inversion of this model yielded a fault plane for the triggered earthquake with a strike of 47° and a dip of 86°. Considering that the faulting and coseismic slip for the mainshock of both the one-fault and mainshock-triggered earthquake models are equivalent, the mainshock-triggered earthquake model will be used for ΔCFS analysis.

The December 1st Momotombo eruption may have been due to positive normal stress change from the April 10th earthquake, which would induce fault/dike dilation. To investigate possible dike dilatation, the ΔCFS and normal stress change from the preferred model for the April 2014 earthquake were calculated for a normal receiver fault with a dip of 90° and a strike of 30°. This strike was chosen because it approximates the trend of many lineaments and surface ruptures mapped in the vicinity of Momotombo after the earthquake (INETER Bulletin, April 2014).

3.5 Results

3.5.1 Earthquake Fault Geometry and Kinematics

Upper-plate earthquakes in Nicaragua represent the partial moment release of the CAFA-CA shear accommodation. Identifying the faulting and sense of motion of these earthquakes also reveals the mode in which shear is being accommodated. Below, the results of inversion of GPS coseismic displacements for the three upper-plate earthquakes (M_w 6.1 April 10th, 2014, M_w 5.7 September 15th, 2016, and M_w 5.5 September 28th, 2016) are presented.

3.5.1.1 April 10th, 2014

Three models were derived in the inversion of coseismic displacements for the April 2014 earthquake: (1) right-lateral coseismic slip with fixed vertical dip, (2) right-lateral coseismic slip, and (3) oblique coseismic slip. All models produced faults with similar trends (NW) but differing fault widths, depths, dips, and coseismic slip (Figures **3-13**, **3-14**, & **3-15**). The model that only allowed right-lateral slip with a fixed depth produced slip of 0.9 m. While the other two models produced equivalent amounts of right-lateral slip (~0.6 m). The model where the dip was fixed to be vertical and only allowed right-lateral slip has a depth of the top of the fault being 1.9 km, a fault length of 16 km, and a width of 6.1 m (Table **3-13**). The right-lateral-slip-only model has a fault depth that is almost at the surface (0.5 km), a length of 16 km, and dips to NE (Table **3-14**). The oblique-slip model has a fault depth of ~3 km, a much longer length (~27 km), and dips to the SW (Table **3-15**). The misfit for the oblique-slip model (21.9) shows an improvement of the right-lateral-slip-only vertical dip model (38.7) and the right-lateral-slip-only model's misfit (40.5). F-tests were carried out to determine which model most likely represents the observed displacements. The right-lateral with fixed vertical dip model most likely fits the observed displacements than the right-lateral model, where inversion yielded a dip of 85° (F-value of 3.2). There is a 94% probability that the right-lateral with a vertical dip model fits the data better than the right-lateral slip model. The F-value, and probability of the oblique-slip model better fitting the data than the right-lateral model is 2.4, and 90%, respectively. There is a 99% probability that the oblique-slip model fits the data better than the model with right-lateral slip and vertical dip, with an F-value of 23.1. The parameter joint distributions for all models are plotted in Figures **3-16**, **3-17**, and **3-18**. The PDFs for all models are plotted in Figures **3-19**, **3-20**, and **3-21**.

Table **3-13**: Faulting parameters for the right-lateral-slip-only and fixed vertical dip model for the April 10th, 2014 earthquake.

Strike	314° ± 4°
Fault Depth	1.9 ± 2.7 km
Fault Length	16.1 ± 3.7 km
Fault Width	6.1 ± 1.0 km
Strike-Slip Displacement	0.9 ± 1.2 m
Poisson Ratio	0.37 ± 0.1
Equivalent Mw	6.2
Misfit	38.7

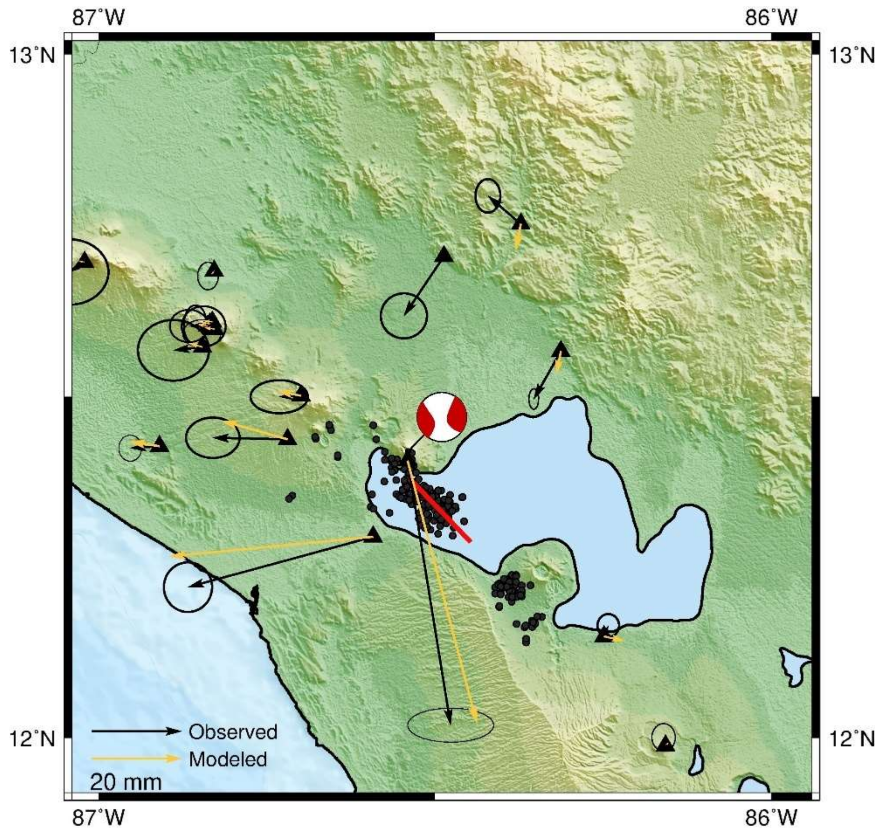

Figure **3-13**: Inversion results for the right-lateral-slip-only with fixed vertical dip model for the April 10th, 2014 earthquake. Black vectors are observed displacements. Yellow vectors are modeled displacements. Relocated aftershocks provided by Karen Fischer, Brown University. Focal mechanisms from GCMT (Dziewonski et al., 1981; Ekström et al., 2012).

Table **3-14**: Faulting parameters for the right-lateral-slip-only model for the April 10th, 2014 earthquake.

Strike	313° ± 5°
Dip	78° ± 7°
Fault Depth	0.5 ± 1.5 km
Fault Length	16.1 ± 3.7 km
Fault Width	7.3 ± 1.1 km
Strike-Slip Displacement	0.6 ± 0.8 m
Poisson Ratio	0.32 ± 0.1
Equivalent Mw	6.1
Misfit	40.5

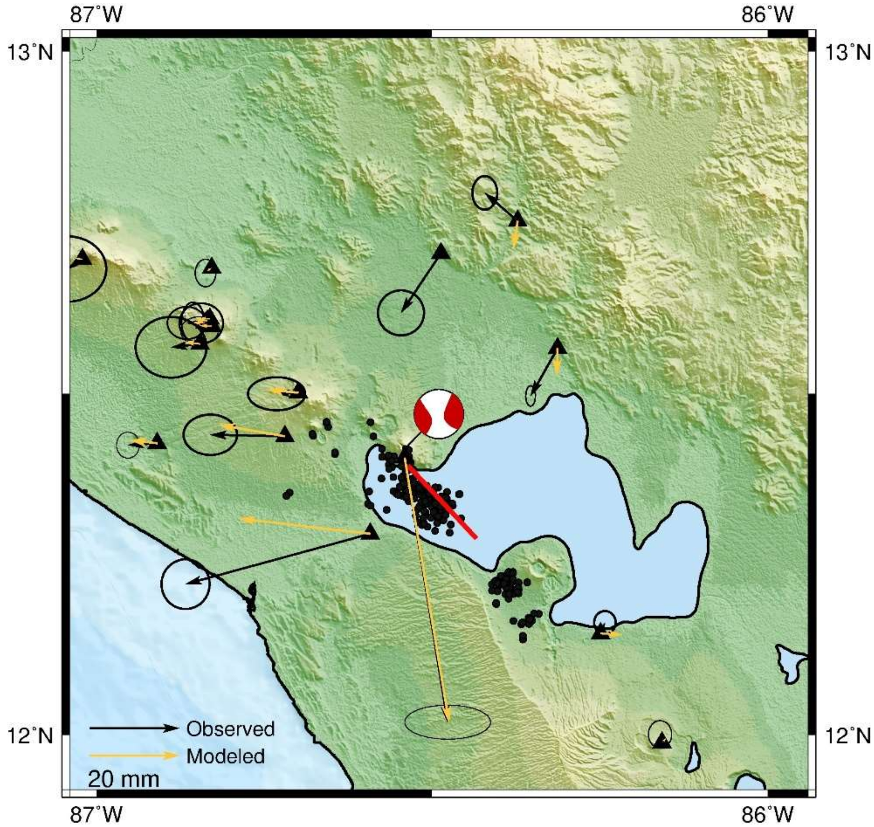

Figure **3-14**: Inversion results for the right-lateral-slip-only model for the April 10th, 2014 earthquake. Black circles are relocated aftershocks that have been translated to the strike of the modeled fault plane. Black vectors are observed displacements. Yellow vectors are modeled displacements. Relocated aftershocks provided by Karen Fischer, Brown University. Focal mechanisms from GCMT (Dziewonski et al., 1981; Ekström et al., 2012).

Table **3-15**: Faulting parameters for the oblique-slip model for the April 10th, 2014 earthquake.

Strike	140° ± 6°
Dip	79° ± 13°
Fault Depth	2.9 ± 4 km
Fault Length	26.7 ± 4.3 km
Fault Width	4.4 ± 1.4 km
Strike-Slip Displacement	0.65 ± 0.13 m
Dip-Slip Displacement	0.67 ± 0.17 m
Poisson Ratio	0.38 ± 0.1
Equivalent Mw	6.2
Misfit	21.9

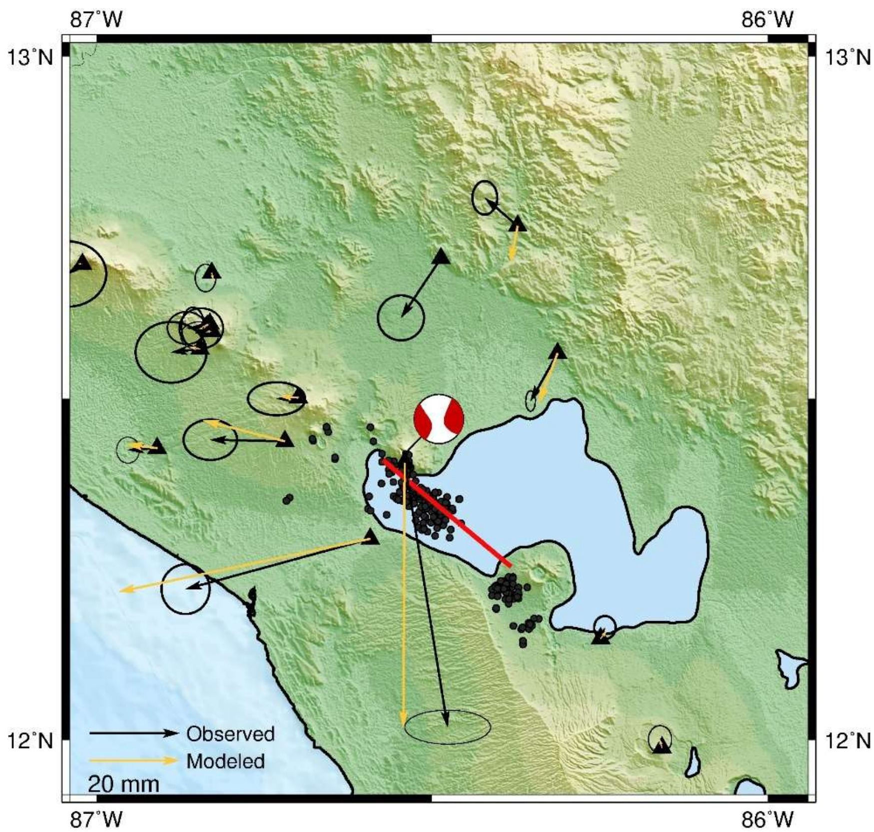

Figure **3-15**: Inversion results for the oblique-slip model for the April 10th, 2014 earthquake. Earthquake symbols are the same as in Figure **3-14**. Focal mechanisms from GCMT (Dziewonski et al., 1981; Ekström et al., 2012).

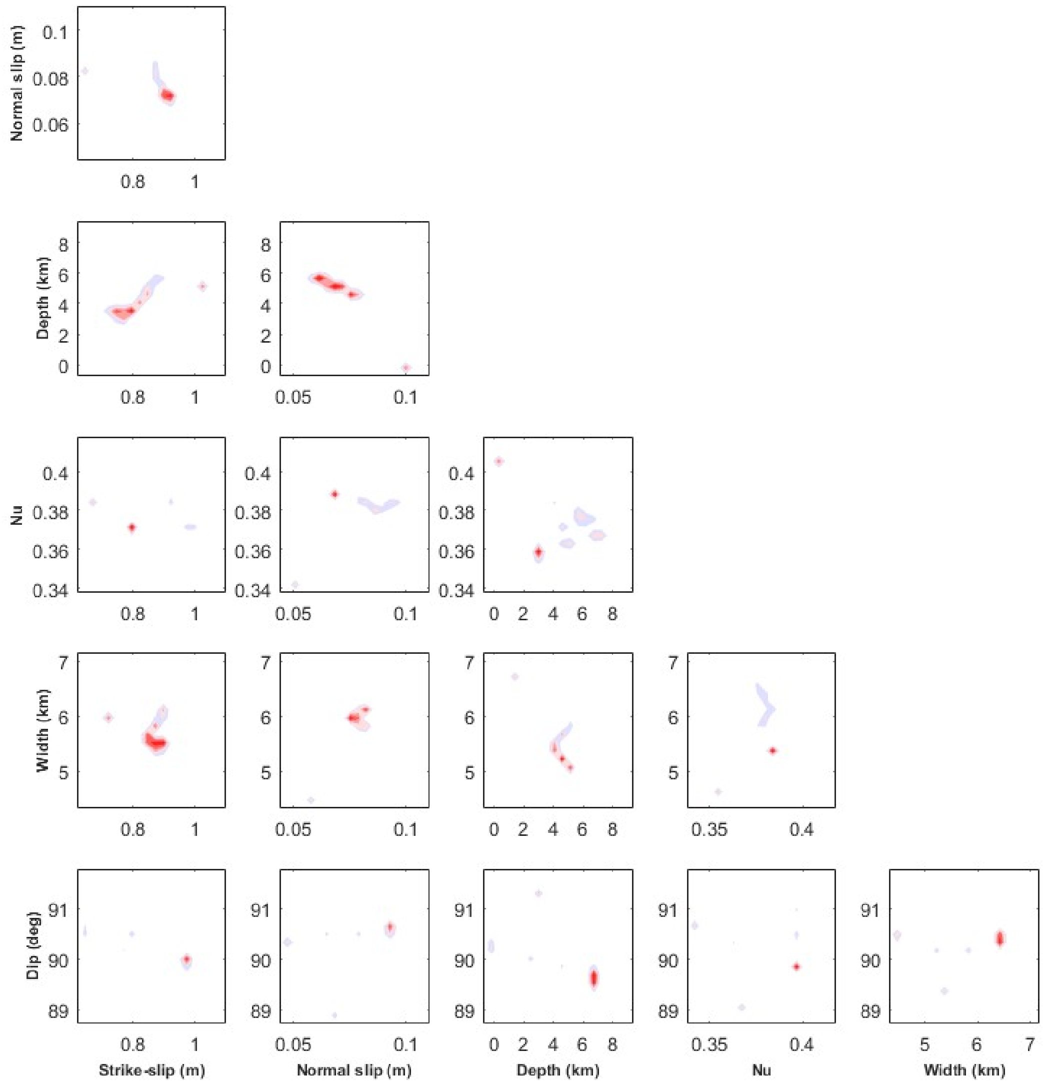

Figure **3-16**: Parameter joint distribution limited to 2σ for inversion results for the right-lateral slip with fixed vertical dip model for the April 10th, 2014 earthquake.

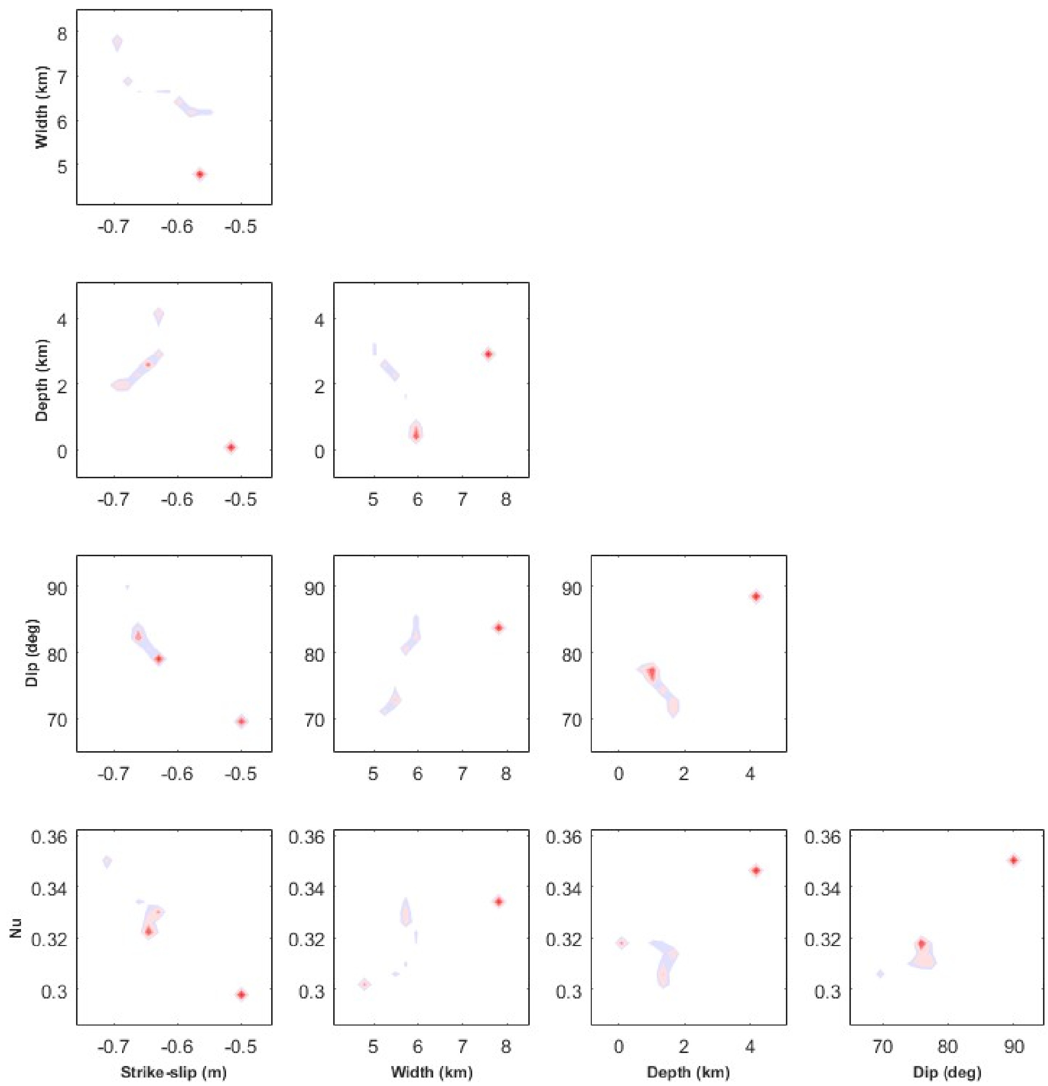

Figure **3-17**: Parameter joint distribution limited to 2σ for inversion results for the right-lateral-slip-only model for the April 10th, 2014 earthquake.

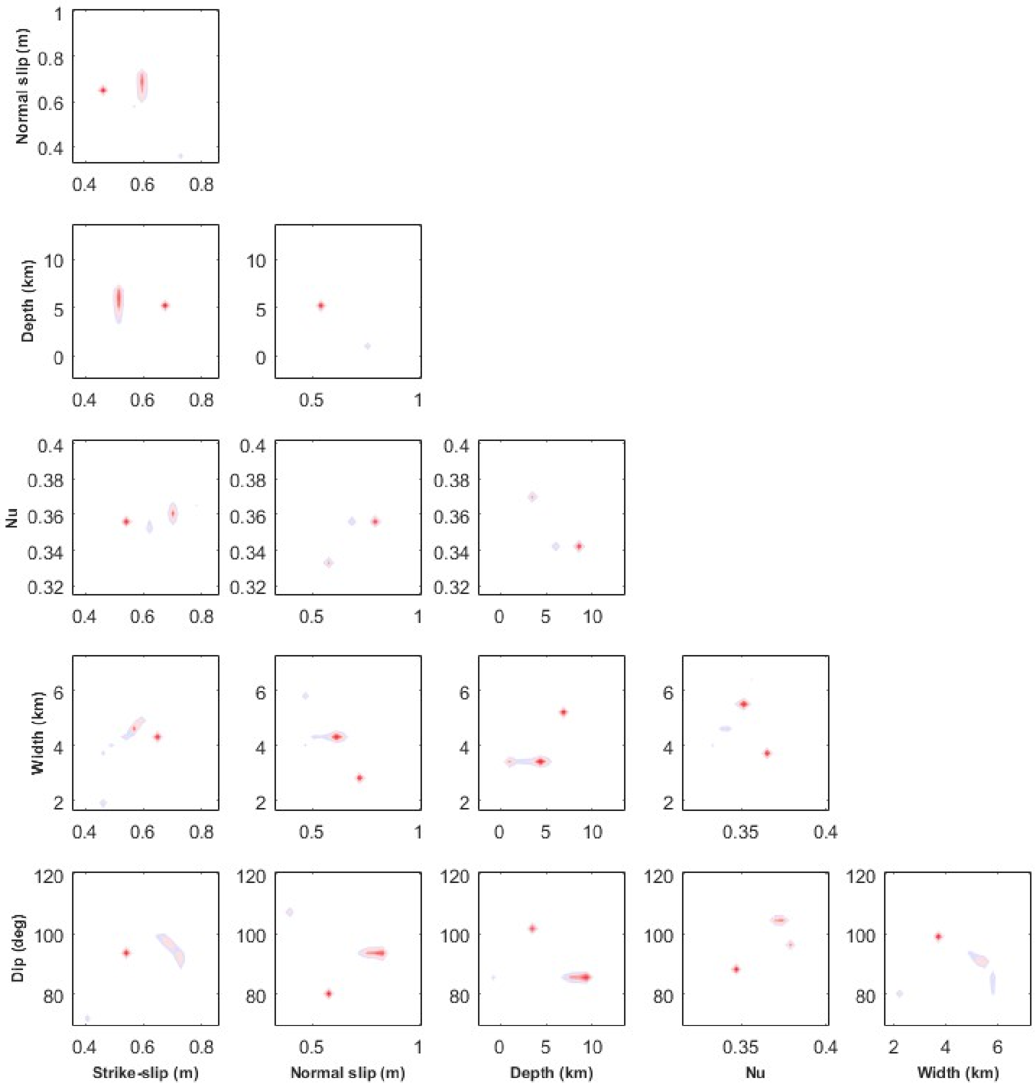

Figure **3-18**: Parameter joint distribution limited to 2σ for inversion results for the oblique-slip model for the April 10th, 2014 earthquake.

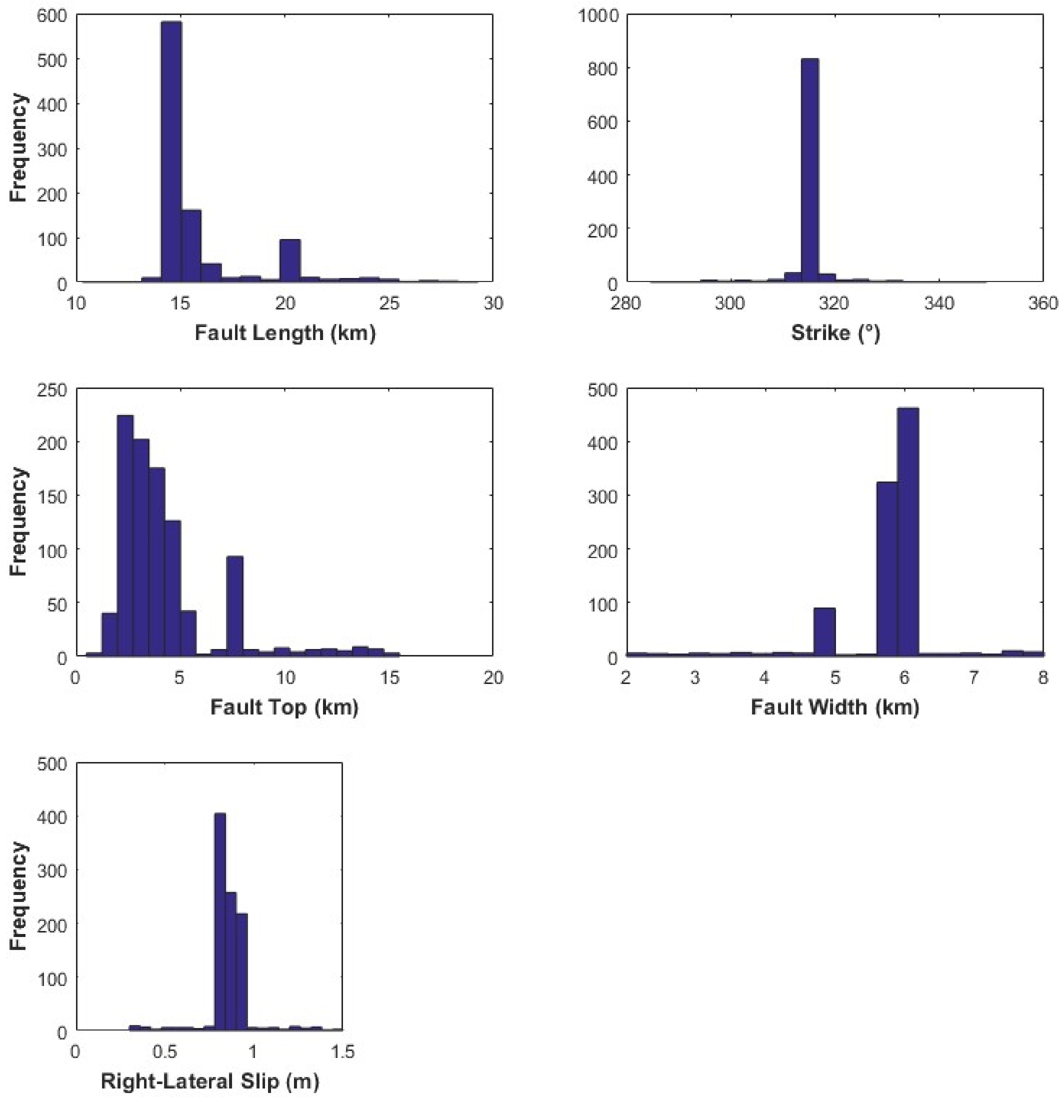

Figure **3-19**: Parameter probability density function for the model that only allowed right-lateral slip with a fixed vertical dip for the April 10th, 2014 earthquake.

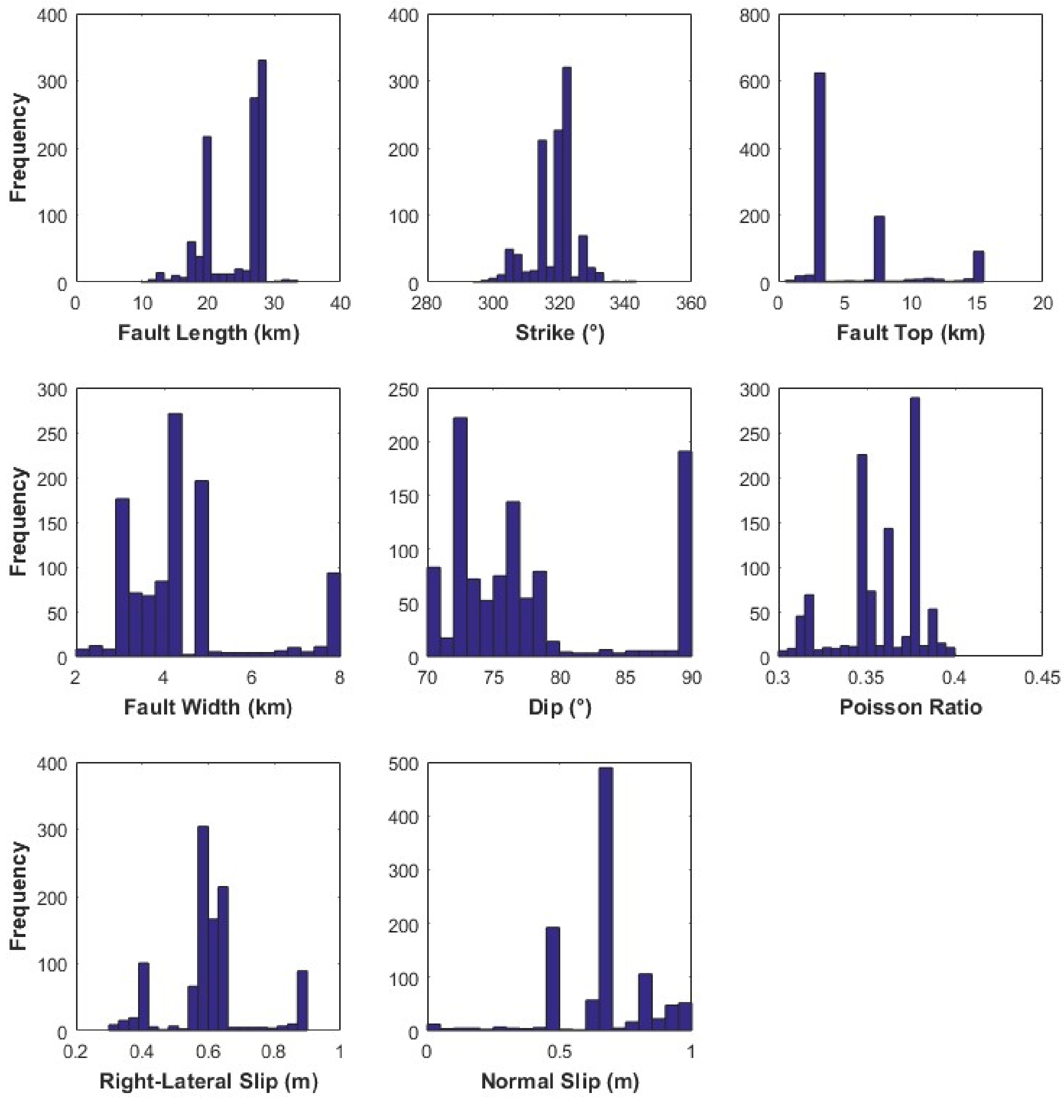

Figure **3-20**: Parameter probability density function for right-lateral-only slip model for the April 10th, 2014 earthquake.

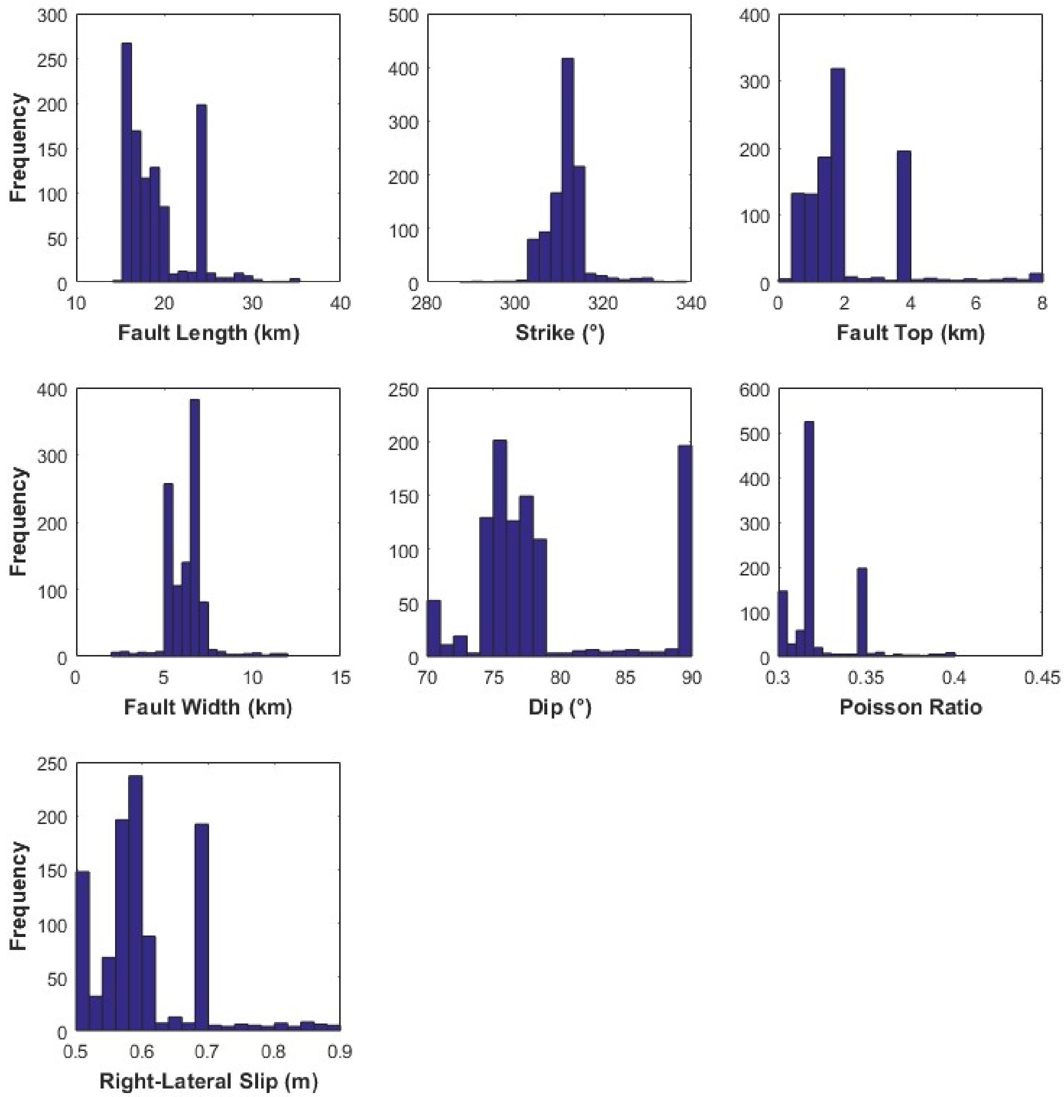

Figure **3-21**: Parameter probability density function for the oblique-slip model for the April 10th, 2014 earthquake.

3.5.1.2 September 15th, 2016

Two inversions of the coseismic displacements for the M_w 5.7 September 15th, 2016 earthquake were carried out. The first model with a single fault (Table **3-16** and Figure **3-22**), produced residuals (Figure **3-23**) that suggest that the observed displacements may be the integrated displacements of the mainshock and a triggered earthquake (Table **3-17** and Figure **3-24**). Both the models have similar mainshock fault planes that are near vertical, with similar strikes (~54°) and width (~2.6 km), and lies on a NE-tending structure on the eastern flank of the El Hoyo volcano complex (Figure **3-25** & **3-26**). Both models are left-lateral with a significant component of dip-slip but the oblique displacement of the single-fault model is 10 cm greater than the jointly inverted mainshock and triggered earthquake model. The modeled triggered earthquake has approximately the same near vertical fault plane and strike as the modeled mainshock and coincident with a mapped NE-trending structure between Cerro Negro and the Las Pilas-El Hoyo volcanic complex (Figure **3-26**). The coseismic slip of the triggered earthquake was entirely dip-slip (7 cm, normal faulting). The misfits for the mainshock and mainshock-triggered earthquake models are 26.6 and 54.2, respectively. The misfit for the mainshock-triggered earthquake model is higher due to the penalty (50) imposed on models with magnitudes greater than M_w 0.2 of the reported magnitude. The resulting model parameters of the triggered earthquake yield a magnitude of M_w 5.4 which is greater than the reported mb 4.7 that occurred five minutes after the mainshock. Both models cannot be compared due to the mainshock-triggered earthquake model having a greater number of estimated parameters (20) than the number of observations (14). This renders the mainshock-triggered earthquake model a statistically unidentifiable model. The parameter joint distributions of both the mainshock and mainshock-triggered earthquake models are plotted in Figures **3-27**, **3-28**, and **3-29**. The PDFs for both models are plotted in Figures **3-30**, **3-31**, and **3-32**.

Table **3-16**: Faulting parameters for inversion of the mainshock-only model for the September 15th, 2016 earthquake.

Strike	53° ± 10°
Dip	89° ± 3°
Fault Depth	2.1 ± 1.5 km
Fault Length	10.9 ± 3.4 km
Fault Width	2.4 ± 0.8 km
Strike-Slip Displacement	-0.70 ± 0.3 m
Dip-Slip Displacement	-0.34 ± 0.08 m
Poisson Ratio	0.31 ± 0.02
Equivalent Mw	5.8
Misfit	25.8

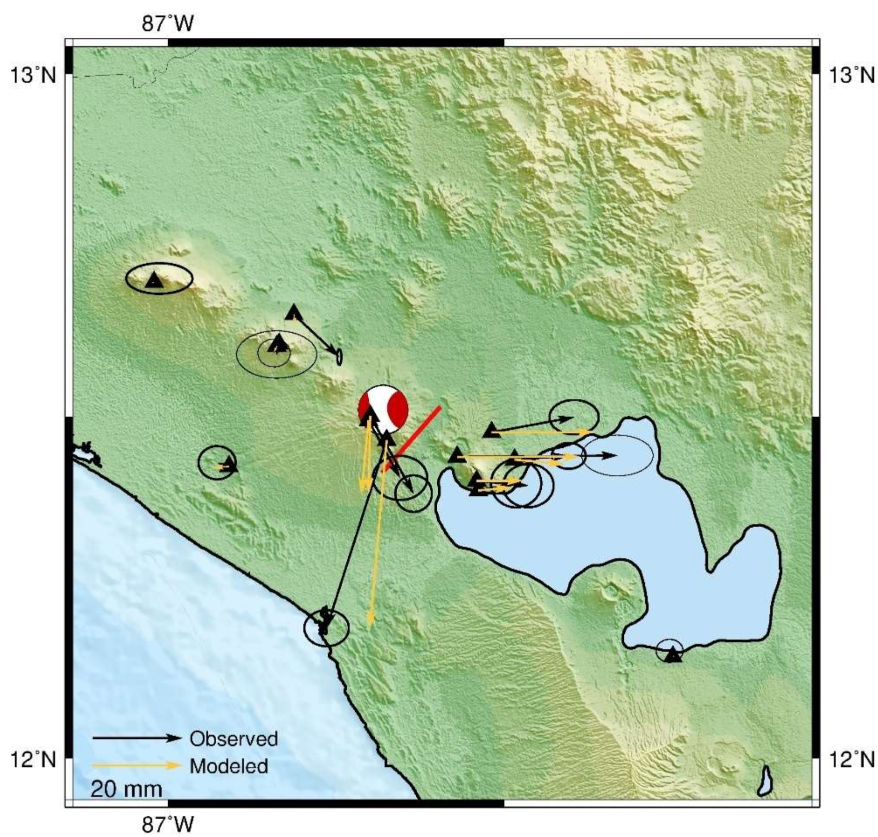

Figure **3-22**: Inversion results for the mainshock-only model for the September 15th, 2016 earthquake. Black vectors are observed displacements. Yellow vectors are modeled displacements. Focal mechanisms from GCMT (Dziewonski et al., 1981; Ekström et al., 2012).

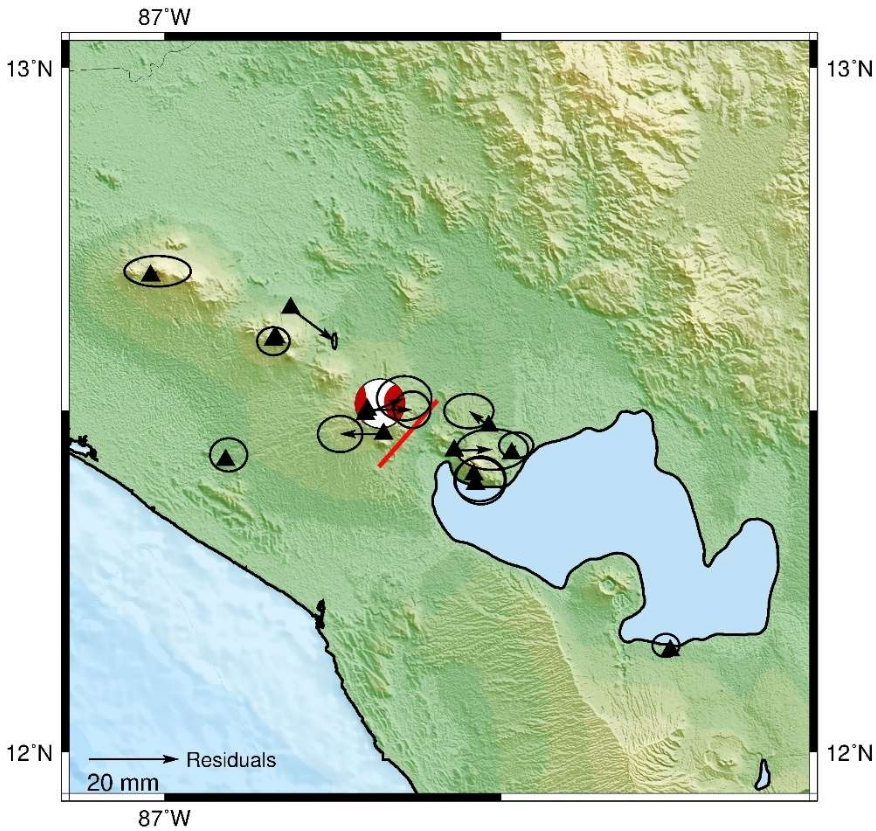

Figure **3-23**: Model residuals for the one-fault model of the September 15th, 2016 earthquake. Focal mechanisms from GCMT (Dziewonski et al., 1981; Ekström et al., 2012).

Table **3-17**. Faulting parameters for the joint inversion of the mainshock and triggered earthquake model for the September 15th, 2016 earthquake.

Mainshock		**Triggered Earthquake**	
Strike	55° ± 4	**Strike**	47° ± 8
Dip	89.7° ± 2	**Dip**	86.2° ± 4
Fault Depth	1.1 ± 1.4 km	**Fault Depth**	1.8 ± 0.2 km
Fault Length	9.8 ± 0.4 km	**Fault Length**	7.7 ± 1.8 km
Fault Width	2.7 ± 0.9 km	**Fault Width**	7.0 ± 1.3 km
Strike-Slip Displacement	-0.62 ± 0.12 m	**Strike-Slip Displacement**	0.0 m ± 0.03 m
Dip-Slip Displacement	-0.24 ± 0.17 m	**Dip-Slip Displacement**	-0.07 m ± 0.03 m
Equivalent Mw	5.7	**Equivalent Mw**	5.3
Poisson Ratio	0. 35 ± 0.04		
Misfit	54.24		

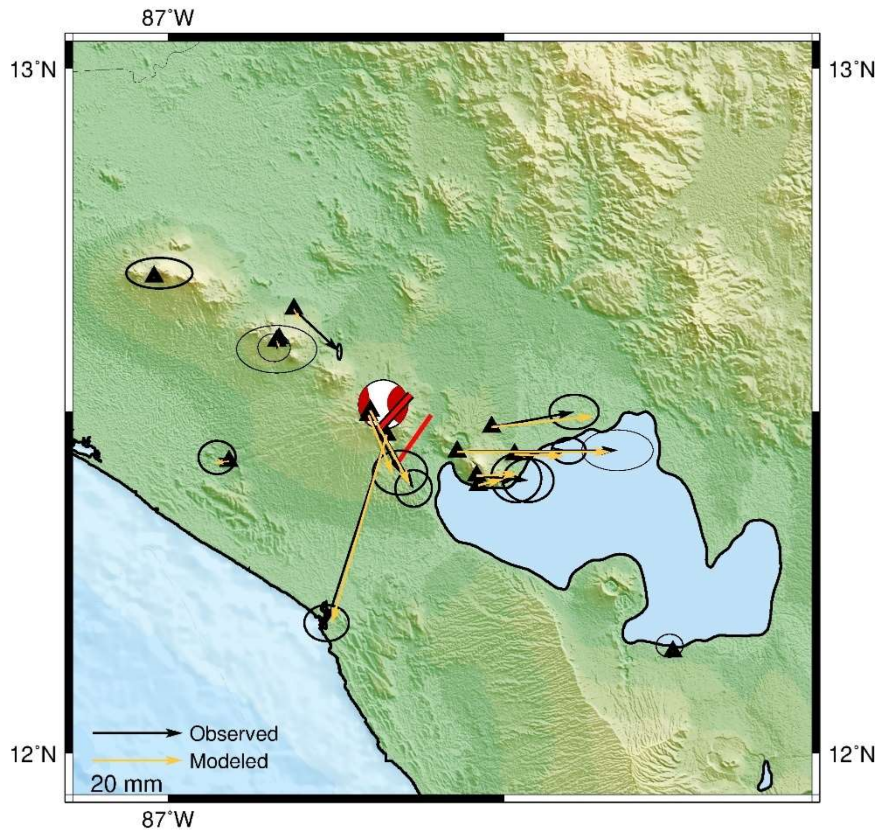

Figure **3-24**: Joint inversion results of the mainshock-triggered earthquake model for the September 15th, 2016 earthquake. Black vectors are observed displacements. Yellow vectors are modeled displacements. Focal mechanisms from GCMT (Dziewonski et al., 1981; Ekström et al., 2012).

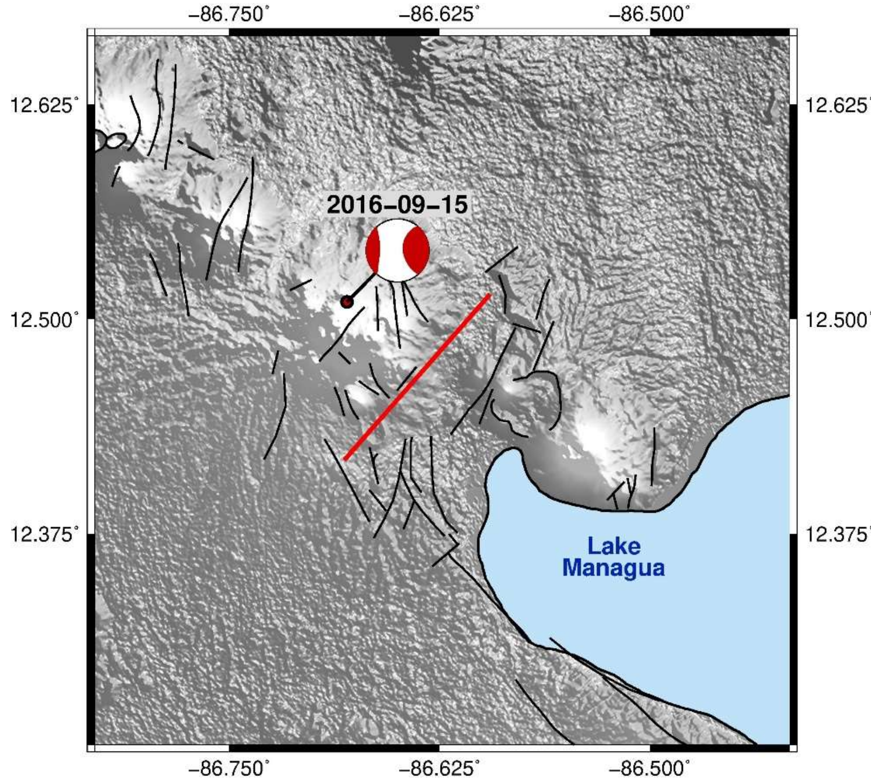

Figure **3-25**: Fault trace of the mainshock-only model for the September 15th, 2016 earthquake. The surface trace is coincident with a known NE trending structure on the flanks of the El Hoyo volcano. Focal mechanisms from GCMT (Dziewonski et al., 1981; Ekström et al., 2012).

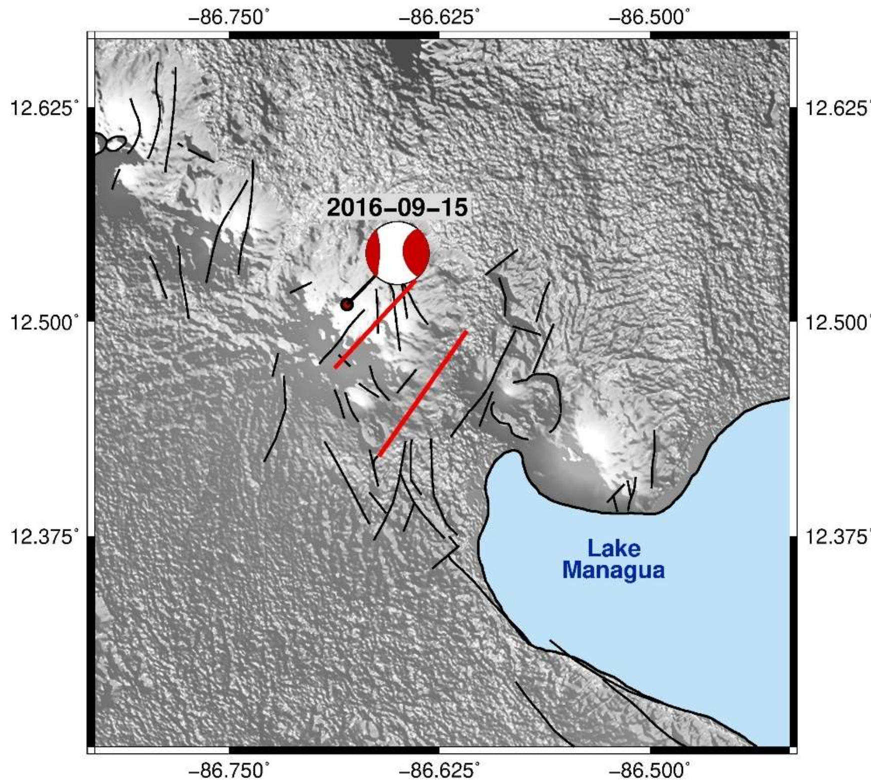

Figure **3-26**: Fault traces for mainshock and triggered earthquake of the mainshock-triggered earthquake model for the September 15th, 2016 earthquake. Both surface traces of the mainshock and triggered earthquake are coincident with NE trending structures in Cero Negro-Las Pilas-El Hoyo volcanic complex. Focal mechanisms from GCMT (Dziewonski et al., 1981; Ekström et al., 2012).

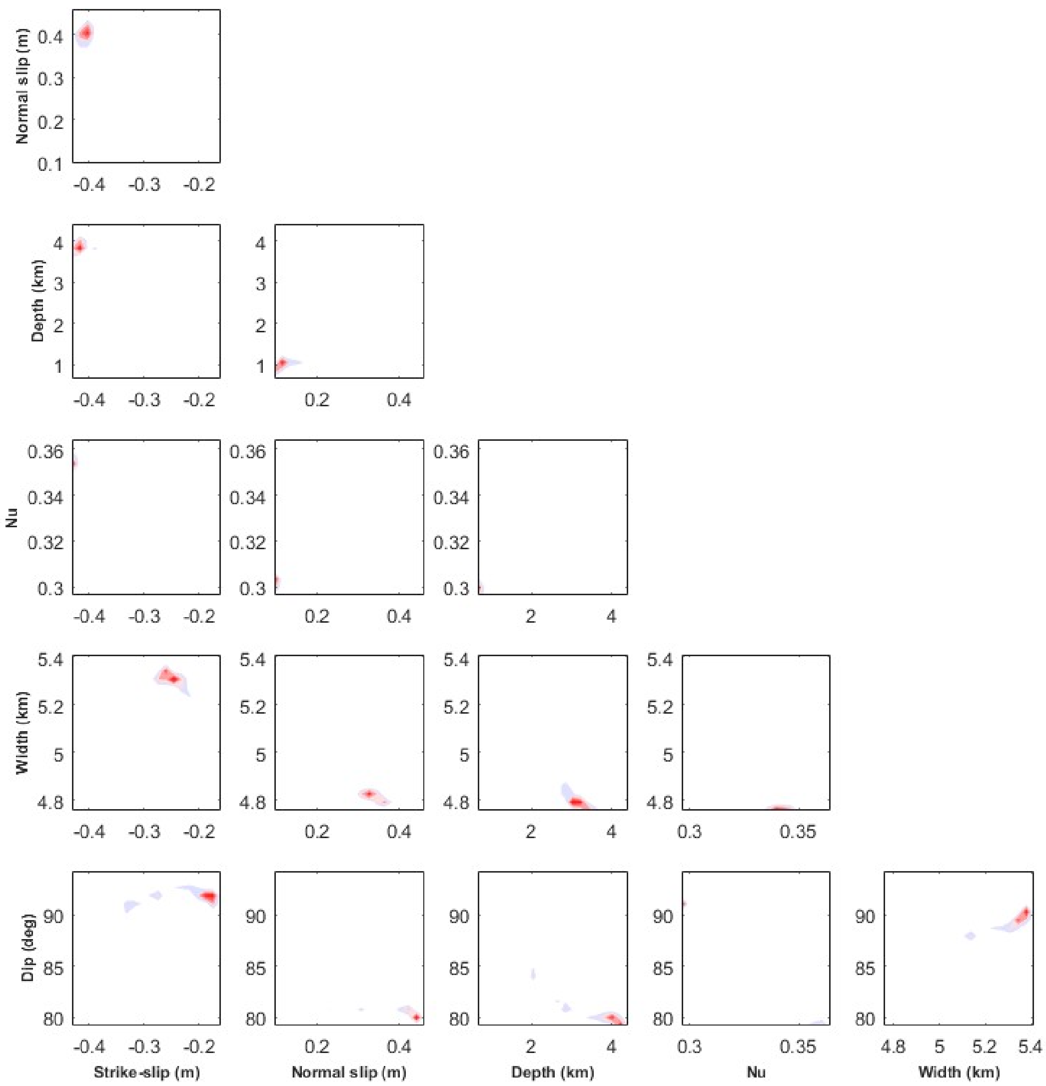

Figure **3-27**: Parameter joint distribution limited to 2σ for inversion results for the mainshock model for the September 15th, 2016 earthquake.

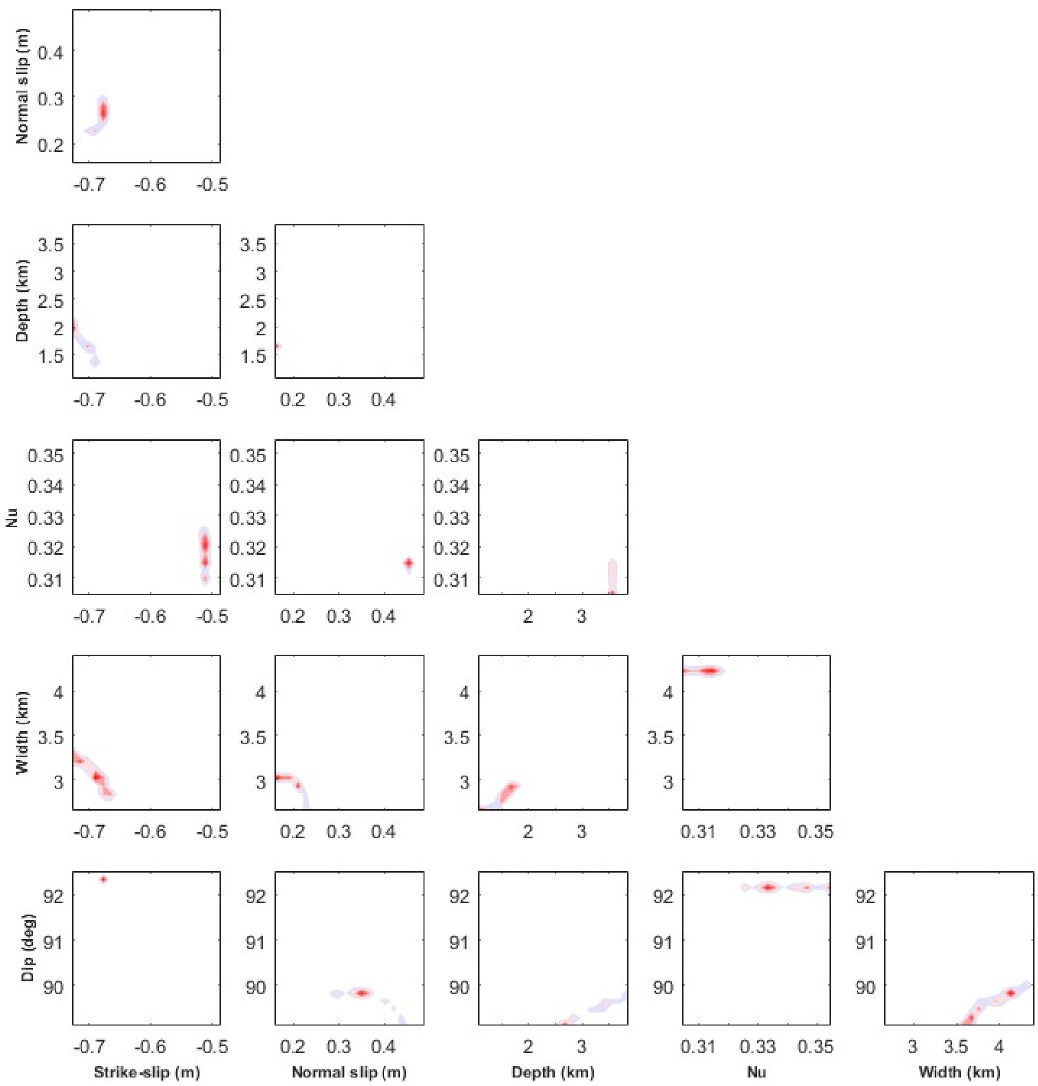

Figure **3-28**: Parameter joint distribution limited to 2σ for inversion results of mainshock for mainshock-triggered earthquake model for the September 15th, 2016 earthquake.

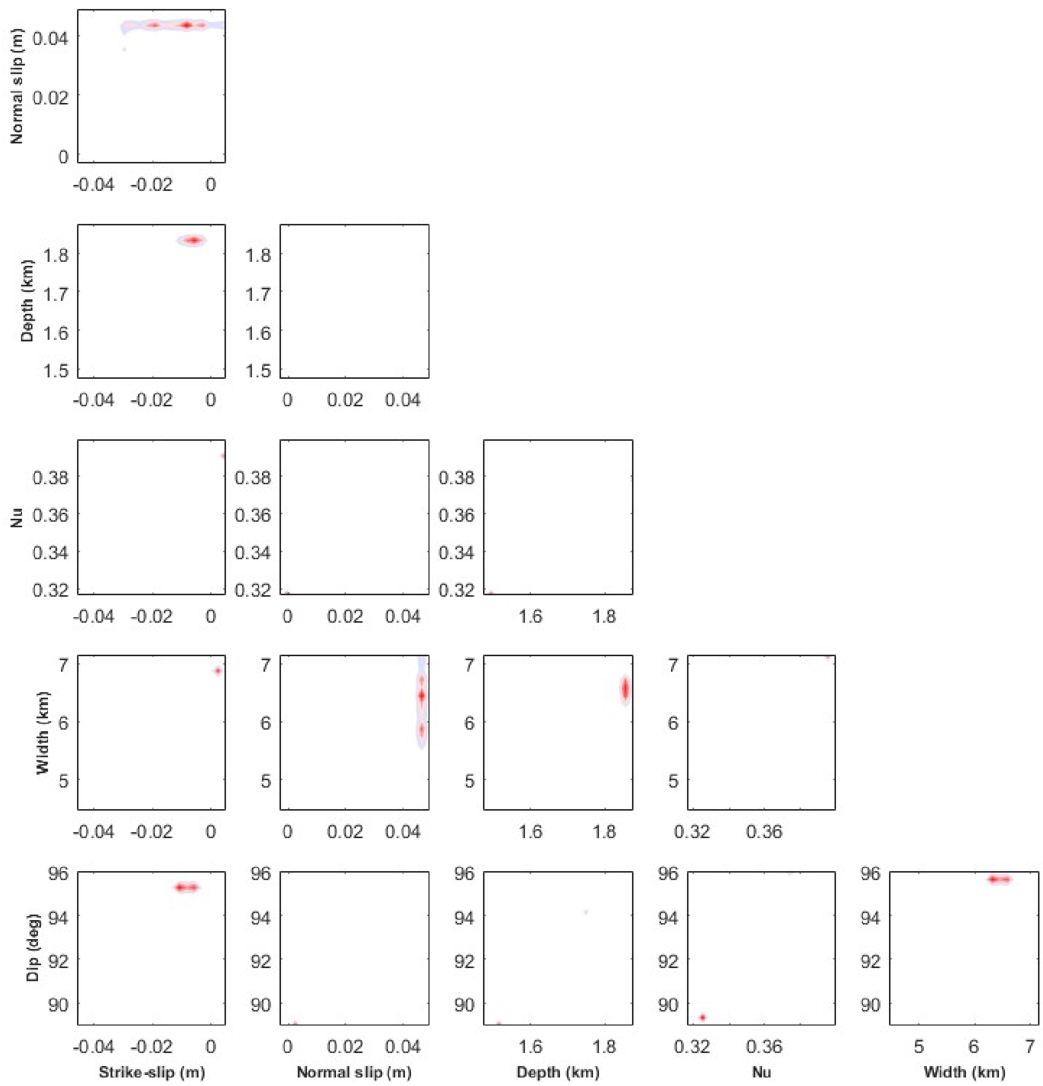

Figure **3-29**: Parameter joint distribution limited to 2σ for inversion results of triggered earthquake for mainshock-triggered earthquake model for the September 15th, 2016 earthquake.

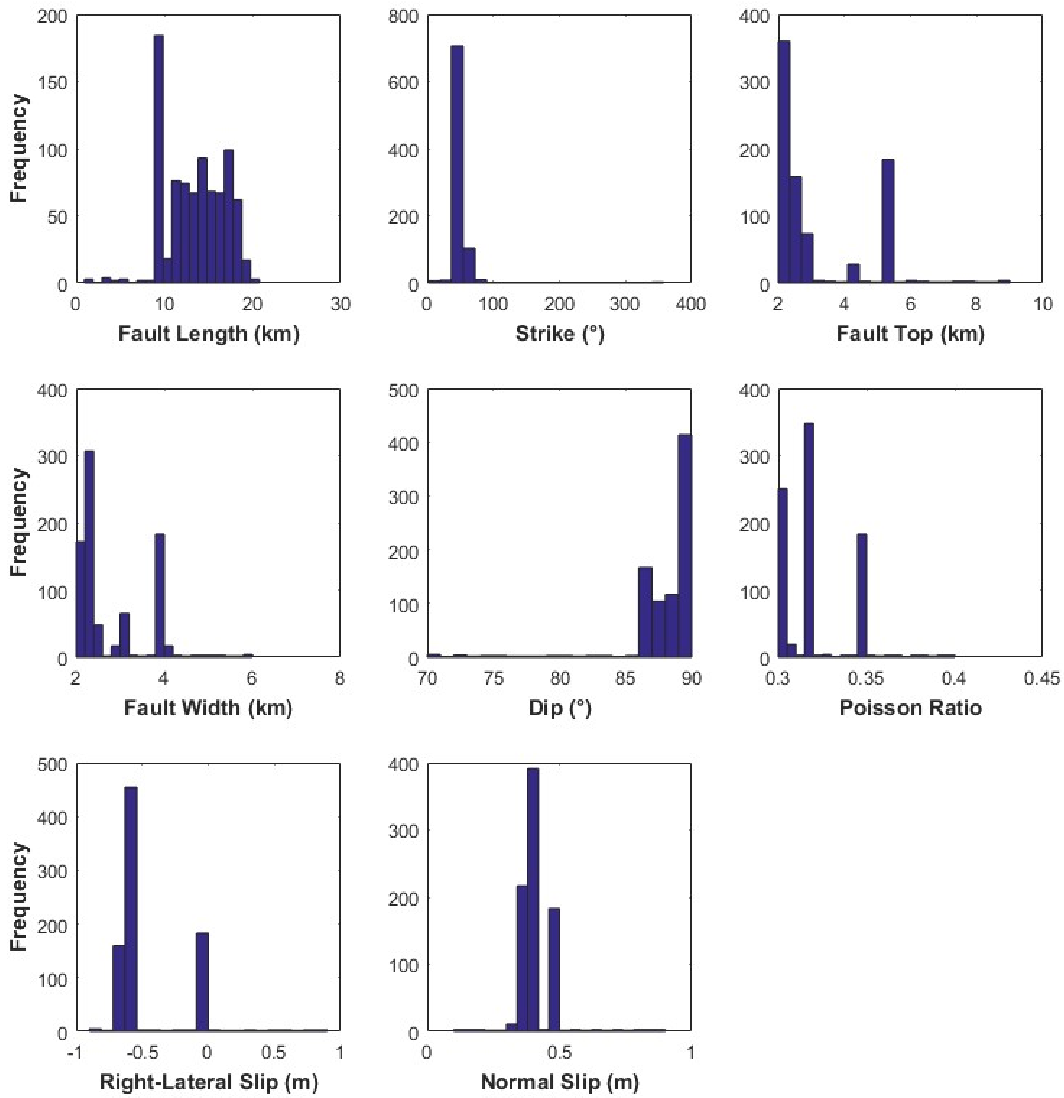

Figure **3-30**: Parameter probability density function for the one-fault model for the September 15th, 2016 earthquake.

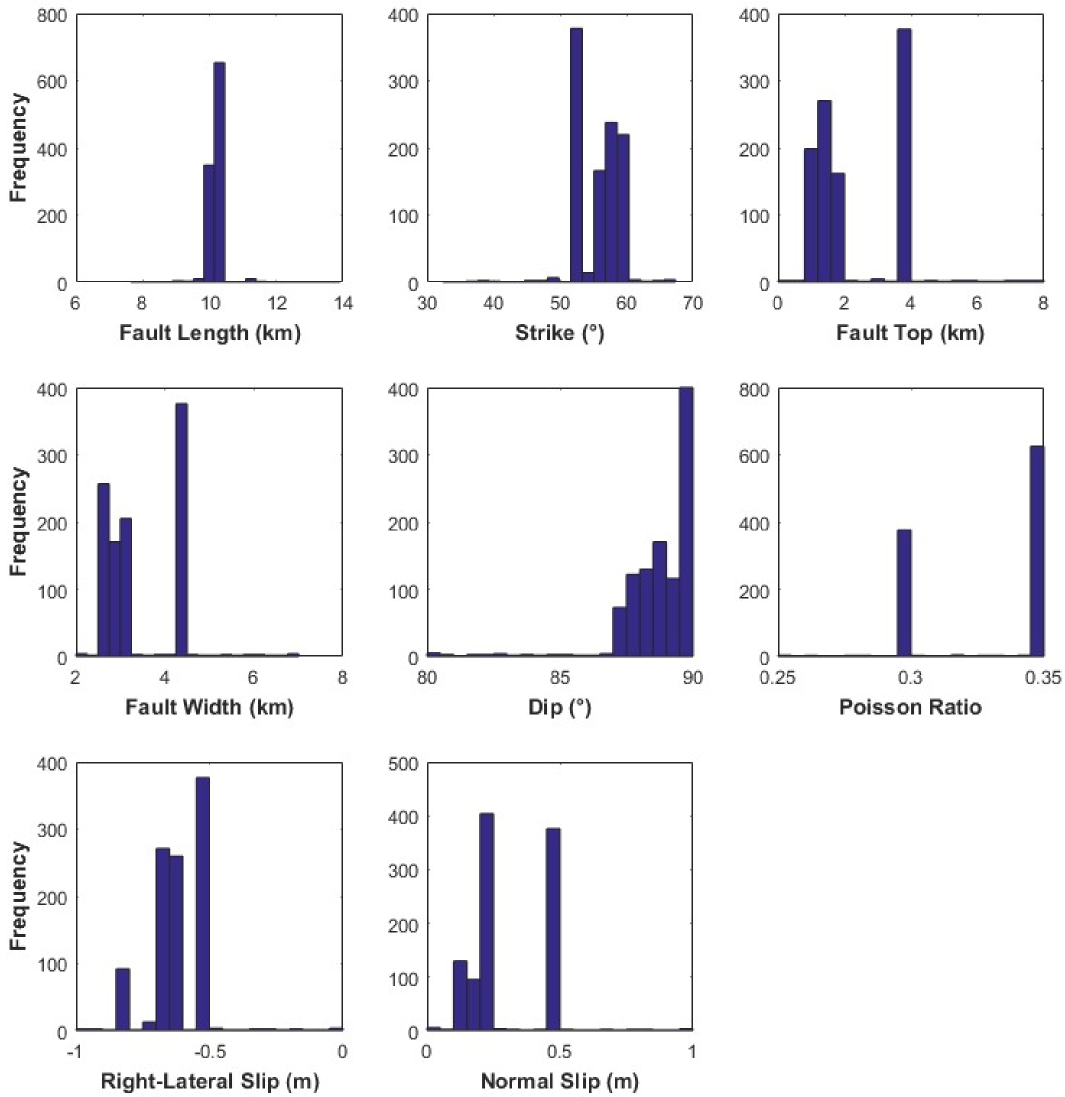

Figure **3-31**: Parameter probability density function for mainshock of the mainshock-triggered earthquake model for the September 15th, 2016 earthquake.

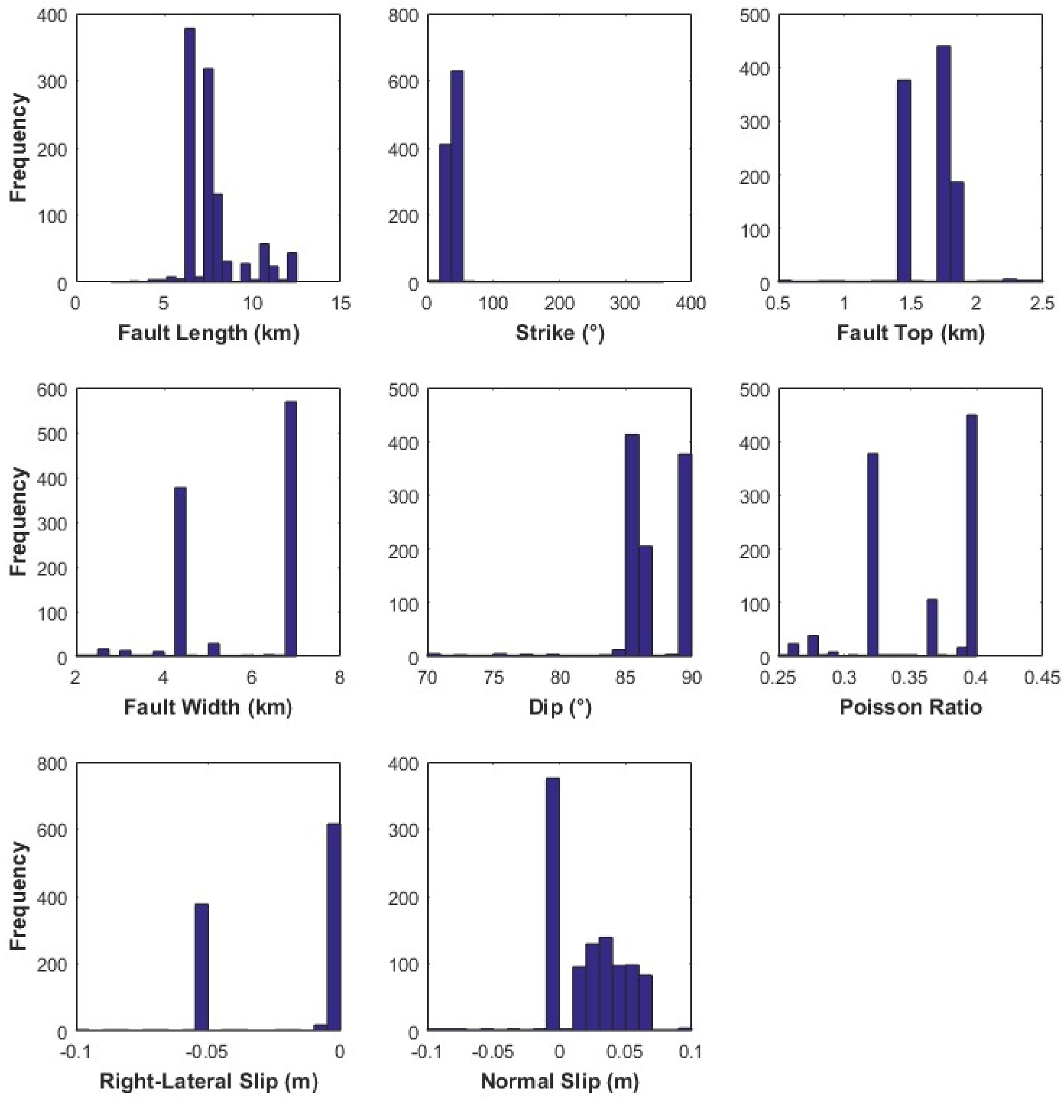

Figure **3-32**: Parameter probability density function for the triggered earthquake of the mainshock-triggered earthquake model for the September 15th, 2016 earthquake.

3.5.1.3 September 28th, 2016

The two inversion approaches of the M_w 5.5 September 28th, 2016 earthquake, where models were spatially constrained to a NE-trending structure west of the Momotombo volcano and within the La Paz Centro fault zone, yielded different faulting styles. The model constrained to the western flank of Momotombo volcano has mostly dip-slip (28 cm, normal faulting) on a nearly vertical fault (dip of 85°) with a strike of 202°, a fault length of 7.1 km and width of 3.3 km, and a misfit of 9.2 mm (Figure **3-33** & Table **3-18**). The model whose inversion was, to a lesser degree spatially (±20 km), constrained to the La Paz Centro fault zone, has a misfit of 12.6, produced a fault with a strike of 216°, a length of 21 km, and a width of 4.9 km (Figure **3-34** & Table **3-19**). The coseismic oblique slip of this model has equivalent components of right-lateral strike-slip (0.06 m) and dip-slip (0.04 m). The model that was constrained to the geomorphic structure west of the Momotombo has a fault trace that is coincident with the structure (Figure **3-35**). The model that was constrained to the La Paz Centro fault zone has a fault trace that is aligned with mapped faults in the La Paz Centro fault zone (Figure **3-36**). However, the fault trace also intersects NE-trending left-lateral faults that have been seismically active in the recent past (Díez et al., 2005; LaFemina et al., 2004). The parameter joint distributions of both models are plotted in Figures **3-37** and **3-38**. The probability density functions for both models are plotted in Figures **3-39** and **3-40**.

Table **3-18**. Faulting parameters for inversion of the September 28th, 2016 earthquake constrained to the western flank of the Momotombo volcanic complex.

Strike	22° ± 37°
Dip	85° ± 5°
Fault Depth	5.5 ± 1.9 km
Fault Length	7.1 ± 3.8 km
Fault Width	3.3 ± 0.7 km
Strike-Slip Displacement	-0.06 ± 0.2 m
Dip-Slip Displacement	-0.28 ± 0.1 m
Poisson Ratio	0.31 ± 0.03
Equivalent Mw	5.5
Misfit	9.2

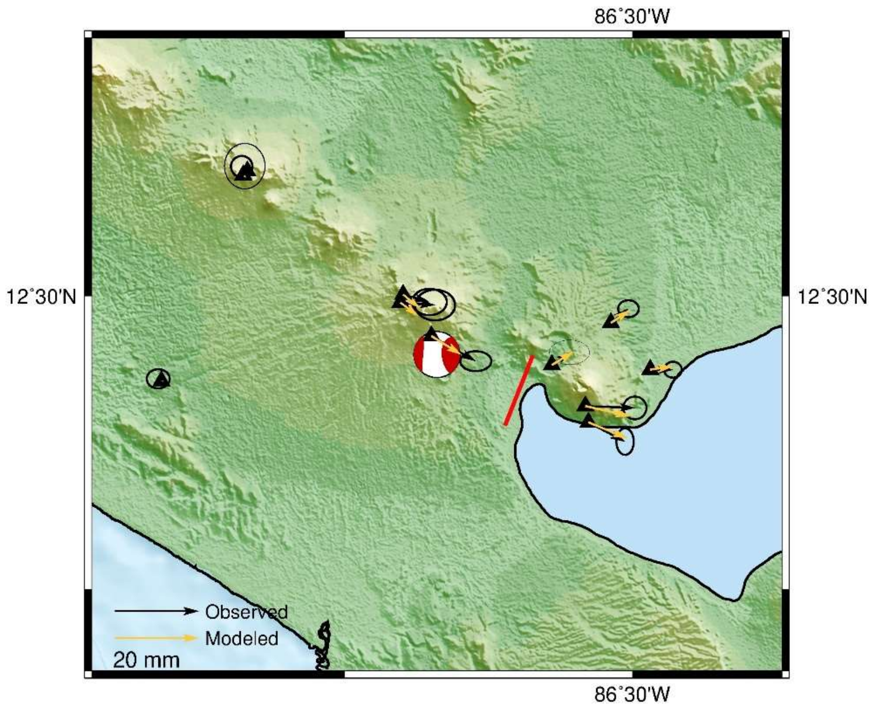

Figure **3-33**: Inversion results for the September 28th, 2016 earthquake constrained to the western flank of the Momotombo volcanic complex. Focal mechanisms from GCMT (Dziewonski et al., 1981; Ekström et al., 2012).

Table **3-19**: Faulting parameters for inversion of the September 28th, 2016 earthquake constrained to the La Paz Centro fault zone.

Strike	311° ± 4°
Dip	84° ± 8°
Fault Depth	1.5 ± 2.8 km
Fault Length	16.5 ± 1.9 km
Fault Width	4.7 ± 1.2 km
Strike-Slip Displacement	0.09 ± 0.5 m
Normal Displacement	-0.05 ± 0.2 m
Poisson Ratio	0.39 ± 0.04
Equivalent Mw	5.5
Misfit	21.7

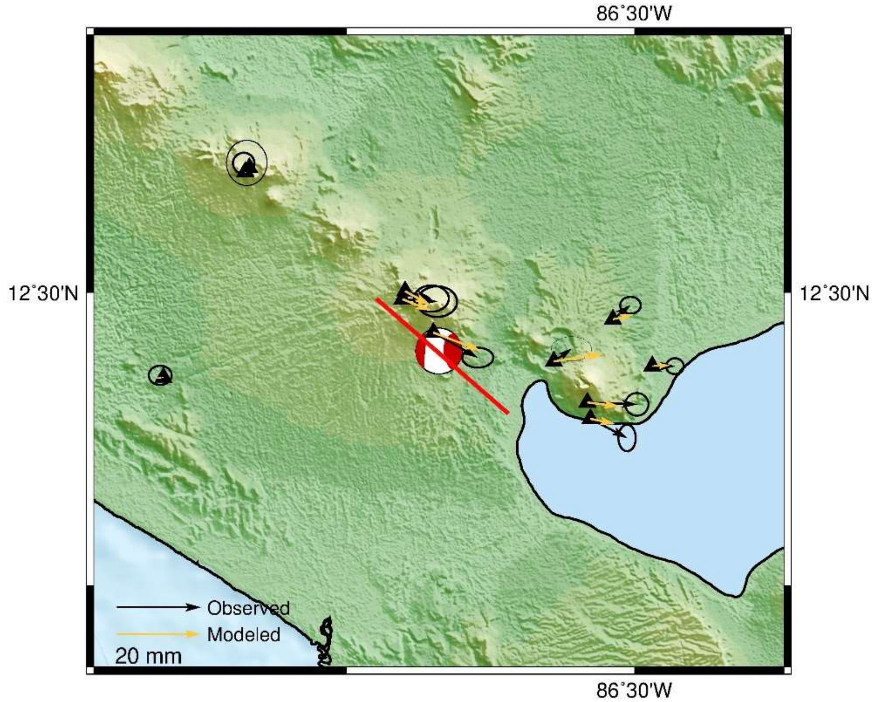

Figure **3-34**: Inversion results for the September 28th, 2016 earthquake constrained to the La Paz Centro fault zone. Focal mechanisms from GCMT (Dziewonski et al., 1981; Ekström et al., 2012).

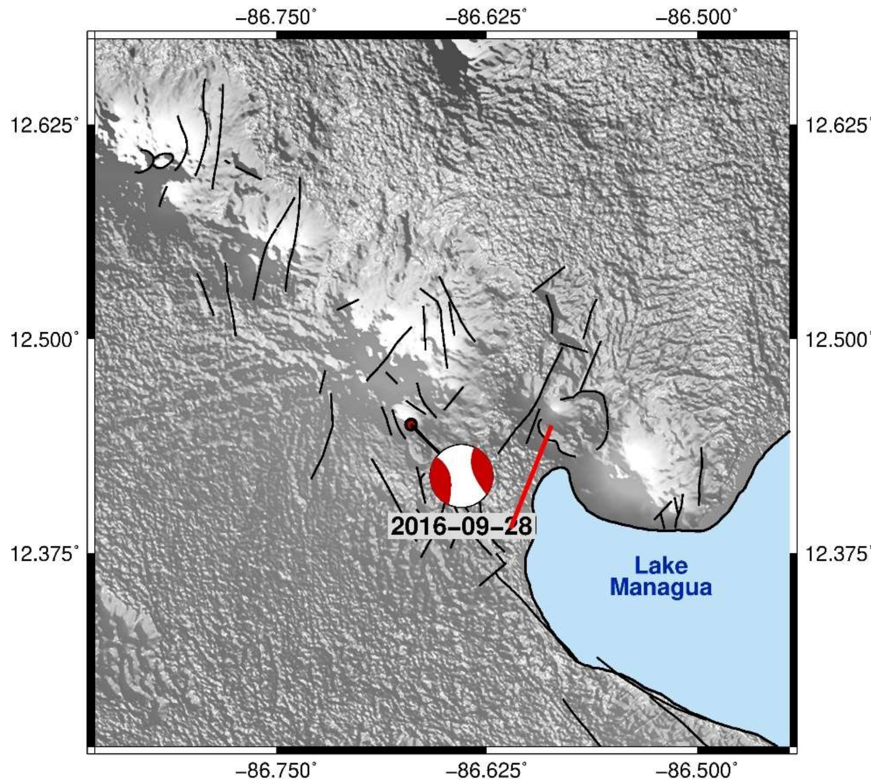

Figure **3-35**: Fault trace of the September 28th, 2016 earthquake model constrained to the western flank of the Momotombo volcanic complex. Focal mechanisms from GCMT (Dziewonski et al., 1981; Ekström et al., 2012).

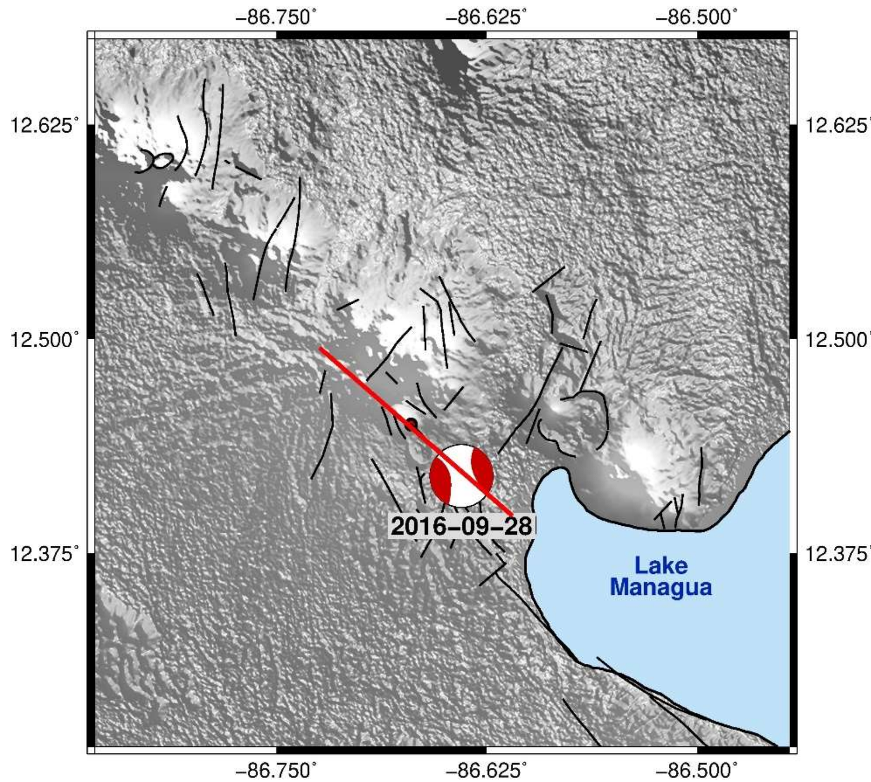

Figure **3-36**: Fault trace of September 28th, 2016 earthquake model constrained to the La Paz Centro fault zone Focal mechanisms from GCMT (Dziewonski et al., 1981; Ekström et al., 2012).

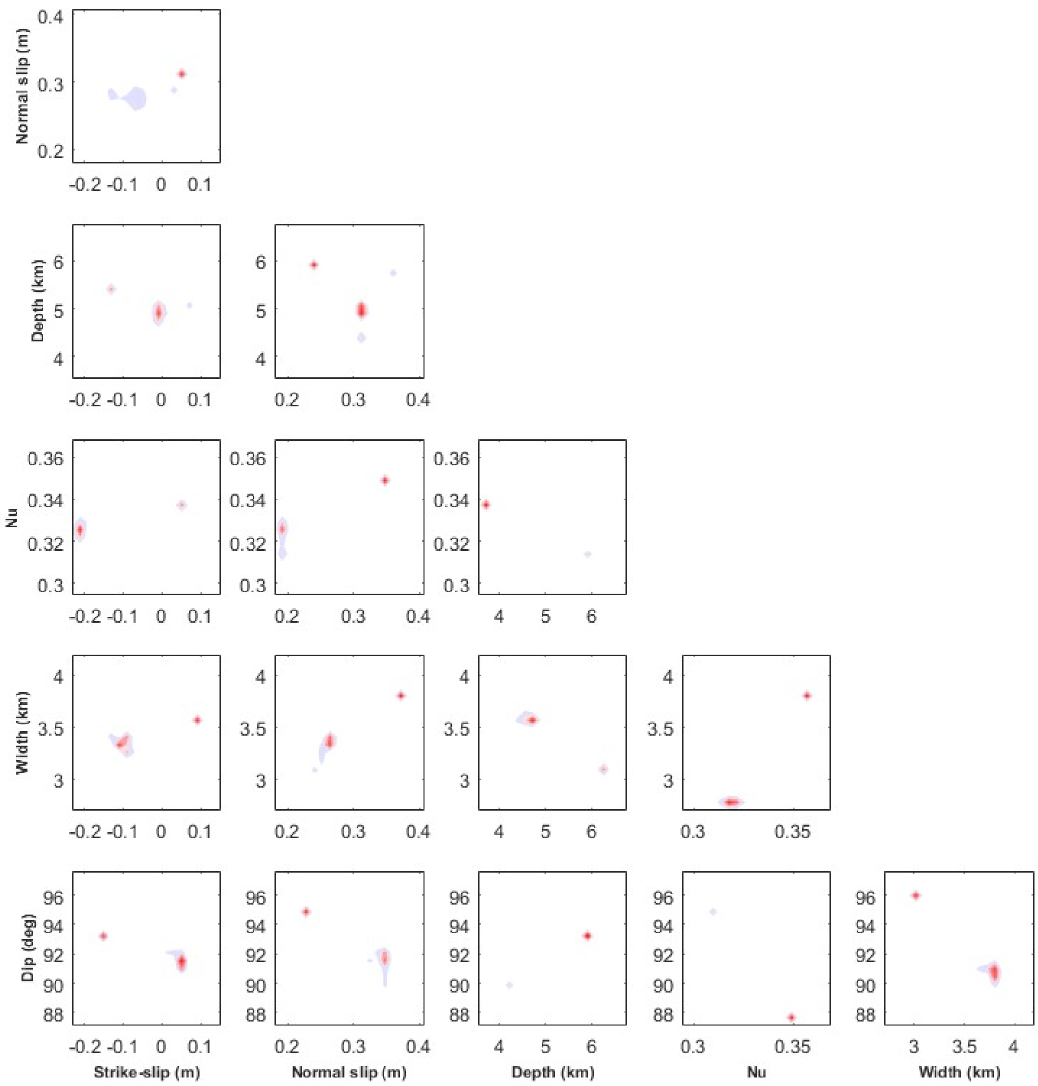

Figure **3-37**: Parameter joint distribution limited to 2σ for inversion results of the September 28th, 2016 earthquake model constrained to the western flank of the Momotombo volcanic center.

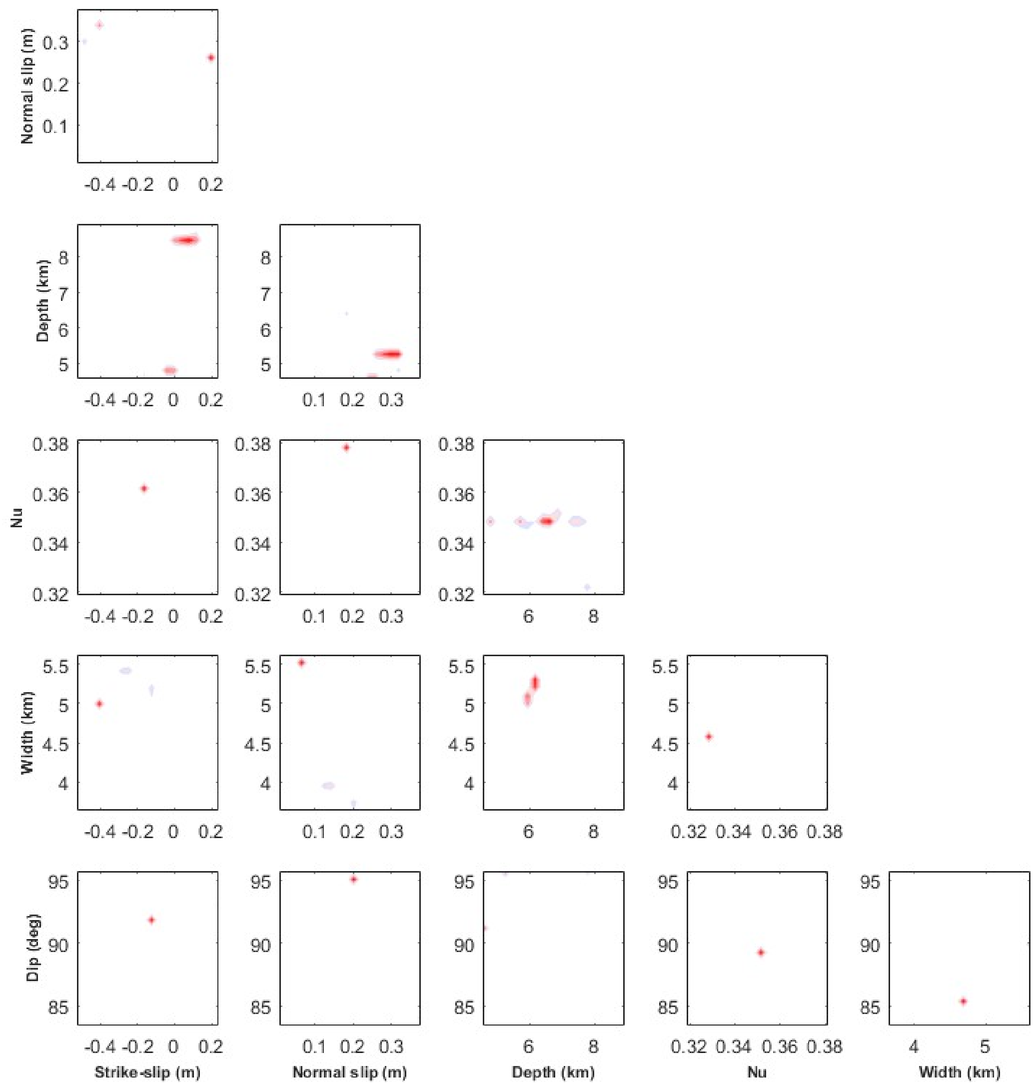

Figure **3-38**: Parameter joint distribution limited to 2σ for inversion results of September 28th, 2016 earthquake model constrained to the La Paz Centro fault zone.

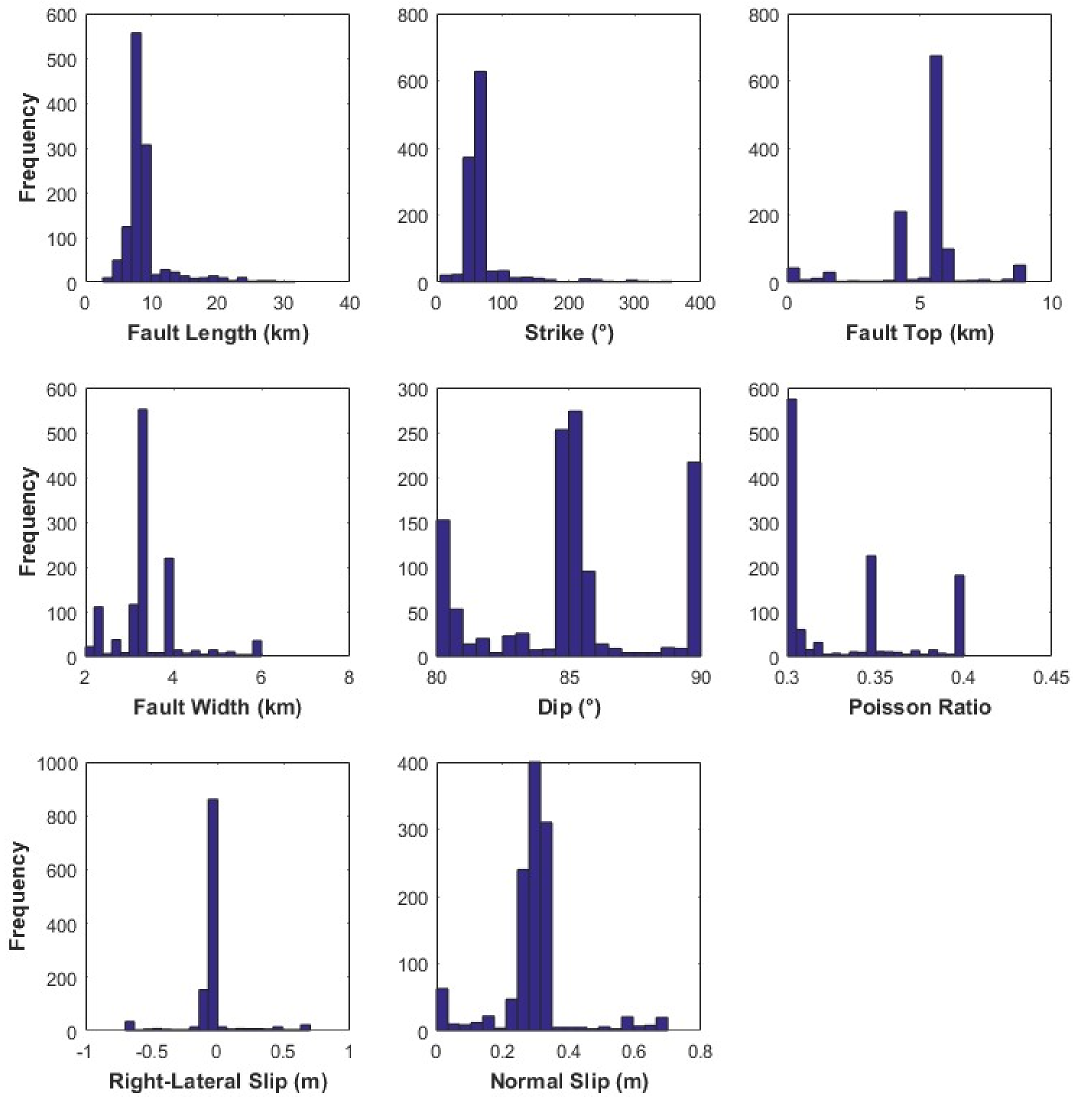

Figure **3-39**: Parameter probability density function for the model spatially constrained to Momotombo for the September 28th, 2016 earthquake.

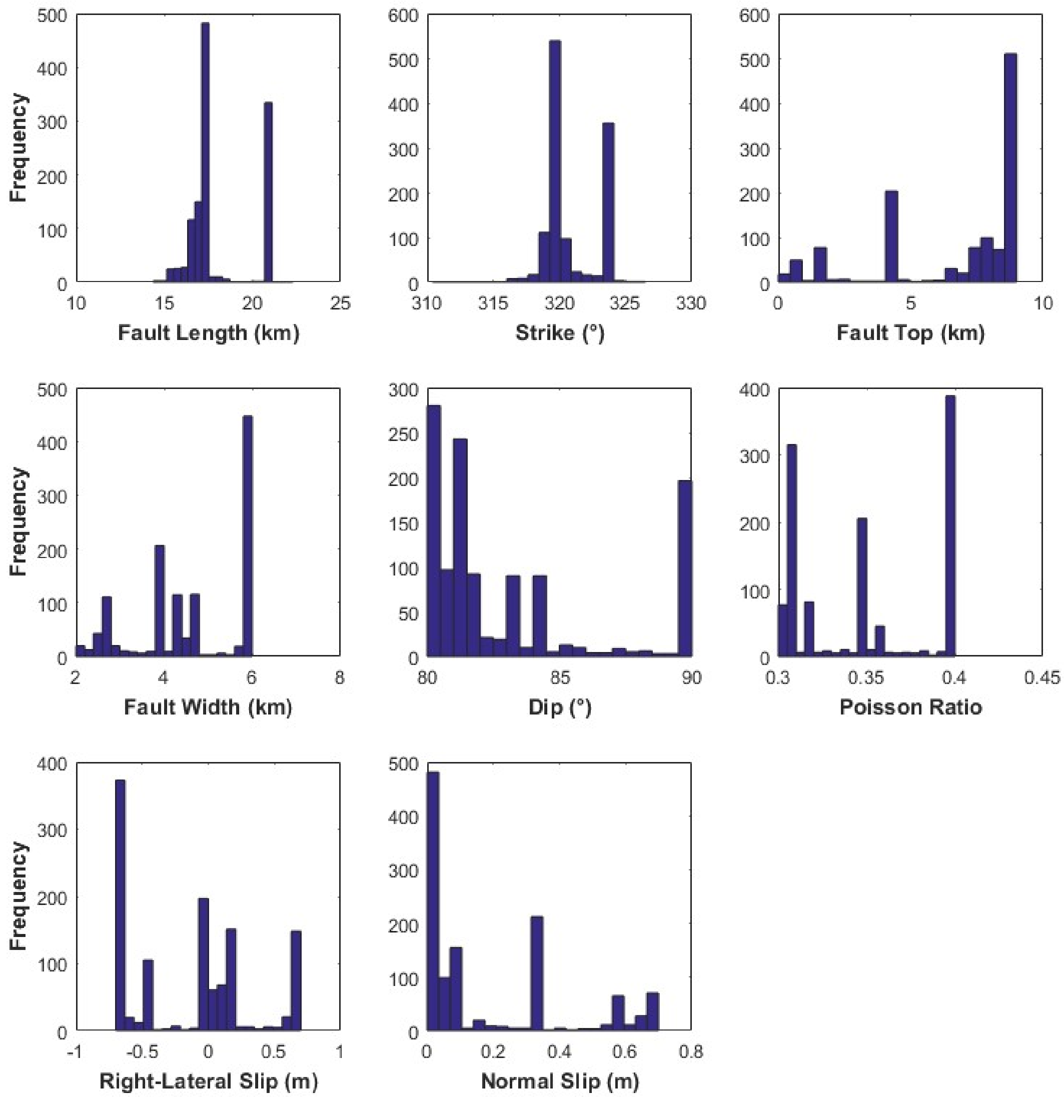

Figure **3-40**: Parameter probability density function for the model spatially constrained to the La Paz Centro fault zone for the September 28th, 2016 earthquake.

3.5.2 Static Stress Change

ΔCFS analyses were carried out to determine if these earthquakes are a triggered sequence and determine if there is any correlation of stress state following the April 10th, 2014 earthquake and the December 1st, 2015 eruption of Momotombo. The ΔCFS induced by the April 10th, 2014 earthquake was determined for receiver fault planes of the September 2016 earthquakes, which had an average strike of 40° and were left-lateral. The inverted model that was chosen for the April 10th earthquake is the right-lateral-slip-only model and its selection is detailed in the Discussion section. A ΔCFS analysis following the April 10th earthquake was also carried out to investigate if the seismically active faults of the Managua graben may have been pushed closer to failure. Two ΔCFS analyses were carried out for stress change induced by the September 15th earthquake for receiver faults of the September 28th earthquake and the triggered earthquake that occurred within 5 minutes after the mainshock. The December 2015 Momotombo eruption may have been due to the April 10th, 2014 earthquake dilating the magmatic plumbing system. To investigate this, a ΔCFS analysis was performed to explore the stress change following the April 10th earthquake for a left-lateral receiver fault that with a strike of 30°.

3.5.2.1 M_w 6.1 April 10th, 2014 ΔCFS for NE-Trending Left-Lateral Receiver Faults

The April 10th earthquake may have promoted failure on the faults responsible for the September 15th and 28th earthquakes. Figure **3-41** shows the ΔCFS for a left-lateral receiver fault with a strike of 40° and a dip of 90° at depth of 6 km. Fault traces for both September 2016 earthquakes are in a positive ΔCFS lobe. Figure **3-43** also shows the same ΔCFS with relocated aftershocks. There is a correlation of positive ΔCFS and the location of aftershocks cluster southeast of the fault plane. These aftershocks were the Mw 5.2 April 14, 2014 earthquake, located in the vicinity of the Apoyoque volcano, with a discrete set of aftershocks.

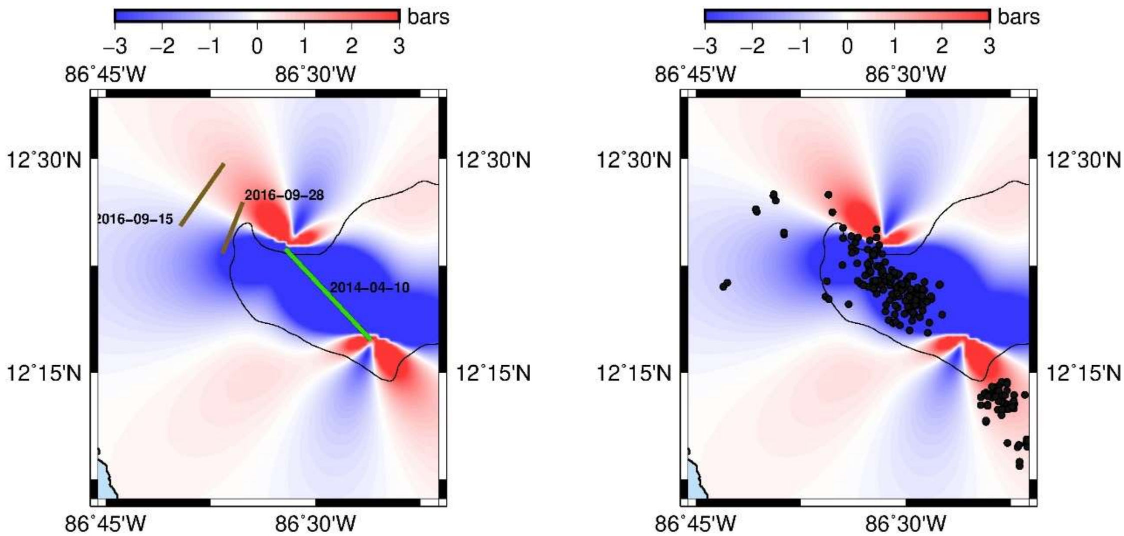

Figure **3-41**: Left: ΔCFS for left-lateral receiver faults with a strike of 40° and a dip of 90° at depth of 6 km. Right: Same ΔCFS with relocated aftershocks that were translated to modeled fault trace. The modeled source fault is the green line. ΔCFS analysis used the right-lateral-slip-only model for the April 2014 earthquake.

3.5.2.2 M_w 6.1 April 10th, 2014 ΔCFS for N-Trending Left-Lateral Receiver Faults

The Managua graben has many active faults that may have been pushed closer to failure after the April 10th earthquake. ΔCFS analysis was carried out for a north-striking left-lateral receiver fault with a vertical dip (Figure **3-44**). The analysis shows that the main active faults, the Nijapa-Miraflores alignment, Tiscapa, and Confradia faults, all lie in a positive ΔCFS regime (Figure **3-42**). Figure **3-42** also shows the normal stress change where the Nijapa-Miraflores and Tiscapa faults are in a positive normal stress regime.

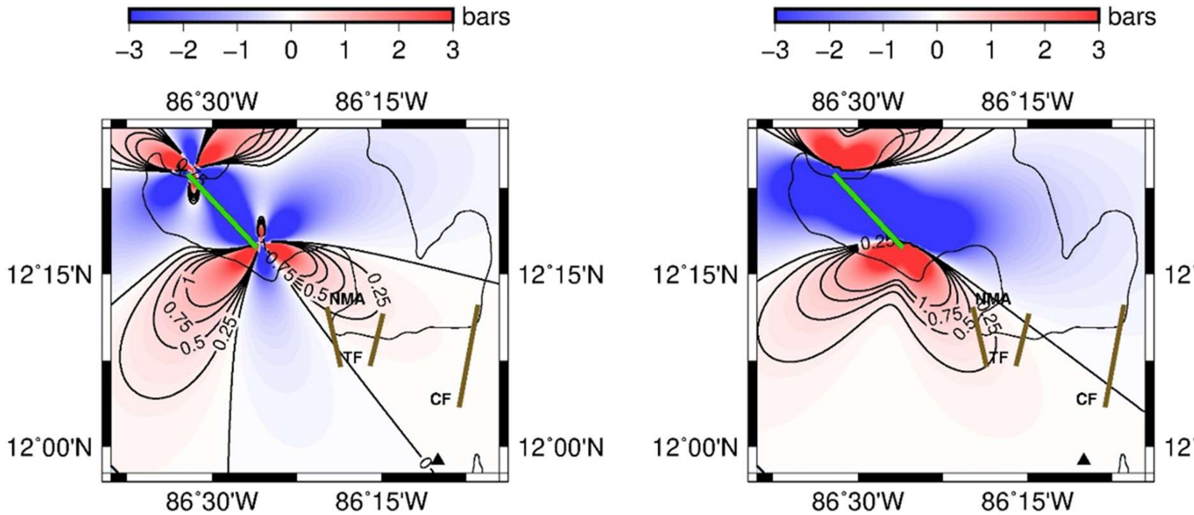

Figure **3-42**: Left: ΔCFS for left-lateral receiver faults with a strike of 0° and a dip of 90° at a depth of 6 km. Right: The normal stress change for left-lateral receiver faults with a strike of 0° and vertical dip. ΔCFS analysis used the right-lateral-slip model for the April 2014 earthquake. NMA – Neja-Miraflores alignment. TF – Tiscapa fault. CF – Confradia fault.

3.5.2.3 M_w 5.7 Sept. 15th, 2016 ΔCFS for N-Trending Left-Lateral Receiver Faults

The September 15th earthquake may have triggered the September 28th earthquake. It is also possible that the modeled triggered earthquake was triggered by the mainshock. To investigate this, using the mainshock-triggered earthquake model results, ΔCFS analysis was carried out after the September 15th earthquake for the receiver fault of the September 28th earthquake (Figures **3-43** & **3-44**) and the modeled triggered earthquake (Figures **3-45** & **3-46**). The September 28th receiver fault had a strike of 22° and a dip of 85° with normal (i.e., dip-slip) motion. The receiver fault for the triggered earthquake had a strike of 47° and a dip of 86°. Figures **3-43** and **3-44** shows that the fault plane of the September 28th earthquake is in a ΔCFS state following the September 15th earthquake. The triggered earthquake's fault plane is also in a ΔCFS state following the September 28th earthquake (Figures **3-45** & **3-46**).

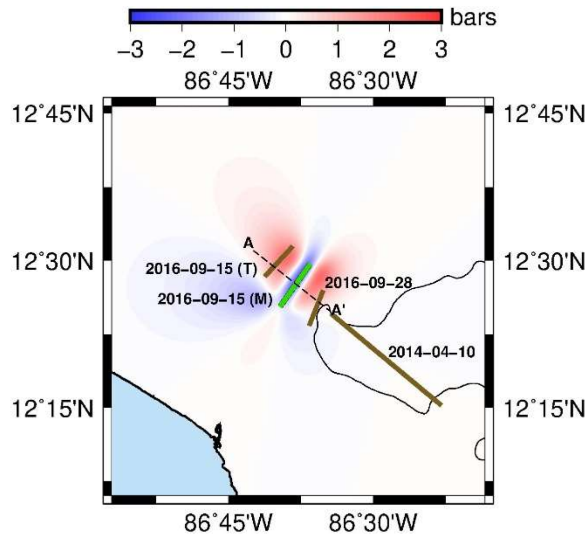

Figure **3-43**: ΔCFS for a normal receiver fault with a strike of 22° and a dip of 87° (September 28th fault plane) at a depth of 7 km. Source fault is the green line, which is the mainshock of the September 15th earthquake.

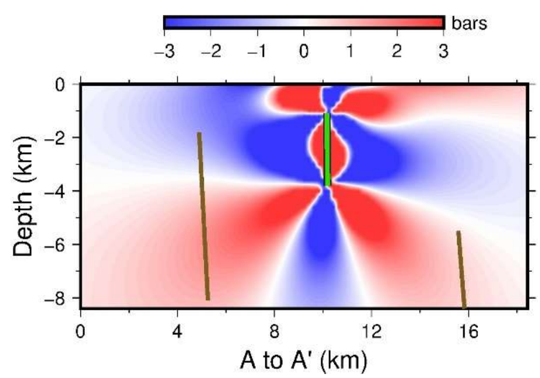

Figure **3-44**: Cross-section (A to A' in Figure **4-43**) of ΔCFS for a normal receiver fault with a strike of 22° and a dip of 85° (September 28th fault plane, rightmost fault in figure). Source fault is the green line, which is the mainshock of the September 15th earthquake.

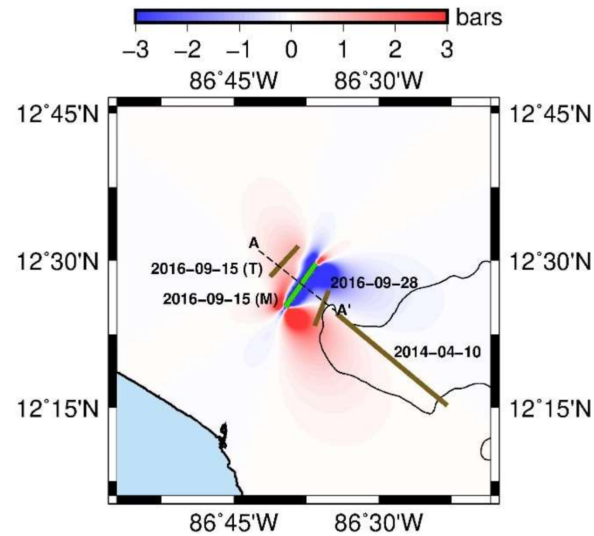

Figure **3-45**: ΔCFS for a normal receiver fault with a strike of 47° and a dip of 86° (triggered earthquake) at a depth of 4 km. Source fault is the green line.

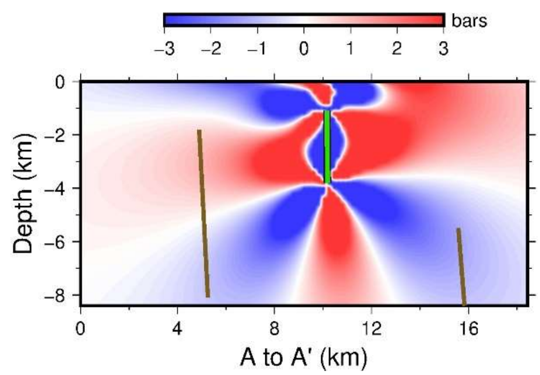

Figure **3-46**: Cross-section (A to A' in Figure **3-32**) of ΔCFS for a left-lateral receiver fault with a strike of 47° and a dip of 86° (leftmost fault). Source fault is the green line.

3.5.2.4 Magma-Tectonic Interaction April 10th, 2014: April 10, 2014 Earthquake and December 15, 2015 eruption of Momotombo

Momotombo erupted on December 1st, 2015, 19 months after the April 10th, 2014 earthquake. ΔCFS analysis was carried out to determine if the earthquake would have dilated the Momotombo magmatic system. This analysis used a receiver fault with a strike of 30° and a dip of 90°, which approximates the trend of many lineaments and surface ruptures mapped in the vicinity of Momotombo after the earthquake (INETER Bulletin, April 2014). Figures **3-47** to **3-51** show the normal stress change due to the April 10th, 2014 earthquake for depths of 2 km, 4 km, 6 km, and 8 km. There is up to 1.2 MPa normal stress change associated with the region beneath Momotombo. The dilatation due to the earthquake was also inspected (Figure **3-52** & **3-53**). From the surface to a depth of 8 km beneath Momotombo would have experienced a dilatation of 2 x 10^{-4}, after the earthquake.

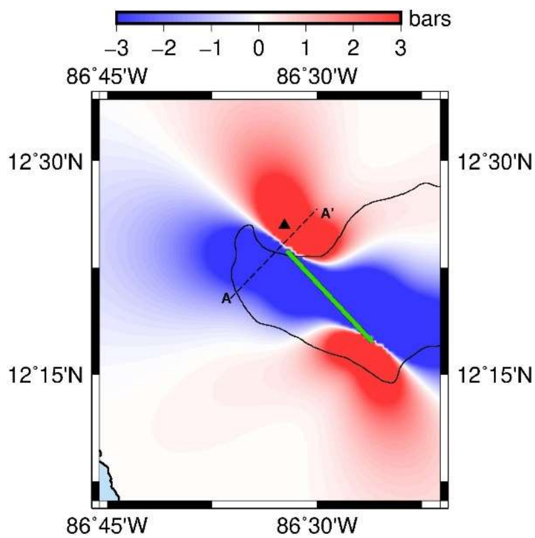

Figure **3-47**: Normal stress change at a depth of 2 km from the right-lateral-only April 2014 earthquake model. Black triangle is the location of the Momotombo summit vent.

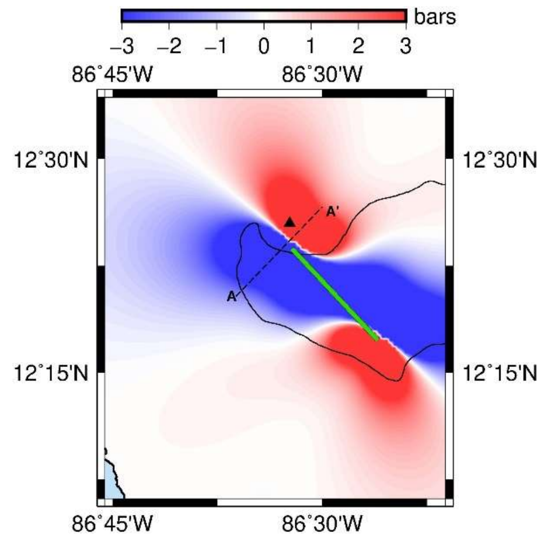

Figure **3-48**: Normal stress change at depth of 4 km. Black triangle is the location of the Momotombo summit vent.

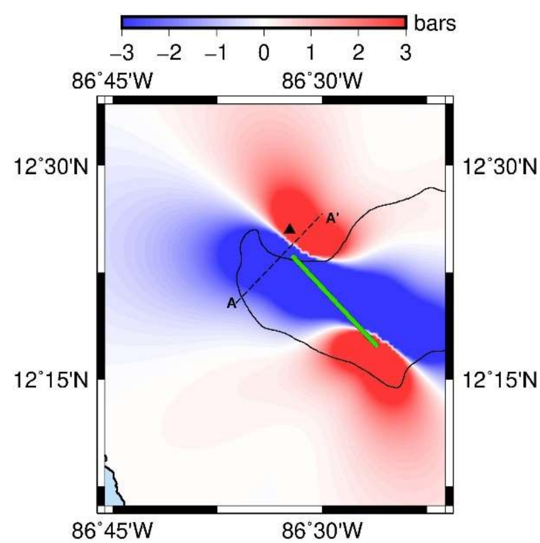

Figure **3-49**: Normal stress change at depth of 6 km from right-lateral-only April 2014 earthquake model. Black triangle is the location of the Momotombo summit vent.

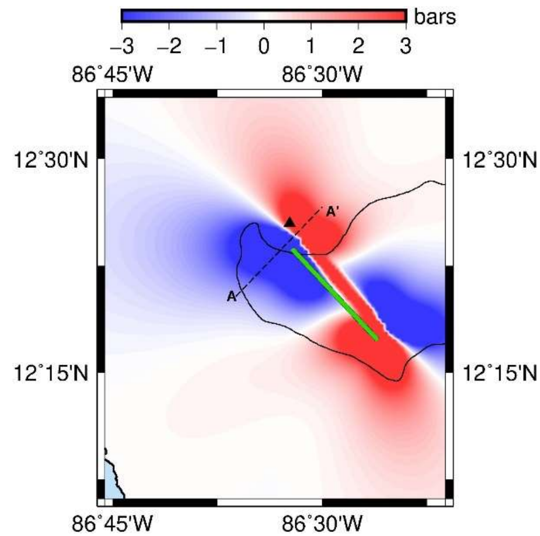

Figure **3-50**: Normal stress change at depth of 8 km from right-lateral-only April 2014 earthquake model. Black triangle is the location of the Momotombo summit vent.

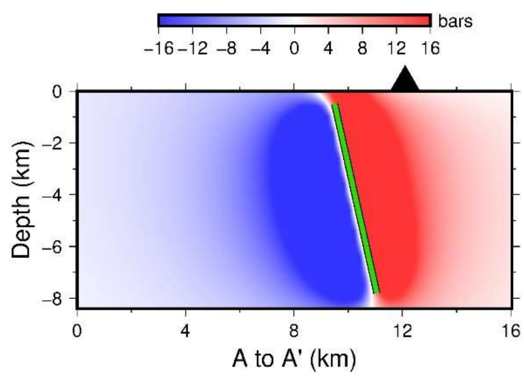

Figure **3-51**: Cross-section of normal stress change from right-lateral-only April 2014 earthquake model. Black triangle is the location of the Momotombo.

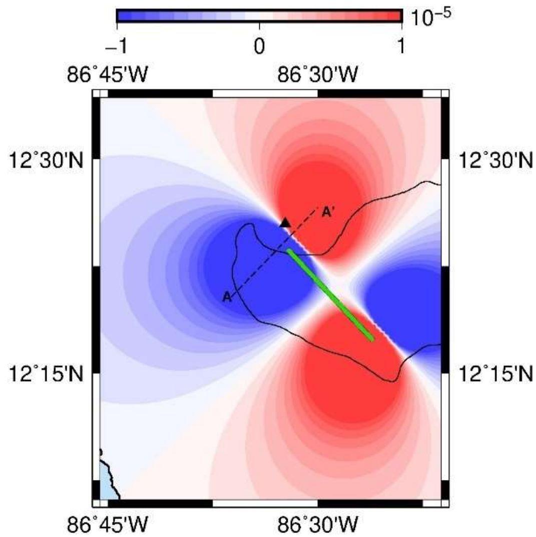

Figure **3-52**: Dilatation strain at a depth of 8 km due to the April 10th earthquake.

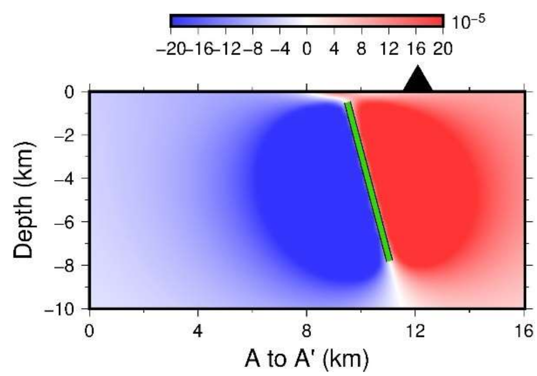

Figure **3-53**: Cross-section of dilation strain due to the April 10th earthquake.

3.6 Discussion

At obliquely convergent margins, strain portioning occurs between the megathrust and the overriding plate. Strain partitioning typically results in the development of margin-parallel shear often located near the volcanic arc. The CAFA sliver translates to the NW at a rate of 8 mm/yr to 14 mm/yr relative to the Caribbean plate (Ellis et al., 2019; Turner et al., 2007; Alvarado et al., 2010; Staller et al., 2016; LaFemina et al., 2009; Kobayashi et al., 2014). In the Nicaraguan segment of the CAFA, bookshelf faulting is the primary mechanism that accommodates this relative motion (LaFemina et al., 2002). This project investigates three moderate magnitude upper-plate earthquakes that are a triggered sequence and identifies the faults that are associated with bookshelf faulting in NW Nicaragua. This project also highlights that in Nicaragua there is tectonic-magmatic interaction by presenting static stress changes in the vicinity of the Momotombo volcano following the M_w 6.1 April 10, 2014 earthquake. The static stress field may have led to the VEI 2 December 1st, 2015 eruption of Momotombo.

3.6.2 CAFA-CA Shear Accommodation

Inversion of coseismic GPS displacements for the three earthquakes produced faults that are both right-lateral NW-trending and left-lateral and NE-trending. These fault trends and sense of motion reveal the complexity of shear accommodation in NW Nicaragua and support the bookshelf faulting model for accommodating the CAFA-CA shear.

Three models of the M_w 6.1 April 2014 earthquake are considered: a right-lateral-slip-only with vertical dip model, a right-lateral-slip-only model, and an oblique-slip model. The right-lateral-slip-only model, an inversion that also estimated the dip, is the preferred model even though it has a worse misfit (40.5) compared to the right-lateral-slip-only with vertical dip model (38.7) and the oblique-slip model (21.9) (Tables **3-13**, **3-14**, and **3-15**). The ~1 m coseismic slip for the right-lateral-slip-only with vertical dip model (Table **3-13**) is unreasonably high for strike-slip faulting (Harris

2017). The oblique-slip model produced a fault that is longer (27 km) than the relocated aftershocks (Figure **3-15**). The right-lateral-slip-only model produced a fault with strike (313°) and dip (78°) that is supported by relocated aftershocks (Figure **3-14**). Consider the ratio of seismic moment of this forearc segment for the last 100 years and that of the seismic moment of the April 10th, 2014 earthquake is ~18, there is a high likelihood that the reoccurrence interval of this earthquake is short (< 200 years with a lower bound of 90 years) or there are other faults accommodating shear. If we consider a reoccurrence interval of 200 years then repeated earthquakes on this segment in the last 10,000 years would produce a ~48 m vertical offset. Lake Managua is shallow (~20 m) and while a 5 m scarp has been identified along the southwestern shore and described as a synthetic fault to the Mateare fault (Funk et al., 2009), there are no fault scarps that are coincident with the modeled fault, which lends support to the right-lateral-only slip model.

Inversion of the GPS-derived coseismic displacements for the M_w September 15th, 2016 earthquake yielded two models: a mainshock and a mainshock-triggered earthquake (Figures **3-22** & **3-24**). The single-fault mainshock model does not fit the observed GPS displacements well (Figure **3-23**), while the mainshock-triggered earthquake does fit the displacements, albeit with a higher misfit due to the penalty of the triggered earthquake having a greater magnitude (M_w 5.3) compared to the mb 4.7 earthquake that occurred 5 minutes after the mainshock. It is possible that GPS displacements are due to a doublet that cannot be distinguished during hypocenter determination or the reported magnitude of the earthquake that occurred 5 minutes later was underestimated. Following Scordilis (2006) the body wave magnitude of 4.7 is equivalent to M_w of 5.0 with an upper limit of 5.42. The mainshock-triggered model most likely represents the integrated coseismic displacements of the temporally close mainshock and triggered mb 4.7 earthquakes. Both earthquakes occurred on faults that are NE-trending and dip to the SE with a normal dip-slip component in the sense of motion (Table

3-17). The coseismic slip of the mainshock was 65 cm of oblique slip while the triggered earthquake's coseismic slip was 7 cm of pure dip-slip motion.

The inversion of the M_w 5.5 September earthquake was spatially constrained to a NE-trending geomorphic structure on the western flank of Momotombo volcano and the La Paz Center fault zone. The resulting two models have differing faulting styles with the Momotombo fault plane being NE-trending with oblique slip with a left-lateral component (Figure **3-20**), while the La Paz Centro fault plane is NW-trending and right-lateral oblique-slip (Figure **3-21**). The La Paz Centro model not only has a poorer misfit than the Momotombo model but the fault trace intersects known active left-lateral faults of the fault zone (La Femina et al., 2004; Díez et al., 2005), and is therefore geologically not feasible. The alignment of the Momotombo model's fault plane corresponds to a mapped structure on the western flank of the Momotombo volcano, making this the likely model that better represents the geodetic displacements observed.

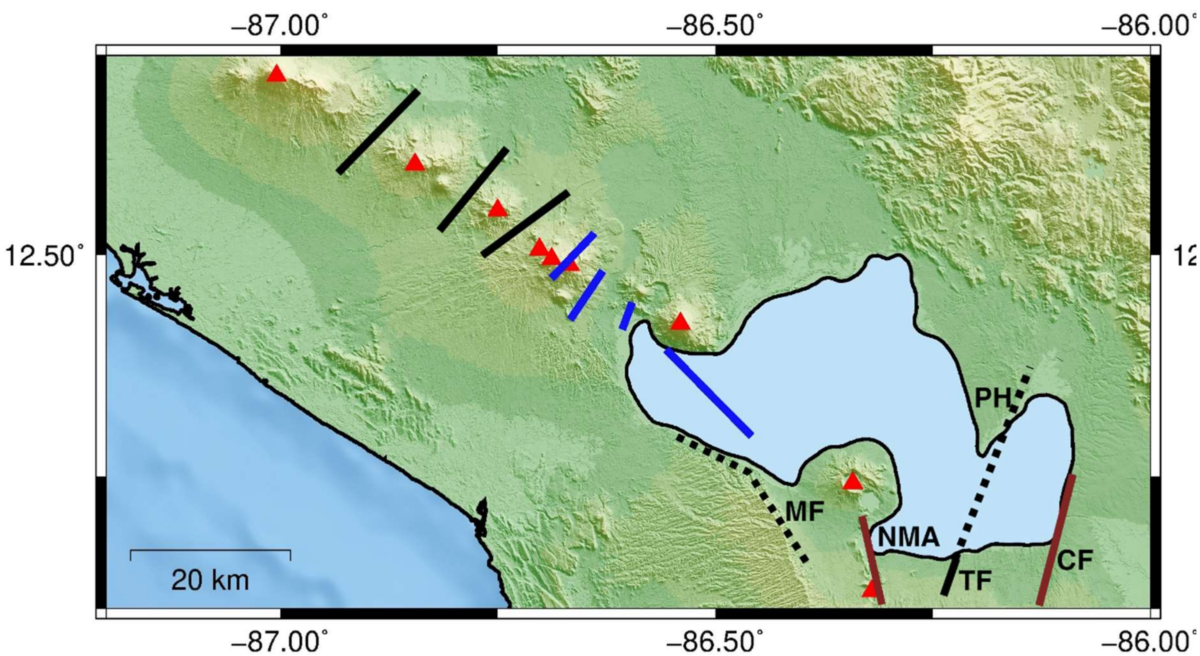

Figure **3-54**: Inversion fault traces (blue), known structures and faults associated with seismicity (black), and mapped faults (dashed black line). Brown lines are faults that bound the Managua

Graben. CF – Confradia fault, MF – Mateare fault, NMA – Nejapa–Miraflores–Apoyeque alignment, PH – Punta Huete fault, TF – Tiscapa fault.

The faulting and sense of motion of three moderate magnitude earthquakes reveal that bookshelf faulting is accommodating CAFA-CA dextral shear in NW Nicaragua. Inversion of the September 2016 earthquakes revealed an array of faults that are NE-trending with normal faulting and left-lateral slip. The location of these faults, between volcanic centers, (Figure **3-46**) supports the work of Cailleau et al. (2007) who found that the thermal regime of volcanic centers promotes stress in the stronger lithosphere between volcanos. Faults with similar strike and sense of motion have also been identified in the El Salvador Fault Zone where bookshelf faulting occurs (Alvarado et al., 2010). The right-lateral fault of the April 10^{th}, 2014 earthquake is a transition zone from the active Managua Graben (Figure **3-54**) that is undergoing E-W extension, to bookshelf faulting in the volcanic arc of NW Nicaragua.

3.6.2 Earthquake Sequence

The three earthquakes constitute a triggered sequence. The ΔCFS analysis indicates that the April 2014 earthquake promoted failure of the faults for the two September 2016 earthquakes. The fault traces of the two earthquakes lie in a region of positive ΔCFS following the April 2014 earthquakes (Figure **3-26**). ΔCFS analysis also shows that the M_w 5.7 September 15^{th}, 2016 triggered an earthquake five minutes after the mainshock and another M_w 5.5 earthquake that occurred 13 days later (Figures **3-29**, **3-31** & **3-33**). These earthquakes represent a triggered sequence, which indicates that seismicity can migrate through the central NW Nicaraguan volcanic arc. This has been observed before in the CAFA where sequences of earthquakes that occurred in the periods of 1951 to 1955 and 1999 to 2000 indicate southwest migration of seismicity due to stress transfer (Cannon 2014). Migration of seismicity on parallel faults has also been observed in the South Iceland Seismic Zone, the Eastern California Shear Zone, and the Central Nevada Seismic Belt (Stefánsson et al., 2000; Scholz, 2010).

The static stress change following the April 10th, 2014 earthquake, also triggered the Mw 5.2 April 14th earthquake near the Apoyoque volcano and imparted a positive ΔCFS on the faults in the Managua graben. The destructive Ms 6.2 1972 Managua earthquake occurred on the Tiscapa fault. The change in static stress for this fault implies that failure is promoted on the fault and the period of earthquake cycle may have been shortened, which has seismic hazard implications.

3.6.3 Magma-Tectonic Interactions: April 10, 2014 and December 15, 2015 eruption of Momotombo

In the CAFA there have been few observed cases of magma-tectonic interaction. The 1917 San Salvador eruption occurred 30 minutes after a Ms 6.4 earthquake that was located 30 km west of the volcano (White et al., 1987). The August 1999 VEI 1 eruption of Cerro Negro volcano occurred 11 hours after a swarm of moderate-magnitude earthquakes, whose strikes are aligned with those of the lineaments of the volcanic center, increased the static stress state of the volcano, allowing magma injection (Díez et al., 2005; La Femina et al., 2004). The December 1st, 2015 VEI 2 Momotombo strombolian eruption occurred ~19 months after the Mw 6.1 April 2014 earthquake. The volcano is persistently active since monitoring began (1975) but the last eruption was in 1905 (Moore et al., 1981). There is evidence that a dilated dike and magma injection drove the eruption. The eruption was preceded by seismic swarms that began on November 24th (INETER Bulletin, November 2015) and no pre-eruption ground deformation was observed by a cGPS station on the southern flank of the volcano. This station was displaced ~6 cm after the April 10th, 2014 earthquake (Figure **3-4**). Preceding the eruption, pressure within geothermal wells in the Momotombo geothermal field began increasing in June 2015 (personal communications ORMAT Momotombo Power Company). The April 2014 earthquake may have dilated the dike and allowed magma injection and ascent.

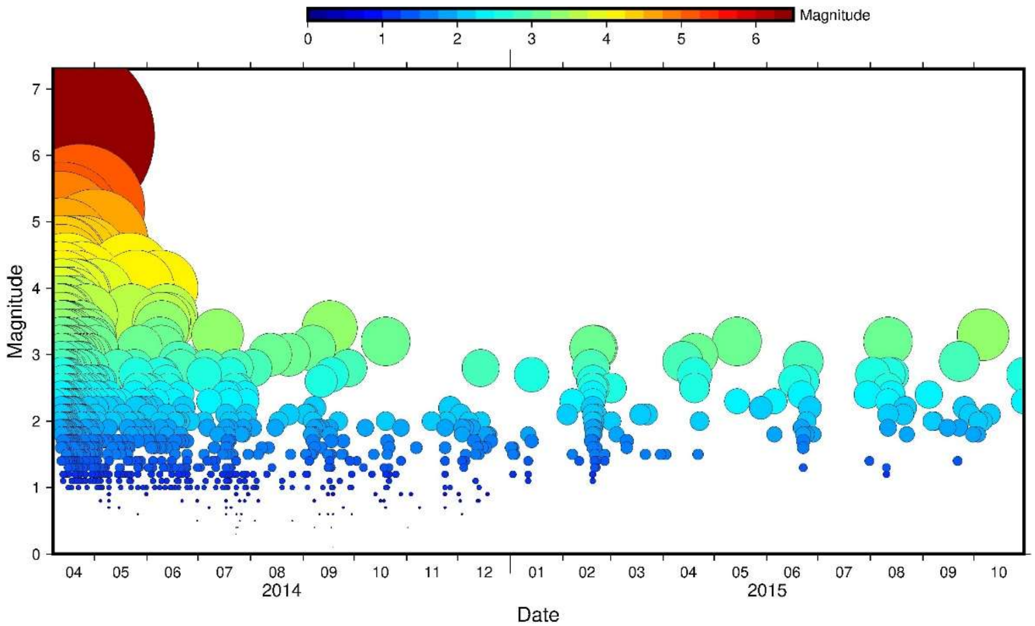

Figure **3-55**: Magnitude and date (year-month) of aftershocks and volcano tectonic earthquakes from April 10th, 2014 to November 23th, 2015. Earthquake data are sourced from the INETER catalog.

Normal static stress change and dilatation strain analysis (Figures **3-47** to **3-53**) shows that the magmatic plumbing, up to 8 km beneath Momotombo, would have experienced up to 1.2 MPa normal stress change, and dilation of 2 x 10^{-4}. This change in the normal stress field is also correlated with a low-velocity zone beneath (<10 km) Momotombo (Obermann et al. 2019). La Femina et al. (2004) and Díez et al. (2005) demonstrated that a normal stress change of 0.01 to 0.1 MPa at the Cerro Negro volcano allowed the injection, extrusion, and fountaining of 0.001 km^3 of magma. The April 2014 earthquake would have induced a change in the state of the magmatic plumbing. Following the earthquake, and up to 7 months later, several M 0.9 to M 2 volcanic tectonic earthquakes were recorded around Momotombo (Figure **3-55**). The earthquake and subsequent eruption do indicate a magma-tectonic interaction but further studies that address melt origin, residence times, and ascent velocities are needed to understand the tectonic stress change and eruption relationship (Roman et al. 2019).

3.7 Conclusions

Accommodation of CAFA-CA dextral shear in NW Nicaragua is complex where right-lateral NW-trending faulting in western Lake Managua represents a transitional zone from the Managua Graben undergoing E-W extension, to bookshelf faulting in the Maribios Range to the northwest. This was revealed by three moderate magnitude earthquakes. The M_w 6.1 April 10th, 2014 earthquake occurred on a southwest dipping fault with a strike of 313°. The M_w 5.7 September 15th, 2016 on a fault that had a vertical dip and strike of 55° while the earthquake that occurred 5 minutes after the mainshock had a dip of 86° and a strike of 47°. The M_w 5.5 September 28th earthquake occurred on a fault with a dip of 85° and strike of 22°. This sequence of earthquakes also represents the promotion of failure of the bookshelves following the initial event (i.e., a triggered sequence). The M_w 6.1 April 10th, 2014 earthquake may have induced dike dilation of the Momotombo, thereby allowing magma injection and the December 1st, 2015 eruption.

3.8 References

Agostini, Samuele, Giacomo Corti, Carlo Doglioni, Eugenio Carminati, Fabrizio Innocenti, Sonia Tonarini, Piero Manetti, Gianfranco Di Vincenzo, and Domenico Montanari. 2006. "Tectonic and Magmatic Evolution of the Active Volcanic Front in El Salvador: Insight into the Berlín and Ahuachapán Geothermal Areas." *Geothermics* 35 (4): 368–408. https://doi.org/10.1016/j.geothermics.2006.05.003.

Algermissen, S. T., J. W. Dewey, C. J. Langer, and W. H. Dillinger. 1974a. "The Managua, Nicaragua, Earthquake of December 23, 1972: Location, Focal Mechanism, and Intensity Distribution." *Bulletin of the Seismological Society of America* 64 (4): 993–1004. https://doi.org/10.1086/622062.

Algermissen, S T, J W Dewey, C J Langer, and W H Dillinger. 1974b. "The Managua, Nicaragua, Earthquake of December 23, 1972: Location, Focal Mechanism, and Intensity Distribution." *Bulletin of the Seismological Society of America* 64 (4): 993–1004.

Alvarado, D., C. DeMets, B. Tikoff, D. Hernández, T.F. Wawrzyniec, C. Pullinger, G. Mattioli, H.L. Turner, M. Rodriguez, and F. Correa-Mora. 2010. "Forearc Motion and Deformation between El Salvador and Nicaragua: GPS, Seismic, Structural, and Paleomagnetic Observations." *Lithosphere* 3 (1): 3–21. https://doi.org/10.1130/l108.1.

Alvarez, Leonardo, Ana Maria Rodriguez, O Leary Gonzalez, Bladimir Moreno, and Amilcar Cabrera. 2018. "Seismotectonics of the Nicaraguan Depression from Recent Seismicity." *Journal of Geology & Geophysics* 07 (05). https://doi.org/10.4172/2381-8719.1000446.

Ambraseys, N. N., J. J. Bommer, E. Buforn, and A. Udías. 2001. "The Earthquake Sequence of May 1951 at Jucuapa, El Salvador." *Journal of Seismology* 5 (1): 23–39. https://doi.org/10.1023/A:1009883313414.

Araya, Maria C, and Juliet Biggs. 2020. "Deformation Associated with Sliver Transport in Costa Rica: Seismic and Geodetic Observations of the July 2016 Bijagua Earthquake Sequence." *Geophysical Journal International* 220 (1): 585–97. https://doi.org/10.1093/gji/ggz474.

Authemayou, C., G. Brocard, C. Teyssier, T. Simon-Labric, A. Guttiérrez, E. N. Chiquín, and S. Morn. 2011. "The Caribbean-North America-Cocos Triple Junction and the Dynamics of the Polochic-Motagua Fault Systems: Pull-up and Zipper Models." *Tectonics* 30 (3): 1–23. https://doi.org/10.1029/2010TC002814.

Avé Lallemant, H. G., and J. S. Oldow. 2000. "Active Displacement Partitioning and Arc-Parallel Extension of the Aleutian Volcanic Arc Based on Global Positioning System Geodesy and Kinematic Analysis." *Geology* 28 (8): 739–42. https://doi.org/10.1130/0091-7613(2000)28<739:ADPAAE>2.0.CO;2.

Bagnardi, Marco, and Andrew Hooper. 2018. "Inversion of Surface Deformation Data for Rapid Estimates of Source Parameters and Uncertainties: A Bayesian Approach." *Geochemistry, Geophysics, Geosystems* 19 (7): 2194–2211. https://doi.org/10.1029/2018GC007585.

Bayes, Thomas. 1763. "LII. An Essay towards Solving a Problem in the Doctrine of Chances. By the Late Rev. Mr. Bayes, FRS Communicated by Mr. Price, in a Letter to John Canton, AMFR S." *Philosophical Transactions of the Royal Society of London*, no. 53: 370–418.

Brown, R. D., P. L. Ward, and G. Plafker. 1974. "Geologic and Seismologic Aspects of the Managua, Nicaragua, Earthquakes of December 23, 1972: US Geological Survey Professional Paper 838, 1973." *Bulletin of the Seismological Society of America* 64 (4): 1031.

Cailleau, B., P. C. Lafemina, and T. H. Dixon. 2007. "Stress Accumulation between Volcanoes: An Explanation for Intra-Arc Earthquakes in Nicaragua?" *Geophysical Journal International* 169 (3): 1132–38. https://doi.org/10.1111/j.1365-246X.2007.03353.x.

Cannon, Sandra. 2014. "Seismicity in Nicaragua: Earthquake Triggering along the Central American

Forearc." The Pennsylvania State University.

Canora, Carolina, José J. Martínez-Díaz, Alejandra Staller, Ramón Capote, Kelvin Berryman, Jose A. Álvarez-Gómez, Pilar Villamor, and Manuel Diaz. 2014. "Structural Evolution of the El Salvador Fault Zone: An Evolving Fault System within a Volcanic Arc." *Journal of Iberian Geology* 40 (3): 471–88. https://doi.org/10.5209/rev_jige.2014.v40.n3.43559.

Carr, Michael J., and Richard E. Stoiber. 1977. "Geologic Setting of Some Destructive Earthquakes in Central America." *Geological Society of America Bulletin* 88 (1): 151–56.

Carr, Michael J. 1976. "Underthrusting and Faulting Central America." *Bulletin of the Geological Society of America*.

Correa-Mora, F., C. DeMets, D. Alvarado, H. L. Turner, G. Mattioli, D. Hernandez, C. Pullinger, M. Rodriguez, and C. Tenorio. 2009. "GPS-Derived Coupling Estimates for the Central America Subduction Zone and Volcanic Arc Faults: El Salvador, Honduras and Nicaragua." *Geophysical Journal International* 179 (3): 1279–91. https://doi.org/10.1111/j.1365-246x.2009.04371.x.

Corti, Giacomo, Eugenio Carminati, Francesco Mazzarini, and Marvyn Oziel Garcia. 2005. "Active Strike-Slip Faulting in El Salvador, Central America." *Geology* 33 (12): 989–92. https://doi.org/10.1130/G21992.1.

Cowan, By Hugh, Michael N Machette, Xavier Amador, Karen S Morgan, Richard L Dart, and Lee-ann Bradley. 2000. "Map and Database of Quaternary Faults in the Vicinity of Managua, Nicaragua." *US Geological Survey*.

DeMets, Charles, Richard G. Gordon, and Donald F. Argus. 2010. "Geologically Current Plate Motions." *Geophysical Journal International* 181 (1): 1–80. https://doi.org/10.1111/j.1365-246X.2009.04491.x.

Dewey, J.W., and S.T. Algermissen. 1974. "Seismicity of the Middle America Arc-Trench System near Managua, Nicaragua." *Bulletin of the Seismological Society of America* 64 (4): 1033–48.

Díez, M., P. C. La Femina, C. B. Connor, W. Strauch, and V. Tenorio. 2005. "Evidence for Static Stress Changes Triggering the 1999 Eruption of Cerro Negro Volcano, Nicaragua and Regional Aftershock Sequences." *Geophysical Research Letters* 32 (4): 1–4. https://doi.org/10.1029/2004GL021788.

Duffield, W. A., G. H. Heiken, K. H. Wohletz, L. W. Maassen, G. Dengo, E. H. Mckee, and Oscar Castañeda. 1992. "Geology and Geothermal Potential of the Tecuamburro Volcano Area, Guatemala." *Geothermics* 21 (4): 425–46. https://doi.org/10.1016/0375-6505(92)90001-P.

Dziewonski, A. M., T. A. Chou, and J. H. Woodhouse. 1981. "Determination of Earthquake Source Parameters from Waveform Data for Studies of Global and Regional Seismicity." *Journal of Geophysical Research: Solid Earth* 86 (B4): 2825–52.

Ekström, G., M. Nettles, and A. M. Dziewoński. 2012. "The Global CMT Project 2004-2010: Centroid-Moment Tensors for 13,017 Earthquakes." *Physics of the Earth and Planetary Interiors* 200–201: 1–9. https://doi.org/10.1016/j.pepi.2012.04.002.

Ellis, A, C DeMets, Robert McCaffrey, P Briole, Beatriz Cosenza Muralles, Omar Flores, Marco Guzmán-Speziale, et al. 2019. "GPS Constraints on Deformation in Northern Central America from 1999 to 2017, Part 2: Block Rotations and Fault Slip Rates, Fault Locking and Distributed Deformation." *Geophysical Journal International* 218 (2): 729–54.

Femina, P. C. La, C. B. Connor, B.E. Hill, W. Strauch, and J. A. Saballos. 2004. "Magma-Tectonic Interactions in Nicaragua: The 1999 Seismic Swarm and Eruption of Cerro Negro Volcano." *Journal of Volcanology and Geothermal Research* 137 (1-3 SPEC. ISS.): 187–99. https://doi.org/10.1016/j.jvolgeores.2004.05.006.

Femina, P. C. La, T. H. Dixon, and W. Strauch. 2002. "Bookshelf Faulting in Nicaragua." *Geology* 30 (8): 751–54. https://doi.org/10.1130/0091-7613(2002)030<0751:BFIN>2.0.CO;2.

Femina, Peter La, Timothy H. Dixon, Rob Govers, Edmundo Norabuena, Henry Turner, Armando Saballos, Glen Mattioli, Marino Protti, and Wilfried Strauch. 2009. "Fore-Arc Motion and Cocos Ridge Collision in Central America." *Geochemistry, Geophysics, Geosystems* 10 (5). https://doi.org/10.1029/2008GC002181.

Fitch, Thomas J. 1972. "Plate Convergence, Transcurrent Faults, and Internal Deformation Adjacent to Southeast Asia and the Western Pacific." *Journal of Geophysical Research* 77 (23): 4432–60.

French, S. W., L. M. Warren, K. M. Fischer, G. A. Abers, W. Strauch, J. M. Protti, and V. Gonzalez. 2010. "Constraints on Upper Plate Deformation in the Nicaraguan Subduction Zone from Earthquake Relocation and Directivity Analysis." *Geochemistry, Geophysics, Geosystems* 11 (3): 1–17. https://doi.org/10.1029/2009GC002841.

Frischbutter, A. 2002. "Structure of the Managua Graben, Nicaragua, from Remote Sensing Images." *Geofisica Internacional* 41 (2): 87–102. https://doi.org/10.22201/igeof.00167169p.2002.41.2.279.

Funk, Justin, Paul Mann, Kirk McIntosh, and Jason Stephens. 2009. "Cenozoic Tectonics of the Nicaraguan Depression, Nicaragua, and Median Trough, El Salvador, Based on Seismic-Reflection Profiling and Remote-Sensing Data." *Bulletin of the Geological Society of America* 121 (11–12): 1491–1521. https://doi.org/10.1130/B26428.1.

Gardner, T. W., D. Verdonck, N. M. Pinter, R. Slingerland, K. P. Furlong, T. F. Bullard, and S. G. Wells. 1992. "Quaternary Uplift astride the Aseismic Cocos Ridge, Pacific Coast, Costa Rica." *Geological Society of America Bulletin* 104 (2): 219–32. https://doi.org/10.1130/0016-7606(1992)104<0219:QUATAC>2.3.CO;2.

Garibaldi, Nicolás, Basil Tikoff, and Walter Hernández. 2016. "Neotectonic Deformation within an Extensional Stepover in El Salvador Magmatic Arc, Central America: Implication for the Interaction of Arc Magmatism and Deformation." *Tectonophysics* 693: 327–39. https://doi.org/10.1016/j.tecto.2016.05.015.

Geist, Eric L, Jonathan R Childs, and David W Scholl. 1988. "The Origin of Summit Basins of the Aleutian Ridge: Implications for Block Rotation of an Arc Massif." *Tectonics* 7 (2): 327–41.

Genrich, J. F., Y- Bock, R. McCaffrey, L Prawirodirdjo, C W Stevens, S. S. O. Puntodewo, C. Subarya, and S. Wdowinski. 2000. "Distribution of Slip at the Northern Sumatran Fault System." *Journal of Geophysical Research: Solid Earth* 105 (B12): 28327–41. https://doi.org/10.1029/2000jb900158.

Harlow, D. H., R. A. White, M. J. Rymer, and S. Alvarez G. 1993. "The San Salvador Earthquake of 10 October 1986 and Its Historical Context." *Bulletin of the Seismological Society of America* 83 (4): 1143–54.

INETER. 2014. "Boletín Mensual Sismos y Volcanes de Nicaragua Instituto Nicaragüense de Estudios Territoriales, Abril 2014." Vol. April. Managua, Nicaragua. https://webserver2.ineter.gob.ni/boletin/2014/04/boletin-1404.pdf.

———. 2015. "Boletín Mensual Sismos de Nicaragua Instituto Nicaragüense de Estudios Territoriales, Deciembre 2015." Managua, Nicaragua. https://webserver2.ineter.gob.ni/boletin/2015/12/boletin-1512.pdf.

———. 2016. "Boletín Mensual Sismos y Volcanes de Nicaragua Instituto Nicaragüense de Estudios Territoriales, Sept 2016." Vol. September. Managua, Nicaragua.

Jarrard, Richard D. 1986. "Relations among Subduction Parameters." *Reviews of Geophysics* 24 (2): 217--284.

Jones, Donald R, Matthias Schonlau, and William J Welch. 1998. "Efficient Global Optimization of Expensive Black-Box Functions." *Journal of Global Optimization* 13 (4): 455–92.

Kobayashi, D., P. LaFemina, H. Geirsson, E. Chichaco, A. A. Abrego, H. Mora, and E. Camacho.

2014. “Kinematics of the Western Caribbean: Collision of the Cocos Ridge and Upper Plate Deformation.” *Geochemistry, Geophysics, Geosystems* 15 (5): 1671–83. https://doi.org/10.1002/2014GC005469.Received.

Langer, C J, M G Hopper, S T Algermissen, and J W Dewey. 1974. “Aftershocks of the Managua, Nicaragua, Earthquake of December 23, 1972.” *Bulletin of the Seismological Society of America* 64 (4): 1005–16.

Legrand, D, G Marroquín, C Demets, L Mixco, A García, M Villalobos, D Ferr, D Escobar, R Torres, and D Hern. 2020. “Active Deformation in the San Salvador Extensional Stepover , El Salvador from an Analysis of the April – May 2017 Earthquake Sequence and GPS Data.” *Journal of South American Earth Sciences* 104 (August). https://doi.org/10.1016/j.jsames.2020.102854.

Lewis, Jonathan C., Adam C. Boozer, Allan López, and Walter Montero. 2008. “Collision versus Sliver Transport in the Hanging Wall at the Middle America Subduction Zone: Constraints from Background Seismicity in Central Costa Rica.” *Geochemistry, Geophysics, Geosystems* 9 (7). https://doi.org/10.1029/2007GC001711.

MacMillan, Ian, Phillip B. Gans, and Guillermo Alvarado. 2004. “Middle Miocene to Present Plate Tectonic History of the Southern Central American Volcanic Arc.” *Tectonophysics* 392 (1–4): 325–48. https://doi.org/10.1016/j.tecto.2004.04.014.

Marshall, Jeffrey S, Donald M Fisher, and Thomas W Gardner. 2000. “Central Costa Rica Deformed Belt: Kinematics of Diffuse Faulting across the Western Panama Block.” *Tectonics* 19 (20): 468--492.

Martínez-Díaz, José J., José A. Álvarez-Gómez, Belén Benito, and Douglas Hernández. 2004. “Triggering of Destructive Earthquakes in El Salvador.” *Geology* 32 (1): 65–68. https://doi.org/10.1130/G20089.1.

McBirney, A. R., and Howel Williams. 1964. “The Origin of the Nicaraguan Depression.” *Bulletin Volcanologique* 27 (1): 63–63. https://doi.org/10.1007/BF02597510.

McCaffrey, Robert. 1992. “Oblique Plate Convergence, Slip Vectors, and Forearc Deformation.” *Journal of Geophysical Research: Solid Earth* 97 (B6): 8905–15.

Minson, S. E., M. Simons, J. L. Beck, F. Ortega, J. Jiang, S. E. Owen, A. W. Moore, A. Inbal, and A. Sladen. 2014. “Bayesian Inversion for Finite Fault Earthquake Source Models - II: The 2011 Great Tohoku-Oki, Japan Earthquake.” *Geophysical Journal International* 198 (2): 922–40. https://doi.org/10.1093/gji/ggu170.

Montero, P.W., J.C. Lewis, J.S. Marshall, S. Kruse, and P. Wetmore. 2013. “Neotectonic Faulting and Forearc Sliver Motion along the Atirro-Río Sucio Fault System, Costa Rica, Central America.” *Bulletin of the Geological Society of America* 125 (5–6): 857–76. https://doi.org/10.1130/B30471.1.

Montero, Walter, Jonathan C. Lewis, and Maria Cristina Araya. 2017. “The Guanacaste Volcanic Arc Sliver of Northwestern Costa Rica.” *Scientific Reports* 7 (1): 1–9. https://doi.org/10.1038/s41598-017-01593-8.

Moore, James L, Erik Osbun, and Paul V Storm. 1981. “Geology and Temperature Distribution of Momotombo Geothermal Field, Nicaragua.”

Morell, Kristin D., Eric Kirby, Donald M. Fisher, and Matthijs Van Soest. 2012. “Geomorphic and Exhumational Response of the Central American Volcanic Arc to Cocos Ridge Subduction.” *Journal of Geophysical Research: Solid Earth* 117 (4). https://doi.org/10.1029/2011JB008969.

Norabuena, Edmundo, Timothy H. Dixon, Susan Schwartz, Heather DeShon, Andrew Newman, Marino Protti, Victor Gonzalez, et al. 2004. “Geodetic and Seismic Constraints on Some Seismogenic Zone Processes in Costa Rica.” *Journal of Geophysical Research: Solid Earth* 109 (11): 1–25. https://doi.org/10.1029/2003JB002931.

Obermann, Anne, Irene Molinari, Jean Philippe Métaxian, Francesco Grigoli, Wilfried Strauch, and Stefan Wiemer. 2019. "Structure of Masaya and Momotombo Volcano, Nicaragua, Investigated with a Temporary Seismic Network." *Journal of Volcanology and Geothermal Research* 379: 1–11. https://doi.org/10.1016/j.jvolgeores.2019.04.013.

Okada, Y. 1985. "Surface Deformation Due to Shear and Tensile Faults in a Half-Space." *Bulletin of the Seismological Society of America* 75 (4): 1135–54.

Protti, M., F. Gu, and K. McNally. 1994. "The Geometry of the Wadati-Benioff Zone under Southern Central America and Its Tectonic Significance: Results from a High-Resolution Local Seismographic Network." *Physics of the Earth and Planetary Interiors* 84 (1–4): 271–87.

Roman, Diana C., Peter C. LaFemina, Rebecca Bussard, Kirsten Stephens, Christelle Wauthier, Machel Higgins, Maureen Feineman, et al. 2019. "Mechanisms of Unrest and Eruption at Persistently Restless Volcanoes: Insights From the 2015 Eruption of Telica Volcano, Nicaragua." *Geochemistry, Geophysics, Geosystems* 20 (8): 4162–83. https://doi.org/10.1029/2019GC008450.

Scholz, Christopher H. 2010. "Large Earthquake Triggering, Clustering, and the Synchronization of Faults." *Bulletin of the Seismological Society of America* 100 (3): 901–9. https://doi.org/10.1785/0120090309.

Schonlau, Matthias, William J Welch, and Donald R Jones. 1998. "Global versus Local Search in Constrained Optimization of Computer Models." *Lecture Notes-Monograph Series*, 11–25.

Scordilis, E. Manolis. 2006. "Empirical Global Relations Converting MS and Mb to Moment Magnitude." *Journal of Seismology* 10 (2): 225–36. https://doi.org/10.1007/s10950-006-9012-4.

Sieh, Kerry, and Danny Natawidjaja. 2000. "Neotectonics of the Sumatran Fault, Indonesia." *Journal of Geophysical Research: Solid Earth* 105 (B12): 28295–326. https://doi.org/10.1029/2000jb900120.

Snoek, Jasper, Hugo Larochelle, and Ryan P Adams. 2012. "Practical Bayesian Optimization of Machine Learning Algorithms." In *Advances in Neural Information Processing Systems*, 2951–59.

Staller, A., J.J. Martínez-Díaz, B. Benito, J. Alonso-Henar, D. Hernández, R. Hernandez-Rey, and M. Diaz. 2016. "Present-Day Crustal Deformation along the El Salvador Fault Zone from ZFESNet GPS Network." *Tectonophysics* 670: 66–81. https://doi.org/10.1016/j.tecto.2015.12.017.

Stefánsson, Ragnar, Gunnar B. Guomundsson, and Páll Halldórsoon. 2000. "The Two Large Earthquakes in the South Iceland Seismie Zone on June 17 and 21, 2000," no. July: 1–8.

Suárez, Gerardo, Angélica Muñoz, Isaac A. Farraz, Emilio Talavera, Virginia Tenorio, David A. Novelo-Casanova, and Antonio Sánchez. 2016. "The 10 April 2014 Nicaraguan Crustal Earthquake: Evidence of Complex Deformation of the Central American Volcanic Arc." *Pure and Applied Geophysics* 173 (10–11): 3305–15. https://doi.org/10.1007/s00024-015-1201-z.

Syracuse, Ellen M., Geoffrey A. Abers, Karen Fischer, Laura MacKenzie, Catherine Rychert, Marino Protti, Víctor González, and Wilfried Strauch. 2008. "Seismic Tomography and Earthquake Locations in the Nicaraguan and Costa Rican Upper Mantle." *Geochemistry, Geophysics, Geosystems* 9 (7): 1–22. https://doi.org/10.1029/2008GC001963.

Turner, Henry L., Peter LaFemina, Armando Saballos, Glen S. Mattioli, Pamela E. Jansma, and Timothy Dixon. 2007. "Kinematics of the Nicaraguan Forearc from GPS Geodesy." *Geophysical Research Letters* 34 (2): 1–5. https://doi.org/10.1029/2006GL027586.

Weinberg, Roberto Ferrez. 1992. "Neotectonic Development of Western Nicaragua." *Tectonics* 11 (5): 1010–17. https://doi.org/10.1029/92TC00859.

Werner, Reinhard, Kaj Hoernle, Paul Van Den Bogaard, Cesar Ranero, Roland Von Huene, and

Dietmar Korich. 1999. "Drowned 14-m.y.-Old Galapagos Archipelago off the Coast of Costa Rica: Implications for Tectonic and Evolutionary Models." *Geology* 27 (6): 499–502. https://doi.org/10.1130/0091-7613(1999)027<0499:DMYOGP>2.3.CO;2.

White, R. A., and D. H. Harlow. 1993. "Destructive Upper-Crustal Earthquakes of Central America since 1900." *Bulletin of the Seismological Society of America* 83 (4): 1115–42.

White, R. A., D. H. Harlow, and S. Alvarez. 1987. "The San Salvador Earthquake of October 10, 1986—Seismological Aspects and Other Recent Local Seismicity." *Earthquake Spectra* 3 (3): 419–34.

Williams, Christopher K I, and Carl Edward Rasmussen. 2006. *Gaussian Processes for Machine Learning*. Vol. 2. MIT press Cambridge, MA.

Wunderman, Richard L, and William I Rose. 1984. "Amatitlán, an Actively Resurging Cauldron 10 Km South of Guatemala City." *Journal of Geophysical Research: Solid Earth* 89 (B10): 8525–39.

Zeumann, Stefanie, and Andrea Hampel. 2017. "Impact of Cocos Ridge (Central America) Subduction on the Forearc Drainage System." *Geology* 45 (10): 907–10. https://doi.org/10.1130/G39251.1.

Chapter 4
The Across-Strike Geodetic Signature of the Central American Forearc-Caribbean Plate in Nicaragua

4.1 Introduction

Strain partitioning between the overriding plate and subduction mega-thrust in convergence margins is attributed to oblique convergence (Jarrard 1986b; Fitch 1972) and strong coupling on the subduction interface (McCaffrey 1992). Strain partitioning may result in trench-parallel transport of the forearc, like the forearc of the Indo-Australia-Eurasian plate boundary in Sumatra, where the relative motion is accommodated by the Great Sumatran fault, a dextral transform fault system within the volcanic arc (Genrich et al., 2000; Sieh & Natawidjaja 2000). The Central American Forearc (CAFA), in the Cocos-Caribbean plate convergence zone, is an escaping tectonic unit due to oblique convergence and the collision and indentation of the Cocos-Ridge with the Caribbean plate (LaFemina et al., 2009; Kobayashi et al., 2014), which initiated 0.5 to 3.5 Mya (Gardner et al., 1992; MacMillan et al., 2004; Morell et al., 2012 and references therein; Zeumann & Hampel 2017). The CAFA-CA relative motion in Central America is accommodated in the Holocene volcanic arc (LaFemina et al. 2009; Kobayashi et al. 2014; Ellis et al. 2019). However, in Nicaragua, there is no through-going (margin parallel) dextral fault system, like the Great Sumatra Fault, that accommodates the CAFA-CA relative motion. In Nicaragua, margin normal faults, termed bookshelf faults, is the primary mechanism that accommodates CAFA-CA shear (La Femina et al., 2002).

In Nicaragua, the CAFA-CA relative motion of ~14 mm/yr is accommodated by bookshelf faulting, where rotating tectonic units are separated by northeast-striking left-lateral faults (Figure **4-1**; LaFemina et al., 2002). Bookshelf faulting in the Nicaraguan segment of the CAFA is supported by earthquake studies where left-lateral motion occurs on arc-normal to transverse faults (Algermissen, et al., 1974; French et al., 2010; La Femina et al., 2002; White & Harlow, 1993). LaFemina et al. (2002), using focal mechanisms of upper-plate earthquakes and geomorphological trends, identified the bookshelf faulting mechanism responsible for forearc transport in Nicaragua. In Nicaragua, shallow (<20 km) upper-plate earthquakes are destructive, frequent, have a maximum magnitude Ms 6.5, and are confined to a 25 km band centered on the volcanic arc (White & Harlow 1993; Syracuse et al., 2008; Carr & Stoiber 1977; Dewey & Algermissen 1974; LaFemina et al., 2009; Kobayashi et al., 2014). The focal mechanisms of these earthquakes indicate that faulting could either be arc-normal and left-lateral or arc-parallel and right-lateral (Figure **4-2**). The destructive M_s 6.2 1972 Managua earthquake occurred on the northeast striking left-lateral Tiscapa fault in the Managua graben (Algermissen et al., 1974; Brown et al., 1974; Ward et al., 1974). The results of Chapter 3 of this dissertation demonstrate that upper-plate earthquakes, within the volcanic arc of the northwestern Nicaraguan CAFA segment (Maribios Range), occur on left-lateral faults that are perpendicular to the direction of shear, as well as a margin parallel fault between the Momotombo and Apoyoque volcanoes in Lake Managua (Figure **4-2**). Bookshelf faulting is the primary mechanism for accommodating the CAFA-CA shear in Nicaragua (Figure **4-3**).

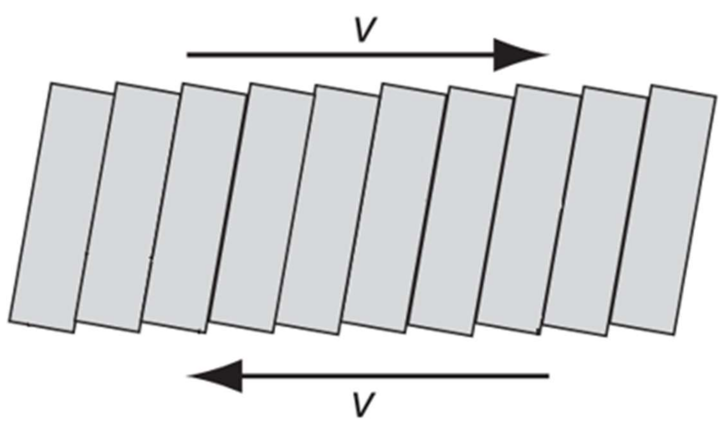

Figure **4-1**: Schematic of bookshelf faulting (from LaFemina in prep).

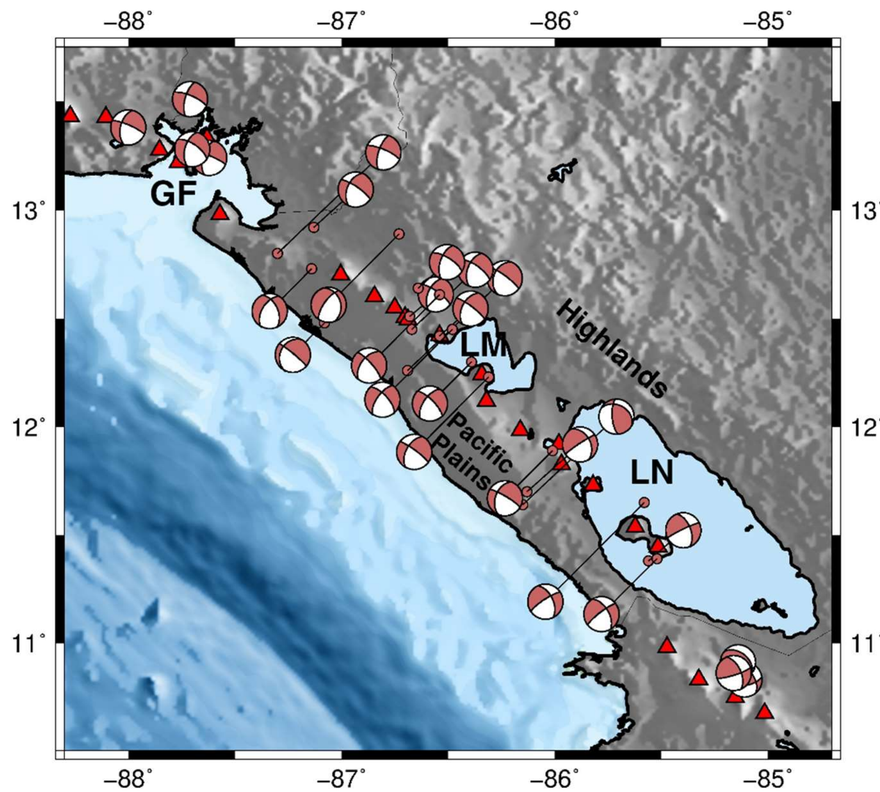

Figure **4-2**: Nicaraguan segment of the Central American forearc (CAFA). The Nicaragua Depression is located between the Highlands and Pacific Plains. GF – Gulf of Fonseco. LM – Lake Managua. LN – Lake Nicaragua. Red triangles are Holocene volcanos. Focal mechanisms of earthquakes with a maximum depth of 20 km and minimum magnitude of M_w 5 from the GCMT catalog (Ekström et al., 2012). Some focal mechanisms are offset from their epicentral locations by thin black lines for clarity.

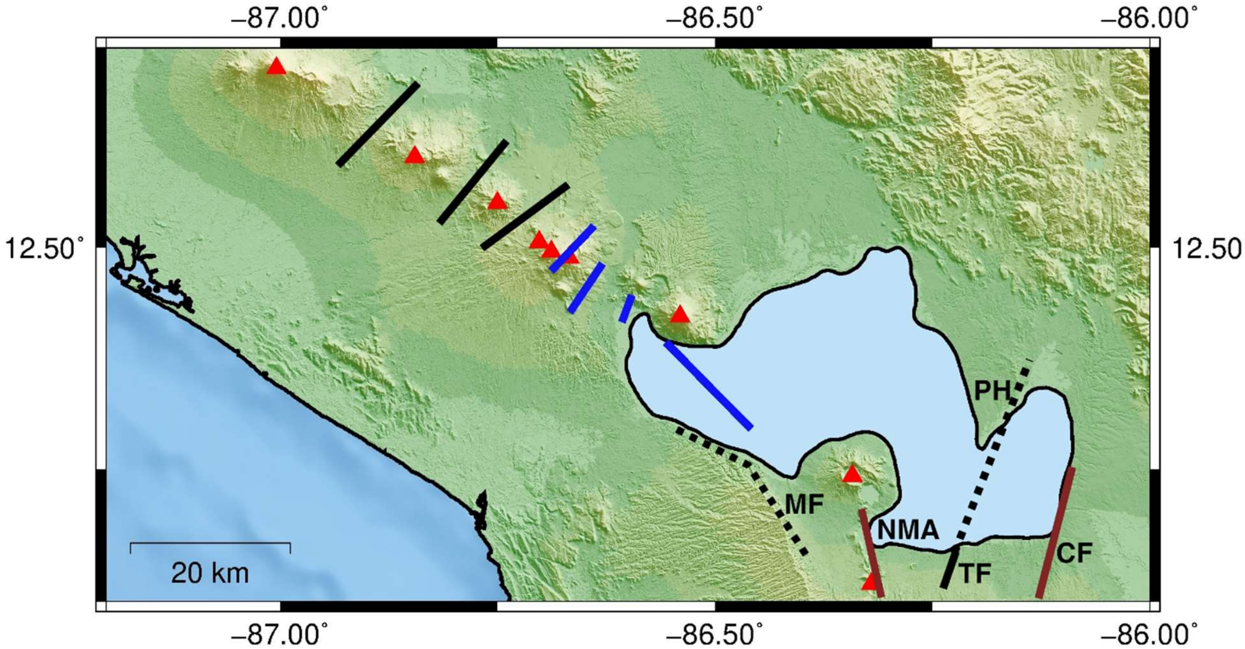

Figure **4-3**: Inversion derived fault traces from Chapter 3 (blue), known structures and faults associated with seismicity (black), and mapped faults (dashed black line). Brown lines are faults that bound the Managua Graben. CF – Confradia fault, MF – Mateare fault, NMA – Nejapa–Miraflores–Apoyeque alignment, PH – Punta Huete fault, TF – Tiscapa fault.

Cailleau et al., (2007), using finite element Coulomb failure analysis, showed that the thermally weakened lithosphere of volcanic centers promotes faulting and seismicity in the lithosphere between volcanic centers. The arc-normal bookshelf faults between volcanic centers are seismogenic but it is possible that faults cutting across volcanic centers (e.g., Van Wyk De Vries and Merle, 1998) creep. Volcanoes within the Holocene arc of the CAFA are characterized as having north-south alignments of vents and are spatially associated with north-striking grabens (McBirney & Williams, 1964; Weinberg, 1992; LaFemina et al., 2002;). Telica, Momotombo, and Cerro Negro are active volcanos, all erupting several times in the last 30 years. At the time of writing, Telica has erupted 15 times, Momotombo has erupted once, and Cerro Negro has erupted twice (Venzke 2020).

The expected mechanism that could be accommodating CAFA-CA relative motion, a throughgoing right-lateral fault system, is not well expressed. The Nicaragua Depression, a conspicuous geomorphic feature of western Nicaragua and the result of Miocene - Pliocene fore-arc extension due to slab retreat (Weinberg 1992; Cailleau and Oncken 2008), is a NW-trending structure and contains both Lakes Nicaragua and Managua. The Nicaragua Depression is bounded by the Nicaragua Highlands to the northeast and the Pacific Plains to the southwest and hosts the Late Pliocene to recent volcanic arcs (Figure **4-2**; Saginor et al., 2013). The depression is a half-graben with normal (down-to-the-southwest) displacement on the southwest boundary (Funk et al., 2009), but no historical seismicity is associated with this structure. The boundary faults of the Nicaragua Depression are therefore unlikely to accommodate the CAFA-CA relative motion.

Bookshelf faulting is not unique to this region as there are similar analogues such as the South Iceland Seismic Zone and Reykjanes Peninsula, Iceland, where east-west transform motion is accommodated by north-south trending faults, which approximates a transform fault in a ridge-transform-ridge system (Decriem et al., 2010; Sigmundsson et al., 1995). Bookshelf faulting also occurs on the southern San Andreas fault, where, between the San Andreas and San Jacinto fault segments, small clockwise rotating crustal blocks are expressed as left-lateral and normal faults (Nicholson et al. 1986). The faults are reactivated faults from a previous phase of deformation (Nicholson et al. 1986). This project explores the geodetic signature that is observed across-strike of the Nicaraguan segment of the CAFA-CA boundary in northwestern Nicaragua using episodic and continuous Global Positioning System data and analytical dislocation and boundary element models. The model results show that the main features of the geodetic signature can be reproduced with an array of faults perpendicular to the direction of shear, i.e., the bookshelf faulting model.

4.2 Data

Campaign-style and continuous Global Positioning Data (GPS) were used to investigate the across-strike geodetic signature of the Nicaraguan segment of the CAFA-CA shear zone. Daily GPS static positions were produced using the same strategy described in Chapter 2 and offsets due to megathrust earthquakes (e.g., 2012 Nicoya and El Salvador megathrust earthquakes), upper-plate earthquakes (see Chapter 3), and volcanic unrest episodes were removed. Seasonal signals in the continuous GPS daily position time series were also removed and velocities and their associated uncertainties (Figure **4-4** and Table **4-1**) were estimated with the Hector software (Bos et al., 2013). Velocities for campaign-style GPS daily position time series were estimated by linear least-squares and uncertainties determined by the RMS of residuals of the linear fit.

The horizontal GPS velocities (Table **4-1**) were rotated into the Caribbean plate reference frame (Table **4-2**; Figure **4-4**) (Kreemer et al., 2014). The resulting horizontal velocity field shows a maximum of ~14 mm/yr of NW translation of the CAFA at the Nicaraguan Pacific coast, the volcanic arc accommodating most of the CAFA-CA shear, and residual strain in the back-arc as velocities asymptotic to 2 mm/yr and do not approach 0 mm/yr (i.e., stable Caribbean Plate motion). The horizontal velocities were projected into an arc-parallel line with an azimuth of 302° (Figures **4-4**). Arc-normal velocities profiles across the Telica, Cerro Negro, and Momotombo volcanic complexes were created (Figures **4-5** and **4-6**).

Table **4-1**: Horizontal GPS velocities used in this project in the ITRF08 reference frame (Altamimi et al., 2012).

Station	**Longitude (°)**	**Latitude (°)**	**V_e (mm/yr)**	**V_n (mm/yr)**	**σ_{ve} (mm/yr)**	**σ_{vn} (mm/yr)**
CALV	-86.8456	12.5724	-23.4	-0.7	1.0	1.0
CN22	-87.0447	12.3841	-25.6	-0.5	0.2	0.2
CORI	-87.1996	12.5166	-24.2	0.4	0.3	0.3
DIA2	-86.7190	12.4846	-20.1	-2.2	2.1	0.7
ELMA	-86.6748	12.4658	-17.5	1.2	1.0	1.0
HERH	-86.8310	12.6093	-22.4	-0.7	0.2	0.2
HOYN	-86.8281	12.5987	-21.4	-3.7	0.2	0.2
JCFI	-86.8283	12.6837	-19.3	-5.7	0.2	0.2
KIOS	-86.7017	12.4943	-16.5	2.2	1.0	1.0
LAGA	-86.3132	12.5663	-14.7	-4.8	0.4	0.7
LEME	-86.9095	12.4274	-23.5	0.4	0.2	0.2
LUIS	-86.5763	12.6783	-16.2	-3.3	0.6	0.3
MALP	-86.6776	12.5460	-20.8	1.9	0.6	0.7
MOM0	-86.5409	12.4061	-19.6	-3.9	1.0	0.2
PAZC	-86.5921	12.2948	-25.6	-2.4	0.5	0.4
PLAP	-86.7923	12.5010	-23.8	1.9	0.9	0.7
POLS	-86.8129	12.6493	-18.3	-3.7	0.2	0.2
PONE	-87.0209	12.3830	-23.7	-1.4	0.3	0.3
QUEN	-86.8519	12.5918	-22.4	-0.7	0.2	0.2
ROSA	-86.3727	12.7524	-14.8	-4.6	0.7	0.5
SALN	-86.8561	12.6177	-20.4	-2.7	0.2	0.2
TECF	-86.8383	12.6031	-22.4	-2.7	0.2	0.2
TELN	-86.8348	12.6064	-22.4	-2.7	0.2	0.2
TROZ	-86.6321	12.6156	-17.1	-3.2	0.8	1.5

Table **4-2**: Horizontal GPS velocities used in this project. Velocities are in the Caribbean plate reference frame (GSRM 2.1; Kreemer et al., 2014).

Station	**Longitude (°)**	**Latitude (°)**	**V_e (mm/yr)**	**V_n (mm/yr)**	**σ_{ve} (mm/yr)**	**σ_{vn} (mm/yr)**
CALV	-86.8456	12.5724	-10.7	4.7	1.0	1.0
CN22	-87.0447	12.3841	-12.8	4.8	0.2	0.2
CORI	-87.1996	12.5166	-11.4	5.5	0.3	0.3
DIA2	-86.719	12.4846	-7.4	3.2	2.1	0.7
ELMA	-86.6748	12.4658	-4.8	6.6	0.2	0.2
HERH	-86.831	12.6093	-9.7	4.7	0.2	0.2
HOYN	-86.8281	12.5987	-8.7	1.7	0.2	0.2
JCFI	-86.8283	12.6837	-6.6	-0.3	0.2	0.2
KIOS	-86.7017	12.4943	-3.7	7.6	0.2	0.2
LAGA	-86.3132	12.5663	-2.0	0.7	0.4	0.7
LEME	-86.9095	12.4274	-10.8	5.7	0.2	0.2
LUIS	-86.5763	12.6783	-3.6	2.1	0.6	0.3
MALP	-86.6776	12.546	-8.1	7.3	0.6	0.7
MOM0	-86.5409	12.4061	-6.8	1.5	1.0	0.0
PAZC	-86.5921	12.2948	-12.8	3.1	0.5	0.4
PLAP	-86.7923	12.501	-11.1	7.3	0.9	0.7
POLS	-86.8129	12.6493	-5.7	1.7	0.2	0.2
PONE	-87.0209	12.383	-10.9	3.8	0.3	0.3
QUEN	-86.8519	12.5918	-9.7	4.7	0.2	0.2
ROSA	-86.3727	12.7524	-2.1	0.9	0.7	0.5
SALN	-86.8561	12.6177	-7.7	2.7	0.2	0.2
TECF	-86.8383	12.6031	-9.7	2.7	0.2	0.2
TELN	-86.8348	12.6064	-9.7	2.7	0.2	0.2
TROZ	-86.6321	12.6156	-4.4	2.3	0.8	1.5
VIST	-86.4869	12.7052	-3.2	0.2	0.8	0.4

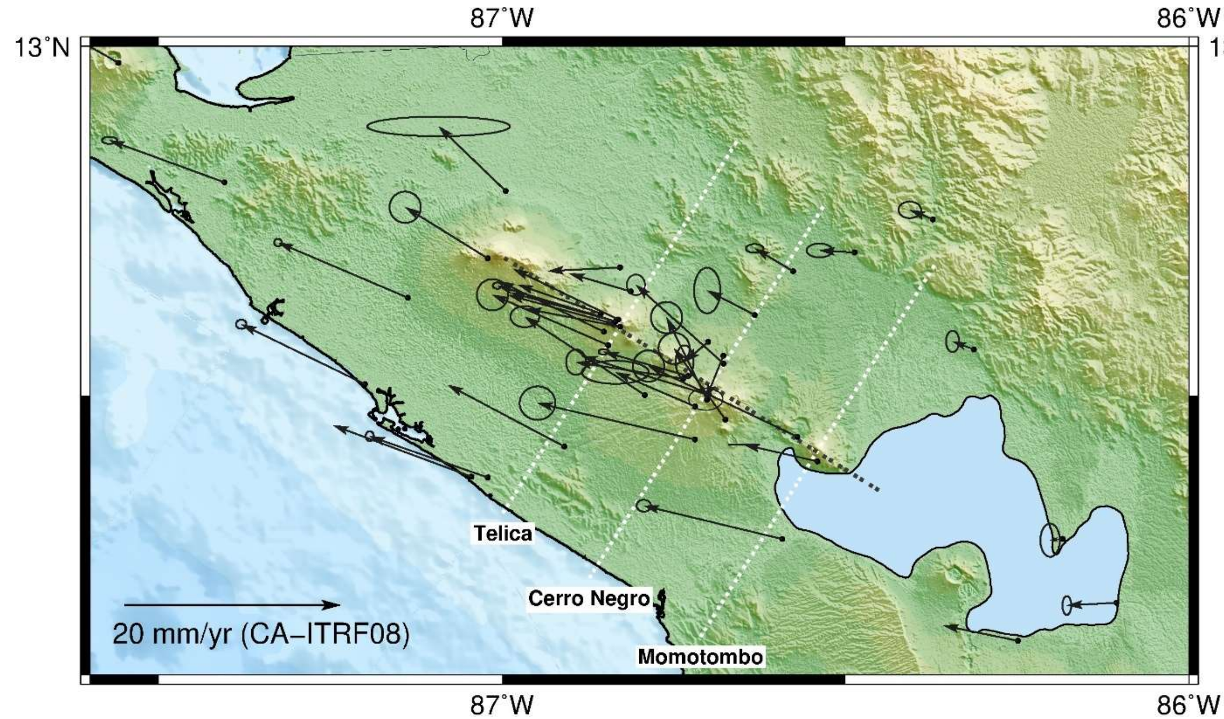

Figure **4-4**: Horizontal GPS velocities used in this project. Velocities are in the Caribbean plate reference frame (Kreemer et al., 2014). Black dashed line – volcanic arc axis (azimuth of 302°) that velocities are projected into.

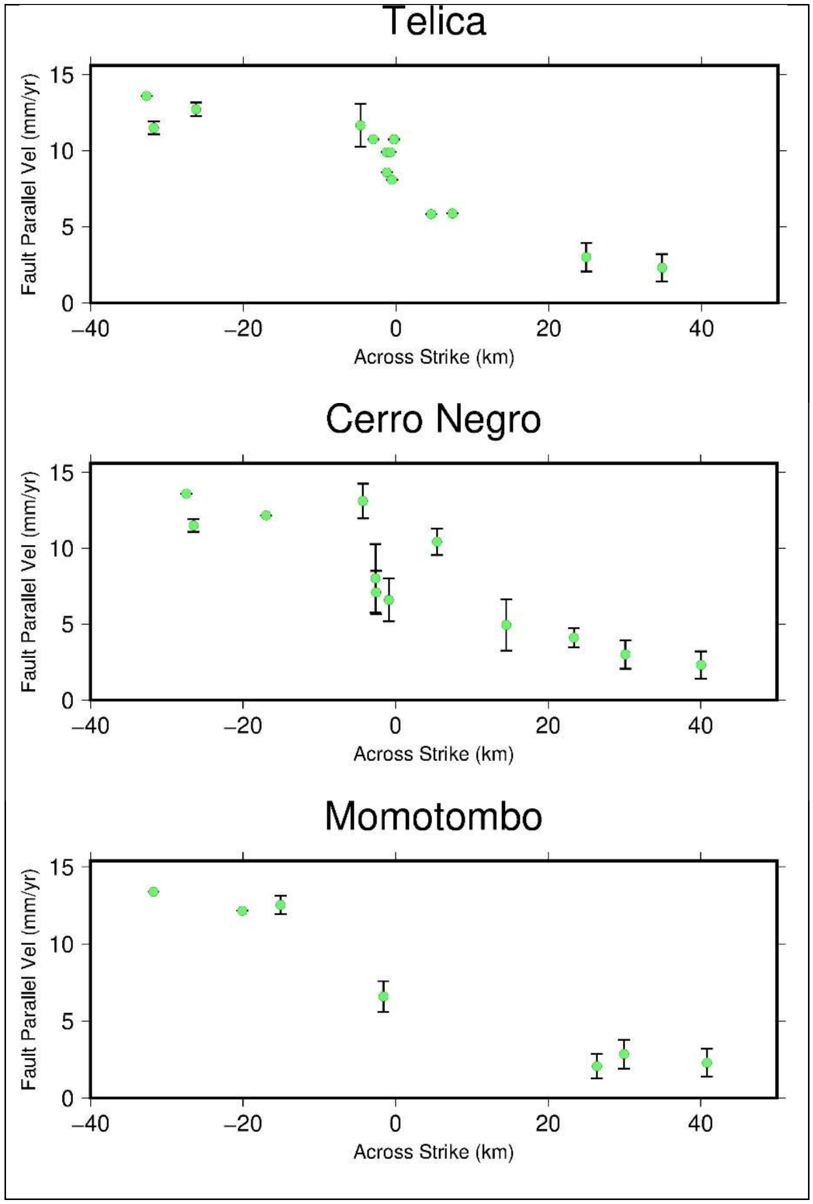

Figure **4-5**: Arc-parallel horizontal velocities on arc-normal profiles across the Telica (top panel), Cerro Negro (middle panel), and Momotombo (bottom panel) volcanoes.

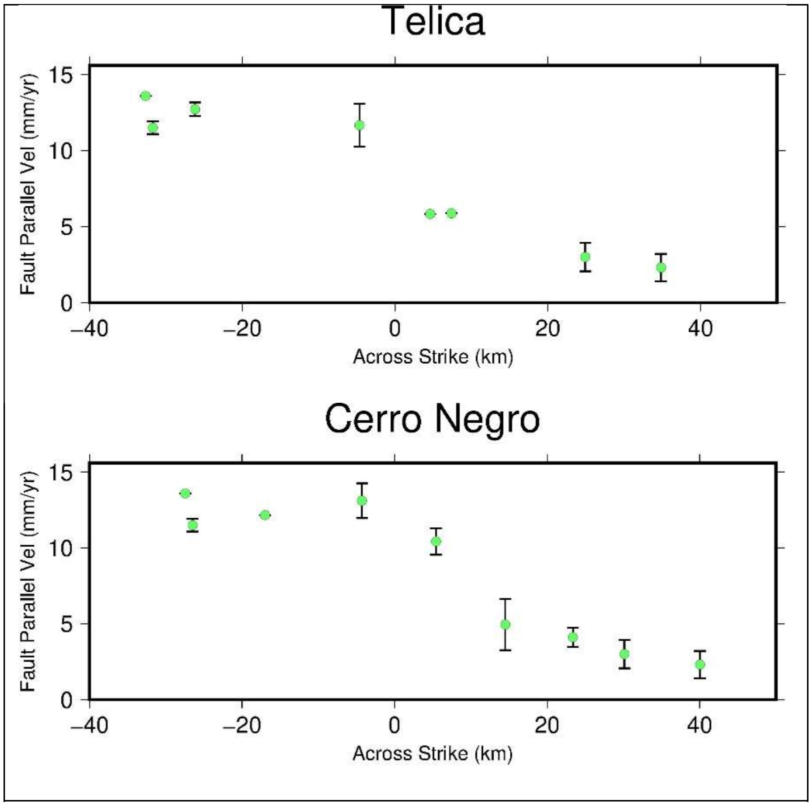

Figure **4-6**: Arc-parallel horizontal velocities on arc-normal profiles across the Telica (top panel), Cerro Negro (middle panel), and Momotombo (bottom panel) volcanoes with GPS stations on the volcanic systems removed.

The across-strike geodetic signature (Figures **4-5** and **4-6**) indicates dextral-shear across the arc and is suggestive of a shear zone at depth and interseismic strain accumulation (e.g., Chapter 3 study of the CA-SA transform plate boundary). This is evident in the asymptotic nature of the velocities in the back-arc. While there is not an equivalent amount of data for the three velocity profiles, the Telica and Cerro Negro velocity profiles do show a similar signature.

4.2 Modeling

The horizontal velocities across the CAFA-CA plate boundary indicate dextral shear centered on the volcanic arc. The velocity field is similar to other geodetically studied transform plate boundaries (e.g., Chapter 2). However, as previously described, the boundary is kinematically more similar to the South Iceland Seismic Zone and/or Reykjanes Peninsula, whereby dextral shear is accommodated on margin normal faults (i.e., the bookshelf faulting model). To explore the kinematics of how the CAFA-CA dextral shear is accommodated two modes of shear were tested: (1) arc-parallel faulting and (2) arc-normal faulting. A model of an arc-parallel throughgoing fault system was first attempted using the elastic dislocation (Savage and Burford, 1973) for the Telica, Cerro Negro, and Momotombo velocity profiles. Following the results of arc-parallel throughgoing fault, several other models were inverted to explain the observed velocities. The observed velocities could be attributed to two arc-parallel right-lateral faults and, for this reason, the velocities were inverted for a two-fault elastic dislocation model. The velocity signature may be due to change in crustal rheology or a compliant zone. For these reasons one- and two-fault hetero-elastic dislocation models (Le Pichon et al., 2005; Segall, 2010) were also inverted. To explore shear via arc-normal faults (bookshelf faulting) and the resulting surface displacements, the boundary element method was used (Gomberg and Ellis 1993).

Both the elastic and hetero-elastic dislocation models were inverted using the same hybrid Monte Carlo strategy as Chapter 2. The velocity profiles were perturbed by randomly sampling within the observed velocity uncertainties and the solution sought using the *fmincon* minimizer in the Matlab software. Uncertainties were calculated from the resulting probability distributions. To discount the possible influence of volcanic centers and associated processes, the elastic and hetero-elastic dislocation models were fitted to velocity profiles without GPS stations sited on the active volcanos. The exception was Momotombo because most of the stations are off the flanks of the volcano (Figure

4-4). Due to the paucity of data for the Momotombo velocity profile, inversions for two subparallel faults elastic and hetero-elastic dislocation models were also not performed. The fits of the dislocation models to the data were evaluated using the reduced chi-square statistic, which is described by Equation 1,

$$\bar{\chi}^2 = \chi^2/v \quad \textbf{4-13}$$

where v is the degrees of freedom (i.e., number of data – number of parameters), and chi-square (χ^2) which is weighted by the square of the uncertainty of observed velocities σ^2, shown in Equation 2

$$\chi^2 = \sum_i \frac{(o_i - m_i)^2}{\sigma_i^2} \quad \textbf{4-14}$$

where o is the observed velocity and m is the modeled velocity.

4.2.1 Arc-Parallel Fault Elastic Dislocation Model

4.2.1.1 Modeling

The mode of shear via an arc-parallel right-lateral fault was explored by inverting the observed GPS velocities using the elastic dislocation model. The elastic dislocation model (Savage and Burford 1973) describes the elastic strain of a strike-slip fault and assumes, if there is locking, the resultant surface displacements are due to shear beneath the locked fault. The elastic dislocation model is described by equation 3,

$$v(x) = \frac{v_{ff}}{\pi} tan^{-1}\left(\frac{x}{D}\right) \quad \textbf{4-15}$$

where $v(x)$ is the velocity at x distance from the fault, the fault is locked from the surface to depth D km, v_{ff} is the far-field velocity. The inversion solved for the locking depth, far-field velocity, and location of the fault relative to the volcanic arc. The constraints for all models are detailed in Table **4-3**.

Table **4-3:** Constraints used during inversion of all one-fault dislocation models. x – fault location relative to volcanic arc. V_{ff} – the far-field velocity. D – locking depth. C – velocity profile offset.

Parameter	**Lower Bound**	**Upper Bound**
***x* (km)**	-5	5
V_{ff} (mm/yr)	6	14
D (km)	0	30
C (mm/yr)	0	4

4.2.1.2 Arc-Parallel Fault Elastic Dislocation Model Results and Discussion

The results for the elastic dislocation model set are detailed in Table **4-4** and Figures **4-7** to **4-12** where all inverted models yielded an equivalent far-field velocity of ~10 mm/yr. All models within this set produced shallow locking depths within uncertainty except the Cerro Negra profile that was inverted using the full data set, i.e., including velocities on the flanks of volcanos, yielded the deepest locking depth with a large uncertainty (22.6 ± 19.2 km; Table **4-4** and Figure **4-7c**). The fit for the Cerro Negro and Telica profiles improved when the inversion included GPS data sited at volcanos (Table **4-4**).

Table **4-4**: Elastic dislocation model results for one arc-parallel fault. x – fault location relative to volcanic arc. V_{ff} – the far-field velocity. D – locking depth. C – profile offset.

Profile	**Model**	***x* (km)**	**V_{ff} (mm/yr)**	**D (km)**	**C (mm/yr)**	$\overline{\chi}^2$	**No. of GPS Velocities**
Telica	With Volcano GPS Stations	2.6 ± 0.3	8.8 ± 0.6	1.9 ± 0.7	3.6 ± 0.6	10.556	15
	No Volcano GPS Stations	2.9 ± 0.4	10.3 ± 0.9	0.5 ± 6.9	2.5 ± 0.9	8.597	10
Cerro Negro	With Volcano GPS Stations	4.2 ± 3.6	14.0 ± 0.1	22.3 ± 3.5	1.0 ± 2.6	2.97	12
	No Volcano GPS Stations	5.0 ± 0.6	8.4 ± 1.6	0.5 ± 1.6	8.0 ± 0.3	7.829	7
Momotombo	--	-2.8 ± 2.6	10.5 ± 0.7	2.7 ± 7.2	3.3 ± 0.7	0.862	7

A

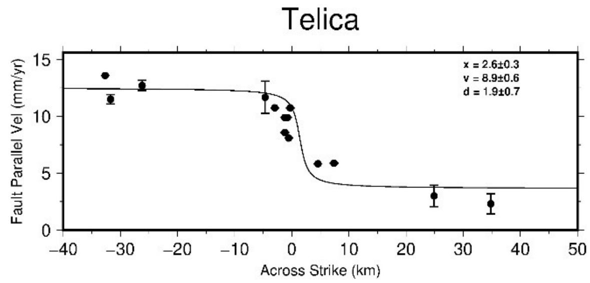
Telica
x = 2.6±0.3
v = 8.9±0.6
d = 1.9±0.7
Fault Parallel Vel (mm/yr)
Across Strike (km)

B

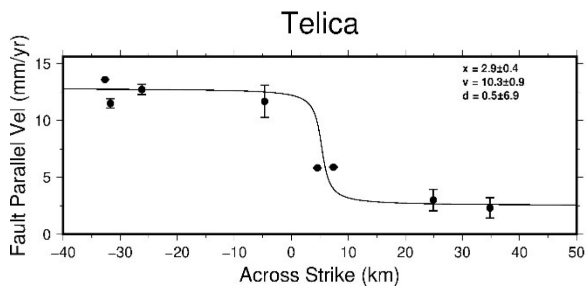
Telica
x = 2.9±0.4
v = 10.3±0.9
d = 0.5±6.9
Fault Parallel Vel (mm/yr)
Across Strike (km)

C

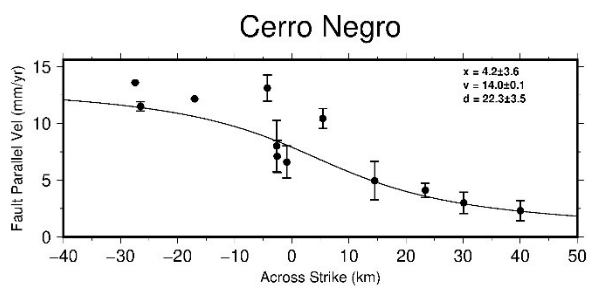
Cerro Negro
x = 4.2±3.6
v = 14.0±0.1
d = 22.3±3.5
Fault Parallel Vel (mm/yr)
Across Strike (km)

D

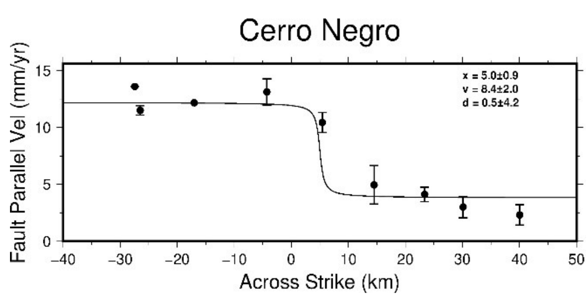
Cerro Negro
x = 5.0±0.9
v = 8.4±2.0
d = 0.5±4.2
Fault Parallel Vel (mm/yr)
Across Strike (km)

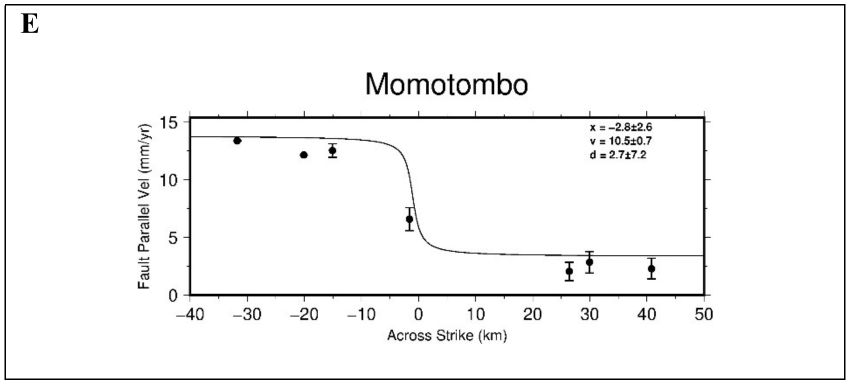

Figure **4-7:** Elastic dislocation model profile for one arc-parallel fault. A – Telica velocity profile and model fit. B – Telica velocity profile and model fit for inversion that did not use velocities of GPS stations sited at volcanos. C – Cerro Negro velocity profile and model fit. D – Cerro Negro velocity profile and model fit for inversion that did not use velocities of GPS stations sited at volcanos. E – Momotombo velocity profile and model fit.

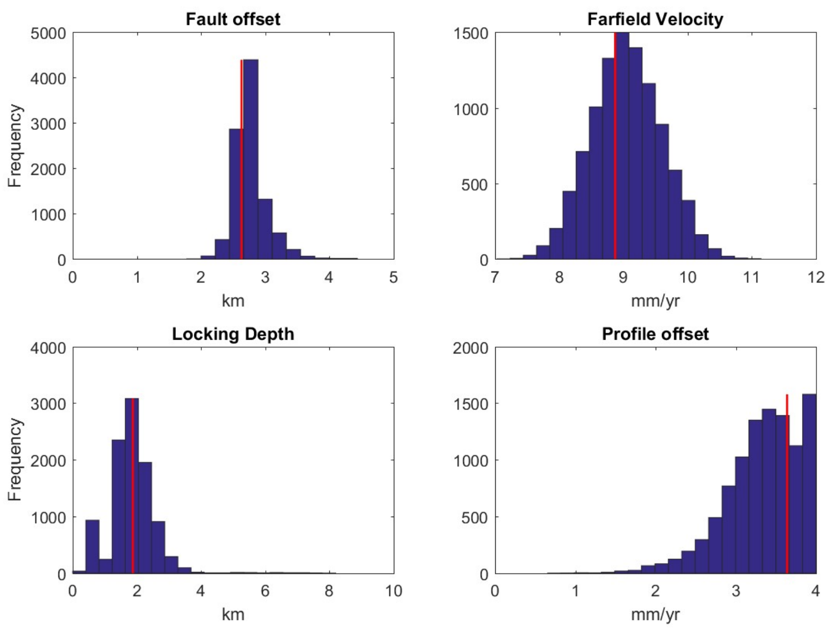

Figure **4-8**: Telica velocity profile parameter probability density functions of one-fault elastic dislocation model. Red line indicates parameter value for the best-fitting model.

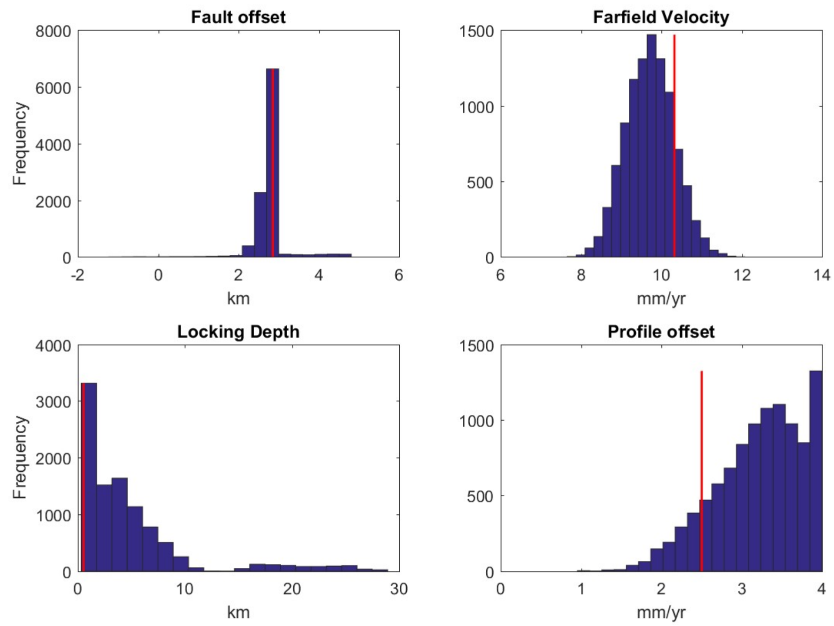

Figure **4-9:** Telica velocity profile parameter probability density functions of one-fault elastic dislocation model where GPS velocities for GPS stations on volcanos were excluded from inversion. Red line indicates parameter value for the best-fitting model.

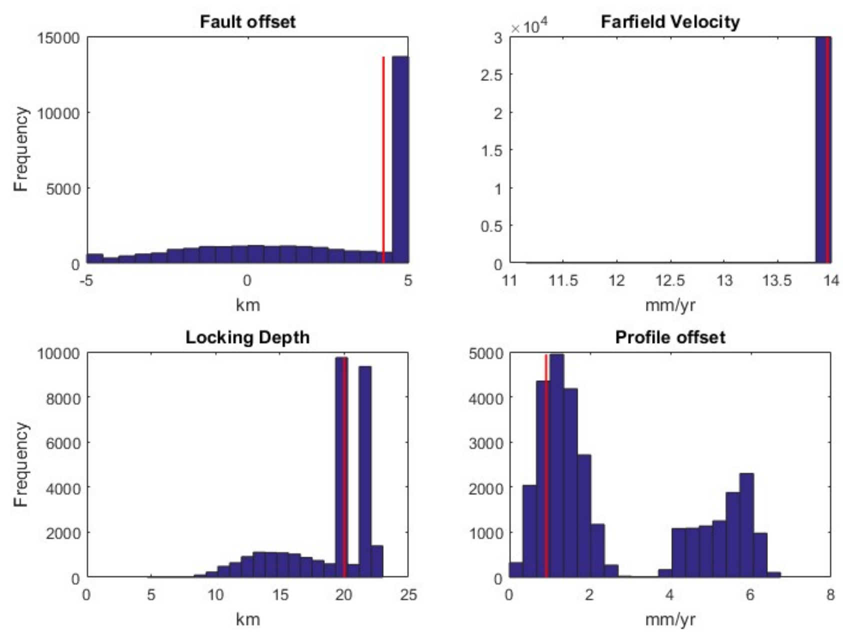

Figure **4-10**. Cerro Negro velocity profile parameter probability density functions of one-fault elastic dislocation model. Red line indicates parameter value for the best-fitting model.

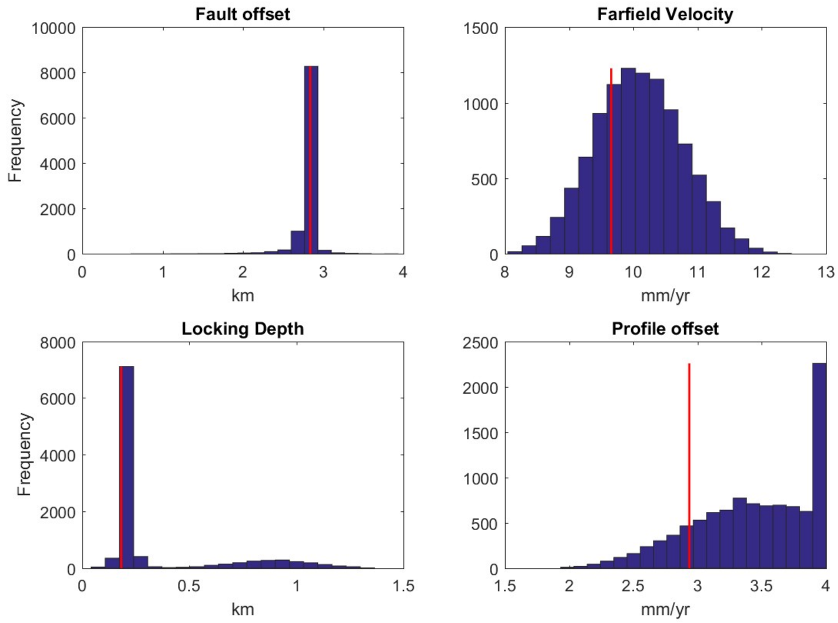

Figure **4-11:** Cerro Negro velocity profile parameter probability density functions of one-fault elastic dislocation model where GPS velocities for GPS stations on volcanos were excluded from inversion. Red line indicates parameter value for the best-fitting model.

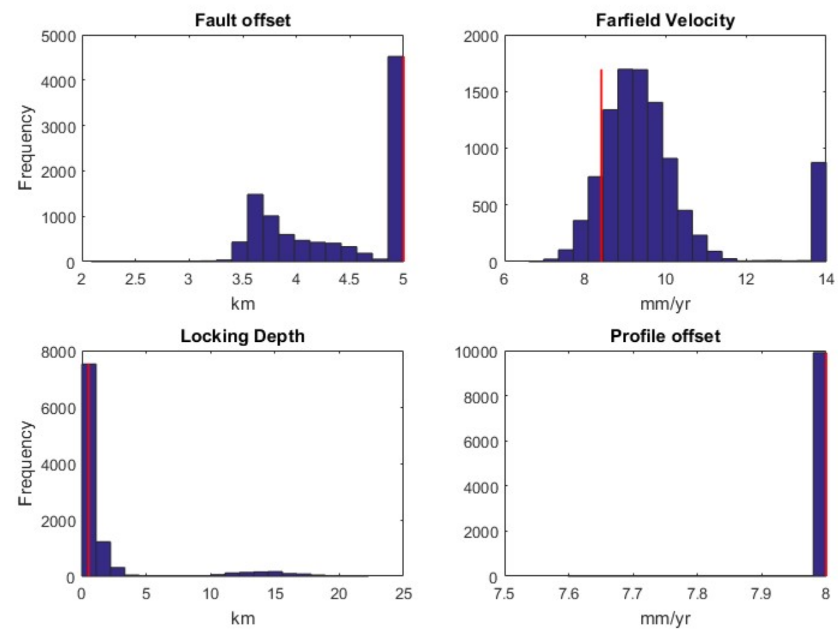

Figure **4-12:** Momotombo velocity profile parameter probability density functions of one-fault elastic dislocation model. Red line indicates parameter value for the best-fitting model.

The one-fault elastic dislocation model did not fit the data well, except for the Telica profile that did not include GPS stations on its flanks. The residuals (Figure **4-13**) show a consistent misfit for the geodetic velocities in the volcanic arc and back-arc. An arc-parallel throughgoing right-lateral fault system does not reproduce the observed velocities.

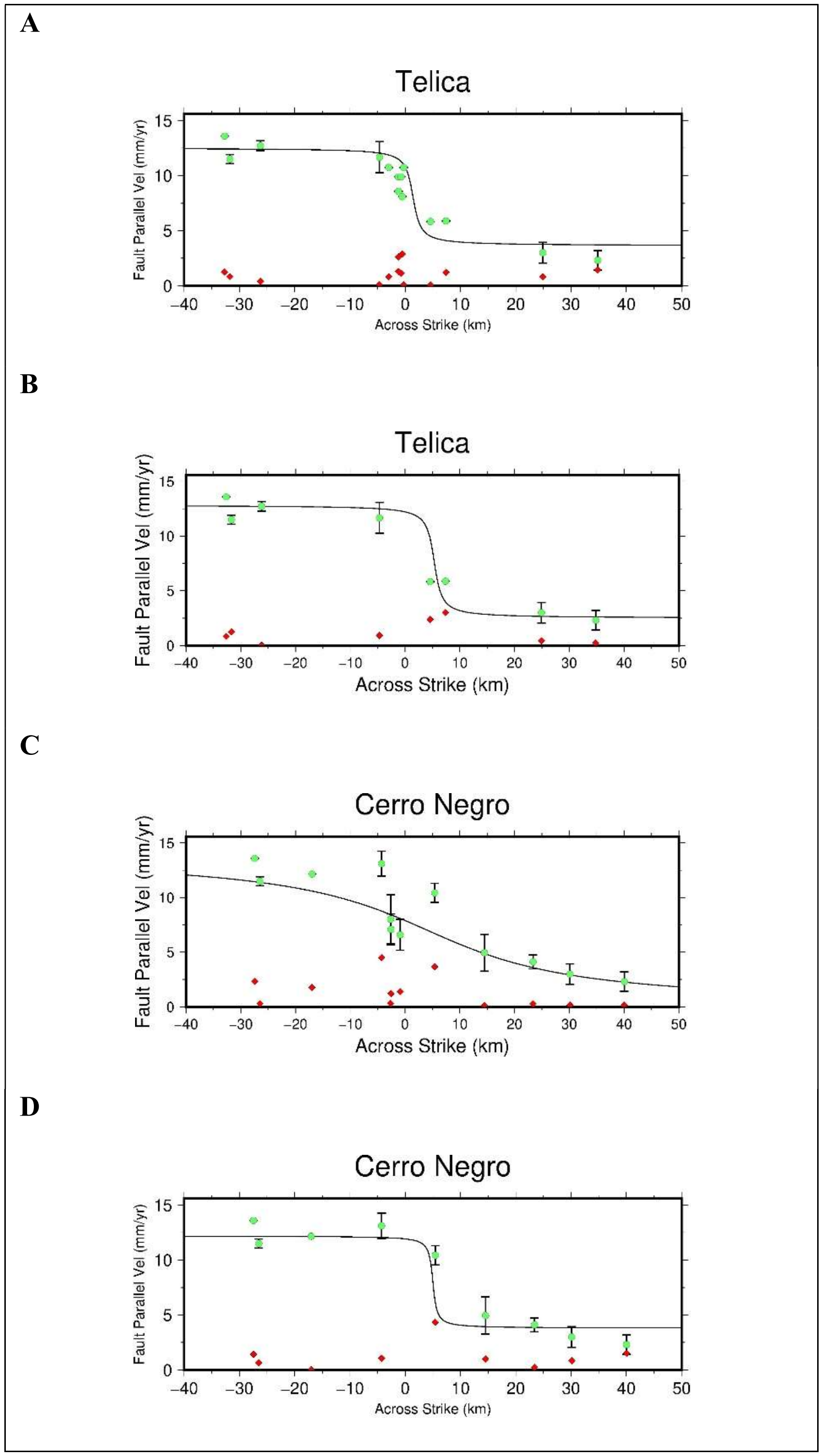
A
Telica
Fault Parallel Vel (mm/yr)
Across Strike (km)
B
Telica
Fault Parallel Vel (mm/yr)
Across Strike (km)
C
Cerro Negro
Fault Parallel Vel (mm/yr)
Across Strike (km)
D
Cerro Negro
Fault Parallel Vel (mm/yr)
Across Strike (km)

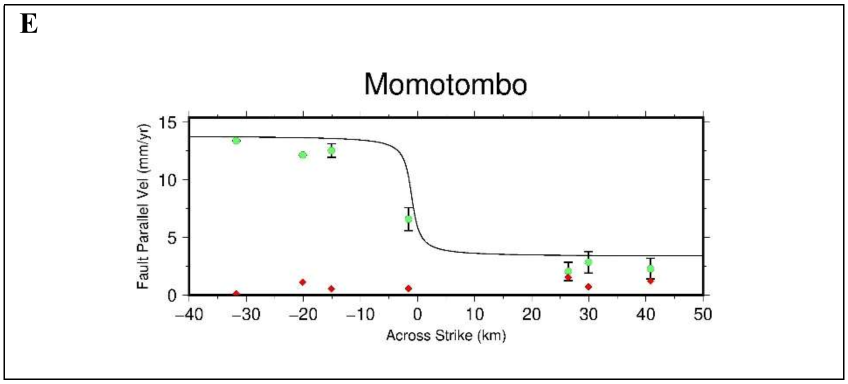

Figure **4-13:** Results for the one-faults elastic dislocation model. Green circles are data. Red diamonds are the residuals of the model to the data.

4.2.2 Two Arc-Parallel Faults Elastic Dislocation

4.2.2.1 Modeling

The one-fault elastic dislocation inversion did not fit the observed GPS velocities. However, the velocities in the back-arc (Figure **4-5**) suggest that a two-fault system may be accommodating the CAFA-CA shear. To investigate this, the observed velocities were inverted using a model with two arc-parallel faults with the elastic dislocation model. The northeast extent of the Nicaragua Depression is 25 km to 30 km from the volcanic arc, which nominally should be located at 0 km across-strike. Beyond the northeast extent of the Nicaragua Depression is the Highlands and stable Caribbean plate, indicating that a likely candidate for a yet to be observed active fault should be within 30 km of the volcanic arc. Two model sets were tested: (1) one set that constrained the across-strike location of the NE fault to 30 km, and (2) one set that relaxed the location constraint allowing for a NE fault to be located between 20 km to 55 km. Models were also inverted (a) with and (b) without GPS velocities for stations located on the flanks of volcanos. Table **4-4** shows the parameter constraints for this model set.

Table **4-5:** Constraints used during inversion of all two-fault dislocation models. x_1 – the along-profile location of volcanic arc fault. x_2 – the along-profile location of northeast fault. $V_{ff\text{-}1}$ – the far-field velocity for volcanic arc fault. . $V_{ff\text{-}2}$ – the far-field velocity for northeast fault. D_1 – locking depth of volcanic arc fault. D_2 – locking depth of northeast fault. C – profile offset.

Parameter	**Lower Bound**	**Upper Bound**
x_1 (km)	-5	5
x_2 (km)	10	30*, 55
$V_{ff\text{-}1}$ (mm/yr)	2	14
$V_{ff\text{-}2}$ (mm/yr)	2	14
D_1 (km)	0	30
D_2 (km)	0	30
C (mm/yr)	0	5

Fault location constraints with * are for models where the location of the northeast fault was constrained to 30 km from volcanic arc.

4.2.2.2 Two Arc-Parallel Faults Elastic Dislocation Model Results and Discussion

It is possible that the CAFA-CA shear may be accommodated by a two-fault system considering GPS velocities show residual strain in the back-arc. These two faults would be located in the volcanic arc and proximal to the northeast boundary of the depression. This mechanism of shear was explored by inverting GPS velocities for the elastic dislocation model for two sub-parallel faults. Two sets of models were inverted: (1) the northeast fault was constrained to 30 km from the volcanic arc, and (2) the northeast fault constraint was relaxed to 55 km from the volcanic arc. The intention of models with relaxed constraints on the location of the northeast fault is to test if the two-fault dislocation models would place this fault in the Highlands (Figure **4-2**), where no NW-trending right-lateral fault has been identified. To discount the possible influence of volcanic processes, two model subsets were inverted for both the elastic and hetero-elastic dislocation models: (a) with and (b) without velocities of GPS stations sited at volcanic centers.

4.2.2.2.1 Elastic Dislocation- Northeast Fault Constrained

The results for the inversion of the two-fault elastic dislocation model subsets, where the location of the northeast fault is constrained to within 30 km of the volcanic arc, are detailed in Table **4-6** and Figures **4-14** to **4-18**. Inversion of the model set yielded locking depths of 0.0 km to 7.2 km on the volcanic arc fault and 2.8 km to 24.2 km on the northeast fault. The models of the Telica profile placed the northeast fault within 10 km of the volcanic (Table **4-6**) while the models of Cerro Negro profiles placed the fault within ~23 km of the volcanic arc (Table **4-6**). The total across-strike velocity is ~13 mm/yr for this model set. The models of the Telica profile that included and excluded volcano GPS stations produced far-field velocities that were lower for the volcanic arc fault (2.1 ± 3.4 mm/yr and 4.7 ± 2.5 mm/yr) than the northeast fault (12.6 ± 3.7 mm/yr and 6.3 ± 3.1 mm/yr) (Table **4-6**). The model that used all data to fit the Cerro Negro profile had the most far-field velocity on the volcanic arc fault (9.7 ± 3.2 mm/yr). However, the model for the Cerro Negro profile that excluded GPS volcano stations produced far-field velocities that were lower (5.6 ± 3.2 mm/yr) for the volcanic arc fault compared to the northeast fault (8.4 ± 2.5 mm/yr) (Table **4-6**). Except for the Cerro Negro profile inverted without GPS stations on the volcano flanks (Figure **4-14d**), the model fit for the two-fault elastic dislocation model to the observed data were poor.

Table **4-6**. Elastic dislocation model results for model set with northeast fault constrained to within 30 km from the volcanic arc. x_1 – the along-profile location of volcanic arc fault. x_2 – the along-profile location of northeast fault. V_{ff-1} – the far-field velocity for volcanic arc fault. . V_{ff-2} – the far-field velocity for northeast fault. D – locking depth. C – profile offset.

Profile	**Model**	x_1 **(km)**	x_2 **(km)**	V_{ff-1} **(mm/yr)**	V_{ff-2} **(mm/yr)**	D_1 **(km)**	D_2 **(km)**	**C (mm/yr)**	$\overline{\chi}^2$	**No. of GPS Velocities**
Telica	With VGPS	5.8 ± 1.6	10.6 ± 8.9	2.1 ± 3.4	12.6 ± 3.7	0.0 ± 2.7	24.2 ± 11.5	0.0 ± 0.9	0.31	15
	No VGPS	0.1 ± 1.7	11.2 ± 8.5	4.7 ± 2.5	6.3 ± 3.1	0.2 ± 2.4	2.8 ± 11.8	1.6 ± 0.9	0.56	10
Cerro Negro	With VGPS	-1.5 ± 2.1	26.5 ± 6.1	9.7 ± 3.2	2.2 ± 2.2	7.2 ± 7.1	4.0 ± 9.2	1.6 ± 0.5	0.55	12
	No VGPS	5.0 ± 4.1	20.5 ± 5.8	5.6 ± 2.3	8.4 ± 2.5	2.1 ± 12.7	11.2 ± 4.3	0.6 ± 1.0	3.21	7

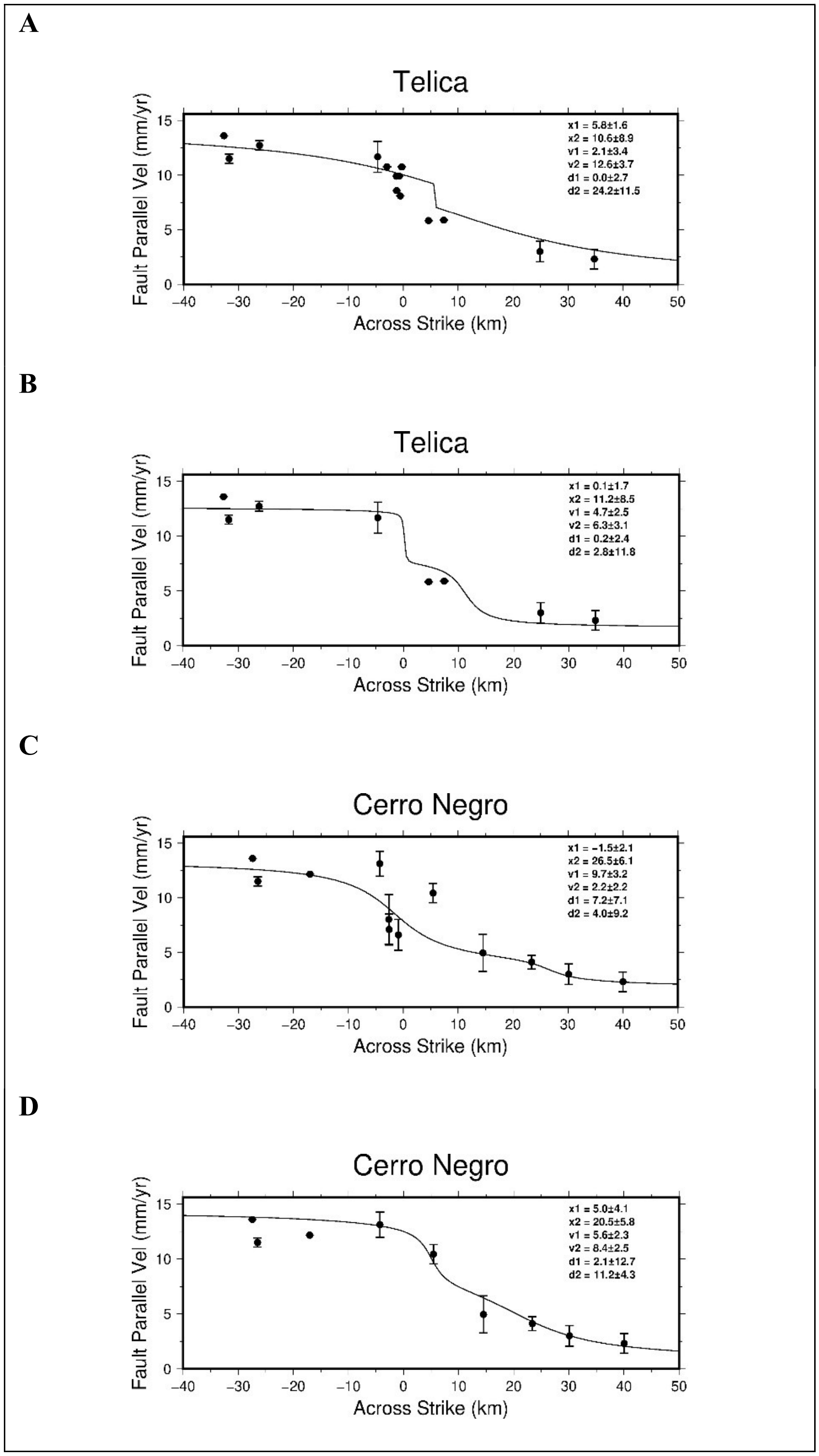
A
Telica
Fault Parallel Vel (mm/yr)
Across Strike (km)
x1 = 5.8±1.6
x2 = 10.6±8.9
v1 = 2.1±3.4
v2 = 12.6±3.7
d1 = 0.0±2.7
d2 = 24.2±11.5
B
Telica
Fault Parallel Vel (mm/yr)
Across Strike (km)
x1 = 0.1±1.7
x2 = 11.2±8.5
v1 = 4.7±2.5
v2 = 6.3±3.1
d1 = 0.2±2.4
d2 = 2.8±11.8
C
Cerro Negro
Fault Parallel Vel (mm/yr)
Across Strike (km)
x1 = −1.5±2.1
x2 = 26.5±6.1
v1 = 9.7±3.2
v2 = 2.2±2.2
d1 = 7.2±7.1
d2 = 4.0±9.2
D
Cerro Negro
Fault Parallel Vel (mm/yr)
Across Strike (km)
x1 = 5.0±4.1
x2 = 20.5±5.8
v1 = 5.6±2.3
v2 = 8.4±2.5
d1 = 2.1±12.7
d2 = 11.2±4.3

Figure **4-14**: Two-fault elastic dislocation model profile fits for two arc-parallel faults. During inversion location of the northeast fault was constrained to 20 km to 30 km. A – Telica velocity profile and model fit. B – Telica velocity profile and model fit for inversion that did not use velocities of GPS stations sited at volcanos. C – Cerro Negro velocity profile and model fit. D – Cerro Negro velocity profile and model fit for inversion that did not use velocities of GPS stations sited at volcanos. E – Momotombo velocity profile and model fit.

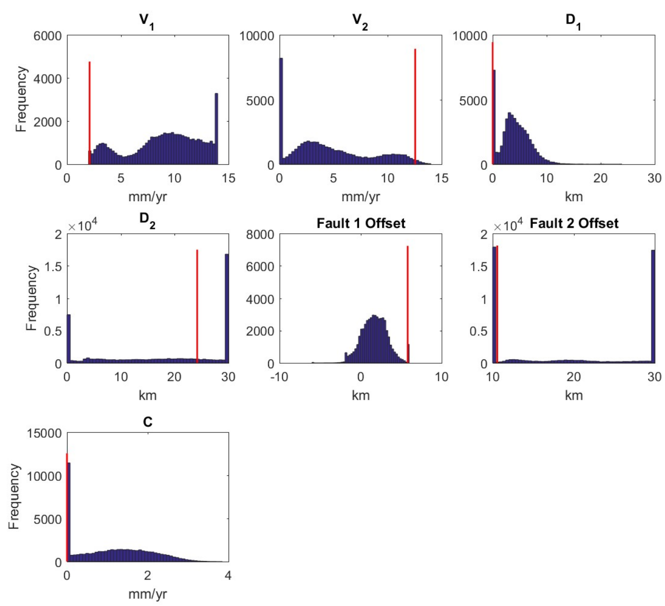

Figure **4-1**: Telica velocity profile parameter probability density functions of two-fault hetero-elastic dislocation model where the northeast fault was constrained to 20 km to 30 km. Red line indicates parameter value for the best-fitting model.

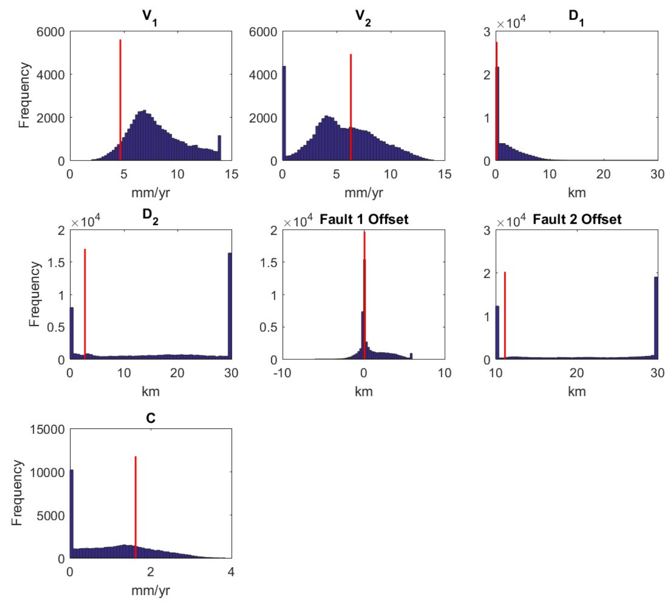

Figure **4-2**: Telica velocity profile parameter probability density functions of one-fault hetero-elastic dislocation model where GPS velocities for GPS stations on volcanos were excluded from inversion and northeast fault was constrained to 20 km to 30 km. Red line indicates parameter value for the best-fitting model.

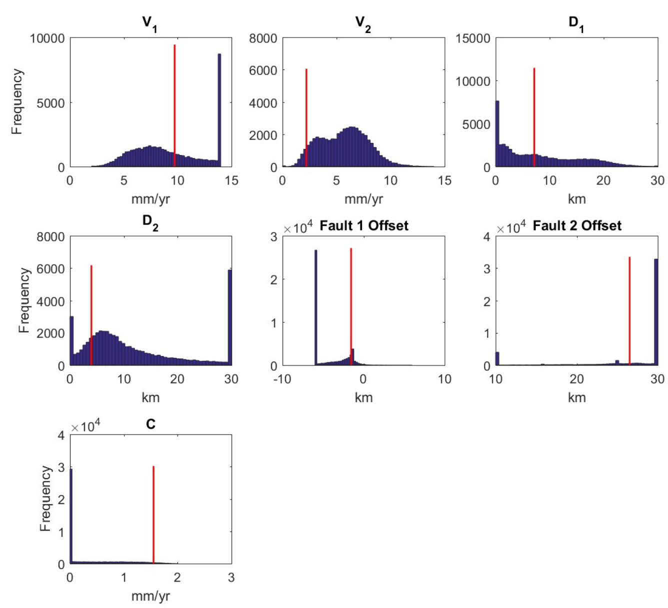

Figure **4-3**: Cerro Negro velocity profile parameter probability density functions of two-fault hetero-elastic dislocation model where the northeast fault was constrained to 20 km to 30 km. Red line indicates parameter value for the best-fitting model.

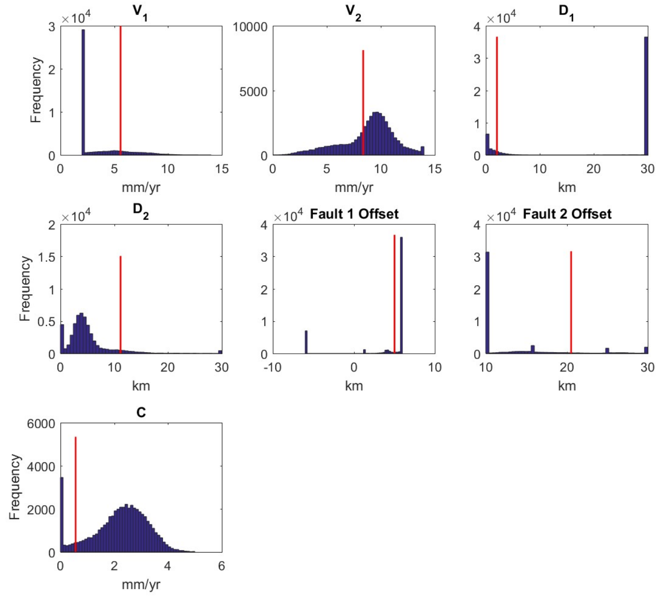

Figure **4-18**: Cerro Negro velocity profile parameter probability density functions of two-fault hetero-elastic dislocation model where GPS velocities for GPS stations on volcanos were excluded from inversion and northeast fault was constrained to 20 km to 30 km. Red line indicates parameter value for the best-fitting model.

4.2.2.2.2 Elastic Dislocation- Relaxed Northeast Fault Constraint

The inversion of the two-fault elastic dislocation model subsets with relaxed constraints on the location of the northeast fault (10 km to 55km) produced models that overall had better fits to the data compared to the northeast fault constrained models (Table **4-7**; Figures **4-27** to **4-31**). Inversion of all profiles yielded comparable locations of the northeast fault, within uncertainty, but the location is greater than 30 km. The inversion of this model set yielded a range of locking depths for the volcanic arc fault of 1.4 km to 7.3 km, while the range of locking depths for the northeast fault is 0.0 km to 4.6 km. The total across-strike velocities for the models are comparable (~13 mm/yr), within uncertainty.

Table **4-7**: Two-fault elastic dislocation model results for model set with northeast fault constrained to within 55 km from the volcanic arc. x_1 – the along-profile location of volcanic arc fault. x_2 – the along-profile location of northeast fault. V_{ff-1} – the far-field velocity for volcanic arc fault. V_{ff-2} – the far-field velocity for northeast fault. D_1 – locking depth of volcanic arc fault. D_2 – locking depth of northeast fault. C – profile offset.

Profile	**Model**	x_1 **(km)**	x_2 **(km)**	V_{ff-1} **(mm/yr)**	V_{ff-2} **(mm/yr)**	D_1 **(km)**	D_2 **(km)**	**C (mm/yr)**	$\bar{\chi}^2$
Telica	With VGPS	-0.8 ± 1.5	32.7 ± 14.6	9.2 ± 3.4	5.6 ± 3.6	4.6 ± 2.8	4.6 ± 12.1	0.5 ± 0.9	0.85
	No VGPS	1.6 ± 1.6	34.5 ± 12.8	8.0 ± 2.7	3.0 ± 3.1	1.4 ± 2.5	5.8 ± 11.9	1.7 ± 0.9	0.41
Cerro Negro	With VGPS	-2.2 ± 1.9	32.8 ± 11.6	9.3 ± 3.0	4.1 ± 2.2	7.3 ± 6.6	1.2 ± 9.2	0.9 ± 0.5	0.78
	No VGPS	3.8 ± 3.2	32.5 ± 5.9	8.6 ± 2.1	3.9 ± 2.4	2.9 ± 13.9	0.0 ± 4.1	1.8 ± 1.1	1.99

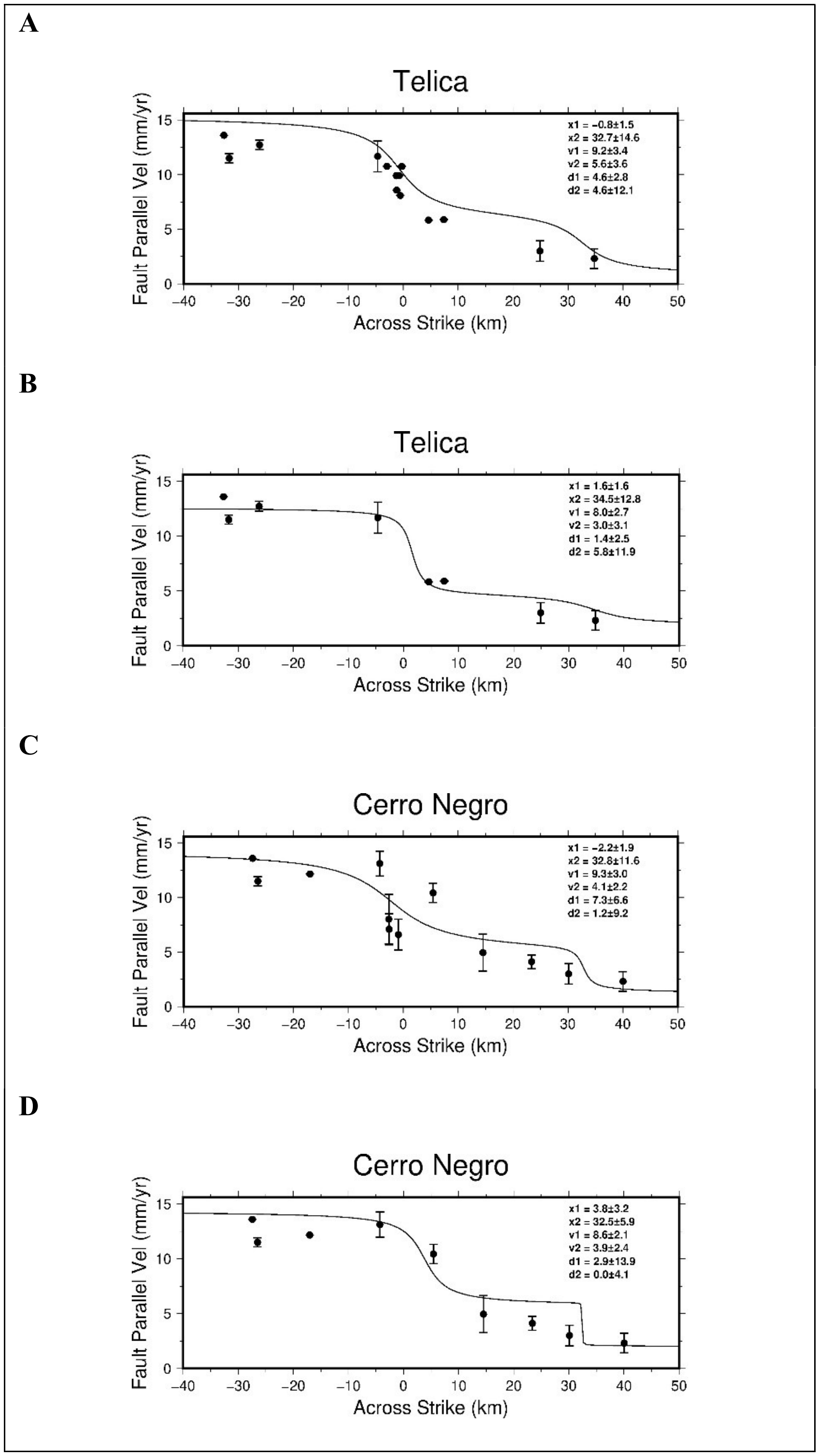

Figure **4-19**: Two-fault elastic dislocation model profile fits for two arc-traverse faults. During inversion location constraint of the northeast fault was relaxed (20 km to 55 km). A – Cerro Negro velocity profile and model fit. B – Cerro Negro velocity profile and model fit for inversion that did not use velocities of GPS stations sited at volcanos. C – Telica velocity profile and model fit. D –

Telica velocity profile and model fit for inversion that did not use velocities of GPS stations sited at volcanos.

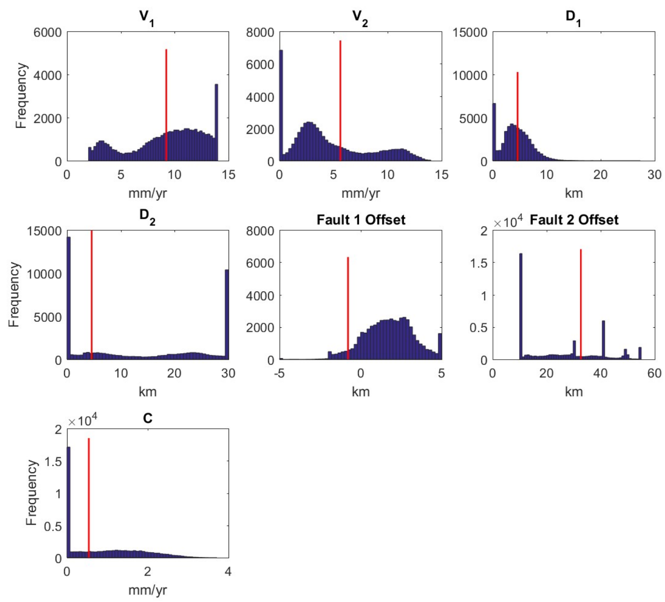

Figure **4-20**: Telica velocity profile parameter probability density functions of two-fault elastic dislocation model where northeast fault location constraint was relaxed (20 km to 55 km). Red line indicates parameter value for the best-fitting model.

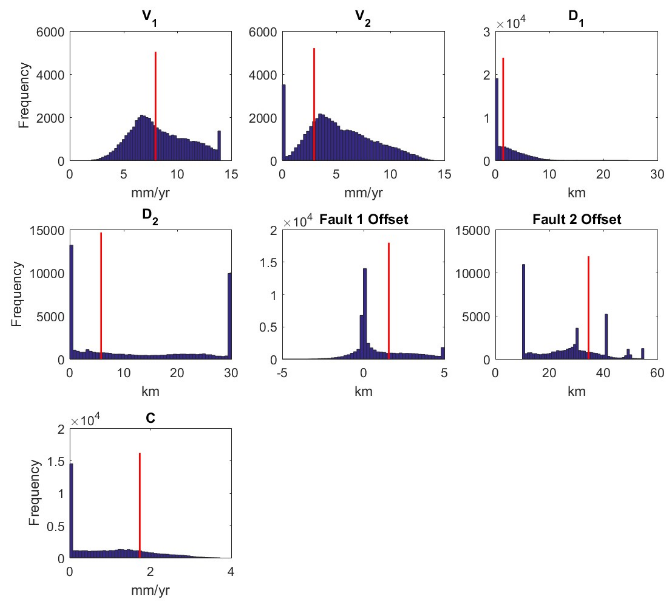

Figure **4-21**: Telica velocity profile parameter probability density functions of two-fault elastic dislocation model where GPS velocities for GPS stations on volcanos were excluded from inversion and northeast fault location constraint was relaxed (20 km to 55 km). Red line indicates parameter value for the best-fitting model.

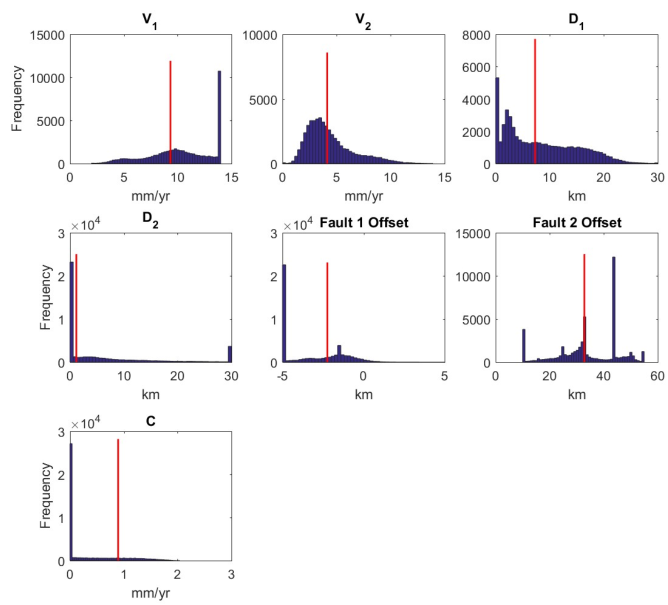

Figure **4-22**: Cerro Negro velocity profile parameter probability density functions of two-fault elastic dislocation model where northeast fault location constraint was relaxed (20 km to 55 km). Red line indicates parameter value for the best-fitting model.

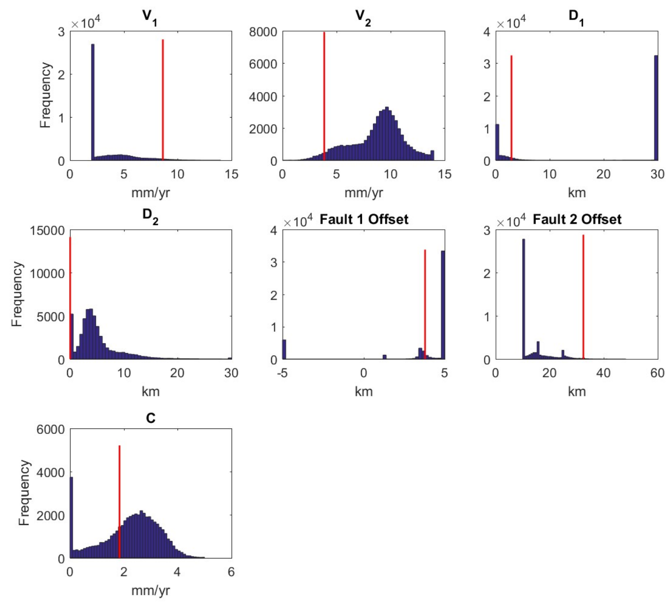

Figure **4-23**: Cerro Negro velocity profile parameter probability density functions of two-fault elastic dislocation model where GPS velocities for GPS stations on volcanos were excluded from inversion and northeast fault location constraint was relaxed (20 km to 55 km). Red line indicates parameter value for the best-fitting model.

4.2.3 Arc-Parallel Fault Hetero-Elastic Dislocation Model

The one-fault and two-fault elastic dislocation models did not fit the data well. This may be due to an across-strike change in rheology, i.e., the rheology of the forearc, volcanic arc, back-arc may differ, or a compliant zone. This is may be the case given the presence of the active volcanic arc. The hetero-elastic dislocation model was used to investigate if there is any across-strike change in rheology and locking on an arc-parallel fault.

4.2.3.1 Modeling

The hetero-elastic dislocation model, a modification of the elastic dislocation model, parameterizes the rheology on each side of the fault interface and is ideal for this use case where the Holocene volcanic arc may have thermally weakened surrounding crust, or the CAFA may be rheologically different than the CA crust. The hetero-elastic dislocation is described by Equation 4,

$$v(x) = \frac{2Kv_{ff}}{\pi} tan^{-1}\left(\frac{x}{D}\right); \ x \geq 0$$
$$v(x) = \frac{2(1-K)v_{ff}}{\pi} tan^{-1}\left(\frac{x}{D}\right); \ x < 0,$$ **4-16**

where $v(x)$ is the velocity at x distance from the fault, the fault is locked from the surface to depth D km, v_{ff} is the far-field velocity, and $K = \mu_1/(\mu_1 + \mu_2)$ is the asymmetry coefficient for which μ_1 and μ_2 are the shear moduli for two regions on either side of the fault (Figure **4-24**).

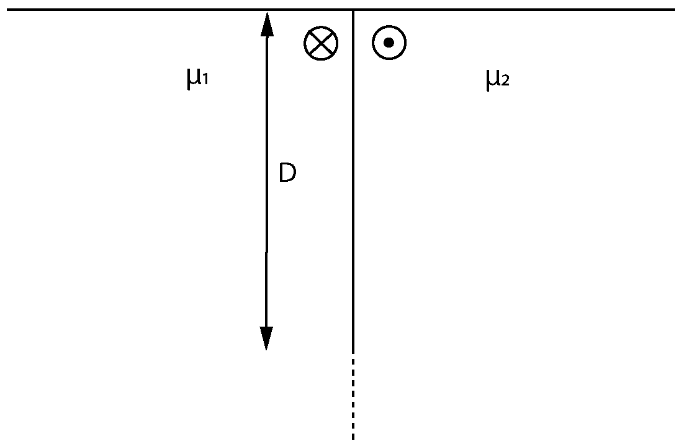

Figure **4-24**: Schematic of the hetero-elastic fault system. Solid black is locked fault. The dashed line is fault creeping at depth. D – locking depth. μ - shear modulus.

The observed GPS velocities were inverted using hetero-elastic dislocation model with constraints that are similar to the one-fault elastic dislocation model where the parameters are identical (Table **4-8**). The range for the shear modulus for either side of the fault was constrained to 20 GPa < μ < 30 GPa (Heap et al., 2020).

Table **4-8**: Constraints used during inversion of all one-fault dislocation models. x – fault location relative to volcanic arc. V_{ff} – the far-field velocity. D – locking depth. C – velocity profile offset. μ_1 – shear modulus of forearc. μ_2 – shear modulus of back-arc.

Parameter	**Lower Bound**	**Upper Bound**
***x* (km)**	-5	5
V_{ff} (mm/yr)	6	14
D (km)	0	30
C (mm/yr)	0	4
μ_1 (GPa)	20	30
μ_2 (GPa)	20	30

4.2.3.2 Arc-Parallel Fault Hetero-Elastic Dislocation Model Results and Discussion

The results for the inversion of the hetero-elastic dislocation model sets produced equivalent far-field velocities (~14.6 mm/yr) with locking depths of 9 km – 18 km (Table **4-9**; Figures **4-25** to **4-30**). This model set yielded no consistent value in the shear moduli for the forearc and back-arc (Table **4-9**). Inversions that did not use GPS stations sited at volcanoes produced shear moduli for the back-arc that are equivalent to the upper bound of the constraint (30 GPa). All models produced shear moduli for the back-arc that were greater than the forearc, except for the Telica profile that included all data during inversion. The Telica profile, where the inversion used the full data set, had a shear modulus of 27.2 ± 6.5 GPa for the back-arc and 22.3 ± 7.0 GPa for the forearc. This model also had the lowest reduced chi-square of the model set.

Table **4-9**: Hetero-elastic dislocation model results for one arc-parallel fault. x – fault location relative to volcanic arc. V_{ff} – the far-field velocity. D – locking depth. μ_1 – shear modulus of forearc. μ_2 – shear modulus of back-arc. VGPS – GPS stations sited on volcanic centers.

Profile	**Model**	***x* (km)**	**V_{ff} (mm/yr)**	**D (km)**	**μ_1 (GPa)**	**μ_2 (GPa)**	$\overline{\chi}^2$	**No. of GPS Velocities**
Telica	With VGPS	9.6 ± 5.8	14.9 ± 0.6	16.3 ± 6.2	22.3 ± 7.0	27.2 ± 6.5	0.24	15
	No VGPS	6.0 ± 2.8	14.0 ± 0.6	9.8 ± 2.0	30.0 ± 0.74	23.2 ± 3.1	0.30	10
Cerro Negro	With VGPS	0.5 ± 3.0	14.6 ± 0.4	17.9 ± 3.9	28.0 ± 6.8	21.6 ± 1.6	0.86	12
	No VGPS	10.0 ± 0.5	15.0 ± 0.2	11.3 ± 2.8	30.0 ± 10.0	20.0 ± 0.0	0.32	7
Momotombo	With VGPS	6.2 ± 3.3	14.4 ± 0.6	18.1 ± 4.9	29.3 ± 1.6	20.5 ± 1.3	1.02	7

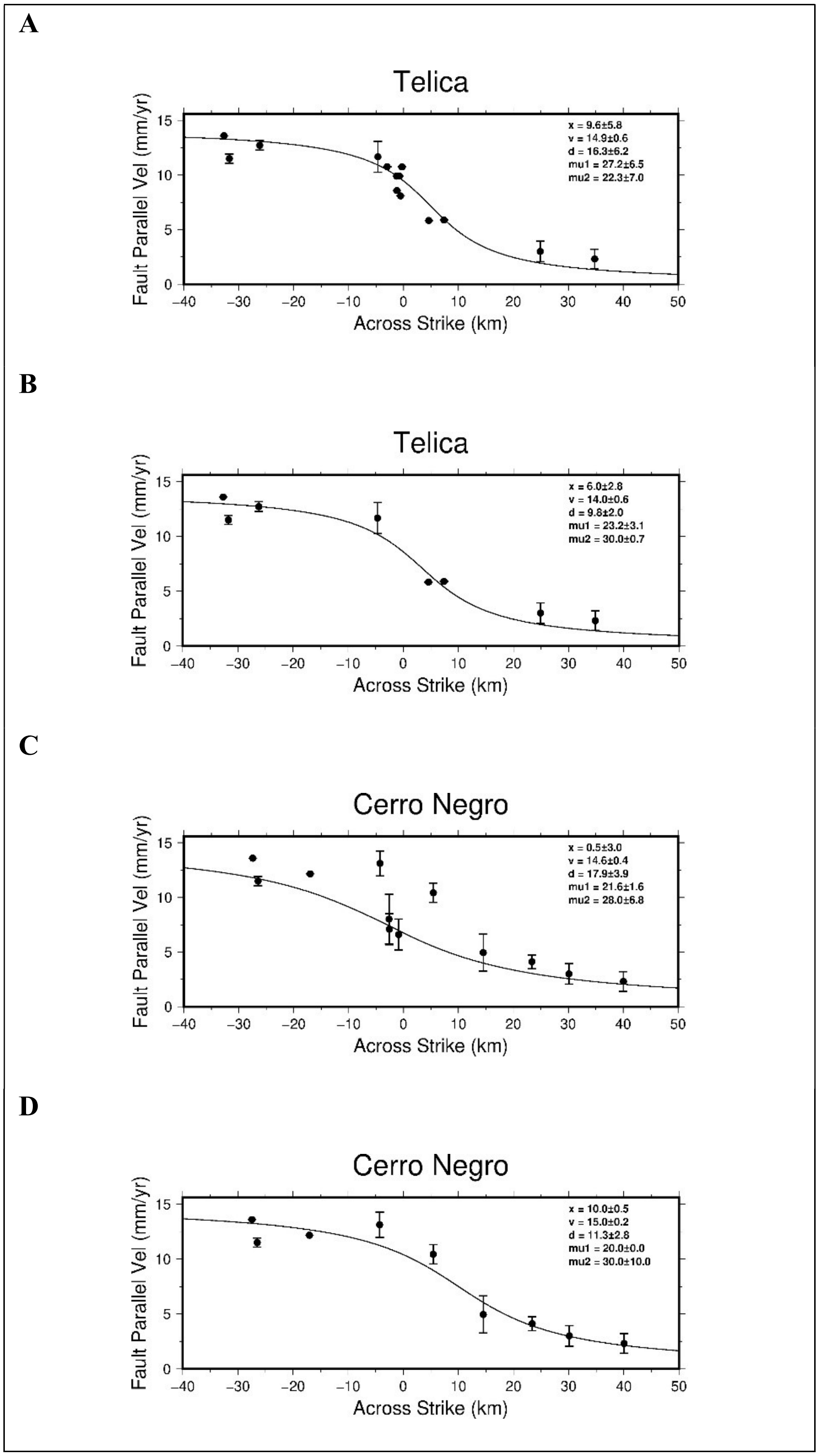
A
Telica
Fault Parallel Vel (mm/yr)
Across Strike (km)
x = 9.6±5.8
v = 14.9±0.6
d = 16.3±6.2
mu1 = 27.2±6.5
mu2 = 22.3±7.0
B
Telica
Fault Parallel Vel (mm/yr)
Across Strike (km)
x = 6.0±2.8
v = 14.0±0.6
d = 9.8±2.0
mu1 = 23.2±3.1
mu2 = 30.0±0.7
C
Cerro Negro
Fault Parallel Vel (mm/yr)
Across Strike (km)
x = 0.5±3.0
v = 14.6±0.4
d = 17.9±3.9
mu1 = 21.6±1.6
mu2 = 28.0±6.8
D
Cerro Negro
Fault Parallel Vel (mm/yr)
Across Strike (km)
x = 10.0±0.5
v = 15.0±0.2
d = 11.3±2.8
mu1 = 20.0±0.0
mu2 = 30.0±10.0

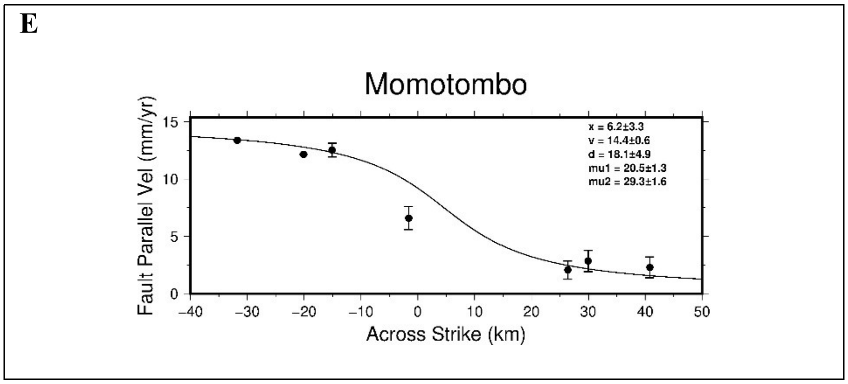

Figure **4-25**: Hetero-elastic dislocation model profile for one arc-parallel fault. A – Telica velocity profile and model fit. B – Telica velocity profile and model fit for inversion that did not use velocities of GPS stations sited at volcanos. C – Cerro Negro velocity profile and model fit. D – Cerro Negro velocity profile and model fit for inversion that did not use velocities of GPS stations sited at volcanos. E – Momotombo velocity profile and model fit.

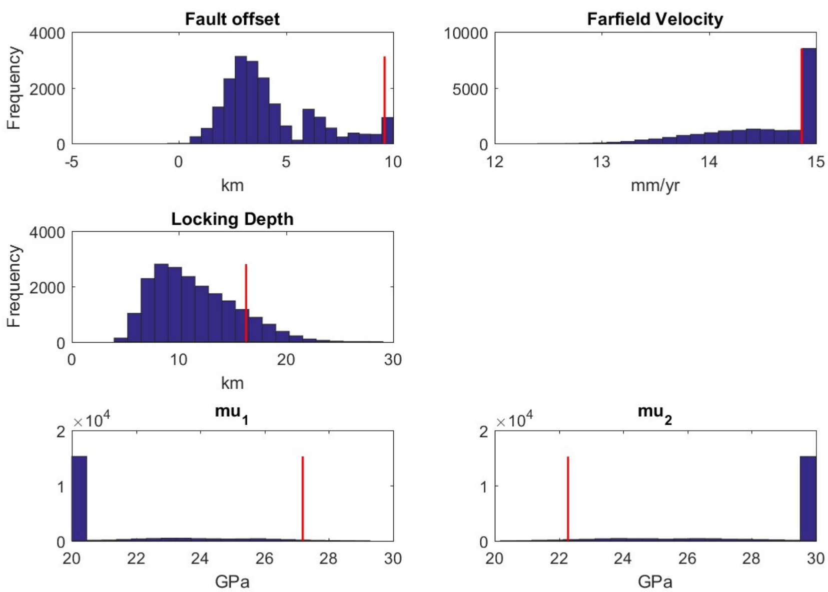

Figure **4-26**: Telica velocity profile parameter probability density functions of one-fault hetero-elastic dislocation model. mu (μ) – shear modulus. Red line indicates parameter value for the best-fitting model.

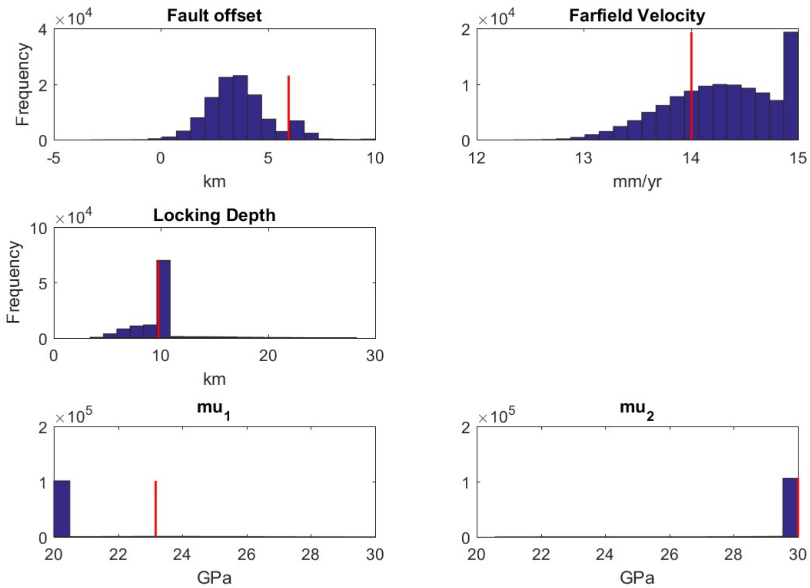

Figure **4-27**: Telica velocity profile parameter probability density functions of one-fault hetero-elastic dislocation model where GPS velocities for GPS stations on volcanos were excluded from inversion. mu (μ) – shear modulus. Red line indicates parameter value for the best-fitting model.

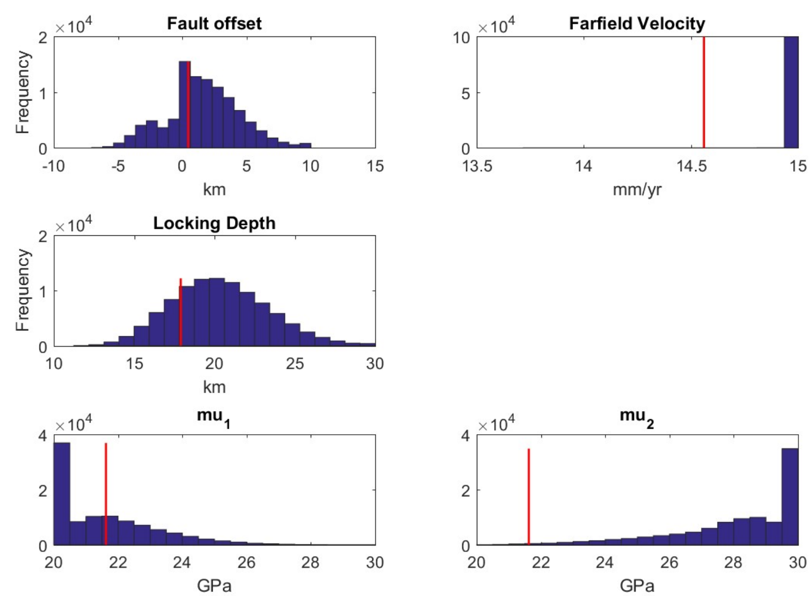

Figure **4-28**: Cerro Negro velocity profile parameter probability density functions of one-fault hetero-elastic dislocation model. mu (μ) – shear modulus. Red line indicates parameter value for the best-fitting model.

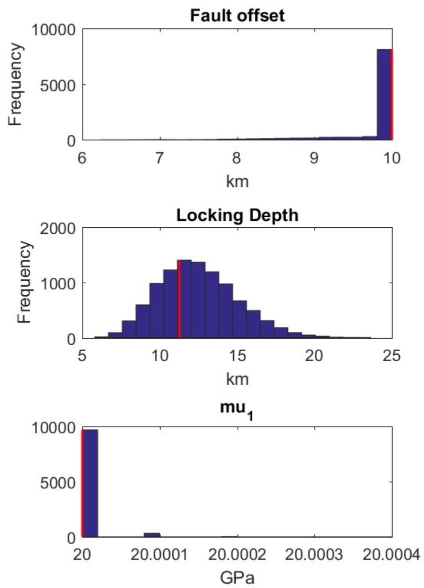

Figure **4-29**: Cerro Negro velocity profile parameter probability density functions of one-fault hetero-elastic dislocation model where GPS velocities for GPS stations on volcanos were excluded from inversion. mu (μ) – shear modulus. Red line indicates parameter value for the best-fitting model.

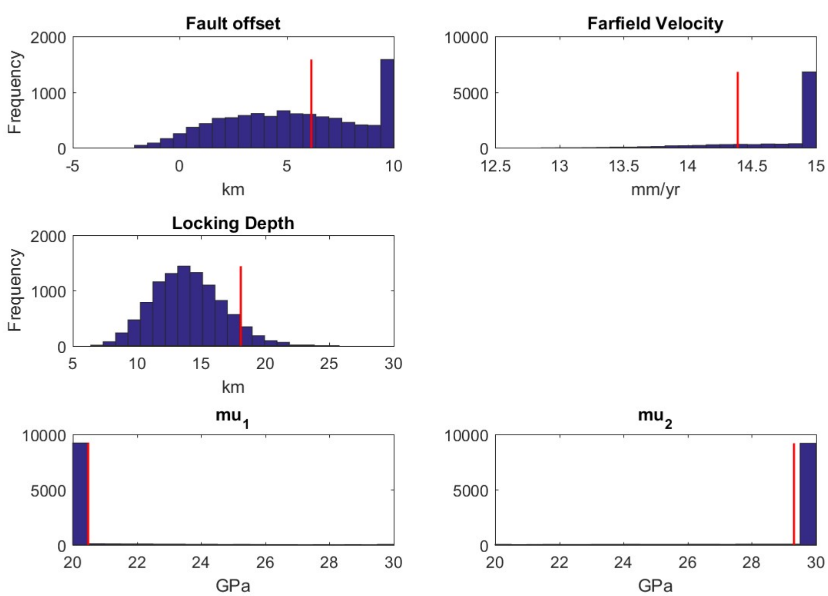

Figure **4-30**: Momotombo velocity profile parameter probability density functions of one-fault hetero-elastic dislocation model. mu (μ) – shear modulus. Red line indicates parameter value for the best-fitting model.

4.2.4 Two Arc-Parallel Faults Hetero-Elastic Dislocation

4.2.4.1 Modeling

If the CAFA-CA shear is being accommodated by two right-lateral transform faults, it is possible that these faults bound regions, in particular, the volcanic arc, that may have varying rheology or a compliant zone (Figure **4-31**). To investigate if a change in rheology and two faults are responsible for the observed velocities, a two-fault hetero-elastic dislocation model was inverted. This model will solve for independent shear moduli for each region separated by two faults (Figure **4-31**). Like the elastic-dislocation models, the model was divided into two sets that (1) constrain the across-strike location of the northeast fault to 30 km, and (2) relaxed constraint on the location of the northeast fault (10 km to 55 km). Models were also inverted with (a) the full GPS data set for each profile and (b) without the velocities of GPS stations on the flanks of volcanos. The constraints for the two subparallel hetero-elastic models are detailed in Table **4-10**. The constraint for the shear modulus was 25 GPa < μ < 30 GPa.

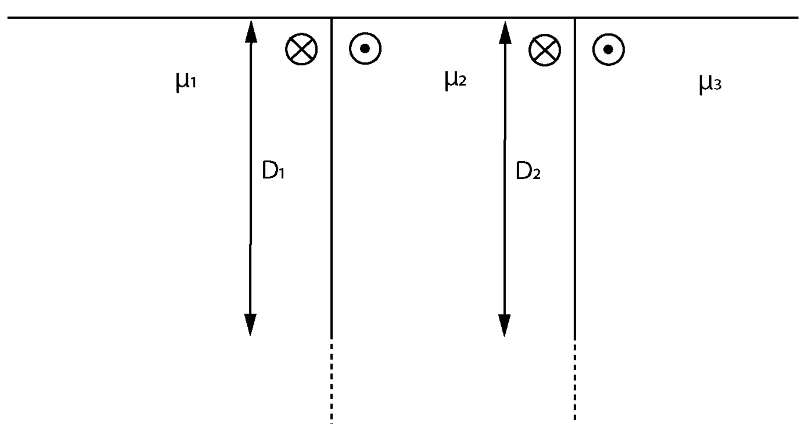

Figure **4-31**: Schematic of the two-fault hetero-elastic model in a dextral shear zone. Solid black is locked fault. The dashed line the fault slipping at depth. D – locking depth. μ - shear modulus.

Table **4-10**: Constraints used during inversion of all two-fault hetero-elastic dislocation models. x_1 – the along-profile location of volcanic arc fault. x_2 – the along-profile location of northeast fault. $V_{ff\text{-}1}$ – the far-field velocity for volcanic arc fault. . $V_{ff\text{-}2}$ – the far-field velocity for northeast fault. D_1 – locking depth of volcanic arc fault. D_2 – locking depth of northeast fault. μ_1 – shear modulus of forearc. μ_2 – shear modulus of region between the two faults. μ_3 – shear modulus of back-arc.

4.2.4.2 Two Arc-Parallel Faults Hetero-Elastic Dislocation Results and Discussion

Parameter	**Lower Bound**	**Upper Bound**
x_1 (km)	-5	5
x_2 (km)	10	30*, 55
$V_{ff\text{-}1}$ (mm/yr)	2	14
$V_{ff\text{-}2}$ (mm/yr)	2	14
D_1 (km)	0	30
D_2 (km)	0	30
μ_1 (GPa)	25	31
μ_2 (GPa)	25	31
μ_3 (GPa)	25	31

* Fault location constraints for models where the location of the northeast fault was constrained to 30 km from volcanic arc.

4.2.4.2 Two Arc-Parallel Faults Hetero-Elastic Dislocation Results and Discussion

4.2.4.2.1 Hetero-Elastic Dislocation - Northeast Fault Constrained

Inversion of the two-fault hetero-elastic dislocation model subset, where the location of the northeast fault was constrained to within 30 km of the volcanic, arc yielded results where almost all the parameters were estimated to be the lower or upper bound of their constraints (Table **4-11**; Figures **4-32** to **4-36**). The estimated location of the northeast fault, for all models, was estimated to be 30 km within uncertainty, which is equivalent to the upper bound constraint. For all models that used the full GPS data set, the shear modulus of the forearc is 25 ± < 1.5 GPa (lower bound of the constraint), while models that did not include volcano GPS velocities yielded shear moduli of 31 ± < 2.0 GPa (upper bound of constraint) for the forearc (Table **4-11**). Except for the model that fit the Cerro Negro profile that did not include volcano GPS velocities (Table **4-11**, Figure **4-32d**), all models produced shear moduli of ~25.0 GPa for the volcanic arc. There is no clear consistency in the shear moduli for the back-arc (Table **4-11**). Most models produce a lower far-field velocity for the volcanic arc fault (~6.1 mm/yr) than the northeast fault (~8 mm/yr). Only the model that fit the Cerro Negro profile using the full GPS data set produced a higher far-field velocity for the volcanic arc (11.3 ± 4.0 mm/yr) than the northeast fault (4.0 ± 3.8 mm/yr). The total across-strike far-field velocities are equivalent for this model set (~ 14 mm/yr). For all models, the fit worsened when inversion excluded volcano GPS velocities.

Table **4-11**: Two-fault hetero-elastic dislocation model results for model set with northeast fault constrained to within 30 km from the volcanic arc. x_1 – the along-profile location of volcanic arc fault. x_2 – the along-profile location of northeast fault. V_{ff-1} – the far-field velocity for volcanic arc fault. . V_{ff-2} – the far-field velocity for northeast fault. D_1 – locking depth of volcanic arc fault. D_2 – locking depth of northeast fault. μ_1 – shear modulus of forearc. μ_2 – shear modulus of region between the two faults. μ_3 – shear modulus of back-arc.

Profile	**Model**	***x_1* (km)**	***x_2* (km)**	**V_{ff-1} (mm/yr)**	**V_{ff-2} (mm/yr)**	**D_1 (km)**	**D_2 (km)**	**μ_1 (GPa)**	**μ_2 (GPa)**	**μ_3 (GPa)**	$\overline{\chi}^2$	**No. of GPS Vels**
Telica	With VGPS	-2.3 ± 3.1	27.6 ± 6.0	6.0 ± 3.0	8.5 ± 2.1	3.2 ± 15.2	20.8 ± 9.5	26.4 ± 4.0	25.0 ± 1.2	31.0 ± 1.9	0.71	15
	No VGPS	5.6 ± 3.5	25.0 ± 3.8	6.2 ± 0.8	7.7 ± 1.4	3.7 ± 24.0	17.8 ± 7.0	29.9 ± 1.6	25.8 ± 3.5	28.6 ± 2.6	2.19	10
Cerro Negro	With VGPS	6.0 ± 2.0	30.0 ± 7.4	11.3 ± 4.0	4.0 ± 3.8	13.3 ± 8.3	16.8 ± 10.4	31.0 ± 1.7	25.0 ± 1.2	31.0 ± 1.9	4.78	12
	No VGPS	6.0 ± 3.8	25.9 ± 4.4	6.2 ± 0.8	8.1 ± 1.1	5.5 ± 22.3	13.2 ± 10.3	29.4 ± 1.4	31.0 ± 2.8	25.0 ± 1.7	0.37	7

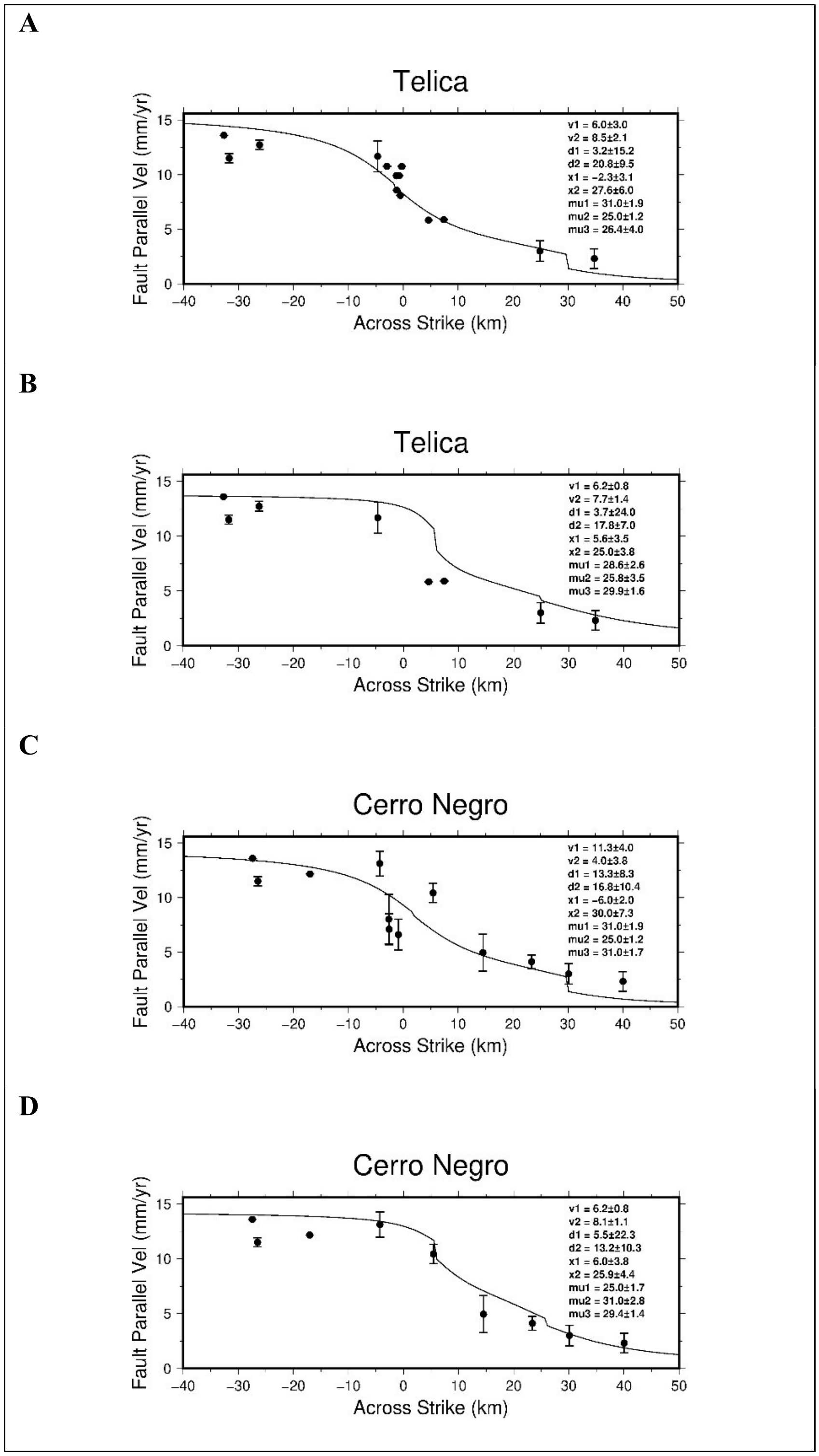

Figure **4-32**: Two-fault hetero-elastic dislocation model profile fits for two arc-transverse faults. During inversion location of the northeast fault was constrained to 20 km to 30 km. A – Cerro Negro velocity profile and model fit. B – Cerro Negro velocity profile and model fit for inversion that did not use velocities of GPS stations sited at volcanos. C – Telica velocity profile and model fit. D – Telica velocity profile and model fit for inversion that did not use velocities of GPS stations sited at volcanos.

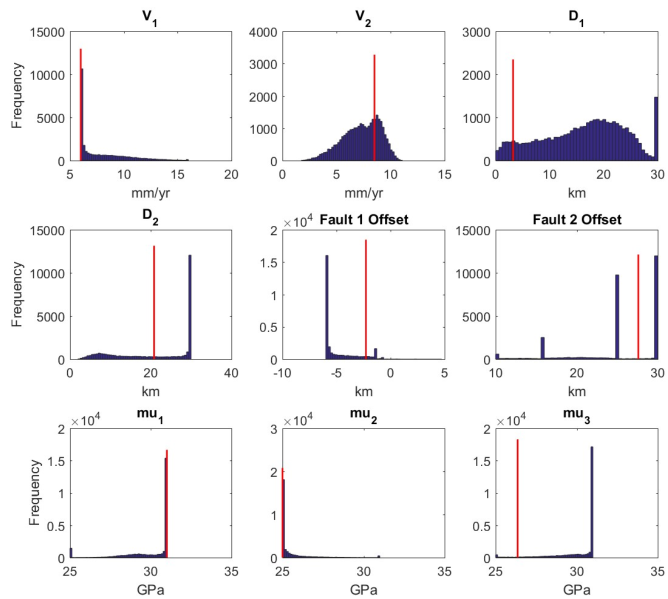

Figure **4-33**: Telica velocity profile parameter probability density functions of two-fault hetero-elastic dislocation model where northeast fault was constrained to 20 km to 30 km. mu (μ) – shear modulus. Red line indicates parameter value for the best-fitting model.

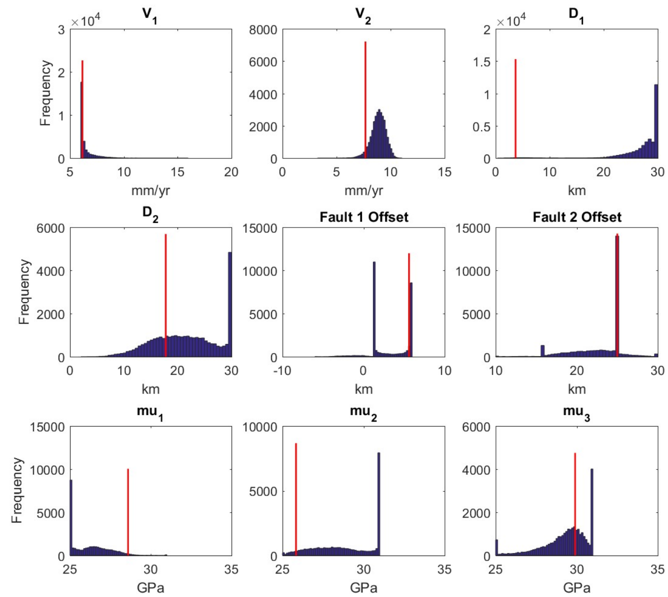

Figure **4-34**: Telica velocity profile parameter probability density functions of two-fault hetero-elastic dislocation model where GPS velocities for GPS stations on volcanos were excluded from inversion and northeast fault was constrained to 20 km to 30 km. mu (μ) – shear modulus. Red line indicates parameter value for the best-fitting model.

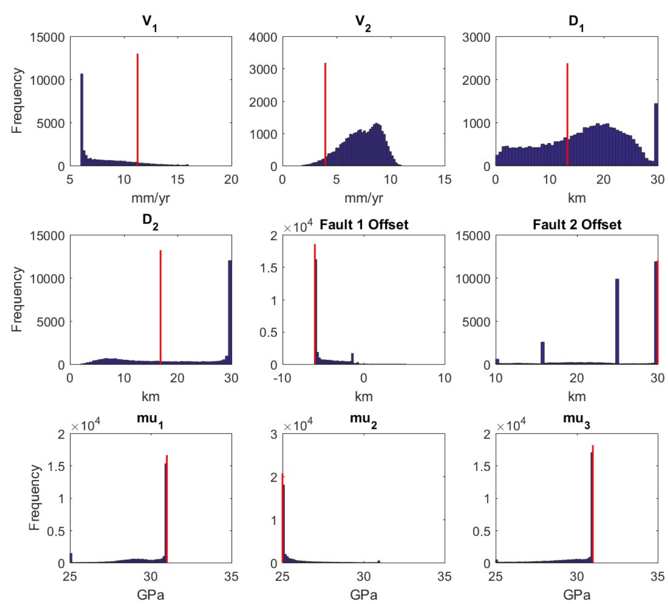

Figure **4-35**: Cerro Negro velocity profile parameter probability density functions of two-fault hetero-elastic dislocation model where the northeast fault was constrained to 20 km to 30 km. mu (μ) – shear modulus. Red line indicates parameter value for the best-fitting model.

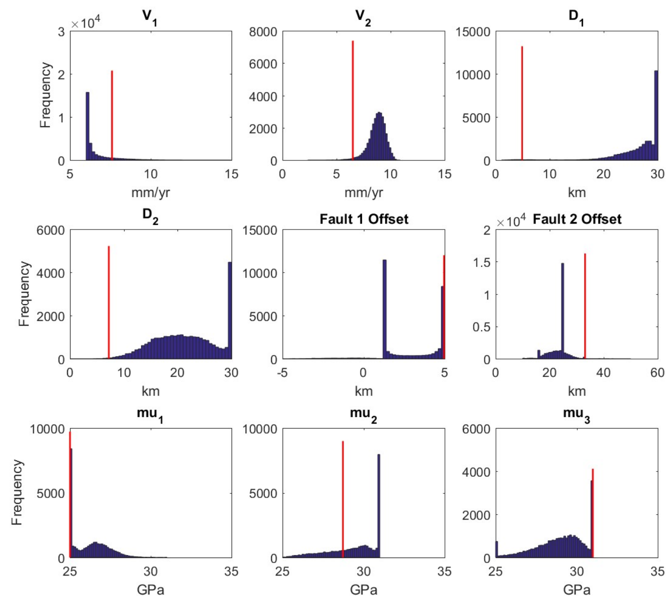

Figure **4-35**: Cerro Negro velocity profile parameter probability density functions of two-fault hetero-elastic dislocation model where GPS velocities for GPS stations on volcanos were excluded from inversion and northeast fault was constrained to 20 km to 30 km. mu (μ) – shear modulus. Red line indicates parameter value for the best-fitting model.

4.2.4.2.2 Hetero-Elastic Dislocation - Relaxed Northeast Fault Constraint

Inversion of the model set for the two-fault hetero-elastic dislocation model with relaxed constraints for the location of the northeast fault (20 km to 55 km) yielded improved model fits compared to the model set that constrained the location of the northeast fault (Table **4-12**; Figures **4-37** to **4-41**). The location of the northeast fault for most models is greater than 30 km from the volcanic arc. The model of the Telica profile, which did not include volcano GPS velocities, is the only model that placed the northeast fault within 30 km of the volcanic arc, at an along profile distance of 18.7 ± 6.0 km from the volcanic arc. The models produced locking depths for the volcanic arc fault of 1.0 km to 30 km and for the northeast faults, locking depths of 1.2 km to 23.4 km (Table **4-12**). The model set also produced shear moduli that were at the lower (25 GPa) and upper bounds (30 GPa) of the constraints. All models produced a shear modulus of 25 ± <17 GPa for the forearc, except the model that fit the Cerro Negro profile that used all GPS velocities, which yielded a shear modulus of 27.7 ± 2.5 GPa (Figure **4-37c**; Table **4-23**). This model produced a shear modulus of 25.0 ± 2.0 GPa for the volcanic arc while other models yielded shear moduli of ~30 GPa. All models produced a shear modulus of ~30 GPA for the back-arc with the exception of the model that fit the Telica profile that used all GPS velocities during inversion. The Telica profile that was inverted using the full data set produced a shear modulus of 26.3 ± 3.3 GPa for the back-arc. The far-field velocities for both the volcanic arc fault and the northeast fault are equivalent (~7 mm/yr) for all models except the Cerro Negro profile that was inverted using the full GPS data set (Table **4-12**). The model that fit the Cerro Negro profile that used all GPS velocities produced far-field velocities of 11.9 ± 4.3 mm/yr across the volcanic arc and 4.0 ± 3.5 across the northeast fault (Table **4-12**; Figure **4-37c**). The total across-strike velocity is equivalent for all models (~15 mm/yr). Inversions that did not use volcanic GPS velocities produced model fits that are worse than inversions that do include volcanic GPS velocities.

Table **4-12**: Two-fault hetero-elastic dislocation model results for model set with northeast fault constrained to within 55 km from the volcanic arc. x_1 – the along-profile location of volcanic arc fault. x_2 – the along-profile location of northeast fault. V_{ff-1} – the far-field velocity for volcanic arc fault. . V_{ff-2} – the far-field velocity for northeast fault. D_1 – locking depth of volcanic arc fault. D_2 – locking depth of northeast fault. μ_1 – shear modulus of forearc. μ_2 – shear modulus of region between the two faults. μ_3 – shear modulus of back-arc.

Profile	**Model**	x_1 **(km)**	x_2 **(km)**	V_{ff-1} **(mm/yr)**	V_{ff-2} **(mm/yr)**	D_1 **(km)**	D_2 **(km)**	μ_1 **(GPa)**	μ_2 **(GPa)**	μ_3 **(GPa)**	$\overline{\chi}^2$	**No. of GPS Vels**
Telica	With VGPS	-3.9 ± 1.5	37.1 ± 12.7	6.0 ± 4.7	8.0 ± 3.1	1.0 ± 17.7	15.5 ± 12.4	26.3 ± 3.3	31.0 ± 5.0	25.0 ± 4.9	1.32	15
	No VGPS	1.3 ±2.4	18.7 ± 6.0	7.6 ± 1.4	7.8 ± 1.3	29.9 ± 5.2	23.4 ± 6.0	29.6 ± 1.7	30.8 ± 2.1	25.2 ± 1.6	0.52	10
Cerro Negro	With VGPS	-2.8 ± 1.8	46.6 ± 19.5	11.9 ± 4.3	4.0 ± 3.5	13.9 ± 7.9	9.2 ± 15.7	31.0 ± 3.0	25.0 ± 2.0	27.7 ± 2.5	3.26	12
	No VGPS	5.0 ±2.9	33.1 ± 10.2	7.6 ± 1.4	6.5 ± 2.4	4.9 ± 22.3	7.2 ± 15.4	31.0 ± 2.5	28.7 ± 1.7	25.0 ± 1.7	0.36	7

A

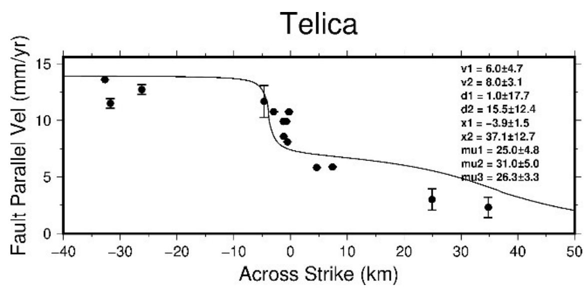
Telica
v1 = 6.0±4.7
v2 = 8.0±3.1
d1 = 1.0±17.7
d2 = 15.5±12.4
x1 = −3.9±1.5
x2 = 37.1±12.7
mu1 = 25.0±4.8
mu2 = 31.0±5.0
mu3 = 26.3±3.3
Fault Parallel Vel (mm/yr)
Across Strike (km)

B

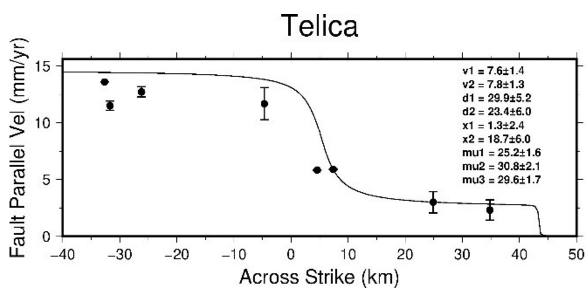
Telica
v1 = 7.6±1.4
v2 = 7.8±1.3
d1 = 29.9±5.2
d2 = 23.4±6.0
x1 = 1.3±2.4
x2 = 18.7±6.0
mu1 = 25.2±1.6
mu2 = 30.8±2.1
mu3 = 29.6±1.7
Fault Parallel Vel (mm/yr)
Across Strike (km)

C

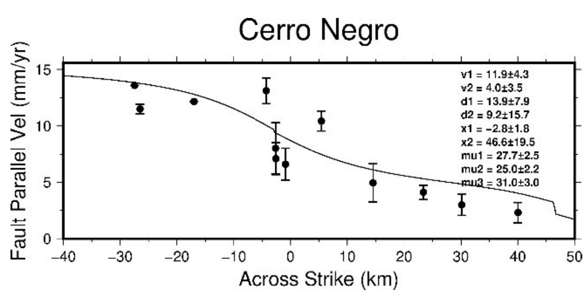
Cerro Negro
v1 = 11.9±4.3
v2 = 4.0±3.5
d1 = 13.9±7.9
d2 = 9.2±15.7
x1 = −2.8±1.8
x2 = 46.6±19.5
mu1 = 27.7±2.5
mu2 = 25.0±2.2
mu3 = 31.0±3.0
Fault Parallel Vel (mm/yr)
Across Strike (km)

D

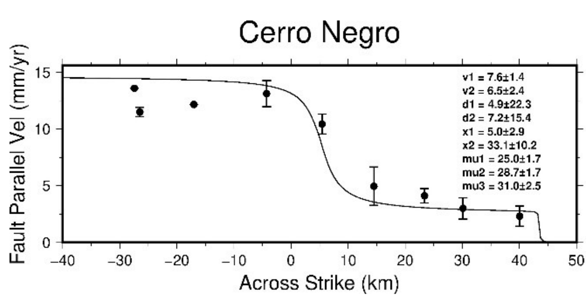
Cerro Negro
v1 = 7.6±1.4
v2 = 6.5±2.4
d1 = 4.9±22.3
d2 = 7.2±15.4
x1 = 5.0±2.9
x2 = 33.1±10.2
mu1 = 25.0±1.7
mu2 = 28.7±1.7
mu3 = 31.0±2.5
Fault Parallel Vel (mm/yr)
Across Strike (km)

Figure **4-37**: Two-fault hetero-elastic dislocation model profile fits for two arc-parallel faults. During inversion location constraint of the northeast fault was relaxed (20 km to 55 km). A – Cerro Negro velocity profile and model fit. B – Cerro Negro velocity profile and model fit for inversion that did not use velocities of GPS stations sited at volcanos. C – Telica velocity profile and model fit. D – Telica velocity profile and model fit for inversion that did not use velocities of GPS stations sited at volcanos.

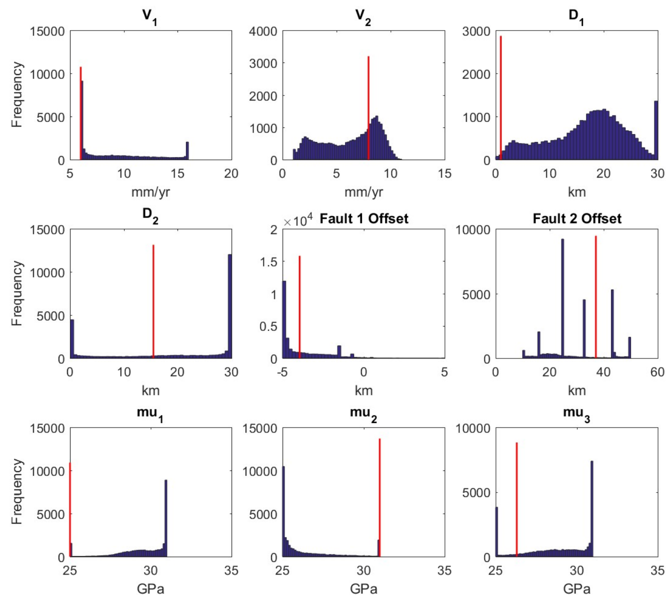

Figure **4-38**: Telica velocity profile parameter probability density functions of two-fault hetero-elastic dislocation model where northeast fault location constraint was relaxed (20 km to 55 km). mu (μ) – shear modulus. Red line indicates parameter value for the best-fitting model.

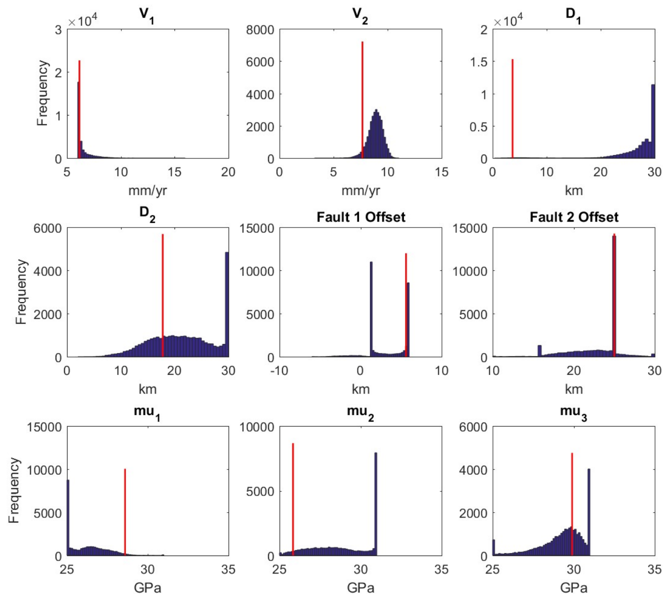

Figure **4-39**: Telica velocity profile parameter probability density functions of two-fault hetero-elastic dislocation model where GPS velocities for GPS stations on volcanos were excluded from inversion and northeast fault location constraint was relaxed (20 km to 55 km). mu (μ) – shear modulus. Red line indicates parameter value for the best-fitting model.

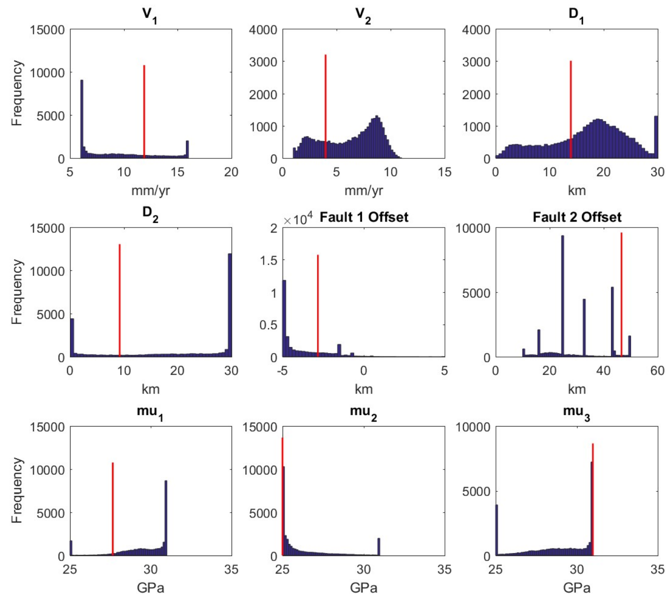

Figure **4-40**: Cerro Negro velocity profile parameter probability density functions of two-fault hetero-elastic dislocation model where northeast fault location constraint was relaxed (20 km to 55 km). mu (μ) – shear modulus. Red line indicates parameter value for the best-fitting model.

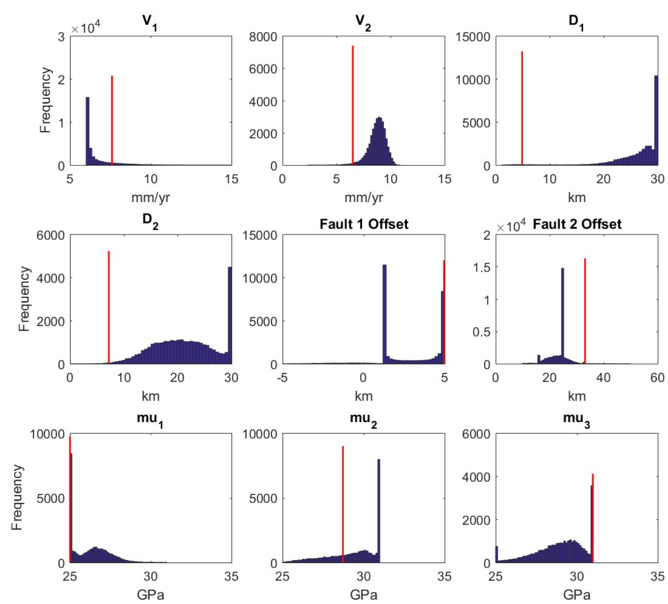

Figure **4-41**: Cerro Negro velocity profile parameter probability density functions of two-fault hetero-elastic dislocation model where GPS velocities for GPS stations on volcanos were excluded from inversion and northeast fault location constraint was relaxed (20 km to 55 km). mu (μ) – shear modulus. Red line indicates parameter value for the best-fitting model.

4.2.3 Bookshelf Faulting – BEM

Shear via an array of sinistral faults with strikes perpendicular to the direction of the dextral shear (i.e., bookshelf faulting) was investigated using the boundary element method (Gomberg and Ellis 1993). The boundary element method (BEM) is advantageous in that it is computationally efficient (compared to the finite element method) and will simultaneously solve for slip on all faults as they interact in a deformation field. A disadvantage of this method is that it does not incorporate heterogeneous rheology. The modeling strategy assumes that the rheology of the forearc and the back-arc is the same. The forearc could be displaced by at most 40 km, given a CAFA translation rate of 14 mm/yr and 3 Myr of ongoing translation since the onset of Cocos Ridge-Caribbean plate collision. This would make it unlikely that rheologically disparate regions are now adjacent like the Carrizo segment of the San Andreas where geodetic, seismic, and geologic evidence indicates an across-strike change in rheology (Schmalzle et al., 2006). It is also assumed that there are arc-normal faults that are creeping due to the presence of volcanic centers, seismogenic arc-normal faults creep at shallow depths (< 10 km), and the interseismic GPS velocities represent the displacement due to creep on these faults. BEM models were also created with slip imposed on faults to explore slip on faults that are locked but slip freely at depth down-dip. All BEM models used a Youngs modulus of 70 GPa. The resulting displacements from the BEM models were compared to observed velocities.

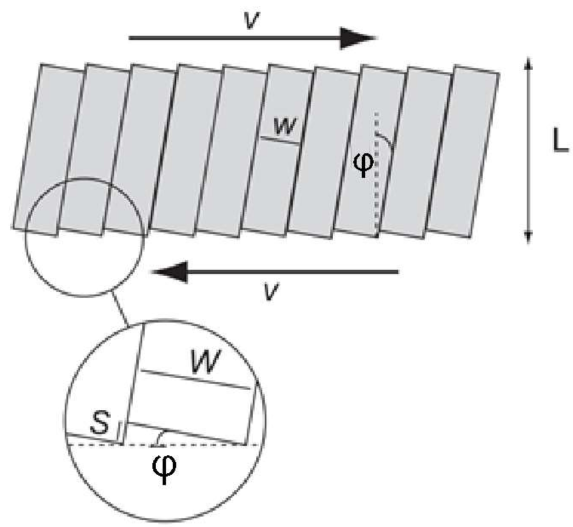

Figure **4-42**: Schematic bookshelf faulting system showing geometric relationships between faults. Modified from Sigmundsson et al., (1995).

The resulting slip on freely slipping arc-normal faults from the BEM was also compared to the expected slip on bookshelf faults using the geometric relationships described by Sigmundsson et al., (1995) for the South Iceland Seismic Zone (Figure **4-42**). The rate of rotation of the arc-normal faults in the CAFA-CA shear zone is described by Equation 5,

$$\dot{\varphi} = 2v/L \quad \textbf{17}$$

where L is the length of each fault, and v = ~7 mm/yr is half the CAFA-CA relative rate. The slip rate on each arc-normal fault is determined using Equation 6,

$$S = w\tan^{-1}\dot{\varphi} = w\dot{\varphi} \quad \textbf{18}$$

where w is the spacing between arc-normal faults.

The deformation field was created using four faults that simulated the motion of the CAFA (Figure **4-43**). This was accomplished by imposing on four north striking faults, at the ends of the model space, either tensile opening or closing. For example, a tensile opening or closing of 7 mm resulted in a linear change in displacement across the model's inspection area of 7 mm to -7 mm. The four faults were spaced 120 km apart, 200 km long, and at depths of the surface to 150 km. Models of arc-normal faults were created with varying fault lengths and spacings from which the surface displacements were inspected. The arc-normal faults are vertical and extend from the surface to 20 km, with modeled lengths of 5 km, 10 km, 15 km, and 20 km and the spacings between these faults being 2 km, 5 km, and 10 km.

Five BEM model sets were created to explore (1) freely slipping faults assuming there is no a priori knowledge of fault slip rates, (2) slip prescribed on arc-normal faults following the kinematic analysis of Sigmundsson et al., (1995). BEM model set were also implemented to explore simulated locked faults by using slip amounts from the bookshelf faulting kinematic analysis on arc-normal faults. The slip was imposed on the faults at down-dip depths of (3) 5 km to 20 km and (4) 10 km to 20 km. To further explore locked arc-normal faults, (5) another model set was created with 10 mm and 14 mm of slip prescribed on the arc-normal faults at down-dip depths of 5 km to 20 km.

4.2.3.1 Freely Slipping Faults

For the BEM model set that allowed faults to slip freely in the deformation field, two subsets of models, A and B, were created. Model set A only has arc-normal faults and model set B includes an arc-parallel fault at depth. The arc-parallel fault represents the shear of the lower lithosphere, where the ductility of the crust is expected to result in shear aligned with the direction of motion. The arc-normal faults are at depths from the surface to 20 km. The arc-parallel fault is at depths of 20 km to 55 km and is 100 km long, long enough to not introduce unwanted displacements at the fault tip in the model inspection area. No slip is prescribed on the arc-normal and arc-parallel faults but they are allowed to slip freely with only strike-slip displacement, i.e., no dip-slip is allowed. Figure **4-44** shows the configuration of models that include arc-normal and arc-parallel faults. Tables **4-13** and **4-14** detail the model names and varying parameters for BEM model sets A and B. A deformation field that created a linear change of -7 mm to 7 mm across the model inspection area was used.

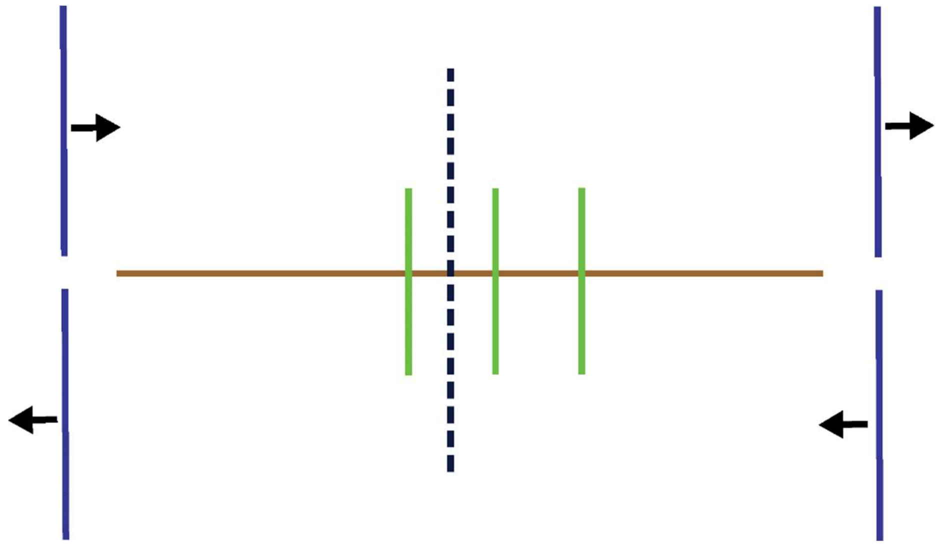

Figure **4-43**: Boundary element method model schematic for faults inducing deformation (dark blue), three arc-normal faults (green), an arc-parallel fault at depth (brown). The dashed line is the profile of the region from which surface displacements will be sampled. Fault lengths are not to scale.

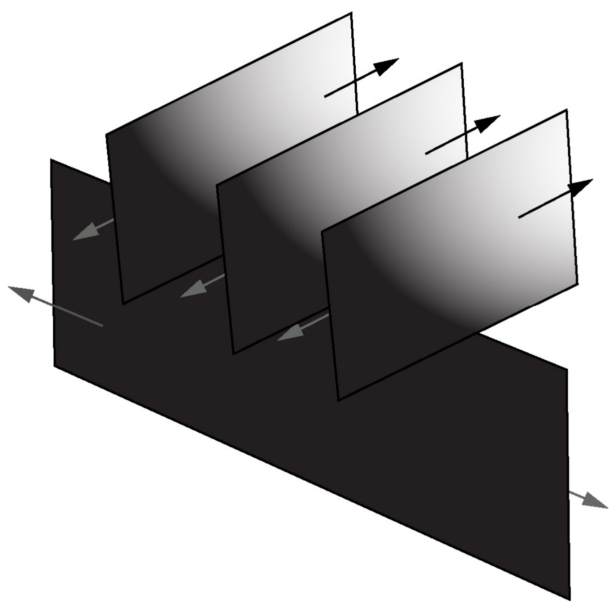

Figure **4-44**. Schematic of the model set up for boundary element models that include arc-normal and arc-parallel faults.

Table **4-13**: Boundary element method models set A with only arc-normal faults.

Model Name	Arc-Normal Fault Length (km)	Arc-Normal Fault Spacing (km)
A1	5	2
A2	5	5
A3	5	10
A4	10	2
A5	10	5
A6	10	10
A7	15	2
A8	15	5
A9	15	10
A10	20	2
A11	20	5
A12	20	10

Table **4-14**: Boundary element method models set with arc-normal and arc-parallel faults.

Model Name	Arc-Normal Fault Length (km)	Arc-Normal Fault Spacing (km)
B1	5	2
B2	5	5s
B3	5	10
B4	10	2
B5	10	5
B6	10	10
B7	15	2
B8	15	5
B9	15	10
B10	20	2
B11	20	5
B12	20	10

Model sets A and B were further explored in different deformation fields considering that the GPS velocities of the CAFA range from 8 mm/yr to 14 mm/yr, which are limited to the coast and the volcanic arc (40 km). It is possible that there is a maximum velocity that is not observed due to the lack of further afield forearc GPS stations. Model set C, which is similar to model set A, was created with a deformation field that has a displacement gradient of -8 mm to 8 mm. Model set D is similar to model set B (arc-parallel fault at depth) and has a deformation field of -8 mm to 8 mm. Model set E is similar to model set A but has a deformation field of -10 mm to 10 mm. Model set F is similar to model set B (arc-parallel fault at depth) but has a deformation field of -10 mm to -10 mm. Models names and configuration for model set C through E are detailed in Tables **4-15**, **4-16**, **4-17**, and **4-18**.

Table **4-15**: Models set C configuration.

Model Name	Arc-Normal Fault Length (km)	Arc-Normal Fault Spacing (km)
C1	5	2
C2	5	5.5
C3	5	10
C4	10	2
C5	10	5
C6	10	10
C7	15	2
C8	15	5
C9	15	10
C10	20	2
C11	20	5
C12	20	10

Table **4-16**: Models set D configuration with arc-parallel fault.

Model Name	Arc-Normal Fault Length (km)	Arc-Normal Fault Spacing (km)
D1	5	2
D2	5	5.5
D3	5	10
D4	10	2
D5	10	5
D6	10	10
D7	15	2
D8	15	5
D9	15	10
D10	20	2
D11	20	5
D12	20	10

Table **4-17**: Models set E configuration

Model Name	**Arc-Normal Fault Length (km)**	**Arc-Normal Fault Spacing (km)**
E1	5	2
E2	5	5.5
E3	5	10
E4	10	2
E5	10	5
E6	10	10
E7	15	2
E8	15	5
E9	15	10
E10	20	2
E11	20	5
E12	20	10

Table **4-18**: Models set F configuration with arc-parallel fault.

Model Name	**Arc-Normal Fault Length (km)**	**Arc-Normal Fault Spacing (km)**
F1	5	2
F2	5	5.5
F3	5	10
F4	10	2
F5	10	5
F6	10	10
F7	15	2
F8	15	5
F9	15	10
F10	20	2
F11	20	5
F12	20	10

4.2.3.2 Slip Prescribed on Faults

To investigate how slip on arc-normal and arc-parallel faults contribute to the across-strike geodetic signal, several models were created where slip was prescribed on faults. These model sets also examined the resulting displacements of these faults slipping with and without a background deformation field and with and without the 20 km deep arc-parallel fault that represents shear at depth.

Models set G was created with the same fault configuration of the model set B (Figure **4-44**), with slip imposed on the arc-normal faults (from the surface to 20 km) following the kinematic analysis of Sigmundsson et al., (1995), right-lateral slip of 14 mm on the arc-parallel fault, and a background deformation field of -7 mm to 7 mm. Model set H is similar to model set G but without the background deformation field. Model set I is also similar to model set G but without the arc-parallel fault. Table **4-19** details the fault configuration and background deformation field for model sets G through I. For model sets G through I, the arc-normal fault lengths are 20 km and models were created for fault spacings of 2 km, 5 km, and 10 km (Table **4-20**).

Table **4-19**: Model sets G through I configuration.

Model Name	**Deformation Field (min to max in mm)**	**Arc-parallel Fault Slip (mm)**
G	7	14
H	None	14
I	7	None

Table **4-20**: Model sets G through I fault spacings.

Model Name	**Arc-Normal Fault Length (km)**	**Arc-Normal Fault Spacing (km)**	**Arc-Normal Fault Slip (mm)**
G1	20	2	1.4
G2	20	5	3.8
G3	20	10	7
H1	20	2	1.4
H2	20	5	3.8
H3	20	10	7
I1	20	2	1.4
I2	20	5	3.8
I3	20	10	7

The bookshelf faults in Nicaragua are seismogenic and the across-strike interseismic GPS velocities may be due to slip down-dip, below the locked part of the faults. Several models were created to explore locked faults with slip down-dip. The slip on these faults follows the kinematic analysis of Sigmundsson et al., (1995). These models also investigated the surface displacements of these locked faults with and without a background deformation field. Model set J has a similar configuration of model set B (includes an arc-parallel fault) with arc-normal faults slip at 10 km to 20 km down-dip and there is no background deformation field. Model set K is similar to model set J but without an arc-parallel fault. Model set L is similar to model set J but with a background deformation field of -7 mm to 7 mm. Model set M is similar to model set J but without a background deformation field nor an arc-parallel fault and slip is imposed on the arc-normal faults down-dip at 5 km to 20 km. Model set N is similar to model set M but with a background deformation field of -7 mm to 7 mm. Table **4-21** details the configuration and background deformation for model sets J through N. For model sets J through N, all arc-normal faults were 20 km long, and spaced 2 km, 5 km, and 10 km (Table **4-22**).

Table **4-21**: Model sets J through N configuration.

Model Name	Deformation Field (-min to +max in mm)	Arc-parallel Fault Slip (mm)	Slip at Down-Dip (km)
J	None	14	15 - 20
K	None	None	10 - 20
L	7	None	10 - 20
M	None	None	5 - 20
N	7	None	5 - 20

Table **4-22**: Model sets G through I fault spacings.

Model Name	Arc-Normal Fault Length (km)	Arc-Normal Fault Spacing (km)	Arc-Normal Fault Slip (mm)
J1	20	2	1.4
J2	20	5	3.8
J3	20	10	7
K1	20	2	1.4
K2	20	5	3.8
K3	20	10	7
L1	20	2	1.4
L2	20	5	3.8
L3	20	10	7
M1	20	2	1.4
M2	20	5	3.8
M3	20	10	7
N1	20	2	1.4
N2	20	5	3.8
N3	20	10	7

Locked arc-normal faults were further investigated by creating models with imposed slip of 10 mm and 14 mm on arc-normal faults. The imposed slip exceeds that of what the kinematic analysis of bookshelf faulting predicts. Model set O has a similar configuration of model set B, i.e., there is an arc-parallel fault at depth, but without the background deformation field and slip of 10 mm was imposed on arc-normal faults at 5 km to 20 km down-dip. Model set P is similar to model set O except a background deformation field of -7 mm to 7 mm is included. Model set Q is similar to model set O but 14 mm of slip was imposed on arc-normal faults. Likewise, the model set R is similar to model set

P except 14 mm of slip was imposed on arc-normal faults. Table **4-23** details the configuration and background deformation for model sets O through R. For model sets O through R, all arc-normal faults were 20 km long, and spaced 2 km, 5 km, and 10 km (Table **4-24**).

Table **4-23**: Model sets O through R configuration.

Model Name	**Deformation Field (min to max in mm)**	**Arc-normal fault Slip (mm)**	**Slip at Down-Dip (km)**
O	None	10	5 - 20
P	7	10	5 - 20
Q	None	14	5 - 20
R	7	14	5 - 20

Table **4-24**: Model sets O through R fault spacings.

Model Name	**Arc-Normal Fault Length (km)**	**Arc-Normal Fault Spacing (km)**	**Arc-Normal Fault Slip (mm)**
O1	20	2	1.4
O2	20	5	3.8
O3	20	10	7
P1	20	2	1.4
P2	20	5	3.8
P3	20	10	7
Q1	20	2	1.4
Q2	20	5	3.8
Q3	20	10	7
R1	20	2	1.4
R2	20	5	3.8
R3	20	10	7

The slip on all faults and background deformation field for all model sets are detailed in Table **4-25**.

Table **4-25:** All BEM model configurations.

Model Name	**Deformation Field (min to max in mm)**	**Arc-parallel Fault Slip (mm)**	**Arc-normal fault Slip (mm)**	**Slip Down-Dip (km)**
A	7	F	None	0 - 20
B	7	F	F	0 - 20
C	8	F	None	0 - 20
D	8	F	F	0 - 20
E	10	F	None	0 - 20
F	10	F	F	0 - 20
G	7	14	S	0 - 20
H	None	14	S	0 - 20
I	7	None	S	0 - 20
J	None	14	S	15 - 20
K	None	None	S	10 - 20
L	7	None	S	10 - 20
M	None	None	S	5 - 20
N	7	None	S	5 - 20
O	None	None	10	5 - 20
P	7	None	10	5 - 20
Q	None	None	14	5 - 20
R	7	None	14	5 - 20

F – free to slip. S – Slip from kinematic analysis (Sigmundsson et al., 1995).

4.2.3.3 Bookshelf Faulting Results

The surface displacements generated by the arc-normal bookshelf faults were explored using the boundary element method. A deformation field was created by prescribing on four faults tensile opening or closing of 7 mm, which created a displacement gradient of 7 mm to -7 mm across (bottom to the top of model space) the model's inspection area (Figures **4-45** and **4-46**). To ensure that the expected deformation field is generated, a model was implemented with an arc-parallel fault (left to right of model space) with fault width from the surface to 30 km and length of 100 km that yielded displacements which approximate an expected step function (Figures **4-47** and **4-48**).

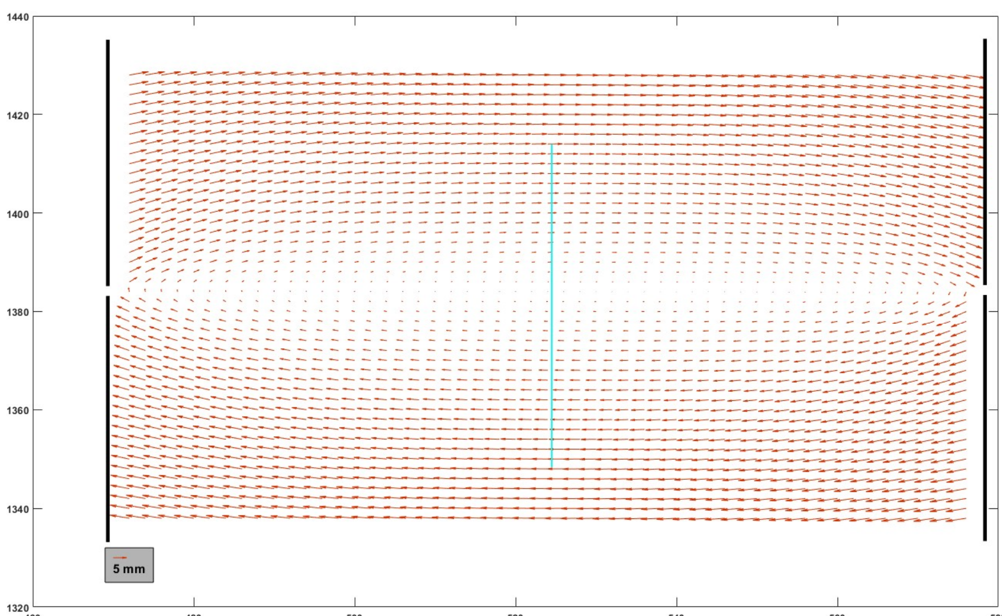

Figure **4-45**: Surface displacement produced by the initial deformation field where the four faults (black lines) are opening or closing to simulate forearc translation. Cyan line is profile line where surface displacements will be inspected.

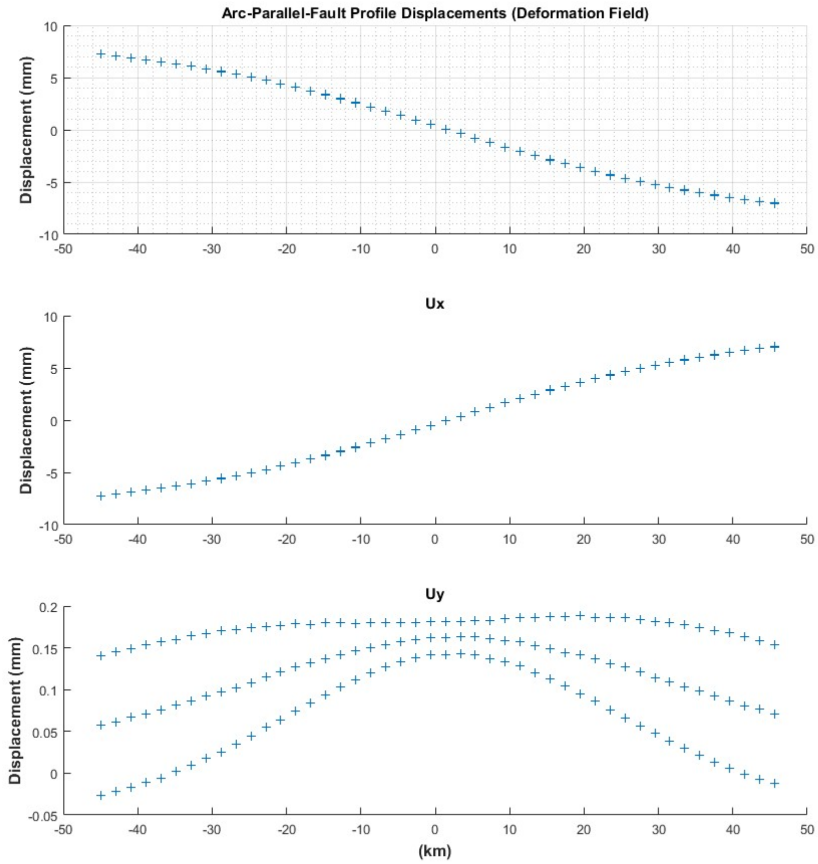

Figure **4-46**: Displacements sampled within a 4 km width along profile line (cyan line in Figure **4-45**). Top panel – profile displacements projected into horizontal line (azimuth = 270°) where westward velocities are positive. Middle panel – profile displacements in the x-direction. Bottom panel – profile displacements in the y-direction.

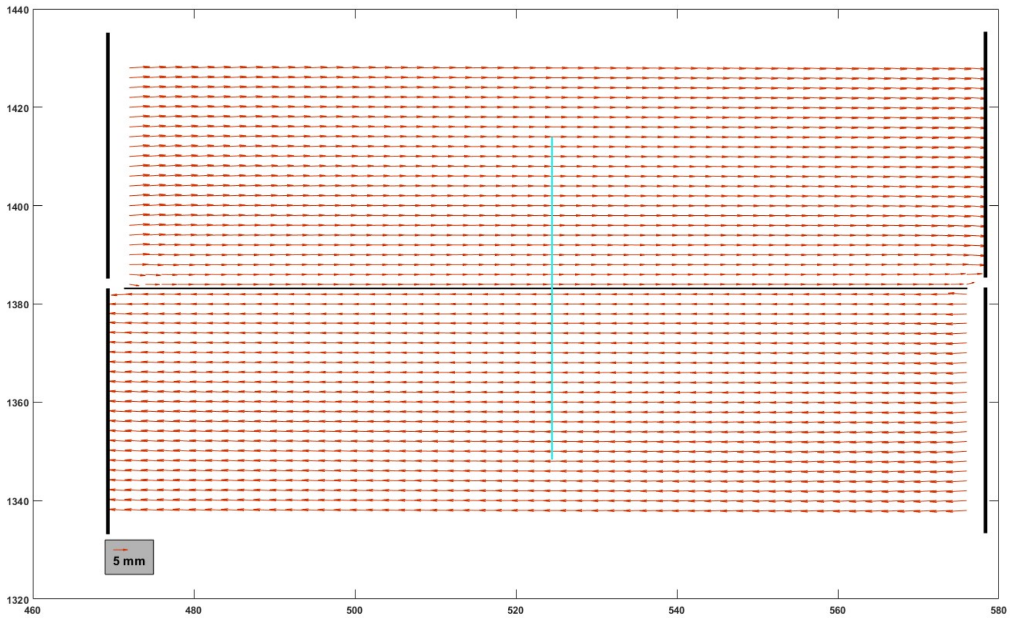

Figure **4-47**: Surface displacement produced by four opening or closing faults (black lines) and horizontal or arc-parallel fault (black line) at depths of 0 km to 30 km and length of 100 km.

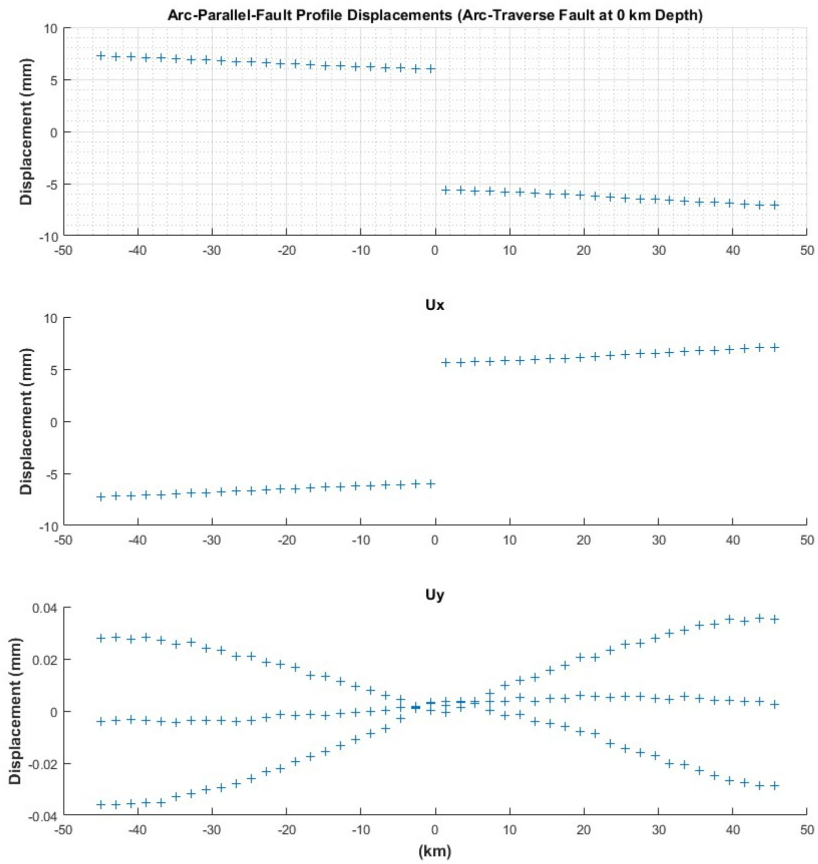

Figure **4-48**: Displacement sampled within a 4 km width of profile produced by four opening or closing faults (black lines) and arc-parallel fault at depths of 0 km to 30 km and length of 100 km. Top panel – profile displacements projected into horizontal line (azimuth = 270°). Middle panel – profile displacements in the x-direction. Bottom panel – profile displacements in the y-direction.

4.3.3.1 Freely Slipping Faults

4.3.3.1.1 Model Sets A & B

All BEM models incorporated arc-normal faults, but to investigate how shear in the ductile lithosphere at depth induces surface displacements, two model sets were created: (i) model set A only incorporated arc-normal faults and (ii) model set B included an arc-parallel fault at depth (30 km to 55 km). The resulting surface displacements are compared to observed displacements (observed GPS velocities over a year). The surface displacements for model set A are plotted in Figures **4-49** to **4-60**. The displacements projected into an arc-parallel (left to right of the model space) profile for model set A are plotted in Figures **4-61** to **4-73**. The surface displacements for model set B are plotted in Figures **4-74** to **4-85**. The displacements model set B that were projected into an arc-normal profile are plotted in Figures **4-86** to **4-98**. Model set A, compared to model set B, better approximates the observed displacements. Both model sets A and B with fault lengths of 15 km and 20 km and spacings of 2 km, 5.5 km, and 10 km appear to well fit the observed displacements in the back-arc, forearc, and about ~10 km away from the volcanic arc (models A7, A8, A9, A10 A11, A12, B7, B8, B9, B10, B11, B12; Figures **4-68** to **4-73** & **4-93** to **4-98**).

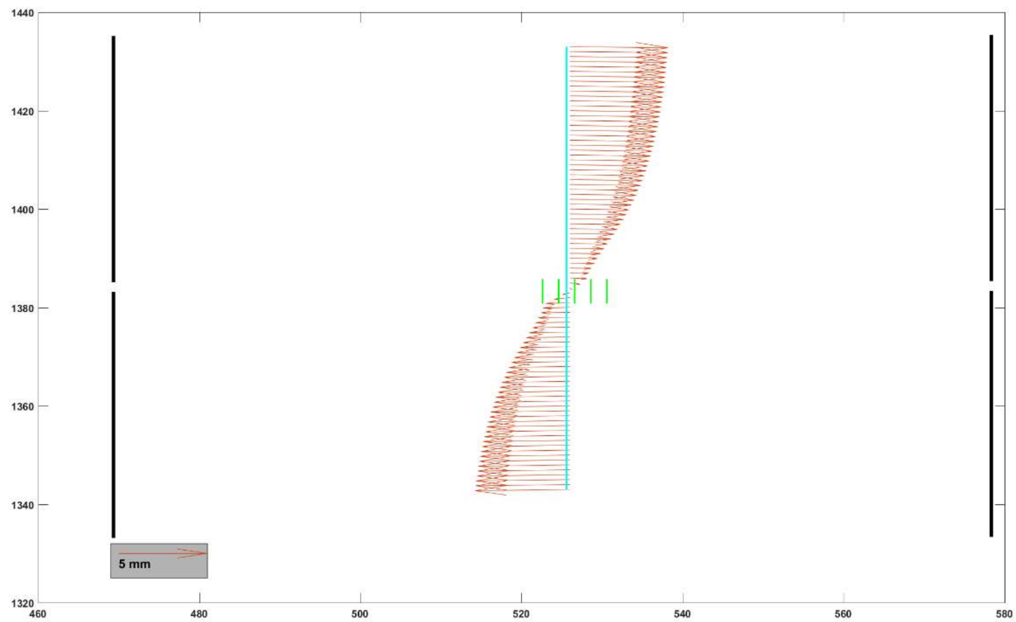

Figure **4-49**. Model A1: surface displacements (red vectors) along-profile line (cyan line). Arc-normal faults' (green lines) length and spacing are 5 km and 2 km respectively. This model has 5 arc-normal faults.

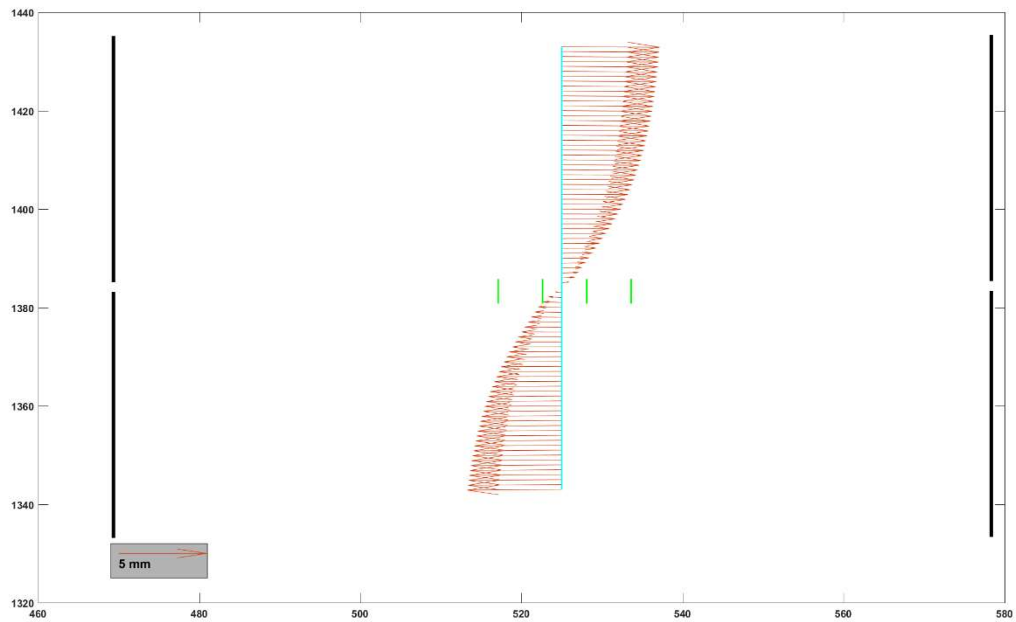

Figure **4-50**. Model A2: surface displacements (red vectors) along-profile line (cyan line). Arc-normal faults' (green lines) length and spacing are 5 km and 5 km respectively. This model has 4 arc-normal faults.

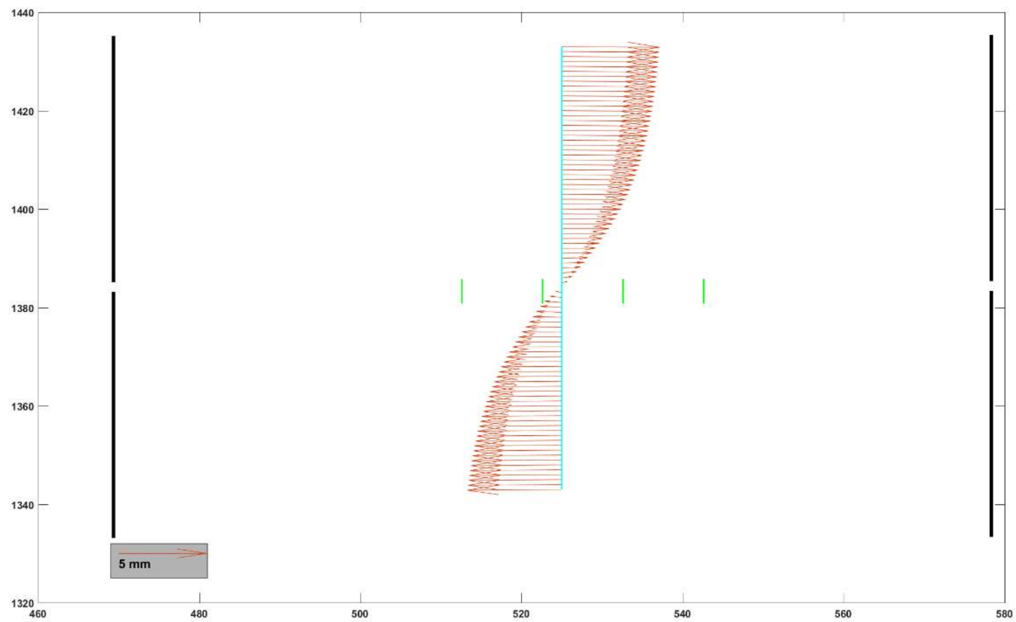

Figure **4-51:** Model A3: surface displacements (red vectors) along-profile line (cyan line). Arc-normal faults' (green lines) length and spacing are 5 km and 10 km respectively. This model has 4 arc-normal faults.

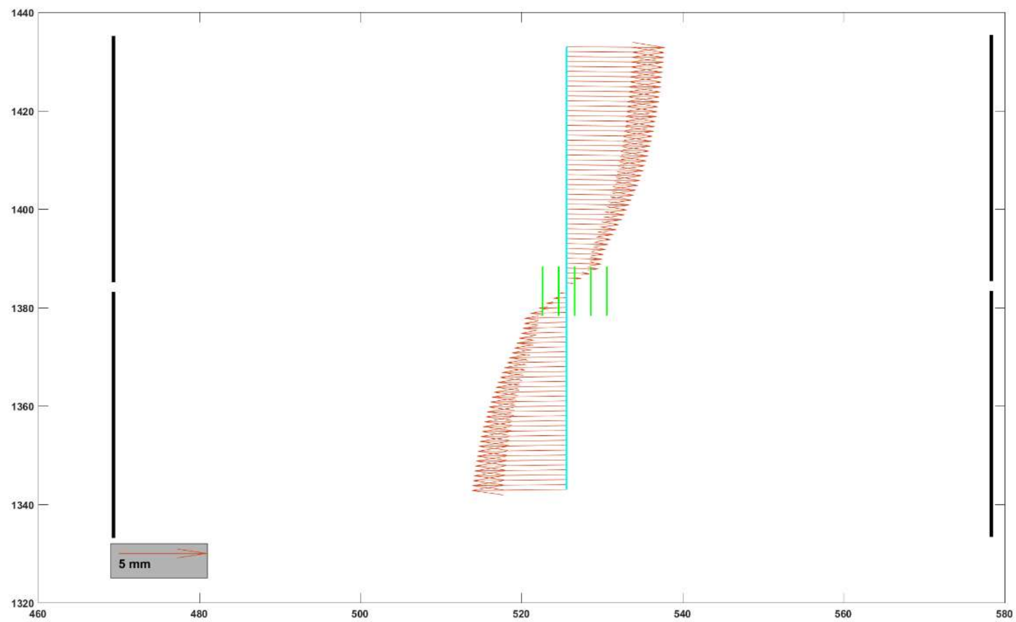

Figure **4-52:** Model A4: surface displacements (red vectors) along-profile line (cyan line). Arc-normal faults' (green lines) length and spacing are 10 km and 2 km respectively. This model has 5 arc-normal faults.

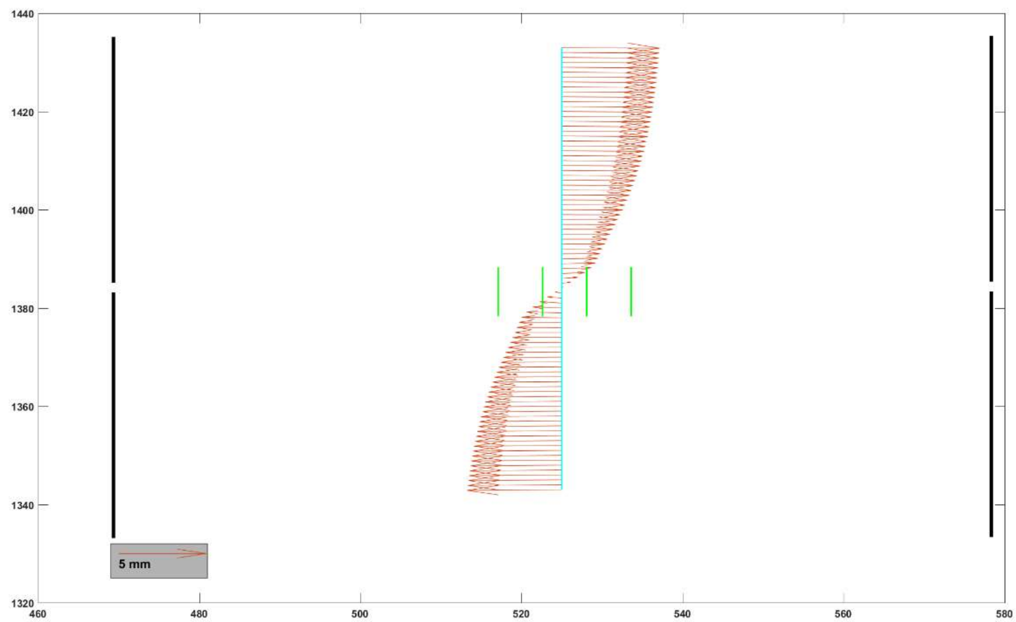

Figure **4-53**: Model A5: surface displacements (red vectors) along-profile line (cyan line). Arc-normal faults' (green lines) length and spacing are 10 km and 5 km respectively. This model has 4 arc-normal faults.

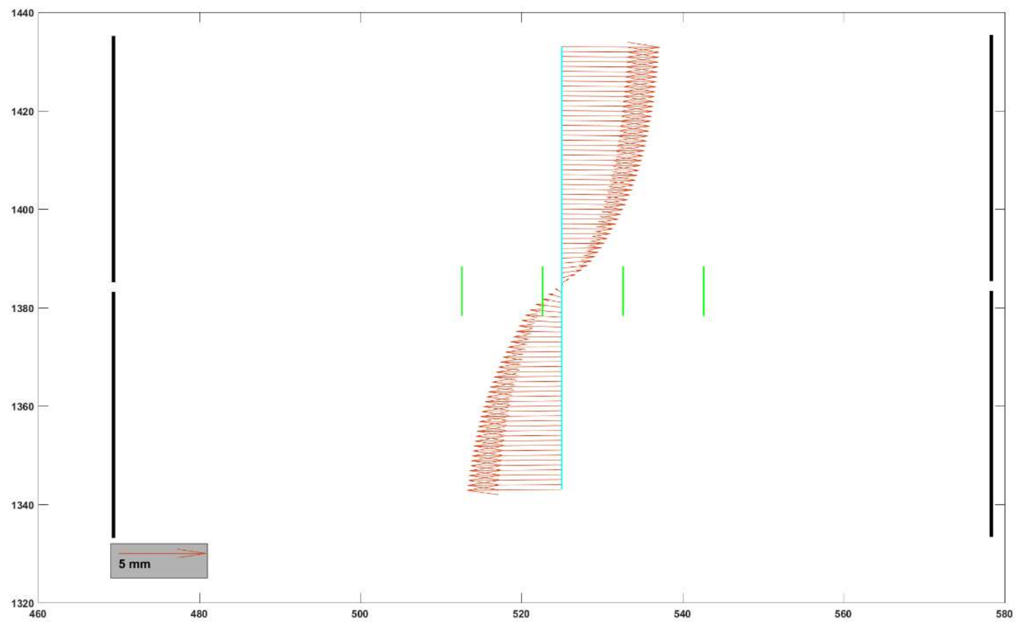

Figure **4-54**: Model A6: surface displacements (red vectors) along-profile line (cyan line). Arc-normal faults' (green lines) length and spacing are 10 km and 10 km respectively. This model has 4 arc-normal faults.

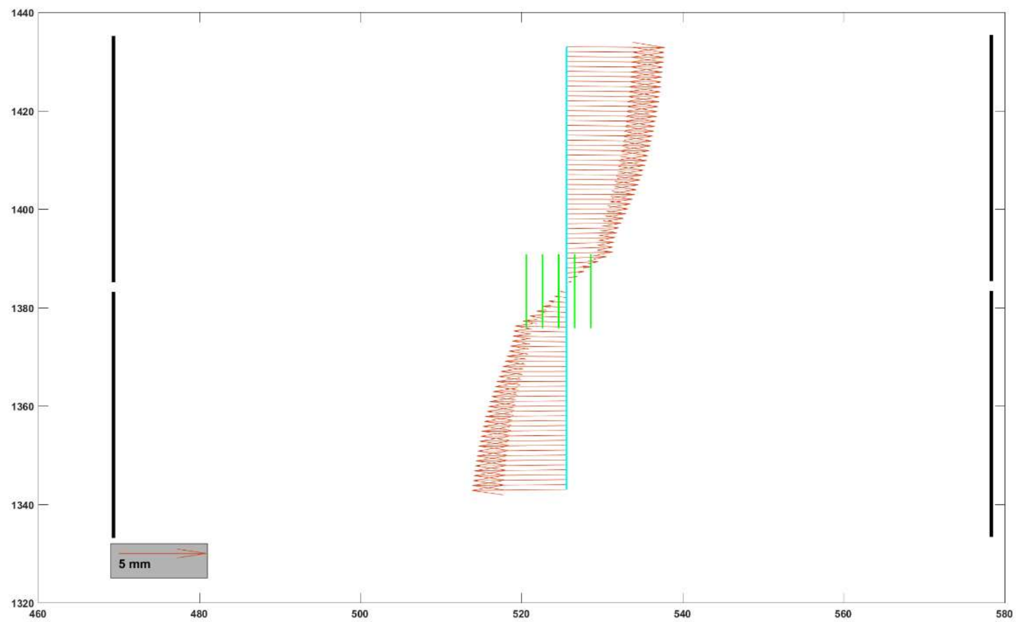

Figure **4-55:** Model A7: surface displacements (red vectors) along-profile line (cyan line). Arc-normal faults' (green lines) length and spacing are 15 km and 2 km respectively. This model has 5 arc-normal faults.

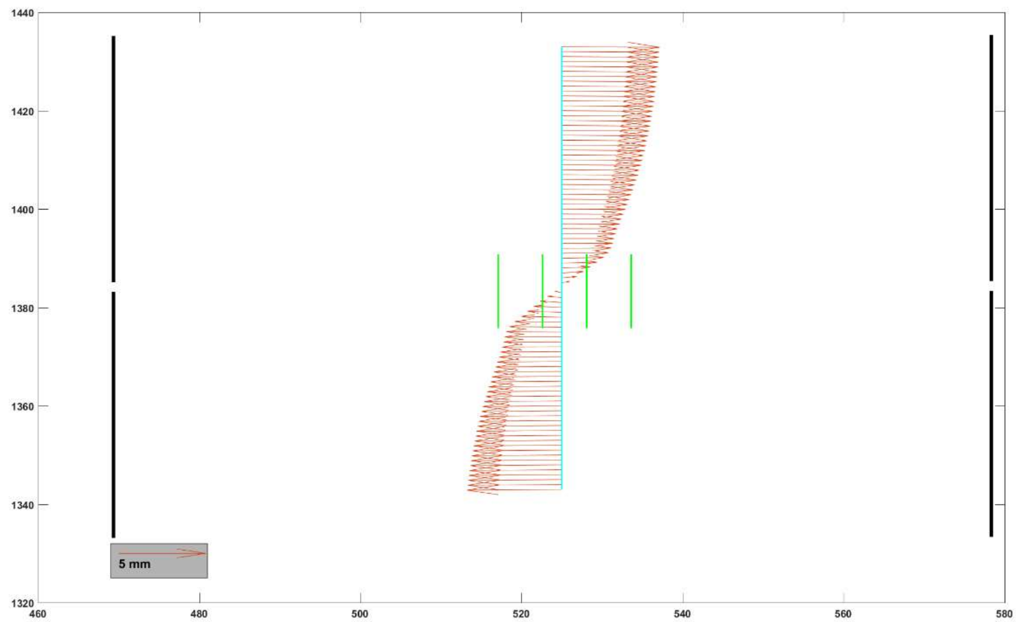

Figure **4-56:** Model A8: surface displacements (red vectors) along-profile line (cyan line). Arc-normal faults' (green lines) length and spacing are 15 km and 5 km respectively. This model has 4 arc-normal faults.

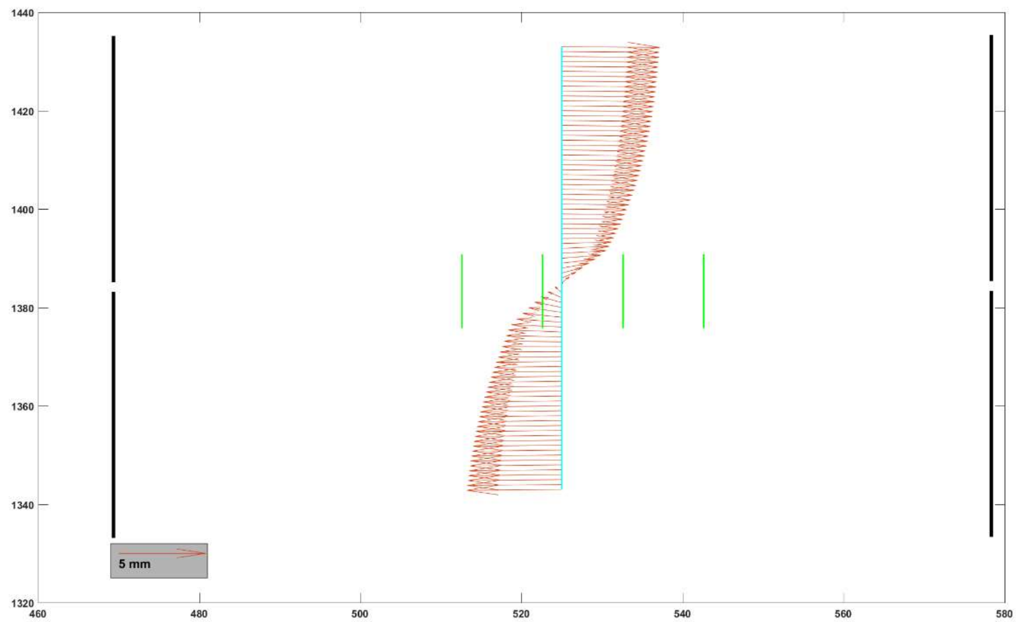

Figure **4-57**: Model A9: surface displacements (red vectors) along-profile line (cyan line). Arc-normal faults' (green lines) length and spacing are 15 km and 10 km respectively. This model has 4 arc-normal faults.

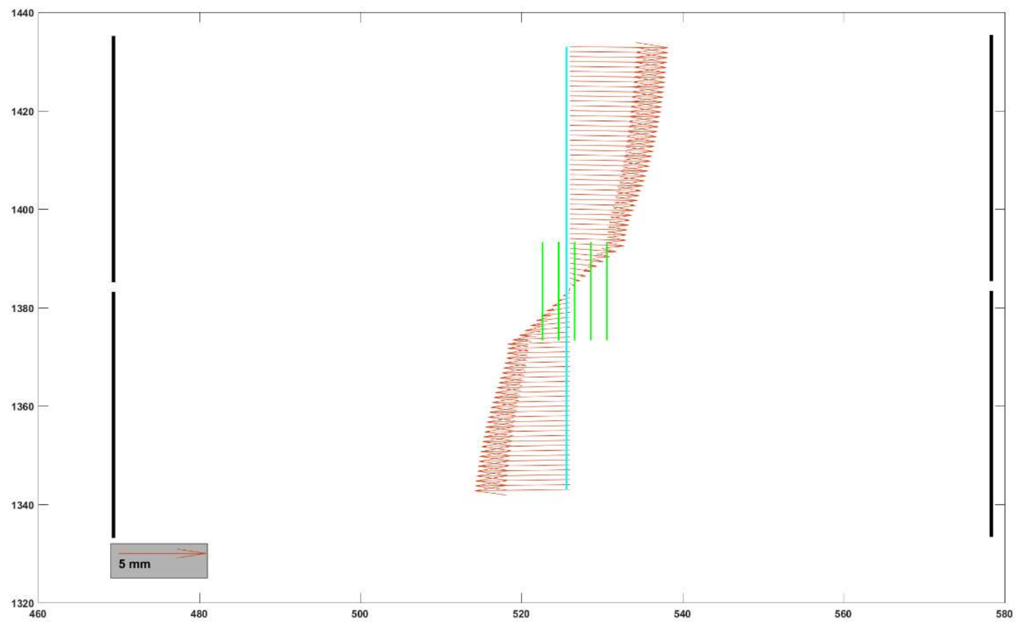

Figure **4-58**: Model A10: surface displacements (red vectors) along-profile line (cyan line). Arc-normal faults' (green lines) length and spacing are 20 km and 2 km respectively. This model has 5 arc-normal faults.

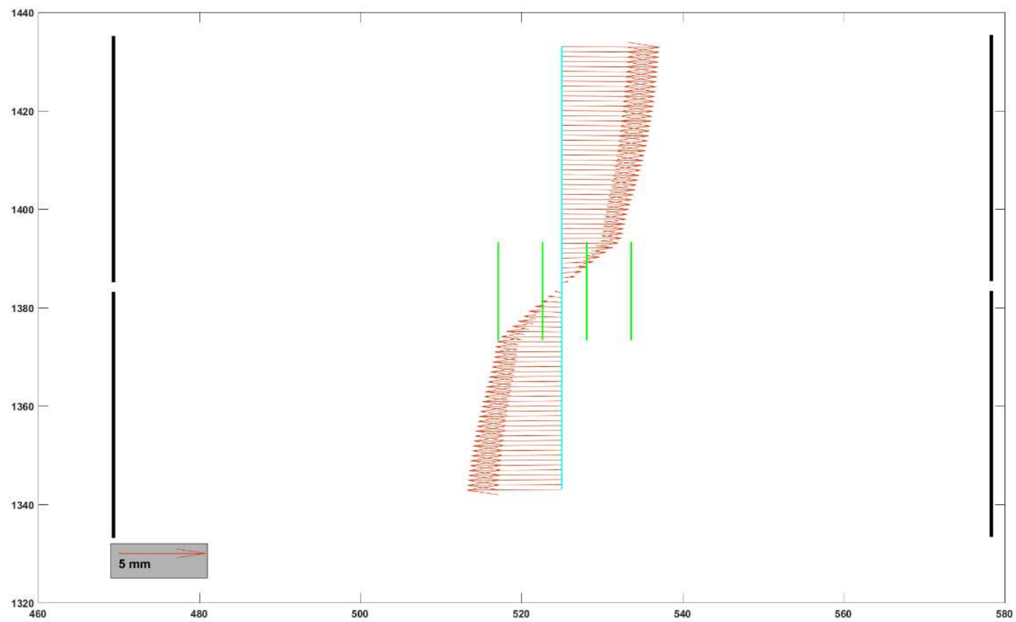

Figure **4-59:** Model A11: surface displacements (red vectors) along-profile line (cyan line). Arc-normal faults' (green lines) length and spacing are 20 km and 5 km respectively. This model has 4 arc-normal faults.

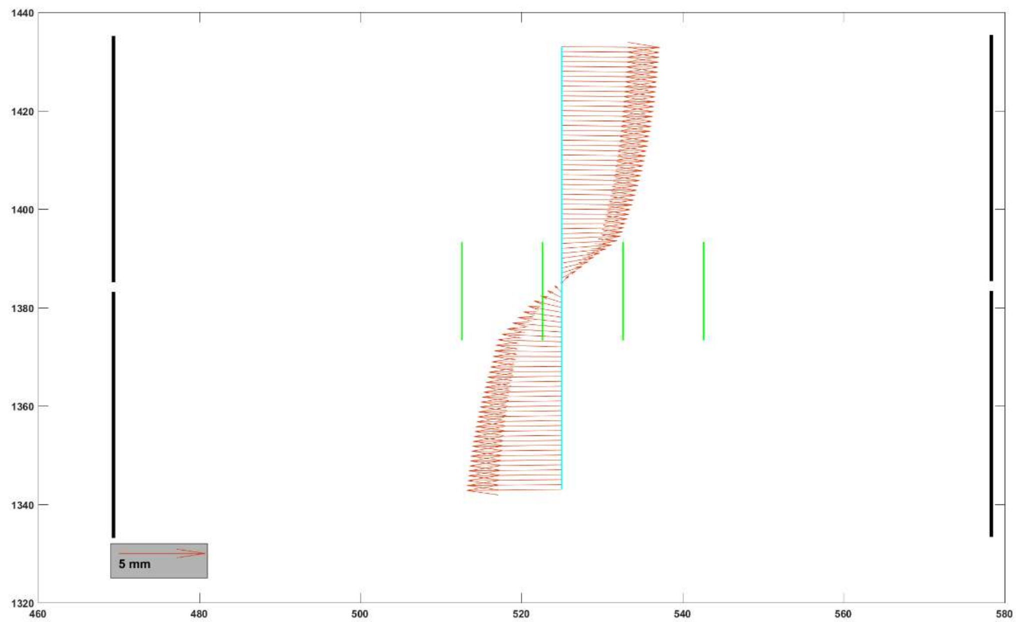

Figure **4-60:** Model A12: surface displacements (red vectors) along-profile line (cyan line). Arc-normal faults' (green lines) length and spacing are 20 km and 10 km respectively. This model has 4 arc-normal faults.

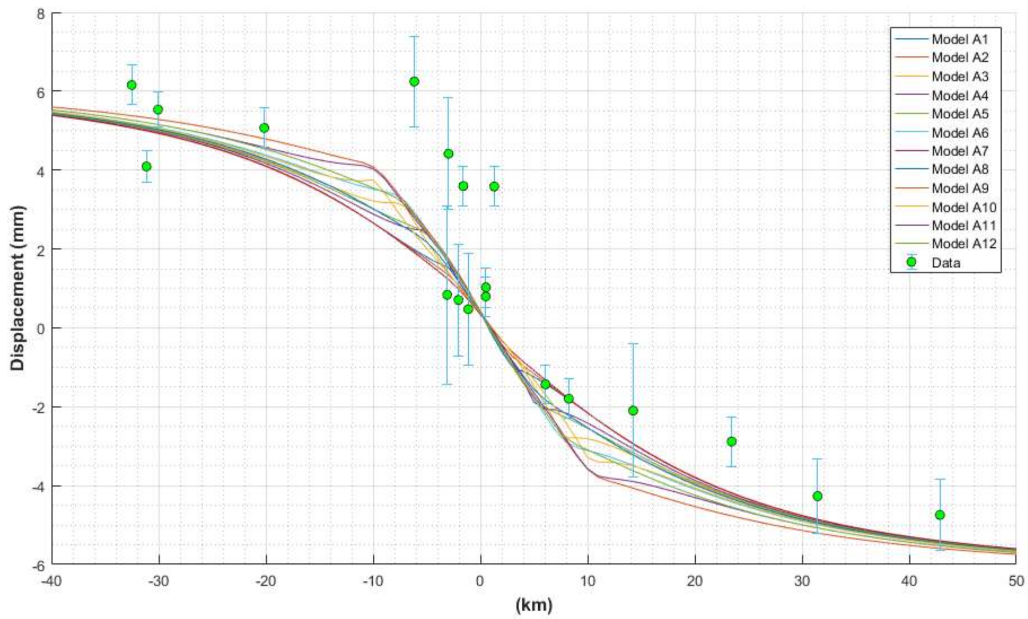

Figure **4-61:** All BEM model set A surface profiles (cyan line in Figures **4-49** to **4-60**).

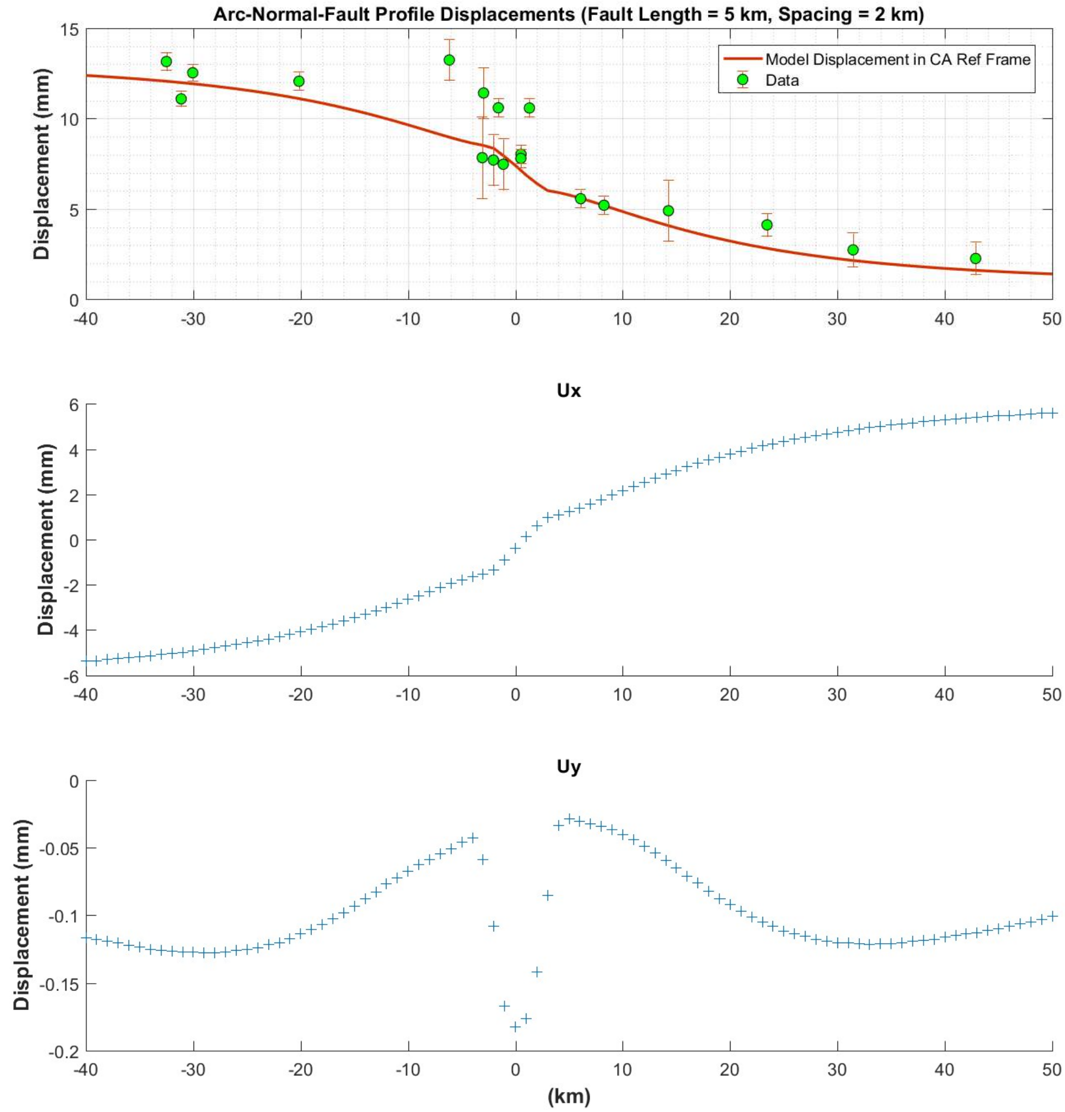

Figure **4-62**. Model A1: displacements along-profile. Arc-normal faults' length and spacing are 5 km and 2 km respectively. Top panel – profile displacements projected into horizontal line (azimuth = 270°). Middle panel – profile displacements in the x-direction. Bottom panel – profile displacements in the y-direction. 'Model Displacement in CA' data sets was created by adding an offset of 7 mm to the model displacements.

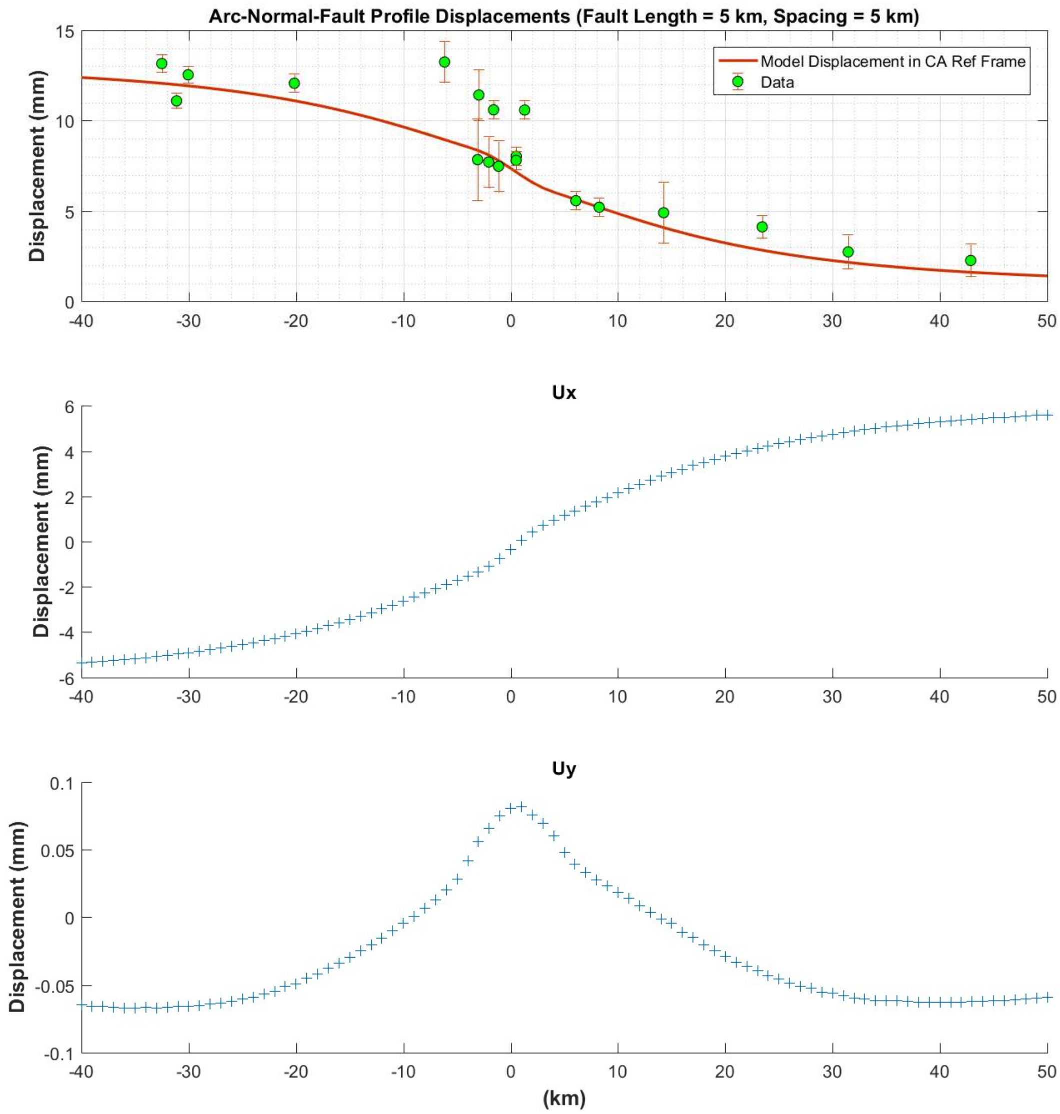

Figure **4-63**. Model A2: displacements along-profile. Arc-normal faults' length and spacing are 5 km and 5 km respectively. Top panel – profile displacements projected into horizontal line (azimuth = 270°). Middle panel – profile displacements in the x-direction. Bottom panel – profile displacements in the y-direction. 'Model Displacement in CA' data sets was created by adding an offset of 7 mm to the model displacements.

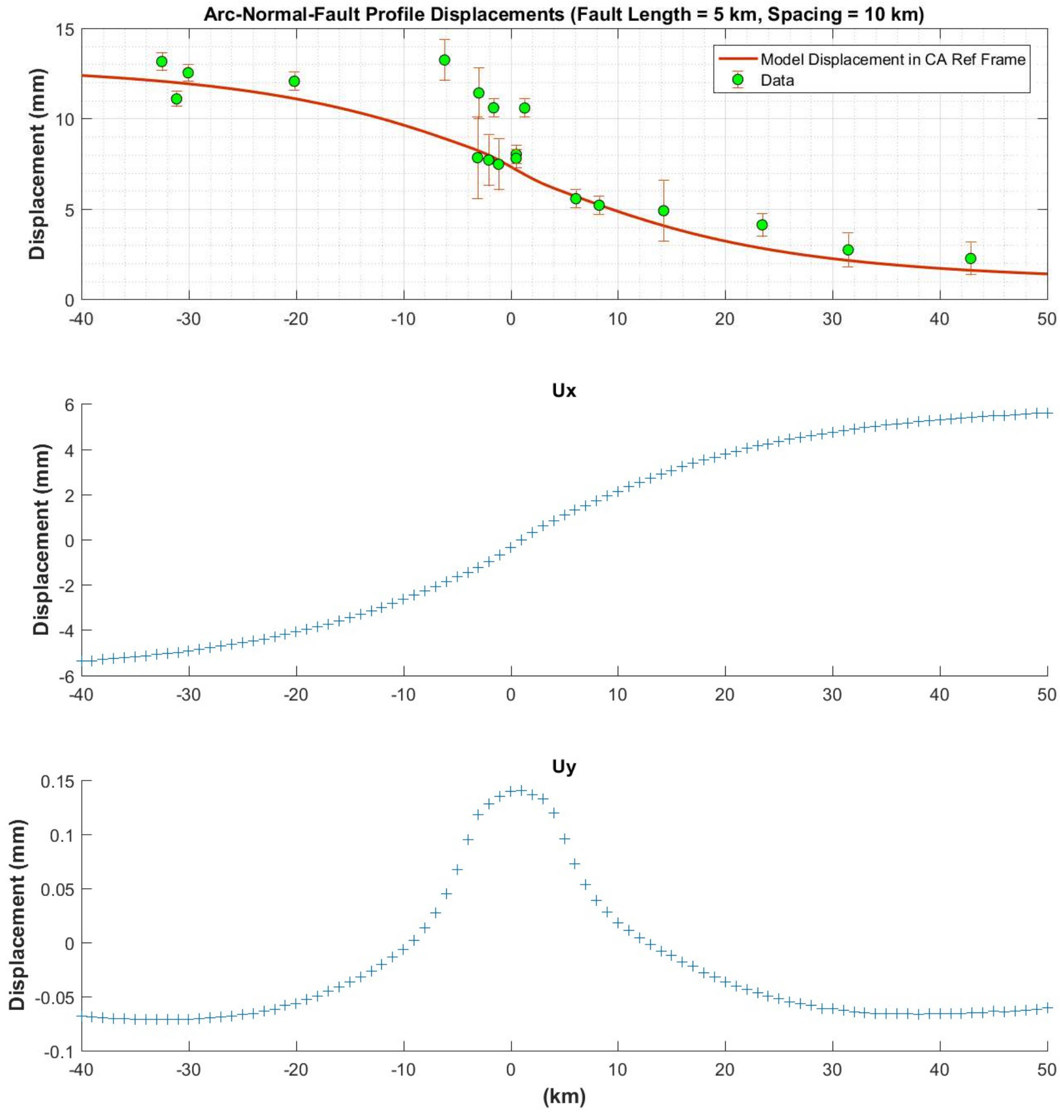

Figure **4-64:** Model A3: displacements along-profile. Arc-normal faults' length and spacing are 5 km and 10 km respectively. Top panel – profile displacements projected into horizontal line (azimuth = 270°). Middle panel – profile displacements in the x-direction. Bottom panel – profile displacements in the y-direction. 'Model Displacement in CA' data sets was created by adding an offset of 7 mm to the model displacements.

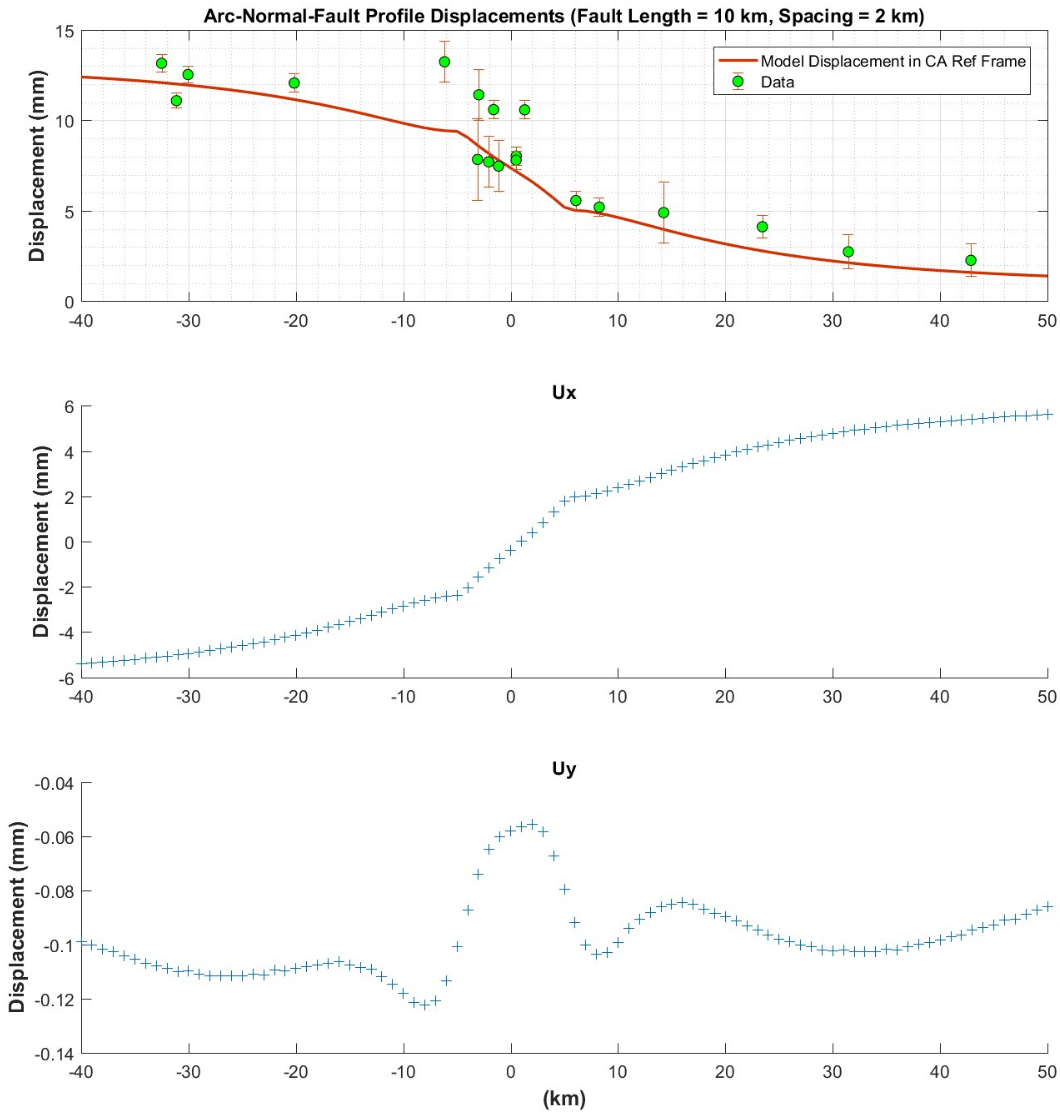

Figure **4-65:** Model A4: displacements along-profile. Arc-normal faults' length and spacing are 10 km and 2 km respectively. Top panel – profile displacements projected into horizontal line (azimuth = 270°). Middle panel – profile displacements in the x-direction. Bottom panel – profile displacements in the y-direction. 'Model Displacement in CA' data sets was created by adding an offset of 7 mm to the model displacements.

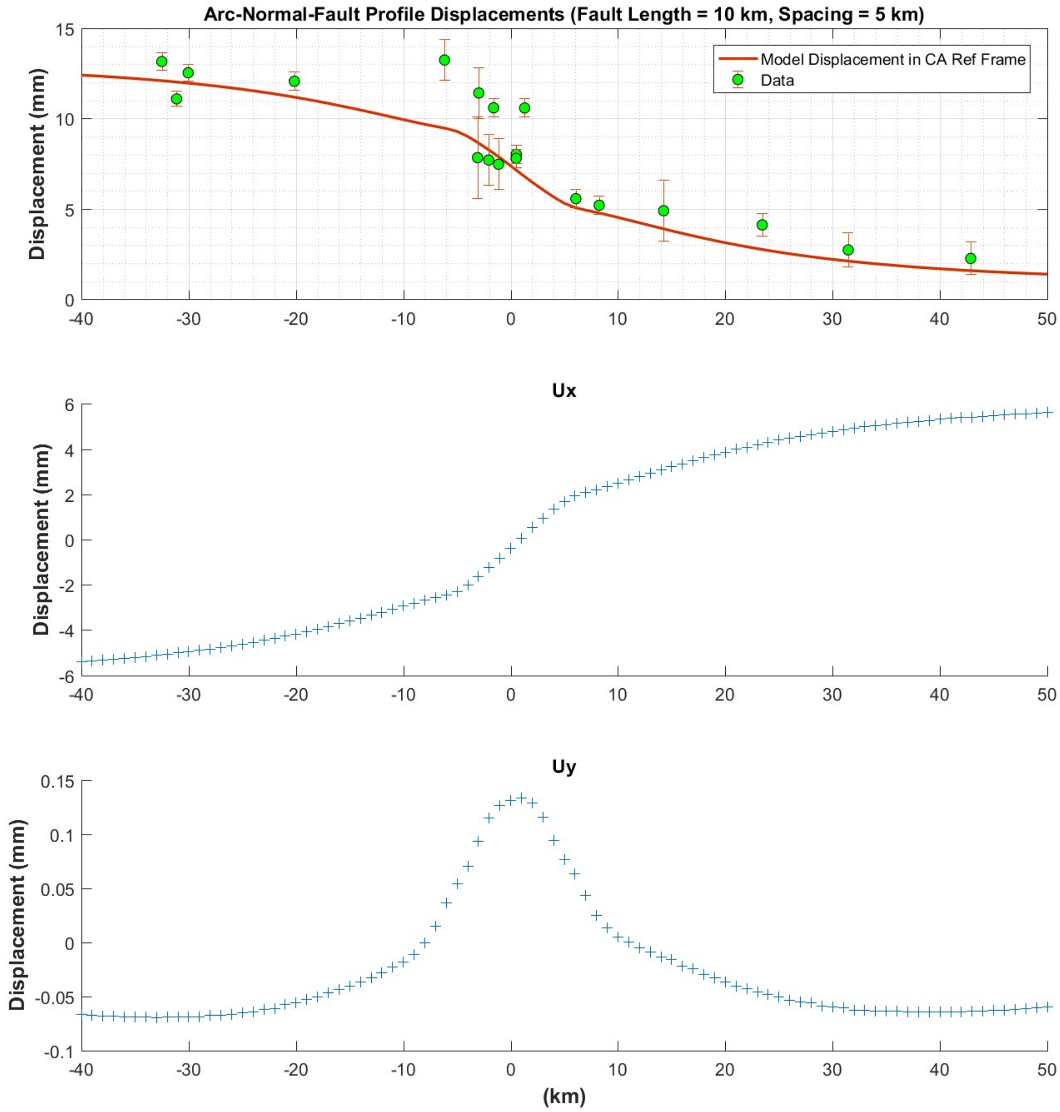

Figure **4-66:** Model A5: displacements along-profile. Arc-normal faults' length and spacing are 10 km and 5 km respectively. Top panel – profile displacements projected into horizontal line (azimuth = 270°). Middle panel – profile displacements in the x-direction. Bottom panel – profile displacements in the y-direction. 'Model Displacement in CA' data sets was created by adding an offset of 7 mm to the model displacements.

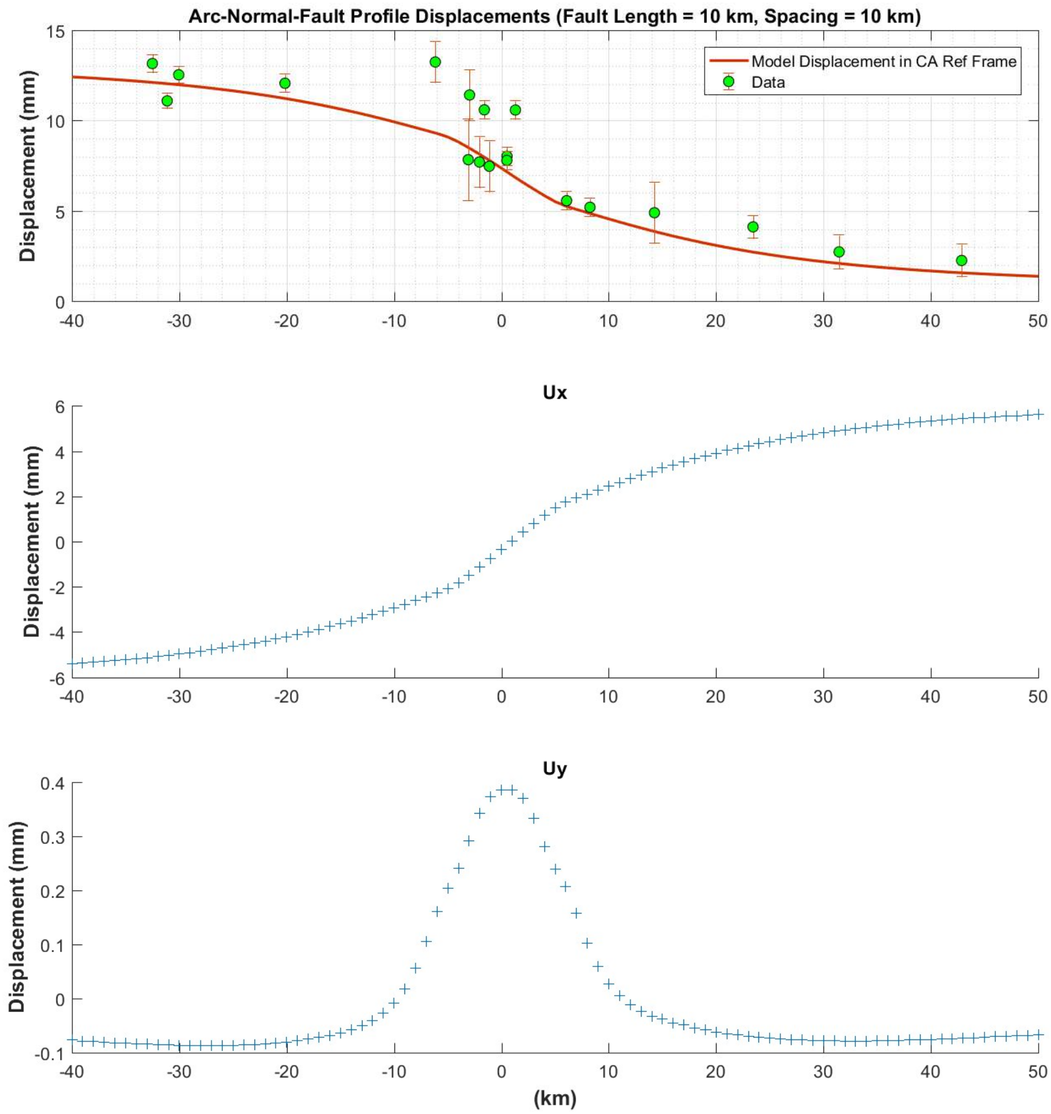

Figure **4-67:** Model A6: displacements along-profile. Arc-normal faults' length and spacing are 10 km and 10 km respectively. Top panel – profile displacements projected into horizontal line (azimuth = 270°). Middle panel – profile displacements in the x-direction. Bottom panel – profile displacements in the y-direction. 'Model Displacement in CA' data sets was created by adding an offset of 7 mm to the model displacements.

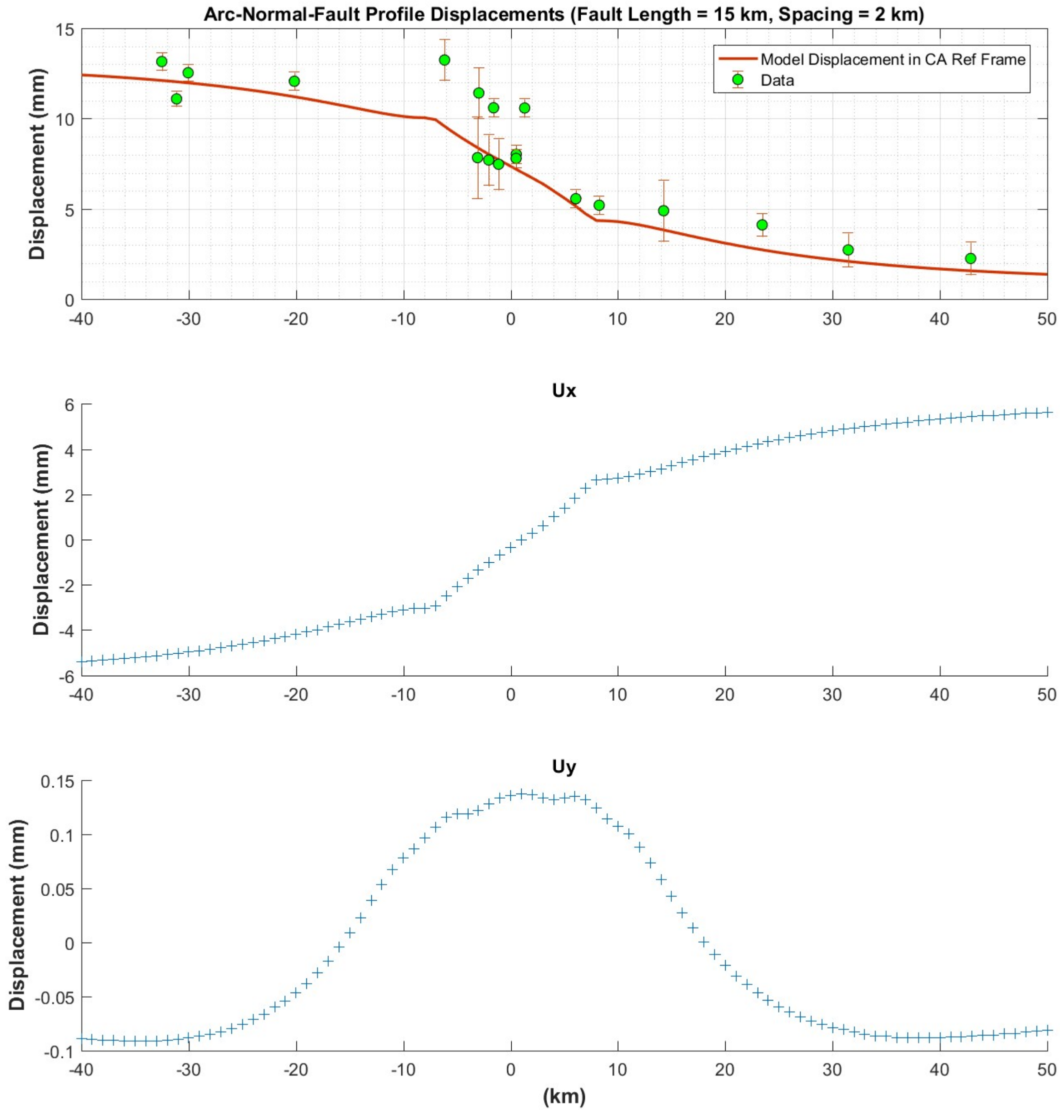

Figure **4-68:** Model A7: displacements along-profile. Arc-normal faults' length and spacing are 15 km and 2 km respectively. Top panel – profile displacements projected into horizontal line (azimuth = 270°). Middle panel – profile displacements in the x-direction. Bottom panel – profile displacements in the y-direction. 'Model Displacement in CA' data sets was created by adding an offset of 7 mm to the modeled displacement.

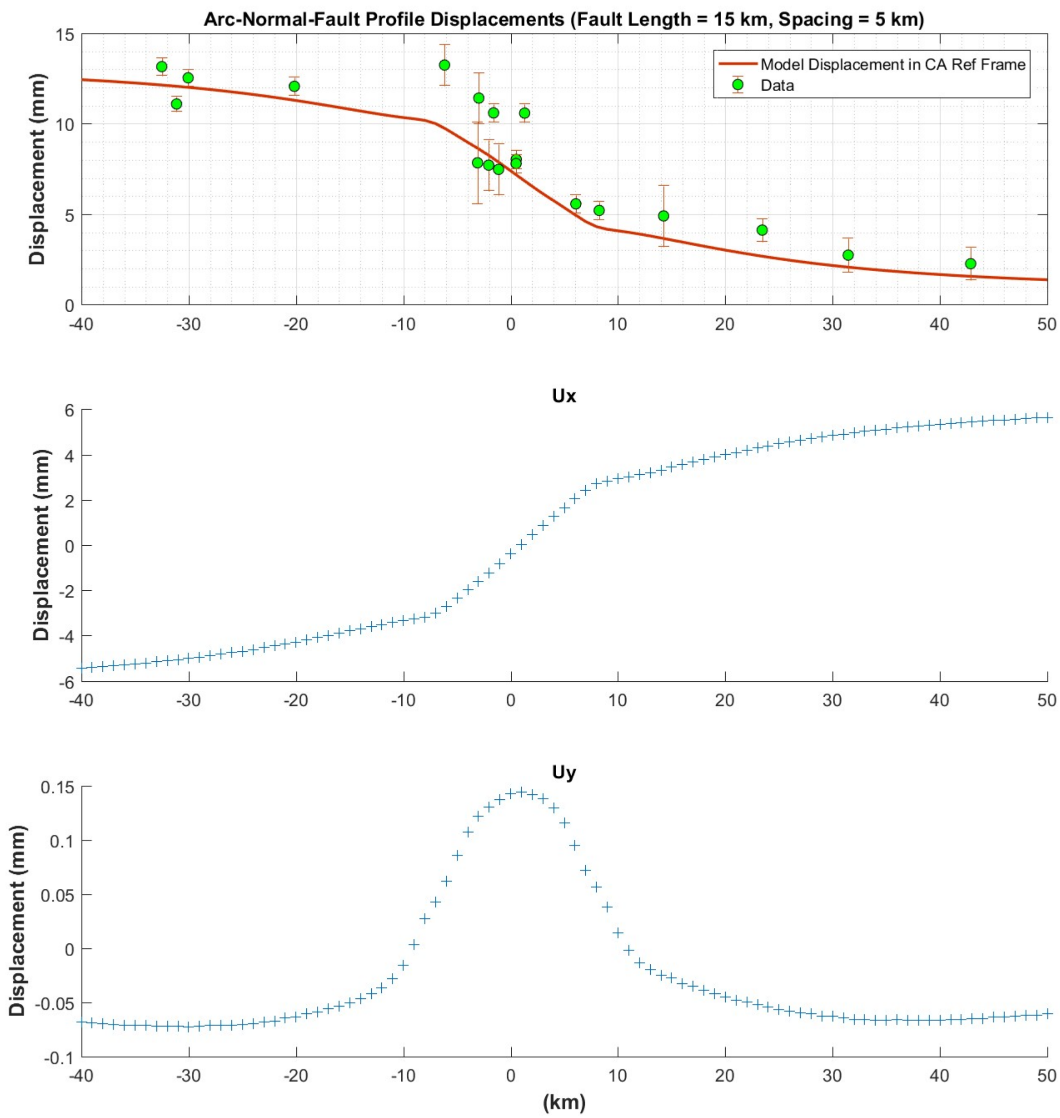

Figure **4-69:** Model A8: displacements along-profile. Arc-normal faults' length and spacing are 15 km and 5 km respectively. Top panel – profile displacements projected into horizontal line (azimuth = 270°). Middle panel – profile displacements in the x-direction. Bottom panel – profile displacements in the y-direction. 'Model Displacement in CA' data sets was created by adding an offset of 7 mm to the modeled displacement.

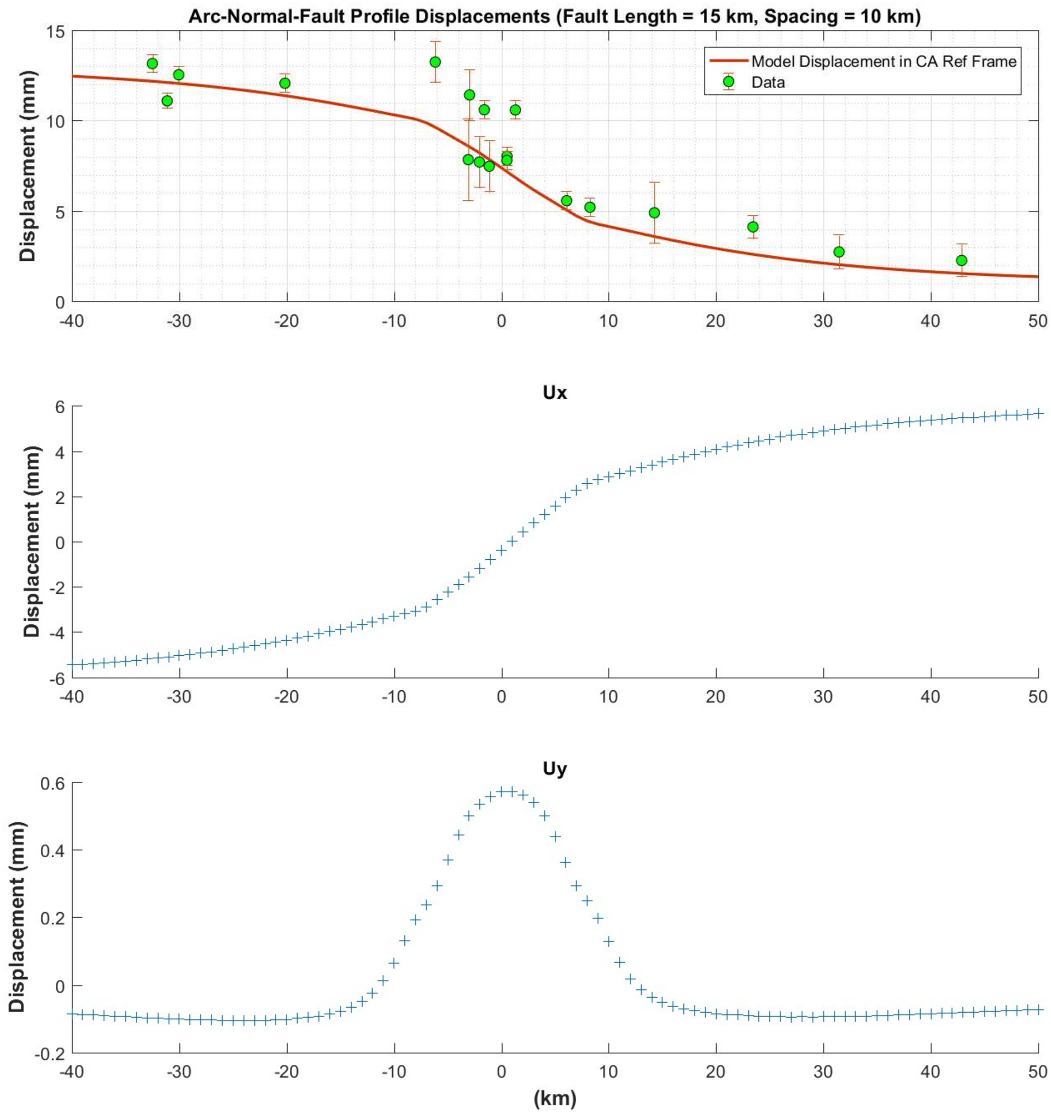

Figure **4-70**. Model A9: displacements along-profile. Arc-normal faults' length and spacing are 15 km and 10 km respectively. Top panel – profile displacements projected into horizontal line (azimuth = 270°). Middle panel – profile displacements in the x-direction. Bottom panel – profile displacements in the y-direction. 'Model Displacement in CA' data sets was created by adding an offset of 7 mm to the modeled displacement.

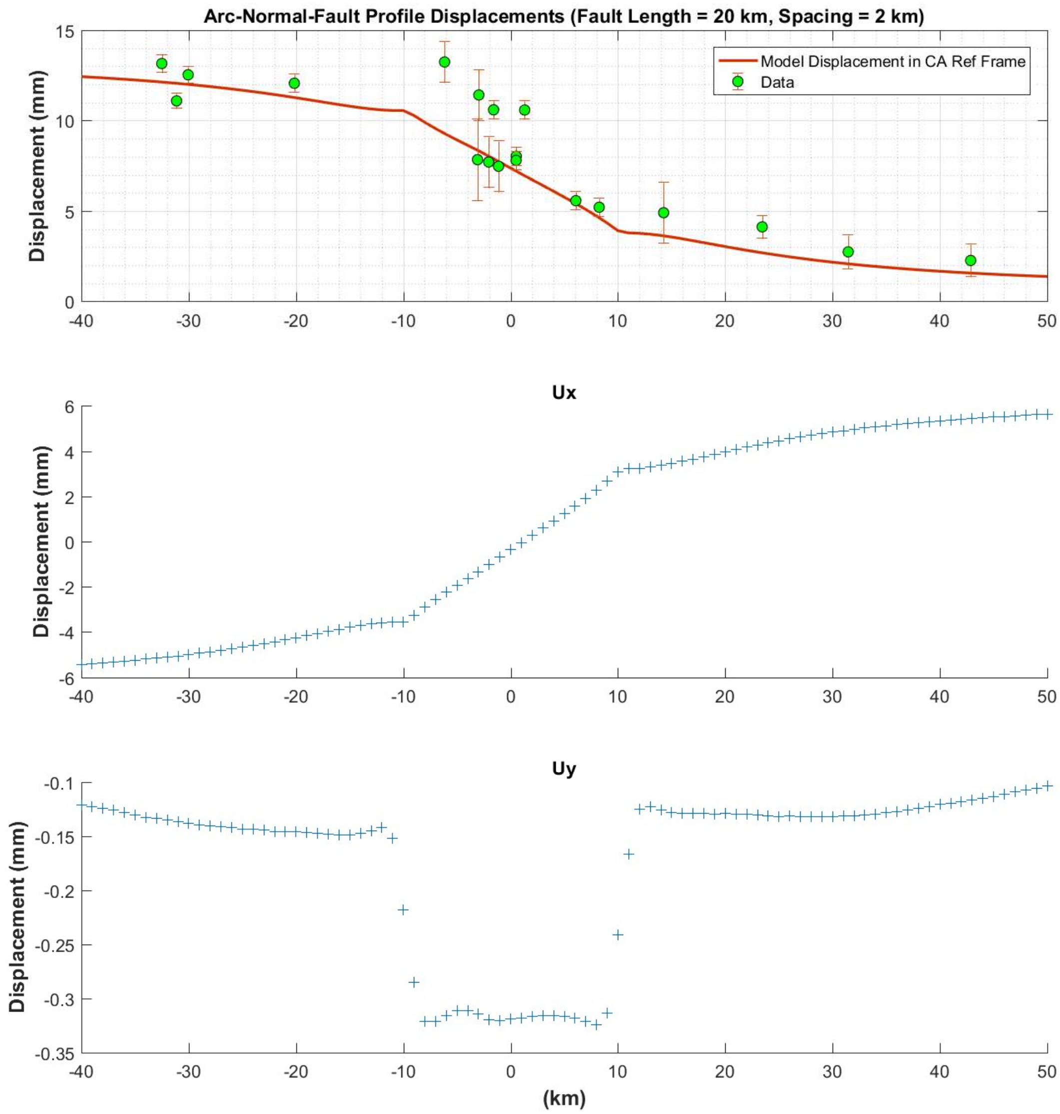

Figure **4-71**. Model A10: displacements along-profile. Arc-normal faults' length and spacing are 20 km and 2 km respectively. Top panel – profile displacements projected into horizontal line (azimuth = 270°). Middle panel – profile displacements in the x-direction. Bottom panel – profile displacements in the y-direction. 'Model Displacement in CA' data sets was created by adding an offset of 7 mm to the model displacements.

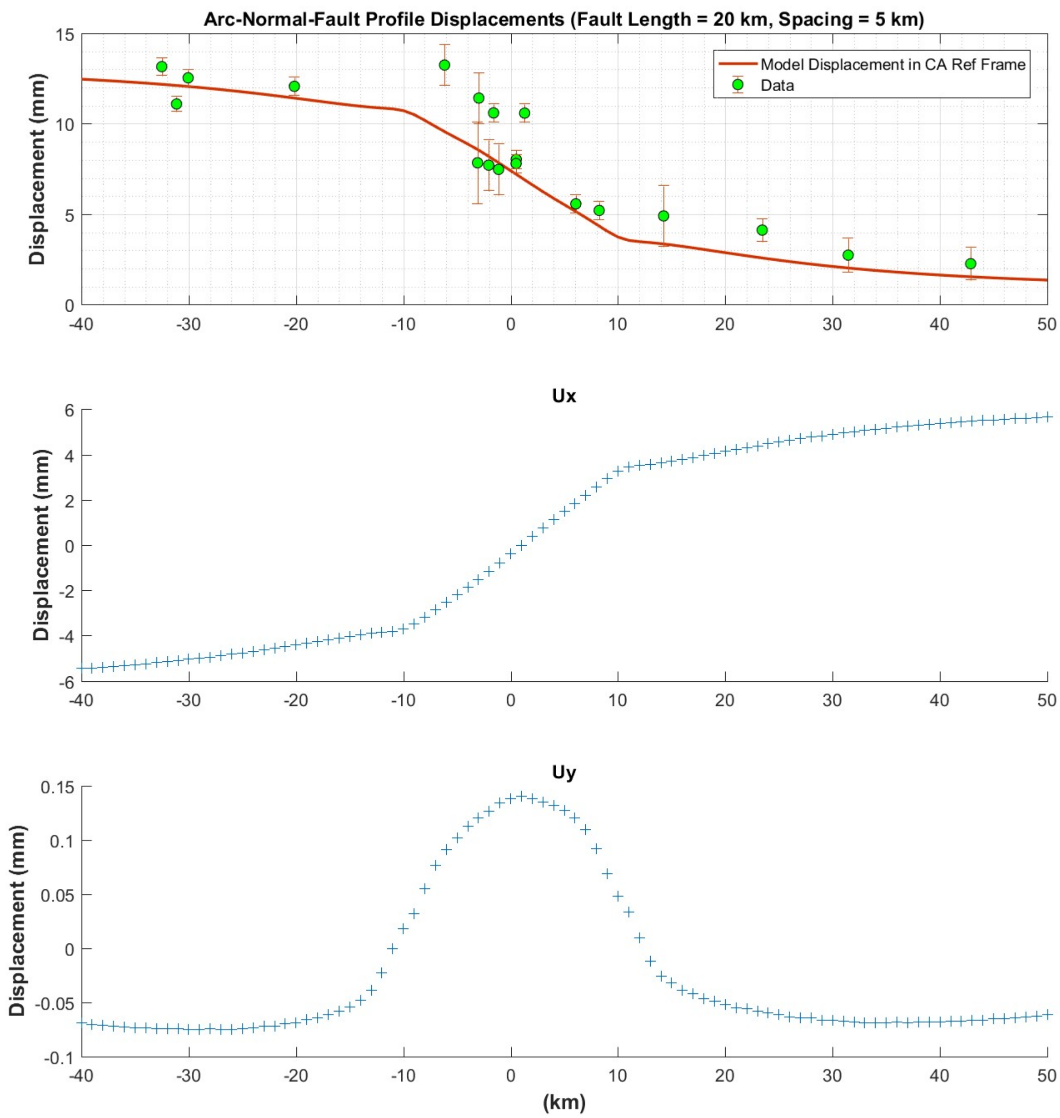

Figure **4-72**. Model A11: displacements along-profile. Arc-normal faults' length and spacing are 20 km and 5 km respectively. Top panel – profile displacements projected into horizontal line (azimuth = 270°). Middle panel – profile displacements in the x-direction. Bottom panel – profile displacements in the y-direction. 'Model Displacement in CA' data sets was created by adding an offset of 7 mm to the model displacements.

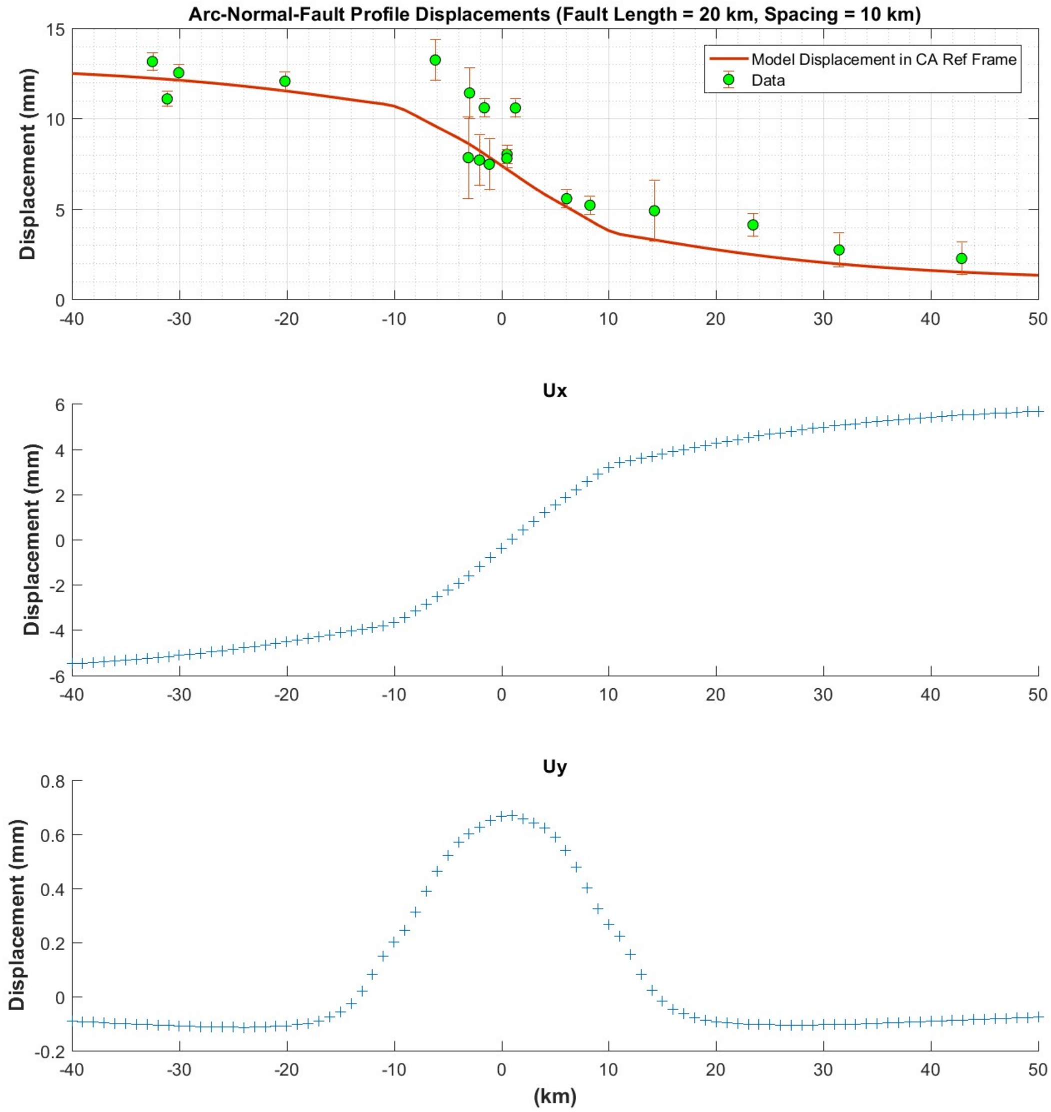

Figure **4-73**. Model A12: displacements along-profile. Arc-normal faults' length and spacing are 20 km and 10 km respectively. Top panel – profile displacements projected into horizontal line (azimuth = 270°). Middle panel – profile displacements in the x-direction. Bottom panel – profile displacements in the y-direction. 'Model Displacement in CA' data sets was created by adding an offset of 7 mm to the model displacements.

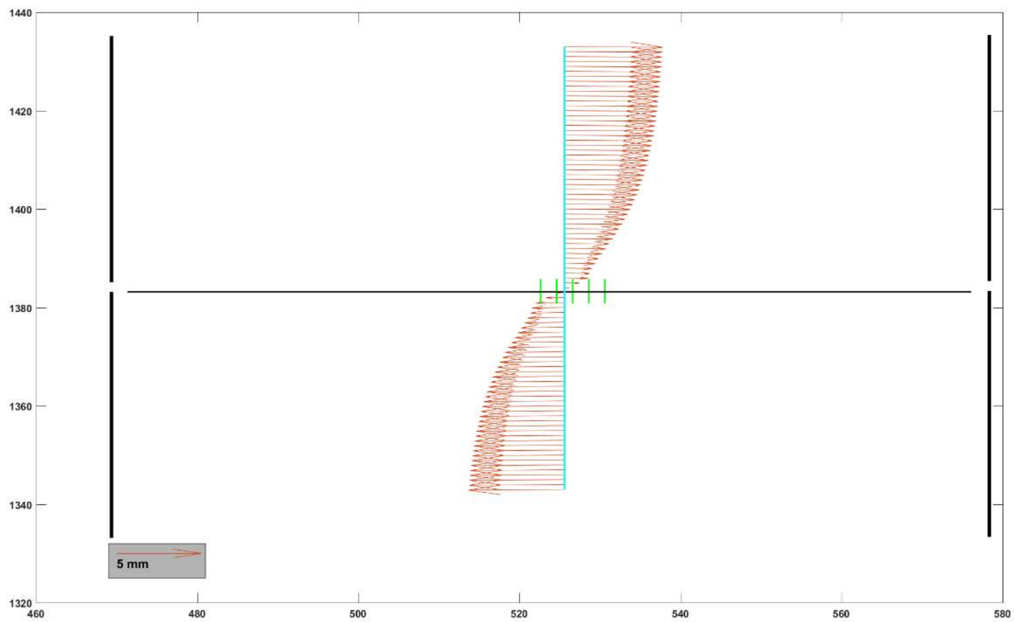

Figure **4-74**. Model B1: surface displacements (red vectors) along-profile line (cyan line). Arc-normal faults' (green lines) length and spacing are 5 km and 2 km respectively. This model has 5 arc-normal faults.

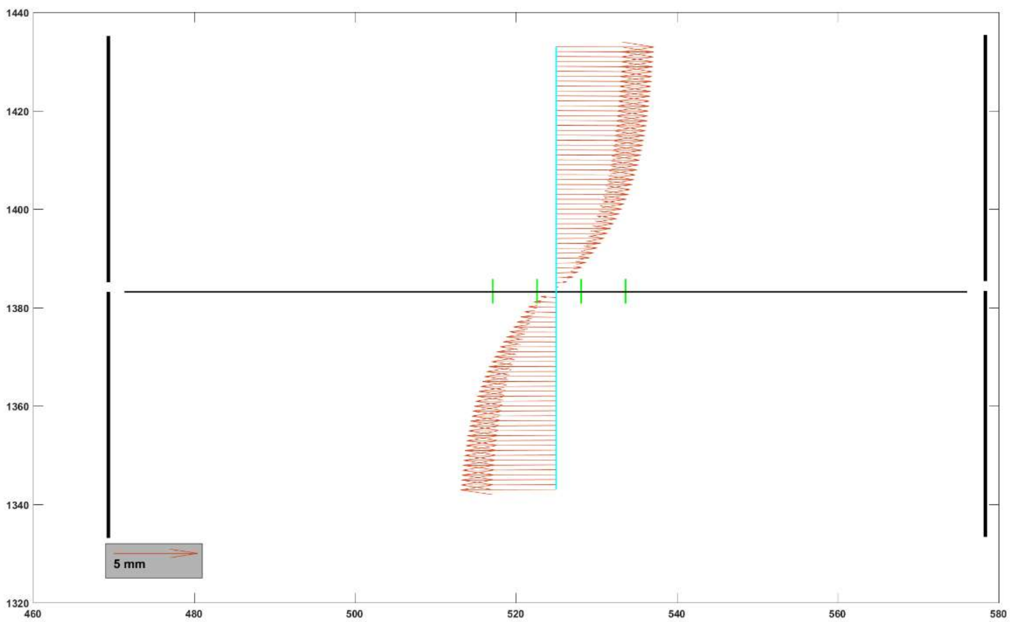

Figure **4-75**. Model B2: surface displacements (red vectors) along-profile line (cyan line). Arc-normal faults' (green lines) length and spacing are 5 km and 5 km respectively. This model has 4 arc-normal faults.

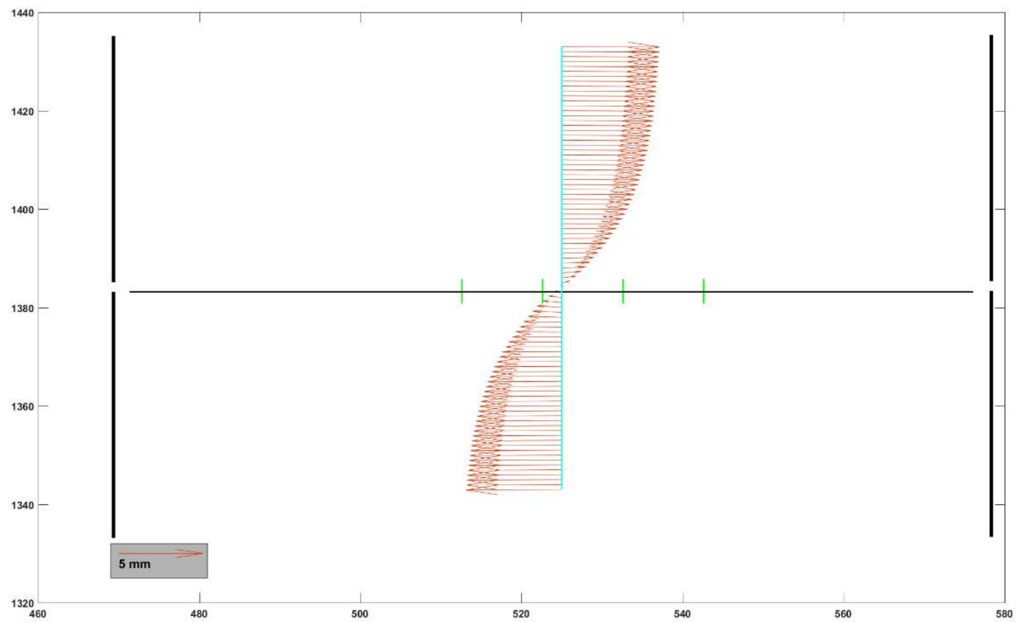

Figure **4-76**. Model B3: surface displacements (red vectors) along-profile line (cyan line). Arc-normal faults' (green lines) length and spacing are 5 km and 10 km respectively. This model has 4 arc-normal faults.

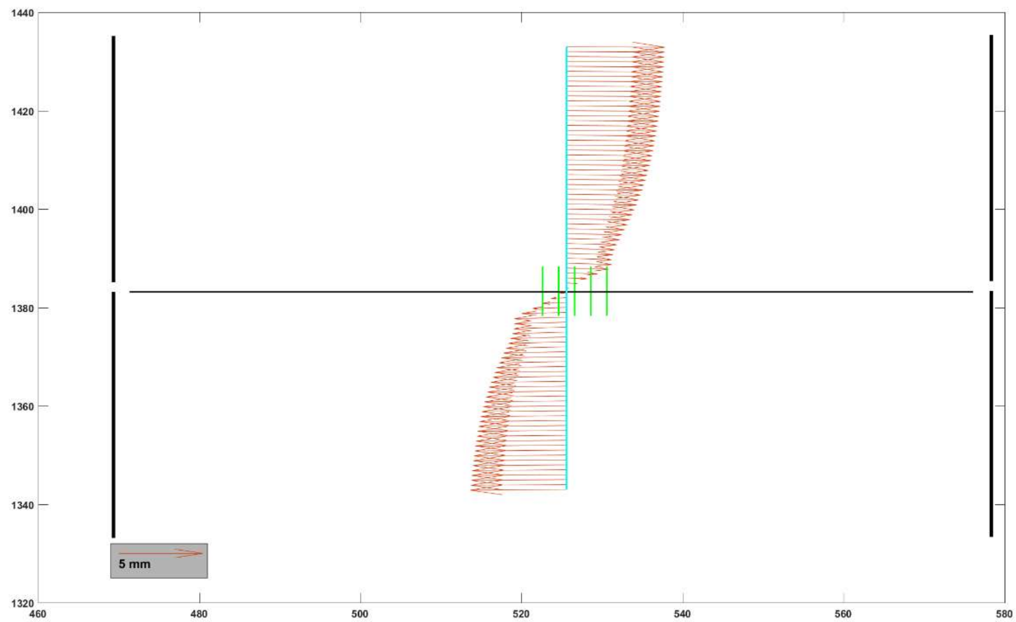

Figure **4-77**. Model B4: surface displacements (red vectors) along-profile line (cyan line). Arc-normal faults' (green lines) length and spacing are 10 km and 2 km respectively. This model has 5 arc-normal faults.

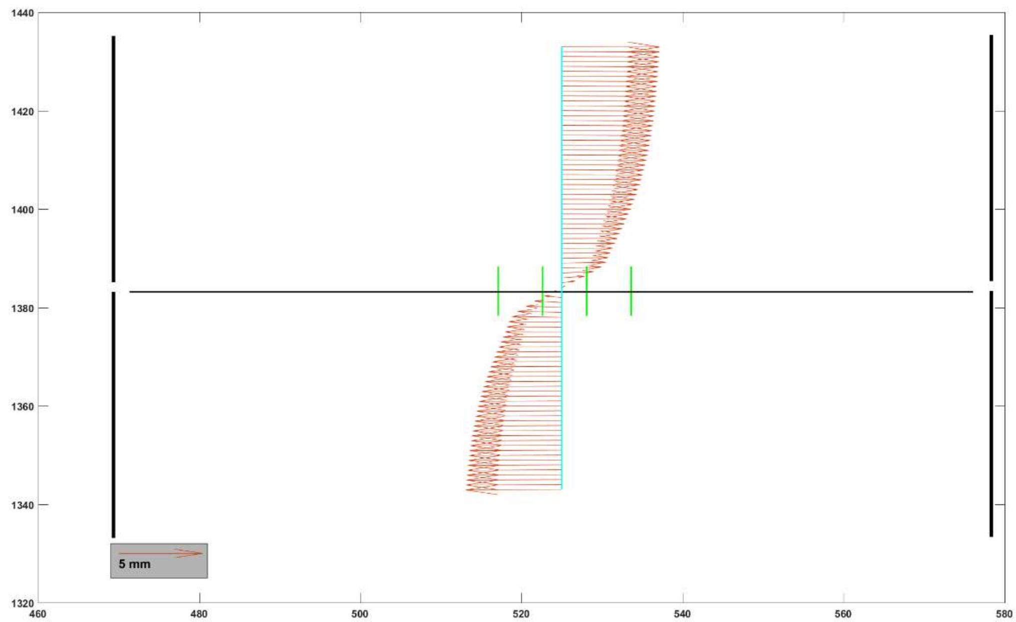

Figure **4-78**. Model B5: surface displacements (red vectors) along-profile line (cyan line). Arc-normal faults' (green lines) length and spacing are 10 km and 5 km respectively. This model has 4 arc-normal faults.

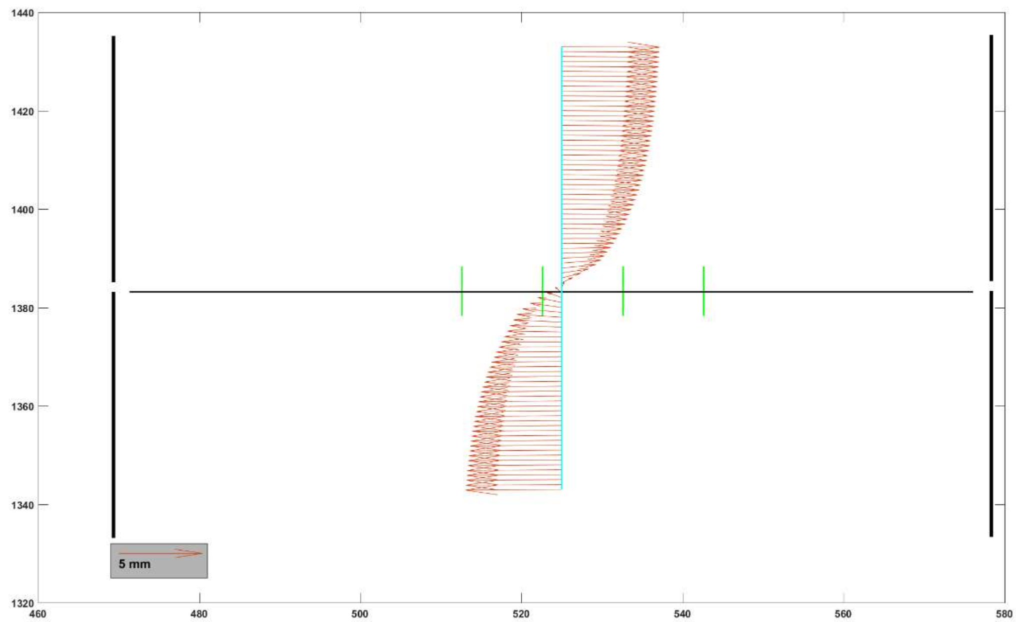

Figure **4-79**. Model B6: surface displacements (red vectors) along-profile line (cyan line). Arc-normal faults' (green lines) length and spacing are 10 km and 10 km respectively. This model has 4 arc-normal faults.

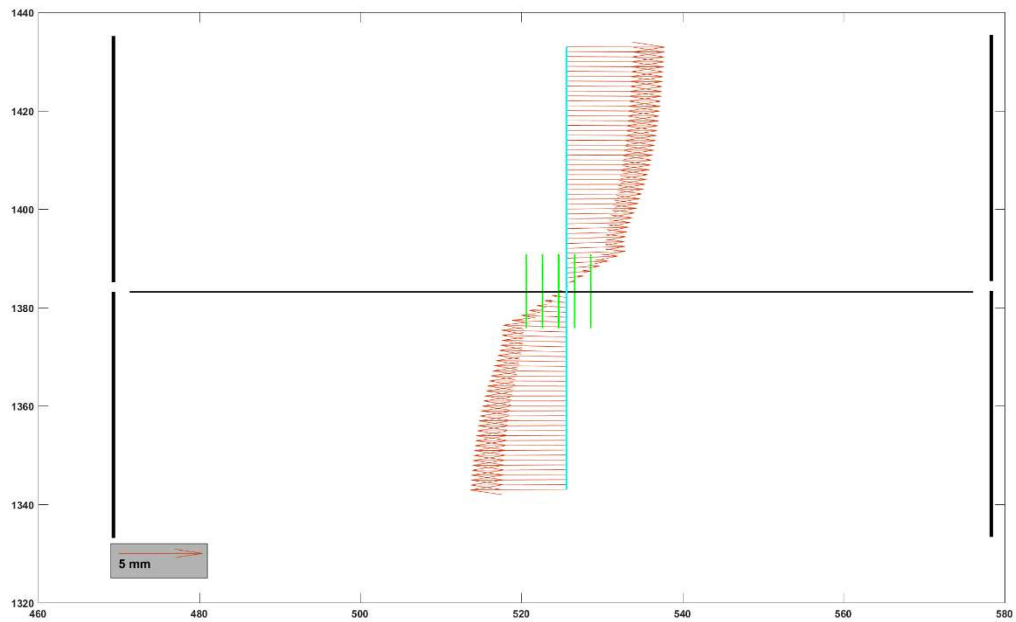

Figure **4-80**. Model B7: surface displacements (red vectors) along-profile line (cyan line). Arc-normal faults' (green lines) length and spacing are 15 km and 2 km respectively. This model has 4 arc-normal faults.

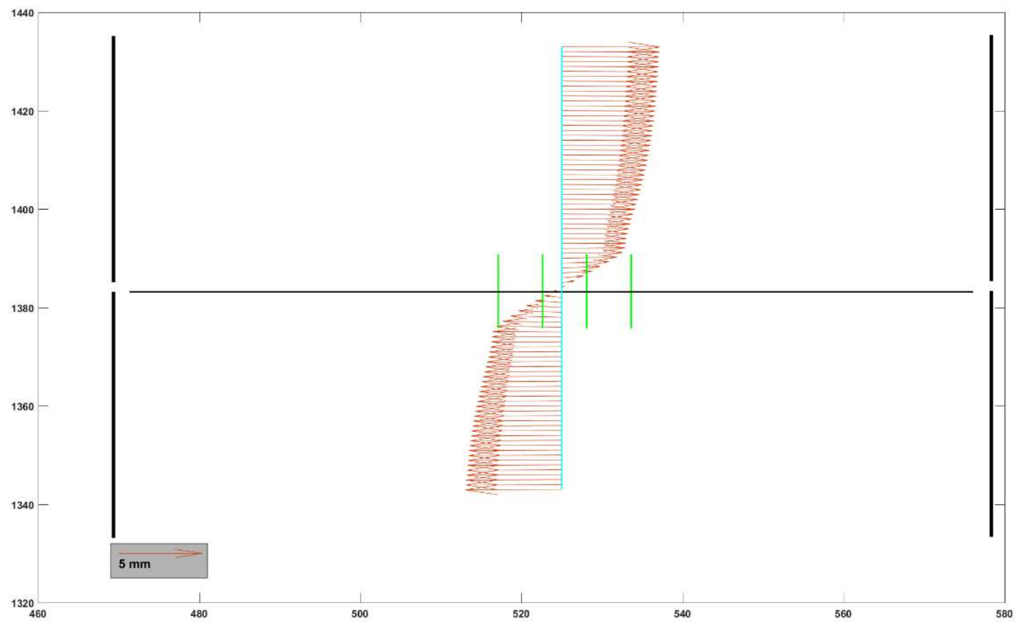

Figure **4-81**. Model B8: surface displacements (red vectors) along-profile line (cyan line). Arc-normal faults' (green lines) length and spacing are 15 km and 5 km respectively. This model has 4 arc-normal faults.

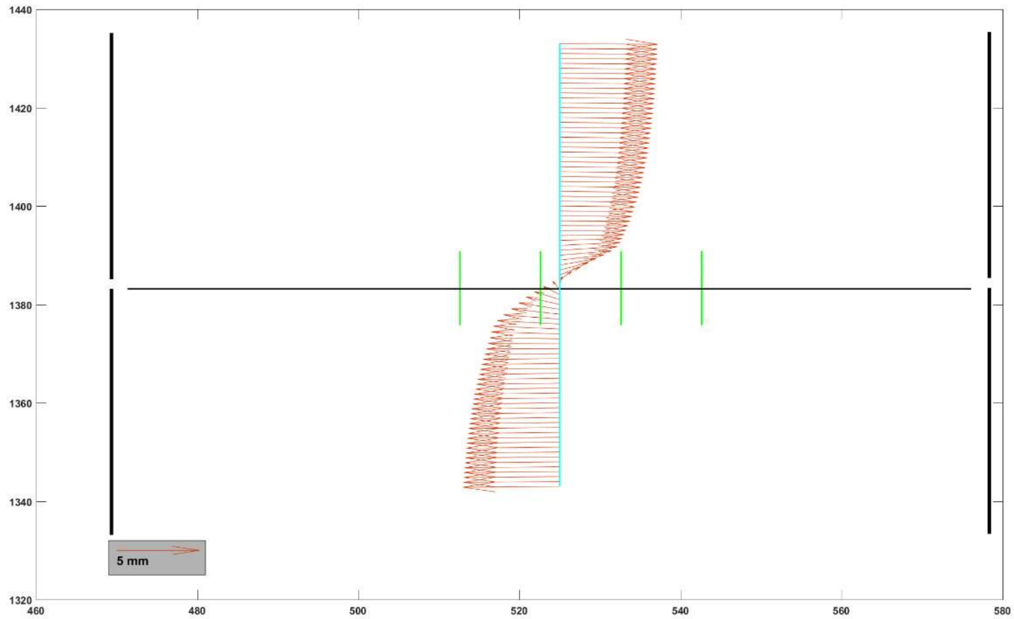

Figure **4-82:** Model B9: surface displacements (red vectors) along-profile line (cyan line). Arc-normal faults' (green lines) length and spacing are 15 km and 10 km respectively. This model has 4 arc-normal faults.

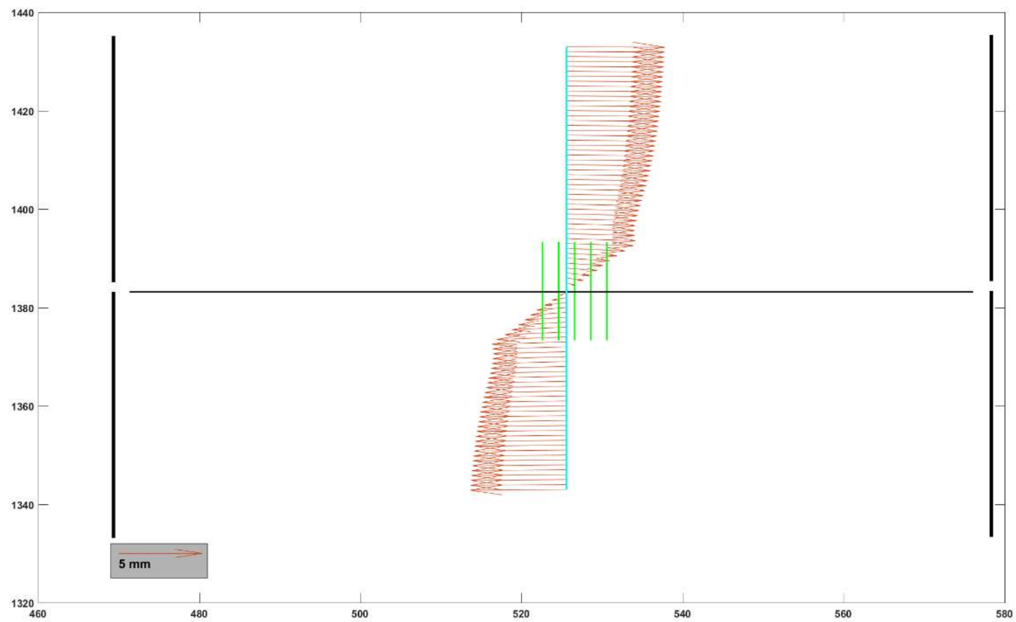

Figure **4-83:** Model B10: surface displacements (red vectors) along-profile line (cyan line). Arc-normal faults' (green lines) length and spacing are 20 km and 2 km respectively. This model has 5 arc-normal faults.

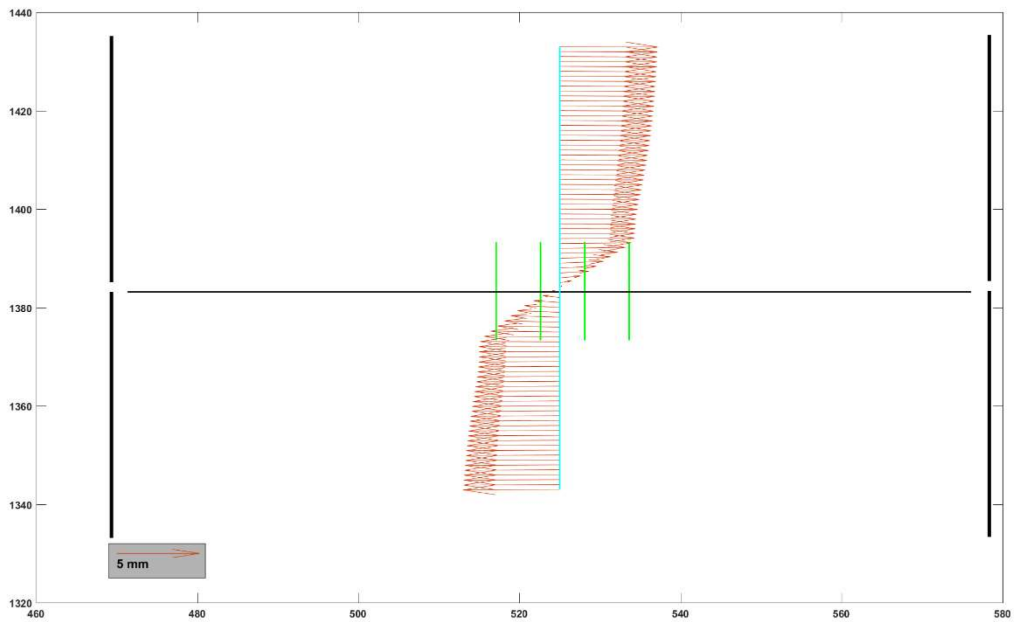

Figure **4-84**. Model B11: surface displacements (red vectors) along-profile line (cyan line). Arc-normal faults' (green lines) length and spacing are 20 km and 5 km respectively. This model has 4 arc-normal faults.

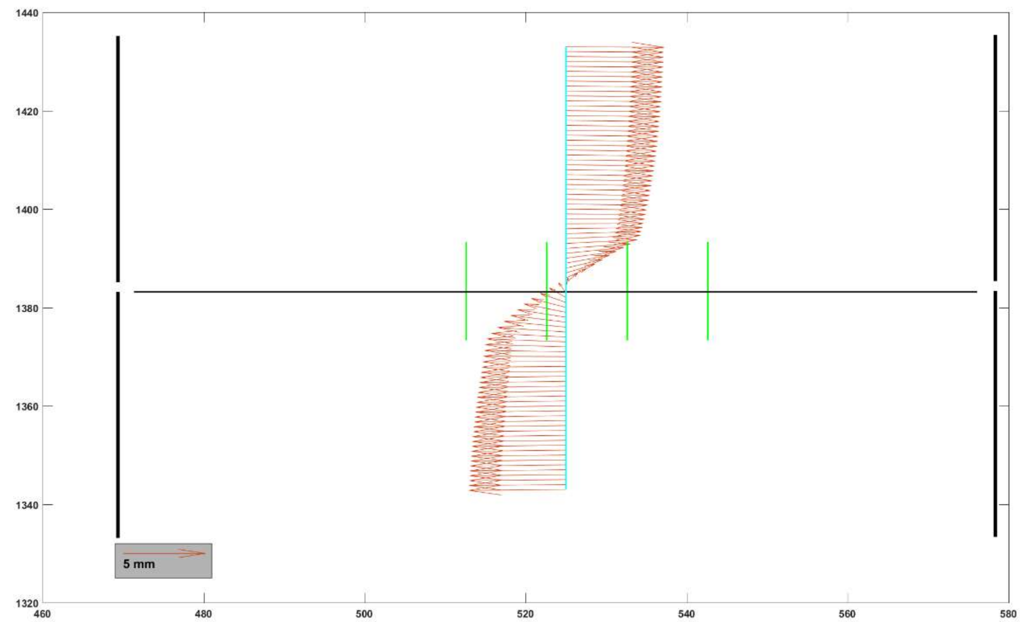

Figure **4-85**. Model B12: surface displacements (red vectors) along-profile line (cyan line). Arc-normal faults' (green lines) length and spacing are 20 km and 10 km respectively. This model has 4 arc-normal faults.

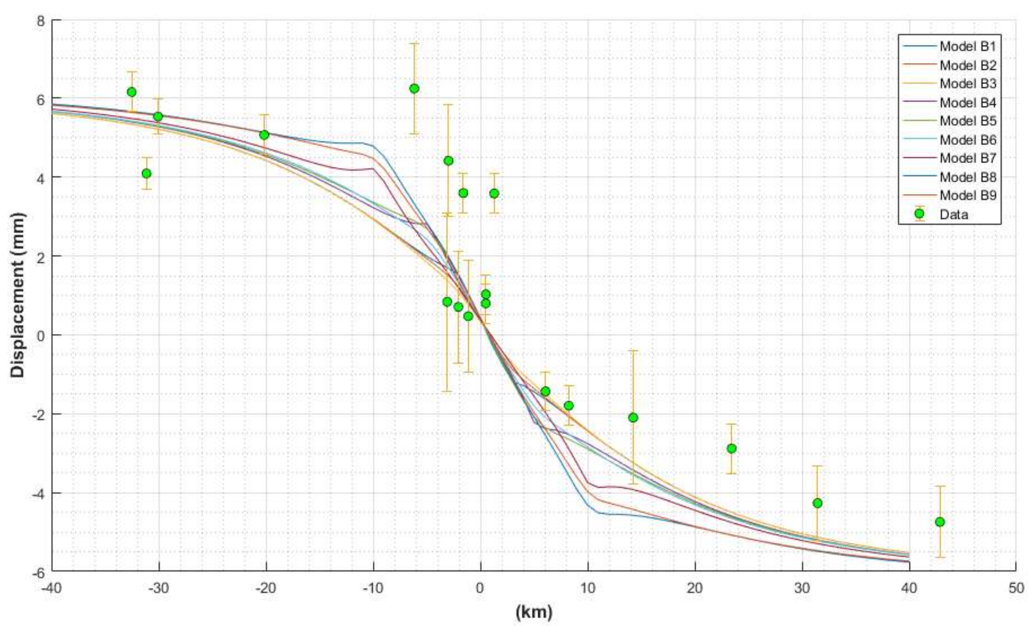

Figure **4-86**. All BEM model B set surface profiles (cyan line in Figures **4-74** to **4-85**).

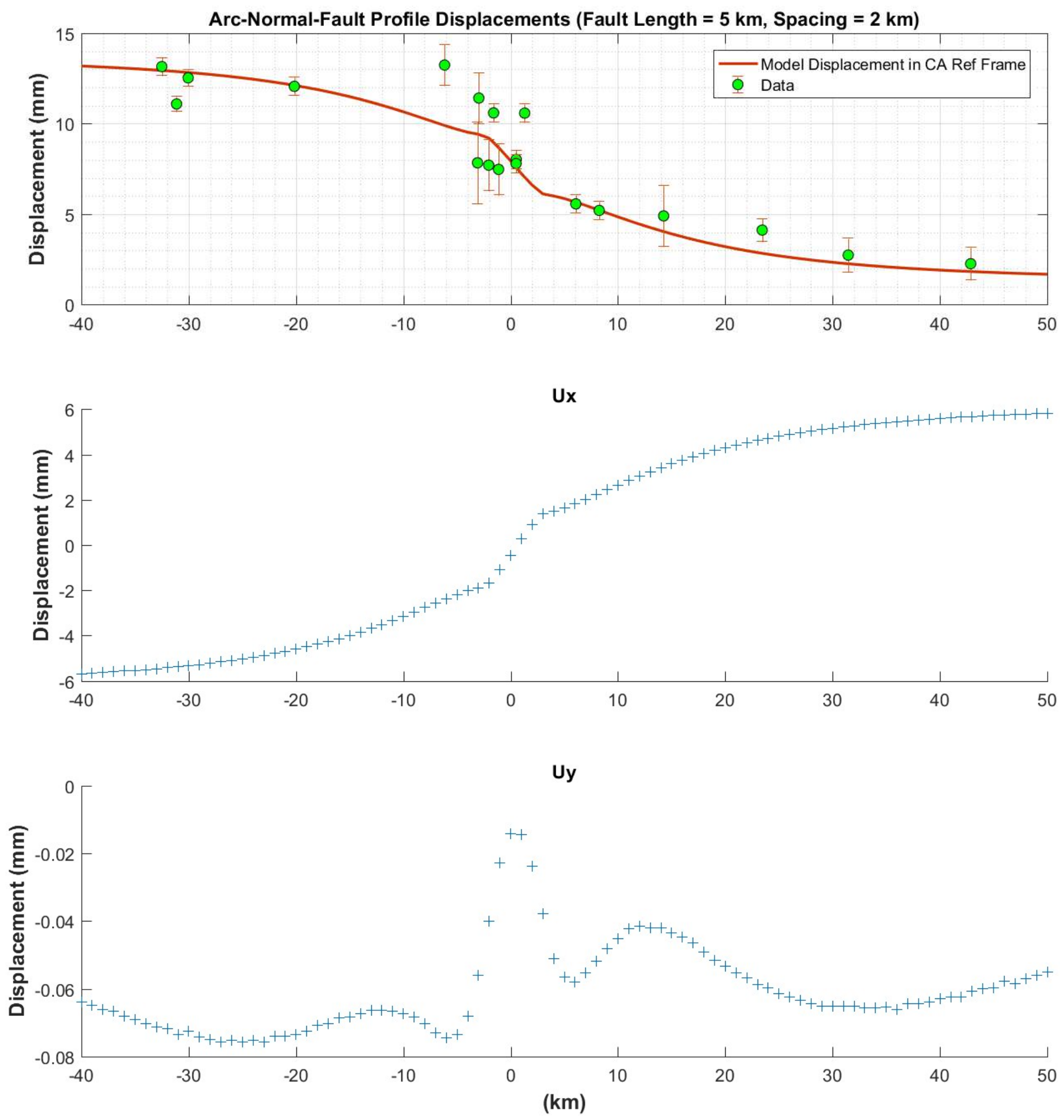

Figure **4-87:** Model B1: displacements along-profile. Arc-normal faults' length and spacing are 5 km and 2 km respectively. Top panel – profile displacements projected into horizontal line (azimuth = 270°). Middle panel – profile displacements in the x-direction. Bottom panel – profile displacements in the y-direction. 'Model Displacement in CA' data sets was created by adding an offset of 7 mm to the model displacements.

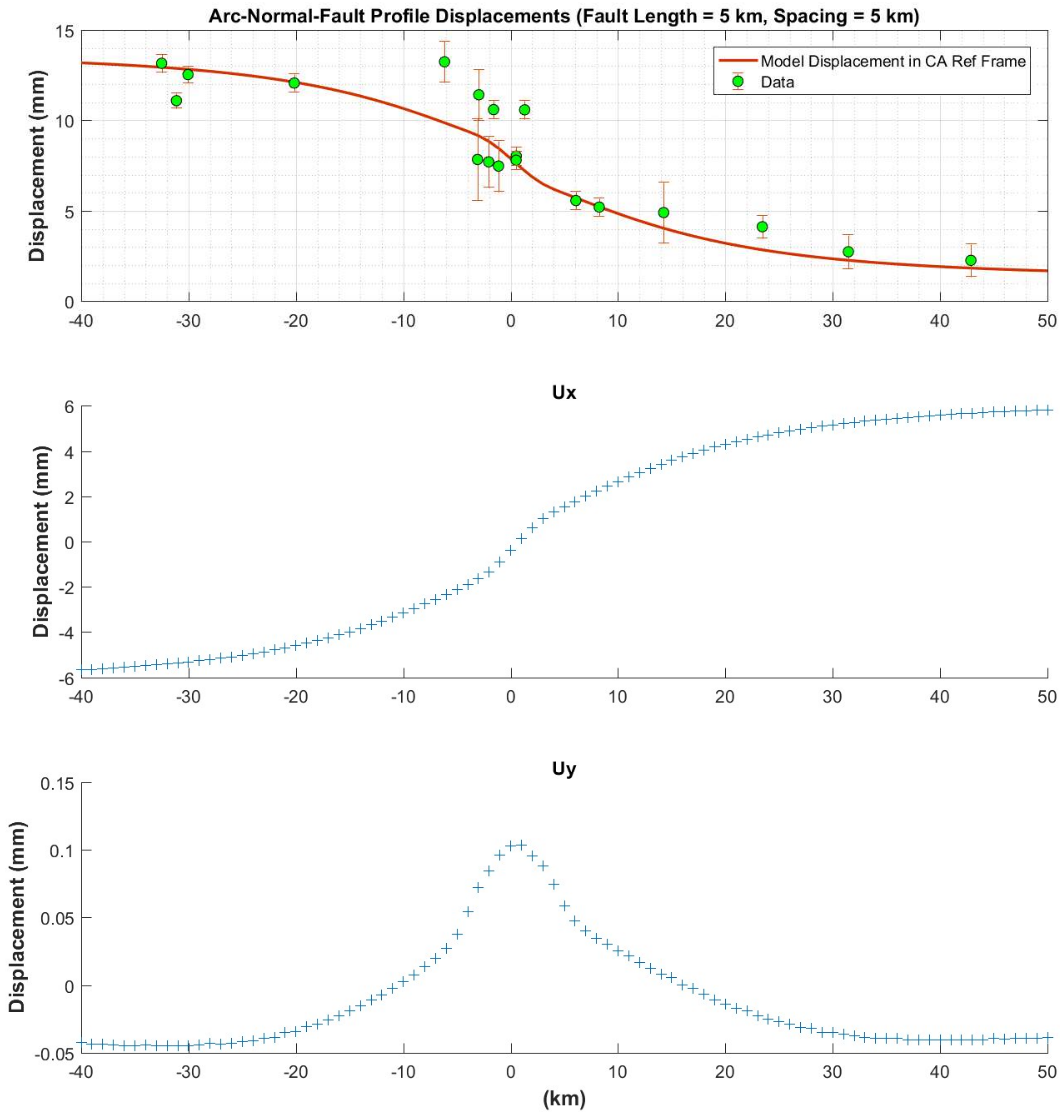

Figure **4-88:** Model B2: displacements along-profile. Arc-normal faults' length and spacing are 5 km and 5 km respectively. Top panel – profile displacements projected into horizontal line (azimuth = 270°). Middle panel – profile displacements in the x-direction. Bottom panel – profile displacements in the y-direction. 'Model Displacement in CA' data sets was created by adding an offset of 7 mm to the model displacements.

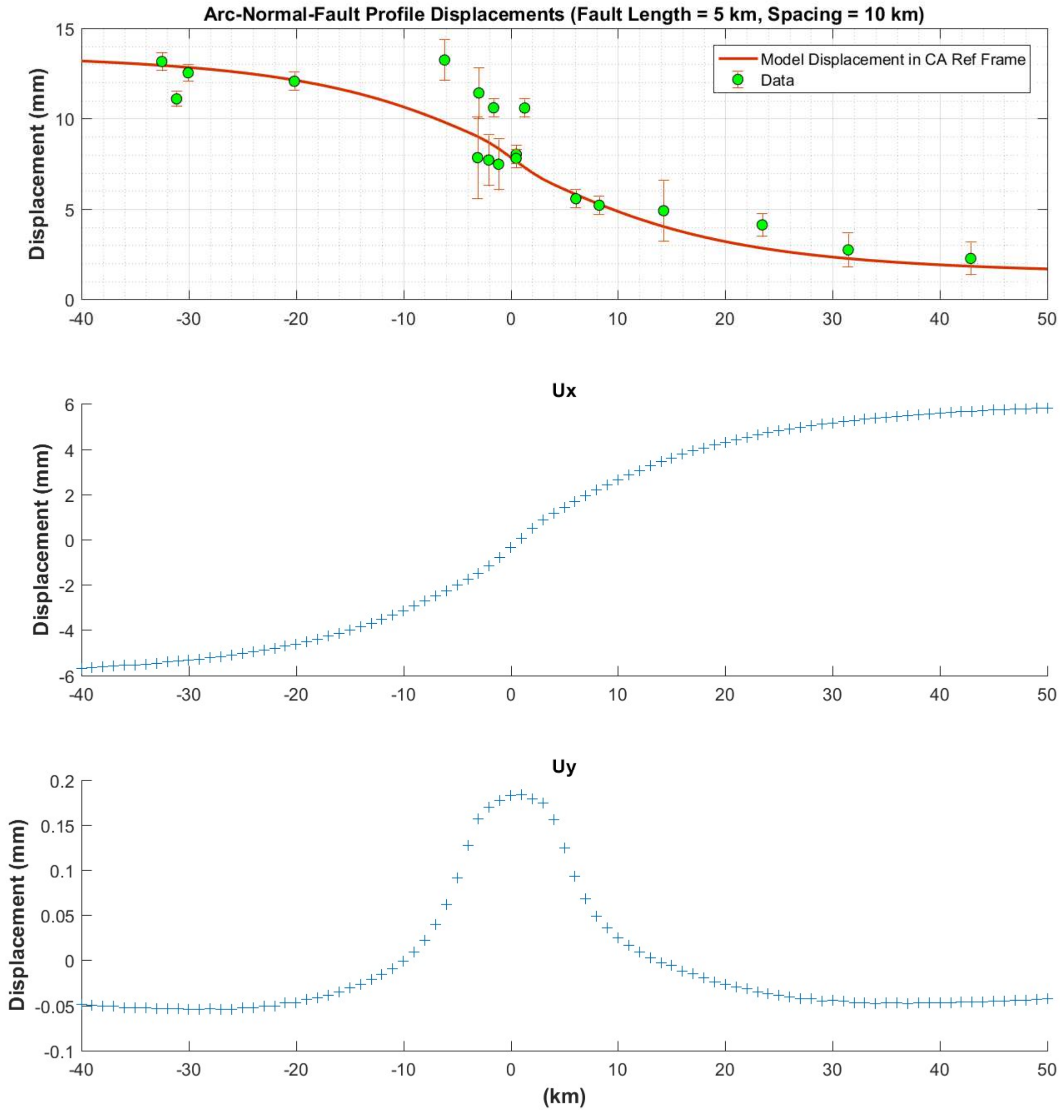

Figure **4-89:** Model B3: displacements along-profile. Arc-normal faults' length and spacing are 5 km and 10 km respectively. Top panel – profile displacements projected into horizontal line (azimuth = 270°). Middle panel – profile displacements in the x-direction. Bottom panel – profile displacements in the y-direction. 'Model Displacement in CA' data sets was created by adding an offset of 7 mm to the model displacements.

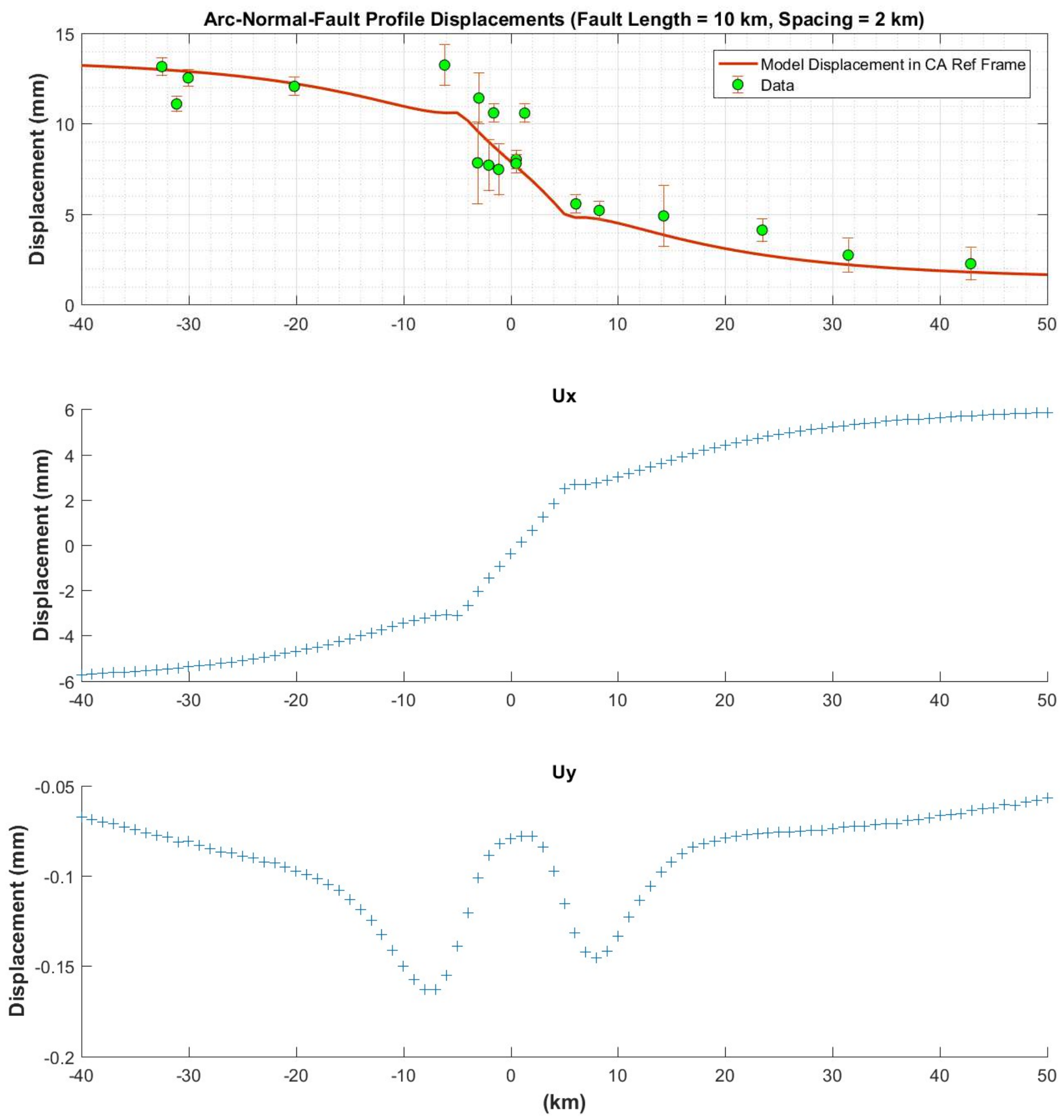

Figure **4-90:** Model B4: displacements along-profile. Arc-normal faults' length and spacing are 10 km and 2 km respectively. Top panel – profile displacements projected into horizontal line (azimuth = 270°). Middle panel – profile displacements in the x-direction. Bottom panel – profile displacements in the y-direction. 'Model Displacement in CA' data sets was created by adding an offset of 7 mm to the model displacements.

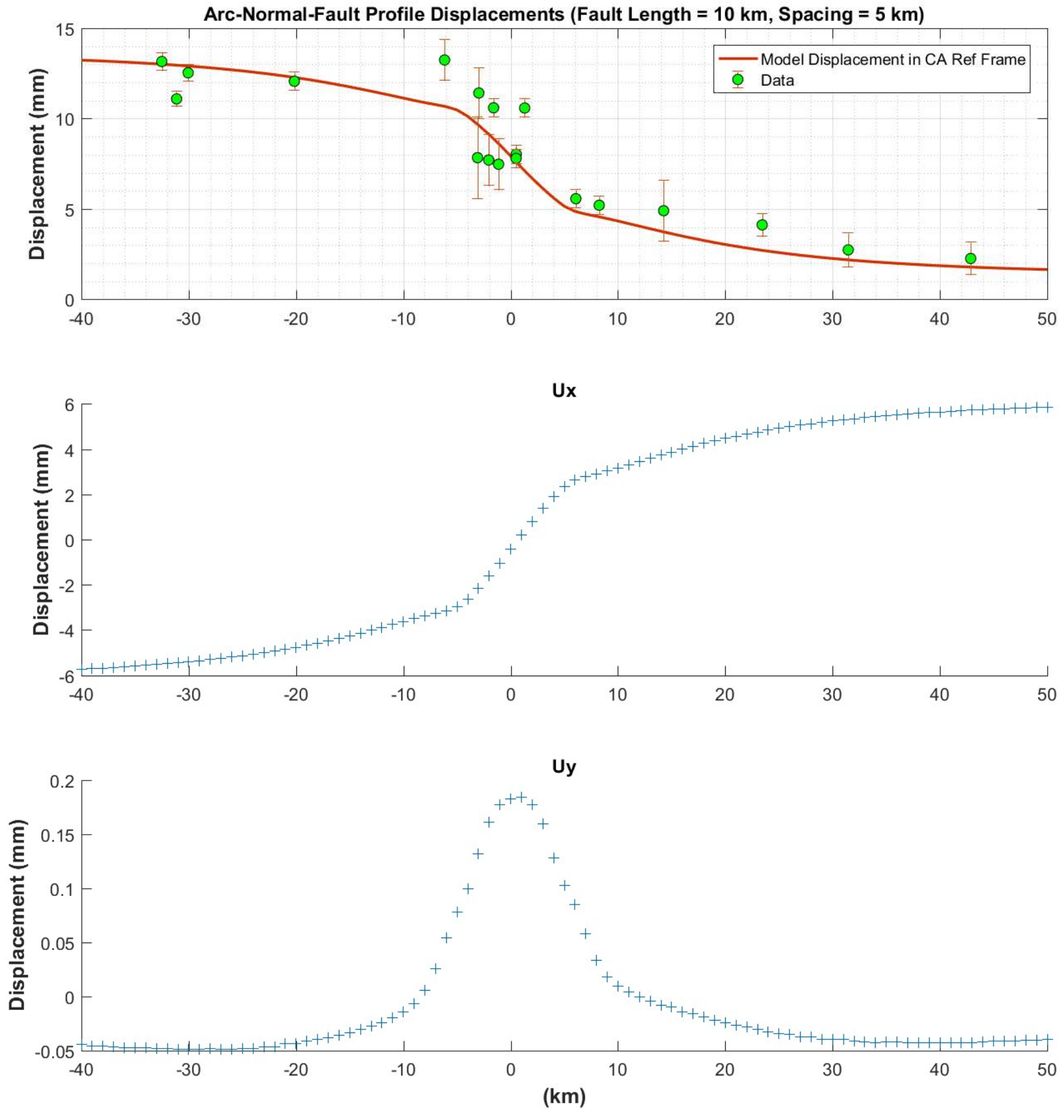

Figure **4-91:** Model B5: displacements along-profile. Arc-normal faults' length and spacing are 10 km and 5 km respectively. Top panel – profile displacements projected into horizontal line (azimuth = 270°). Middle panel – profile displacements in the x-direction. Bottom panel – profile displacements in the y-direction. 'Model Displacement in CA' data sets was created by adding an offset of 7 mm to the model displacements.

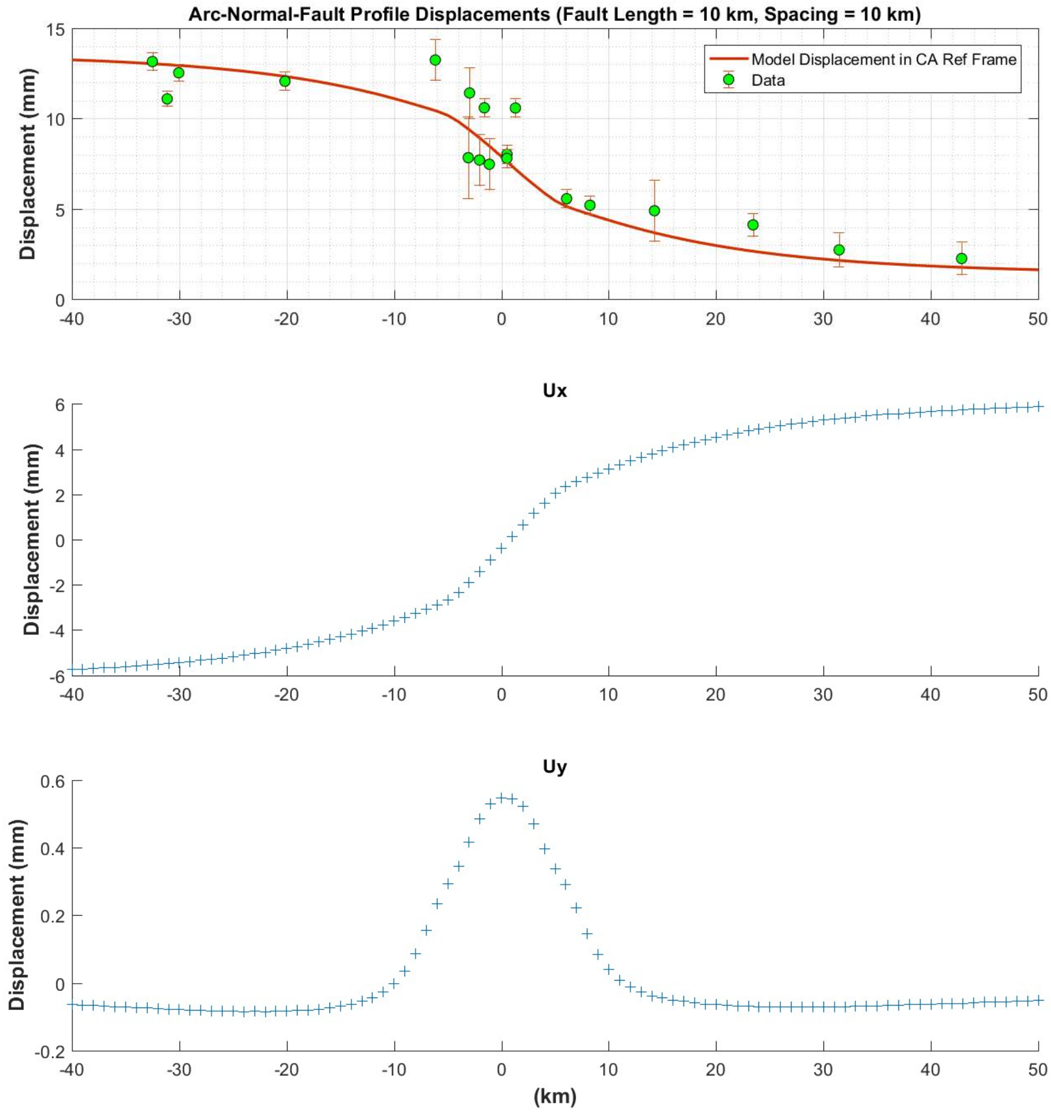

Figure **4-92:** Model B6: displacements along-profile. Arc-normal faults' length and spacing are 10 km and 10 km respectively. Top panel – profile displacements projected into horizontal line (azimuth = 270°). Middle panel – profile displacements in the x-direction. Bottom panel – profile displacements in the y-direction. 'Model Displacement in CA' data sets was created by adding an offset of 7 mm to the model displacements.

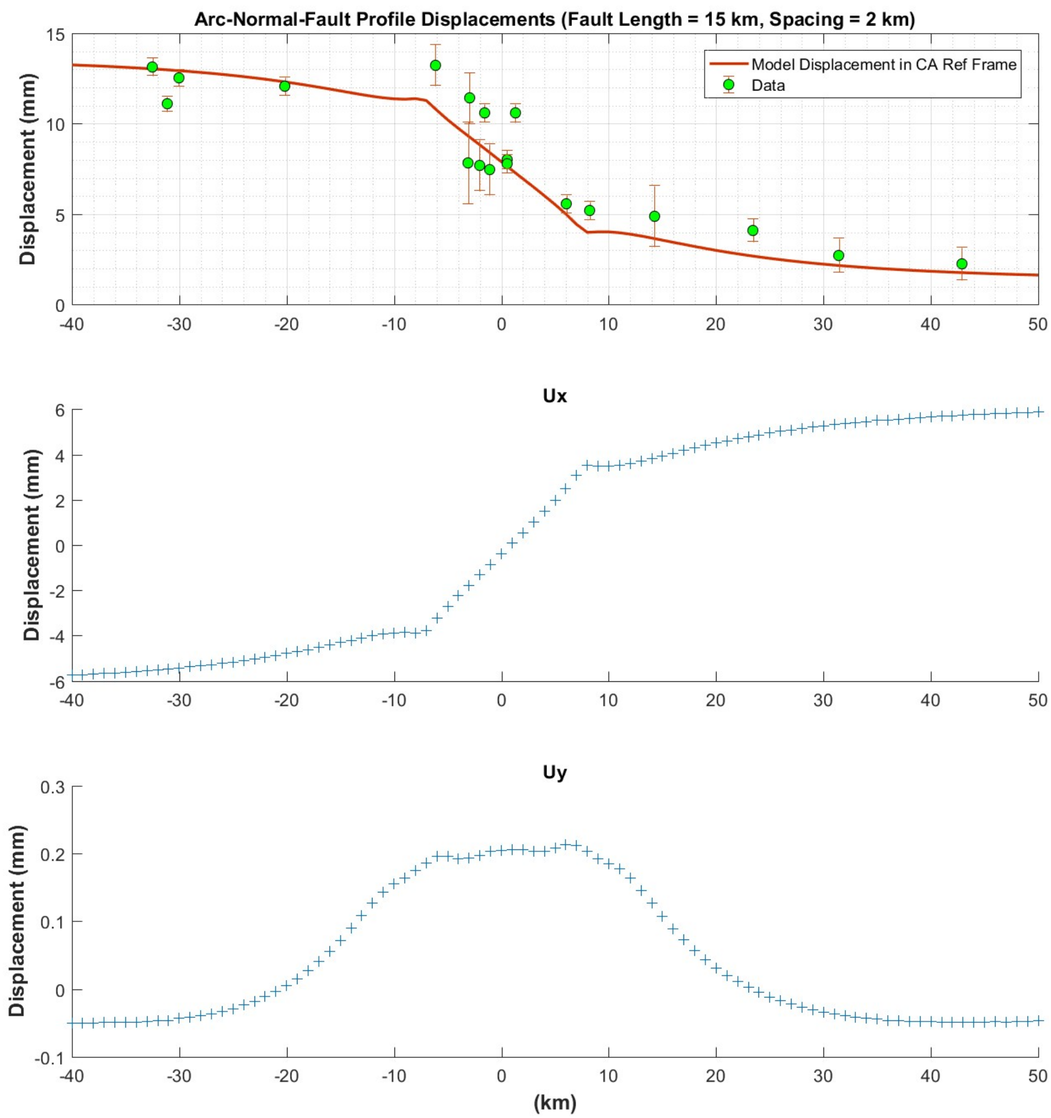

Figure **4-93:** Model B7: displacements along-profile. Arc-normal faults' length and spacing are 15 km and 2 km respectively. Top panel – profile displacements projected into horizontal line (azimuth = 270°). Middle panel – profile displacements in the x-direction. Bottom panel – profile displacements in the y-direction. 'Model Displacement in CA' data sets was created by adding an offset of 7 mm to the model displacements.

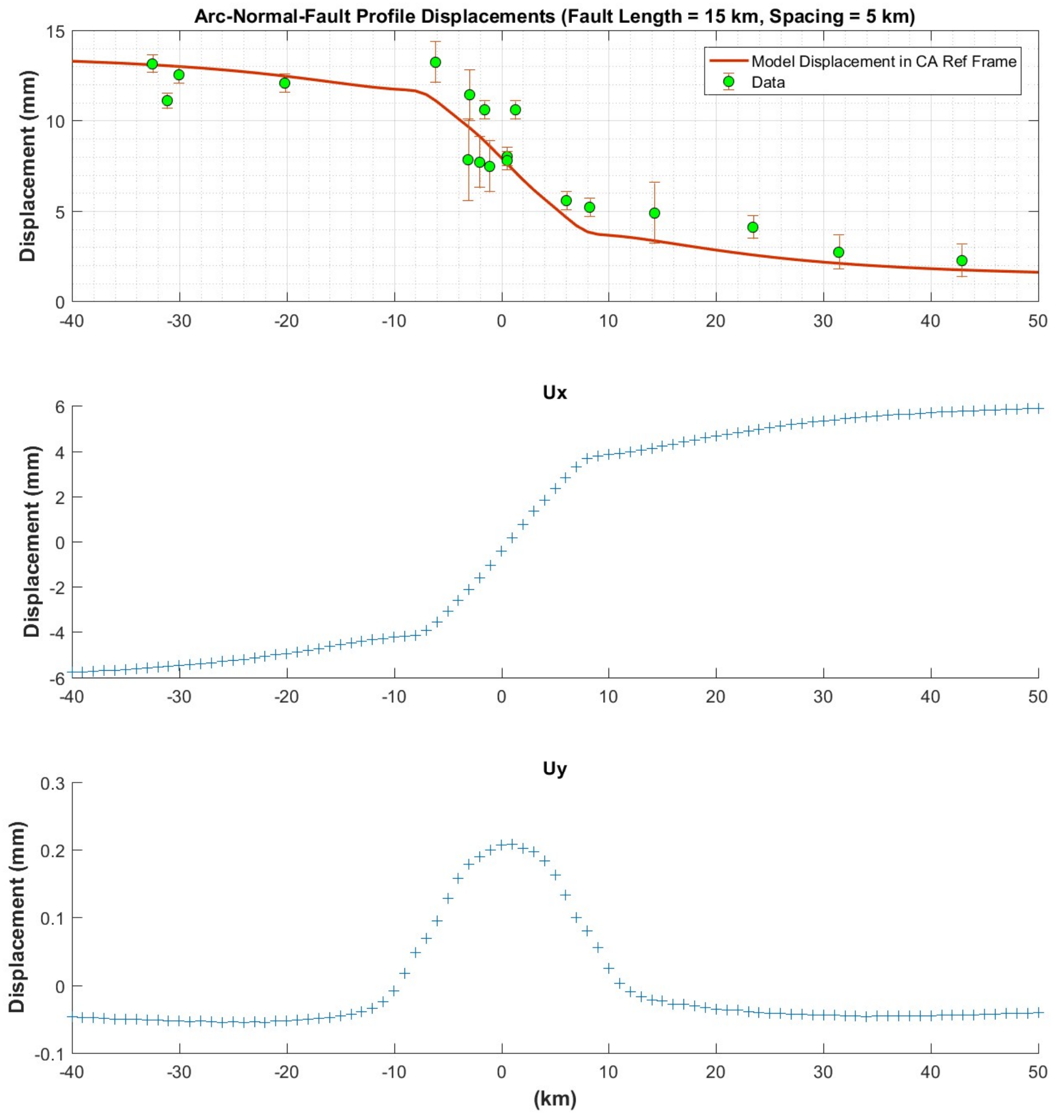

Figure **4-94:** Model B8: displacements along-profile. Arc-normal faults' length and spacing are 15 km and 5 km respectively. Top panel – profile displacements projected into horizontal line (azimuth = 270°). Middle panel – profile displacements in the x-direction. Bottom panel – profile displacements in the y-direction. 'Model Displacement in CA' data sets was created by adding an offset of 7 mm to the model displacements.

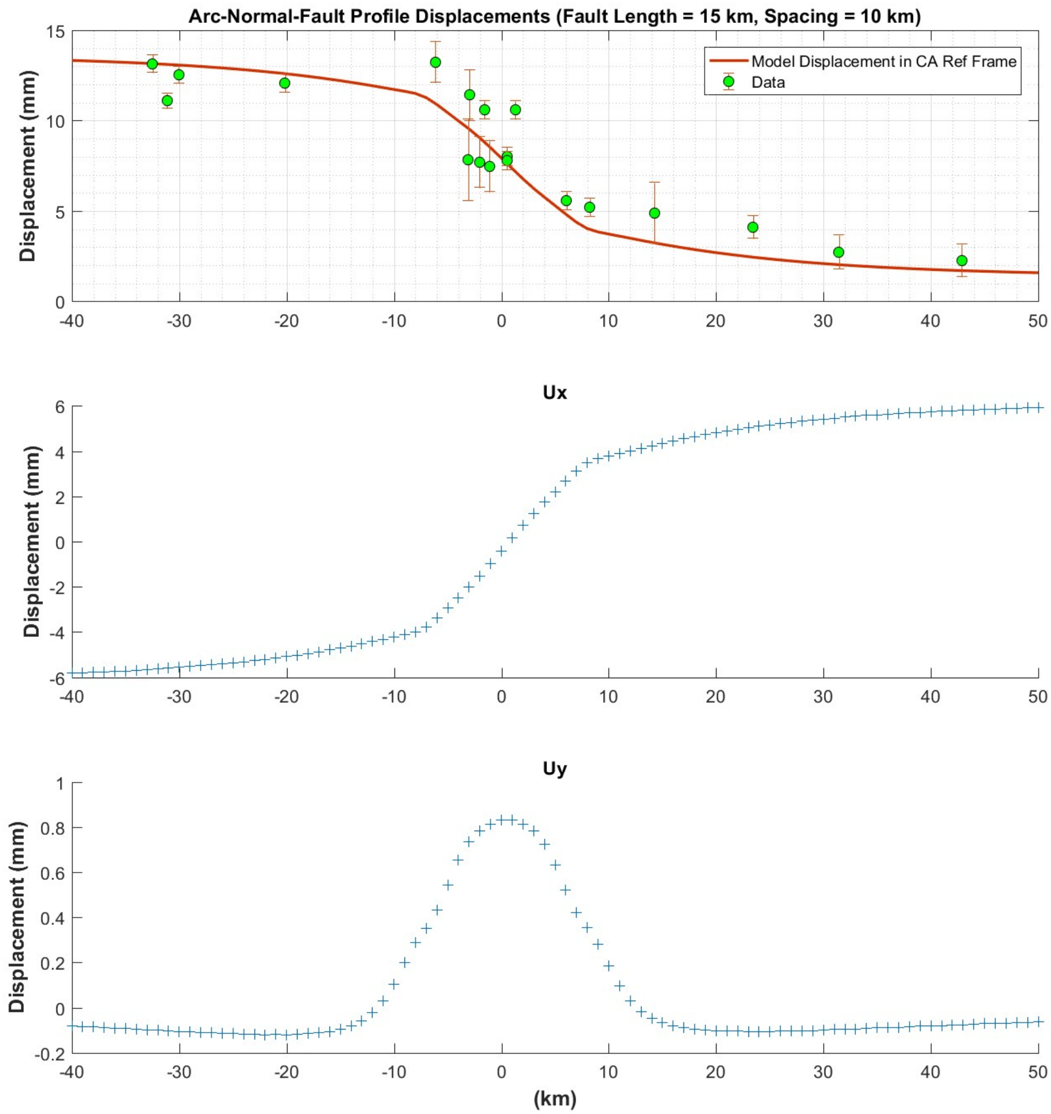

Figure **4-95:** Model B9: displacements along-profile. Arc-normal faults' length and spacing are 15 km and 10 km respectively. Top panel – profile displacements projected into horizontal line (azimuth = 270°). Middle panel – profile displacements in the x-direction. Bottom panel – profile displacements in the y-direction. 'Model Displacement in CA' data sets was created by adding an offset of 7 mm to the model displacements.

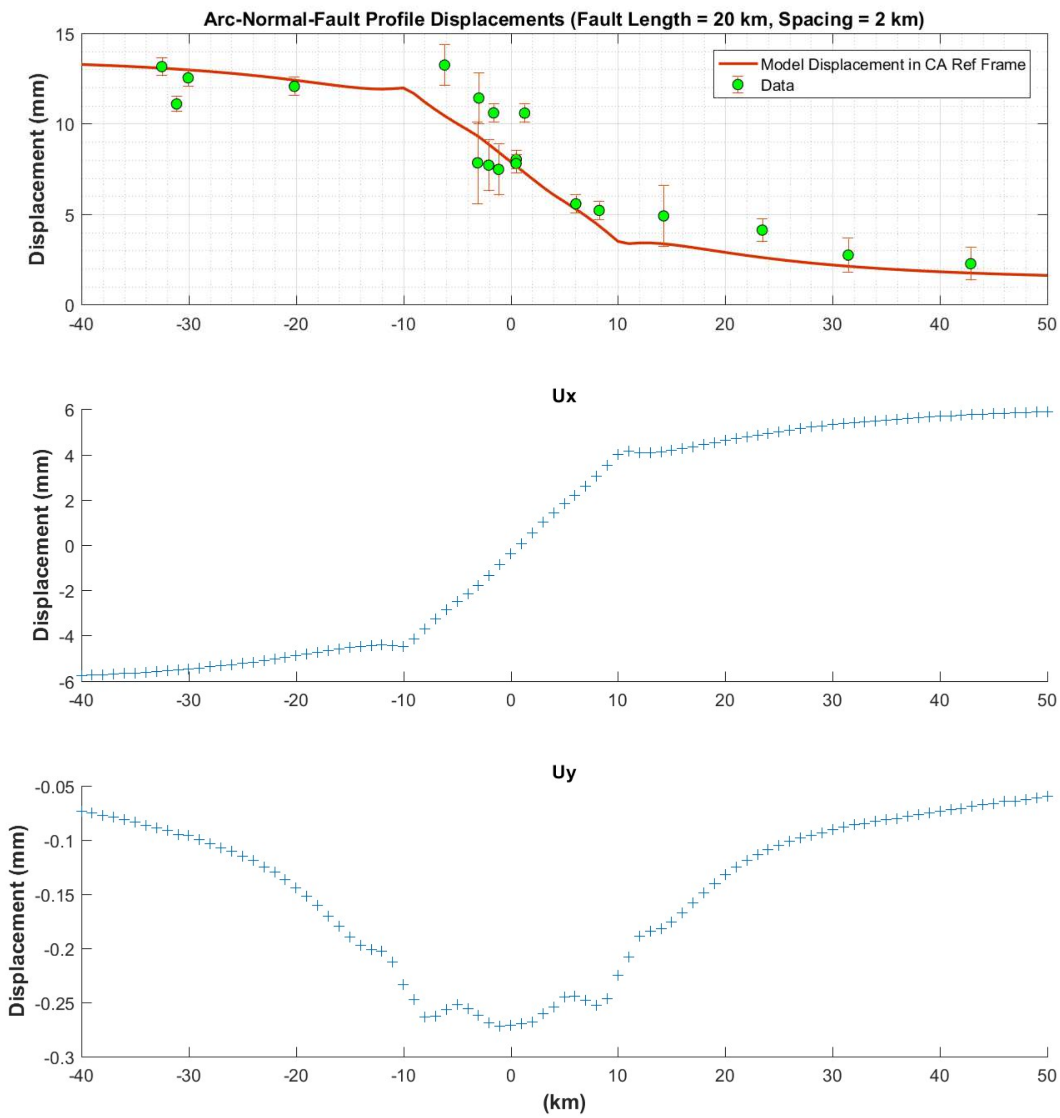

Figure **4-96:** Model B10: displacements along-profile. Arc-normal faults' length and spacing are 20 km and 2 km respectively. Top panel – profile displacements projected into horizontal line (azimuth = 270°). Middle panel – profile displacements in the x-direction. Bottom panel – profile displacements in the y-direction. 'Model Displacement in CA' data sets was created by adding an offset of 7 mm to the model displacements.

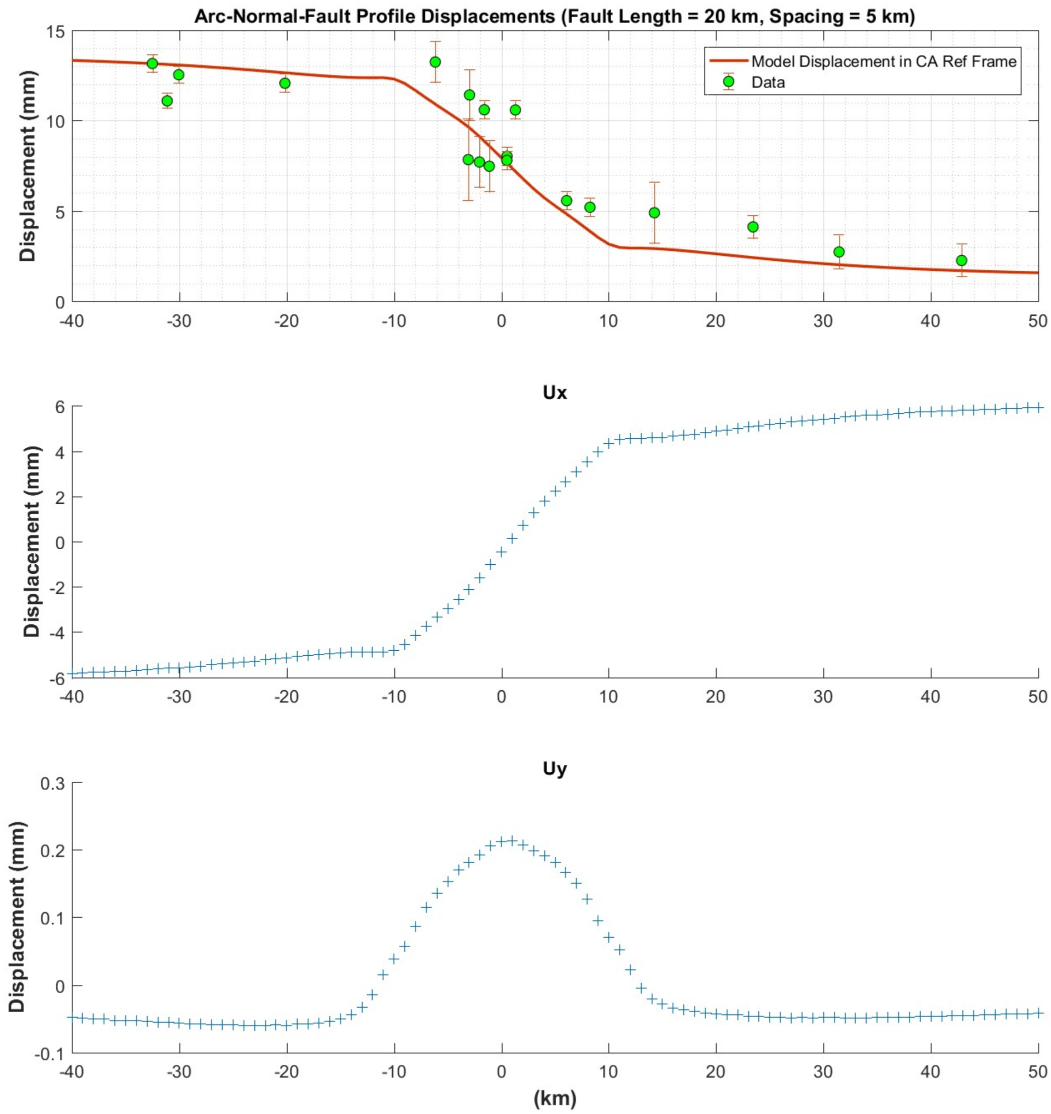

Figure **4-97**. Model B11: displacements along-profile. Arc-normal faults' length and spacing are 20 km and 5 km respectively. Top panel – profile displacements projected into horizontal line (azimuth = 270°). Middle panel – profile displacements in the x-direction. Bottom panel – profile displacements in the y-direction. 'Model Displacement in CA' data sets was created by adding an offset of 7 mm to the model displacements.

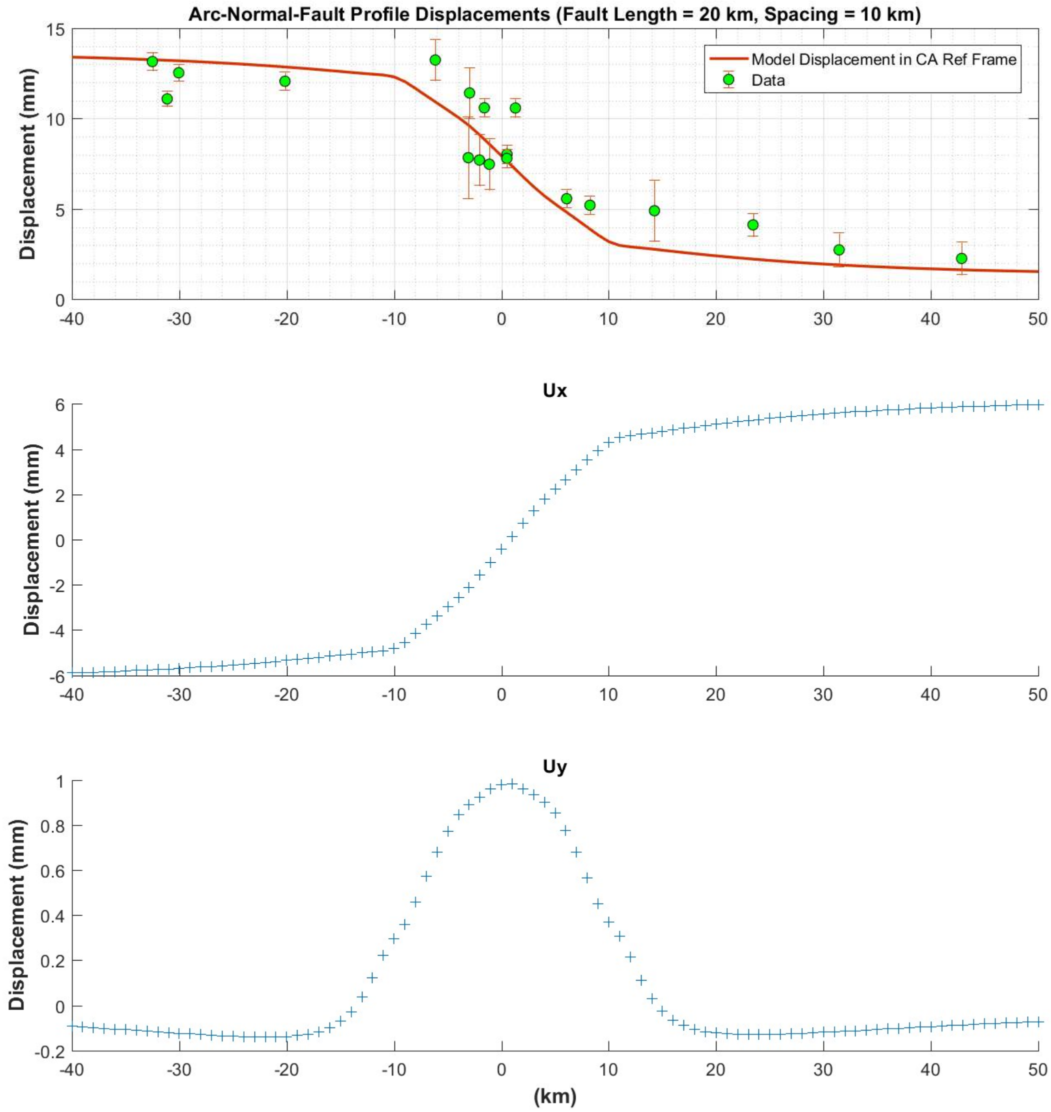

Figure **4-98:** Model B12: displacements along-profile. Arc-normal faults' length and spacing are 20 km and 10 km respectively. Top panel – profile displacements projected into horizontal line (azimuth = 270°). Middle panel – profile displacements in the x-direction. Bottom panel – profile displacements in the y-direction. 'Model Displacement in CA' data sets was created by adding an offset of 7 mm to the model displacements.

The slip of the elements for the arc-normal faults were inspected. For both model sets A and B, all elements of arc-normal faults underwent left-lateral displacement. The maximum left-lateral slip on the arc-normal faults for BEM model set A is 2.5 mm and for model set B, which includes an arc-parallel fault (left to right of model space) at depth, the maximum slip is 6.8 mm (Tables **4-26** & **4-27**). The average and maximum slip on arc-normal faults for both model sets are detailed in Tables **4-26** and **4-27**. Figures **B-1** to **B-24** (in Appendix B) show the frequency of left-lateral slip of elements for the arc-normal faults where the element are at depths of 1.5 km, 4.5 km, 7.5 km, 10 km, and 13.5 km. The fits of the model sets A and B to the observed data were calculated using the reduced chi-square and are detailed in Table **4-28**.

Table **4-26**: Average downdip arc-normal faults in model set A.

Model	**Average Slip at -1.5 km (mm)**	**Average Slip at -4.5 km (mm)**	**Average Slip at -7.5 km (mm)**	**Average Slip at -10.5 km (mm)**	**Average Slip at -13.5 km (mm)**	**Max Slip (mm)**
A1	0.9	0.8	0.8	0.7	0.6	1.1
A2	1	0.9	0.9	0.8	0.7	1.1
A3	1	1	0.9	0.9	0.8	1.5
A4	1.1	1.1	1	0.9	0.8	1.5
A5	1.7	1.6	1.5	1.4	1.1	2.1
A6	2	1.9	1.8	1.6	1.3	2.8
A7	1.2	1.1	1	0.9	0.8	1.7
A8	2	1.9	1.8	1.6	1.3	2.6
A9	2.5	2.4	2.2	2	1.5	3.7
A10	1.2	1.1	1	0.9	0.8	2.1
A11	2.1	2	1.9	1.7	1.3	2.9
A12	2.7	2.6	2.4	2.1	1.6	4.1

Table **4-27**: Average downdip arc-normal faults in model set B.

Model	Average Slip at -1.5 km (mm)	Average Slip at -4.5 km (mm)	Average Slip at -7.5 km (mm)	Average Slip at -10.5 km (mm)	Average Slip at -13.5 km (mm)	Max Slip (mm)
B1	1.2	1.2	1.3	1.5	1.9	2.7
B2	1.3	1.3	1.4	1.7	2.1	2.8
B3	1.3	1.3	1.4	1.7	2.2	3.1
B4	1.6	1.6	1.7	1.7	1.8	3.7
B5	2.4	2.4	2.5	2.6	2.7	4.2
B6	2.7	2.7	2.7	2.9	2.9	4.8
B7	1.6	1.7	1.7	1.6	1.7	4.1
B8	2.9	2.9	2.9	2.9	2.8	5.1
B9	3.5	3.5	3.5	3.5	3.3	6
B10	1.6	1.6	1.6	1.6	1.6	4.5
B11	3	3	3	2.9	2.8	5.7
B12	3.8	3.8	3.8	3.7	3.4	6.8

Table **4-28**: Model set A and B fits.

Model	$\bar{\chi}^2$	Model	$\bar{\chi}^2$
A1	3.939	B1	3.947
A2	3.809	B2	3.745
A3	3.796	B3	3.713
A4	3.354	B4	3.462
A5	3.409	B5	3.594
A6	3.426	B6	3.554
A7	3.120	B7	3.332
A8	3.262	B8	3.299
A9	3.361	B9	3.791
A10	3.368	B10	3.621
A11	3.451	B11	4.465
A12	3.676	B12	4.28

The results of kinematic analysis of the expected slip on bookshelf faults (Sigmundsson et al., 1995), using the same fault configuration (lengths and spacings) as the BEM model sets A and B, are detailed in Table **4-29**. This analysis shows that the maximum slip of 28 mm/yr will occur on arc-normal faults where their length is 5 km and spacing is 10 km. The minimum amount of slip, on bookshelf faults is 1.4 mm/yr, where arc-normal fault lengths are 20 km and spaced every 2 km.

Table **4-29**: Results from geometric analysis of expected slip on bookshelf faults. φ - rotation rate of fault.

Length (km)	**Spacing (km)**	**φ (μrads/yr)**	**Slip (mm/yr)**
5	2	2.8	5.6
5	5.5	2.8	15.4
5	10	2.8	28
10	2	1.4	2.8
10	5.5	1.4	7.7
10	10	1.4	14
15	2	0.9	1.9
15	5	0.9	4.7
15	10	0.9	9.3
20	2	0.7	1.4
20	5.5	0.7	3.8
20	10	0.7	7

4.3.3.1.2 Model Sets C, D, E, & F

GPS velocities of the CAFA range from 8 mm/yr to 14 mm/yr but GPS stations are limited to 40 km across-strike the CAFA, i.e., from the coast to the volcanic arc. The maximum CAFA velocity may not have been observed. To investigate this, model sets C and D (with arc-parallel fault) with a background deformation field of -8 mm to 8 mm were created. The surface displacements for model sets C and D are plotted in Figures **B-25** to **B-36** and **B-48** to **B-59** (in Appendix B), respectively, and their displacement profile in Figures **B-47** to **B-48** and **B-61** to **B-73**, respectively. Model sets E and F (with arc-parallel fault) were created with a background deformation field of -10 mm to 10 mm. The surface displacements for model sets E and F are plotted in Figures **B-73** to **B-84** and **B-97** to **B-108**, respectively, and their displacement profile in Figures **B-85** to **B-96** and **B-109** to **B-120**, respectively. Model sets C, D, E, and F did not fit the observed displacements in the forearc and back-arc.

4.3.3.2 Slip Prescribed on Faults

4.3.3.2.1 Model Sets G, H, & I

Model sets G, H, and I explore imposing slip on the arc-normal faults using the kinematic analysis of Sigmundsson et al. (1995) and arc-parallel fault (slip of 14 mm) with and without a background deformation field. Plots for models that did not fit the data are in Appendix B. Model G has a deformation field of -7 mm to 7 mm and its surface displacements are plotted in Figures **B-121** to **B-123** while its displacement profile is plotted in Figures **B-124** to **B-126**. Model set H does not have a background deformation field and its surface displacements are plotted in Figures **B-127** to **B-129** while the model set displacement profiles are plotted in Figures **B-130** to **B-132**. Model set I has a background displacement field of -7 mm to 7 mm but does not have an arc-parallel fault. The surface displacements of model set I are plotted in Figures **B-133** to **B-135** and the displacement profiles are plotted in Figures **B-136** to **B-138**. Model sets G, H, and I did not fit the observed displacement, except for model I2 (Figures **4-99** and **4-100**).

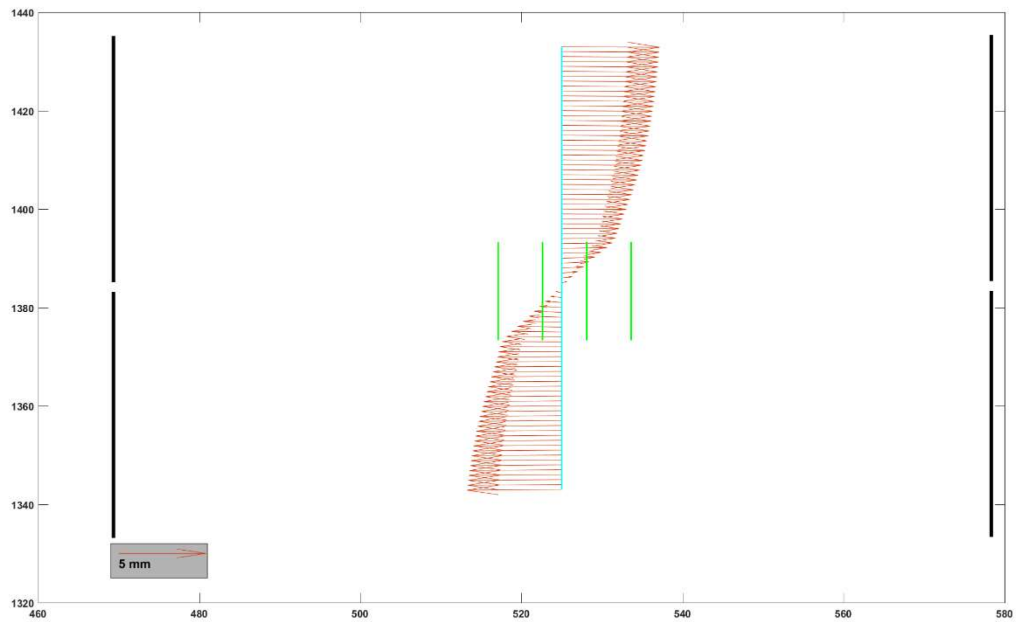

Figure **4-99:** Model I2: surface displacements (red vectors) along-profile line (cyan line). Arc-normal faults' (green lines) length and spacing are 20 km and 5 km respectively. This model has 4 arc-normal faults.

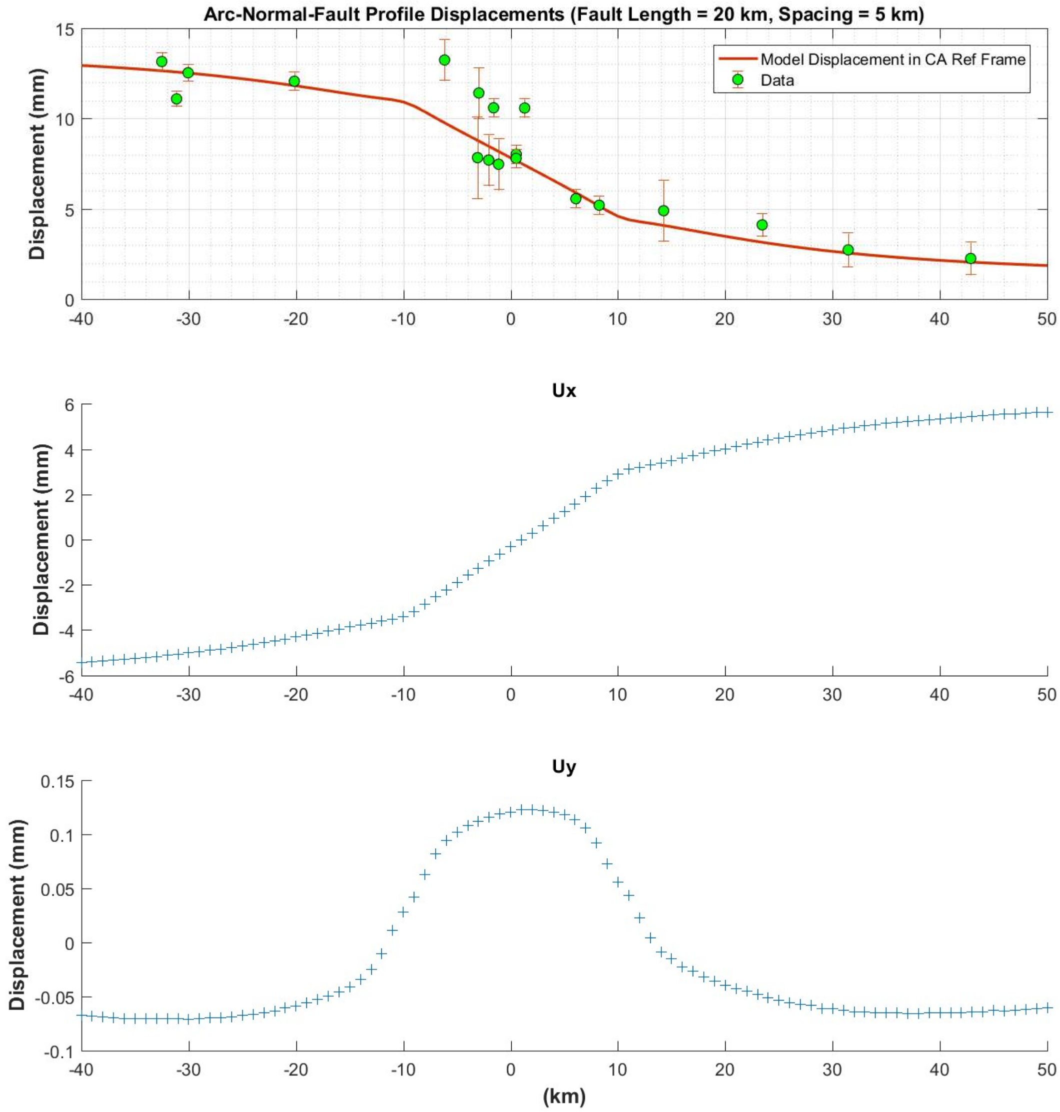

Figure **4-100:** Model I2: displacements along-profile. Arc-normal faults' length and spacing are 20 km and 5 km respectively. Top panel – profile displacements projected into horizontal line (azimuth = 270°). Middle panel – profile displacements in the x-direction. Bottom panel – profile displacements in the y-direction. 'Model Displacement in CA' data sets was created by adding an offset of 7 mm to the model displacements.

4.3.3.2.2 Model Sets J, K, L, M, & N

Model sets J, K, L, M, and N were created to investigate surface displacements of locked arc-normal faults that slip down-dip at an amount described by the kinematic analysis of Sigmundsson et al. (1995). Plots for models that did not fit the data are in Appendix B. Model set J has no deformation field, slip on arc-normal faults at down-dip 15 km to 20 km, and an arc-parallel fault at depth with slip of 14 mm. Surface displacements for model set J are plotted in Figures **B-134** to **B-136** and displacement profiles are plotted in Figures **B-137** to **B-139**. Model set K has no background deformation field, no arc-parallel fault, and arc-normal faults that slip at down-dip depths of 10 km to 20 km. Surface displacements for model set K are plotted in Figures **B-140** to **B-142** and displacement profiles are plotted in Figures **B-143** to **B-145**. Model set L has a background deformation field of -7 mm to 7 mm, no arc-parallel fault, and arc-normal faults slip at down-dip depths of 10 km to 20 km. Surface displacements for model set L are plotted in Figures **B-146** to **B-148** and displacement profiles are plotted in Figures **4-221** to **4-223**. Model set M has no background deformation field, no arc-parallel fault, and arc-normal faults slip at down-dip depths of 5 km to 20 km. Surface displacements for model set M are plotted in Figures **B-101** to **B-103** and displacement profiles are plotted in Figures **B-104** to **B-106**. Model N has a background deformation field of -7 mm to 7 mm, no arc-parallel fault, and arc-normal faults slip at down-dip depths of 5 km to 20 km. Surface displacements for model set N are plotted in Figures **B-107 to B-109** and displacement profiles are plotted in Figures **4-224**, **4-225**, and **B-110**. Model sets J, K, L, M, and N poorly fit the observed displacements. However, models L1, L2, and L3 (spacings of 2km, 10 km, and 5 km, Figures **4-101** to **4-103**) and models N1 and N2 (spacings of 2km and 5 km, Figures **4-104** & **4-105**) did fit the observed displacements in the back-arc and forearc. Models L1, L2, N1, and N2 had background displacement fields.

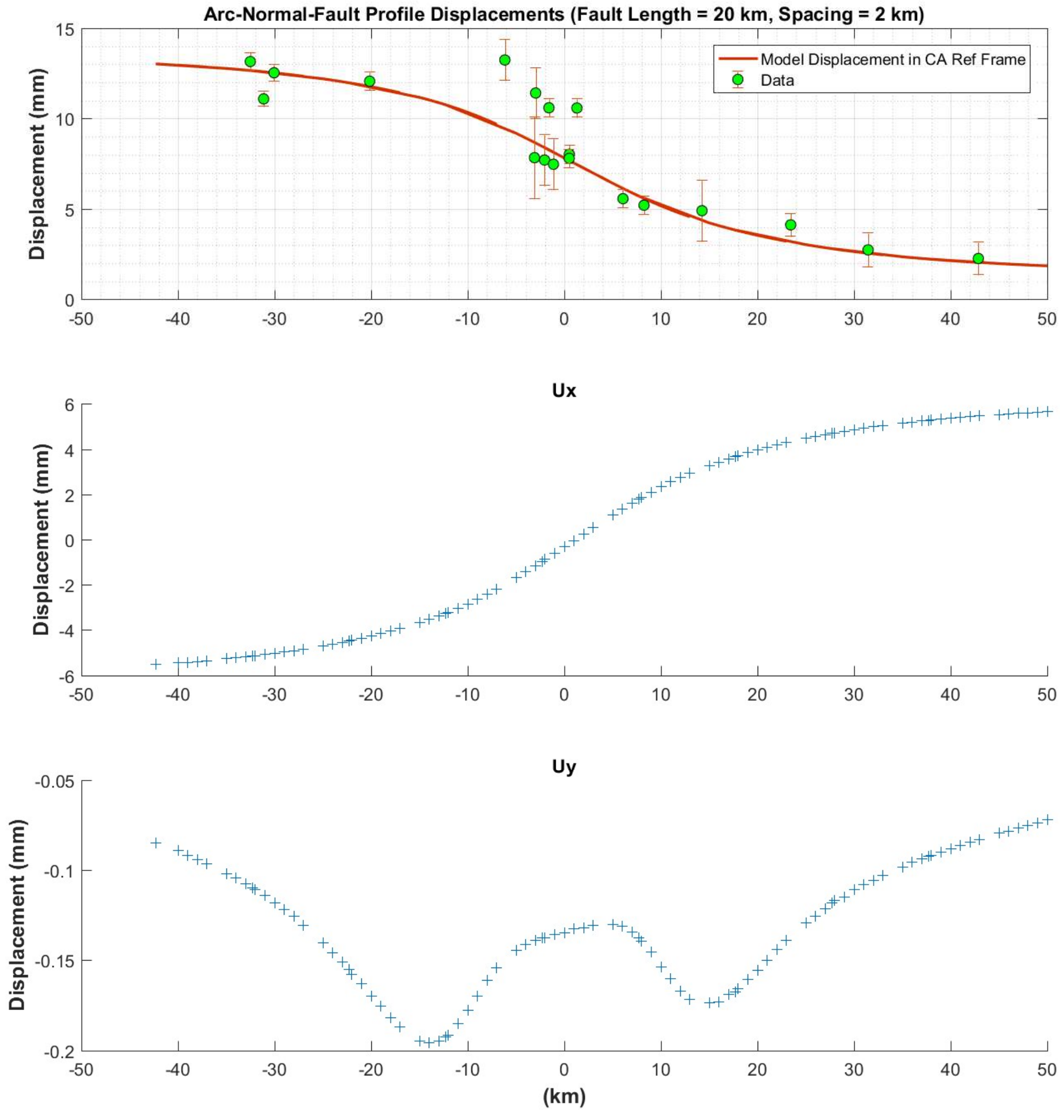

Figure **4-101:** Model L1: displacements along-profile. Arc-normal faults' length and spacing are 20 km and 2 km respectively and had 1.4 mm of slip imposed on them. Top panel – profile displacements projected into horizontal line (azimuth = 270°). Middle panel – profile displacements in the x-direction. Bottom panel – profile displacements in the y-direction. 'Model Displacement in CA' data sets was created by adding an offset of 7 mm to the model displacements.

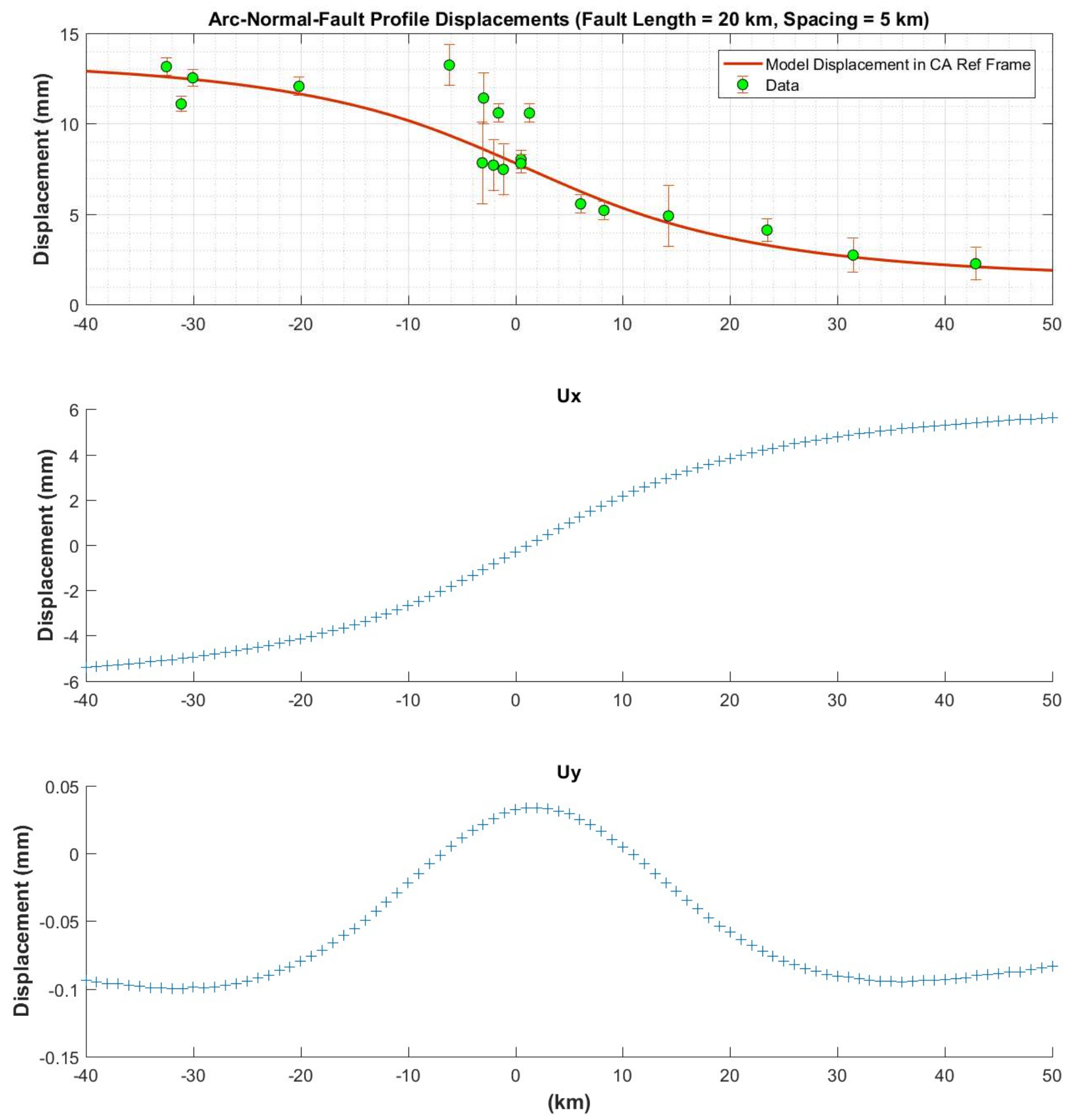

Figure **4-102:** Model L2: displacements along-profile. Arc-normal faults' length and spacing are 20 km and 5 km respectively and had 3.8 mm of slip imposed on them. Top panel – profile displacements projected into horizontal line (azimuth = 270°). Middle panel – profile displacements in the x-direction. Bottom panel – profile displacements in the y-direction. 'Model Displacement in CA' data sets was created by adding an offset of 7 mm to the model displacements.

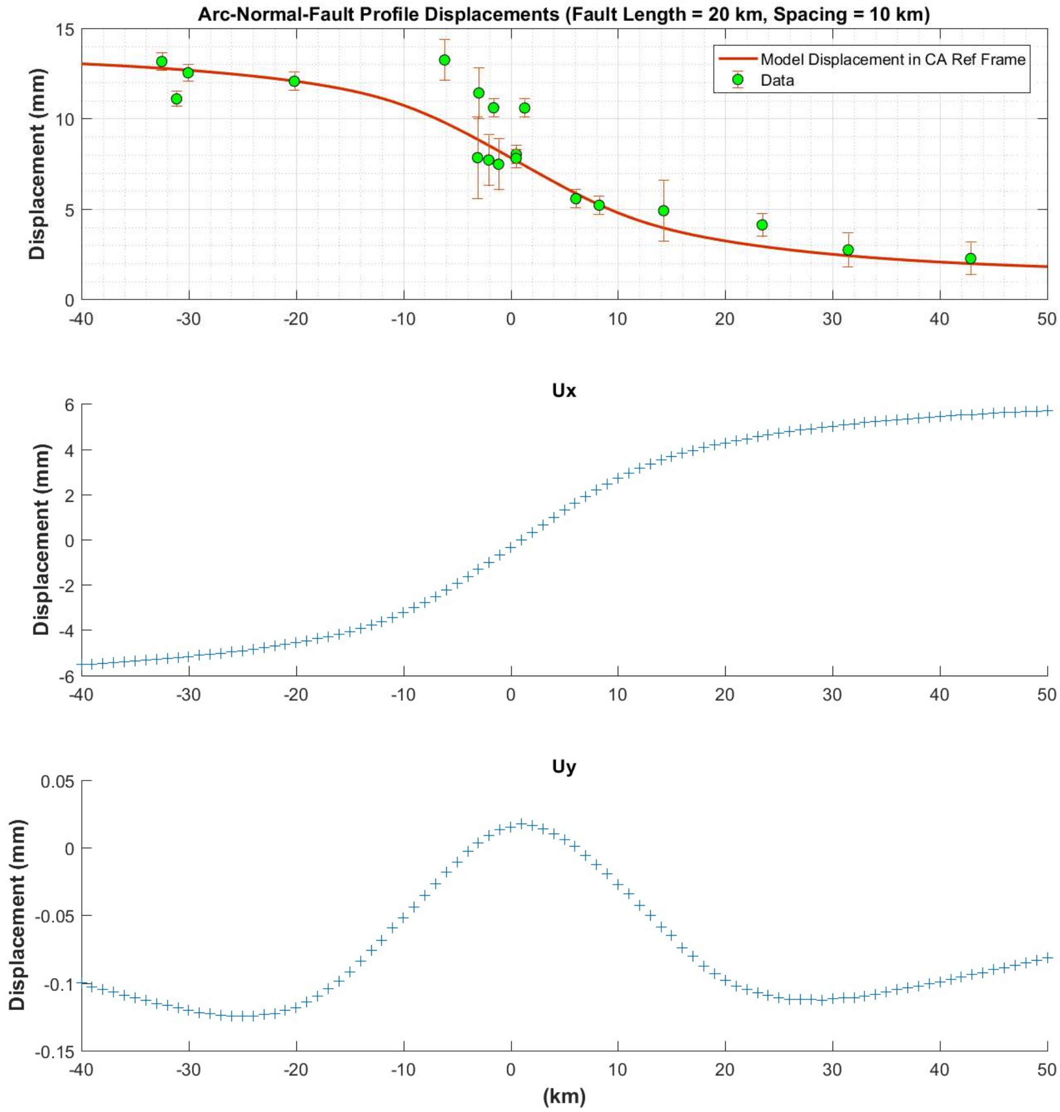

Figure **4-103:** Model L3: displacements along-profile. Arc-normal faults' length and spacing are 20 km and 10 km respectively and had 7 mm of slip imposed on them. Top panel – profile displacements projected into horizontal line (azimuth = 270°). Middle panel – profile displacements in the x-direction. Bottom panel – profile displacements in the y-direction. 'Model Displacement in CA' data sets was created by adding an offset of 7 mm to the model displacements.

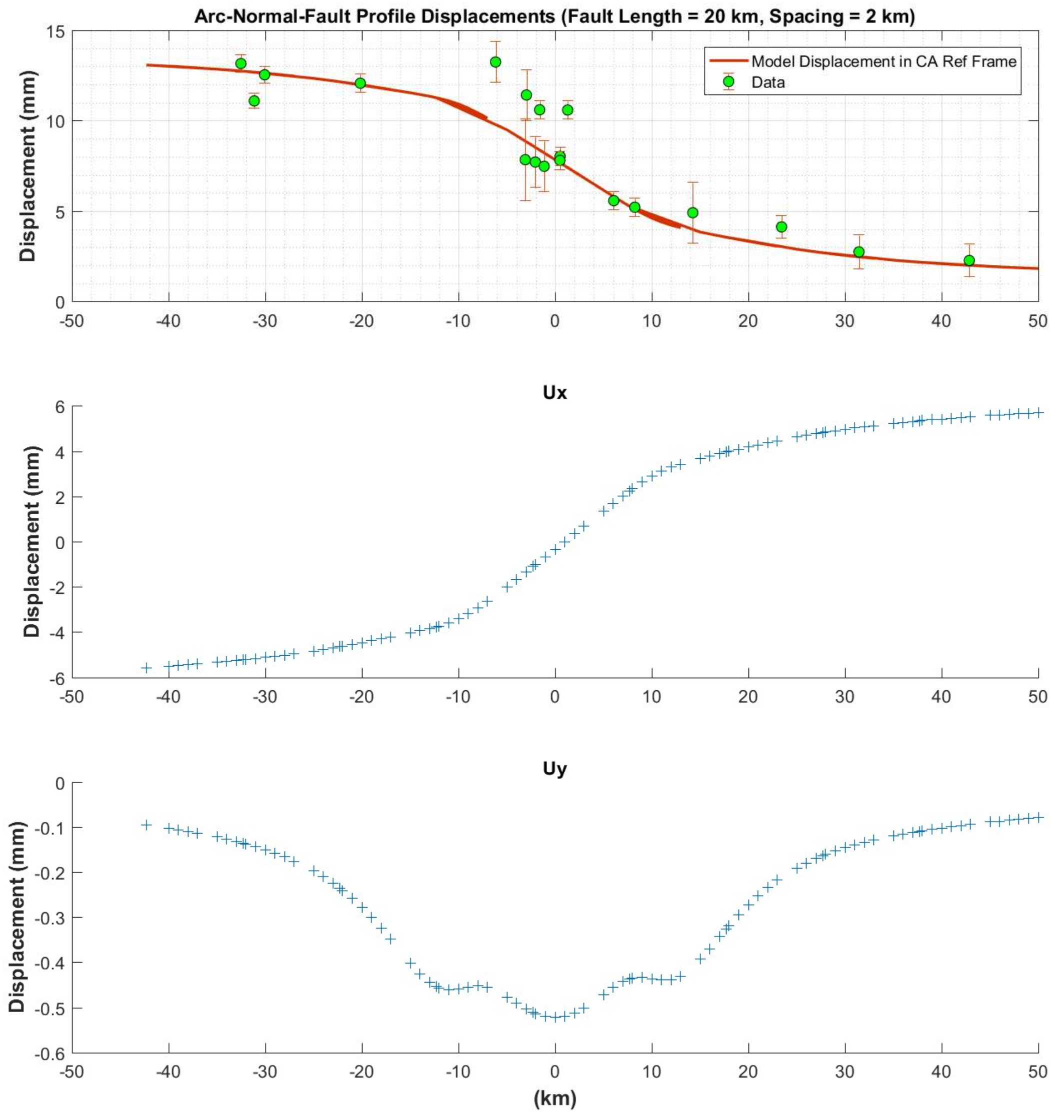

Figure **4-104:** Model N1: displacements along-profile. Arc-normal faults' length and spacing are 20 km and 2 km respectively and had 1.4 mm of slip imposed on them. Top panel – profile displacements projected into horizontal line (azimuth = 270°). Middle panel – profile displacements in the x-direction. Bottom panel – profile displacements in the y-direction. 'Model Displacement in CA' data sets was created by adding an offset of 7 mm to the model displacements.

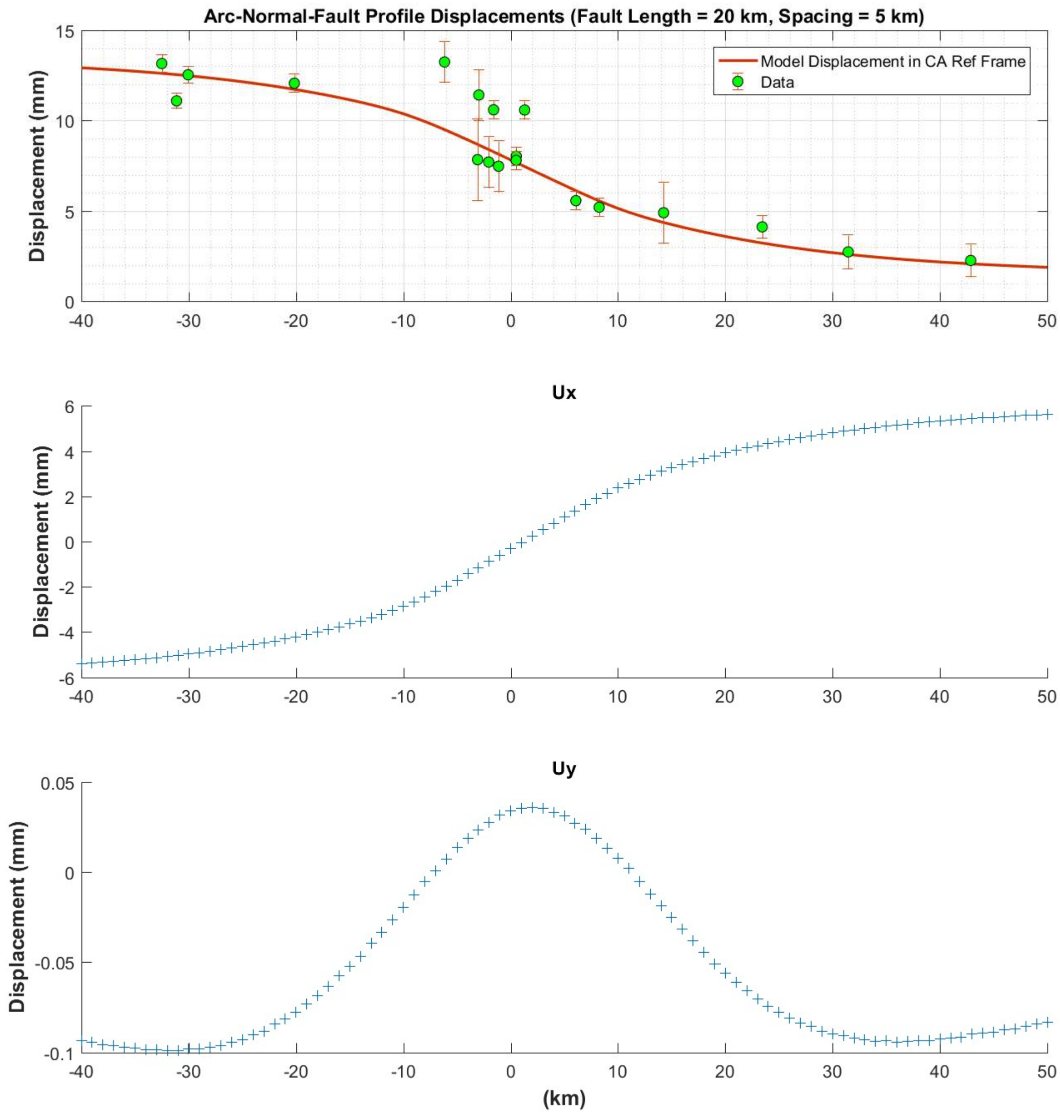

Figure **4-105:** Model N2: displacements along-profile. Arc-normal faults' length and spacing are 20 km and 5 km respectively and had 3.8 mm of slip imposed on them. Top panel – profile displacements projected into horizontal line (azimuth = 270°). Middle panel – profile displacements in the x-direction. Bottom panel – profile displacements in the y-direction. 'Model Displacement in CA' data sets was created by adding an offset of 7 mm to the model displacements.

4.3.3.2.3 Model Sets O, P, Q, & R

Model sets O, P, Q, and R were created to investigate arc-normal faults shallowly locked, i.e., slip at down-dip depths of 5 km to 20 km. Plots for models that did not fit the data are in Appendix B. Models were created that imposed slip of 10 mm (model sets O and P) and 14 mm (model sets Q and R) on the arc-normal faults, which exceeds what is predicted by the kinematic analysis described by Sigmundsson et al. (1995). Model set O had no deformation field while model set P has a background deformation field of -7 mm to 7 mm. The model set Q also has no deformation field while model set R has a background deformation field of -7 mm to 7 mm. The surface displacements for model sets O and P are plotted in Figures **B-160** to **B-162** and **B-166** to **B-168**, respectively, and their displacement profile in Figures **B-163** to **B-165** and **B-169 to B-171,** respectively. The surface displacements for model sets Q and R are plotted in Figures **B-172** to **B-174** and **B-178** to **B-180**, respectively, and their displacement profile in Figures **B-175** to **B-177** and **B-181** to **B-183**, respectively. Model sets O, P, Q, and R did not fit the observed displacements.

4.3 Discussion

At the CAFA-CA boundary, there is no well-expressed throughgoing right-lateral transform fault system (La Femina et al., 2002). Instead, bookshelf faulting appears to be the primary mechanism of accommodating the relative motion, at least in northwestern Nicaragua and Lake Nicaragua (La Femina et al., 2002). Bookshelf faulting can approximate a transform fault and has been observed in the South Iceland Seismic Zone where a system of north-south trending faults approximates a transform fault that connects two ridges (Sigmundsson et al. 1995). A similar type of shear mechanism has been found in the central Afar rift system in Africa where strain is accommodated on bookshelf faults between disconnected rift segments (Sigmundsson 1992; Manighetti et al. 2001). The geodetic signature of this mode of shear has not been previously investigated and the modeling results previously presented suggest that surface displacements can be reproduced with slip on arc-normal faults and shear at depth.

Dislocation models were inverted using GPS velocity data to explore if the CAFA-CA shear can be accommodated by an arc-parallel one-fault or two-fault systems, along with whether there are regions of contrasting rheology. The dislocation models do fit the observed GPS velocities but some models (5 out of 18) overfitted the data ($\bar{\chi}^2 < 1$). Regardless of model fit, many models failed to capture the geodetic signature in the back-arc or the full 14 mm/yr across-strike velocity. The one-fault elastic dislocation model set could not fit this signal and had the worse model fits ($\bar{\chi}^2 > 15$), with the exception of the Momotombo profile which overfitted the data ($\bar{\chi}^2 = 0.862$). The one-fault elastic dislocation models could not fit the velocity profile in the back-arc. The two-fault elastic dislocation models fit ($\bar{\chi}^2 < 5$) both the Cerro Negro and Telica velocity profiles better than the one-fault dislocation models ($\bar{\chi}^2$ ~15). The two-fault elastic dislocation models suggest a northeast fault maybe within 30 to 35 km from the volcanic arc, in the Highlands (Figure **4-2**), outside the Nicaragua Depression. No such NW-trending right-lateral fault has been identified in the Highlands of Nicaragua. The one-fault hetero-elastic model fit the observed velocities well but all model inversions produced unrealistic shear moduli (<25 GPa). The one-fault hetero-elastic dislocation models do better at fitting the data than the one-fault elastic dislocation model. However, these models do not capture the velocities in the forearc (Figure **4-25**) and may have been biased by more data in the back-arc. Results of the two-fault hetero-elastic dislocation models and their fits suggest that the northeast fault is located between 25 km and 37 km from the volcanic arc. For the three velocity profiles, all model fits worsen when inverting data without velocities of GPS stations on volcanic centers, which may suggest that the GPS stations sited at volcanos record the CAFA-CA shear. The elastic and hetero-elastic dislocation models do fit observed GPS velocities but cannot capture the main features of the observed geodetic signature and do not honor the real-world fault configuration.

The boundary element method was used to demonstrate that the observed geodetic signature can be reproduced using arc-normal faults perpendicular to the direction of shear (bookshelf faulting). Model sets A and B were created to allow arc-normal faults and an arc-parallel fault at depth to freely slip in a deformation field that is a displacement gradient of -7 mm to 7 mm. Both model sets A and B produced the main features of the geodetic signal. The surface displacements of Model set A fit the observed data better than Model set B, which had an arc-parallel fault at depths of 20 km to 55 km (e.g., Figure **4-71**). In particular, models with arc-normal fault lengths of 15 km and 20 km, and spacings of 2 km, 5 km, 10 km for both model sets A and B, better approximate the observed displacements (Table **4-28**). The best fitting model is A7 (Table **4-28**, Figure **4-68**), which has arc-normal fault lengths of 15 km and spacings of 2 km and the lowest reduced chi-square value (3.12). However, model A8, with arc-normal fault lengths of 15 km and spacing of 5 km, had a comparable reduced chi-square value of 3.26 (Table **4-28**; Figure **4-69**). Models A4 and B4, with arc-normal fault lengths of 10 km with spacings of 2 km (Table **4-28**; Figures **4-65** and **4-90**), also fit the observed displacements but it is likely that the real-world faults of the CAFA-CA shear zone are longer given the mapped structures presented by La Femina et al. (2002) and the results of Chapter 3 of this dissertation. It should be noted that only the model B10 from model set B, with a reasonable fault configuration (lengths of 20 km and spacings of 2 km) and had a better fit than its equivalent in model set A (A10) (Table **4-28**; Figure **4-96**). Model sets A and B indicate that it is possible that the shear of the northwestern Nicaraguan segment of the CAFA-CA boundary is accommodated by arc-normal faults of lengths 15 km to 20 km and spacings of 5 km or less (Figure **4-106**).

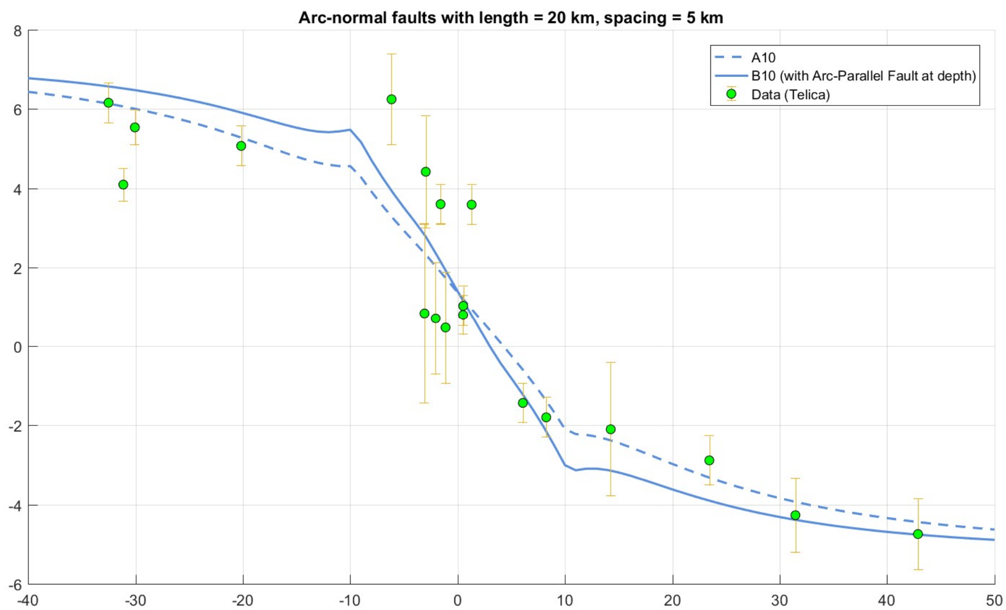

Figure **4-106**: Across profile displacements of models A10 and B10. Data is a combination of Telica and Cerro Negro velocity profiles.

Model set B included an arc-parallel fault at depths of 20 km to 55 km to represent the expected shear of the ductile lithosphere below the brittle-ductile transition zone. This model set did not fit the observed data as well as model set A but the geodynamic reality is that this shear zone at depth must exist and is responsible for most of the geodetic signature observed in northwestern Nicaragua. If such a shear zone exists beneath the volcanic arc, then it would also be shearing the magmatic bodies that supply the arc with magma. Such emplaced sheared magmatic bodies have been observed in the

Cathedral Park Range Late Cretaceous granitic batholiths in the Sierra Nevada, California (Tikoff and Teyssier 1992). The elongated batholiths were emplaced in a strike-slip shear zone associated with the oblique convergence margin of the then Farallon-North American boundary (Tikoff & Teyssier, 1992; and references therein). Likewise, emplaced magmatic bodies in the modern Nicaraguan volcanic arc must be undergoing shear and the modeled shear zone (arc-parallel fault at depth) is a real feature. Also, the fit for model set B to the data would improve if translated +5 km along the profile, albeit, it does not capture many of the displacements in the volcanic arc (Figure **4-107**).

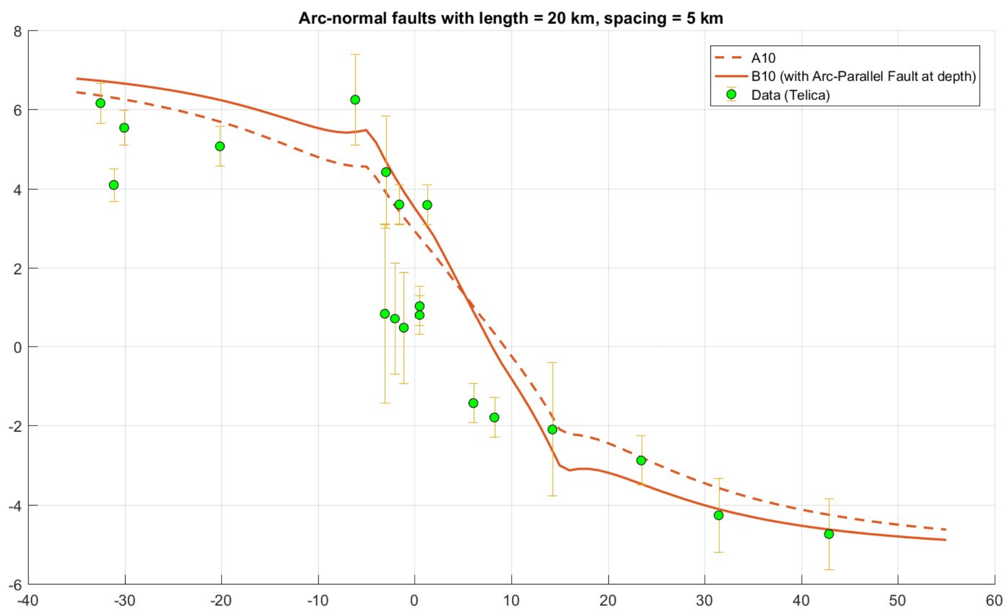

Figure **4-107:** Across profile displacements of models A10 and B10 translated +5km along profile. Data is a combination of Telica and Cerro Negro velocity profiles.

Models A8 and B8, with arc-normal fault lengths of 15 km and spacing of 5 km, might be the closest analogue to the real-world as the faulting of three upper-plate earthquakes described in Chapter 3 of this dissertation found ruptured arc-normal faults that were spaced 5.5 km on average. The average slip on arc-normal faults for Models A8 and B8 is ~2 mm and ~3 mm, which has implications for the return period of shallow moderate magnitude earthquakes that occur in the volcanic arc. If the average slip rate of a seismogenic arc-normal fault is 3 mm/yr, and the fault is 10 km along-strike and 5 km down-dip, and it ruptures to produce a M_w 5.5 earthquake, then the reoccurrence interval for this earthquake would be 50 years.

The arc-normal fault slip produced by the kinematic analysis of Sigmundsson et al. (1995) (Table **4-27**), when considering the same fault configurations of model sets A and B, are not equivalent to that produced by model sets A and B (Tables **4-26** & **4-27**). The kinematic analysis produced slip on the arc-normal faults that were much larger. The kinematic model is ideal and works well for faults of the bookshelf fault model that are separated by distances greater than 10 km. The kinematic model does not take into account the interaction of spatially close faults where a superposition of the displacement fields produced by the faults would reduce the slip on the faults.

Several models were created to explore how prescribed slip on the arc-normal faults and an arc-parallel fault and the deformation field contributes to an across-strike signature. Model sets G, H, and I imposed slip following Sigmundsson et al. (1995) on 20 km long arc-normal faults at down-dip depths of the surface to 20 km. The model set also explored the resulting surface displacements with and without a deformation field and with and without an arc-parallel fault. From these model sets, only model I2 fit the observed displacements in the back-arc and fore-arc (Figure **4-100**). Model I2 had arc-normal faults with length of 20 km and spacing of 5 km, imposed slip of 3.8 mm, no arc-parallel fault at depth, and a background deformation field of -7 mm to 7 mm. This model configuration is equivalent to model A11, which only had a maximum induce slip on the arc-normal faults of ~3 mm. Model sets G, H, and I demonstrated that slip on the arc-normal faults and arc-parallel fault do contribute to the features of the observed geodetic signatures.

Model sets J, K investigated locked arc-normal faults with imposed slip amounts following Sigmundsson et al., 1995 at down-dip depths of 15 km to 20 km, and 10 km to 20 km, respectively. The model set did not have a background deformation field. Model sets J and K produced submillimeter surface displacements and show that locked arc-normal faults that slip at depth do not contribute to the surface displacements (Figures **B-137** to **B-139** & **B-92** to **B-98**). Model set M is similar to model sets J and K but slip was imposed on arc-normal faults at down-dip depths of 5 km to 20 km. Model set M also reinforces that locked arc-normal faults do not contribute much to the surface displacements (Figures **B-152** to **B-154**). Models L1 and L2 had a background deformation field of -7 mm to 7 mm, fault spacings of 2 km (L1) and 5 km (L2), and imposed slip on arc-normal faults of 1.4 mm (L1) and 3.8 mm (L2) at down-dip depths of 10 km to 20 km. Both models L1 and L2 fit the observed geodetic signature (Figures **4-101** & **4-102**). As did model N1 (Figures **4-103**), which is similar to models L1 except slip was imposed on arc-normal faults at down-dip depths of 5 km to 20 km. Results of model sets J through N demonstrated that the background deformation field, which, for these models, is the shear at depth, is required to reproduce the observed geodetic signature and that locked arc-normal faults do not contribute much to this signature.

Model sets O through R impose slip that exceeds that predicted by the kinematic analysis on arc-normal faults at down-dip depths of 5 km to 10 km. The slips that were imposed were 10 mm, for model sets O and P and 14 mm for model sets Q and R. Model sets O and Q did not have a deformation but, as expected with increase slip on the arc-normal faults, the surface displacements were greater (Figures **B-163** to **B-165** & **B-175** to **B-177**) than previous models that explored surface displacements with ≤ 7 mm of slip down-dip, beneath the locked parts of the faults (model sets J, K, and M). Model sets P and R had a background deformation field but did not fit the observed displacements.

There are limitations to using the BEM to simulate CAFA-CA shear. The BEM models were implemented to produce the first-order features of the geodetic signature of the CAFA in Nicaragua, especially the velocity signature in the back-arc. The observed velocity in the back-arc and fore-arc is not due to an unaccounted change in crustal thickness from the coast to the Nicaragua Depression-Highlands boundary or vertical rheological differences. MacKenzie et al. (2008), using seismic receiver functions to image the crust of the CAFA and back-arc (volcanic arc to Nicaragua Depression-Highlands boundary), has shown that the crustal thickness is consistently 30 km. There is likely no across-strike change in rheology as the CAFA has only been displaced by at most 40 km, which would make it unlikely that rheologically disparate regions are now adjacent. Furthermore, the Nicaraguan segment of the CAFA is accreted oceanic crust and has been called the Siuna Terrane in the literature (Andjić et al., 2019; Flores & Gazel, 2020; and references therein). The base of the forearc lithosphere may be compositionally different, and hence, rheologically different, as oceanic crust is transformed to continental crust through melt-crust interaction (Gazel et al. 2019) but these changes are too deep to cause the observed geodetic signal. The BEM strategy does not take into account the thermally weakened crust of the active volcanic centers. The rheology of the local shallow crust may vary and could explain near-field features of the surface displacement but it is unlikely to contribute to the displacements observed in the back-arc. The near-arc displacements (i.e., velocities within 5 km of the volcanic arc), may also be difficult to model given that the arc-normal fault array produces vortices of surface displacements between faults (Figures **4-108** & **4-109**) and the strike and length of these faults will vary in reality.

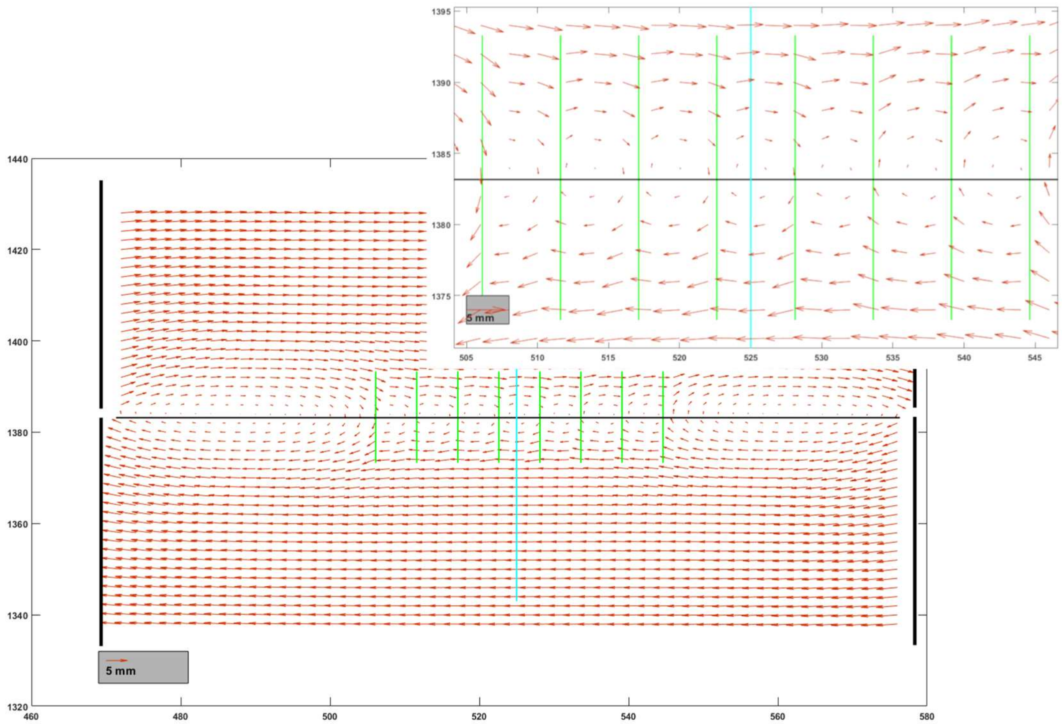

Figure **4-108:** Surface displacements sampled in a 2 km by 2 km grid of a model with arc-normal faults (length 20 km) and arc-parallel faults free to slip in a background deformation field of -7 mm to 7 mm. Inset is a plot of just the arc-normal faults and surface displacements.

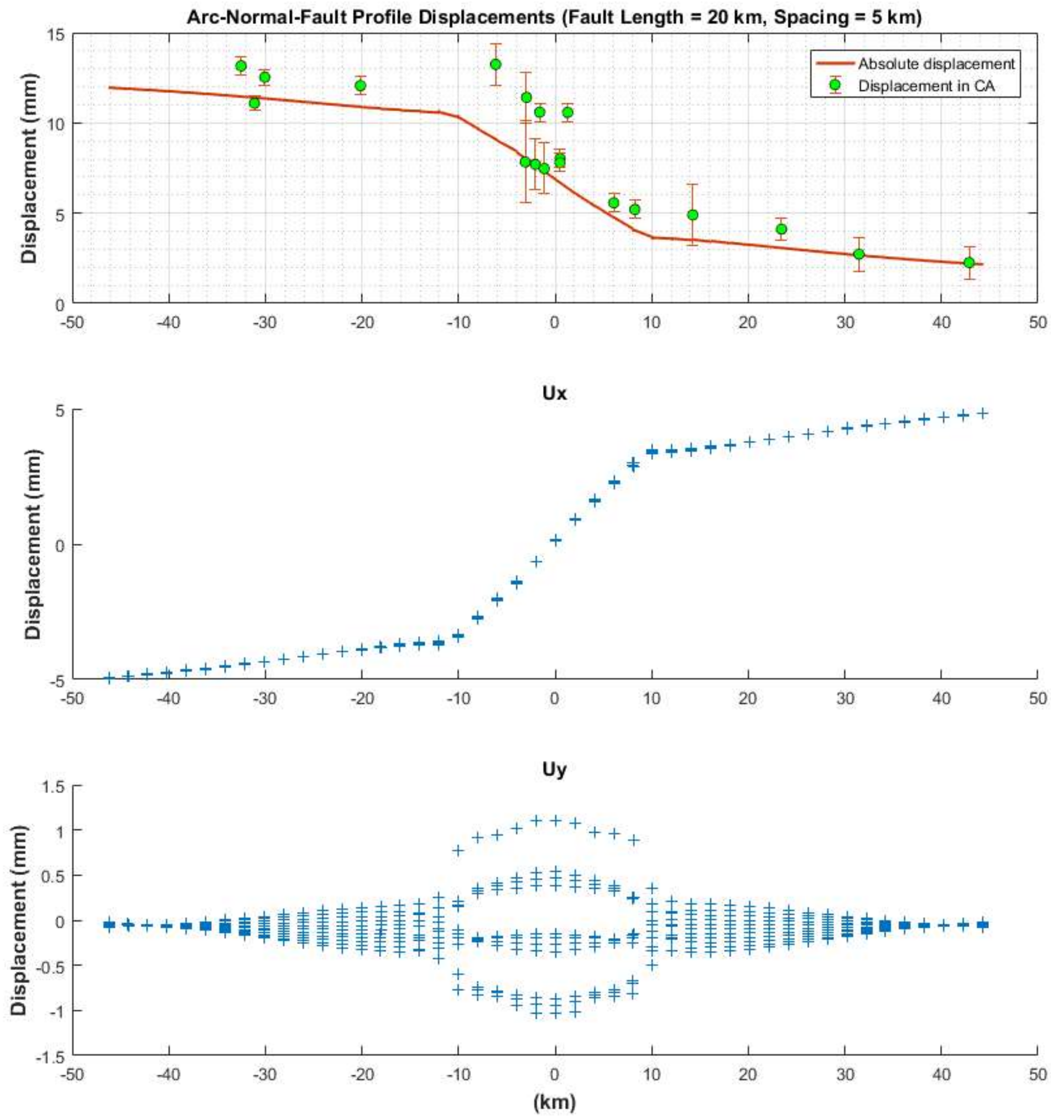

Figure **4-109:** Displacement profile for model shown in Figure **4-108**.

4.4 Conclusion

While two-fault elastic dislocation models can fit the geodetic signature across-strike the Nicaraguan segment of the CAFA and back-arc, they do not reflect the fault configuration. Instead, Bookshelf faulting approximates a transform fault in northwestern Nicaragua. The slip on creeping parts of the arc-normal faults of Bookshelf faulting and shear at depth are responsible for the first-order features of the observed GPS velocities of the CAFA in Nicaragua. Locked arc-normal faults between volcanos do not contribute to the observed geodetic signal. The maximum velocity of the CAFA is 14 mm/yr and the maximum expected slip rate on the arc-normal faults is 3 mm/yr, while the minimum average spacing between these faults is 5 km. Locked arc-normal faults could produce M_w ~5 earthquakes with reoccurrence intervals of 50 years.

4.5 References

Algermissen, S T, J W Dewey, C J Langer, and W H Dillinger. 1974. "The Managua, Nicaragua, Earthquake of December 23, 1972: Location, Focal Mechanism, and Intensity Distribution." *Bulletin of the Seismological Society of America* 64 (4): 993–1004.

Altamimi, Z., L. Métivier, and X. Collilieux. 2012. "ITRF2008 Plate Motion Model." *Journal of Geophysical Research: Solid Earth* 117 (7): 1–14. https://doi.org/10.1029/2011JB008930.

Andjić, Goran, Javier Escuder-Viruete, Claudia Baumgartner-Mora, Peter O. Baumgartner, Simon F. Mitchell, Michèle Caron, and Esmeralda Caus. 2019. "Sedimentary Record of Arc-Continent Collision Along Mesozoic SW North America (Siuna Belt, Nicaragua)." *Tectonics* 38 (12): 4399–4425. https://doi.org/10.1029/2019TC005741.

Bos, M. S., R. M.S. Fernandes, S. D.P. Williams, and L. Bastos. 2013. "Fast Error Analysis of Continuous GNSS Observations with Missing Data." *Journal of Geodesy* 87 (4): 351–60. https://doi.org/10.1007/s00190-012-0605-0.

Brown, R. D., P. L. Ward, and G. Plafker. 1974. "Geologic and Seismologic Aspects of the Managua, Nicaragua, Earthquakes of December 23, 1972: US Geological Survey Professional Paper 838, 1973." *Bulletin of the Seismological Society of America* 64 (4): 1031.

Cailleau, B., P. C. Lafemina, and T. H. Dixon. 2007. "Stress Accumulation between Volcanoes: An Explanation for Intra-Arc Earthquakes in Nicaragua?" *Geophysical Journal International* 169 (3): 1132–38. https://doi.org/10.1111/j.1365-246X.2007.03353.x.

Cailleau, B., and O. Oncken. 2008. "Past Forearc Deformation in Nicaragua and Coupling at the Megathrust Interface: Evidence for Subduction Retreat?" *Geochemistry, Geophysics, Geosystems* 9 (3). https://doi.org/10.1029/2007GC001754.

Carr, Michael J., and Richard E. Stoiber. 1977. "Geologic Setting of Some Destructive Earthquakes in Central America." *Geological Society of America Bulletin* 88 (1): 151–56.

Decriem, J., T. Árnadóttir, A. Hooper, H. Geirsson, F. Sigmundsson, M. Keiding, B. G. Ófeigsson, et al. 2010. "The 2008 May 29 Earthquake Doublet in SW Iceland." *Geophysical Journal International* 181 (2): 1128–46. https://doi.org/10.1111/j.1365-246X.2010.04565.x.

Dewey, J.W., and S.T. Algermissen. 1974. "Seismicity of the Middle America Arc-Trench System near Managua, Nicaragua." *Bulletin of the Seismological Society of America* 64 (4): 1033–48.

Ekström, G., M. Nettles, and A. M. Dziewoński. 2012. "The Global CMT Project 2004-2010: Centroid-Moment Tensors for 13,017 Earthquakes." *Physics of the Earth and Planetary Interiors* 200–201: 1–9. https://doi.org/10.1016/j.pepi.2012.04.002.

Ellis, A, C DeMets, Robert McCaffrey, P Briole, Beatriz Cosenza Muralles, Omar Flores, Marco Guzmán-Speziale, et al. 2019. "GPS Constraints on Deformation in Northern Central America from 1999 to 2017, Part 2: Block Rotations and Fault Slip Rates, Fault Locking and Distributed Deformation." *Geophysical Journal International* 218 (2): 729–54.

Femina, P. C. La, T. H. Dixon, and W. Strauch. 2002. "Bookshelf Faulting in Nicaragua." *Geology* 30 (8): 751–54. https://doi.org/10.1130/0091-7613(2002)030<0751:BFIN>2.0.CO;2.

Femina, Peter La, Timothy H. Dixon, Rob Govers, Edmundo Norabuena, Henry Turner, Armando Saballos, Glen Mattioli, Marino Protti, and Wilfried Strauch. 2009. "Fore-Arc Motion and Cocos Ridge Collision in Central America." *Geochemistry, Geophysics, Geosystems* 10 (5). https://doi.org/10.1029/2008GC002181.

Fitch, Thomas J. 1972. "Plate Convergence, Transcurrent Faults, and Internal Deformation Adjacent to Southeast Asia and the Western Pacific." *Journal of Geophysical Research* 77 (23): 4432–60.

Flores, Kennet E., and Esteban Gazel. 2020. "A 100 m.y. Record of Volcanic Arc Evolution in Nicaragua." *Island Arc* 29 (1): 1–14. https://doi.org/10.1111/iar.12346.

French, S. W., L. M. Warren, K. M. Fischer, G. A. Abers, W. Strauch, J. M. Protti, and V. Gonzalez. 2010. "Constraints on Upper Plate Deformation in the Nicaraguan Subduction Zone from Earthquake Relocation and Directivity Analysis." *Geochemistry, Geophysics, Geosystems* 11 (3): 1–17. https://doi.org/10.1029/2009GC002841.

Funk, Justin, Paul Mann, Kirk McIntosh, and Jason Stephens. 2009. "Cenozoic Tectonics of the Nicaraguan Depression, Nicaragua, and Median Trough, El Salvador, Based on Seismic-Reflection Profiling and Remote-Sensing Data." *Bulletin of the Geological Society of America* 121 (11–12): 1491–1521. https://doi.org/10.1130/B26428.1.

Gardner, T. W., D. Verdonck, N. M. Pinter, R. Slingerland, K. P. Furlong, T. F. Bullard, and S. G. Wells. 1992. "Quaternary Uplift astride the Aseismic Cocos Ridge, Pacific Coast, Costa Rica." *Geological Society of America Bulletin* 104 (2): 219–32. https://doi.org/10.1130/0016-7606(1992)104<0219:QUATAC>2.3.CO;2.

Gazel, Esteban, Jorden L. Hayes, Andres Ulloa, Aristides Alfaro, Drew S. Coleman, and Michael J. Carr. 2019. "The Record of the Transition From an Oceanic Arc to a Young Continent in the Talamanca Cordillera." *Geochemistry, Geophysics, Geosystems* 20 (6): 2733–52. https://doi.org/10.1029/2018GC008128.

Geirsson, Halldor, Mel Rodgers, Peter LaFemina, Molly Witter, Diana Roman, Angelica Muñoz, Virginia Tenorio, et al. 2014. “Multidisciplinary Observations of the 2011 Explosive Eruption of Telica Volcano, Nicaragua: Implications for the Dynamics of Low-Explosivity Ash Eruptions.” *Journal of Volcanology and Geothermal Research* 271: 55–69. https://doi.org/10.1016/j.jvolgeores.2013.11.009.

Genrich, J. F., Y- Bock, R. McCaffrey, L Prawirodirdjo, C W Stevens, S. S. O. Puntodewo, C. Subarya, and S. Wdowinski. 2000. “Distribution of Slip at the Northern Sumatran Fault System.” *Journal of Geophysical Research: Solid Earth* 105 (B12): 28327–41. https://doi.org/10.1029/2000jb900158.

Gomberg, Joan S, and Michael Ellis. 1993. “3D-DEF; a User’s Manual (a Three-Dimensional, Boundary Element Modeling Program).”

Heap, Michael J., Marlène Villeneuve, Fabien Albino, Jamie I. Farquharson, Elodie Brothelande, Falk Amelung, Jean Luc Got, and Patrick Baud. 2020. “Towards More Realistic Values of Elastic Moduli for Volcano Modelling.” *Journal of Volcanology and Geothermal Research* 390: 106684. https://doi.org/10.1016/j.jvolgeores.2019.106684.

Jarrard, Richard D. 1986. “Relations among Subduction Parameters.” *Reviews of Geophysics* 24 (2): 217–84.

Kobayashi, D., P. LaFemina, H. Geirsson, E. Chichaco, A. A. Abrego, H. Mora, and E. Camacho. 2014. “Kinematics of the Western Caribbean: Collision of the Cocos Ridge and Upper Plate Deformation.” *Geochemistry, Geophysics, Geosystems* 15 (5): 1671–83. https://doi.org/10.1002/2014GC005469.Received.

Kreemer, C., E. Klein, Z. K. Shen, M. Wang, L. Estey, S. Wier, and F. Boler. 2014. “A Geodetic Platemotion and Global Strain Rate Model.” *Geochemistry, Geophysics, Geosystems*, 130. https://doi.org/10.1002/2014GC005407.Received.

MacKenzie, Laura, Geoffrey A. Abers, Karen M. Fischer, Ellen M. Syracuse, J. Marino Protti, Victor Gonzalez, and Wilfried Strauch. 2008. “Crustal Structure along the Southern Central American Volcanic Front.” *Geochemistry, Geophysics, Geosystems* 9 (8). https://doi.org/10.1029/2008GC001991.

MacMillan, Ian, Phillip B. Gans, and Guillermo Alvarado. 2004. “Middle Miocene to Present Plate Tectonic History of the Southern Central American Volcanic Arc.” *Tectonophysics* 392 (1–4): 325–48. https://doi.org/10.1016/j.tecto.2004.04.014.

Manighetti, I., P. Tapponnier, V. Courtillot, Y. Gallet, E. Jacques, and P. Y. Gillot. 2001. “Strain Transfer between Disconnected, Propagating Rifts in Afar.” *Journal of Geophysical Research:*

Solid Earth 106 (B7): 13613–65. https://doi.org/10.1029/2000jb900454.

McBirney, A. R., and Howel Williams. 1964. “The Origin of the Nicaraguan Depression.” *Bulletin Volcanologique* 27 (1): 63–63. https://doi.org/10.1007/BF02597510.

McCaffrey, Robert. 1992. “Oblique Plate Convergence, Slip Vectors, and Forearc Deformation.” *Journal of Geophysical Research: Solid Earth* 97 (B6): 8905–15.

Morell, Kristin D., Eric Kirby, Donald M. Fisher, and Matthijs Van Soest. 2012. “Geomorphic and Exhumational Response of the Central American Volcanic Arc to Cocos Ridge Subduction.” *Journal of Geophysical Research: Solid Earth* 117 (4). https://doi.org/10.1029/2011JB008969.

Nicholson, Craig, Leonardo Seeber, Patrick Williams, and Lynn R Sykes. 1986. “Seismic Evidence for Conjugate Slip and Block Rotation within the San Andreas Fault System, Southern California.” *Tectonics* 5 (4): 629–48.

Pichon, Xavier Le, Corné Kreemer, and Nicolas Chamot-Rooke. 2005. “Asymmetry in Elastic Properties and the Evolution of Large Continental Strike-Slip Faults.” *Journal of Geophysical Research B: Solid Earth* 110 (3): 1–11. https://doi.org/10.1029/2004JB003343.

Saginor, Ian, Esteban Gazel, Claire Condie, and Michael J. Carr. 2013. “Evolution of Geochemical Variations along the Central American Volcanic Front.” *Geochemistry, Geophysics, Geosystems* 14 (10): 4504–22. https://doi.org/10.1002/ggge.20259.

Savage, J. C., and R. O. Burford. 1973. “Geodetic Determination of Relative Plate Motion in Central California.” *Journal of Geophysical Research* 78 (5): 832–45.

Schmalzle, Gina, Timothy Dixon, Rocco Malservisi, and Rob Govers. 2006. “Strain Accumulation Accross the Carrizo Segment of the San Andreas Fault, California: Impact of Laterally Varying Crustal Properties.” *Journal of Geophysical Research: Solid Earth* 111 (5): 1–19. https://doi.org/10.1029/2005JB003843.

Segall, Paul. 2010. *Earthquake and Volcano Deformation*. Princeton University Press.

Sieh, Kerry, and Danny Natawidjaja. 2000. “Neotectonics of the Sumatran Fault, Indonesia.” *Journal of Geophysical Research: Solid Earth* 105 (B12): 28295–326. https://doi.org/10.1029/2000jb900120.

Sigmundsson, Freysteinn. 1992. “Tectonic Implications of the 1989 Afar Earthquake Sequence.” *Geophysical Research Letters* 19 (9): 877–80.

Sigmundsson, Freysteinn, Páll Einarsson, Roger Bilham, and Erik Sturkell. 1995. “Rift-Transform Kinematics in South Iceland: Deformation from Global Positioning System Measurements, 1986 to 1992.” *Journal of Geophysical Research: Solid Earth* 100 (B4): 6235–48.

Syracuse, Ellen M., Geoffrey A. Abers, Karen Fischer, Laura MacKenzie, Catherine Rychert, Marino Protti, Víctor González, and Wilfried Strauch. 2008. “Seismic Tomography and Earthquake Locations in the Nicaraguan and Costa Rican Upper Mantle.” *Geochemistry, Geophysics, Geosystems* 9 (7): 1–22. https://doi.org/10.1029/2008GC001963.

Tikoff, Basil, and Christian Teyssier. 1992. “Bridges : A Possible Solution to the Batholithic Room Problem.” *Geology* 20: 927–30.

Venzke, E. 2020. “Volcanoes of the World, Global Volcanism Program.” Smithsonian Institution. https://doi.org/https://doi.org/10.5479/si.GVP.VOTW4-2013.

Ward, Peter L, James Gibbs, David Harlow, and Arturo Aburto Q. 1974. “Aftershocks of the Managua, Nicaragua, Earthquake and the Tectonic Significance of the Tiscapa Fault.” *Bulletin of the Seismological Society of America* 64 (4): 1017–29.

Weinberg, Roberto Ferrez. 1992. “Neotectonic Development of Western Nicaragua.” *Tectonics* 11 (5): 1010–17. https://doi.org/10.1029/92TC00859.

White, R. A., and D. H. Harlow. 1993. “Destructive Upper-Crustal Earthquakes of Central America since 1900.” *Bulletin of the Seismological Society of America* 83 (4): 1115–42.

Wyk De Vries, B. Van, and O. Merle. 1998. “Extension Induced by Volcanic Loading in Regional Strike-Slip Zones.” *Geology* 26 (11): 983–86. https://doi.org/10.1130/0091-7613(1998)026<0983:EIBVLI>2.3.CO;2.

Zeumann, Stefanie, and Andrea Hampel. 2017. “Impact of Cocos Ridge (Central America) Subduction on the Forearc Drainage System.” *Geology* 45 (10): 907–10. https://doi.org/10.1130/G39251.1.

Chapter 5
Dynamics of Trapdoor Faulting During the 2018 Sierra Negra Eruption

5.1 Introduction

The Sierra Negra volcano, in southern Isabela Island, Galapagos, Ecuador (Figure **5-1**), is a basaltic shield volcano where magma movement, fissure location, caldera morphology, and eruptive behavior diverges from its global analogs. Sierra Negra, like all volcanoes of the western province of the Galapagos, has circumferential and radial fissures (Reynolds et al., 1995; Harpp and Geist, 2018; Bell et al., 2021; Bagnardi et al., 2013; Chadwick and Dieterich, 1995; Corbi et al., 2015) and no rift system like that of Kilauea, Hawaii (Neal et al. 2019; Anderson et al. 2019; Tilling and Dvorak 1993) and Bardarbunga, Iceland (Sigmundsson et al., 2014; Gudmundsson et al., 2016). The Sierra Negra volcano is a hot-spot fed volcano, with 13 historical eruptions since 1813 (Siebert et al., 2011; D. J. Geist et al., 2008; Bell et al., 2021), and is the most voluminous shield volcano with the largest caldera in the western volcanic province of the Galapagos Islands (Reynolds et al., 1995; Munro and Rowland, 1996; Harpp and Geist, 2018). The summit caldera is 9.5 km by 7.5 km in extent and 100 m deep (Munro and Rowland, 1996; Harpp and Geist, 2018) and contains a ~14 km long arcuate sinuous ridge ringing the northern, western, and southern section of the caldera. The intra-caldera sinuous ridge is comprised of inward dipping reverse faults that were formed gradually over time by the pivoting of the caldera floor in a "trap door" fashion, leading to the western section rising above the caldera rim (Figures **5-1b & 5-2**; Reynolds et al., 1995; Jónsson et al., 2005; Bell et al., 2021). The Trap Door Fault (TDF), with its hinge in the northeast caldera, governs magma movement and eruptive fissure location (Munro and Rowland 1996; Jónsson 2009; Gregg et al., 2018; Bell et al., 2021). The TDF within the Sierra Negra caldera is also different from the piston-like caldera collapse that occurred during the 2018 eruption at Kilauea (Neal et al., 2019; Anderson et al., 2019).

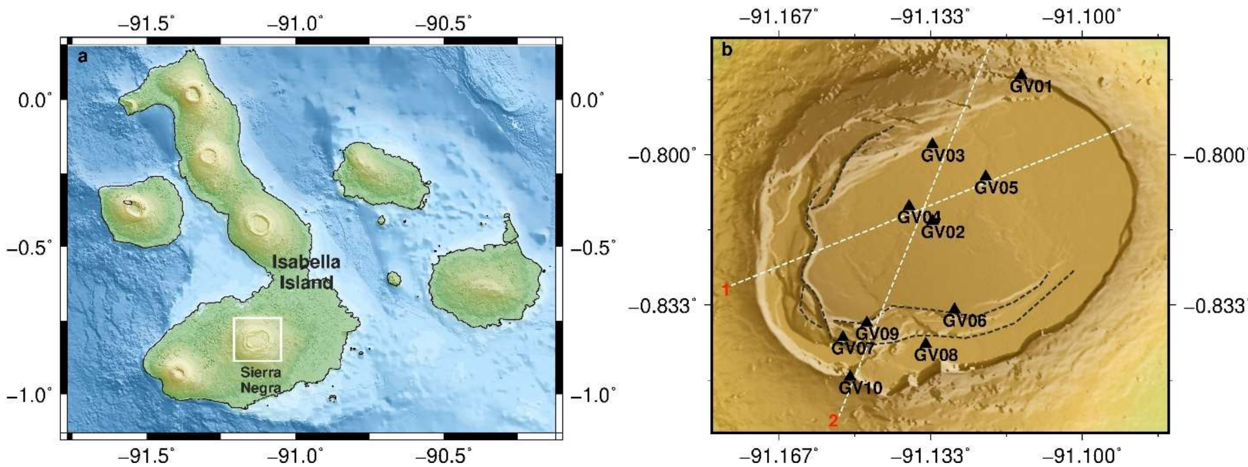

Figure **5-1**: a) Isabella Island, Galapagos, Ecuador with a white box highlighting summit caldera of Sierra Negra. Topography and bathymetry from ETOPO1 (Amante and Eakins 2009). b) Summit caldera of Sierra Negra where black triangles show the locations of GPS stations, sinuous ridge (dashed black lines) and topography profiles 1 and 2 (dashed white lines) in Figure **5-2**. Caldera DEM from Copernicus GLO-30 Digital Elevation Model.

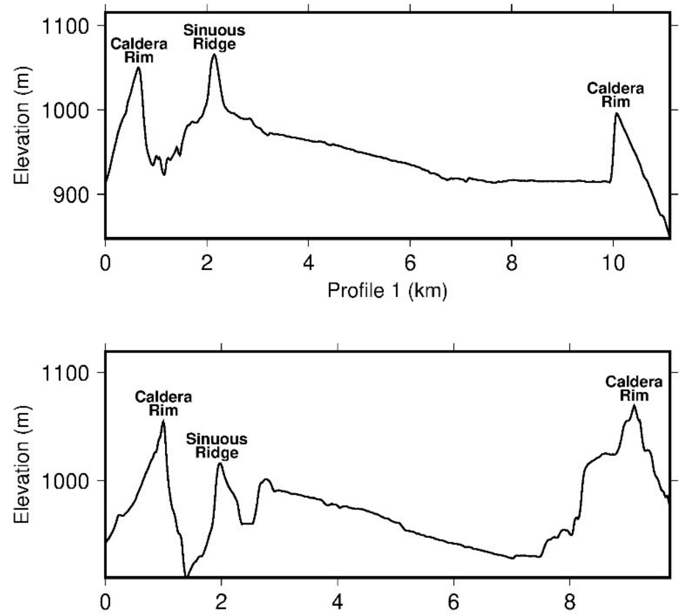

Figure **5-2**: Topographic profiles 1 and 2 (Copernicus GLO-30 Digital Elevation Model) across Sierra Negra caldera. Profile locations are dashed white line in Figure **5-1**.

Calderas are subcircular topographic depressions created by the collapse of a magma chamber, withdrawal or lateral migration of magma, or effusive or explosive eruptions (Cole et al., 2005;

Holohan et al., 2013; e.g., Gudmundsson et al., 2016; Howard et al., 2018;). The vertical displacement on the TDF plays a role in the building a resurgent caldera, which is the cumulative result of inflation and deflation episodes throughout many (>1000) eruption cycles (Bell et al. 2021; Acocella 2007; Galetto et al. 2019). Caldera resurgence via inflation and deflation, along with sub-horizontal sill propagation and radial and circumferential fissures are the two components of building the shield volcanos of the western volcanic province of the Galapagos (Bell et al., 2021; Bagnardi et al., 2013; Galetto et al., 2019). Sierra Negra has gently sloping flanks but the upper flanks steepen towards the caldera rim, which is a feature of repetitive inflation and TDF events (Bell et al., 2021 and references therein).

The Trap Door Fault (TDF) is an intra-caldera fault system where, over the eruptive cycle of the October 22nd, 2005 and June 26th, 2018 eruptions, episodes of rapid vertical displacement have been observed (Amelung et al., 2000; Jónsson et al., 2005; Geist et al., 2006; Chadwick et al., 2006; Bell et al., 2021). The 2005 eruption was preceded 3 hours by a M_w 5.4 earthquake on the TDF (Geist et al., 2008) and, likewise, ~8 hours prior to the 2018 eruption, a M_w 5.3 earthquake occurred on the TDF (Bell et al., 2021). Prior to the October 15th, 2005 eruption, there was a mb 4.5 earthquake on April 16th that produced a maximum of 0.85 m uplift of the caldera floor (Geist et al. 2008). This indicates that the TDF is a feature that accommodates a portion of the uplift of the caldera floor. Previous authors have found the TDF to be an important component of the eruption dynamics of the Sierra Negra volcano. Amelung et al. (2000), using Interferometric Synthetic Aperture Radar (InSAR), with two scenes of the Sierra Negra caldera that span 1997 to 1998 (before the 2005 eruption), modeled an opening sill and displacements on the southern intra-caldera fault. The modeled fault had four segments and followed the mapped southern limb of the TDF. The authors' model results yielded a sill that was roughly the same extent of the caldera floor and at a depth of 2.3 km to 2.9 km with variable thickness. The authors' modeling of the TDF earthquake produced reverse slip of 1.2 m on the faults with a fixed dip of 75°. Chadwick et al. (2006), using both GPS and InSAR data, modeled the sill and the mb 4.6 April 16th, 2005 TDF earthquake before the October 22nd, 2005 eruption. The modeled sill was at a depth of 2.2 km, and the fault had a maximum of 1.9 m of reverse slip, with 13% percent of the slip being strike-slip, on a fault that had a dip of 71° and strike of 259°, a length of 3.3 km, and located along the southern limb of the TDF. The authors also performed Coulomb static stress change analysis and found that the stress change due to the faulting of the earthquake would prevent sill or dike growth further to the south of the caldera. Jonsson et al. (2009), using the same GPS and InSAR datasets as Chadwick et al. (2006), also modeled the sill and the April 16th TDF earthquake. The authors found the sill was at a depth of 2.2 km, and a maximum of 2 m reverse slip, with 16% being right-lateral strike-slip, on a 3 km long fault with a strike of 259° and dip of 71°. The previously mentioned studies and Yun et al. (2006) have all inverted geodetic data to determine that the sub-caldera sill is shallow, at ~2 km. This indicates that the down-dip width of the TDF is from the surface to ~2 km.

The TDF is also responsible for caldera growth where inflation and deflation episodes build the sinuous ridge (Figure **5-2**). This was observed before and after the 2018 eruption due to the benefit of a denser GPS and seismic network and that recorded events of rapid uplift and subsidence of the trapdoor. During the inflation period, GPS stations recorded a maximum of 6.5 m of inflation of the caldera floor (2005 to 2018) and from January 1st to June 26th there was 12 M_l >4 earthquakes on the TDF with mixed focal mechanisms that primarily indicate uplift (Figure **5-3**; Bell et al., 2021). The syn-eruption M_w 5.3 June 26th earthquake displaced GV09 vertically by 1.8 m and its focal mechanism suggests reverse slip with a strike-slip component (Bell et al., 2021). During the eruption, which ended on August 23rd there was a maximum of 8.5 m of subsidence of the caldera floor (Figure **5-4**) and 15 Ml >4 earthquakes on the TDF (Figure **5-3**) with focal mechanisms indicating mostly normal faulting**.** After the eruption, there was a net 1.5 m of uplift recorded at GV06 and GV09 (Bell et al., 2021). A portion of the recorded uplift and subsidence was due to earthquakes on the TDF (Bell et al., 2021). After the 70 day long deflation period, inflation immediately reinitiated (Bell et al., 2021). At the time of writing, since the 2018 eruption, there has been >2.0 m of uplift within the caldera floor (Figure **5-4**).

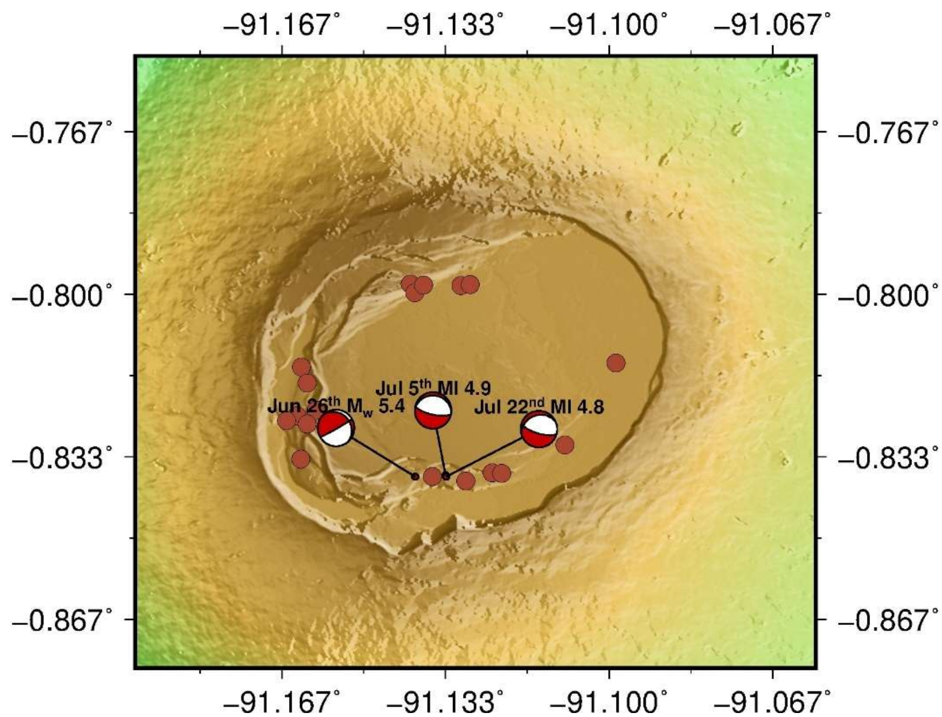

Figure **5-3**: Relocated earthquakes from Bell et al. (2021) with magnitudes greater than M_l 4. Earthquakes with focal mechanisms are earthquakes with magnitudes greater than M_l 4.8 that produced sufficient enough displacements to be used in this study. Aside from the June 26th earthquake, there were no M_l >5 earthquakes in the catalog.

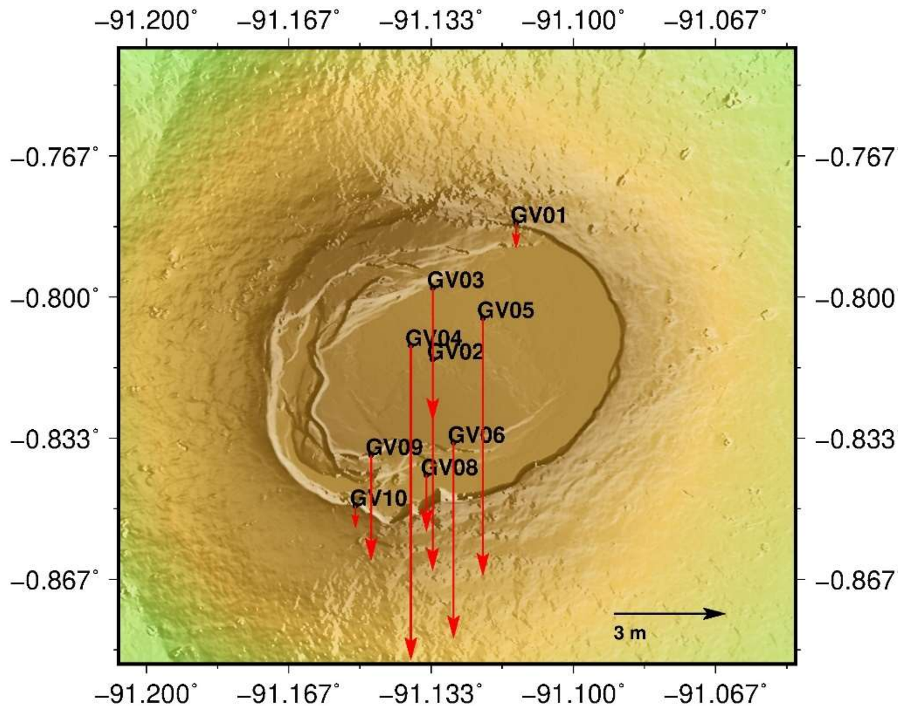

Figure **5-4**: GPS displacements during the deflation phase of the eruption (2018-06-26 to 2018-09-01).

Earthquakes on the TDF play an important role in magma movement and eruptive fissure location at the Sierra Negra volcano. Gregg et al. (2018) modeled the static stress after the Mw 5.4 earthquake that occurred 3 hours before the 2005 eruption, using a fault in the lower-left corner of the arcuate sinuous ridge. The authors chose the fault location, strike, and length based on observed GPS displacements. Their Coulomb static stress change models show that there was increased tensile stress in the northeastern caldera which is where the eruptive fissure was located. After the June 26th, 2018 earthquake, Bell et al. (2021) documented the movement of magma along the northern caldera rim and the eventual fissure opening located on the northeastern caldera rim. The authors calculated the normal stress change for the northern caldera faults system and found that the normal stress regime favored dike propagation along the northern caldera rim and fissure opening in the northeastern caldera rim.

Understanding the faulting events on the TDF is useful in forecasting future fissure locations and sill emplacement at this volcano and the processes of caldera building. This project will use high temporally sampled (30 s) continuous GPS data to model the fault orientation, geometry, and slip of the June 26th, 2018, M_w 5.3 earthquake that preceded the 2018 eruption, and deflation phase earthquakes that occurred on July 5th and July 22nd, with magnitudes of M_l 4.9 and M_l 4.8, respectively.

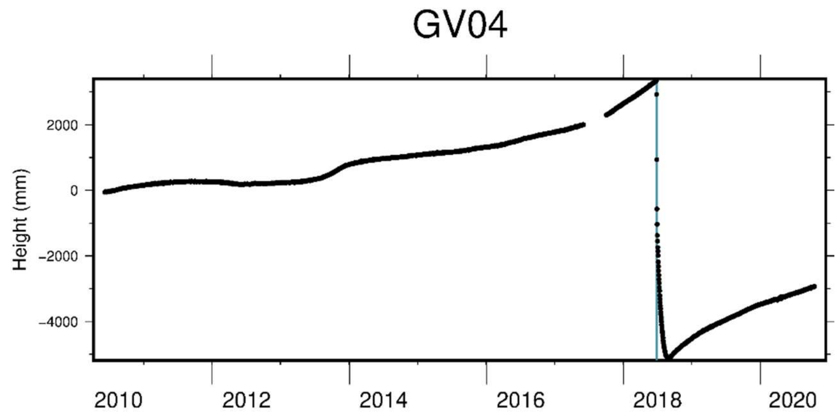

Figure **5-5:** Vertical time series for GPS station GV04. Blue line is the June 26th 2018 eruption. See Figure **5-3** for the location of GV04.

5.2 Data

This project uses high-rate (30-second interval) GPS positions to determine the faulting of the June 26th, July 5th, and 22nd earthquakes on the TDF. The use of high-rate positions was necessary due to the pre- and post-eruption dynamics where rapid inflation before the June 26th earthquake and the syn-eruption deflation would alias the earthquake displacements recorded in the GPS daily static positions (Figure **5-4**). There are 7 continuous GPS (cGPS) within the caldera and two cGPS stations on the caldera rim. Unfortunately, during these earthquakes, only 6 cGPS stations were operational at the time. The June 26th, July 5th, and 22nd earthquakes were also the only Ml >4.5 earthquakes that produced detectable offsets in the high-rate time series.

GPS high-rate data was processed using the kinematic processing procedures in the GIPSY-OASIS software. To limit the effects of the troposphere, tropospheric delays were first estimated, for each station, for the days of the earthquakes (see Malservisi et al., 2015). Tropospheric delays were estimated using the same approach as determining the daily static positions outlined in Chapters 2 and 3.

Earthquake displacements and uncertainties (Tables **5-1**, **5-2**, & **5-3**; Figures **5-6**, **5-7**, & **5-8**) were calculated by averaging positions one half hour before and after each earthquake. Figures **5-6**, **5-7**, and **5-8**, for comparison, also show the displacements and uncertainties from GPS daily static positions, which were calculated using GPS static positions 5 days before and 5 days after the earthquake (Appendix C; Tables **C-1**, **C-2**, & **C-3**). The GPS static daily position analysis is the same as previously described in estimating tropospheric delay. It should be noted that the uncertainties of the vertical displacements derived from high-rate analysis are consistently greater than 1 cm. In particular, the GV06 station has uncertainties of its vertical displacements of 10 cm for the July 5th and 22nd earthquakes.

Table **5-1**: Displacements for the M_w 5.3 June 26th earthquake.

Station	**Longitude**	**Latitude**	**Easting (mm)**	**Northing (mm)**	**Vertical (mm)**	**σE (mm)**	**σN (mm)**	**σV (mm)**
GV01	-91.113	-0.782	-87	-16	-20	5	7	16
GV05	-91.121	-0.805	-14	-19	-253	10	10	20
GV06	-91.128	-0.834	781	511	1425	7	9	17
GV08	-91.134	-0.842	508	-41	-272	9	9	22
GV09	-91.147	-0.837	841	-110	1834	6	6	29
GV10	-91.151	-0.849	227	36	-66	5	7	12

Table **5-2**: Displacements for the M_l 4.9 July 5th earthquake.

Station	**Longitude**	**Latitude**	**Easting (mm)**	**Northing (mm)**	**Vertical (mm)**	**σE (mm)**	**σN (mm)**	**σV (mm)**
GV01	-91.1134	-0.782	14	-1	-8	8	5	19
GV04	-91.1381	-0.811	-87	26	-64	13	7	29
GV06	-91.1281	-0.834	-230	-151	-730	31	20	100
GV08	-91.1344	-0.842	-286	1	146	39	9	28
GV09	-91.1474	-0.837	29	144	-153	6	20	24
GV10	-91.1511	-0.849	-28	-14	18	6	5	17

Table **5-3:** Displacements for the M_l 4.8 July 5th earthquake.

Station	**Longitude**	**Latitude**	**Easting (mm)**	**Northing (mm)**	**Vertical (mm)**	**σE (mm)**	**σN (mm)**	**σV (mm)**
GV01	-91.1134	-0.782	13	-1	-3	7	6	15
GV04	-91.1381	-0.811	-22	-3	-1	6	7	83
GV06	-91.1212	-0.805	-2	-5	-7	7	6	102
GV08	-91.1281	-0.834	-40	-63	-108	8	10	62
GV09	-91.1344	-0.842	-88	7	38	14	7	67
GV10	-91.1474	-0.837	-13	66	-64	5	11	65

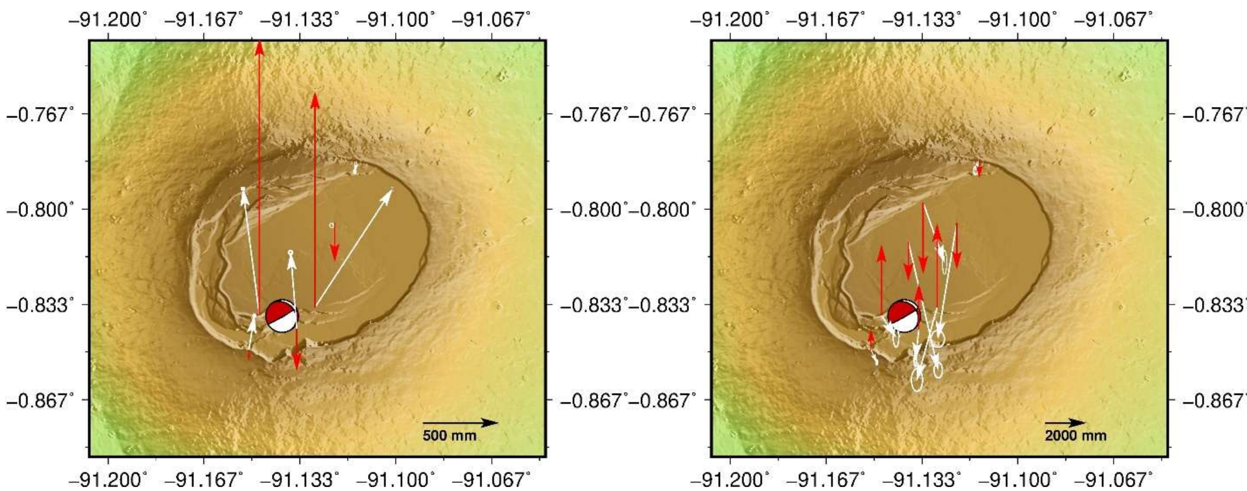

Figure **5-6**: Displacements for June 26th Mw 5.3 earthquake. Left- Displacements from high-rate GPS. Right – Displacements from daily GPS positions. White vectors are the observed horizontal displacements. Red vectors are the observed vertical displacements without error ellipses. Focal mechanism from Bell et al. (2021).

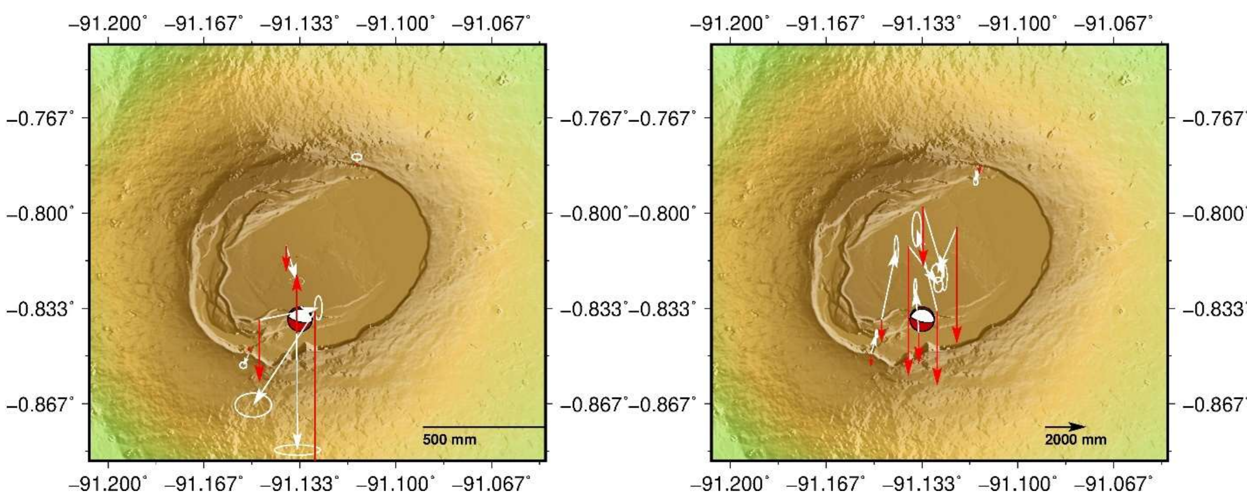

Figure **5-7**: Displacements for July 5th M_l 4.9 earthquake. Left – Displacements from high-rate GPS. Right – Displacements from daily GPS positions. White vectors are the observed horizontal displacements. Red vectors are the observed vertical displacements without error ellipses. Focal mechanism from Bell et al. (2021).

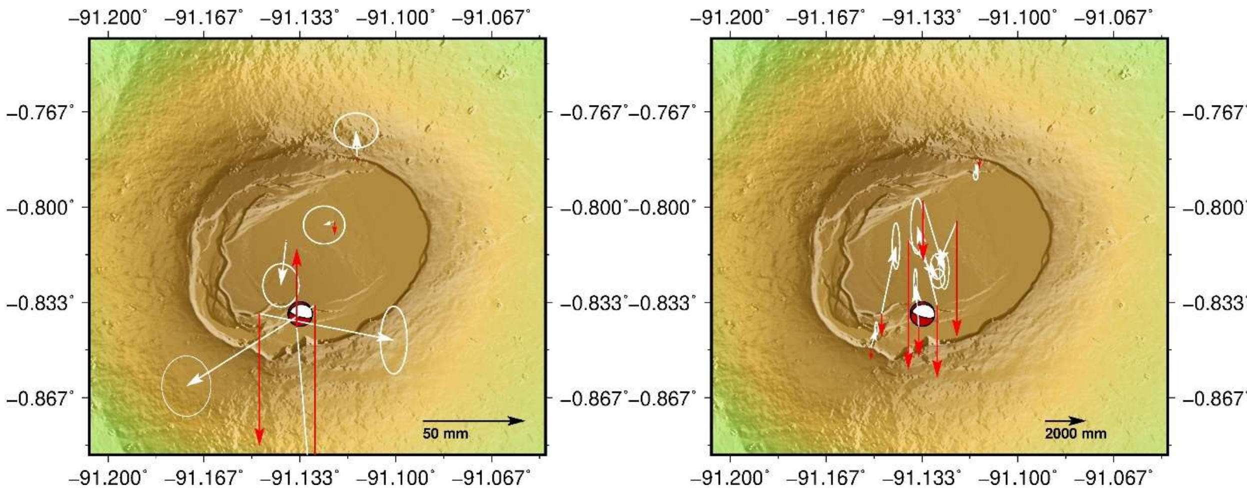

Figure **5-8**: Displacements for July 22nd M_l 4.8 earthquake. Left – Displacements from high-rate GPS. Right – Displacements from daily GPS positions. White vectors are the observed horizontal displacements. Red vectors are the observed vertical displacements without error ellipses. Focal mechanism from Bell et al. (2021).

5.3 Methods

The inversion strategy employed in Chapter 3 of this dissertation was also implemented in determining the faulting of the three M_l >4.8 TDF earthquakes. Inversion for the June 26th, 2018, M_w 5.3 July 5th, and 22nd earthquakes were constrained to the southern TDF. Unlike the methodology of Chapter 3, the surface trace of the fault was not inverted to find the start and end of the fault, instead, a midpoint, fault azimuth, and fault half-length were solved for during inversion. Inversion constraints of the June 26th, July 5th, and 22nd earthquakes are detailed in Tables **5-4**, **5-5**, and **5-6**, respectively. Stations GV06, GV08, and GV09 were downweighted due to their large vertical displacements during all three events and the stations possibly being in the damage zone of the TDF, which tends to amplify displacements (Manconi et al., 2007). Vertical displacements were also downweighted due to the large uncertainties for the inversion of the July 5th and 22nd earthquakes.

Table **5-4**: Inversion constraints for the June 26th earthquake.

Fault Midpoint Longitude	-91.128°
Fault Midpoint Latitude	-0.838°
Midpoint-x	± 2.5 km
Midpoint-y	± 0.5 km
70°< azimuth < 110°	
1 km < half-length < 4 km	
65°< dip < 90°	
0 km < fault top < 1 km	
1.0 km <fault width < 2.8 km	
0.3 < Poisson Ratio < 0.4	
0 m < right-lateral slip < 3 m	
1 m < reverse slip < 5 m	

Table **5-5**: Inversion constraints for the July 5th earthquake.

Fault Midpoint Longitude	-91.128°
Fault Midpoint Latitude	-0.838°
Midpoint-x	± 2.5 km
Midpoint-y	± 0.5 km
70°< azimuth < 110°	
1 km < half-length < 4 km	
65°< dip < 90°	
0 km < fault top < 1 km	
1.0 km <fault width < 2.8 km	
0.3 < Poisson Ratio < 0.4	
-3 m < right-lateral slip < 3 m	
1 m < reverse slip < 5 m	

Table **5-6**: Inversion constraints for the July 22nd earthquake.

Fault Midpoint Longitude	-91.128°
Fault Midpoint Latitude	-0.838°
Midpoint-x	± 2.5 km
Midpoint-y	± 0.5 km
70°< azimuth < 110°	
1 km < half-length < 4 km	
65°< dip < 90°	
0 km < fault top < 1 km	
1.0 km <fault width < 2.8 km	
0.3 < Poisson Ratio < 0.4	
-3 m < right-lateral slip < 3 m	
1 m < reverse slip < 5 m	

5.4 Results

The displacements due to the syn-eruption June 26th Mw 5.4 earthquake and the post-eruption July 5th M_l 4.9 and July 22nd M_l 4.8 earthquakes were inverted to characterize the faulting of the TDF and gain insight into building a resurgent caldera. The June 26th earthquake for one fault plane was inverted and constrained to the southern sinuous ridge. Likewise, the July 5th and July 22nd earthquakes were inverted for one fault plane with fault surface trace constrained to the southern limb of the sinuous ridge.

Inversion results for of the June 26th earthquake yielded a fault of length 4.8 km, a dip of 73°, a width from surface to 1.8 km, and a strike of 264° that closely approximates the mapped fractures of the sinuous ridge (Table **5-7**; Figure **5-9**). The model also yielded 1.8 meters of right-lateral slip and 4.5 m of reverse slip. The parameters' joint distribution and probability density function for this model is plotted in Figure **5-10** and Figure **5-11**, respectively.

Inversion of the July 5th and July 22nd normal faulting earthquakes were constrained the southern sinuous ridge. Results for the July 5th earthquake (Table **5-8**; Figure **5-12**) indicate that the fault did not rupture to the surface with the top of the fault being at 0.5 km. The width of the ruptured fault plane is 1.8 km. The model had 0.4 m of left-lateral slip and 3.2 m of dip-slip on a 1.7 km long fault that dips at 71° with a strike of 259°. The inversion results of the July 22nd earthquake also yielded a fault plane of 1.8 km in length and 0.9 km in width (Table **5-9**; Figure **5-13**) the top of the fault at a depth of 0.7 km, a width of 0.8 km, a dip of 81°, and a strike of 263°. The model yielded right-lateral slip of 0.4 m and dip-slip of 1.7 m. The parameter joint distributions and probability density functions for the inversions of the July 5th earthquakes are plotted in Figures **5-14** and **5-15**, respectively. The parameter joint distributions and probability density functions for and July 22nd earthquake are plotted in Figures **5-16** and **5-17**, respectively.

An inversion that did not allow right-lateral slip was performed for the July 22nd earthquake. That inversion produced a 2.1 km long fault, which had a fault top at a depth of 0.6, a width of 1.2 km, a dip of 77°, and a strike of 261° (Table **5-10**; Figure **5-18**). The inversion produced no strike-slip motion and 1.7 m of coseismic dip-slip. The parameter joint distributions and probability density functions for the inversion of the July 22nd earthquake that did not allow any right-slip are plotted in Figures **5-19** and **5-20**.

Table **5-7**: Results for June 26th earthquake for the one-fault model constrained to the southern sinuous ridge.

Strike	264° ± 4°
Dip	73° ± 4°
Fault Depth	0.2 ± 0.1 km
Fault Length	4.7 ± 0.4 km
Fault Width	1.5 ± 0.4 km
Strike-Slip Displacement	1.8 ± 0.7 m
Reverse Displacement	4.5 ± 1.1 m
Poisson Ratio	0.39 ± 0.1
Equivalent Mw	5.8
WRMS	29.26

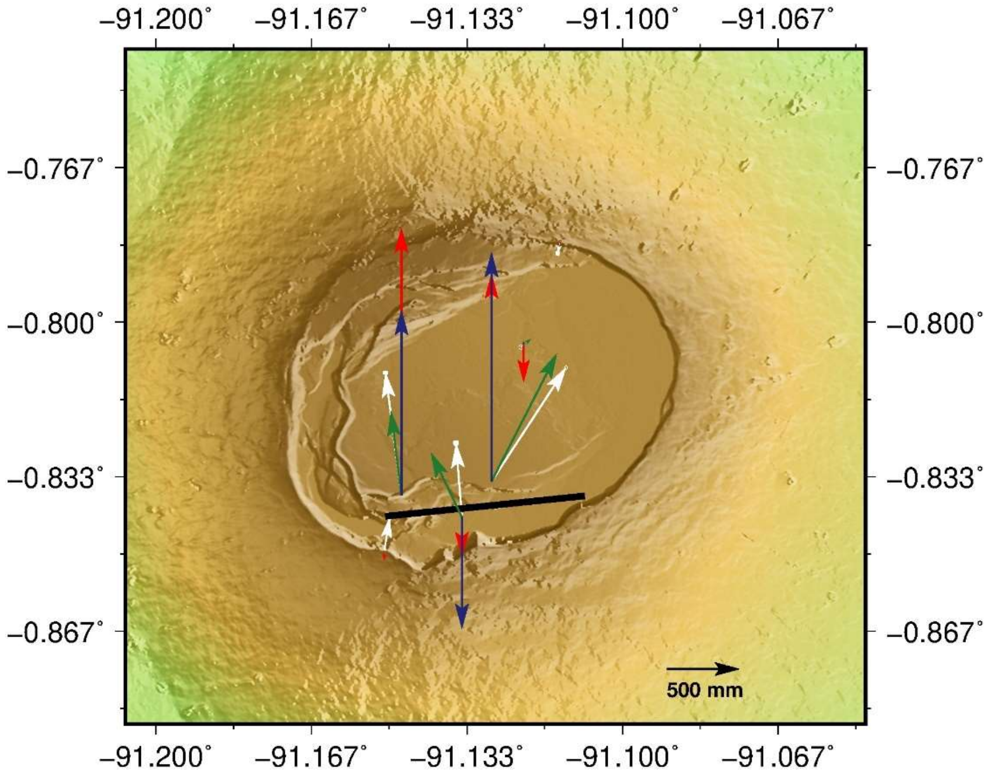

Figure **5-9**: Best-fitting model for June 26th one-fault model constrained to the southern sinuous ridge. Black line is the surface trace of the fault. White vectors are the observed horizontal displacements. Red vectors are the observed vertical displacements without error ellipses. Blue vectors are the modeled vertical displacements. Green vectors are the modeled horizontal displacements.

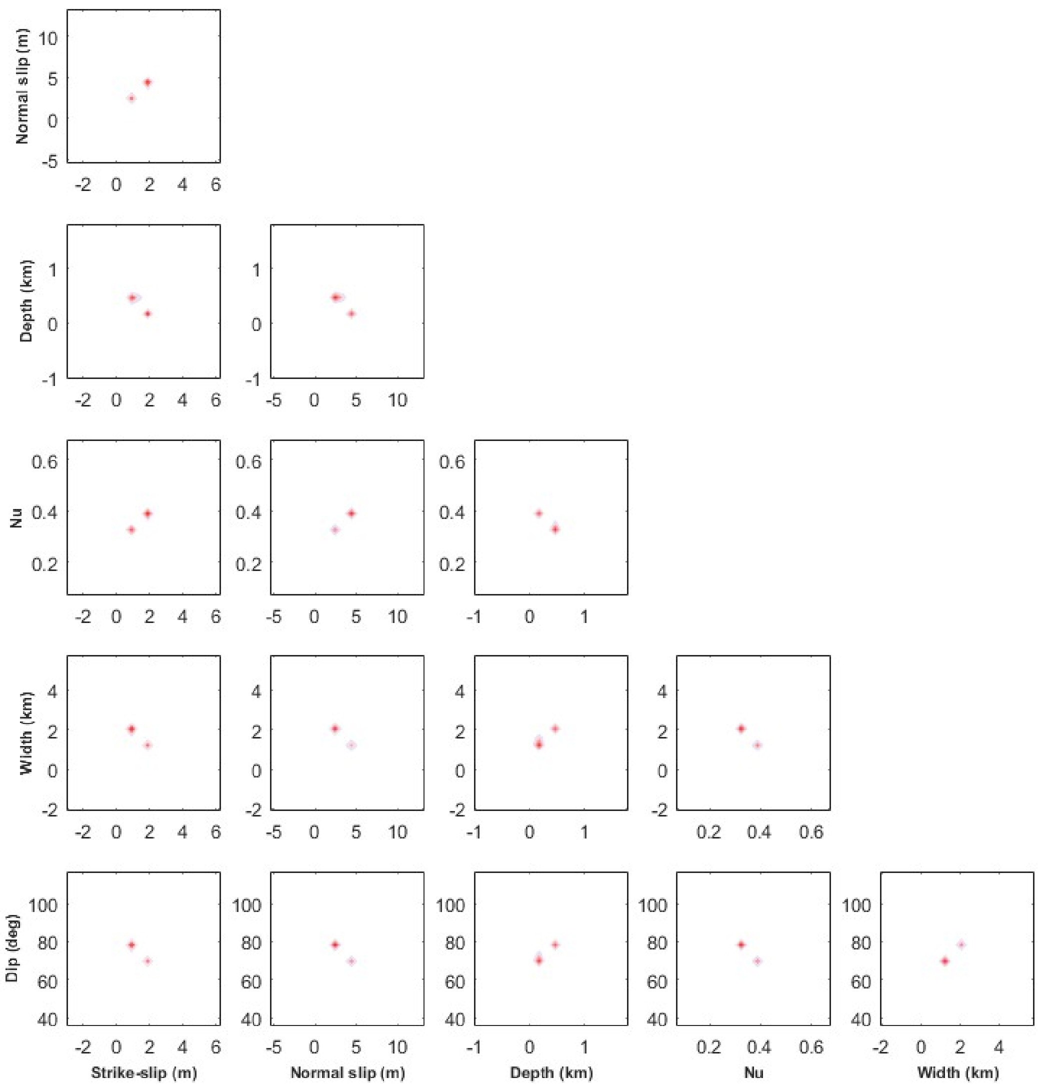

Figure **5-10**: Joint distribution, limited to 2σ, for inversion of the June 26th earthquake displacements that was constrained to the southern sinuous ridge.

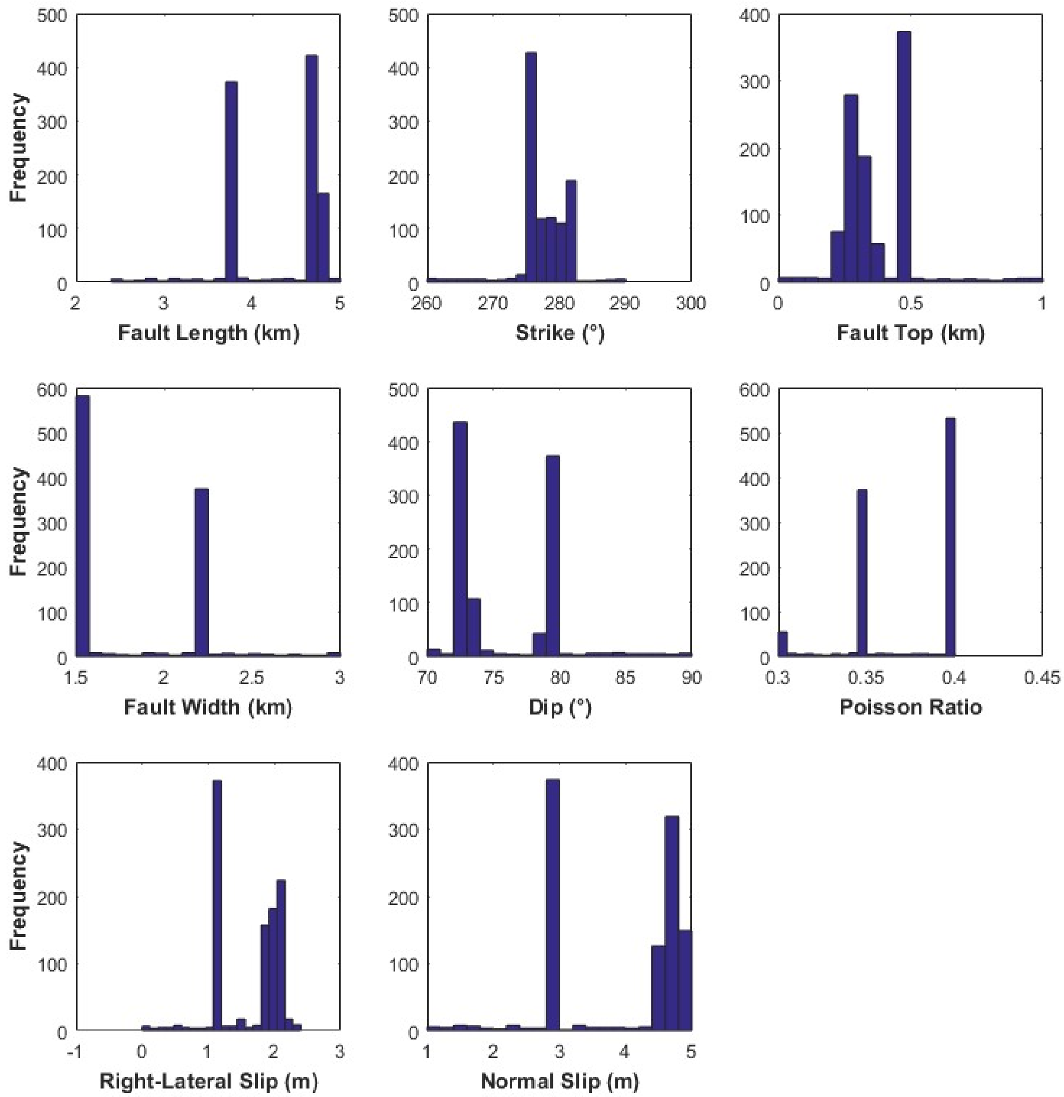

Figure **5-11**: Probability density functions for parameters for June 26th earthquake inversion.

Table **5-8**: Results for July 5th earthquake.

Strike	259° ± 1°
Dip	71° ± 0.01°
Fault Depth	0.5 ± 0.2 km
Fault Length	1.7 ± 0.3 km
Fault Width	1.8 ± 0.5 km
Strike-Slip Displacement	-0.4 ± 0.8 m
Reverse Displacement	-3.2 ± 1.2 m
Poisson Ratio	0.38 ± 0.1
Equivalent Mw	5.6
WRMS	2.42

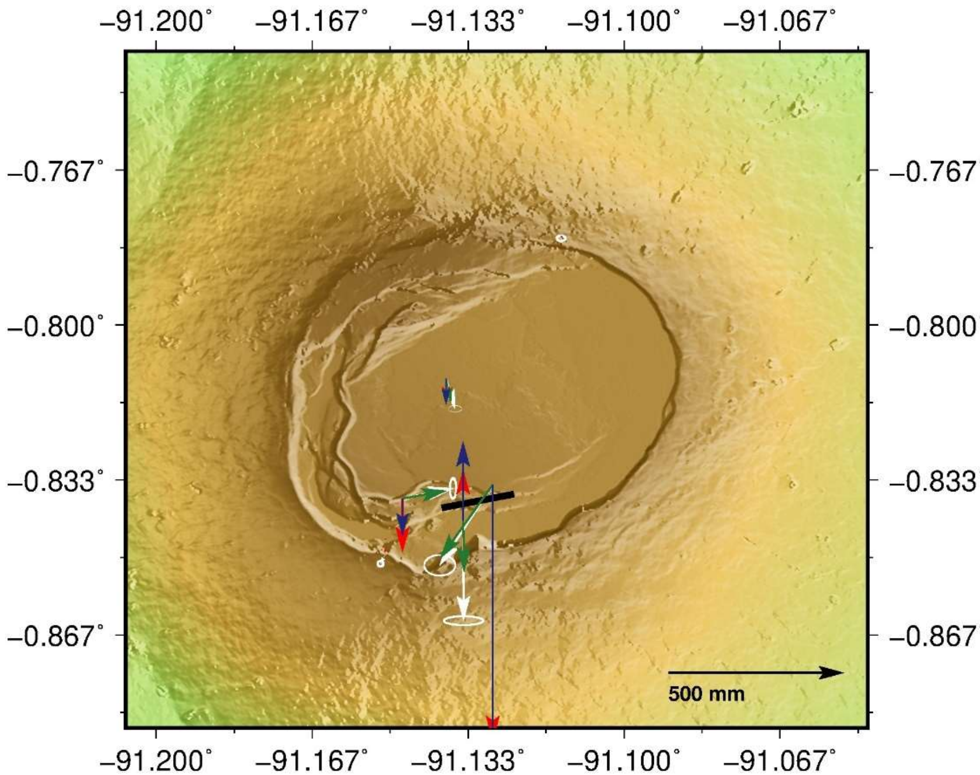

Figure **5-12**: Best-fitting model for July 5th one-fault model. Black line is the surface trace of the fault. White vectors are the observed horizontal displacements. Red vectors are the observed vertical displacements without error ellipses. Blue vectors are the modeled vertical displacements. Green vectors are the modeled horizontal displacements.

Table **5-9**: Results for July 22nd earthquake.

Strike	263° ± 1°
Dip	81° ± 0.1°
Fault Depth	0.6 ± 0.3 km
Fault Length	1.7 ± 0.4 km
Fault Width	0.9 ± 0.4 km
Strike-Slip Displacement	0.4 ± 0.8 m
Reverse Displacement	-1.7 ± 0.9 m
Poisson Ratio	0.38 ± 0.1
Equivalent Mw	5.2
WRMS	0.86

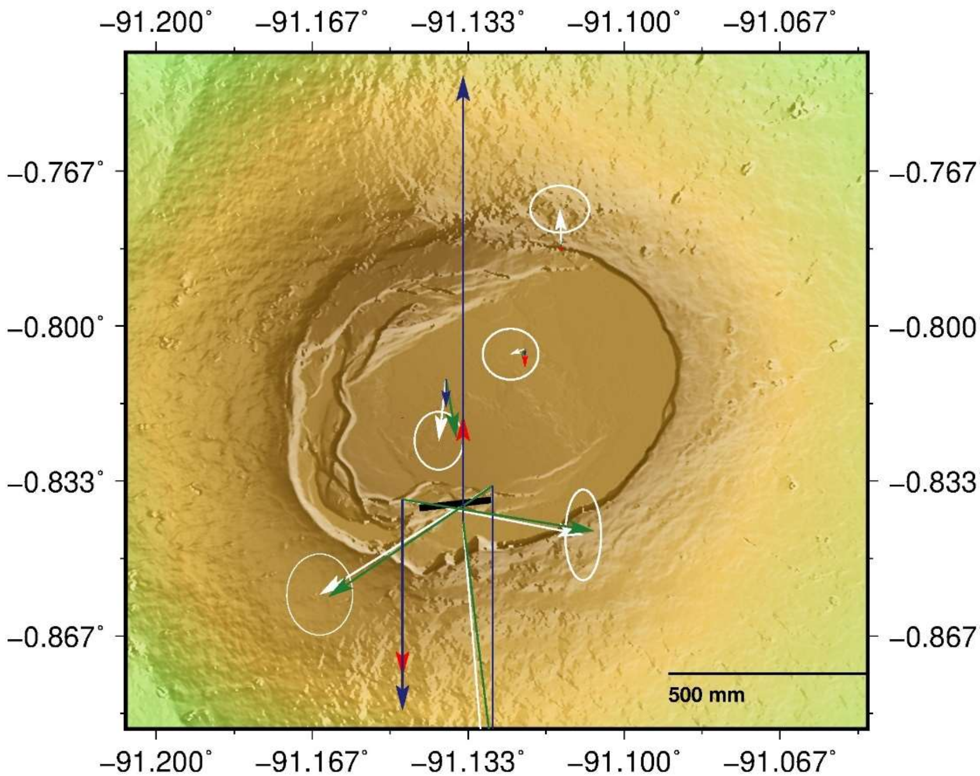

Figure **5-13**: Best-fitting model for July 22nd one-fault model. Black line is the surface trace of the fault. White vectors are the observed horizontal displacements. Red vectors are the observed vertical displacements without error ellipses. Blue vectors are the modeled vertical displacements. Green vectors are the modeled horizontal displacements.

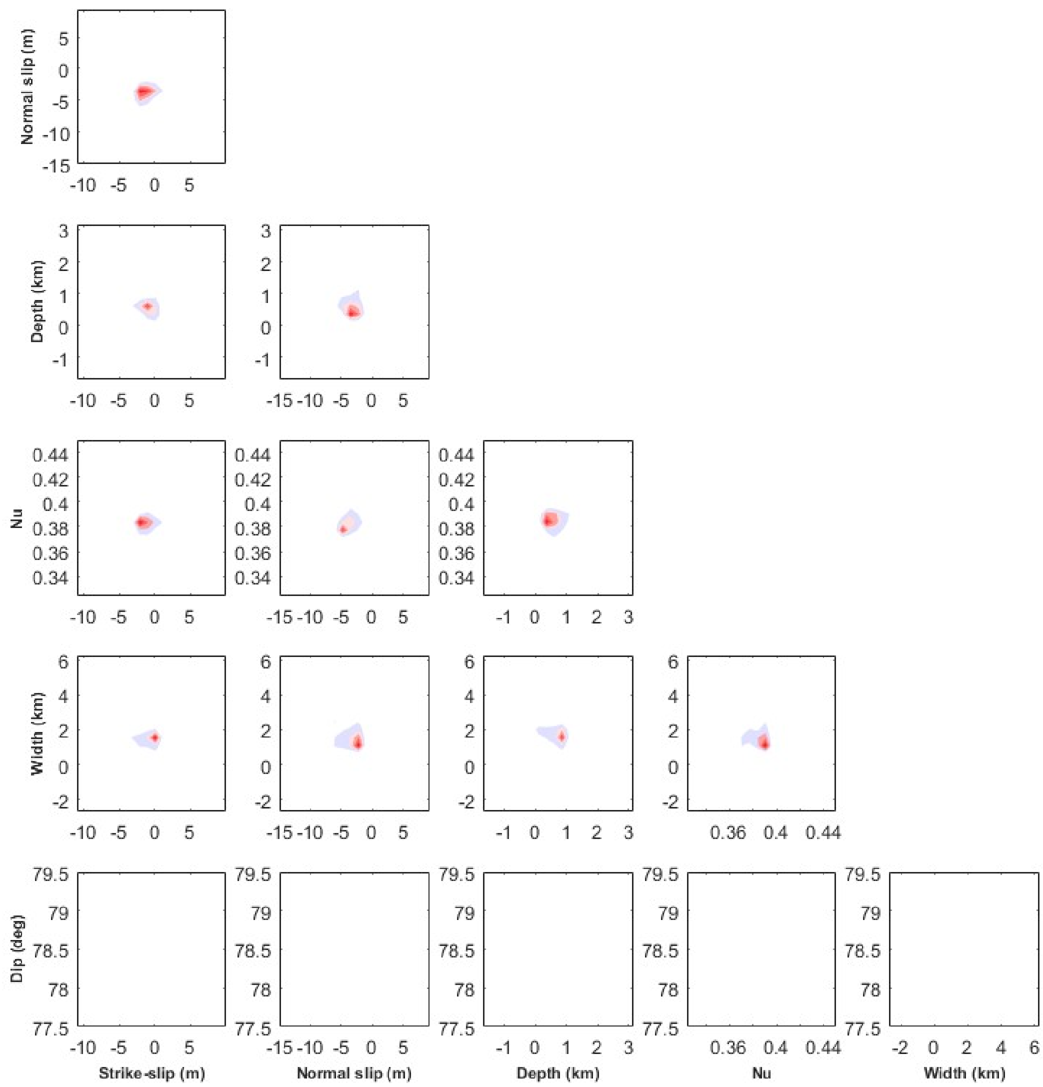

Figure **5-14:** Joint distribution, limited to 2σ, for inversion of the July 5th earthquake displacements. Plots with dip are not empty, the inversion produced a small standard deviation for the dip of 0.01°.

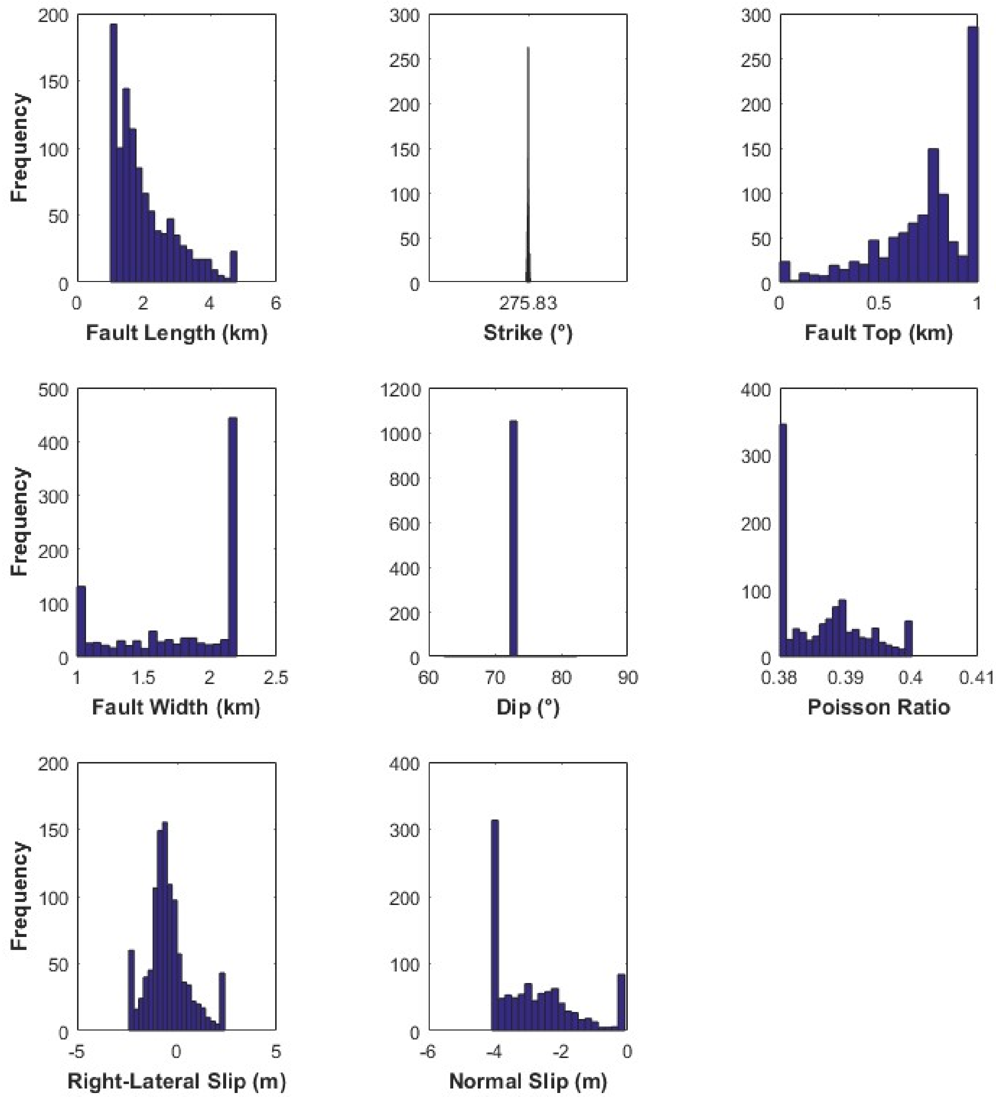

Figure **5-15**: Probability density functions for parameters for July 5th earthquake inversion.

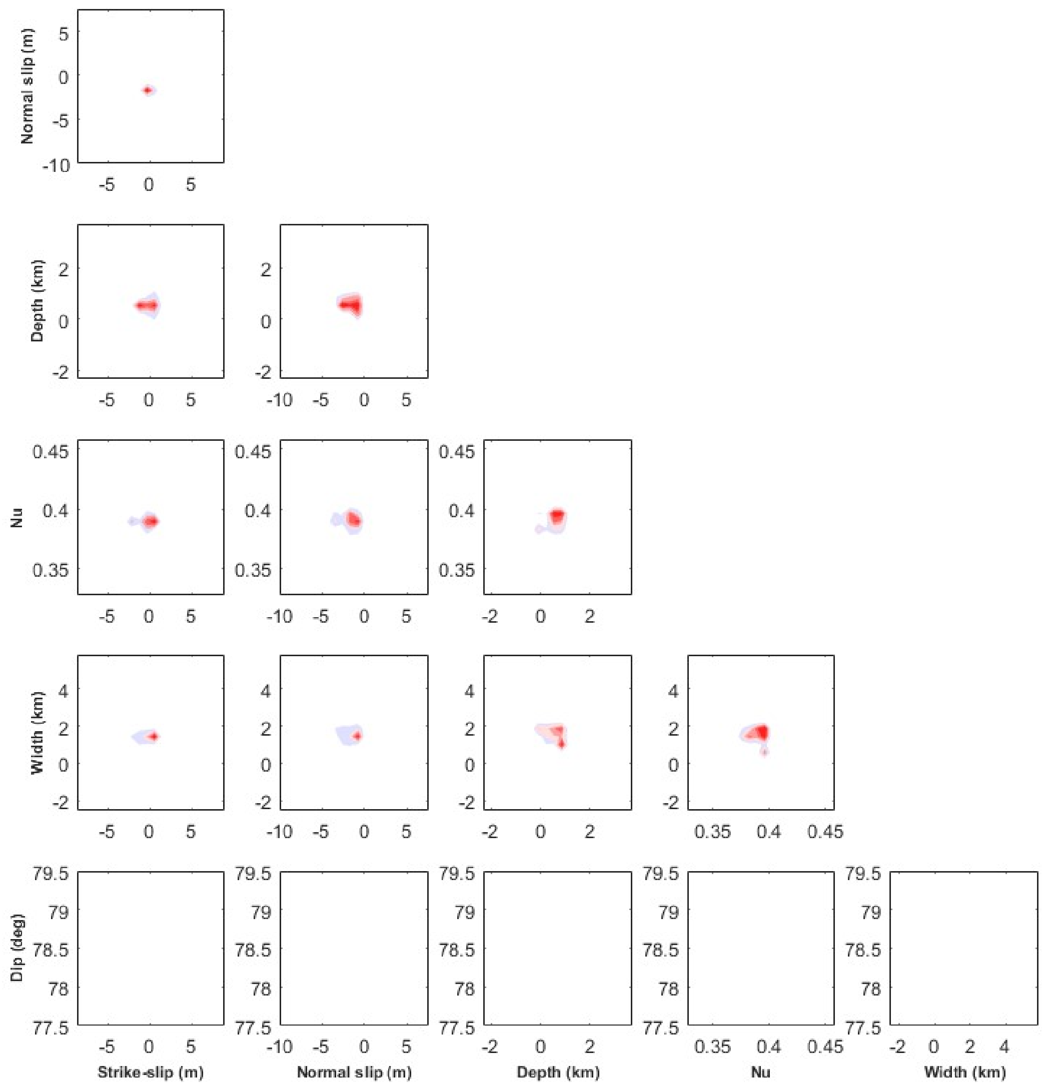

Figure **5-16**: Joint distribution, limited to 2σ, for inversion of the July 22nd earthquake displacements. Plots with dip are not empty, the inversion produced a small standard deviation for the dip of <0.01°.

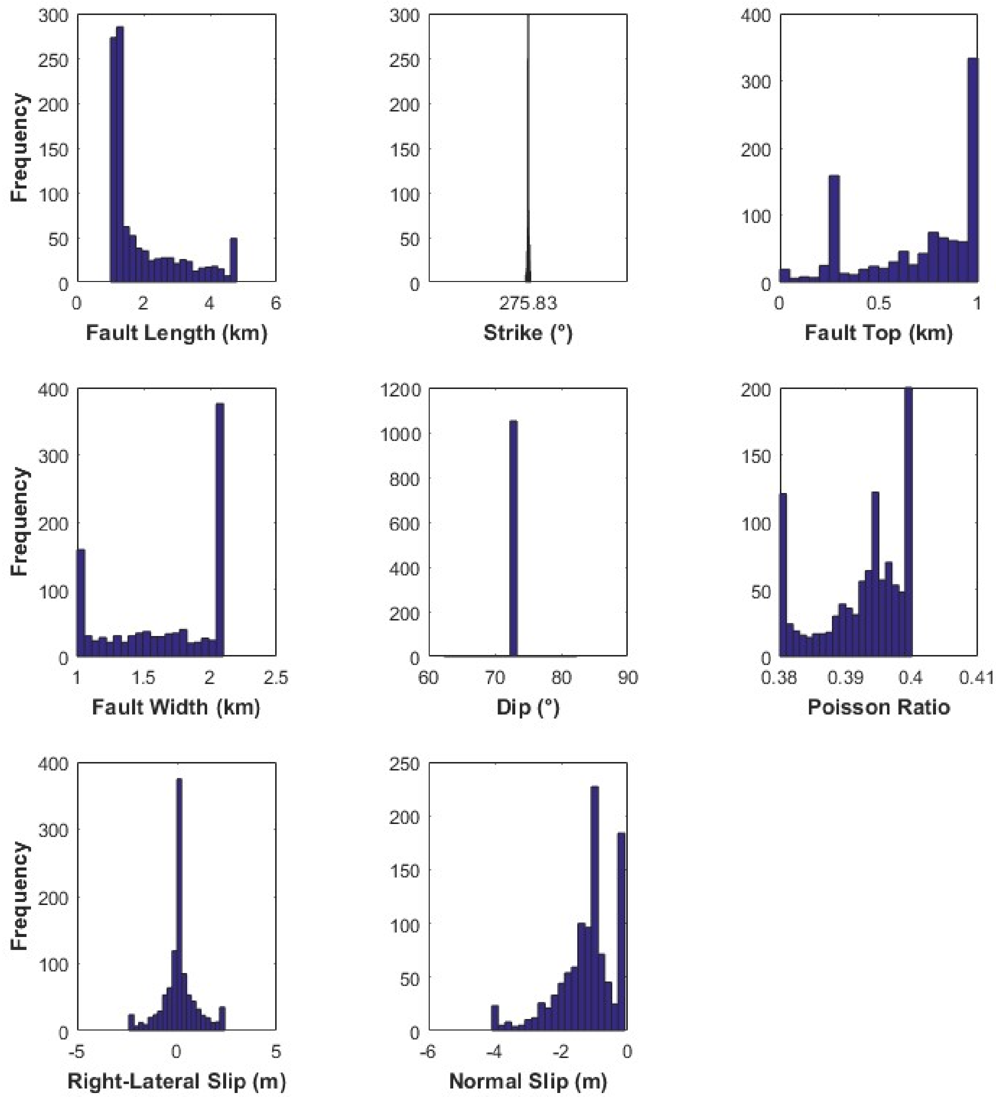

Figure **5-17**: Probability density functions for parameters for July 5th earthquake inversion.

Table **5-10**: Results for July 22nd earthquake that did not allow left-lateral slip.

Strike	262° ± 4°
Dip	77° ± 4°
Fault Depth	0.6 ± 0.1 km
Fault Length	2.1 ± 0.4 km
Fault Width	1.4 ± 0.4 km
Strike-Slip Displacement	0.0 ± 0.7 m
Reverse Displacement	1.2 ± 1.1 m
Poisson Ratio	0.39 ± 0.1
Equivalent Mw	5.2
WRMS	1.05

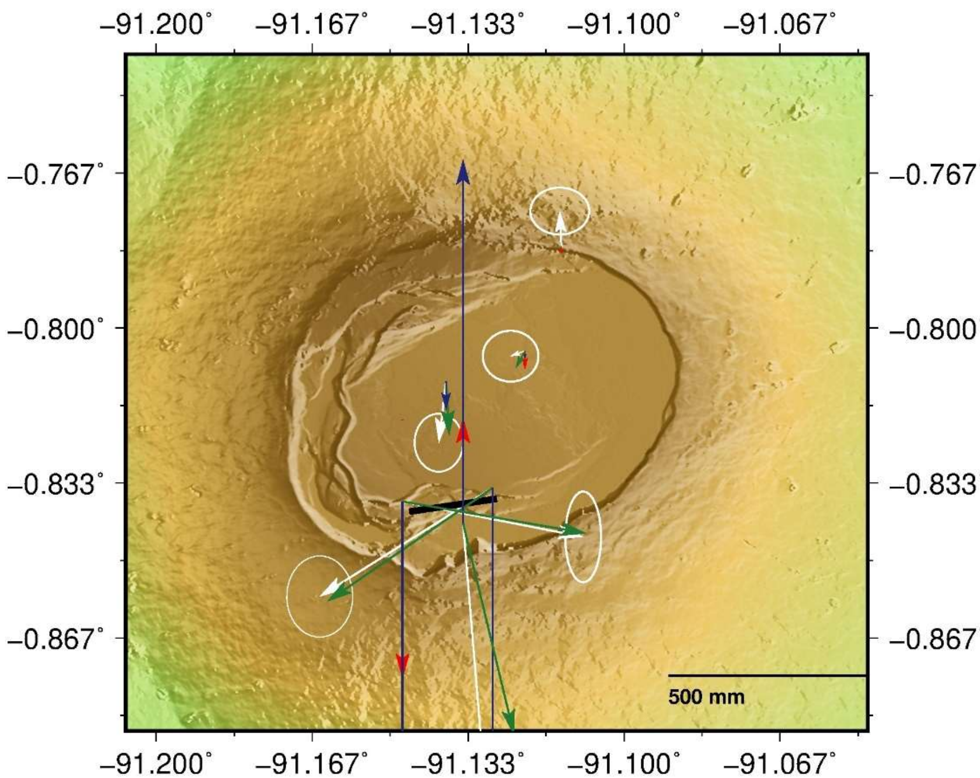

Figure **5-18**: Best-fitting model for July 22nd one-fault model that did not allow left-lateral slip. Black line is the surface trace of the fault. White vectors are the observed horizontal displacements. Red vectors are the observed vertical displacements without error ellipses. Blue vectors are the modeled vertical displacements. Green vectors are the modeled horizontal displacements.

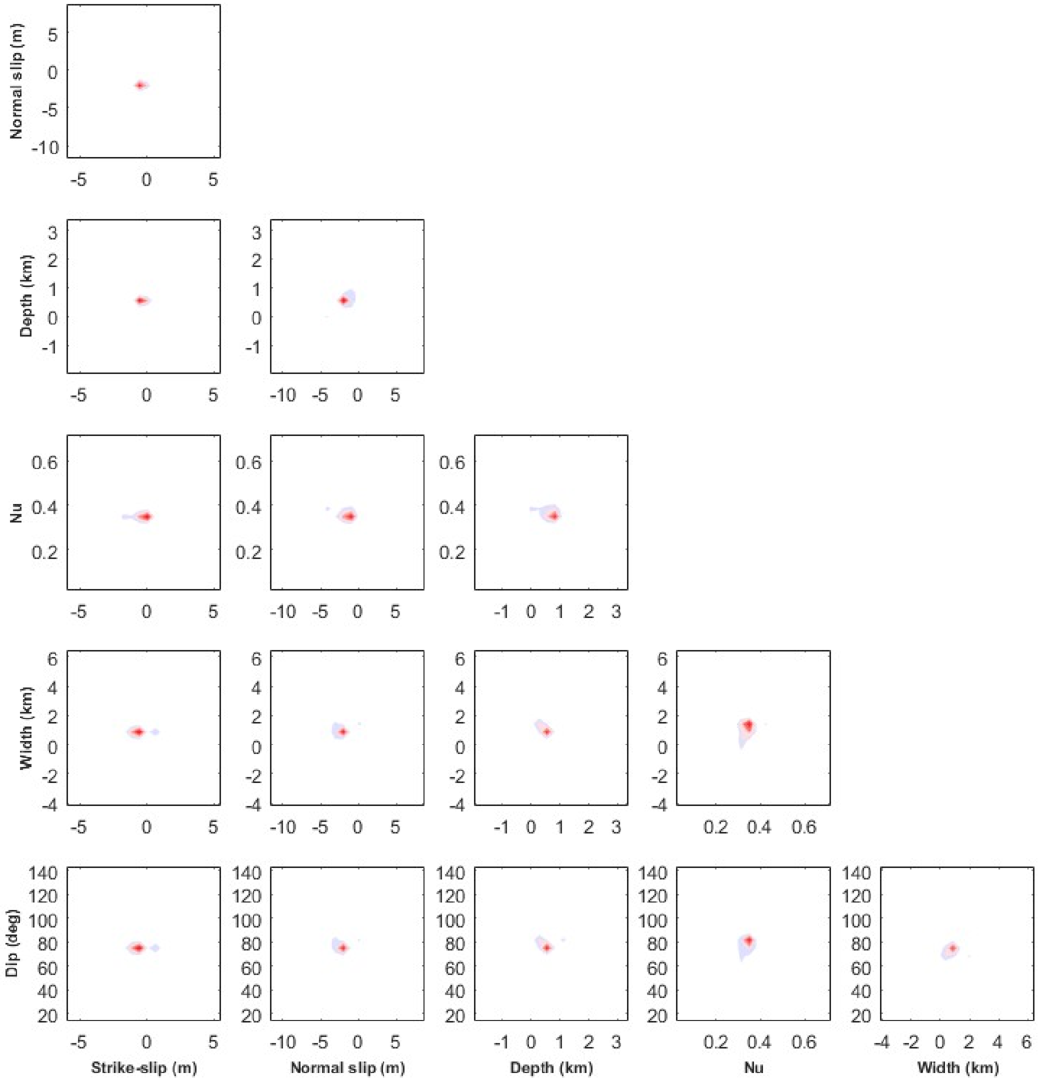

Figure **5-19**: Joint distribution, limited to 2σ, for inversion of the July 22nd earthquake displacements that did not allow right-lateral slip.

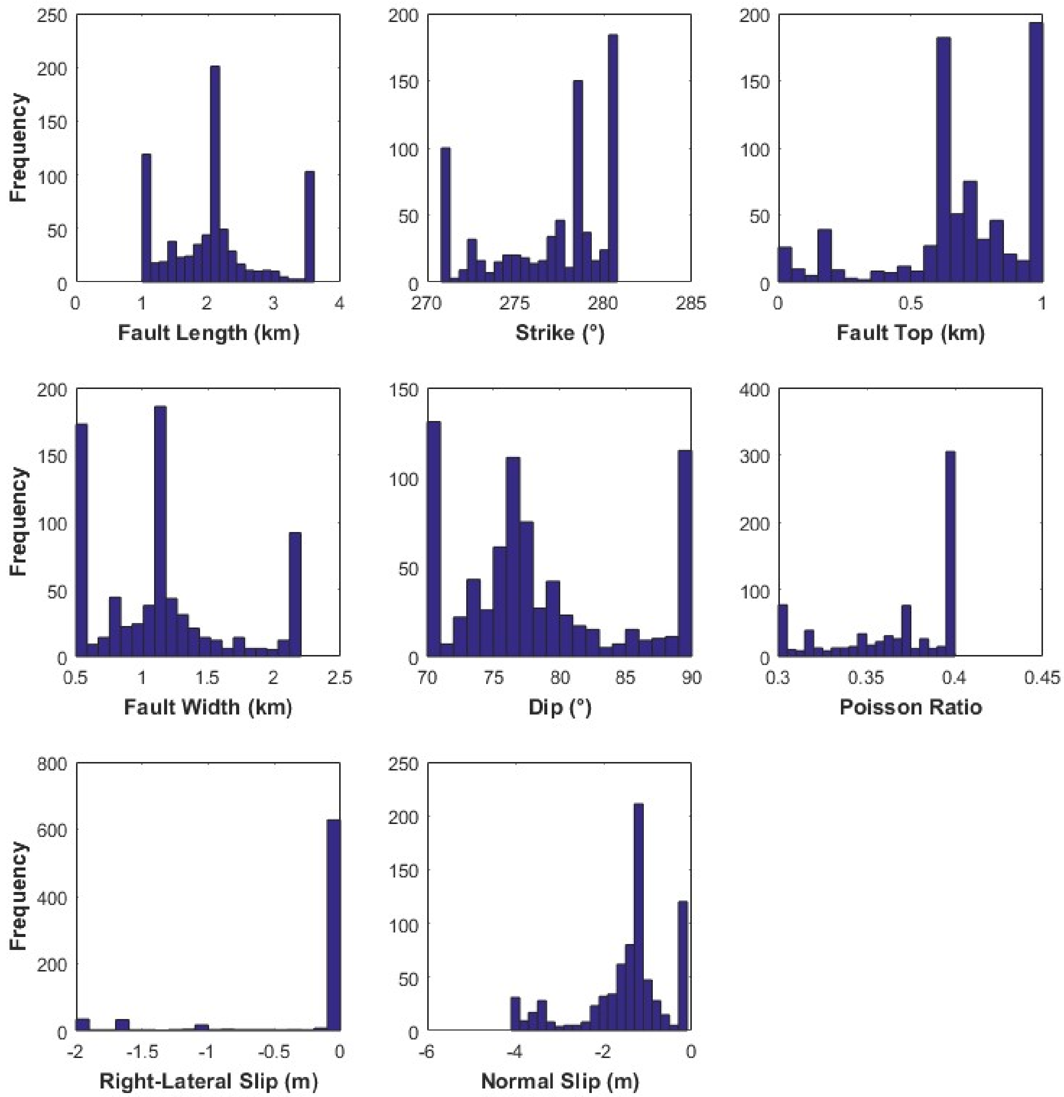

Figure **5-20**: Probability density functions for parameters for July 5th earthquake inversion that did not allow right-lateral slip.

5.4 Discussion

In many basaltic shield volcanos caldera collapse occurs due to magma withdrawal from a shallow reservoir. Such events occur over varying timescales, e.g., caldera collapse took 200+ days during the 2014 Bardarbunga eruption (Gudmundsson et al. 2016), and, during the 2018 Kilauea eruption, caldera collapse occurred over ~10 days (Neal et al., 2019). The 2005 and 2018 eruptions of the Sierra Negra volcano highlight the mechanism by which it undergoes caldera subsidence via trapdoor faulting after the shallow magma reservoir had been drained (Bell et al., 2021; and references therein). The 2018 eruption benefited from having a denser seismic network and more operational GPS stations compared to the 2005 eruption and offered an opportunity to observe the rapid uplift and subsidence of the caldera floor via earthquakes on the TDF. The observations also highlights that the TDF is a key component in building the resurgent caldera as there was a net vertical displacement of ~1.5 m near the TDF (Bell et al., 2021). Using GPS displacements this project explored the faulting of the 2018 TDF earthquakes that were a source of rapid uplift and subsidence. These earthquakes were the syn-eruption June 26th M_w 5.3, July 5th M_l 4.9 and July 22nd M_l 4.8 earthquakes. The results of this project show that significant slip is required to raise and subside the Sierra Negra caldera floor, which is key for caldera resurgence.

The best-fitting model for the June 26th earthquake places the fault on mapped fractures of the southern sinuous ridge, with a fault width from the surface to the sill (1.5 km to 2 km; Amelung et al., 2000; Chadwick et al., 2006; Jónsson, 2009; Yun et al., 2006). The model yielded coseismic slip in both strike-slip and dip-slip that were above 1 m, with 28% of the slip being right-lateral and 72% being dip-slip slip (reverse faulting). This slip is supported by the focal mechanism for this earthquake, which indicates oblique-slip with a right-lateral component (Figure **5-6**). The morphology of the western intra-caldera faults (Figure **5-1b**) also lends credence to the slip derived by this model. The western sinuous ridge is steeper (Figure **5-2**, Profile 1) compared to the southern section of the sinuous ridge (Figure **5-2**, Profile 2; Reynolds et al., 1995). Repetitive TDF earthquakes with a significant amount of right-lateral slip would be required to move the caldera floor to create these well-expressed fault scarps. This would be a long-lived feature if there is ongoing caldera resurgence and syn-eruption earthquakes are larger than the earthquakes during the deflation period, which was the case in the 2018 eruption.

Inversion results of the July 5th and 22nd earthquakes show events of quick subsidence of the trapdoor after the eruption. The coseismic motion of the July 5th earthquake was left-lateral with normal faulting. A model of the July 22nd earthquake yielded right-lateral and normal faulting with a fault width of 0.9 km. The inversion that did not allow right-lateral slip for the July 22nd earthquake produced pure dip-slip (normal faulting) with a fault width of 1.4 km, which is comparable to the July 5th earthquake. The more agreeable fault width of the July 22nd inversion that did not allow right-lateral motion makes this model the preferred model. Models of both earthquakes indicate that there was a total of 4.3 m of rapid dip-slip motion on the TDF. The results also show that, for these two earthquakes, the TDF did not rupture at the surface but at depths ~0.5 km to ~2 km. It is possible the lower 2 km portions of the TDF recovered the vertical displacements during inflation, where there were many reverse faulting earthquakes during this period, including the syn-eruptive June 26th earthquake. This is in line with the thermomechanical modeling that was performed by Gregg et al. (2018). The authors modeling of the inflating sill prior to the 2005 eruption shows that increase in temperature of the host rock is critical in limiting stress accumulation and preventing sill failure. They conclude that weakened (lower elastic moduli) host rocks allowed for prolonged inflation of a stable sill without dike propagation. The rocks down-dip the interface of the TDF may be weaker than those further up-dip. It might also be possible that the top 0.5 km of the TDF is a compliant zone that does not behave elastically. Regardless, the rupturing of the TDF at downdip depths of 0.5 km to the sill after an eruption may also be a component of caldera resurgence. July 5th and 22nd earthquakes are a very small fraction of the total seismic moment released by the southern limb of the TDF during the deflation phase (Figure **5-21**). However, the July 5th and 22nd earthquakes indicate that not all of the TDF slips in large earthquakes and that some parts of the upper portions of the TDF interface are fixed to some degree, leading to the net increase in uplift observed over the eruption. The surface traces of the July 5th and 22nd earthquakes are coincident and fall on the sinuous ridge (Figure **5-22**) implying that the earthquakes happened on the same fault. The surface traces also have strikes that are similar to the June 26th fault but are offset to the north by 0.3 km, which indicates a sub-parallel ring fault system, which is supported by the anastomosing southern sinuous ridge (Figure **5-22**).

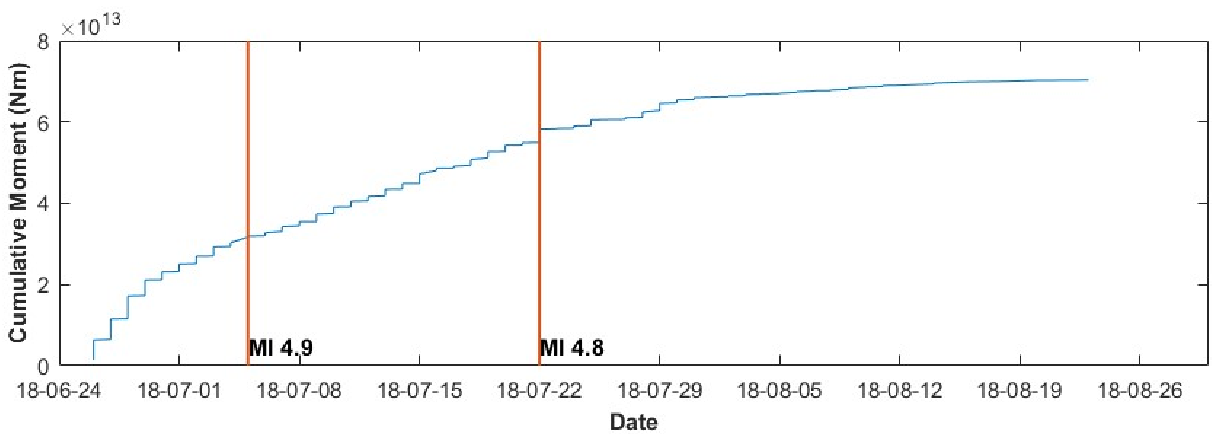

Figure **5-21**: Cumulative moment release for earthquakes for the deflationary period of June 26th, 2018 to September 1st, 2018. Earthquakes are from the relocated catalog of Bell et al. (2021). Earthquakes used in the analysis are those associated with the southern limb of the sinuous ridge.

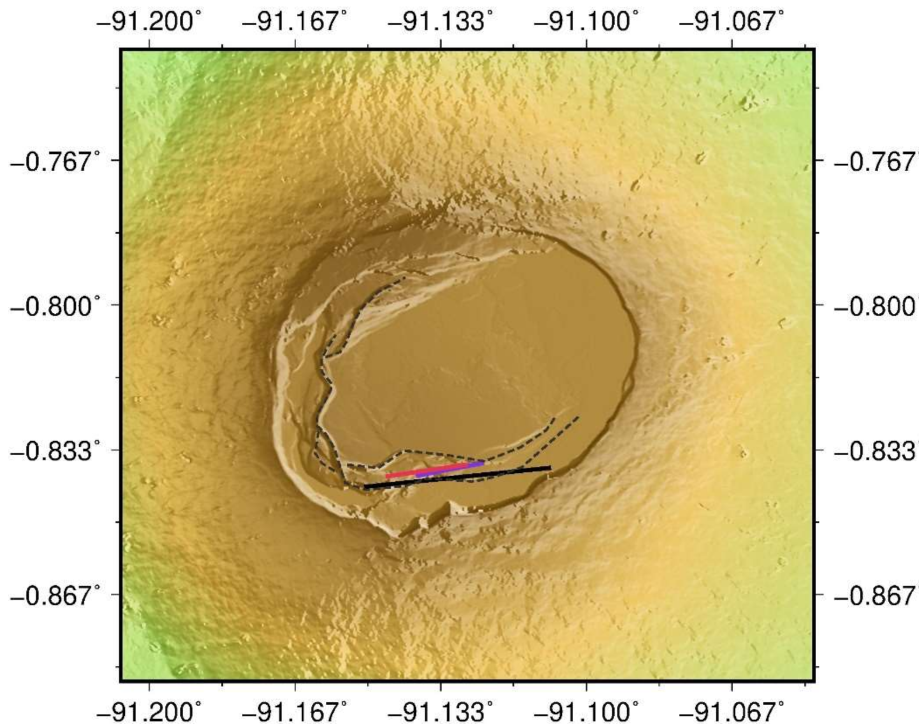

Figure **5-22**: Surface traces for all earthquakes. Black line is the fault trace for the June 26th earthquake. Purple line is the fault trace for the July 5th earthquake. Red line is the fault trace of the July 22nd earthquake. Dashed line is outline of the sinuous ridge.

Model results of the June 26th Mw 5.3, July 5th M_l 4.9, and July 22nd M_l 4.8 earthquakes indicate the active TDF before and during the 2018 eruption is the ~5 km southern sinuous ridge. The total coseismic dip-slip (normal faulting) of the July earthquakes is 4.3 m compared to 4.5 m of dip-slip (reverse faulting) of the syn-eruption June 26th earthquake, which corroborates the net surface uplift of 1.5 m reported by Bell et al. (2021). The coseismic right-lateral displacement of the June 26th earthquake was 1.8 m while the total left-lateral coseismic displacement for the deflation period earthquakes is 0.4 m. This net right-lateral coseismic slip of 1.3 m on the TDF may be building the steep western sinuous ridge (Figure **5-2**) as the sill roof is being pushed to the south over eruptive cycles. Many of the best-fitting models did not well fit vertical displacements, and in some cases, some horizontal displacements, for GV08, GV09, and GV06. This is most likely because these stations are in the damage zone of the TDF and may not behave elastically and record amplified displacements. It also possible that the TDF has a more complex geometry that the number of data cannot resolve.

5.5 Conclusion

The earthquakes on the TDF play an important role in the caldera resurgence and magma movement at the Sierra Negra volcano. Modeling of the syn-eruption June 26th showed that the southern limb of the TDF ruptured with reverse dip-slip motion. Results for the July 5th and July 22nd earthquakes, both occurring during the deflation period, show that the events were normal faulting and southern TDF ruptured with dip-slip motion. The three earthquakes, which occurred over the course of the eruption, had a net coseismic dip-slip of 0.2 m, which is sufficient enough to produce the observed net uplift over the eruption, leading to building the resurgent caldera. These three earthquakes also had significant strike-slip components, which explains the steep western sinuous ridge as the sill roof is pushed to the south. The constraint in the location of the active TDF this project presents will aid in forecasting future eruptive fissure locations.

5.6 References

Acocella, Valerio. 2007. "Understanding Caldera Structure and Development: An Overview of Analogue Models Compared to Natural Calderas." *Earth-Science Reviews* 85 (3–4): 125–60. https://doi.org/10.1016/j.earscirev.2007.08.004.

Amante, C., and B. W. Eakins. 2009. "ETOPO1 1 Arc-Minute Global Relief Model: Procedures, Data Sources and Analysis." Boulder, Colorado.

Amelung, F., S. Jonsson, H. Zebker, and P. Segall. 2000. "Widespread Uplift and 'trapdoor' Faulting on Galapagos Volcanoes Observed with Radar Interferometry." *Nature* 407 (6807): 993–96. https://doi.org/10.1038/35039604.

Anderson, Kyle R., Ingrid A. Johanson, Matthew R. Patrick, Mengyang Gu, Paul Segall, Michael P. Poland, Emily K. Montgomery-Brown, and Asta Miklius. 2019. "Magma Reservoir Failure and the Onset of Caldera Collapse at Kīlauea Volcano in 2018." *Science* 366 (6470). https://doi.org/10.1126/science.aaz1822.

Bagnardi, Marco, Falk Amelung, and Michael P. Poland. 2013. "A New Model for the Growth of Basaltic Shields Based on Deformation of Fernandina Volcano, Galápagos Islands." *Earth and Planetary Science Letters* 377–378: 358–66. https://doi.org/10.1016/j.epsl.2013.07.016.

Bell, Andrew F., Peter C. La Femina, Mario Ruiz, Falk Amelung, Marco Bagnardi, Christopher J. Bean, Benjamin Bernard, et al. 2021. "Caldera Resurgence during the 2018 Eruption of Sierra Negra Volcano, Galápagos Islands." *Nature Communications* 12 (1): 1–9. https://doi.org/10.1038/s41467-021-21596-4.

Chadwick, W. W., and J. H. Dieterich. 1995. "Mechanical Modeling of Circumferential and Radial Dike Intrusion on Galapagos Volcanoes." *Journal of Volcanology and Geothermal Research* 66 (1–4): 37–52. https://doi.org/10.1016/0377-0273(94)00060-T.

Chadwick, William W., Dennis J. Geist, Sigurjón Jónsson, Michael Poland, Daniel J. Johnson, and Charles M. Meertens. 2006. "A Volcano Bursting at the Seams: Inflation, Faulting, and Eruption at Sierra Negra Volcano, Galápagos." *Geology* 34 (12): 1025–28. https://doi.org/10.1130/G22826A.1.

Cole, Jim W., D. M. Milner, and K. D. Spinks. 2005. "Calderas and Caldera Structures: A Review." *Earth-Science Reviews* 69 (1–2): 1–26. https://doi.org/10.1016/j.earscirev.2004.06.004.

Copernicus GLO-30 Digital Elevation Model. 2021. "Copernicus GLO-30 Digital Elevation Model." Sinergise. https://doi.org/10.5069/G9028PQB Accessed: 2021-05-25.

Corbi, F., E. Rivalta, V. Pinel, F. Maccaferri, M. Bagnardi, and V. Acocella. 2015. "How Caldera Collapse Shapes the Shallow Emplacement and Transfer of Magma in Active Volcanoes." *Earth and Planetary Science Letters* 431: 287–93. https://doi.org/10.1016/j.epsl.2015.09.028.

Galetto, Federico, Marco Bagnardi, Valerio Acocella, and Andrew Hooper. 2019. "Noneruptive Unrest at the Caldera of Alcedo Volcano (Galápagos Islands) Revealed by InSAR Data and Geodetic Modeling." *Journal of Geophysical Research: Solid Earth* 124 (4): 3365–81. https://doi.org/10.1029/2018JB017103.

Geist, Dennis, William Chadwick, and Daniel Johnson. 2006. "Results from New GPS and Gravity Monitoring Networks at Fernandina and Sierra Negra Volcanoes, Galápagos, 2000-2002." *Journal of Volcanology and Geothermal Research* 150 (1–3): 79–97. https://doi.org/10.1016/j.jvolgeores.2005.07.003.

Geist, Dennis J., Karen S. Harpp, Terry R. Naumann, Michael Poland, William W. Chadwick, Minard Hall, and Erika Rader. 2008. "The 2005 Eruption of Sierra Negra Volcano, Galápagos, Ecuador." *Bulletin of Volcanology* 70 (6): 655–73. https://doi.org/10.1007/s00445-007-0160-3.

Gregg, P. M., H. Le Mével, Y. Zhan, J. Dufek, D. Geist, and W. W. Chadwick. 2018. "Stress Triggering of the 2005 Eruption of Sierra Negra Volcano, Galápagos." *Geophysical Research*

Letters 45 (24): 13,288-13,297. https://doi.org/10.1029/2018GL080393.

Gudmundsson, Magnús T., Kristín Jónsdóttir, Andrew Hooper, Eoghan P. Holohan, Sæmundur A. Halldórsson, Benedikt G. Ófeigsson, Simone Cesca, et al. 2016. "Gradual Caldera Collapse at Bárdarbunga Volcano, Iceland, Regulated by Lateral Magma Outflow." *Science* 353 (6296). https://doi.org/10.1126/science.aaf8988.

Harpp, Karen S., and Dennis J. Geist. 2018. "The Evolution of Galápagos Volcanoes: An Alternative Perspective." *Frontiers in Earth Science* 6 (May): 1–16. https://doi.org/10.3389/feart.2018.00050.

Holohan, Eoghan P., Thomas R. Walter, Martin P.J. Schöpfer, John J. Walsh, Benjamin Van Wyk De Vries, and Valentin R. Troll. 2013. "Origins of Oblique-Slip Faulting during Caldera Subsidence." *Journal of Geophysical Research: Solid Earth* 118 (4): 1778–94. https://doi.org/10.1002/jgrb.50057.

Howard, Keith A, Tom Simkin, Dennis J Geist, Godfrey Merlen, and Bruce Nolf. 2018. "Large Hydromagmatic Eruption Related to Fernandina Volcano's 1968 Caldera Collapse—Deposits, Landforms, and Ecosystem Recovery." *Field Volcanology: A Tribute to the Distinguished Career of Don Swanson, Special Paper* 538: 385–408.

Jónsson, Sigurjón. 2009. "Stress Interaction between Magma Accumulation and Trapdoor Faulting on Sierra Negra Volcano, Galápagos." *Tectonophysics* 471 (1–2): 36–44. https://doi.org/10.1016/j.tecto.2008.08.005.

Jónsson, Sigurjón, Howard Zebker, and Falk Amelung. 2005. "On Trapdoor Faulting at Sierra Negra Volcano, Galápagos." *Journal of Volcanology and Geothermal Research* 144 (1-4 SPEC. ISS.): 59–71. https://doi.org/10.1016/j.jvolgeores.2004.11.029.

Malservisi, R., S.Y. Schwartz, N. Voss, M. Protti, V. Gonzalez, T.H. Dixon, Y. Jiang, et al. 2015. "Multiscale Postseismic Behavior on a Megathrust : The 2012 Nicoya Earthquake, Costa Rica." *Geochemistry, Geophysics, Geosystems* 1950 (September 2012): 1848–64. https://doi.org/10.1002/2015GC005794.Received.

Manconi, A., T. R. Walter, and F. Amelung. 2007. "Effects of Mechanical Layering on Volcano Deformation." *Geophysical Journal International* 170 (2): 952–58. https://doi.org/10.1111/j.1365-246X.2007.03449.x.

Massé, R P, and R E Needham. 1989. "NEIC-The National Earthquake Information Center." *Earthquakes & Volcanoes (USGS)* 21 (1): 4–44.

Munro, Duncan C., and Scott K. Rowland. 1996. "Caldera Morphology in the Western Galápagos and Implications for Volcano Eruptive Behavior and Mechanisms of Caldera Formation." *Journal of Volcanology and Geothermal Research* 72 (1–2): 85–100. https://doi.org/10.1016/0377-0273(95)00076-3.

Neal, C. A., S. R. Brantley, L. Antolik, J. L. Babb, and Etc. 2019. "The 2018 Rift Eruption and Summit Collapse of Kīlauea Volcano." *Science* 363 (January): 367–74.

Reynolds, R. W., D. Geist, and M. D. Kurz. 1995. "Physical Volcanology and Structural Development of Sierra Negra Volcano, Isabela Island, Galapagos Archipelago." *Geological Society of America Bulletin* 107 (12): 1398–1410. https://doi.org/10.1130/0016-7606(1995)107<1398:PVASDO>2.3.CO;2.

Siebert, Lee, Tom Simkin, and Paul Kimberly. 2011. *Volcanoes of the World*. Univ of California Press.

Sigmundsson, Freysteinn, Andrew Hooper, Sigrún Hreinsdóttir, Kristín S. Vogfjörd, Benedikt G. Ófeigsson, Elías Rafn Heimisson, Stéphanie Dumont, et al. 2014. "Segmented Lateral Dyke Growth in a Rifting Event at Bárðarbunga Volcanic System, Iceland." *Nature* 517 (7533). https://doi.org/10.1038/nature14111.

Tilling, Robert I., and John J. Dvorak. 1993. "Anatomy of a Basaltic Volcano." *Nature* 363 (6425):

125–33. https://doi.org/10.1038/363125a0.
Yun, S., P. Segall, and H. Zebker. 2006. "Constraints on Magma Chamber Geometry at Sierra Negra Volcano, Galápagos Islands, Based on InSAR Observations." *Journal of Volcanology and Geothermal Research* 150 (1–3): 232–43. https://doi.org/10.1016/j.jvolgeores.2005.07.009.

Appendix A

Strain Partitioning and Interseismic Fault Behavior Along the Caribbean-South American Transform Plate Boundary

A.1 GPS Velocities

Table **A-1:** GPS Velocities from this study Reinoza et al. (2015), Pérez et al. (2018), and Weber et al. (2020) in the ITRF2008 reference frame (Altamimi et al., 2012). Stations with an asterisk indicate reanalyzed cGPS velocities.

Station	**Long (°)**	**Lat (°)**	**Ve (mm/yr)**	**Vn (mm/yr)**	**σVe (mm/yr)**	**σVn (mm/yr)**
ALTA	-66.178	9.866	-5.1	9.2	0.5	0.5
ARI0	-63.749	10.511	11.1	12.3	0.2	0.2
ARR	-64.291	10.370	0.8	13.2	0.3	0.2
ARY0	-64.236	10.571	10.8	14.3	0.2	0.2
AUD0	-64.081	10.447	1.3	14.3	0.1	0.1
BIC0	-63.965	10.770	13.5	15.0	0.2	0.2
BLAN	-64.599	11.822	10.7	15.0	2.5	1.8
BNKR	10.340	-61.459	8.7	0.8	11.4	0.7
CAC0	-63.837	10.553	11.6	12.8	0.3	0.3
CALD*	-60.731	11.196	15.0	0.0	14.0	0.0
CAMB	11.320	-60.556	14.2	0.3	14.7	0.5
CASI	-66.960	9.926	-4.2	12.0	0.5	0.5
CHA0	-64.156	10.841	13.7	15.1	0.3	0.2
CN45*	-60.938	10.837	13.0	0.0	13.0	0.0
CN46*	-61.427	12.487	12.0	0.0	16.0	0.0
COI0	-63.116	10.415	-1.6	15.0	0.4	0.4
COR0	-64.184	10.831	13.9	15.1	0.3	0.2
COV0	-63.603	10.136	-2.7	13.2	0.2	0.2
CUMA	-64.195	10.429	1.2	15.0	0.1	0.1
FORT*	-61.683	10.171	-1.0	0.0	11.0	0.0
FTMD	11.154	-60.843	14.7	0.4	15.6	0.7
GAL0	-64.188	10.802	13.7	14.9	0.2	0.2
GALE*	-60.995	10.147	1.0	0.0	7.0	0.0

GRAN*	-61.128	10.586	12.0	0.0	12.0	0.0
GSPO	10.334	-61.423	-4.8	1.1	10.5	0.7
HOR0	-64.291	10.965	14.6	15.6	0.2	0.2
IPU0	-63.751	10.122	-2.9	12.0	1.0	0.9
ISL0	-63.896	10.884	14.7	14.7	0.2	0.2
LFAB	10.098	-61.658	-3.1	0.6	12.7	0.4
LLNE	10.081	-61.317	-3.3	0.7	10.9	0.8
MAN0	-63.895	11.156	15.0	14.6	1.0	0.9
MARG	-64.360	11.042	16.7	16.5	0.2	0.2
MAYO	10.359	-61.364	-5.4	2.2	8.9	1.3
MCH0	-63.811	10.707	13.2	15.0	0.2	0.2
MOC0	-64.344	10.346	-1.3	15.3	0.2	0.2
MTTB	10.681	-61.396	11.9	0.3	12.2	0.6
PALM	10.292	-61.406	-2.4	0.6	9.2	1.0
PAR0	-64.231	10.508	8.7	14.4	0.2	0.2
PCN0	-63.637	10.636	14.0	13.9	0.2	0.2
PER0	-63.767	10.446	-2.4	13.3	0.4	0.3
PIG0	-64.083	10.637	11.9	13.8	0.3	0.2
PLND	10.191	-61.602	-3.5	4.6	3.7	2.3
POST	10.649	-61.514	12.8	0.7	11.8	1.0
PPI0	-62.404	10.547	12.7	14.0	1.0	0.9
PUND	10.377	-61.419	11.8	0.9	11.8	0.3
RAG0	-62.974	10.582	15.0	15.1	0.4	0.4
RES0	-64.209	11.053	14.7	15.2	0.2	0.2
RIC0	-63.120	10.701	15.0	15.3	0.2	0.2
RQUE	-66.678	11.953	14.0	13.4	2.4	1.8
SAL0	-62.274	10.604	12.6	17.8	1.5	1.3
SMI1	-63.519	10.492	2.8	14.5	0.2	0.2
SMRY	10.185	-61.311	-5.4	1.7	7.8	0.7
SNDO	10.281	-61.459	-4.0	2.0	10.2	1.0
SRUX	10.653	-61.401	10.9	0.3	13.8	0.3
SUL0	-63.910	10.757	14.1	14.7	0.3	0.2
SVNH	10.669	-61.513	8.5	1.3	10.2	1.1
TAC0	-63.977	9.954	-3.8	16.3	0.3	0.3
TANK	10.395	-61.438	10.7	0.3	11.8	0.6

TET0	-64.127	10.963	14.9	15.7	0.3	0.3
TOR0	-63.569	10.352	-3.8	16.9	0.2	0.2
TORT	-65.227	10.963	13.3	13.3	2.0	1.7
TTPA	10.594	-61.347	10.9	1.5	14.8	1.2
TTSF*	-61.466	10.277	-2.0	0.0	10.0	0.0
TTUW*	-61.399	10.640	12.0	0.0	14.0	0.0
USB0	-66.792	10.409	-1.1	12.0	0.5	0.5
USB1	-66.883	10.411	-1.4	12.1	0.5	0.5
WESS	10.333	-61.425	-2.3	1.4	9.6	1.3

* Denotes cGPS.

A.2 InSAR Data

Figures A-1 and A-2 show interferograms where displacement is detected along-strike the CRF. Figure A-6 shows the perpendicular and temporal baselines for interferograms that were used in SBAS calculations. Figure S4 shows the interferograms that were used in SBAS calculated velocities. Figure A-5 shows the SBAS produced LOS velocities that appear to have planar trends that may be influenced by persistent atmospherics associated with the relief high of the CRF fault. There are two long-wavelength features in the SBAS calculated velocities (Figure A-5) that were further detrended (Figure A-7). Figure A-8 shows the change in relief of the Central Range, from west to east, which we believe is responsible for atmospheric errors in most interferograms. Profile I1 is across an area of low relief.

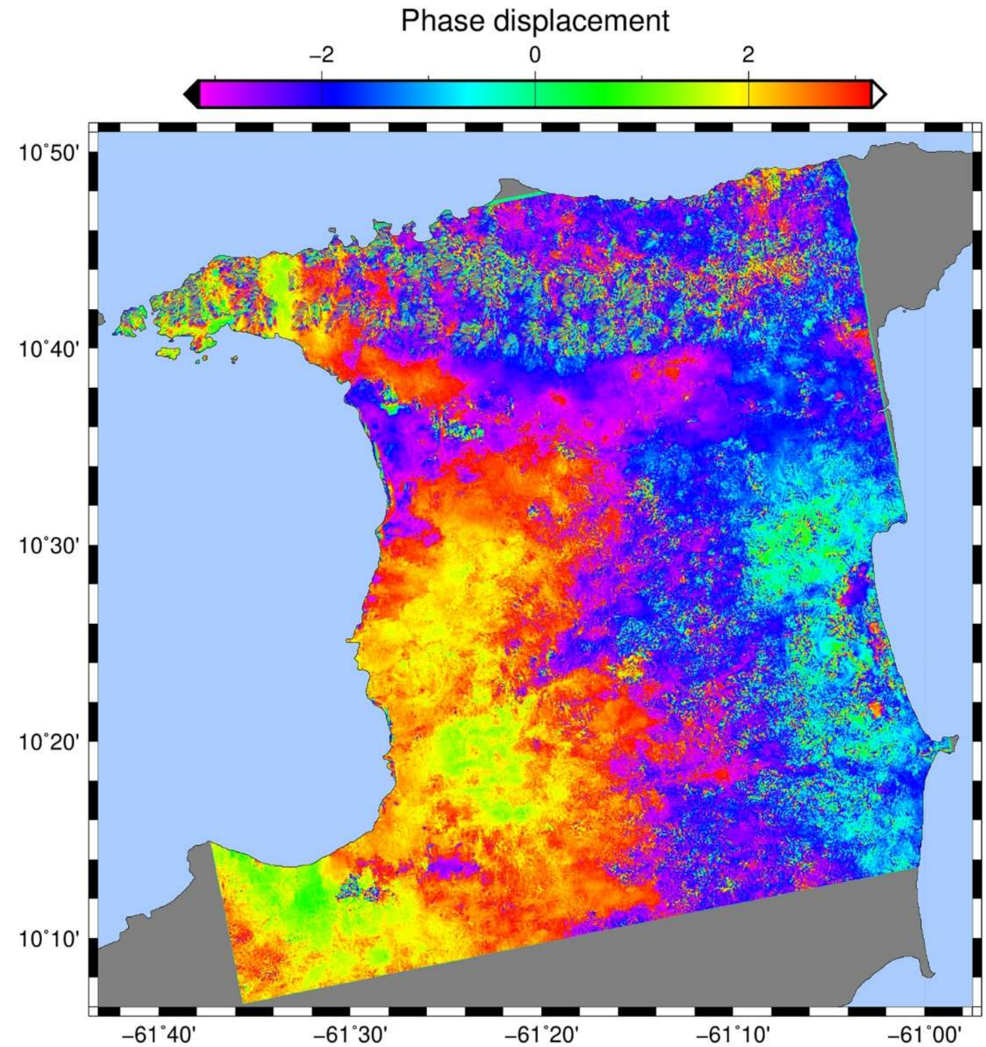

Figure **A-1**: Wrapped interferogram produced by phase differentiating SAR scenes acquired on 2017/02/01 and 2018/03/28. Interferogram resolves the full fault trace of the CRF. The Caroni swamp, in the northwest of the island, and the Nariva swamp, in the east of the land are not masked out.

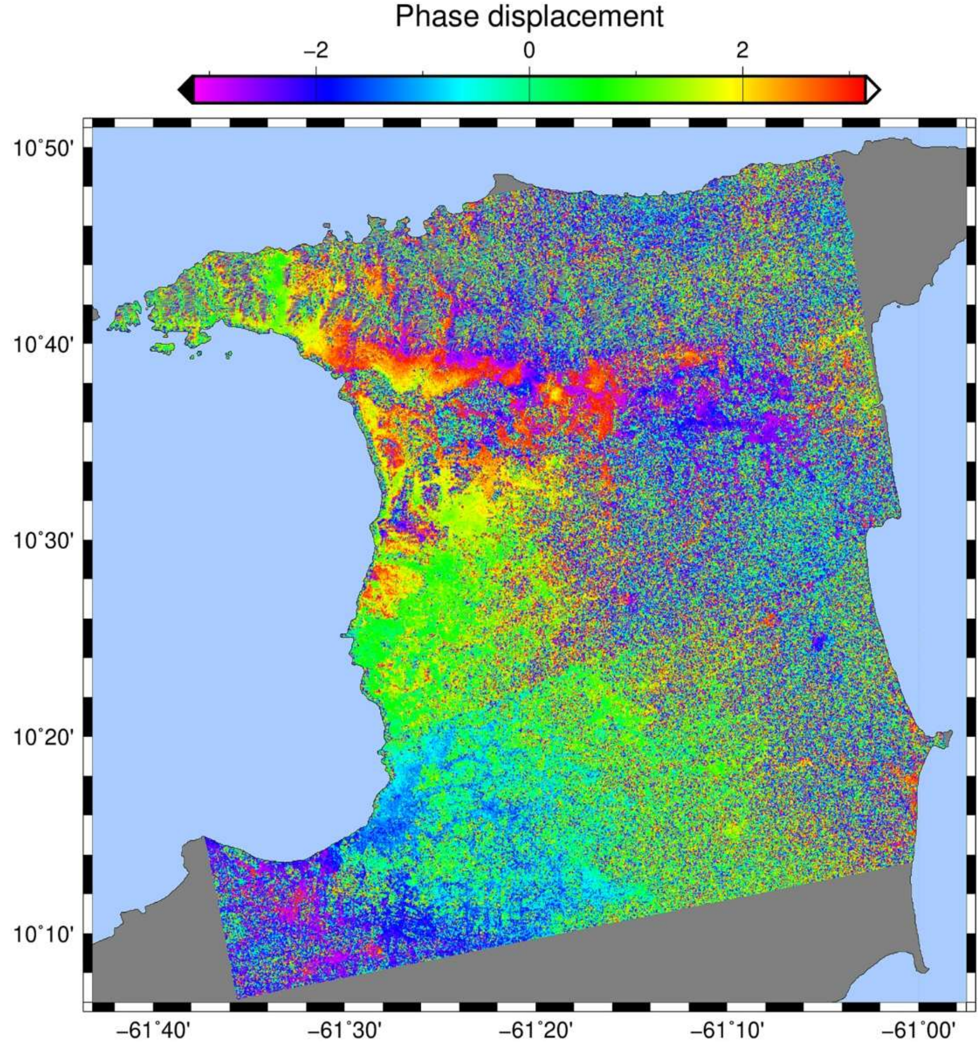

Figure **A-2**: Wrapped interferogram produced by phase differentiating SAR scenes acquired on 2017/02/01 and 2019/03/27. Interferogram resolves the full fault trace of the CRF. The Caroni swamp, in the northwest of the island, and the Nariva swamp, in the east of the land are not masked out.

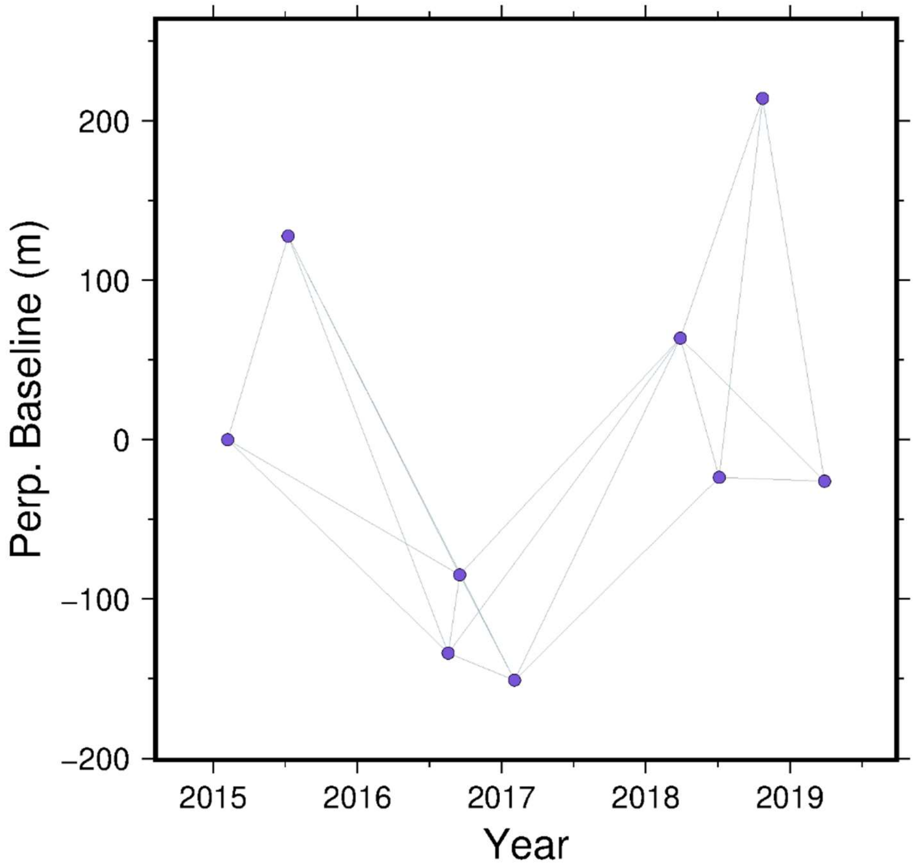

Figure **A-3**: Baseline plot for 19 ALOS-2 interferograms used in SBAS analysis. Perp. Baseline (perpendicular baseline) is the distance between the satellite at two acquisitions.

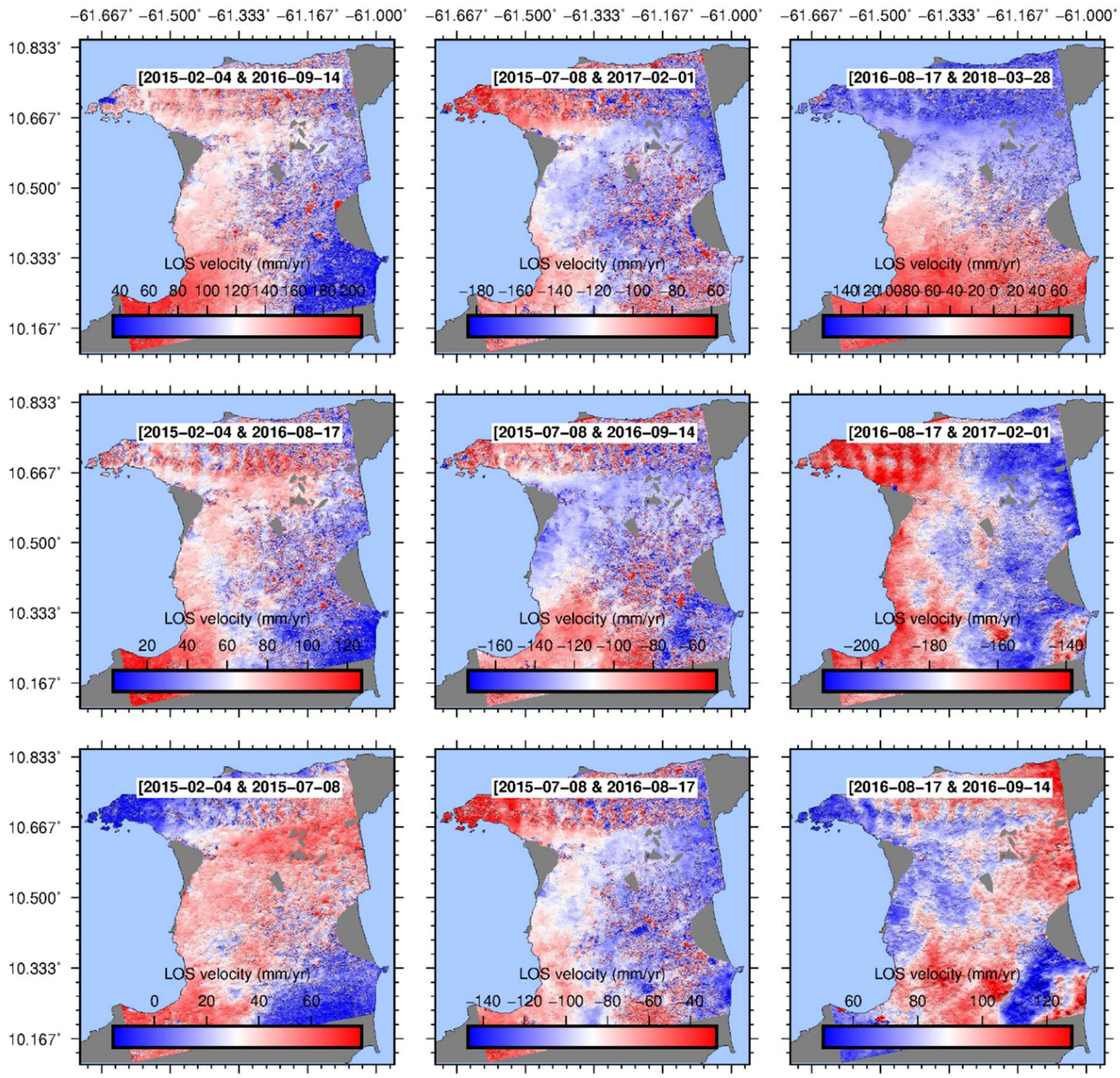

Figure **A-4**: Interferograms used in the SBAS algorithm.

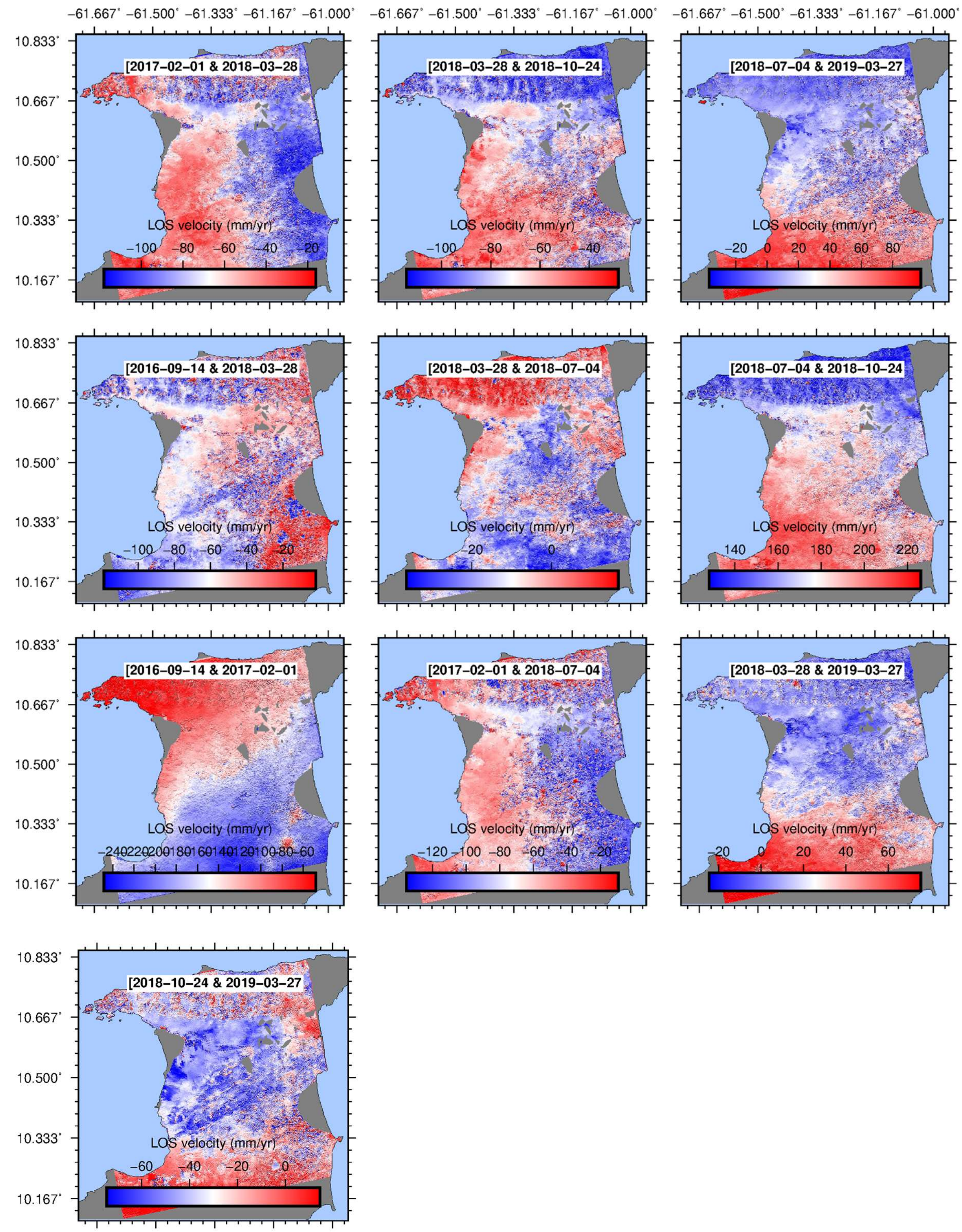

Figure **A-4**: (Continued) Interferograms used in the SBAS algorithm.

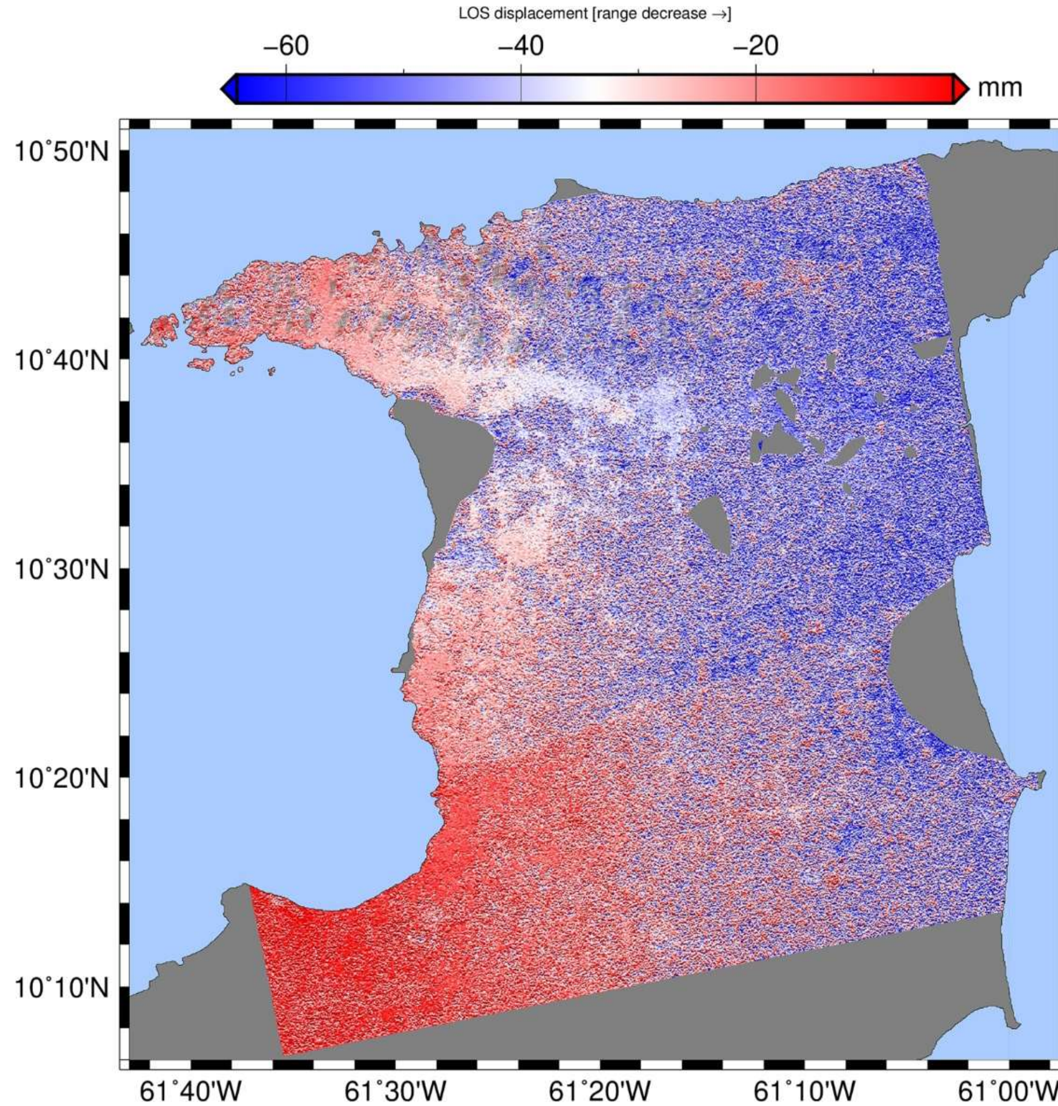

Figure **A-5**: SBAS calculated displacements. There are two long-wavelength planar trends that were removed.

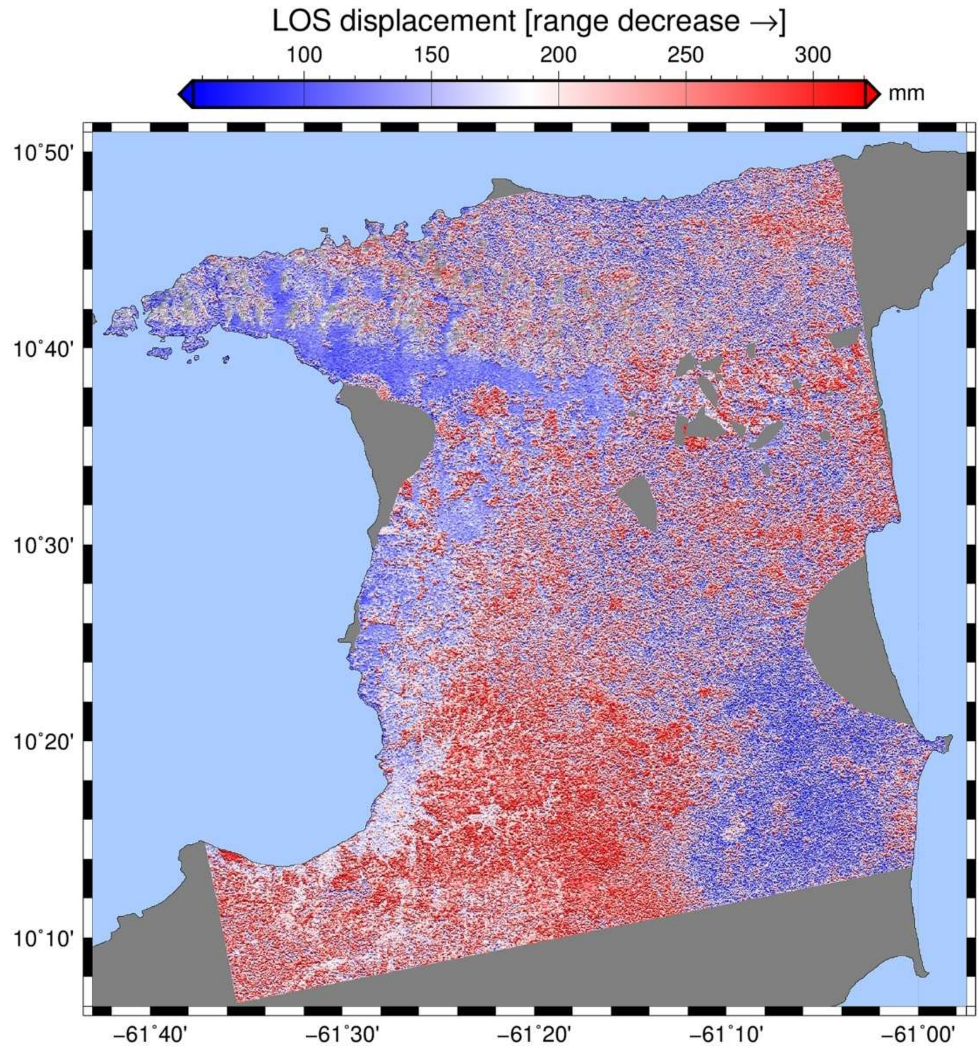

Figure **A-6**: SBAS calculated RMS.

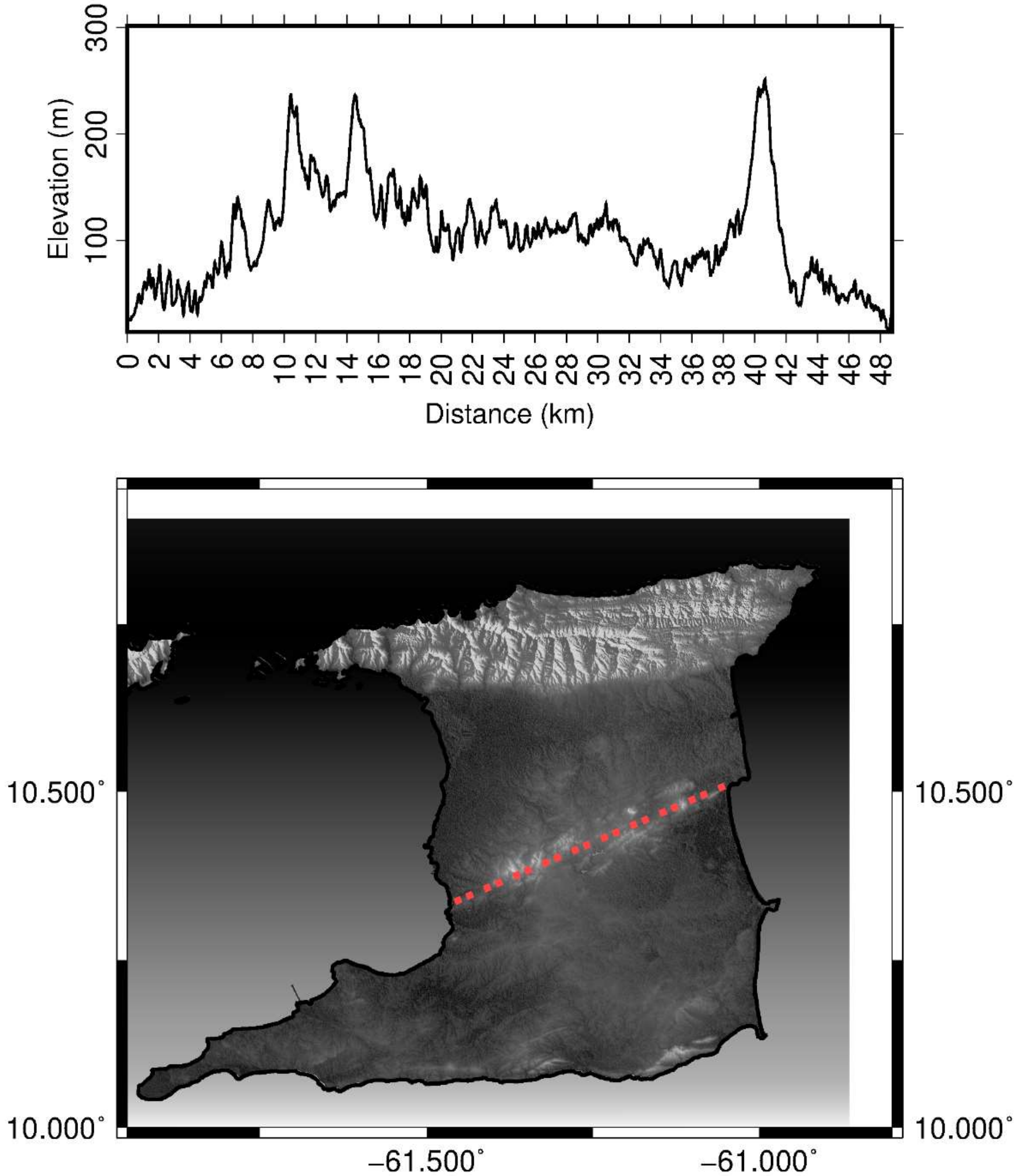

Figure **A-7**: Terrain profile of the Central Range.

A.3 Elastic Dislocation Modeling Statistics

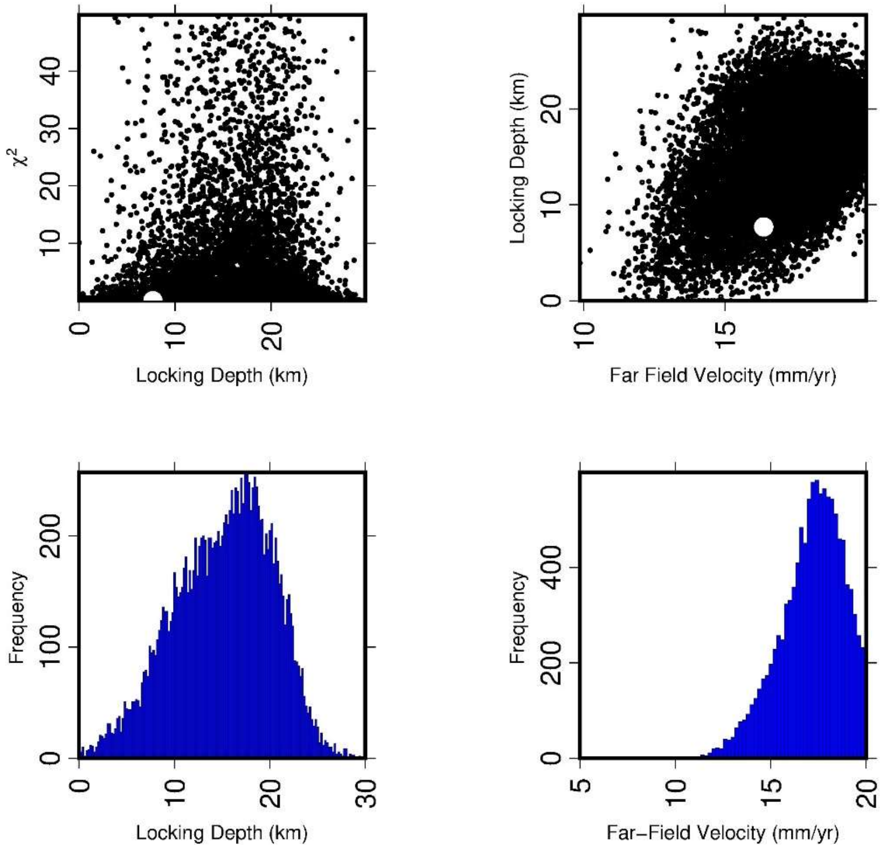

Figure **A-8**: Modeling statistics for the Monte Carlo inversion of the SSF. Top left panel: Locking depth vs $\chi 2$ with a dot being the most likely locking depth. Top right panel: Far-field velocity vs locking depth with a dot representing the most likely values. Bottom left panel: histogram of locking depth. Bottom right panel: histogram of far-field velocities.

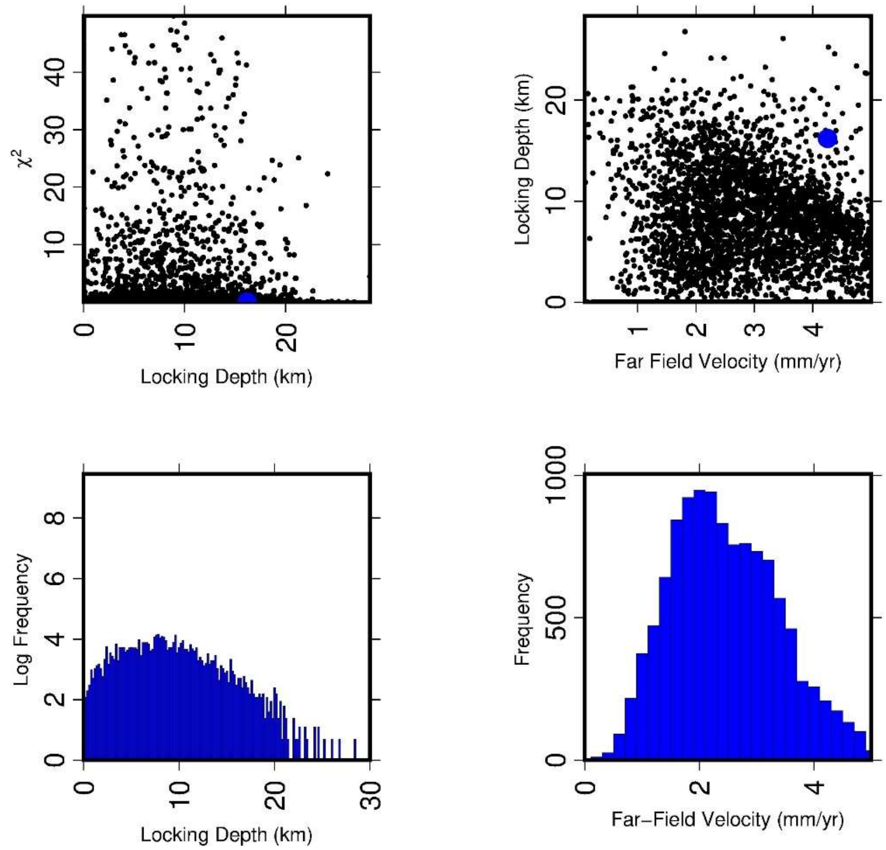

Figure **A-9**: Modeling statistics for the Monte Carlo inversion of the LVF. Top left panel: Locking depth vs χ2 with a dot being the most likely locking depth. Top right panel: Far-field velocity vs locking depth with a dot representing the most likely values. Bottom left panel: histogram of locking depth. Bottom right panel: histogram of far-field velocities.

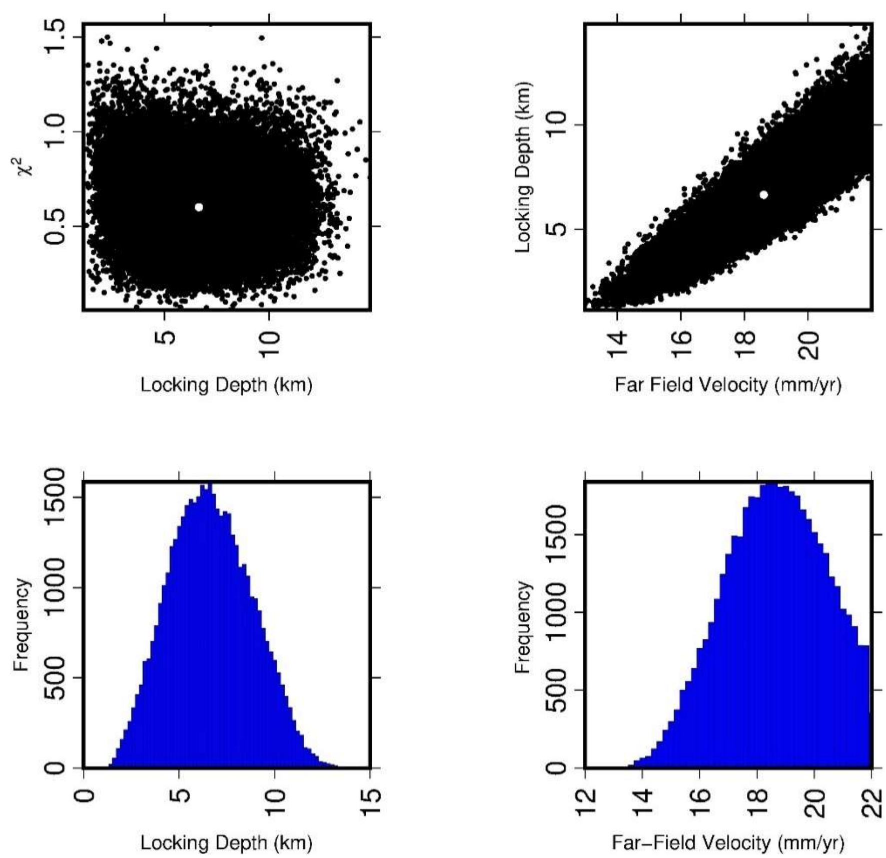

Figure **A-10**: Modeling statistics for the Monte Carlo inversion of Profile A for the EPF. Top left panel: Locking depth vs $\chi 2$ with a dot being the most likely locking depth. Top right panel: Far-field velocity vs locking depth with a dot representing the most likely values. Bottom left panel: histogram of locking depth. Bottom right panel: histogram of far-field velocities.

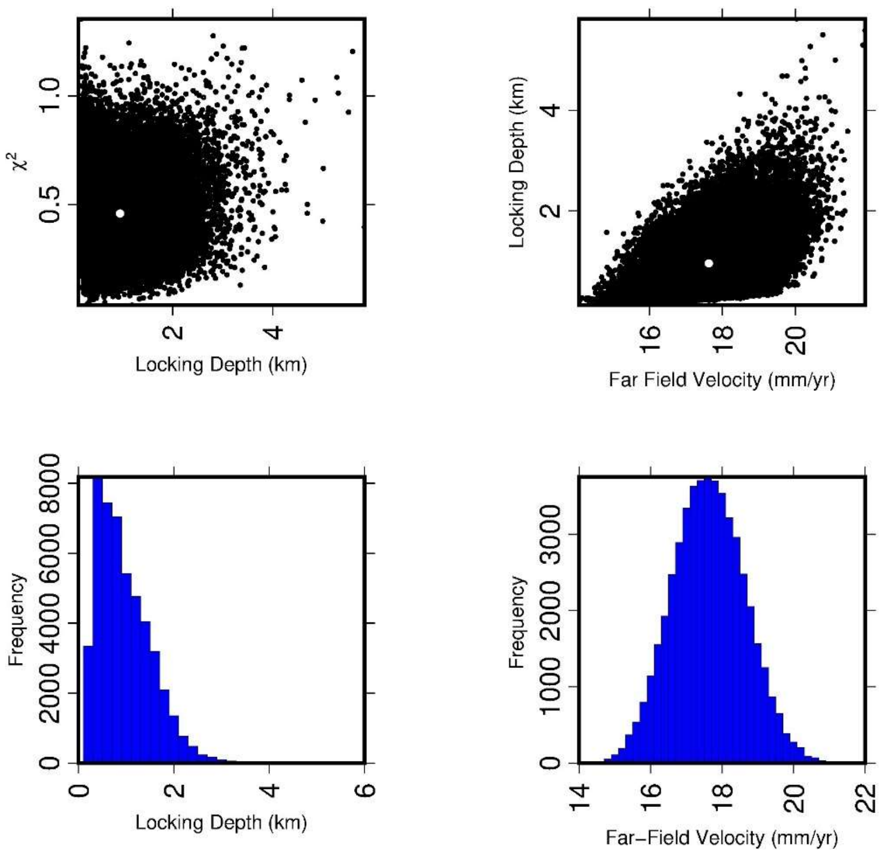

Figure **A-11**: Modeling statistics for the Monte Carlo inversion of Profile B for the EPF. Top left panel: Locking depth vs χ2 with a dot being the most likely locking depth. Top right panel: Far-field velocity vs locking depth with a dot representing the most likely values. Bottom left panel: histogram of locking depth. Bottom right panel: histogram of far-field velocities.

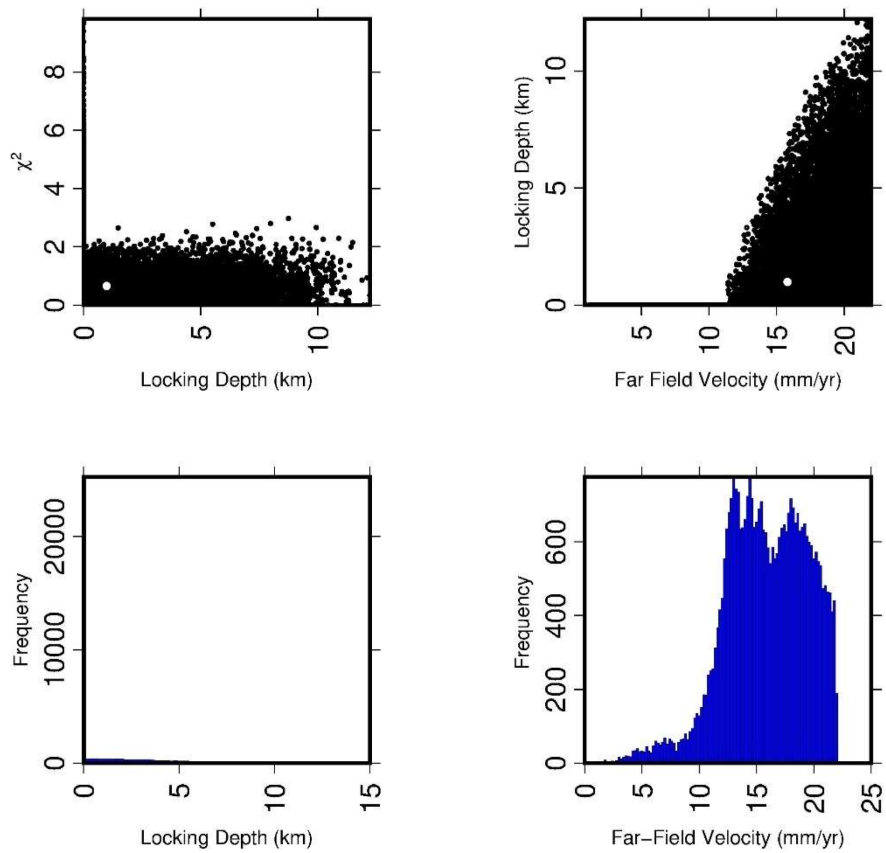

Figure **A-12**: Modeling statistics for the Monte Carlo inversion of Profile C for the EPF. Top left panel: Locking depth vs χ2 with a dot being the most likely locking depth. Top right panel: Far-field velocity vs locking depth with a dot representing the most likely values. Bottom left panel: histogram of locking depth. Bottom right panel: histogram of far-field velocities.

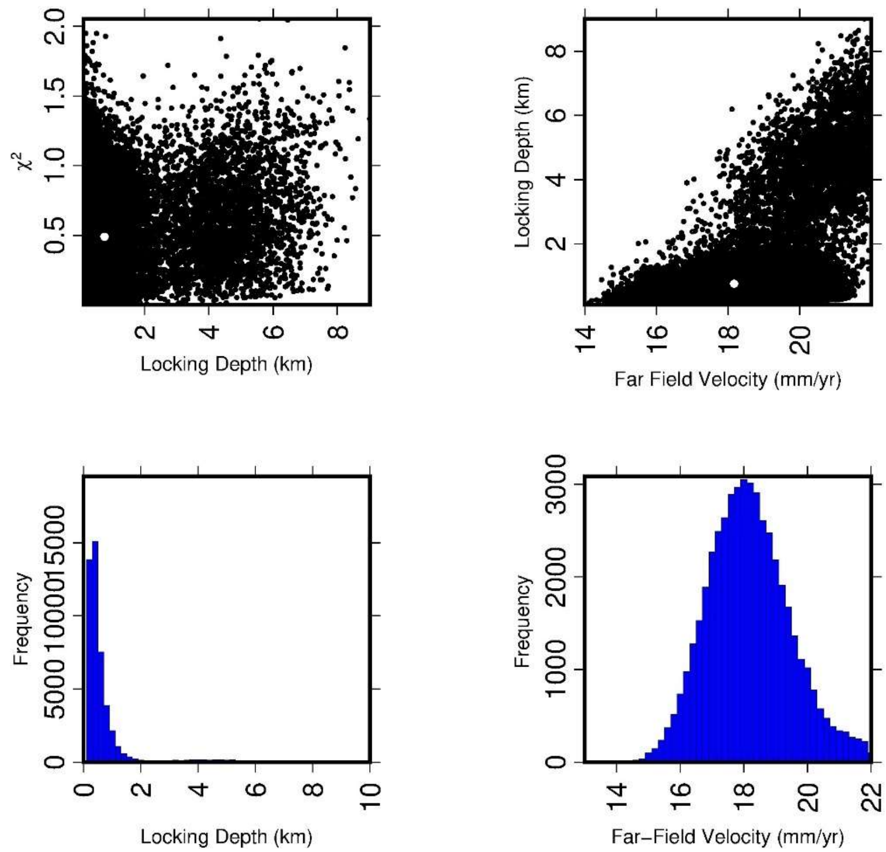

Figure **A-13**: Modeling statistics for the Monte Carlo inversion of Profile D for the EPF. Top left panel: Locking depth vs χ2 with a dot being the most likely locking depth. Top right panel: Far-field velocity vs locking depth with a dot representing the most likely values. Bottom left panel: histogram of locking depth. Bottom right panel: histogram of far-field velocities.

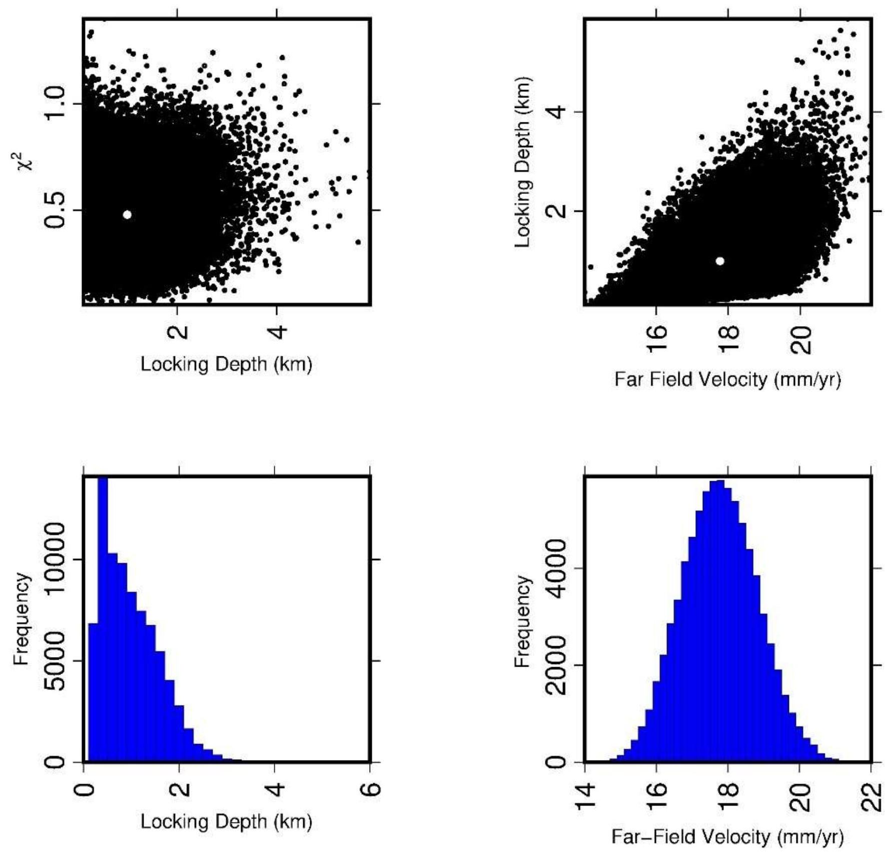

Figure **A-14**: Modeling statistics for the Monte Carlo inversion of Profile E for the EPF. Top left panel: Locking depth vs χ2 with a dot being the most likely locking depth. Top right panel: Far-field velocity vs locking depth with a dot representing the most likely values. Bottom left panel: histogram of locking depth. Bottom right panel: histogram of far-field velocities.

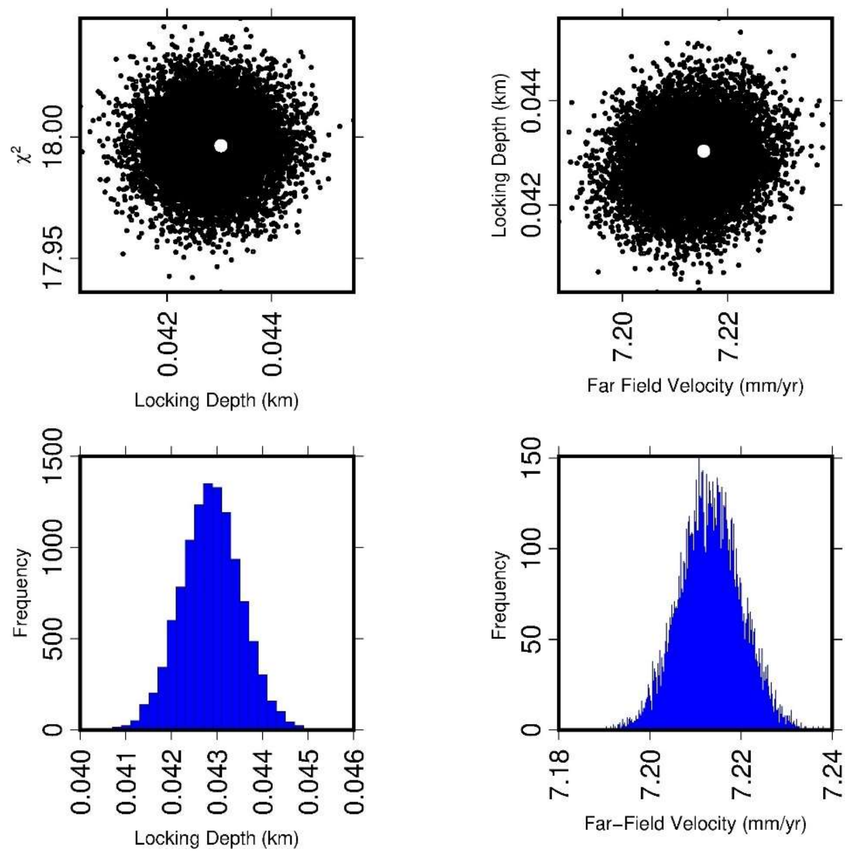

Figure **A-15**: Modeling statistics for the Monte Carlo inversion of Profile I1 for the CRF. Top left panel: Locking depth vs χ2 with a dot being the most likely locking depth. Top right panel: Far-field velocity vs locking depth with a dot representing the most likely values. Bottom left panel: histogram of locking depth. Bottom right panel: histogram of far-field velocities.

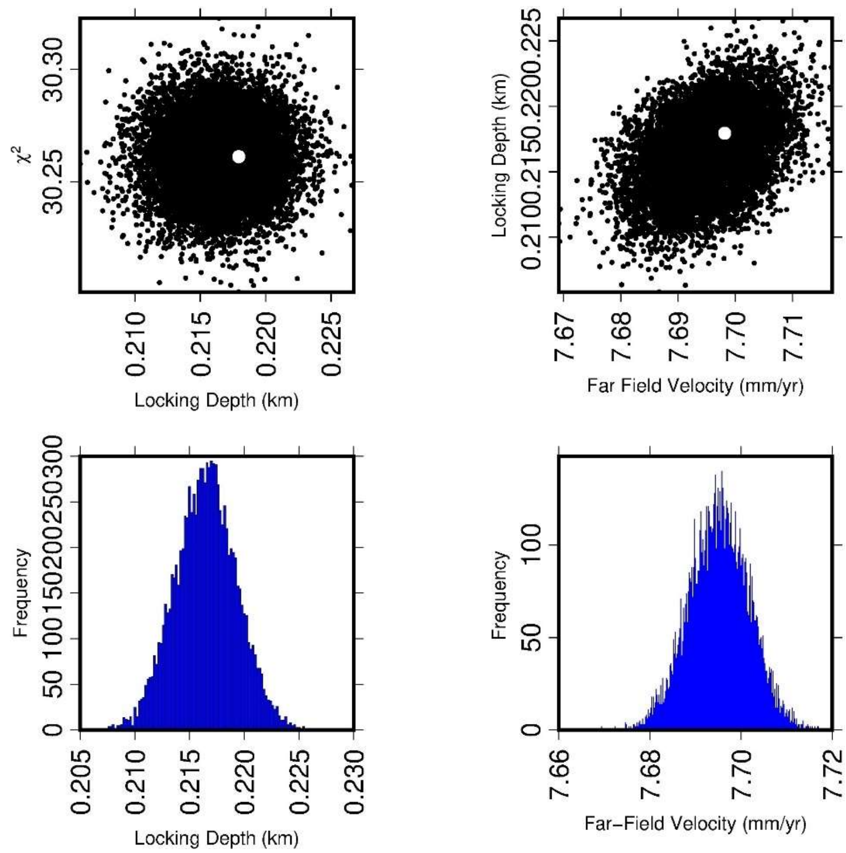

Figure **A-16**: Modeling statistics for the Monte Carlo inversion of Profile I2 for the CRF. Top left panel: Locking depth vs χ2 with a dot being the most likely locking depth. Top right panel: Far-field velocity vs locking depth with a dot representing the most likely values. Bottom left panel: histogram of locking depth. Bottom right panel: histogram of far-field velocities.

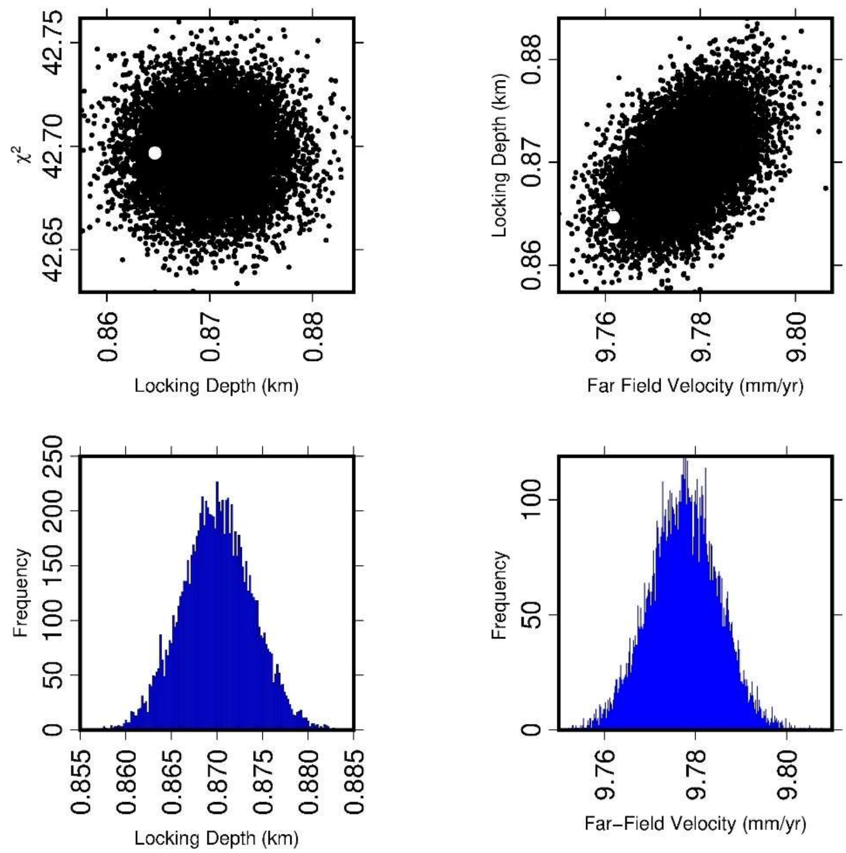

Figure **A-17**: Modeling statistics for the Monte Carlo inversion of Profile I3 for the CRF. Top left panel: Locking depth vs χ2 with a dot being the most likely locking depth. Top right panel: Far-field velocity vs locking depth with a dot representing the most likely values. Bottom left panel: histogram of locking depth. Bottom right panel: histogram of far-field velocities.

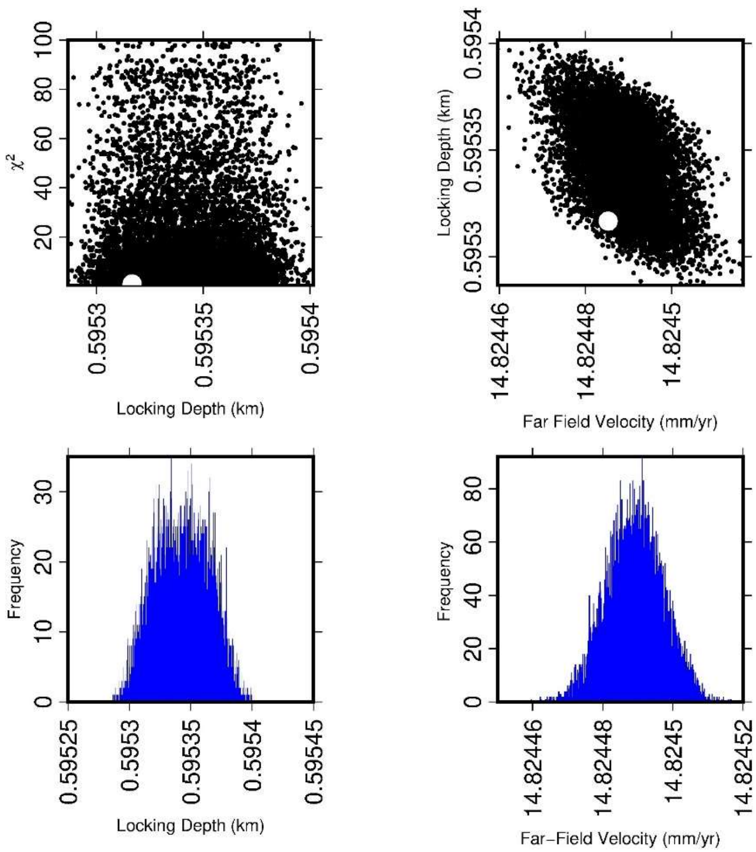

Figure **A-18**: Modeling statistics for the Monte Carlo inversion of GPS velocity profile for the CRF. Top left panel: Locking depth vs $\chi 2$ with a dot being the most likely locking depth. Top right panel: Far-field velocity vs locking depth with a dot representing the most likely values. Bottom left panel: histogram of locking depth. Bottom right panel: histogram of far-field velocities.

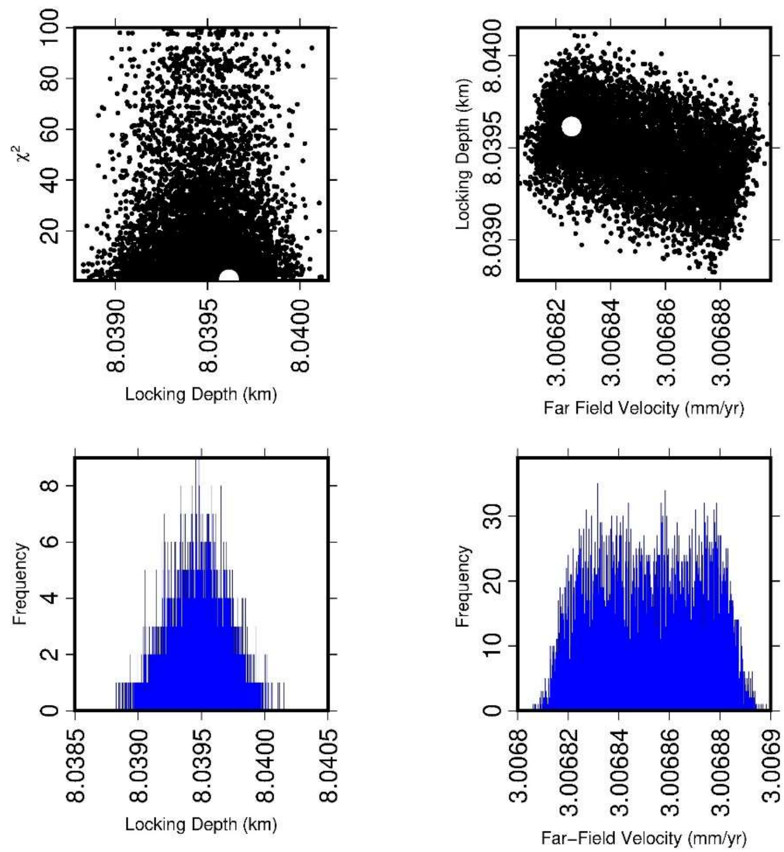

Figure **A-20**: Modeling statistics for the Monte Carlo inversion of GPS velocity profile for the STTF. Top left panel: Locking depth vs χ2 with a dot being the most likely locking depth. Top right panel: Far-field velocity vs locking depth with a dot representing the most likely values. Bottom left panel: histogram of locking depth. Bottom right panel: histogram of far-field velocities.

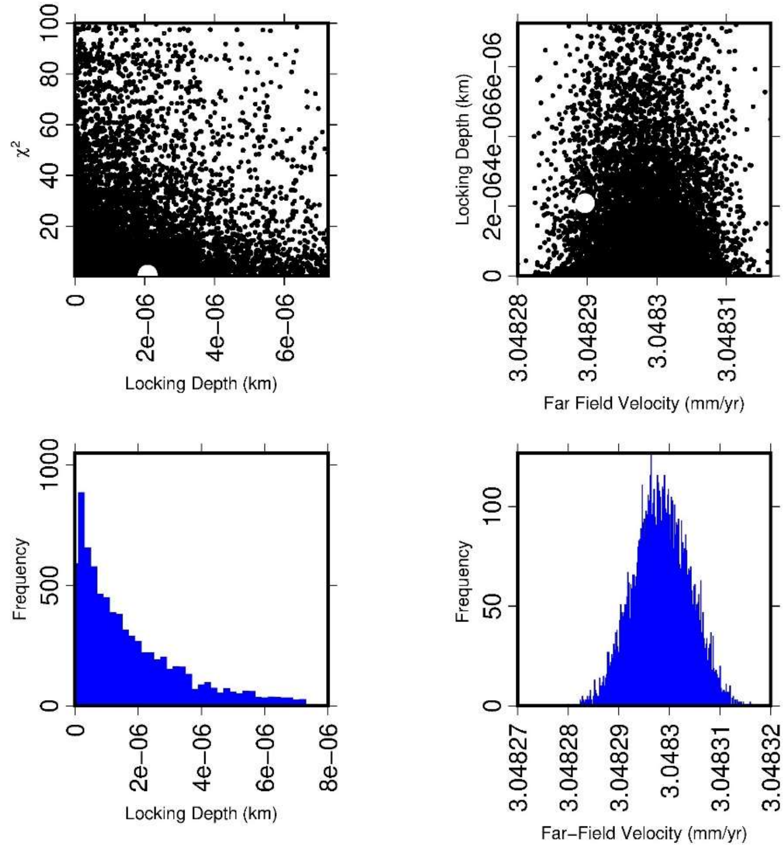

Figure **A-21**: Modeling statistics for the Monte Carlo inversion of GPS velocity profile for the SCF. Top left panel: Locking depth vs $\chi 2$ with a dot being the most likely locking depth. Top right panel: Far-field velocity vs locking depth with a dot representing the most likely values. Bottom left panel: histogram of locking depth. Bottom right panel: histogram of far-field velocities.

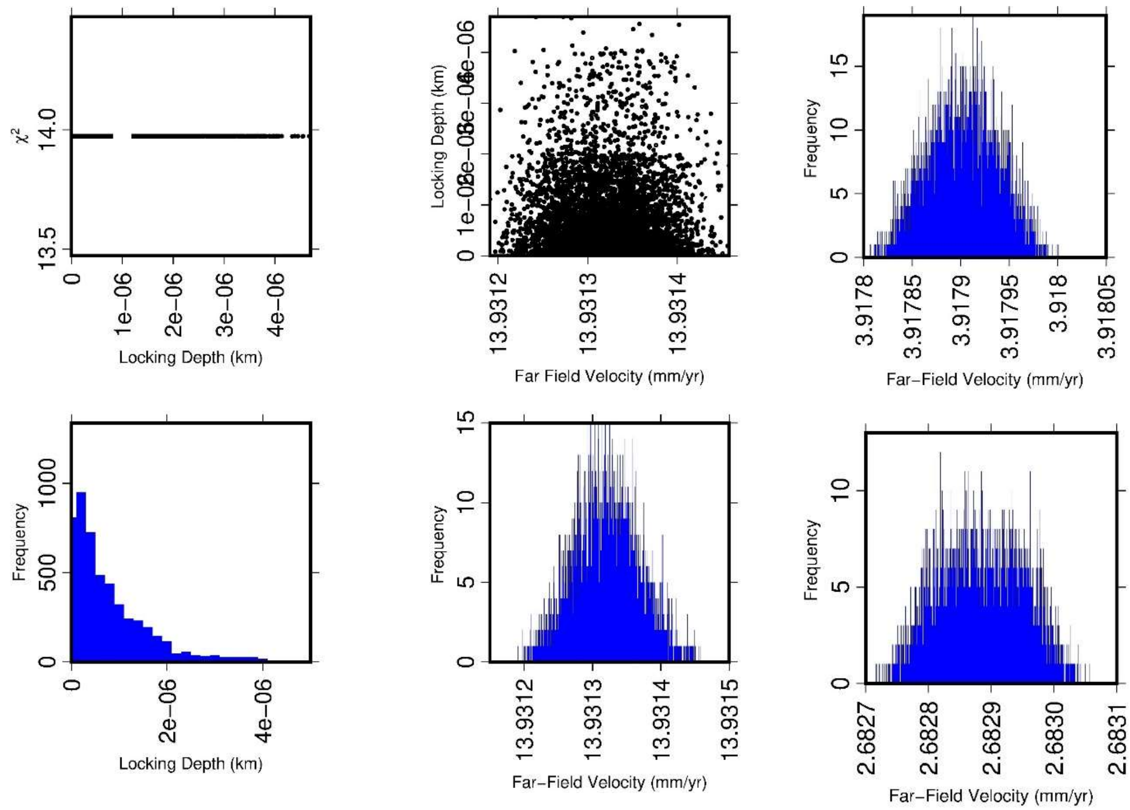

Figure **A-23**: Modeling statistics for the Monte Carlo inversion of GPS velocity profile for the Trinidad and Tobago faults where SCF and STTF locking depths were fixed to 0.1 km. Top left panel: CRF locking depth vs χ2 with a dot being the most likely locking depth. Top center panel: CRF far-field velocity vs locking depth with a dot representing the most likely values. Top right panel: histogram of far-field velocities of STTF. Bottom left panel: histogram of locking depth of CRF. Bottom center panel: histogram of far-field velocities of CRF. Bottom right panel: histogram of far-field velocities of SCF.

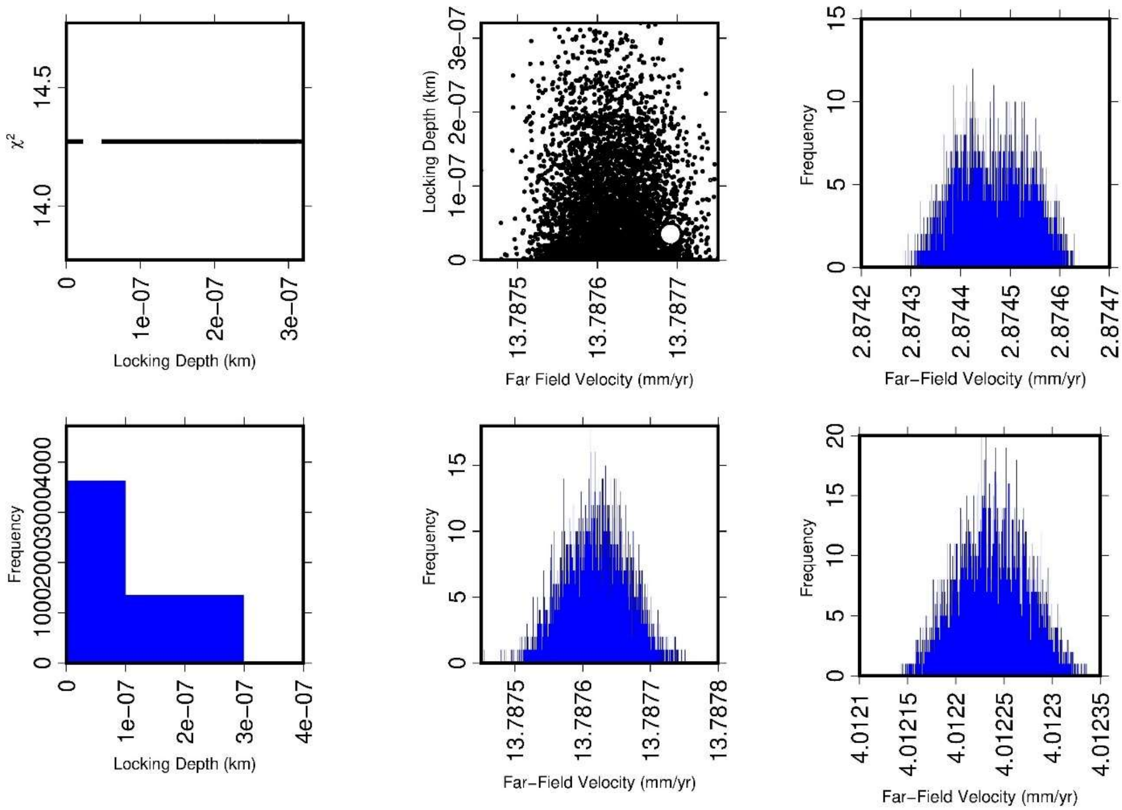

Figure **A-24**: Modeling statistics for the Monte Carlo inversion of GPS velocity profile for the Trinidad and Tobago faults where SCF and STTF locking depths were fixed to 2 km. Top left panel: CRF locking depth vs χ2 with a dot being the most likely locking depth. Top center panel: CRF far-field velocity vs locking depth with a dot representing the most likely values. Top right panel: histogram of far-field velocities of STTF. Bottom left panel: histogram of locking depth of CRF. Bottom center panel: histogram of far-field velocities of CRF. Bottom right panel: histogram of far-field velocities of SCF.

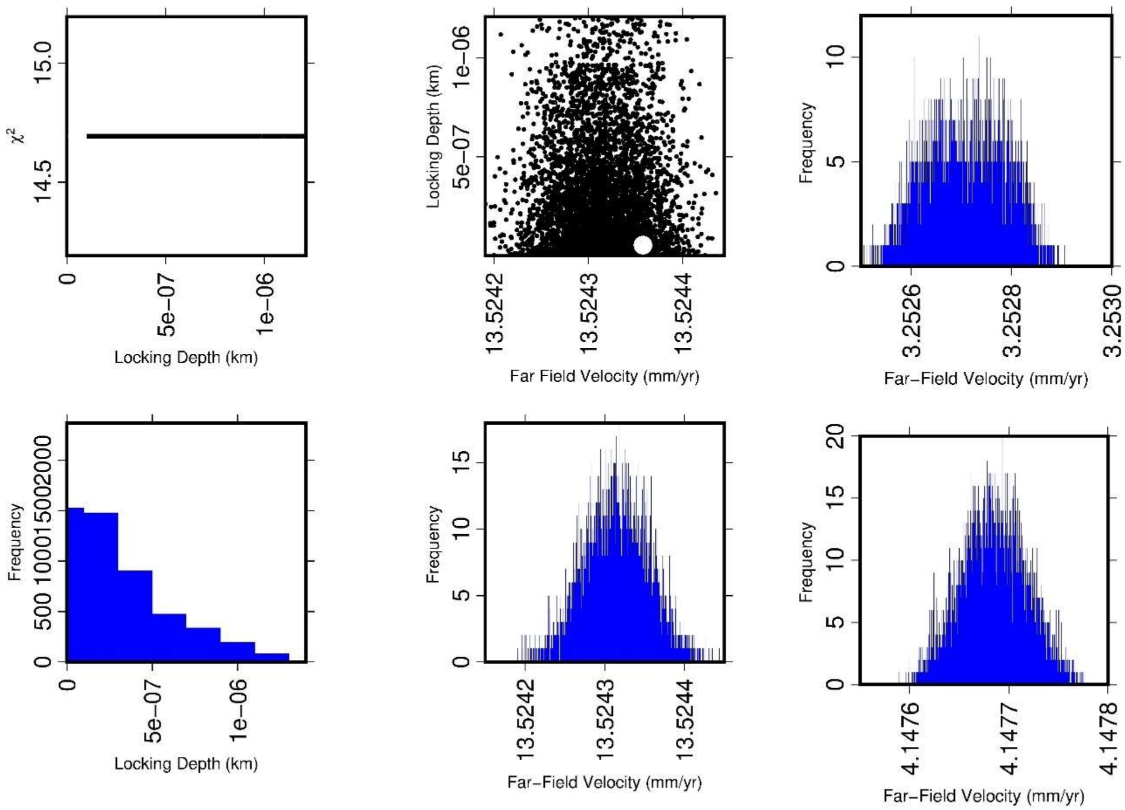

Figure **A-25**: Modeling statistics for the Monte Carlo inversion of GPS velocity profile for the Trinidad and Tobago faults where SCF and STTF locking depths were fixed to 5 km. Top left panel: CRF locking depth vs χ2 with a dot being the most likely locking depth. Top center panel: CRF far-field velocity vs locking depth with a dot representing the most likely values. Top right panel: histogram of far-field velocities of STTF. Bottom left panel: histogram of locking depth of CRF. Bottom center panel: histogram of far-field velocities of CRF. Bottom right panel: histogram of far-field velocities of SCF.

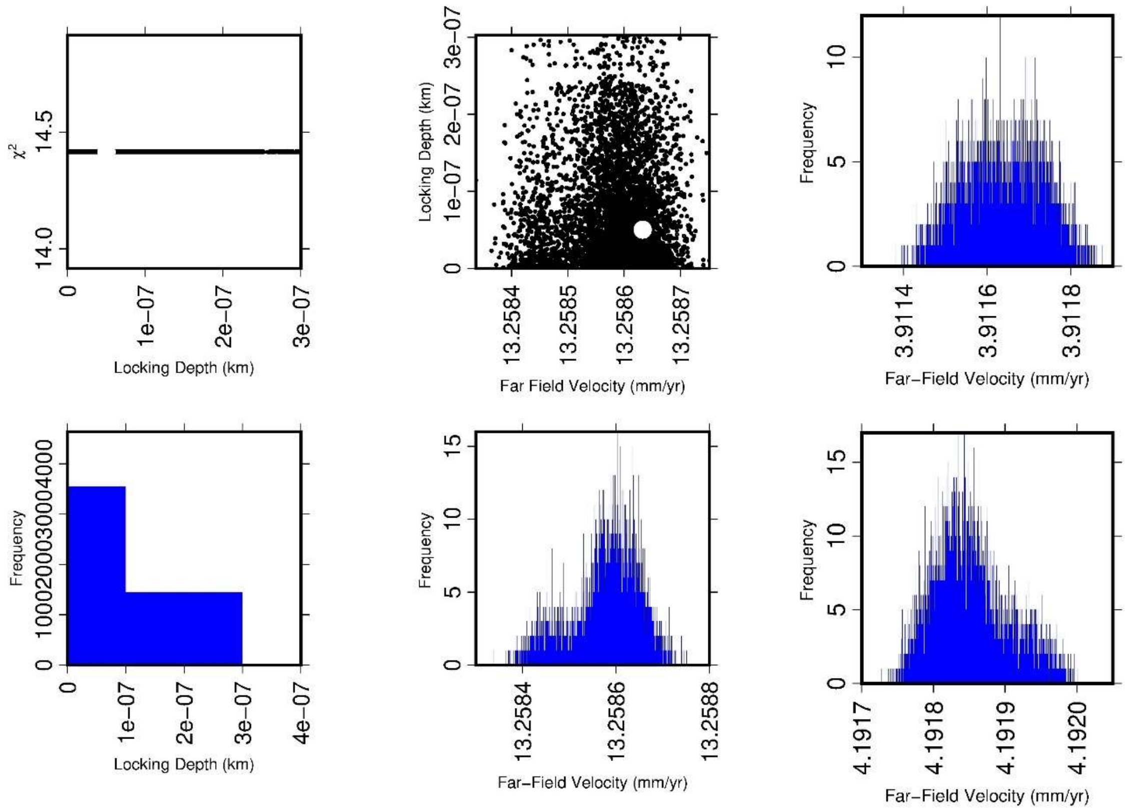

Figure **A-26**: Modeling statistics for the Monte Carlo inversion of GPS velocity profile for the Trinidad and Tobago faults where SCF and STTF locking depths were fixed to 10 km. Top left panel: CRF locking depth vs $\chi 2$ with a dot being the most likely locking depth. Top center panel: CRF far-field velocity vs locking depth with a dot representing the most likely values. Top right panel: histogram of far-field velocities of STTF. Bottom left panel: histogram of locking depth of CRF. Bottom center panel: histogram of far-field velocities of CRF. Bottom right panel: histogram of far-field velocities of SCF.

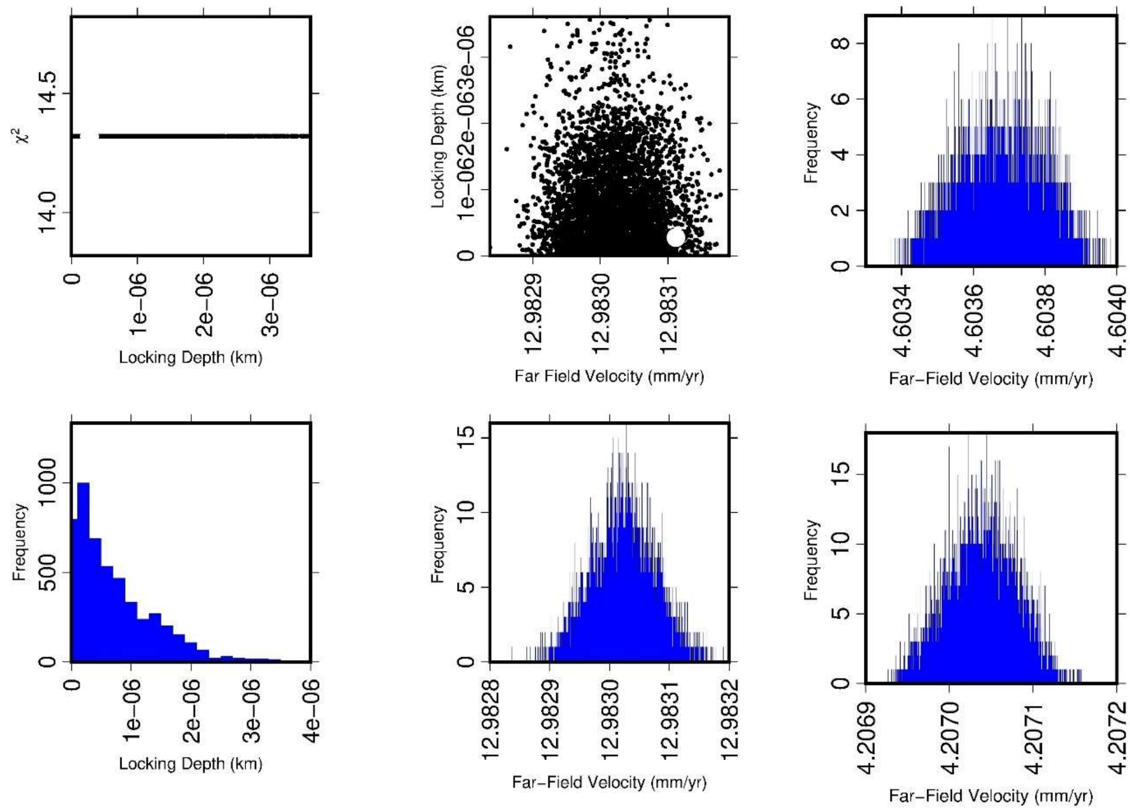

Figure **A-27**: Modeling statistics for the Monte Carlo inversion of GPS velocity profile for the Trinidad and Tobago faults where SCF and STTF locking depths were fixed to 15 km. Top left panel: CRF locking depth vs χ2 with a dot being the most likely locking depth. Top center panel: CRF far-field velocity vs locking depth with a dot representing the most likely values. Top right panel: histogram of far-field velocities of STTF. Bottom left panel: histogram of locking depth of CRF. Bottom center panel: histogram of far-field velocities of CRF. Bottom right panel: histogram of far-field velocities of SCF.

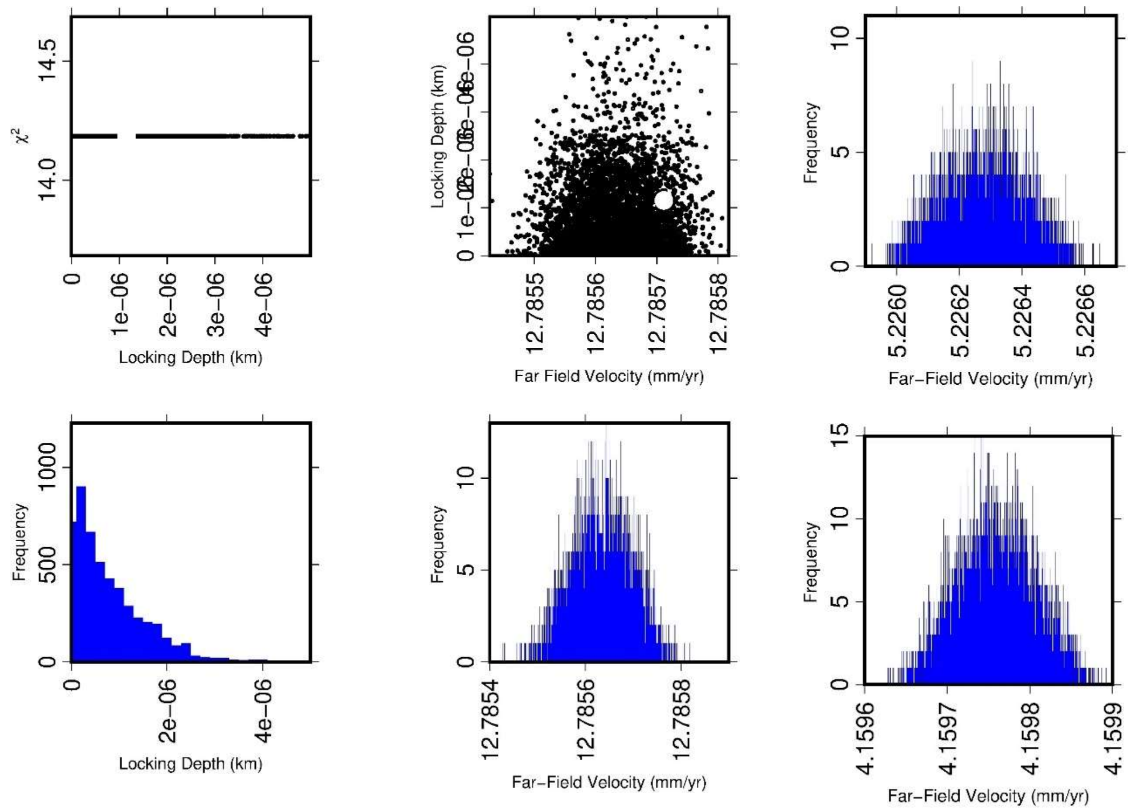

Figure **A-28**: Modeling statistics for the Monte Carlo inversion of GPS velocity profile for the Trinidad and Tobago faults where SCF and STTF locking depths were fixed to 20 km. Top left panel: CRF locking depth vs χ2 with a dot being the most likely locking depth. Top center panel: CRF far-field velocity vs locking depth with a dot representing the most likely values. Top right panel: histogram of far-field velocities of STTF. Bottom left panel: histogram of locking depth of CRF. Bottom center panel: histogram of far-field velocities of CRF. Bottom right panel: histogram of far-field velocities of SCF.

Appendix B
Bookshelf Faulting Plots

B.1 Slip on Arc-Normal Faults for Model Sets A and B

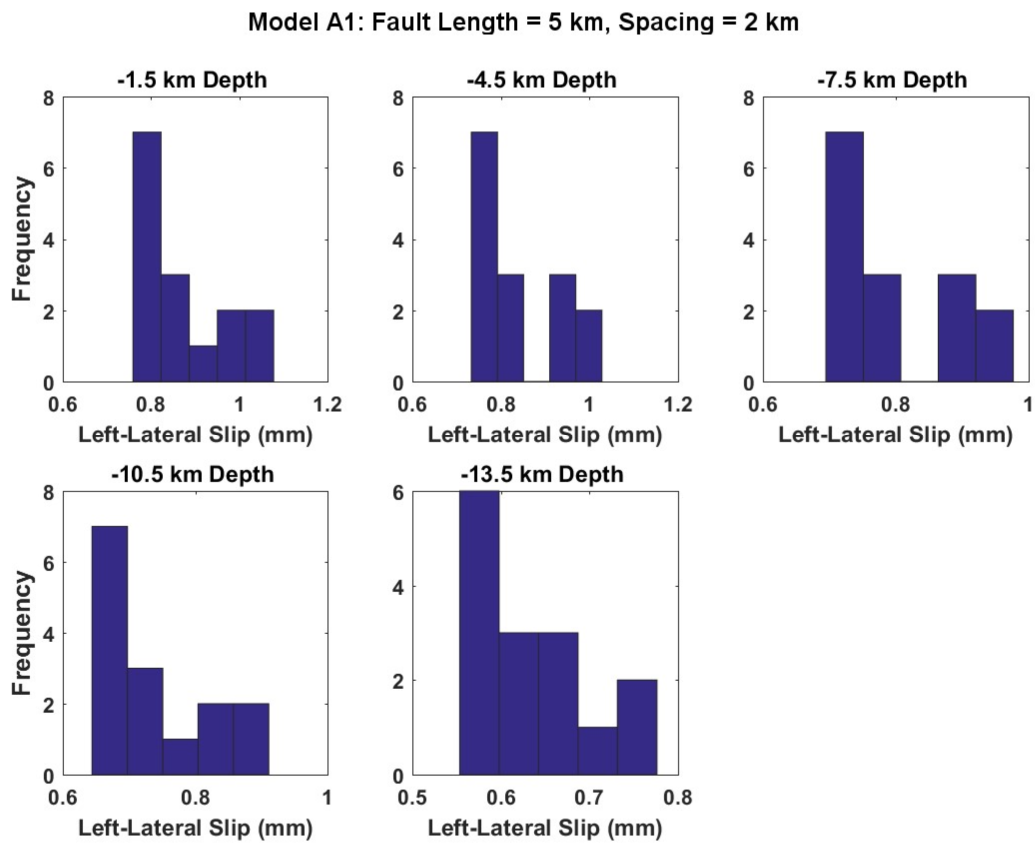

Figure **B-4:** Arc-normal fault downdip elements displacements for model A1.

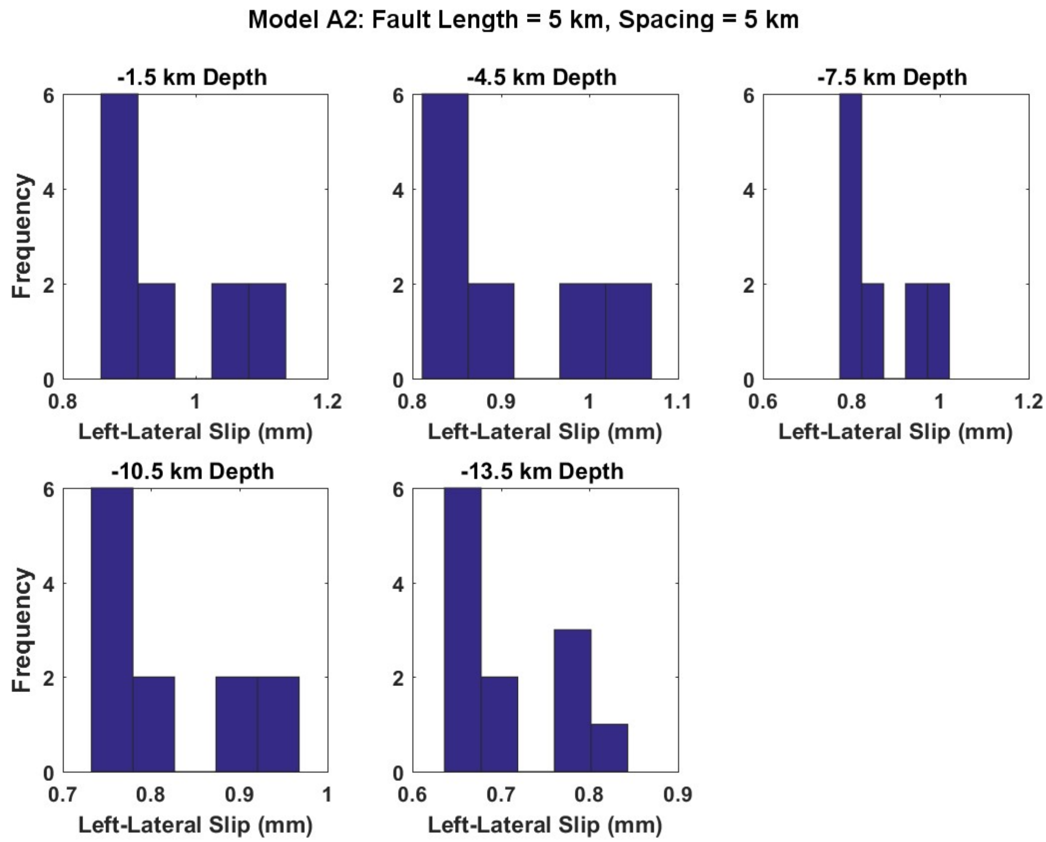

Figure **B-5**: Arc-normal fault downdip elements displacements for model A2.

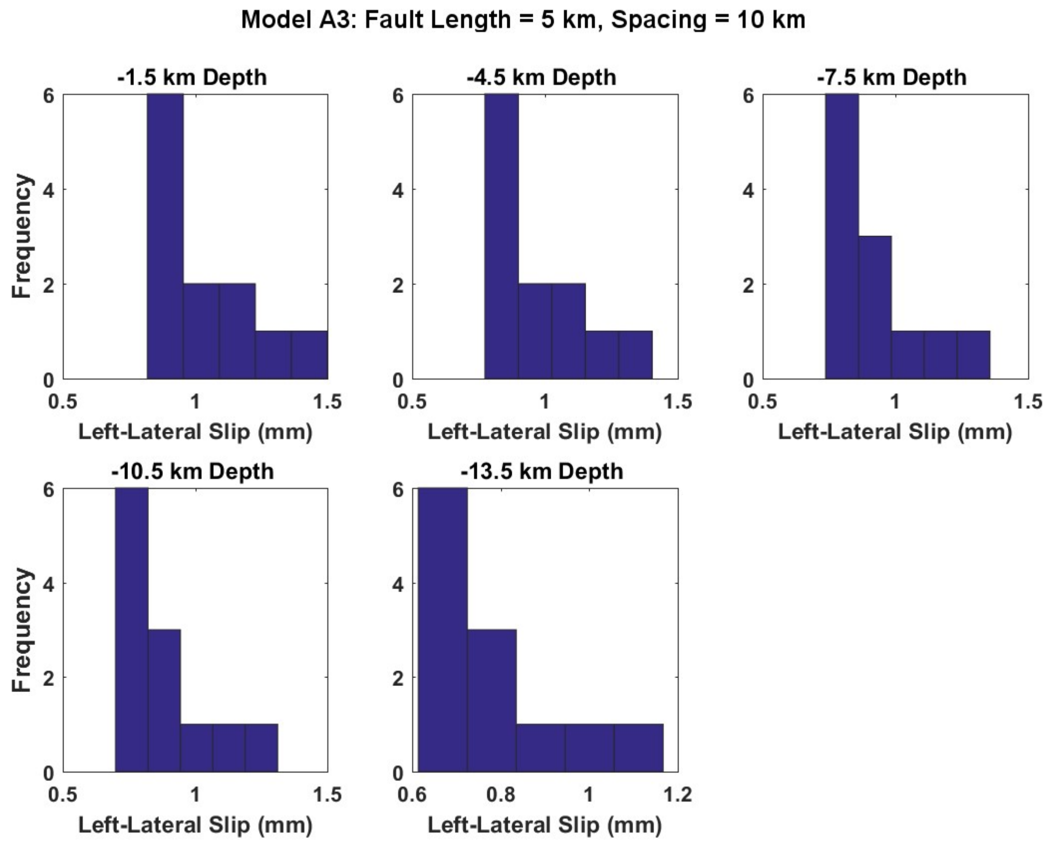

Figure **B-6**: Arc-normal fault downdip elements displacements for model A3.

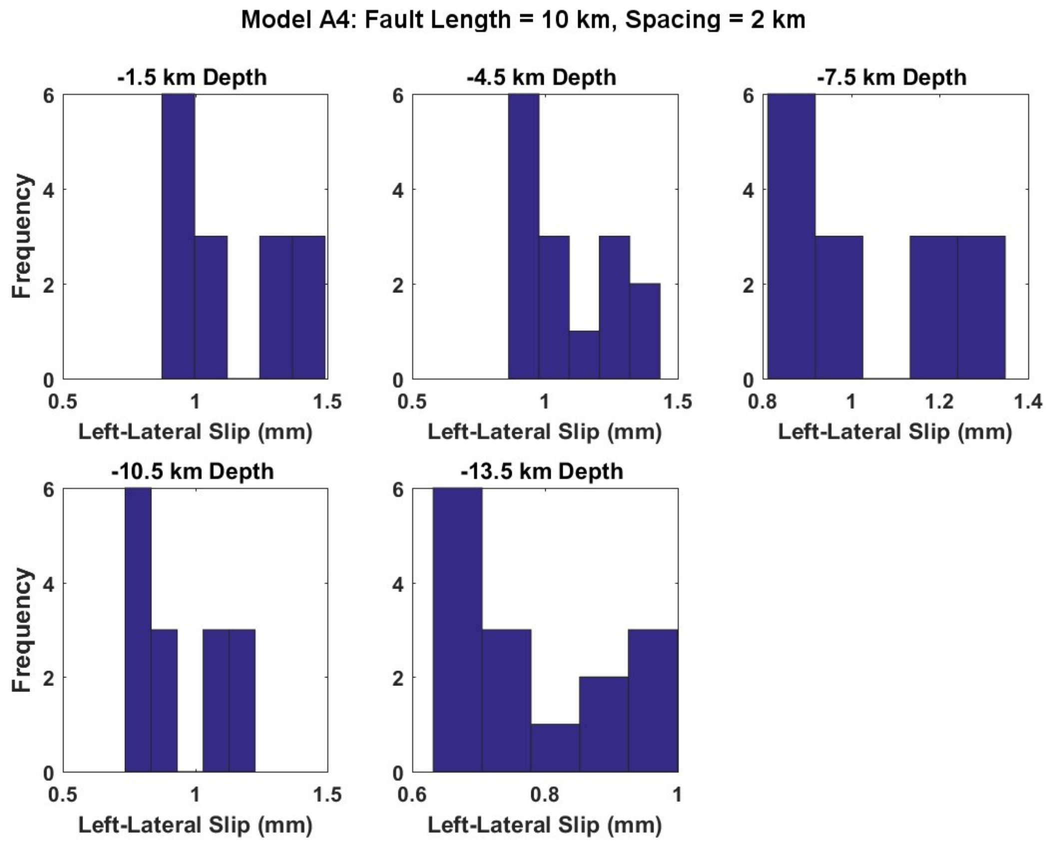

Figure **B-7**: Arc-normal fault downdip elements displacements for model A4.

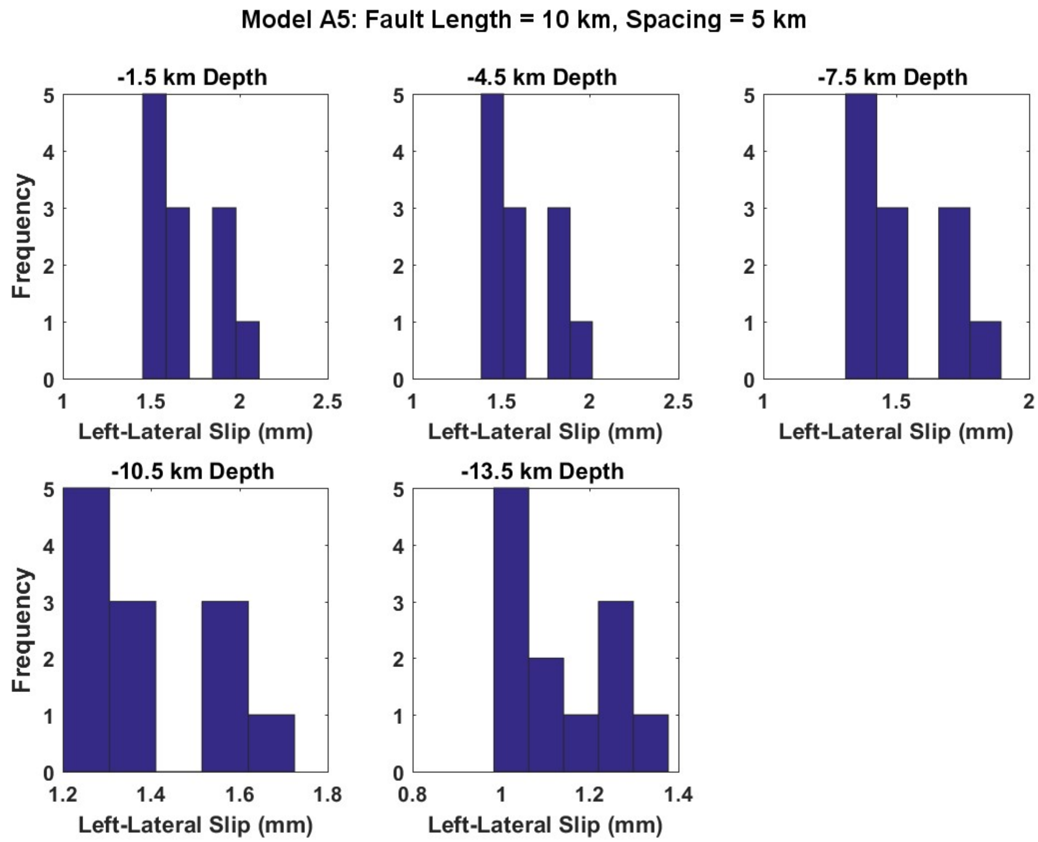

Figure **B-8**: Arc-normal fault downdip elements displacements for model A5.

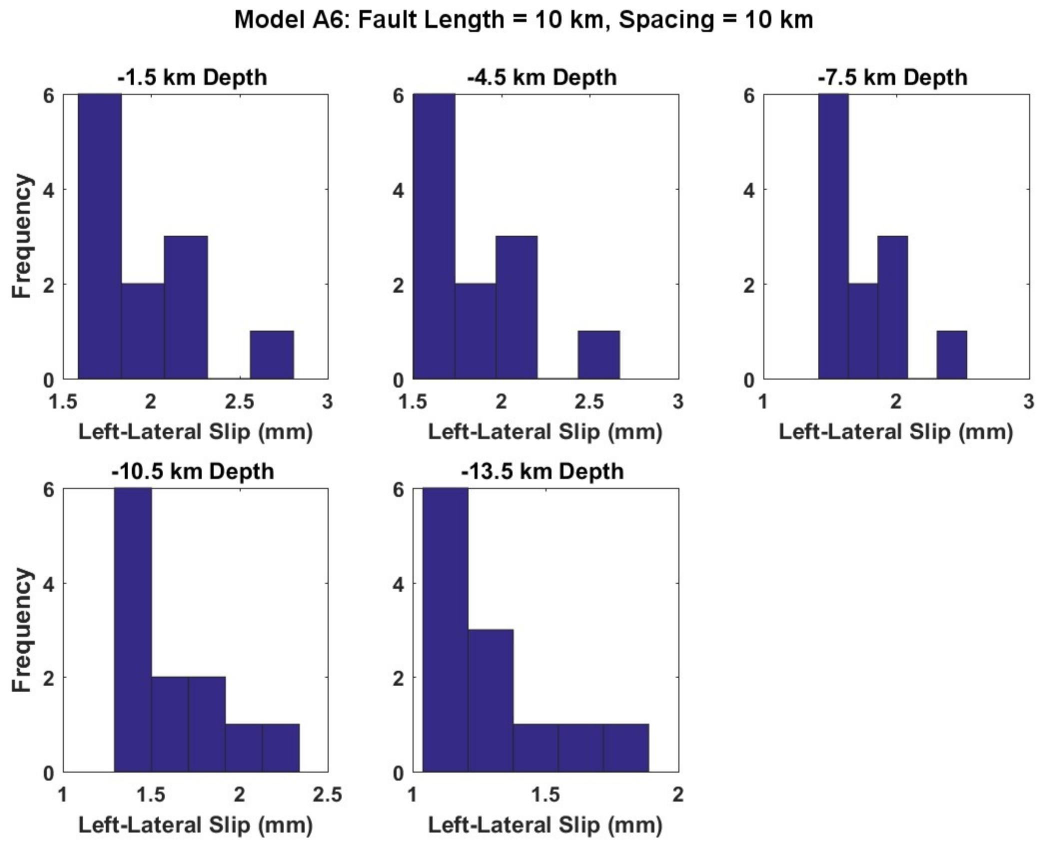

Figure **B-9**: Arc-normal fault downdip elements displacements for model A6.

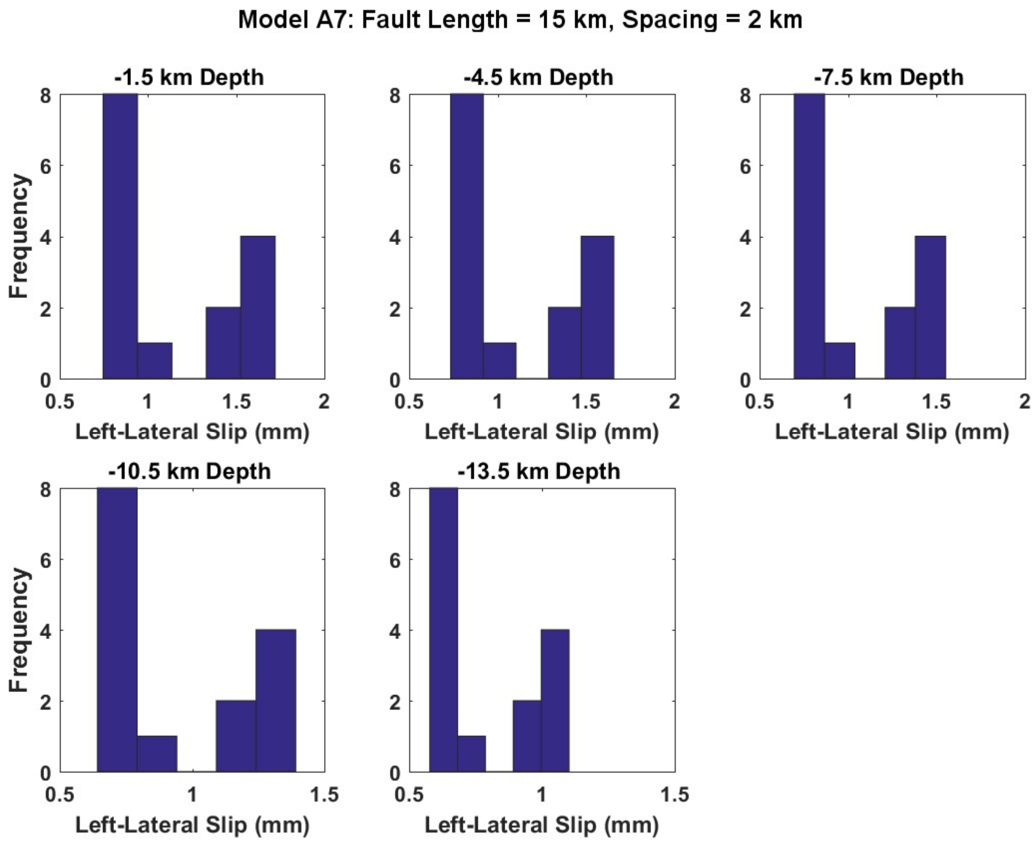

Figure **B-10**: Arc-normal fault downdip elements displacements for model A7.

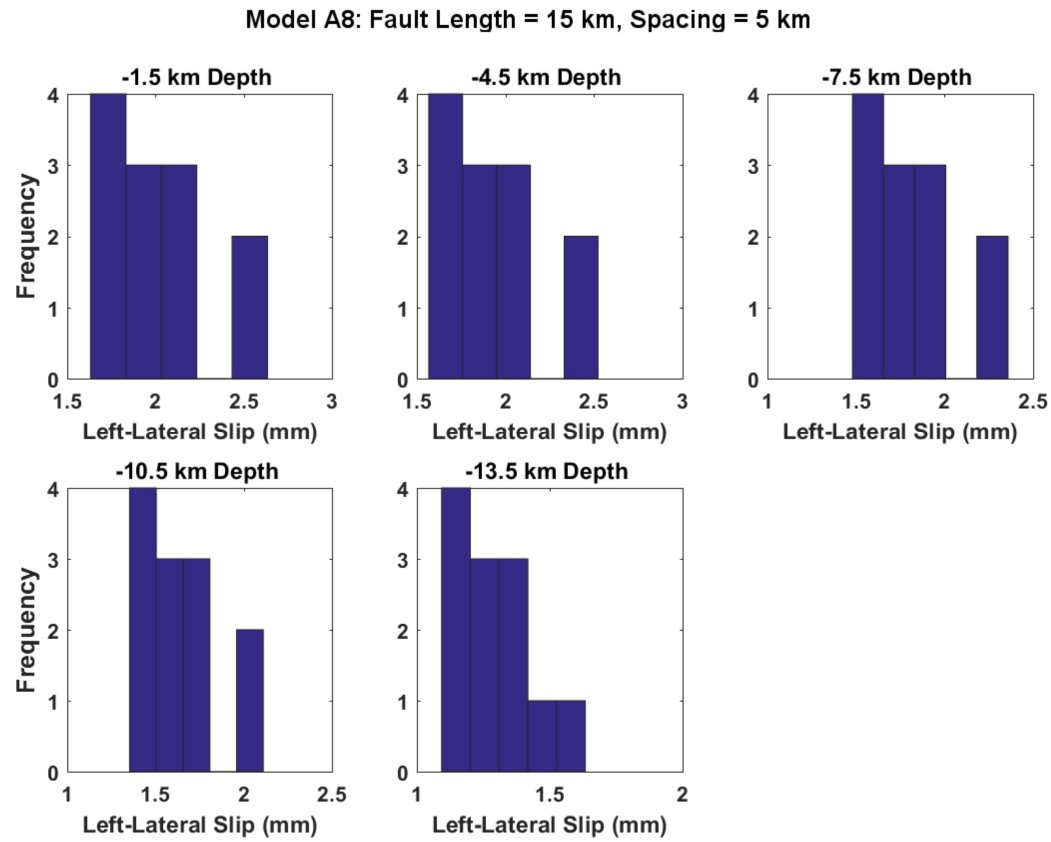

Figure **B-11**: Arc-normal fault downdip elements displacements for model A8.

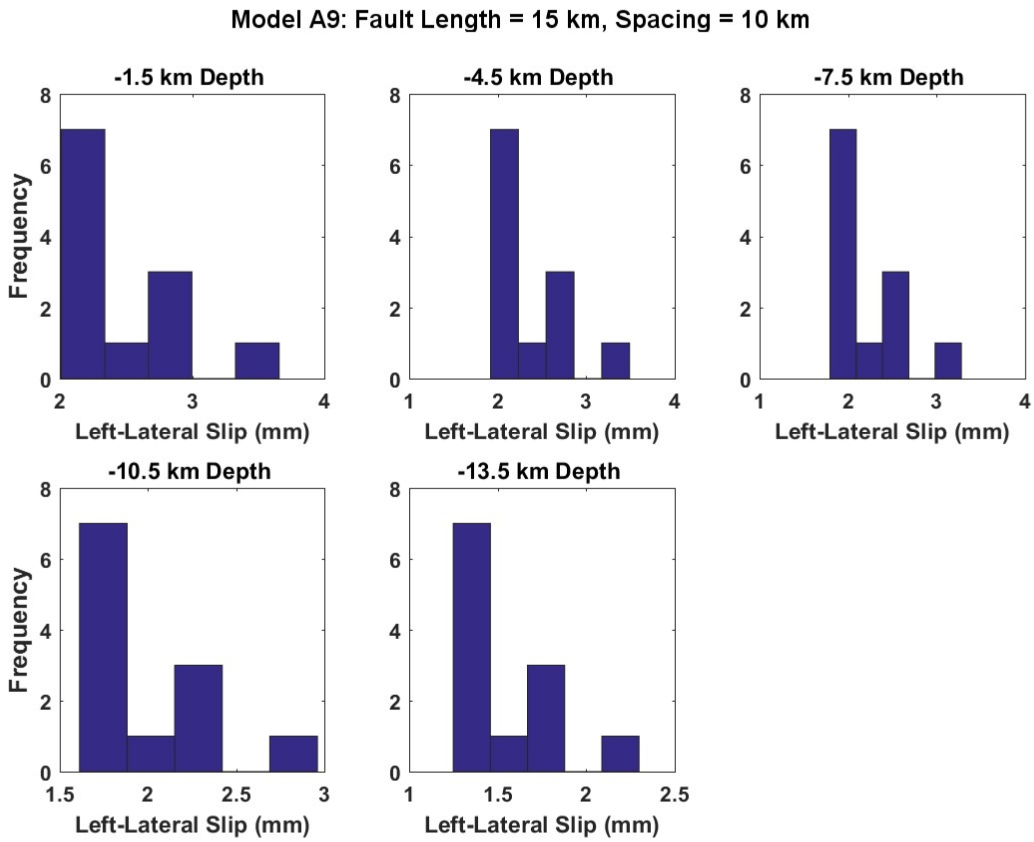

Figure **B-12**: Arc-normal fault downdip elements displacements for model A9.

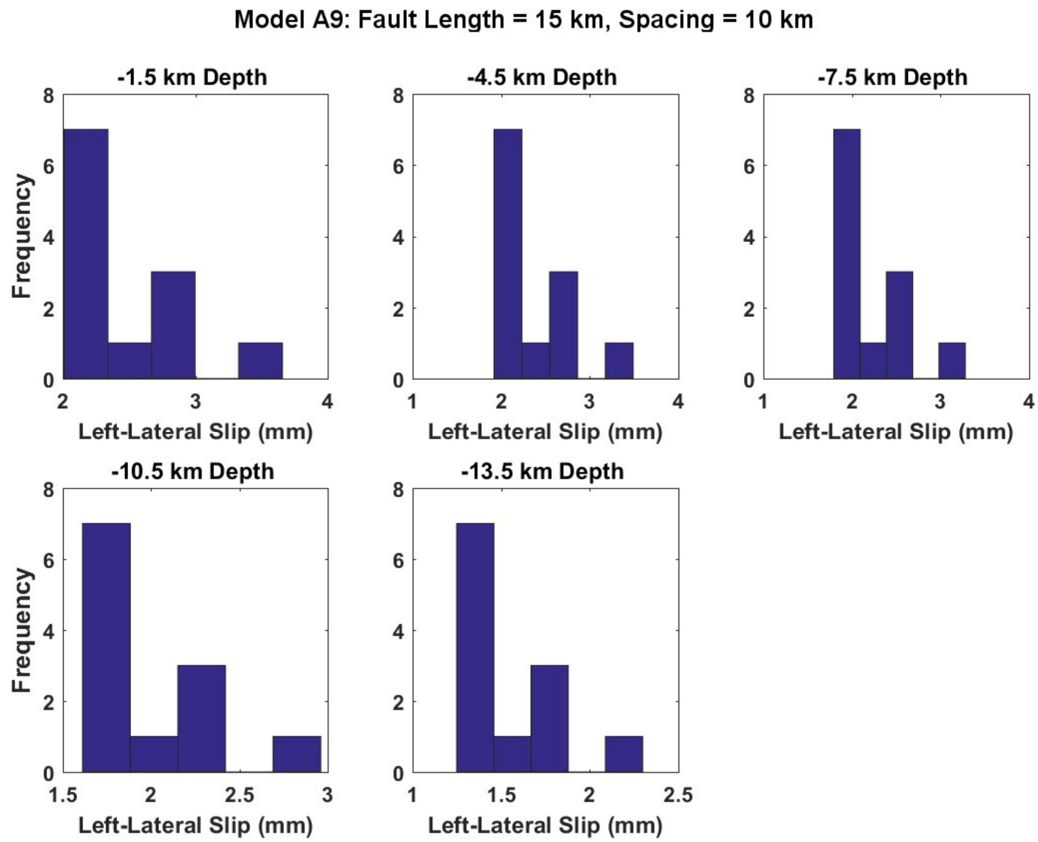

Figure **B-13**: Arc-normal fault downdip elements displacements for model A10.

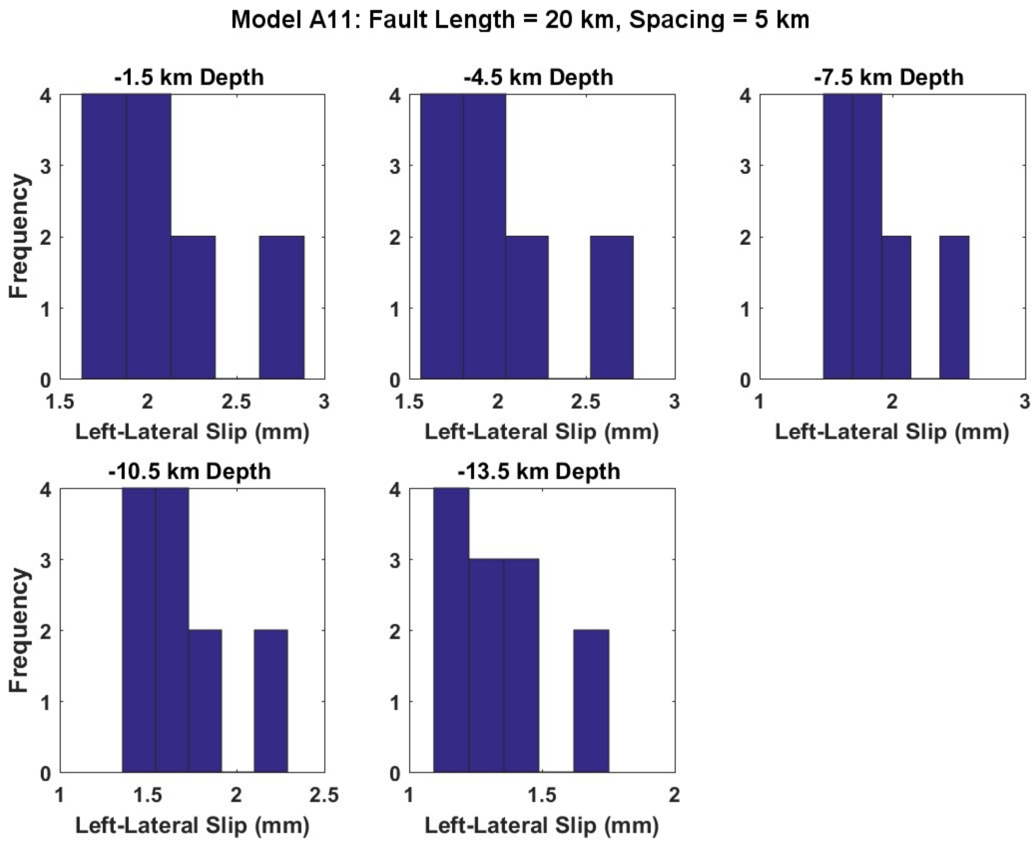

Figure **B-14**: Arc-normal fault downdip elements displacements for model A11.

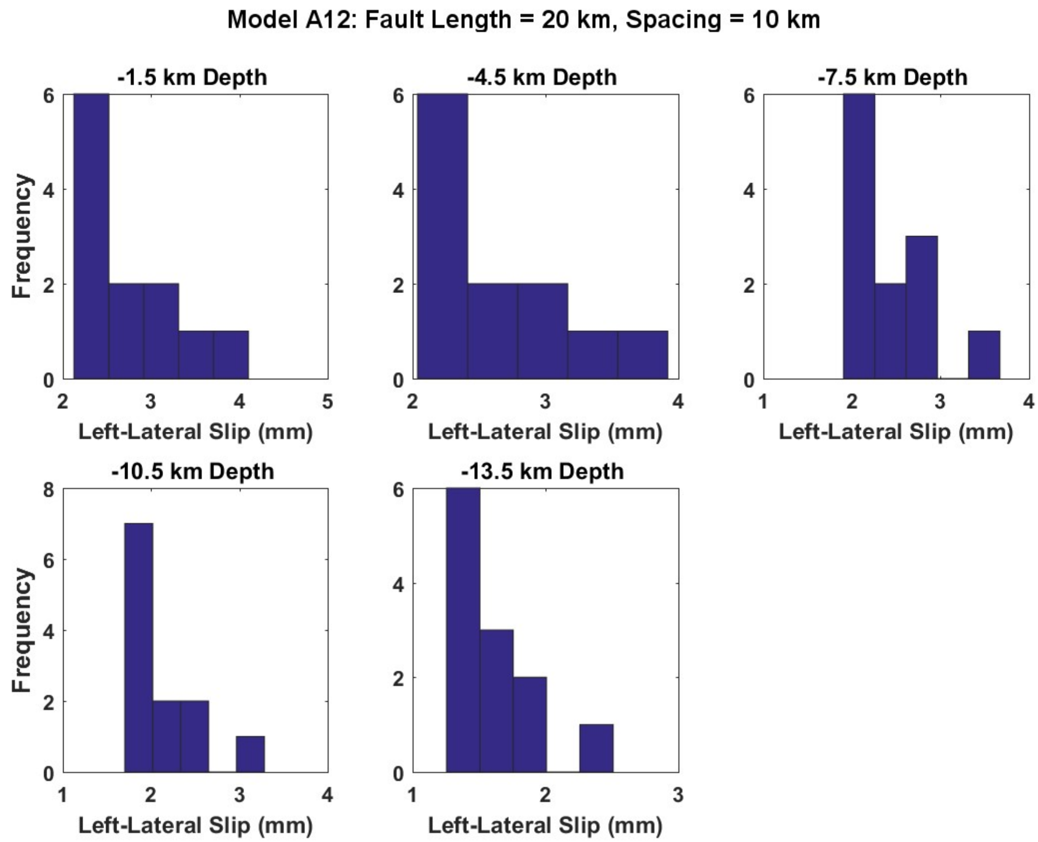

Figure **B-15**: Arc-normal fault downdip elements displacements for model A12.

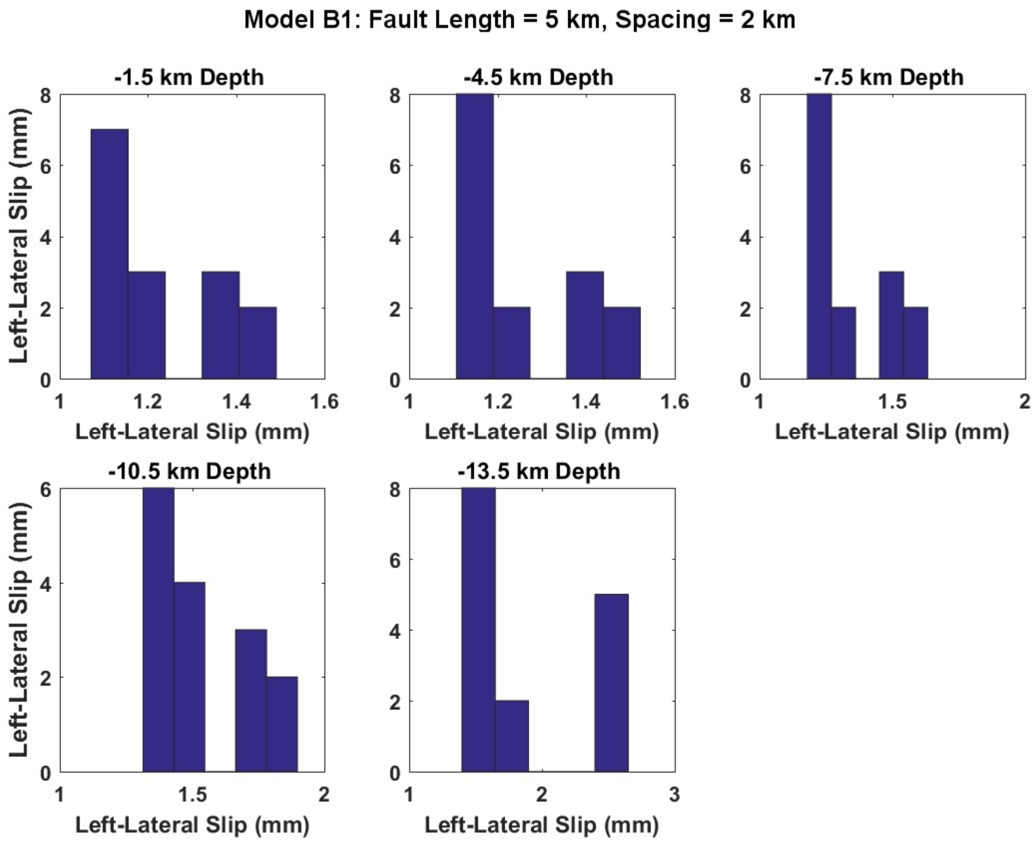

Figure **B-16**: Arc-normal fault downdip elements displacements for model B1.

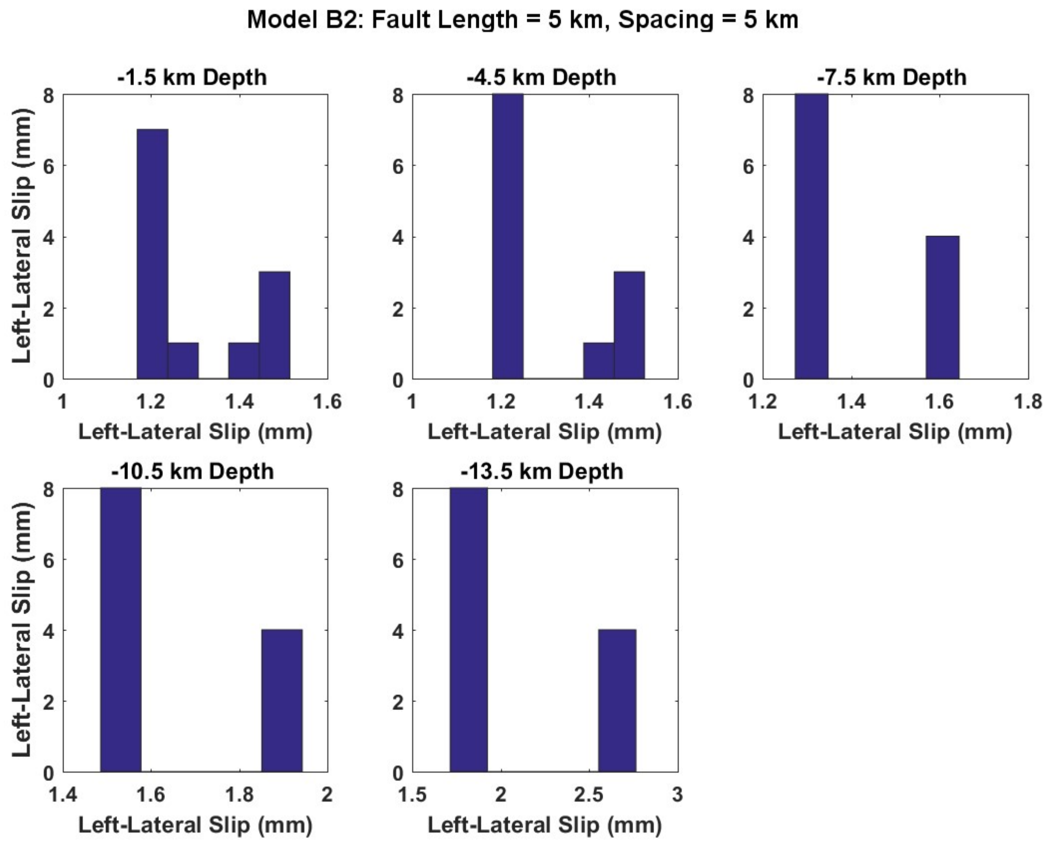

Figure **B-17**: Arc-normal fault downdip elements displacements for model B2.

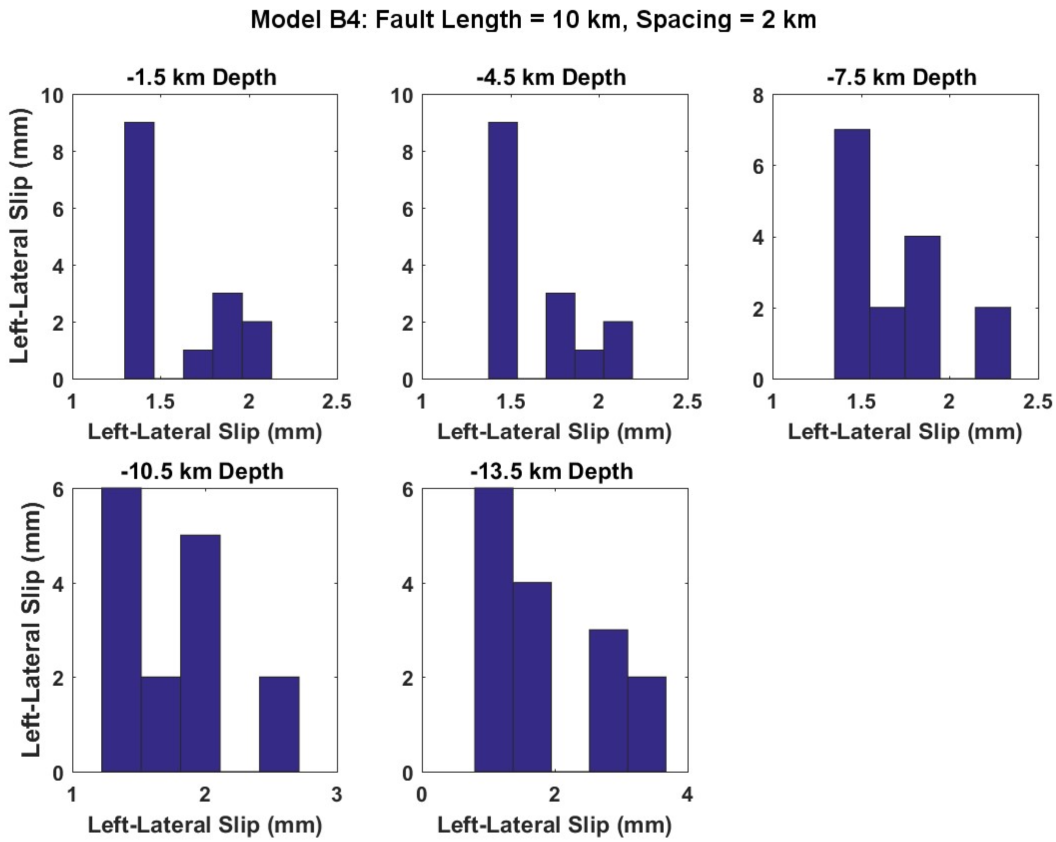

Figure **B-18**: Arc-normal fault downdip elements displacements for model B3.

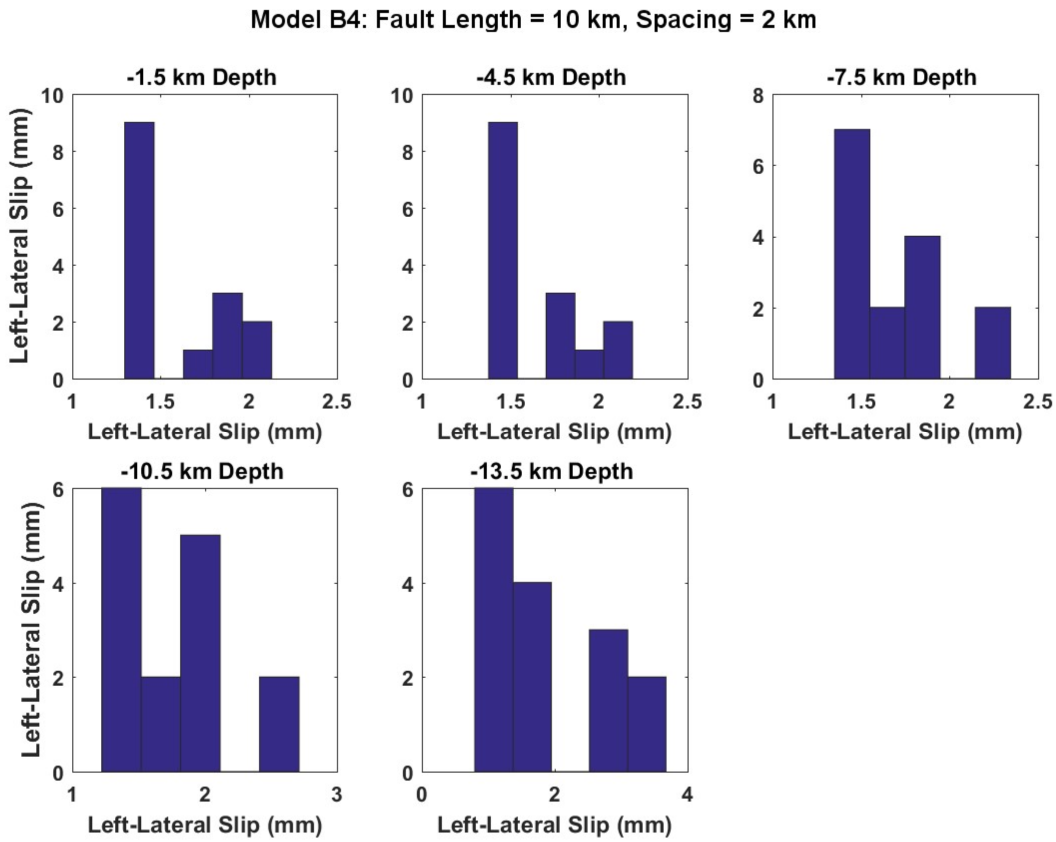

Figure **B-19**: Arc-normal fault downdip elements displacements for model B4.

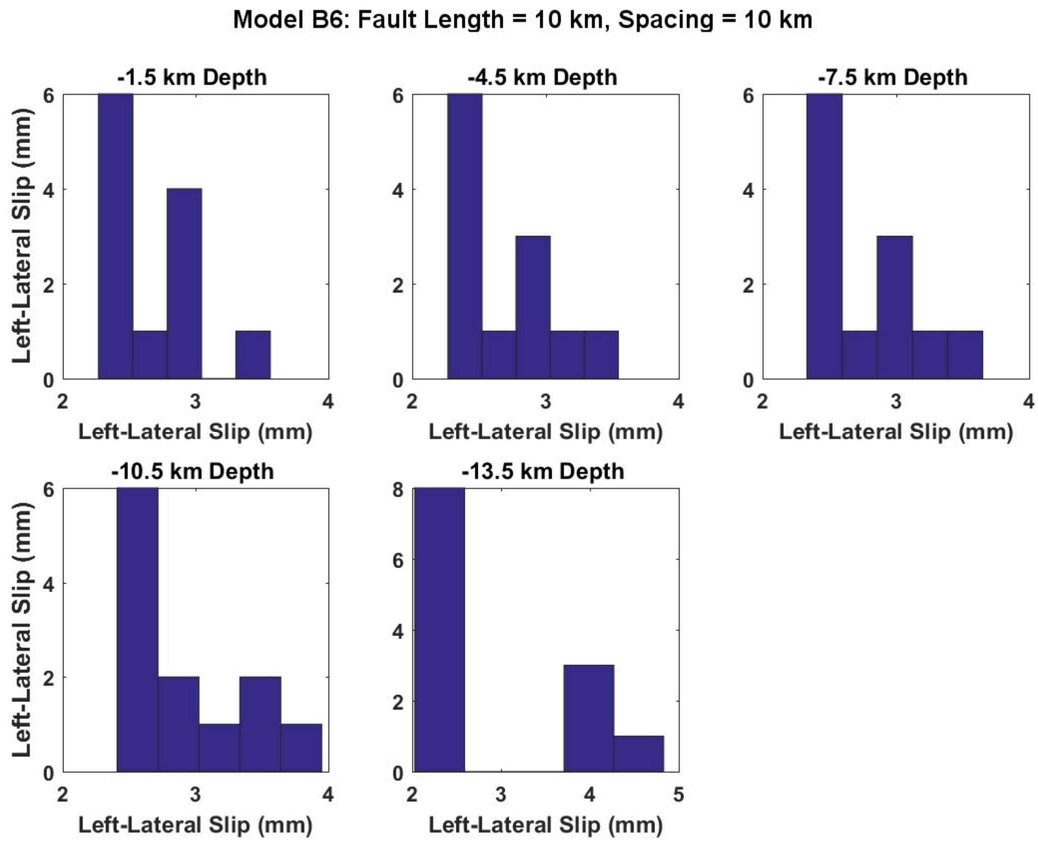

Figure **B-20**: Arc-normal fault downdip elements displacements for model B6.

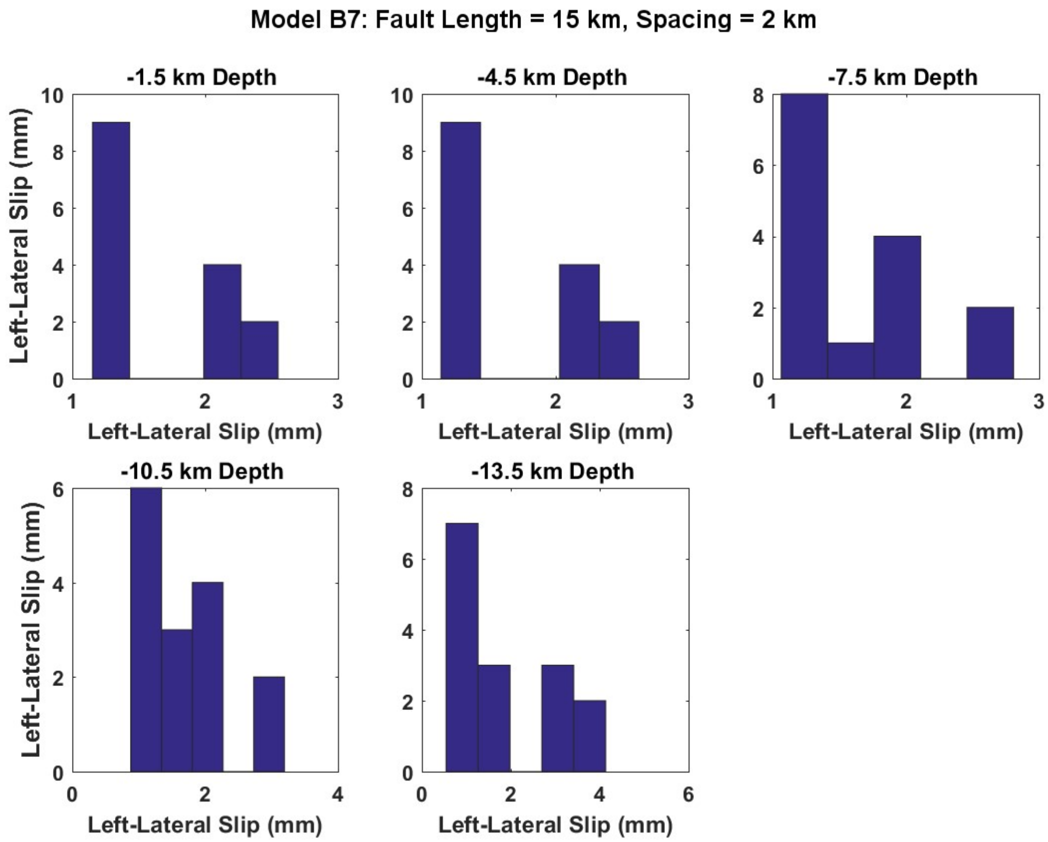

Figure **B-21**: Arc-normal fault downdip elements displacements for model B6.

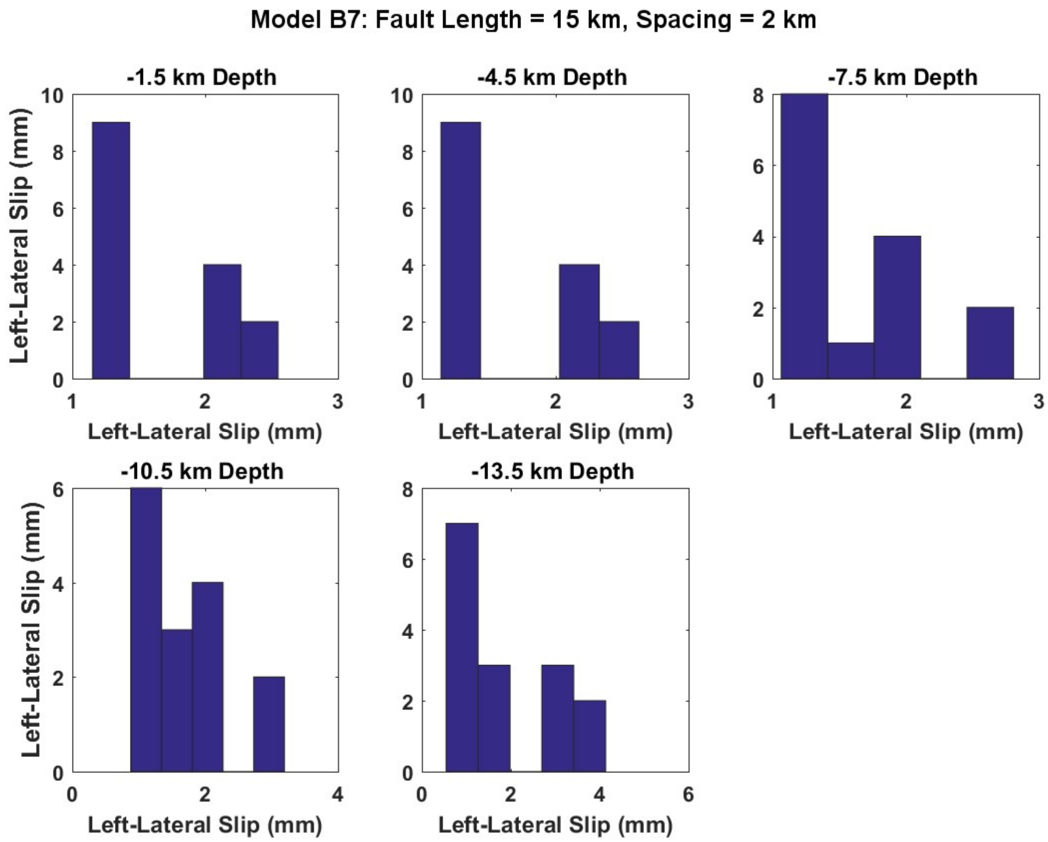

Figure **B-22**: Arc-normal fault downdip elements displacements for model B7.

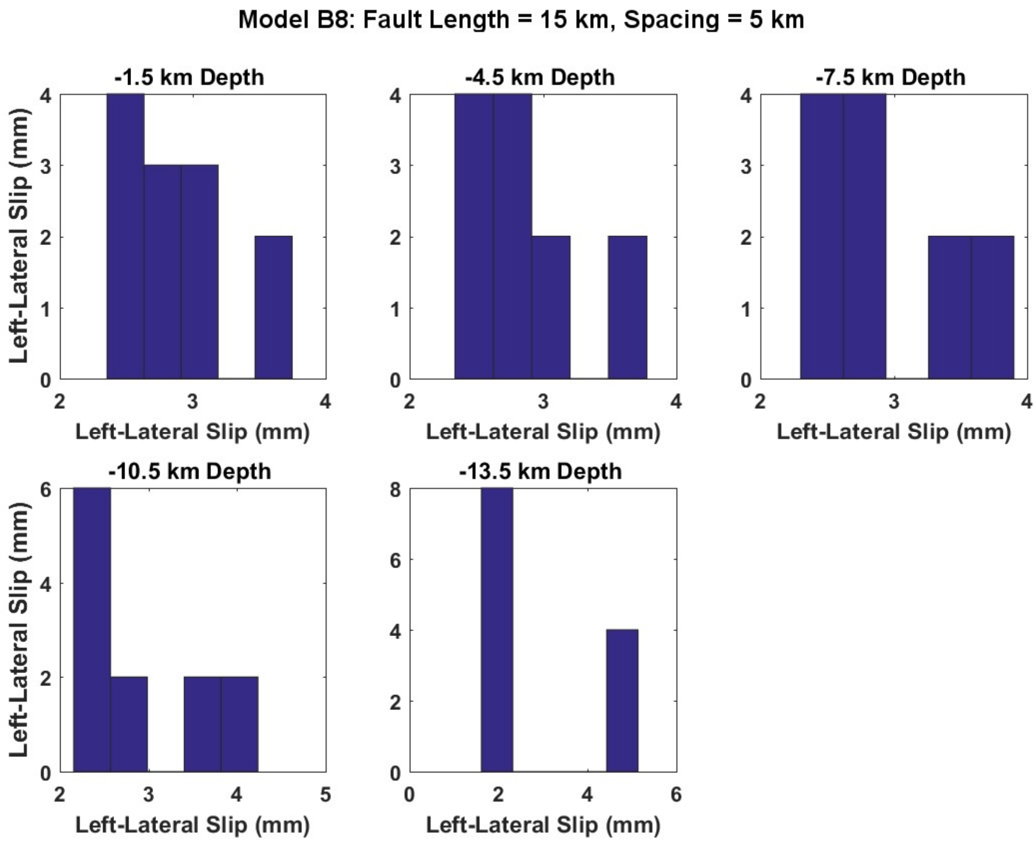

Figure **B-23**: Arc-normal fault downdip elements displacements for model B8.

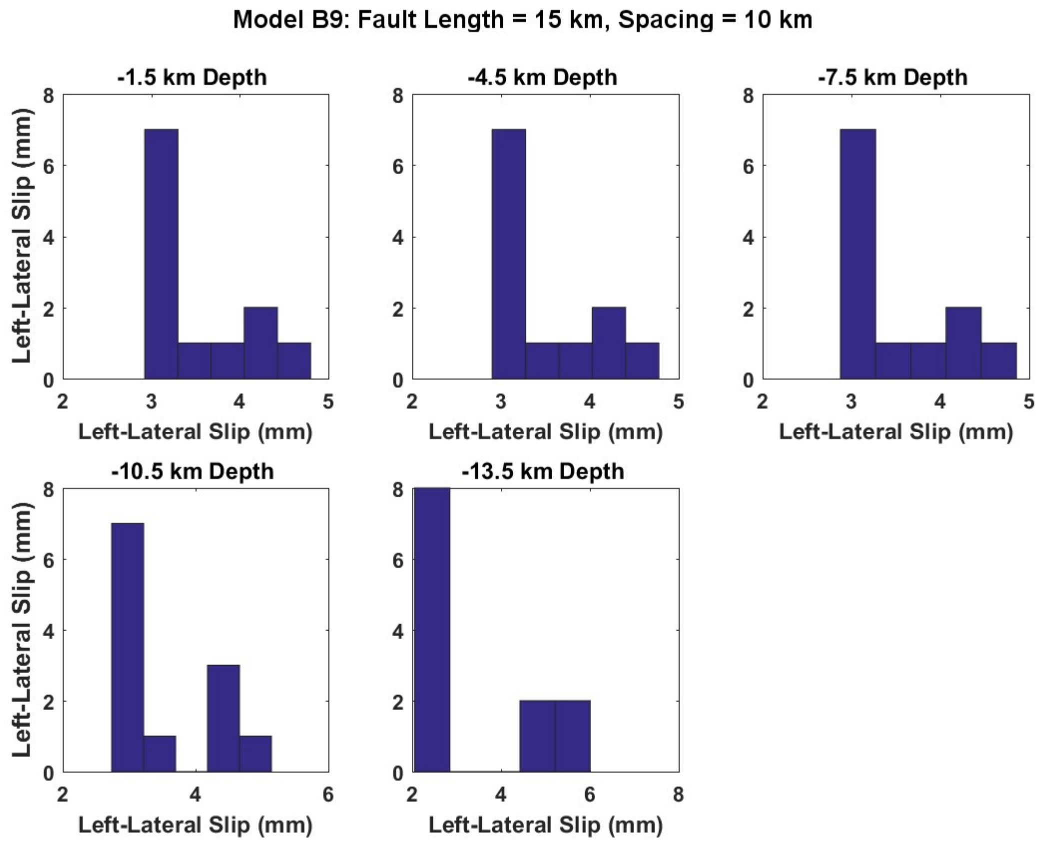

Figure **B-24**: Arc-normal fault downdip elements displacements for model B9.

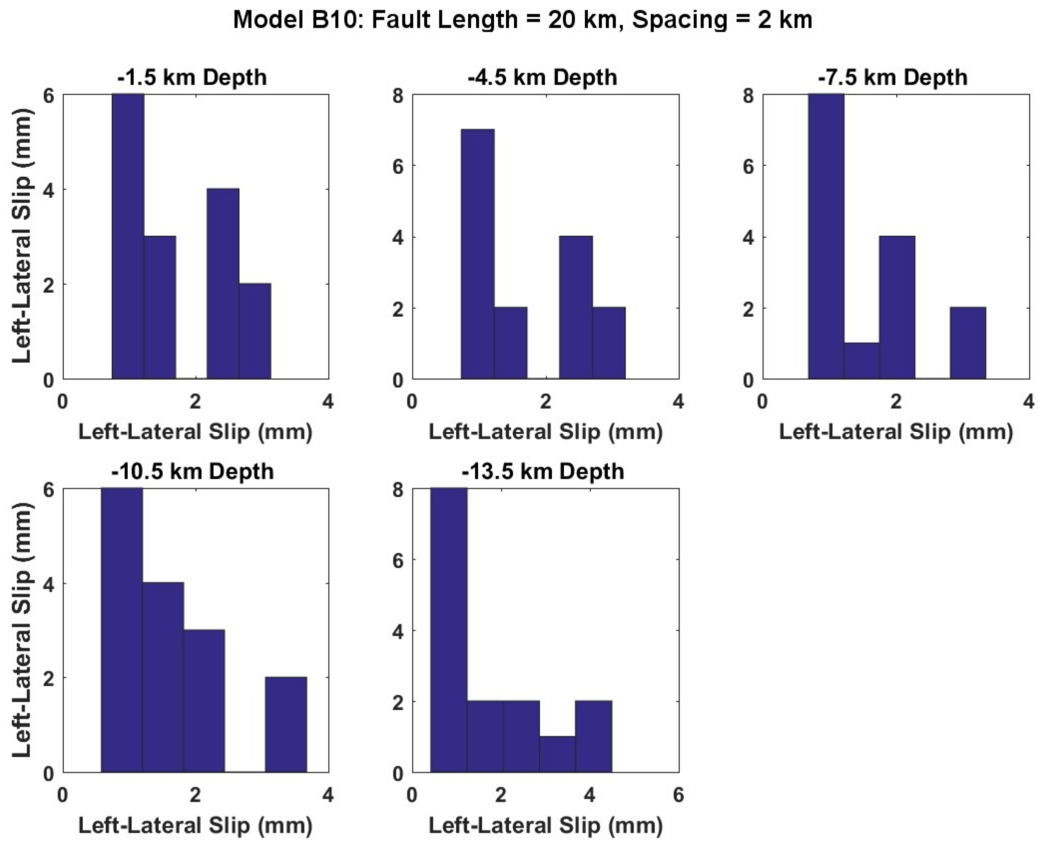

Figure **B-25**: Arc-normal fault downdip elements displacements for model B10.

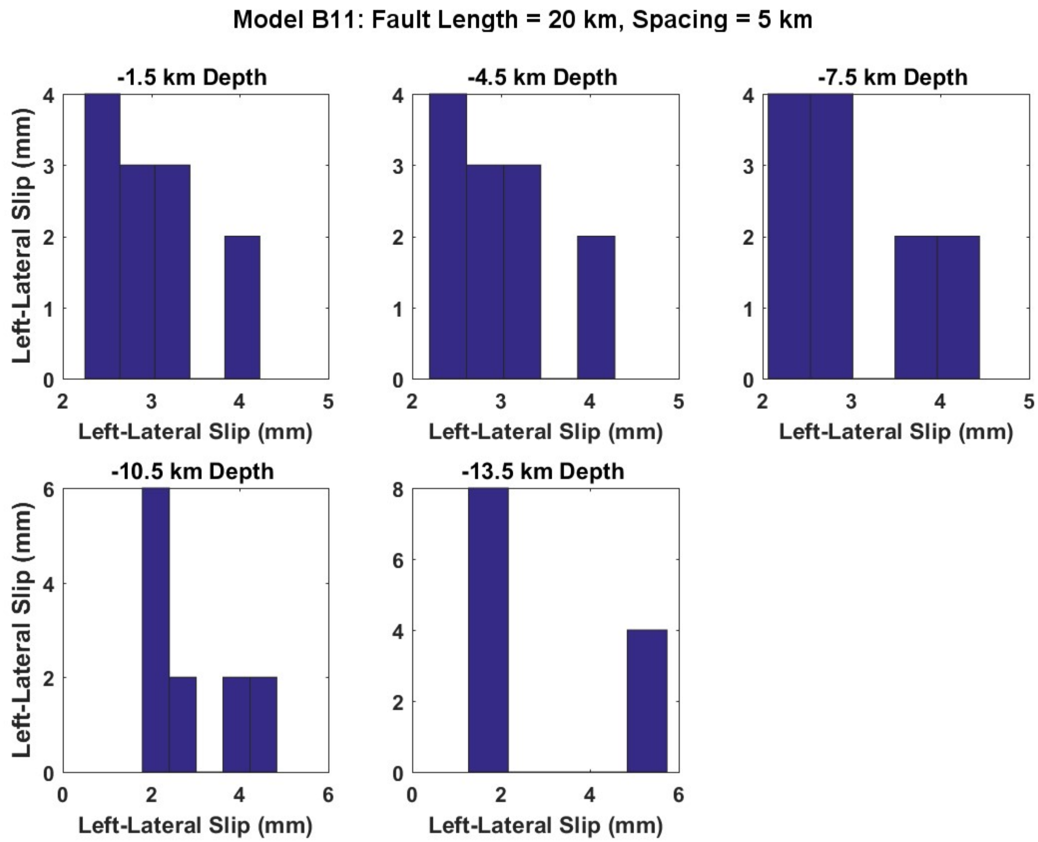

Figure **B-26**: Arc-normal fault downdip elements displacements for model B11.

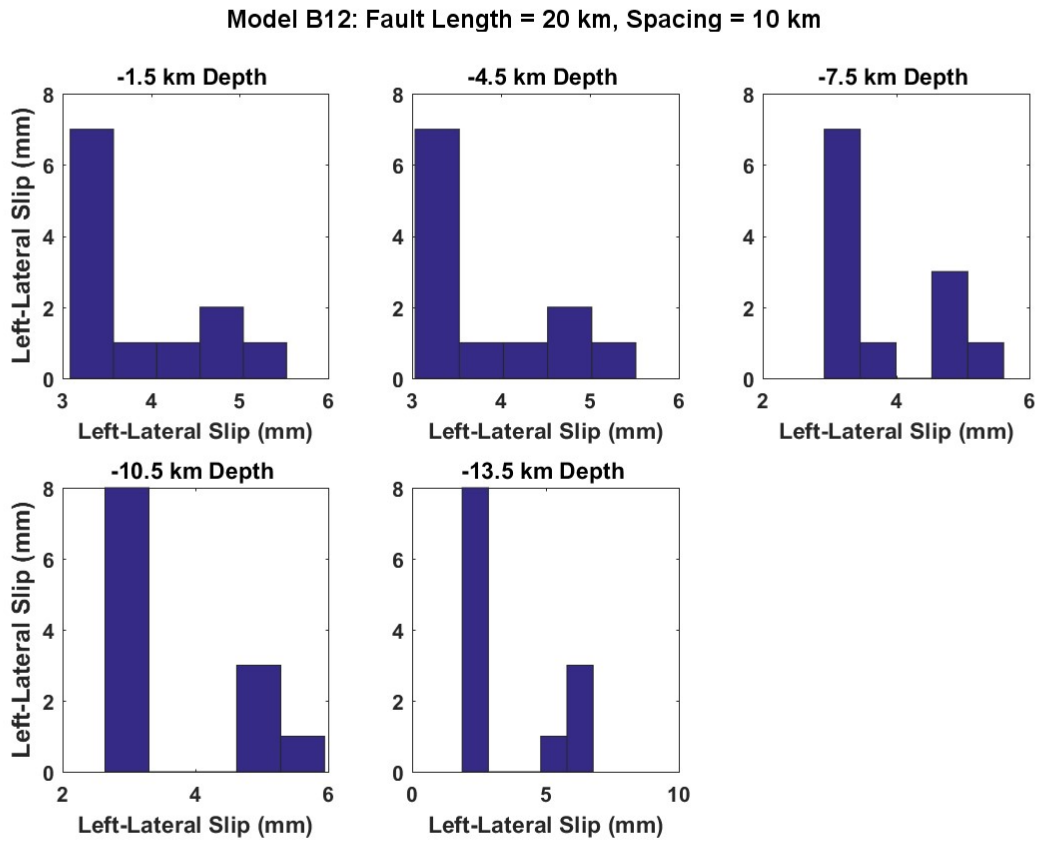

Figure **B-27**: Arc-normal fault downdip elements displacements for model B12.

B.3 Model Set C Plots

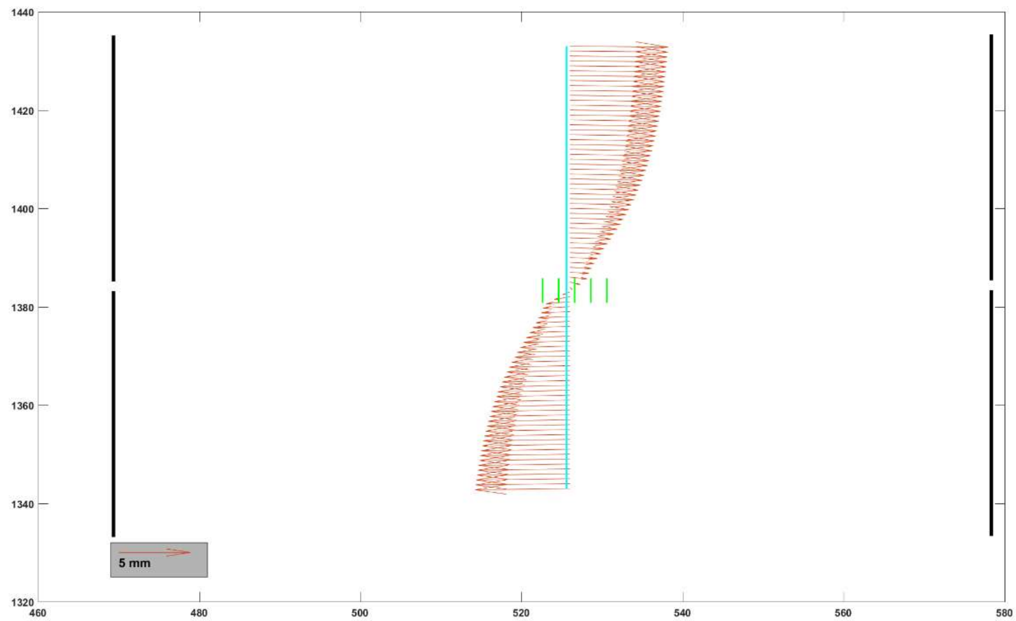

Figure **B-28**: Model C1: surface displacements (red vectors) along-profile line (cyan line). Arc-normal faults' (green lines) length and spacing are 5 km and 2 km respectively. This model has 5 arc-normal faults.

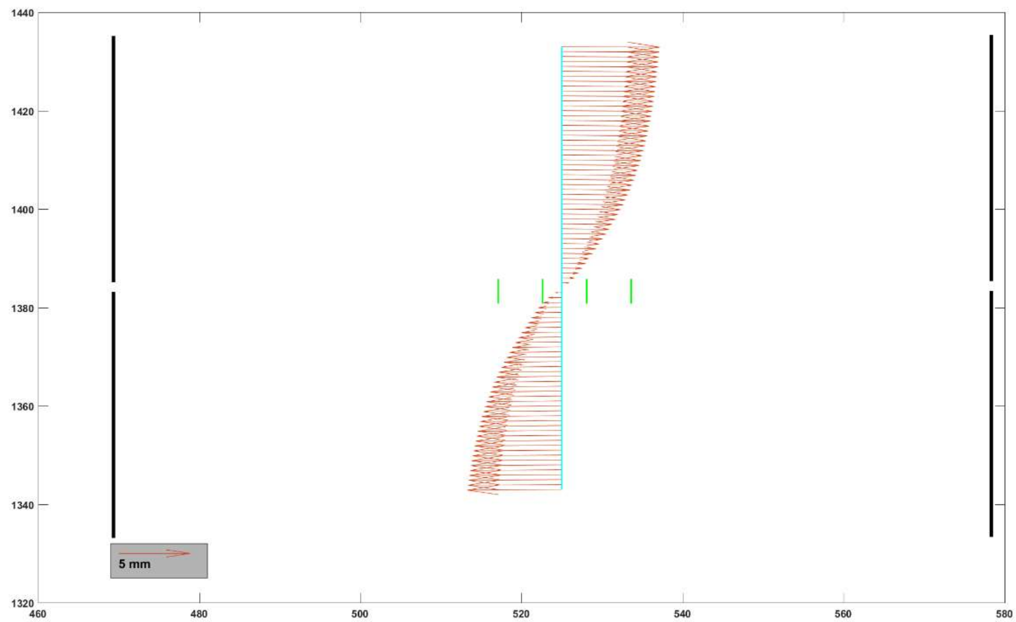

Figure **B-29**: Model C2: surface displacements (red vectors) along-profile line (cyan line). Arc-normal faults' (green lines) length and spacing are 5 km and 5 km respectively. This model has 4 arc-normal faults.

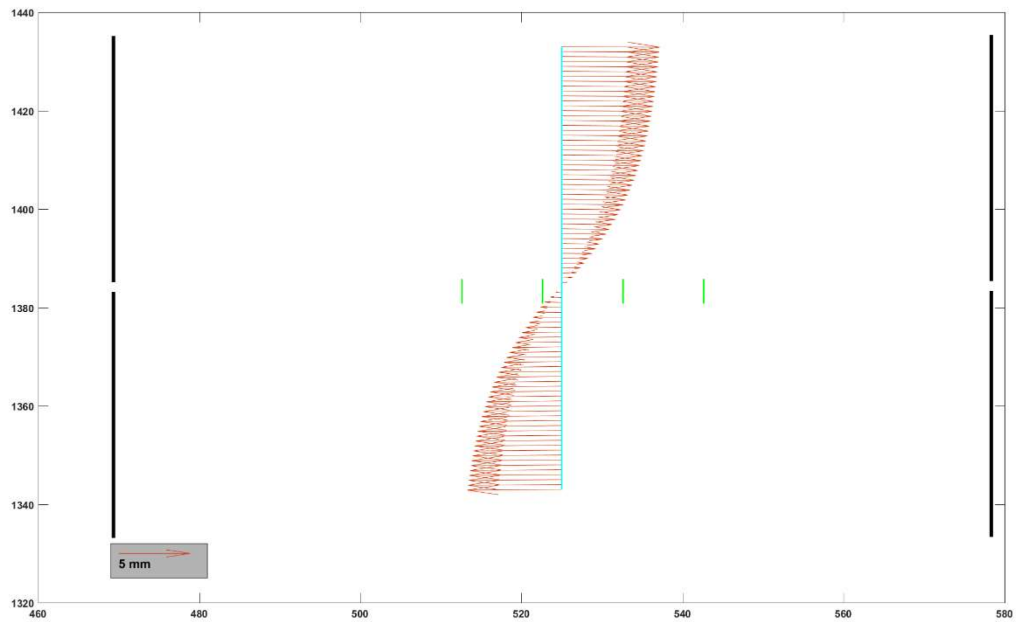

Figure **B-30**: Model C3: surface displacements (red vectors) along-profile line (cyan line). Arc-normal faults' (green lines) length and spacing are 5 km and 10 km respectively. This model has 4 arc-normal faults.

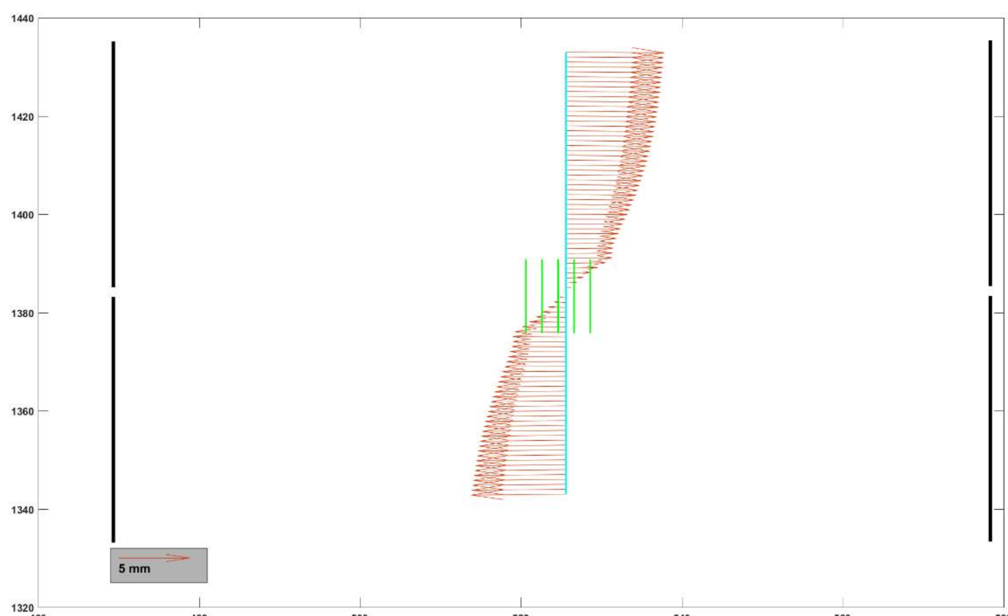

Figure **B-31**: Model C4: surface displacements (red vectors) along-profile line (cyan line). Arc-normal faults' (green lines) length and spacing are 10 km and 2 km respectively. This model has 5 arc-normal faults.

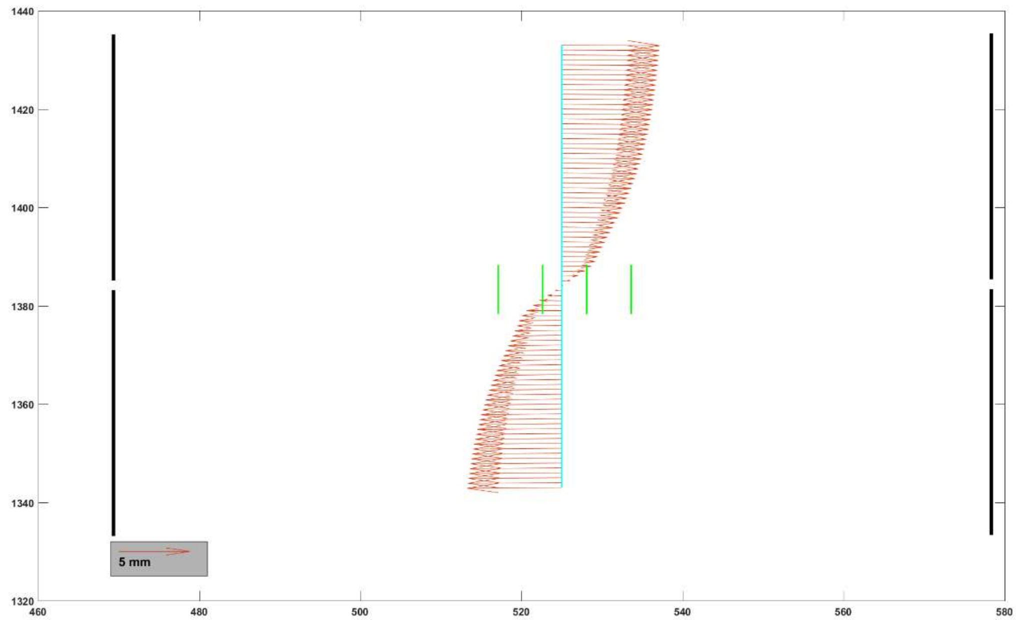

Figure **B-32**: Model C5: surface displacements (red vectors) along-profile line (cyan line). Arc-normal faults' (green lines) length and spacing are 10 km and 5 km respectively. This model has 4 arc-normal faults.

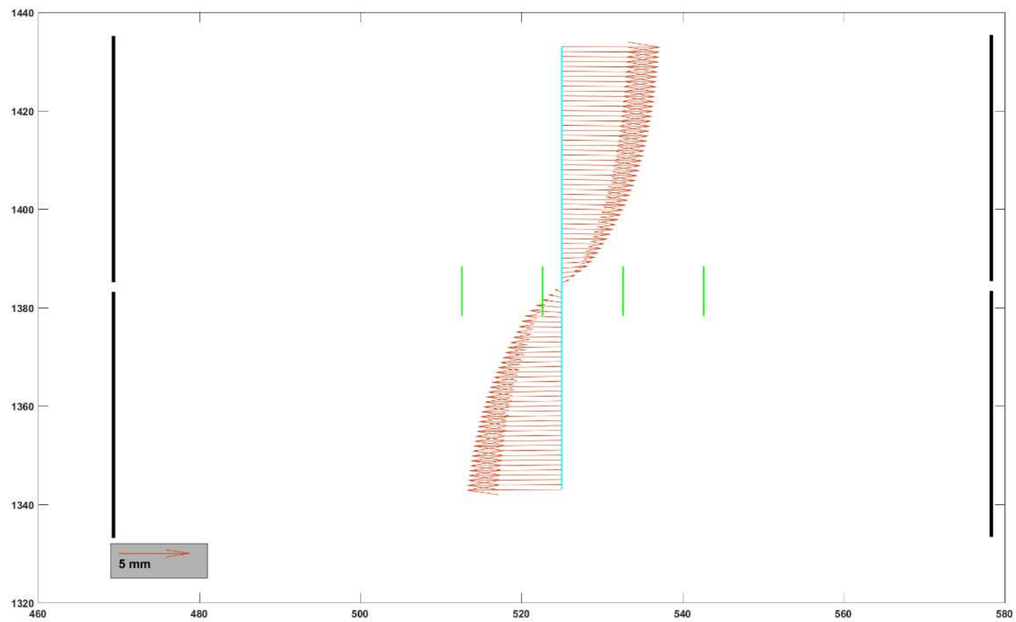

Figure **B-33**: Model C6: surface displacements (red vectors) along-profile line (cyan line). Arc-normal faults' (green lines) length and spacing are 10 km and 10 km respectively. This model has 4 arc-normal faults.

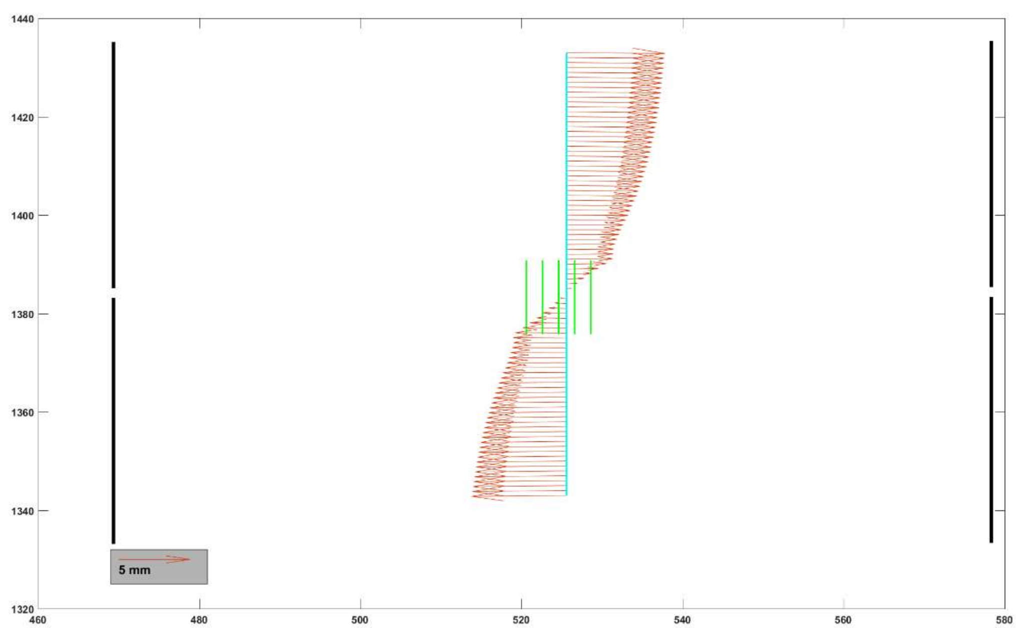

Figure **B-34**: Model C7: surface displacements (red vectors) along-profile line (cyan line). Arc-normal faults' (green lines) length and spacing are 15 km and 2 km respectively. This model has 5 arc-normal faults.

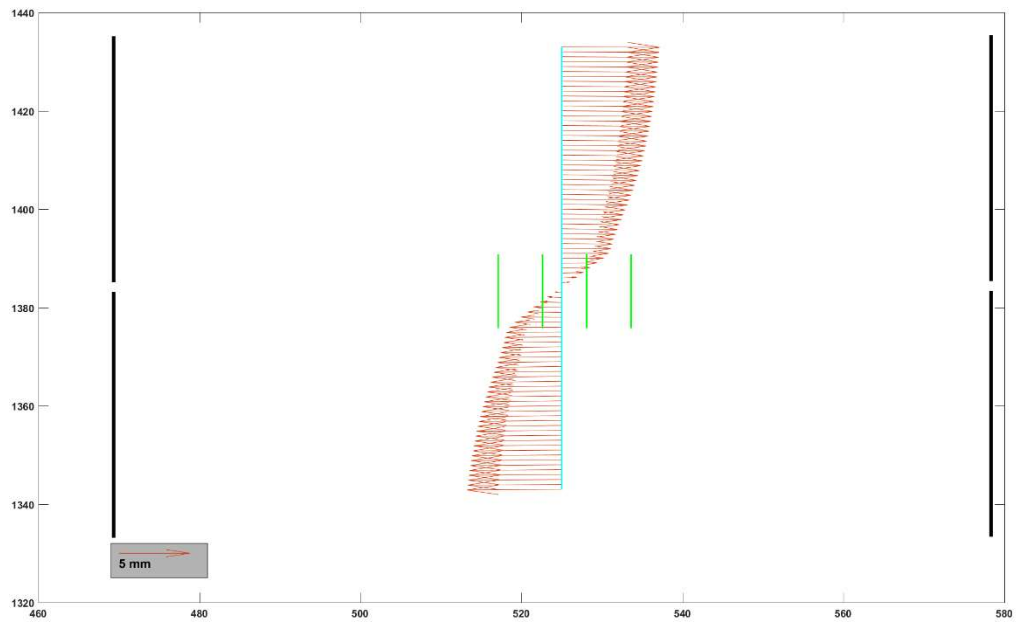

Figure **B-35**: Model C8: surface displacements (red vectors) along-profile line (cyan line). Arc-normal faults' (green lines) length and spacing are 15 km and 5 km respectively. This model has 4 arc-normal faults.

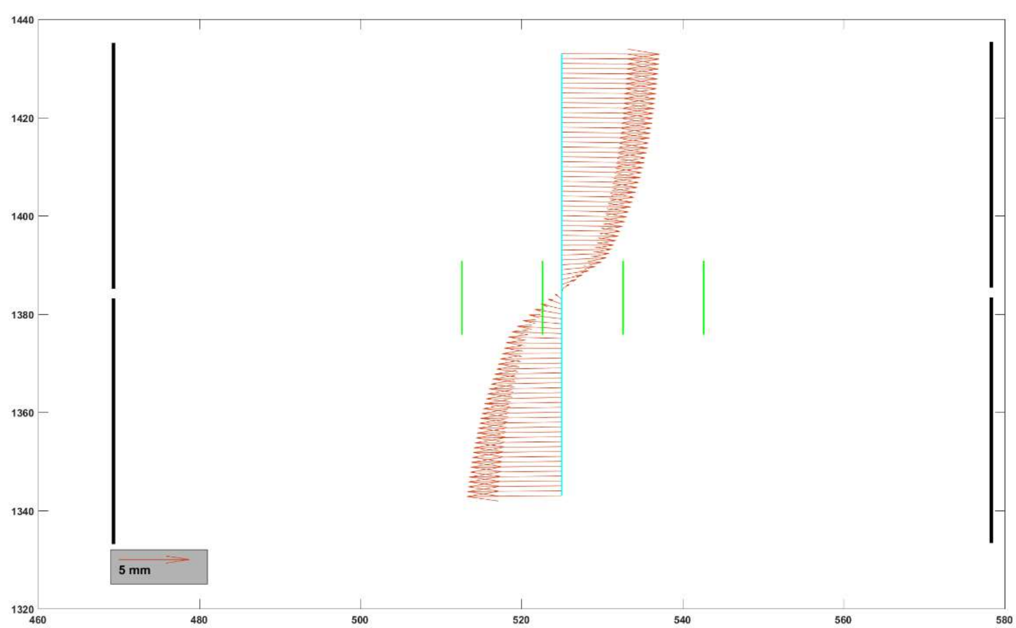

Figure **B-36**: Model C9: surface displacements (red vectors) along-profile line (cyan line). Arc-normal faults' (green lines) length and spacing are 15 km and 10 km respectively. This model has 4 arc-normal faults.

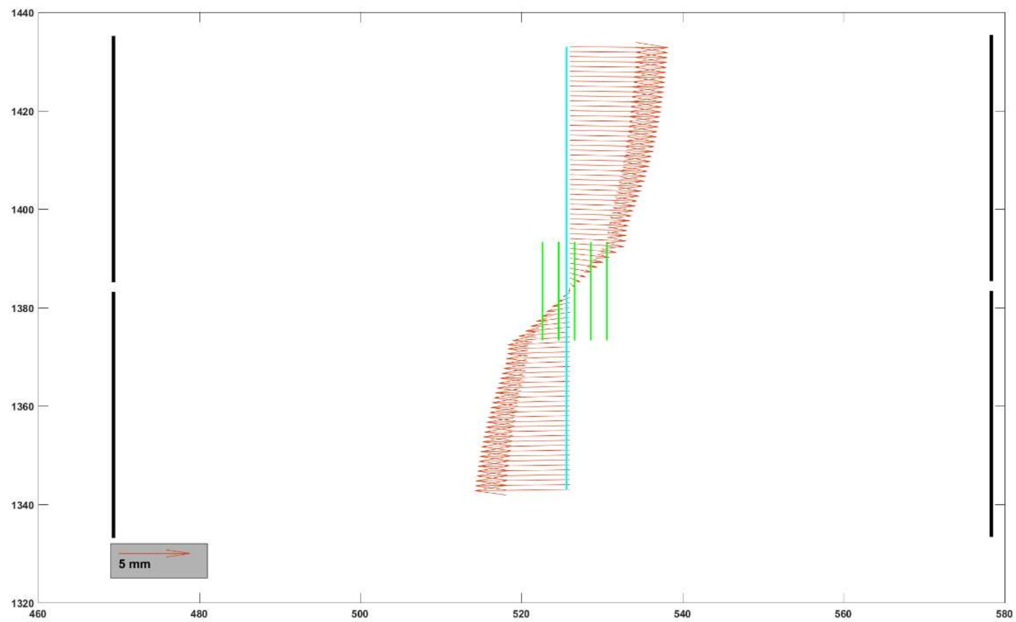

Figure **B-37**: Model C10: surface displacements (red vectors) along-profile line (cyan line). Arc-normal faults' (green lines) length and spacing are 20 km and 2 km respectively. This model has 5 arc-normal faults.

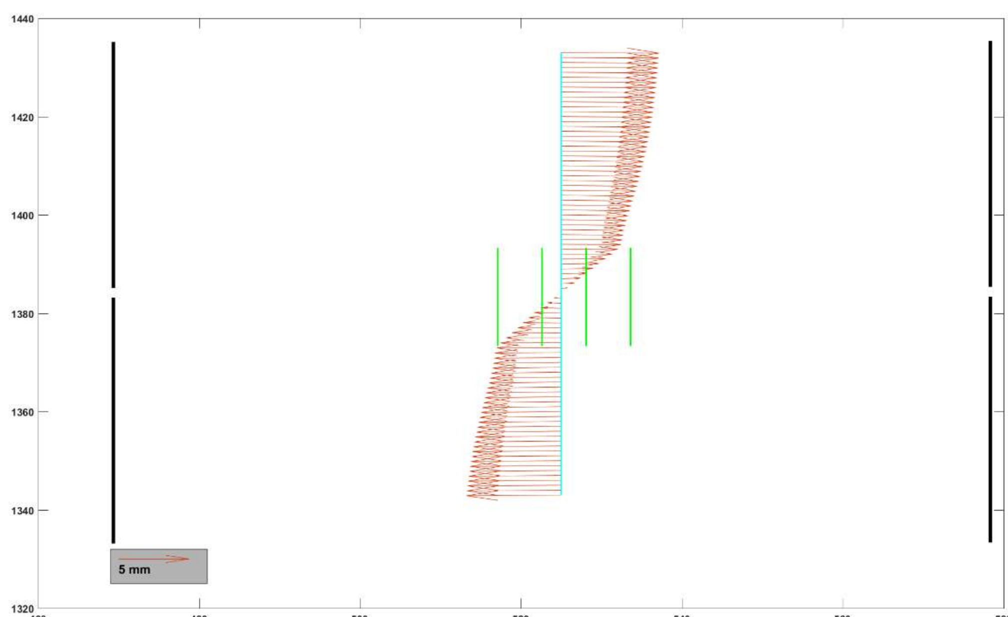

Figure **B-38**: Model C11: surface displacements (red vectors) along-profile line (cyan line). Arc-normal faults' (green lines) length and spacing are 20 km and 5 km respectively. This model has 4 arc-normal faults.

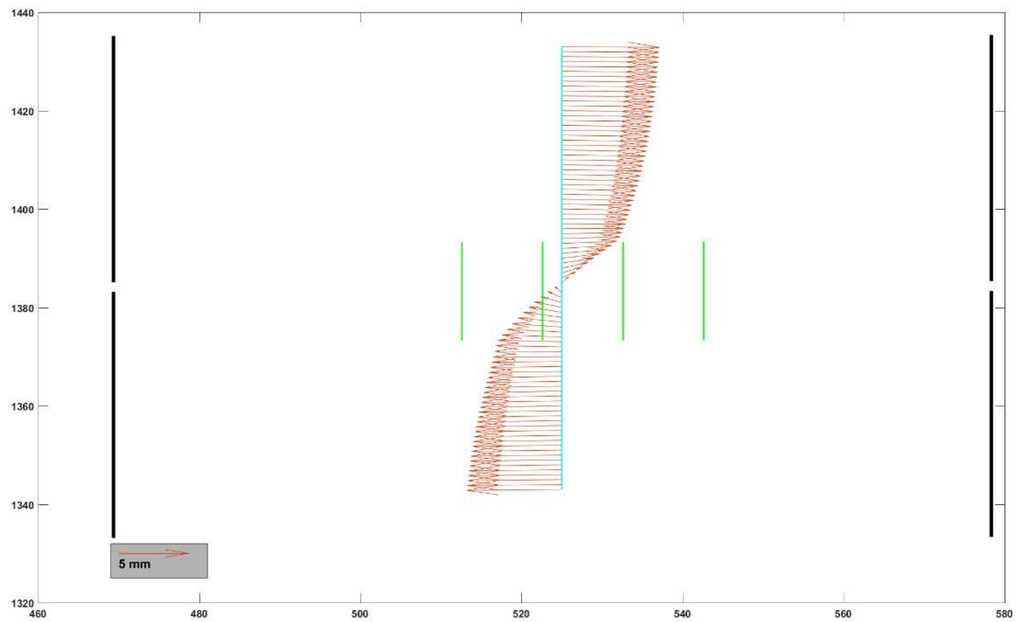

Figure **B-39**: Model C12: surface displacements (red vectors) along-profile line (cyan line). Arc-normal faults' (green lines) length and spacing are 20 km and 10 km respectively. This model has 4 arc-normal faults.

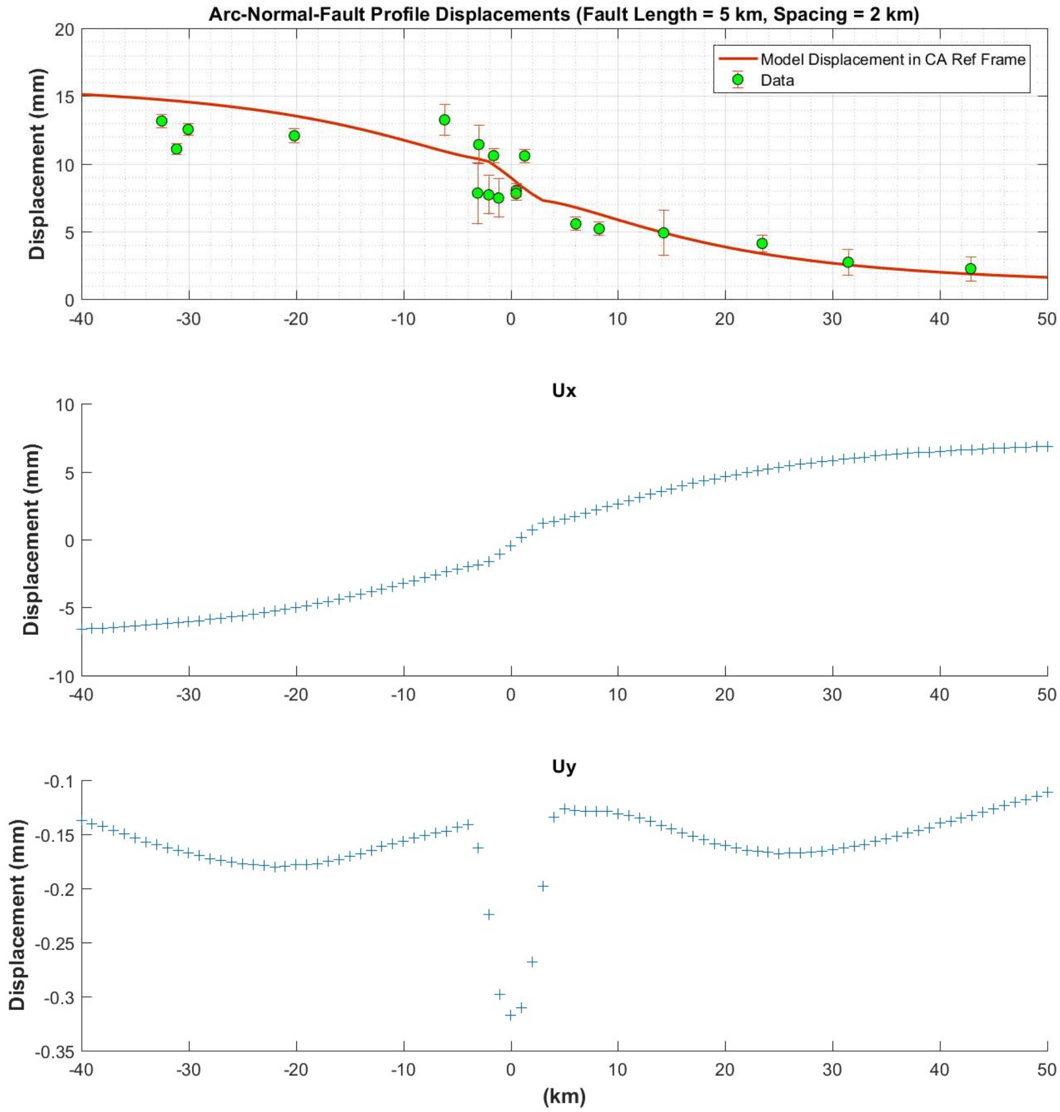

Figure **B-40**: Model C1: displacements along-profile. Arc-normal faults' length and spacing are 5 km and 2 km respectively. Top panel – profile displacements projected into horizontal line (azimuth = 270°). Middle panel – profile displacements in the x-direction. Bottom panel – profile displacements in the y-direction. 'Model Displacement in CA' data sets was created by adding an offset of 7 mm to the model displacements.

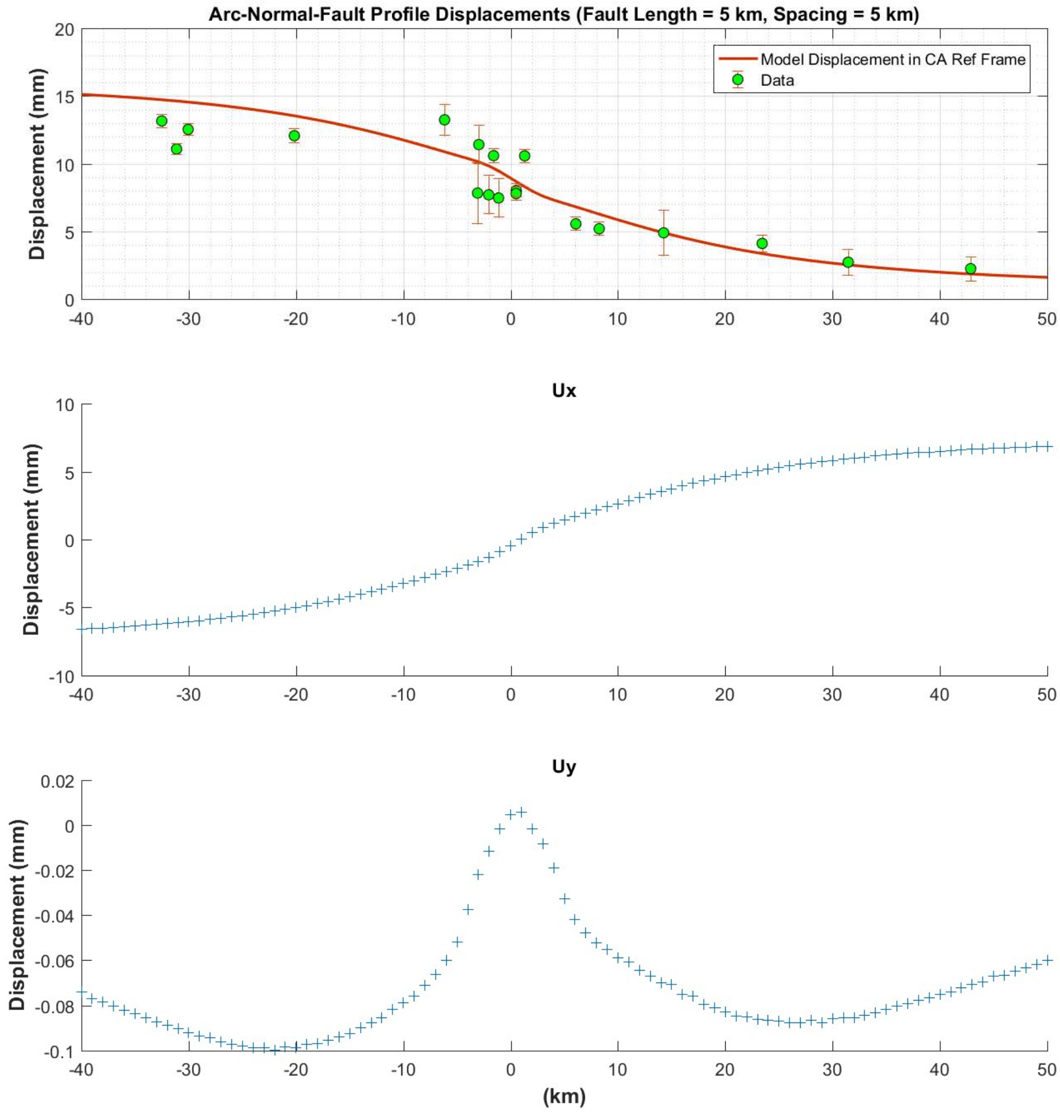

Figure **B-41**: Model C2: displacements along-profile. Arc-normal faults' length and spacing are 5 km and 5 km respectively. Top panel – profile displacements projected into horizontal line (azimuth = 270°). Middle panel – profile displacements in the x-direction. Bottom panel – profile displacements in the y-direction. 'Model Displacement in CA' data sets was created by adding an offset of 7 mm to the model displacements.

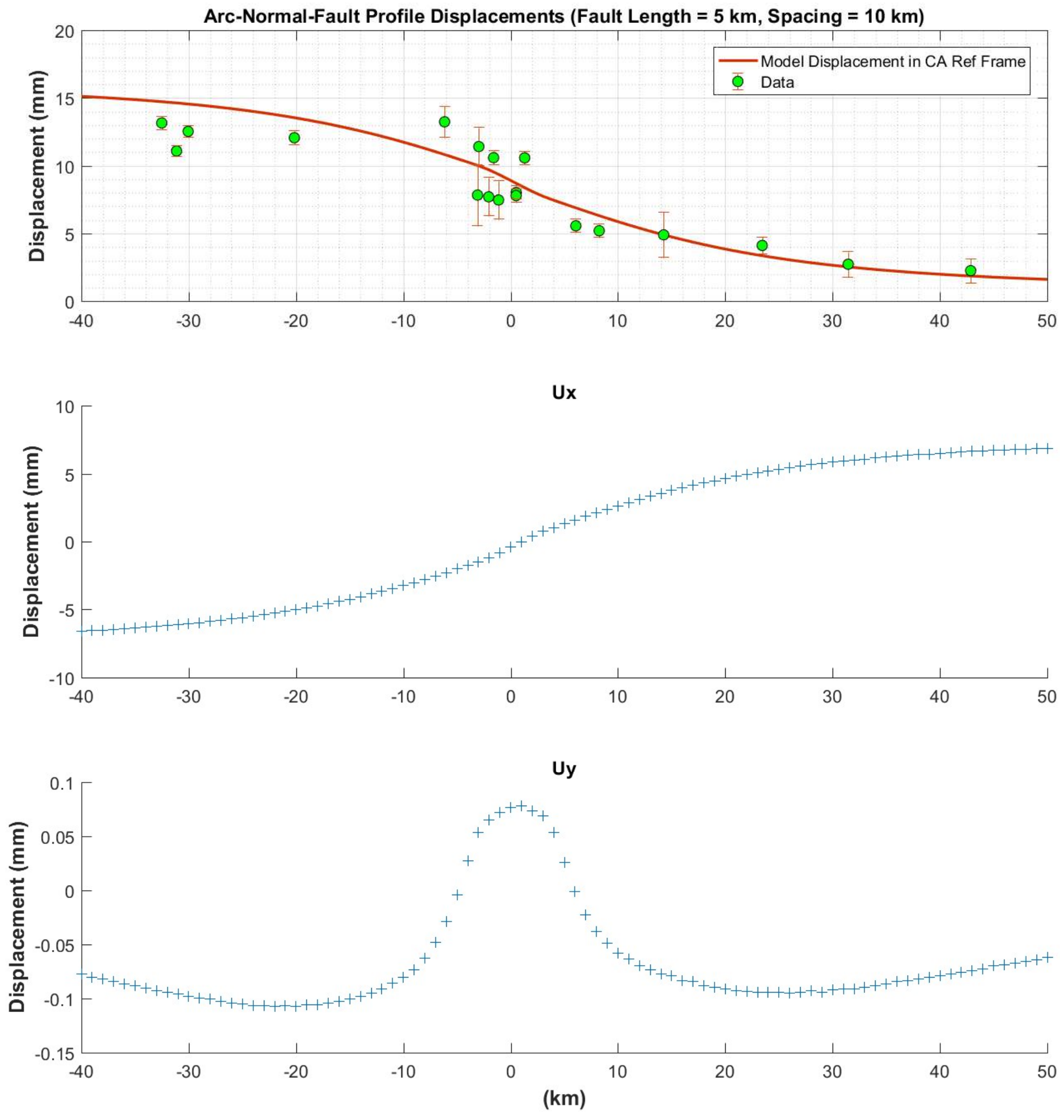

Figure **B-42**: Model C3: displacements along-profile. Arc-normal faults' length and spacing are 5 km and 10 km respectively. Top panel – profile displacements projected into horizontal line (azimuth = 270°). Middle panel – profile displacements in the x-direction. Bottom panel – profile displacements in the y-direction. 'Model Displacement in CA' data sets was created by adding an offset of 7 mm to the model displacements.

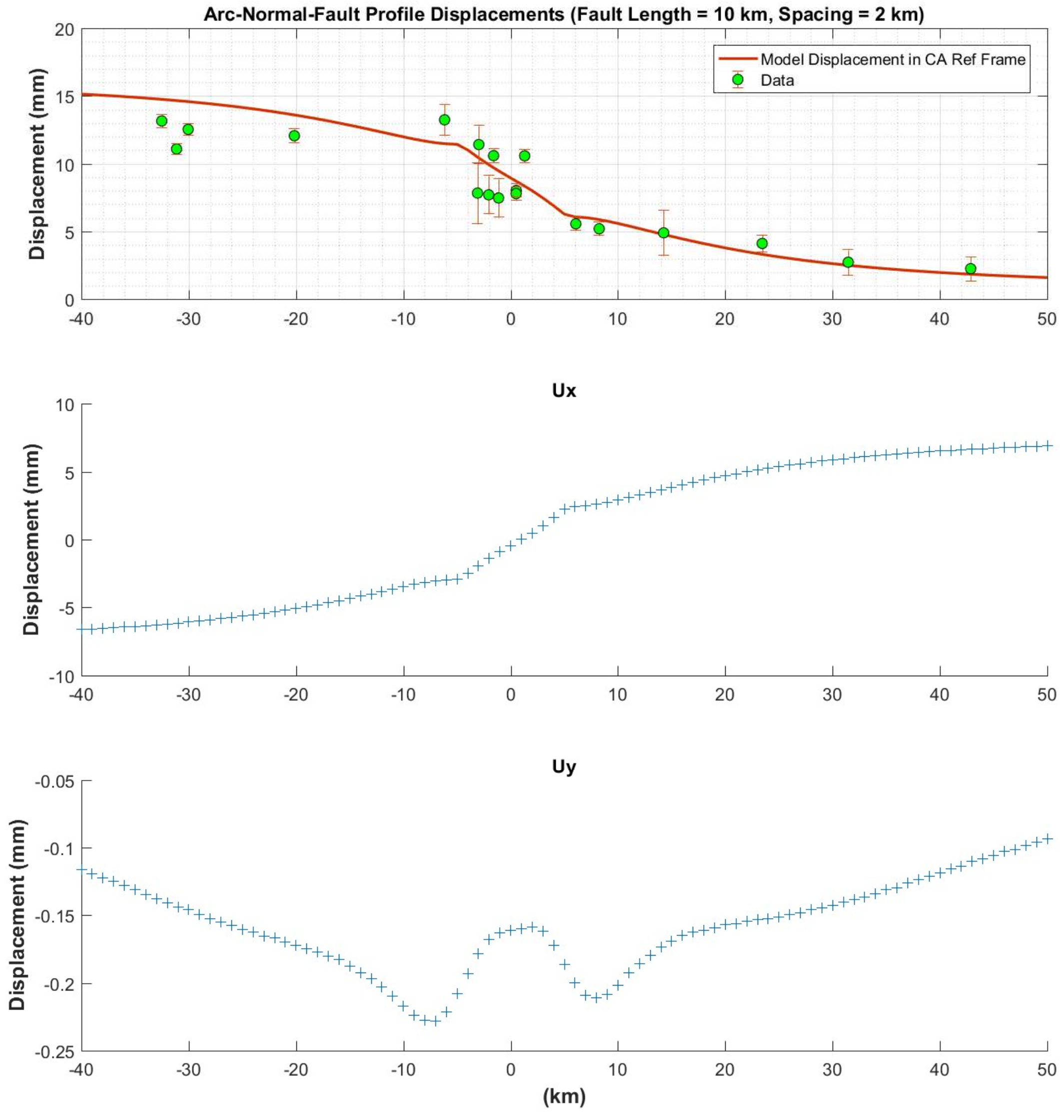

Figure **B-43**: Model C4: displacements along-profile. Arc-normal faults' length and spacing are 10 km and 2 km respectively. Top panel – profile displacements projected into horizontal line (azimuth = 270°). Middle panel – profile displacements in the x-direction. Bottom panel – profile displacements in the y-direction. 'Model Displacement in CA' data sets was created by adding an offset of 7 mm to the model displacements.

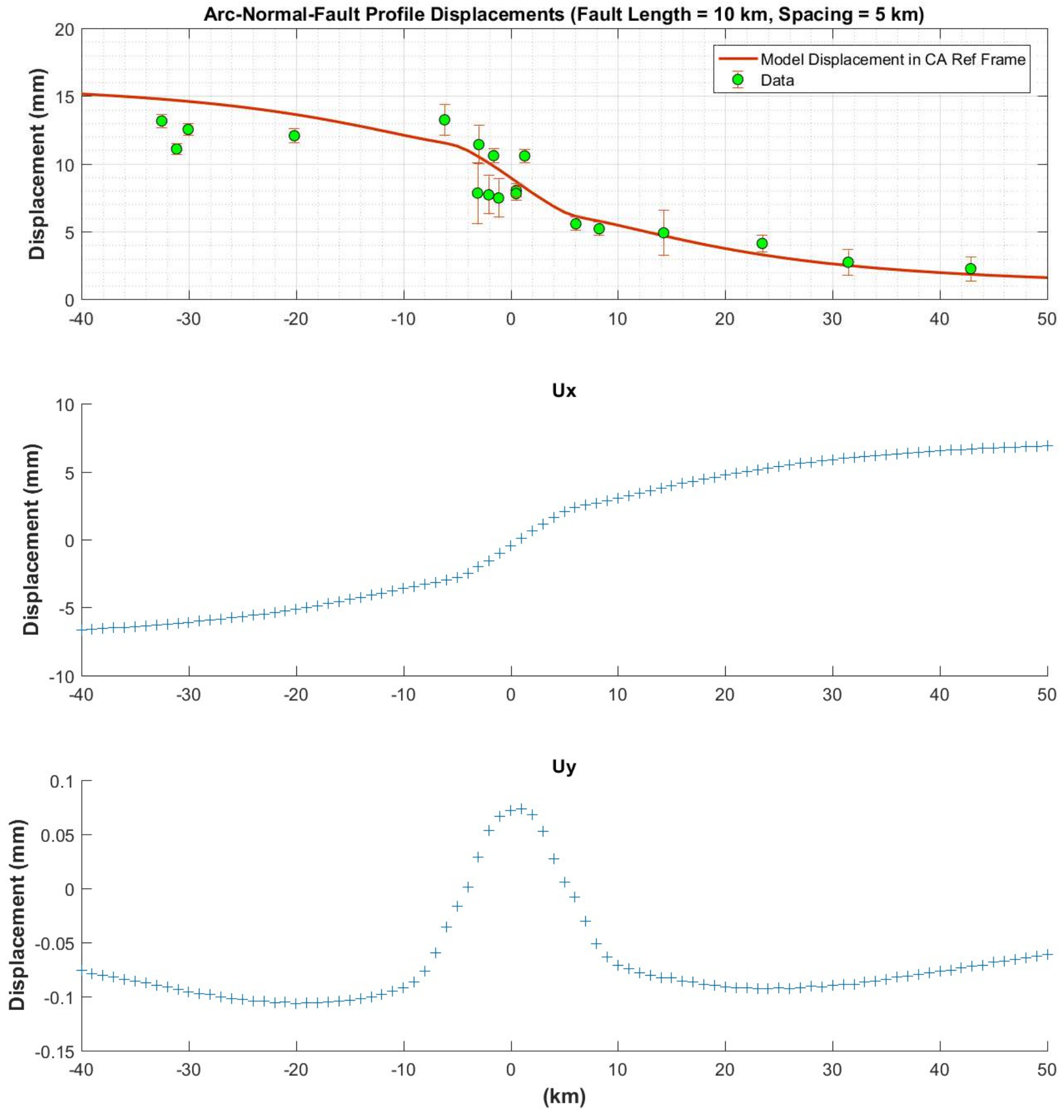

Figure **B-44**: Model C5: displacements along-profile. Arc-normal faults' length and spacing are 10 km and 5 km respectively. Top panel – profile displacements projected into horizontal line (azimuth = 270°). Middle panel – profile displacements in the x-direction. Bottom panel – profile displacements in the y-direction. 'Model Displacement in CA' data sets was created by adding an offset of 7 mm to the model displacements.

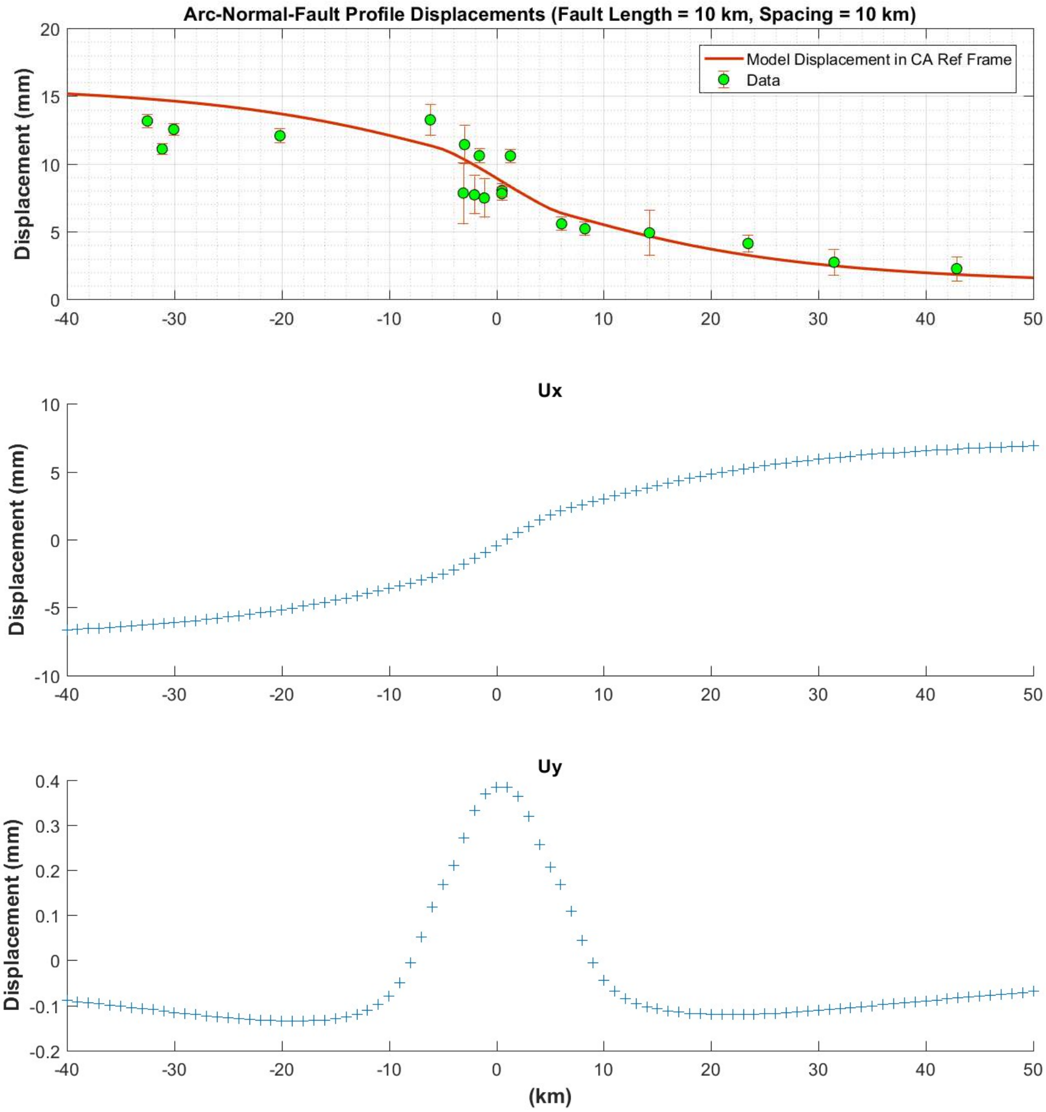

Figure **B-45**: Model C6: displacements along-profile. Arc-normal faults' length and spacing are 10 km and 10 km respectively. Top panel – profile displacements projected into horizontal line (azimuth = 270°). Middle panel – profile displacements in the x-direction. Bottom panel – profile displacements in the y-direction. 'Model Displacement in CA' data sets was created by adding an offset of 7 mm to the model displacements.

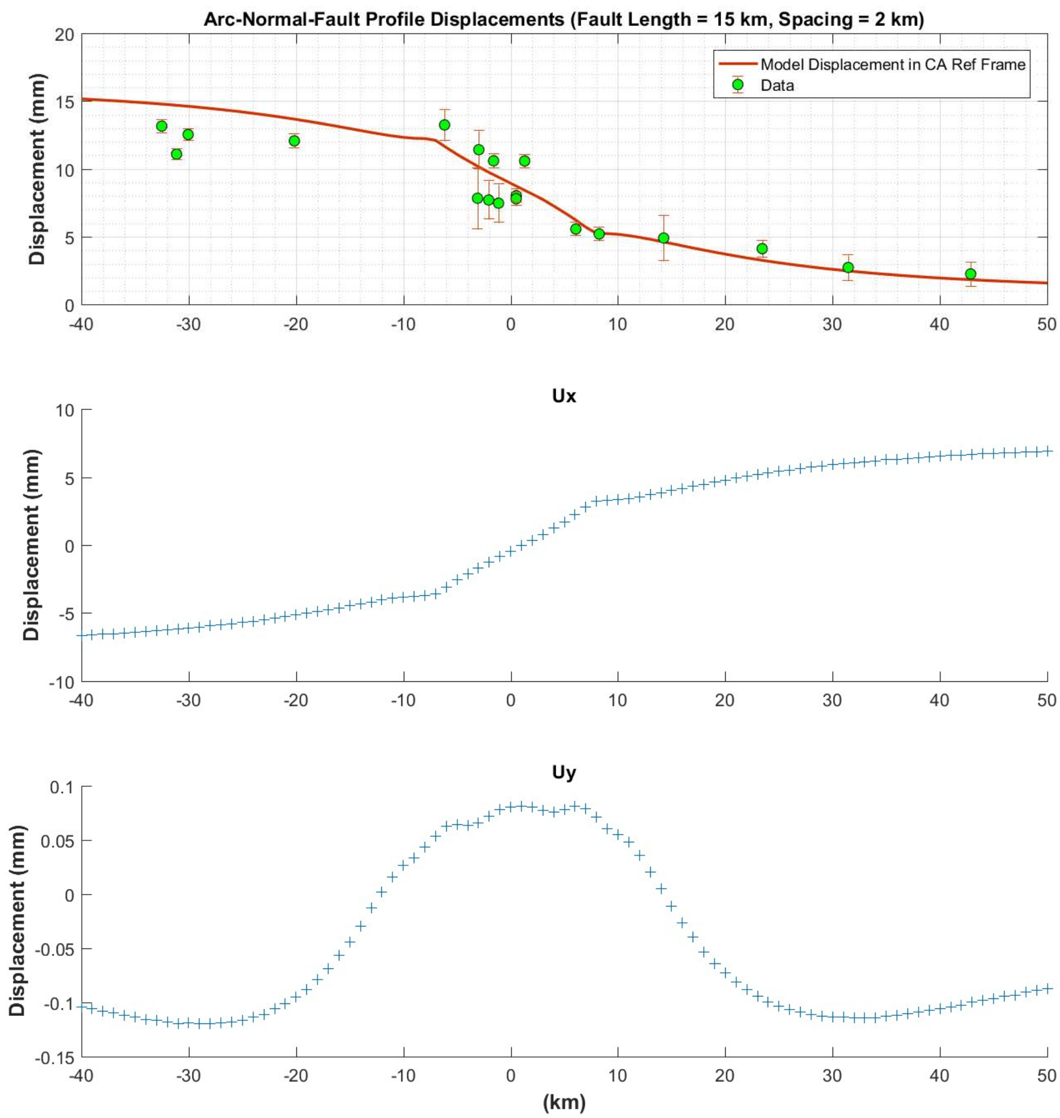

Figure **B-46**: Model C7: displacements along-profile. Arc-normal faults' length and spacing are 15 km and 2 km respectively. Top panel – profile displacements projected into horizontal line (azimuth = 270°). Middle panel – profile displacements in the x-direction. Bottom panel – profile displacements in the y-direction. 'Model Displacement in CA' data sets was created by adding an offset of 7 mm to the modeled displacement.

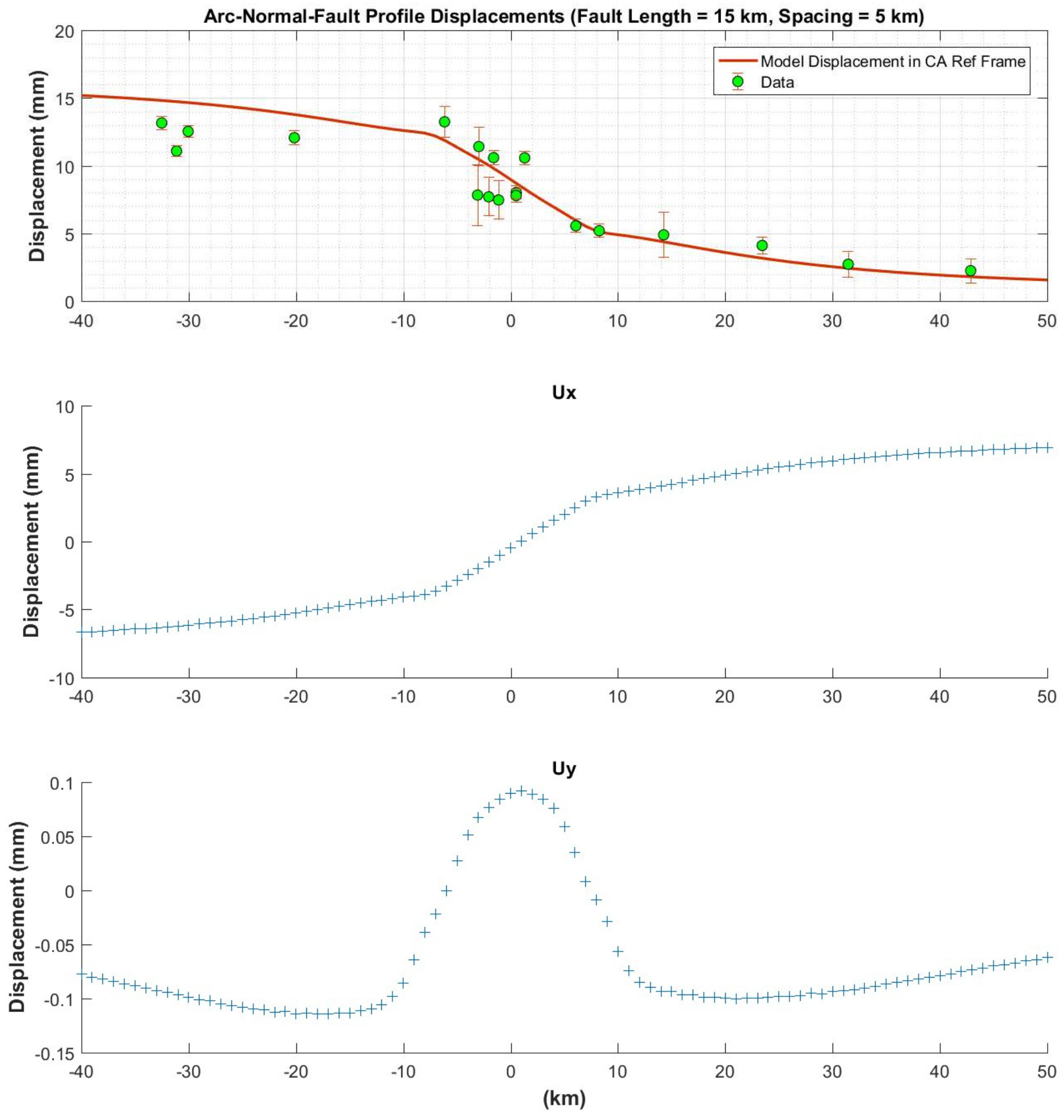

Figure **B-47**: Model C8: displacements along-profile. Arc-normal faults' length and spacing are 15 km and 5 km respectively. Top panel – profile displacements projected into horizontal line (azimuth = 270°). Middle panel – profile displacements in the x-direction. Bottom panel – profile displacements in the y-direction. 'Model Displacement in CA' data sets was created by adding an offset of 7 mm to the modeled displacement.

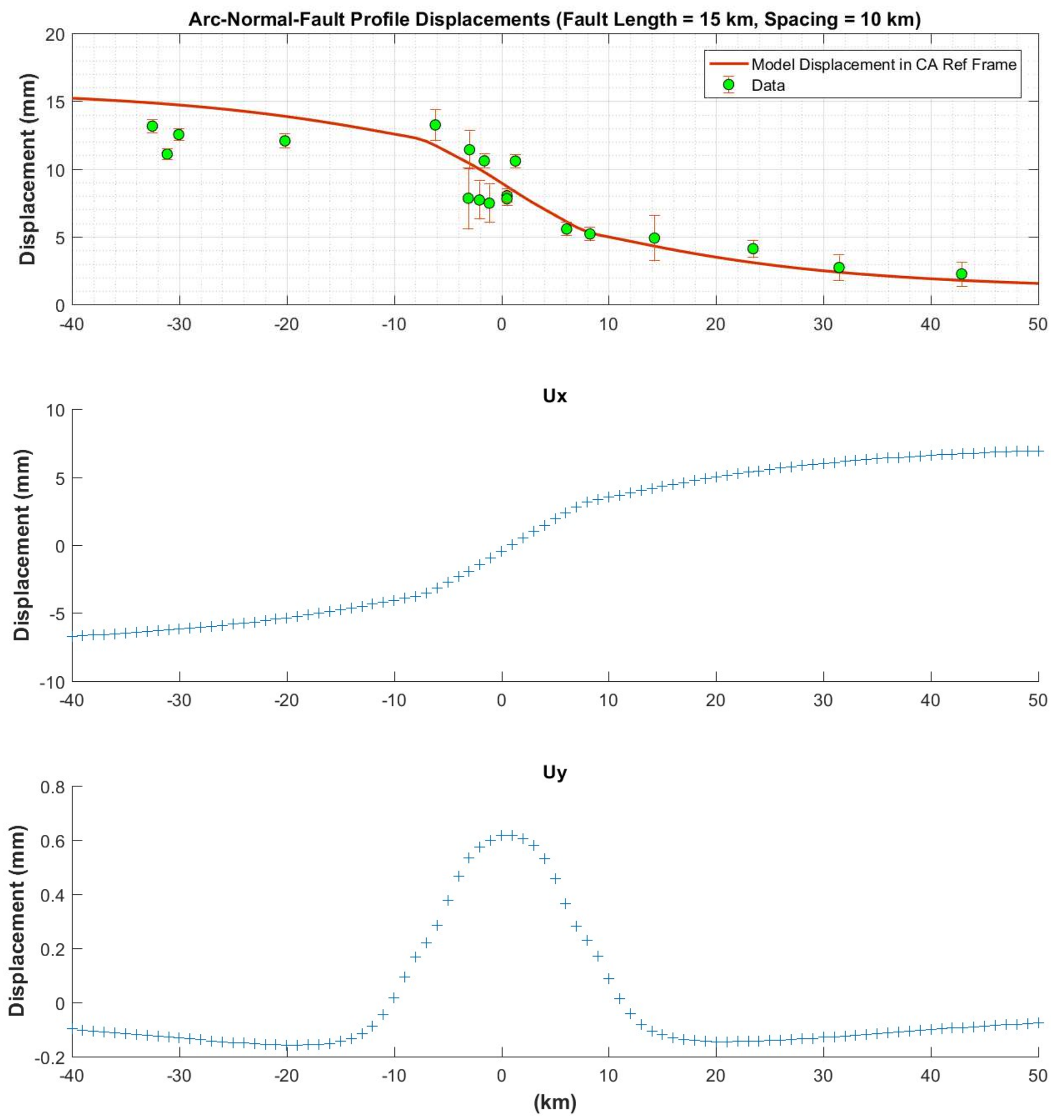

Figure **B-48**: Model C9: displacements along-profile. Arc-normal faults' length and spacing are 15 km and 10 km respectively. Top panel – profile displacements projected into horizontal line (azimuth = 270°). Middle panel – profile displacements in the x-direction. Bottom panel – profile displacements in the y-direction. 'Model Displacement in CA' data sets was created by adding an offset of 7 mm to the modeled displacement.

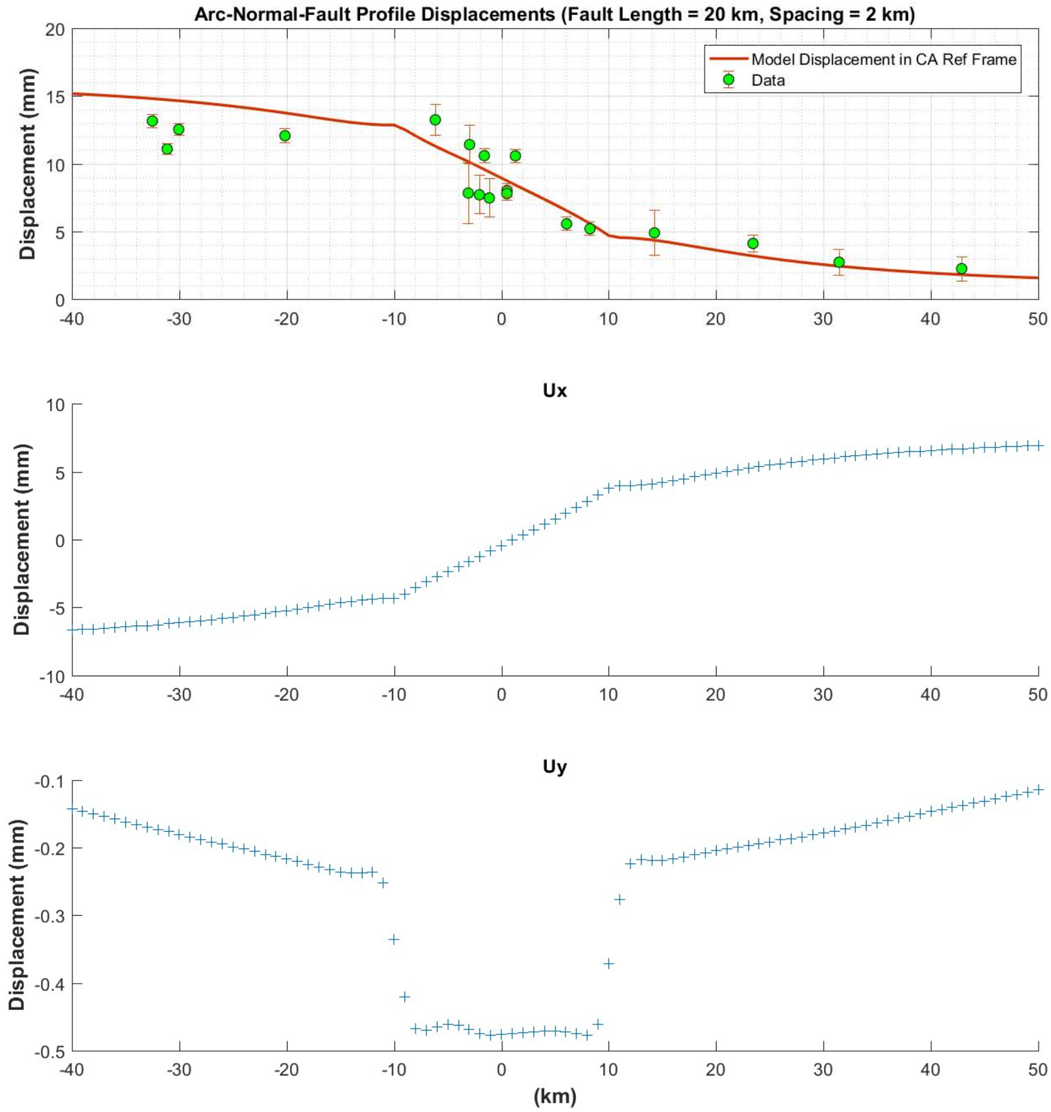

Figure **B-49**: Model C10: displacements along-profile. Arc-normal faults' length and spacing are 20 km and 2 km respectively. Top panel – profile displacements projected into horizontal line (azimuth = 270°). Middle panel – profile displacements in the x-direction. Bottom panel – profile displacements in the y-direction. 'Model Displacement in CA' data sets was created by adding an offset of 7 mm to the model displacements.

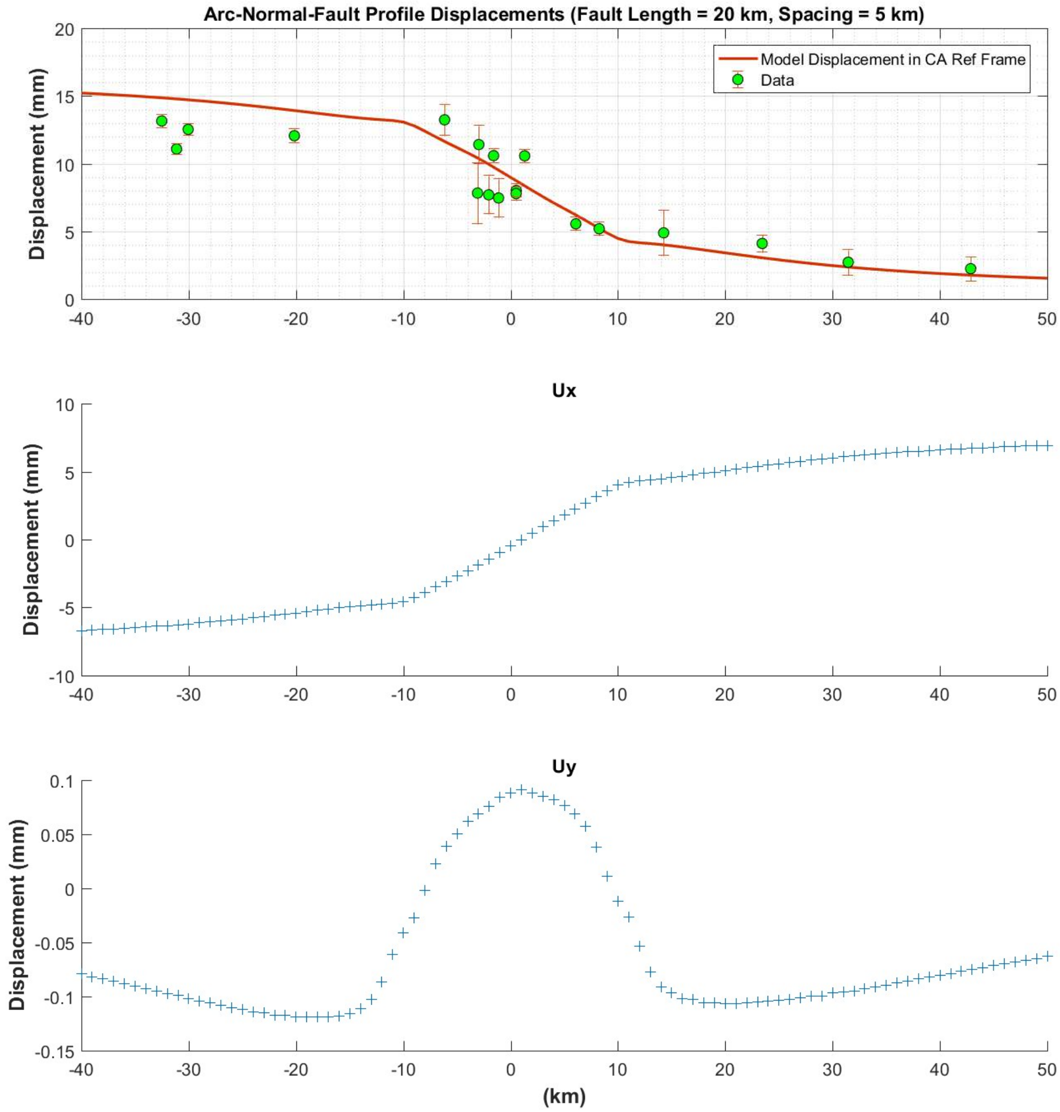

Figure **B-50**: Model C11: displacements along-profile. Arc-normal faults' length and spacing are 20 km and 5 km respectively. Top panel – profile displacements projected into horizontal line (azimuth = 270°). Middle panel – profile displacements in the x-direction. Bottom panel – profile displacements in the y-direction. 'Model Displacement in CA' data sets was created by adding an offset of 7 mm to the model displacements.

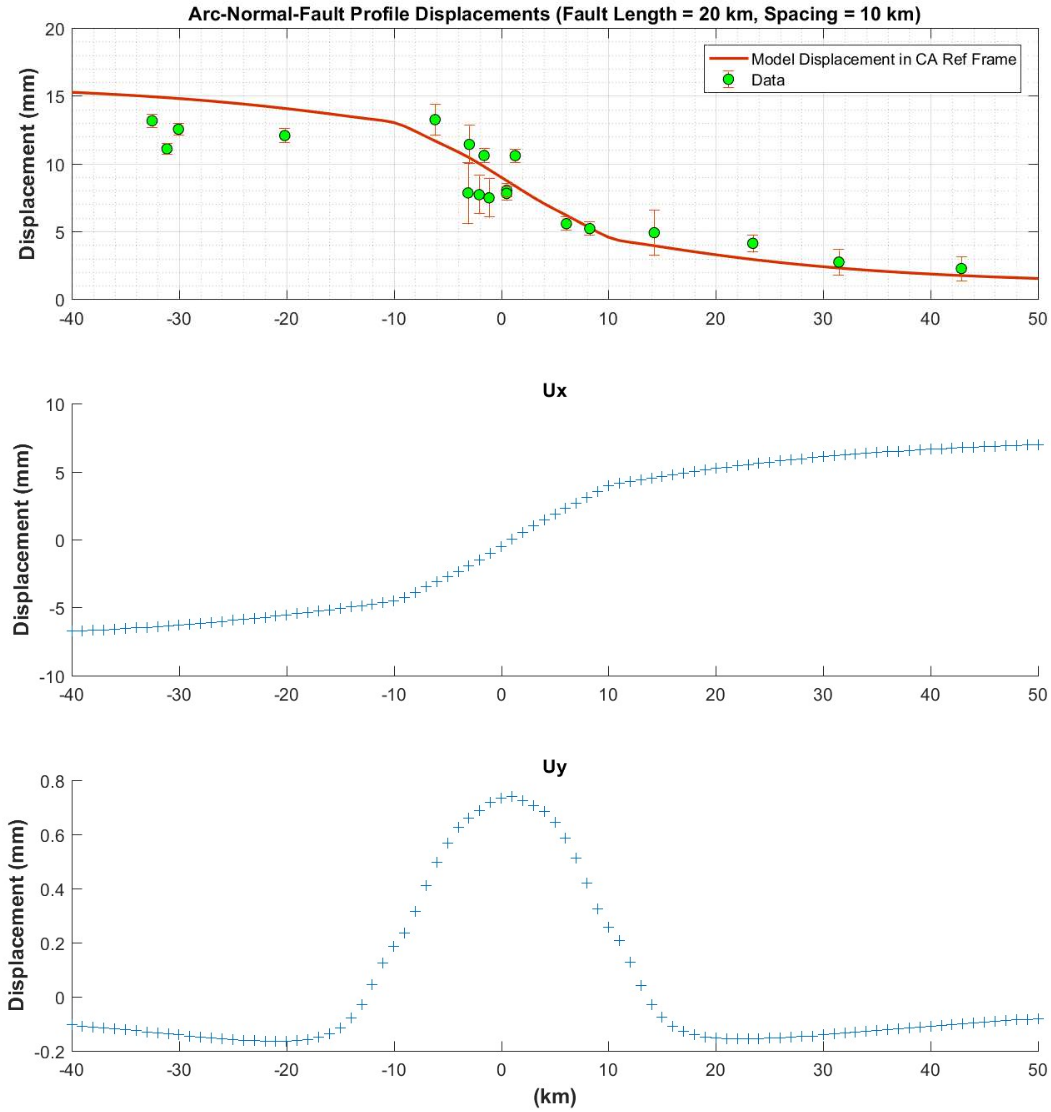

Figure **B-51**: Model C12: displacements along-profile. Arc-normal faults' length and spacing are 20 km and 10 km respectively. Top panel – profile displacements projected into horizontal line (azimuth = 270°). Middle panel – profile displacements in the x-direction. Bottom panel – profile displacements in the y-direction. 'Model Displacement in CA' data sets was created by adding an offset of 7 mm to the model displacements.

B.3 Model Set D Plots

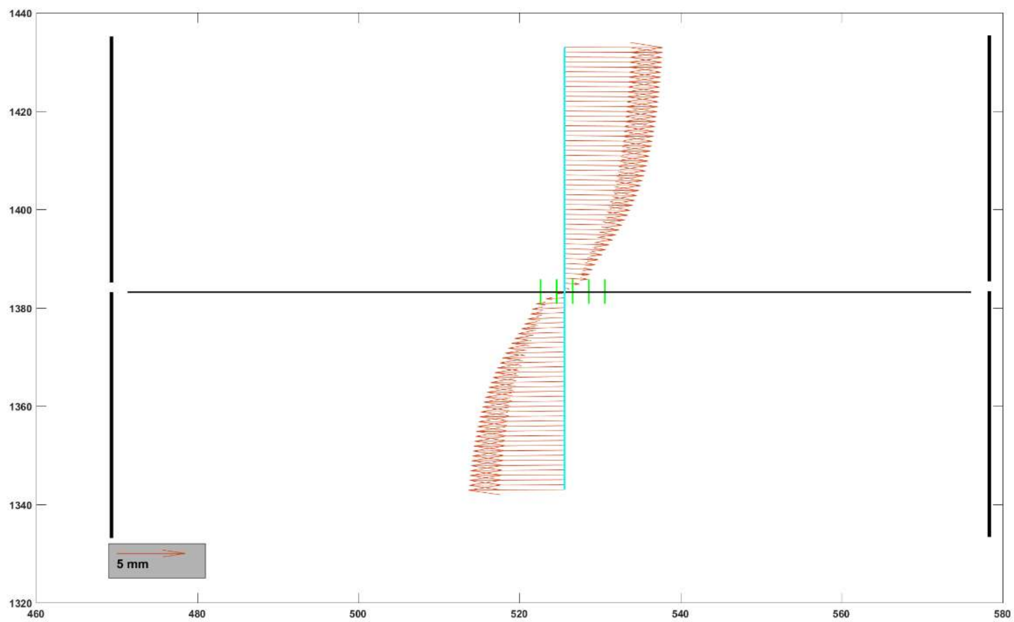

Figure **B-52**: Model D1: surface displacements (red vectors) along-profile line (cyan line). Arc-normal faults' (green lines) length and spacing are 5 km and 2 km respectively. This model has 5 arc-normal faults.

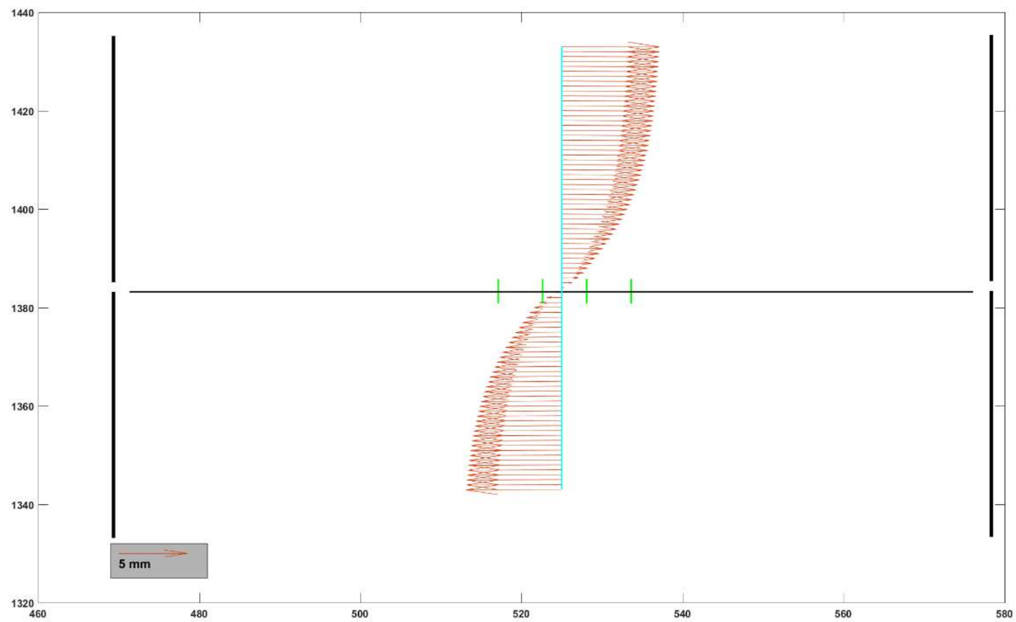

Figure **B-53**: Model D2: surface displacements (red vectors) along-profile line (cyan line). Arc-normal faults' (green lines) length and spacing are 5 km and 5 km respectively. This model has 4 arc-normal faults.

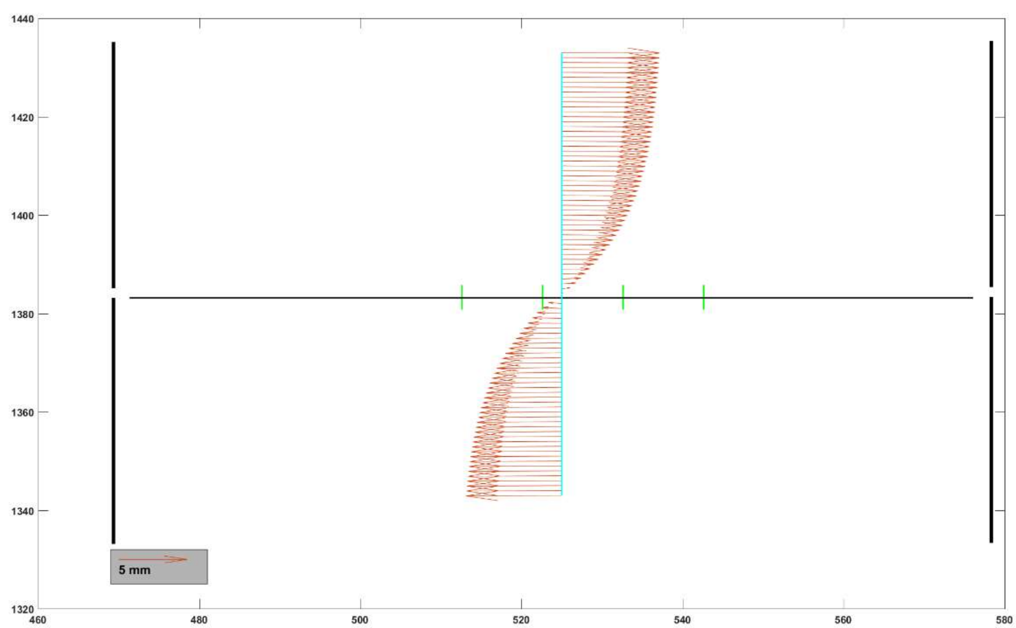

Figure **B-54**: Model D3: surface displacements (red vectors) along-profile line (cyan line). Arc-normal faults' (green lines) length and spacing are 5 km and 10 km respectively. This model has 4 arc-normal faults.

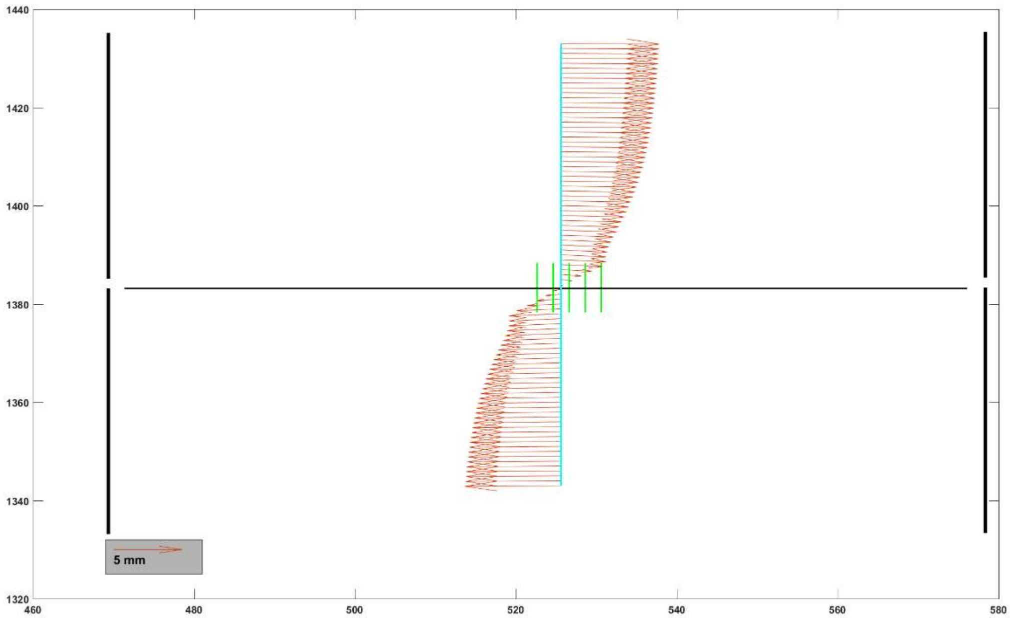

Figure **B-55**: Model D4: surface displacements (red vectors) along-profile line (cyan line). Arc-normal faults' (green lines) length and spacing are 10 km and 2 km respectively. This model has 5 arc-normal faults.

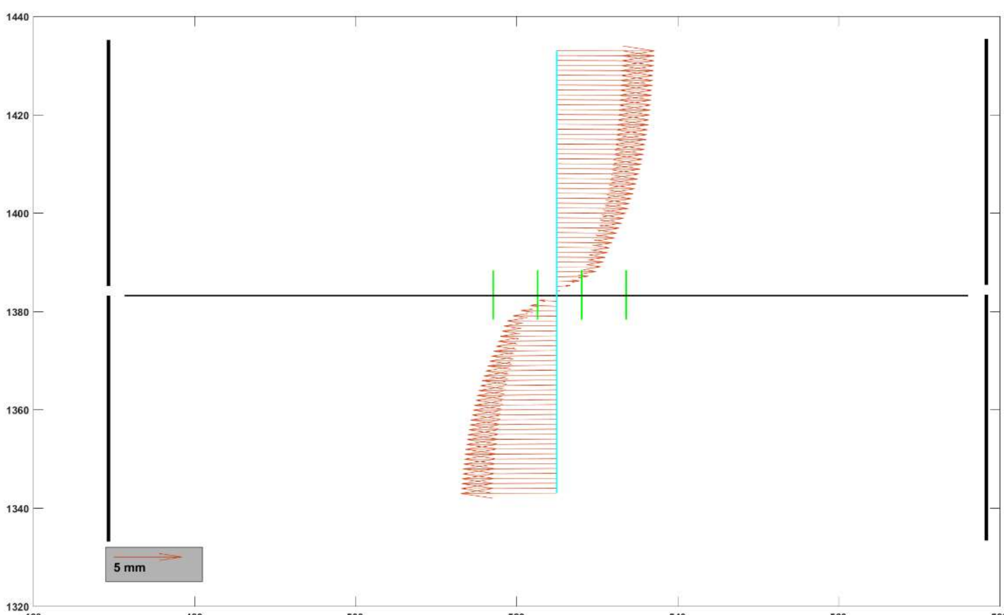

Figure **B-56**: Model D5: surface displacements (red vectors) along-profile line (cyan line). Arc-normal faults' (green lines) length and spacing are 10 km and 5 km respectively. This model has 4 arc-normal faults.

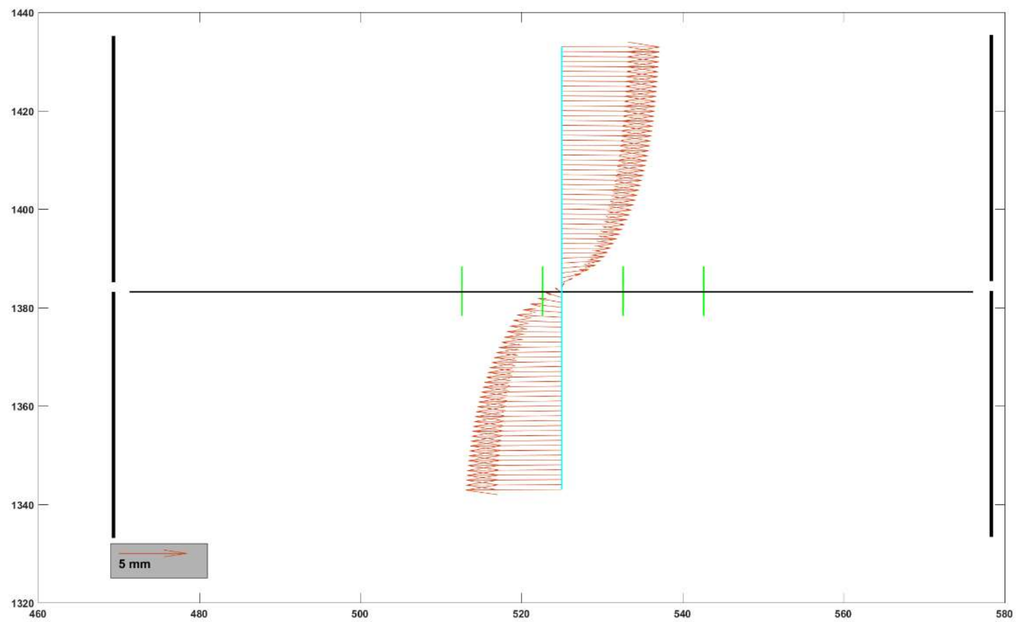

Figure **B-57**: Model D6: surface displacements (red vectors) along-profile line (cyan line). Arc-normal faults' (green lines) length and spacing are 10 km and 10 km respectively. This model has 4 arc-normal faults.

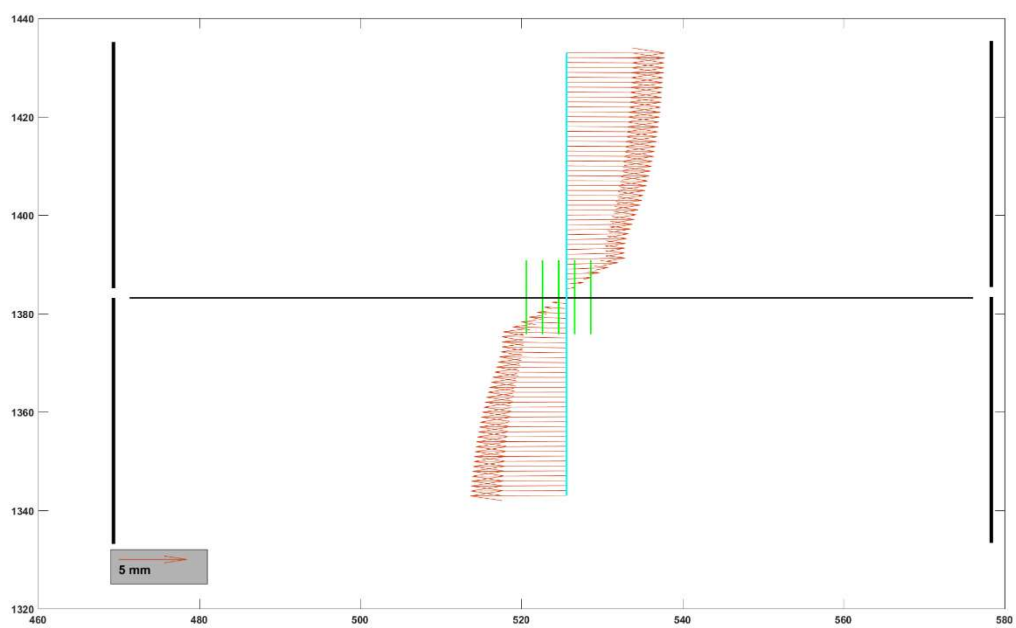

Figure **B-58**: Model D7: surface displacements (red vectors) along-profile line (cyan line). Arc-normal faults' (green lines) length and spacing are 15 km and 2 km respectively. This model has 4 arc-normal faults.

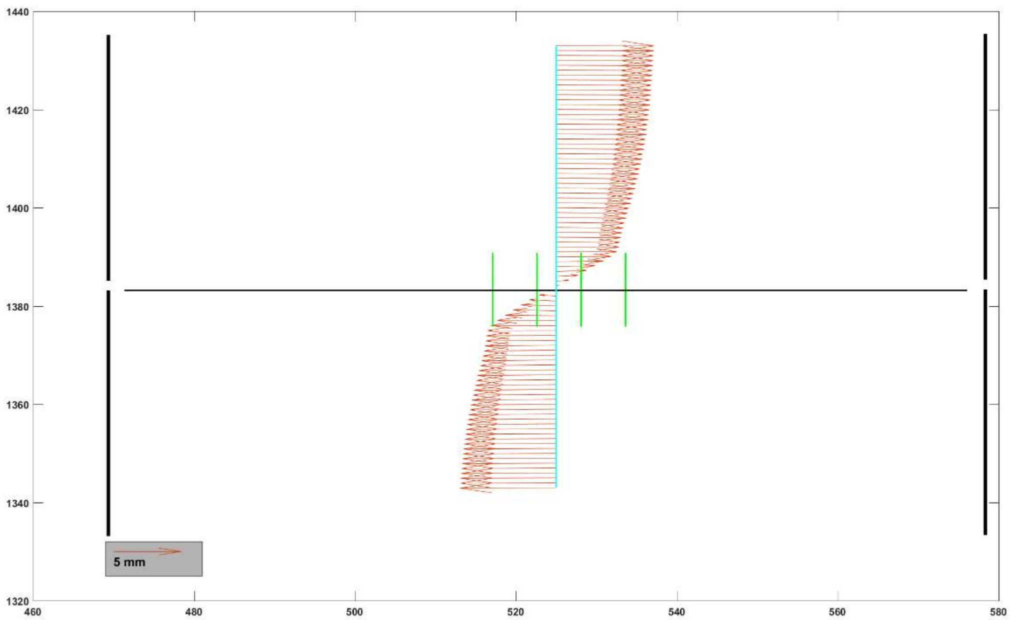

Figure **B-59**: Model D7: surface displacements (red vectors) along-profile line (cyan line). Arc-normal faults' (green lines) length and spacing are 15 km and 5 km respectively. This model has 4 arc-normal faults.

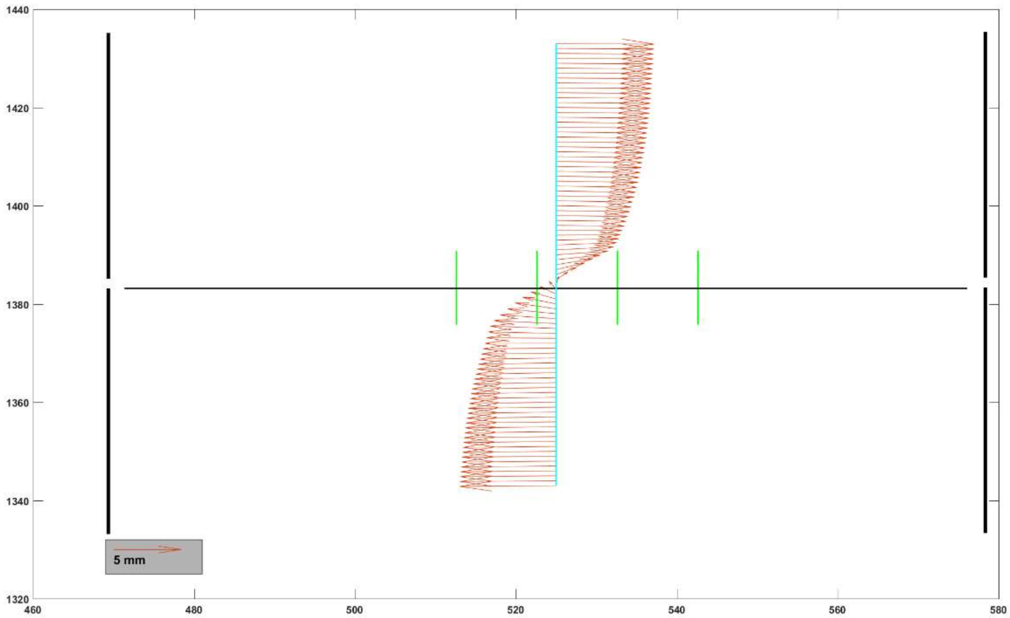

Figure **B-60**: Model D6: surface displacements (red vectors) along-profile line (cyan line). Arc-normal faults' (green lines) length and spacing are 15 km and 10 km respectively. This model has 4 arc-normal faults.

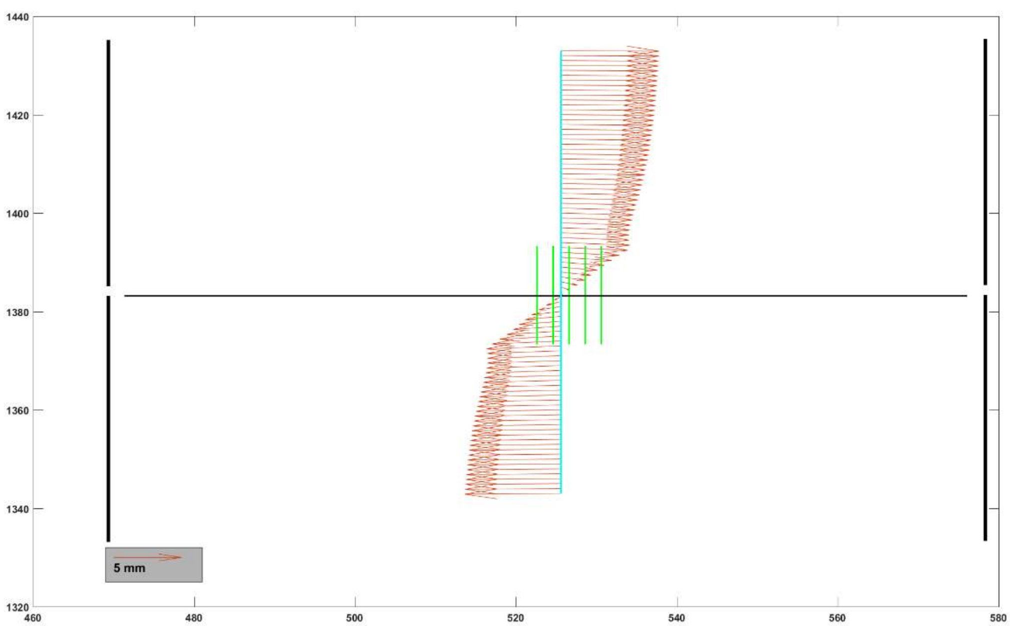

Figure **B-61**: Model D7: surface displacements (red vectors) along-profile line (cyan line). Arc-normal faults' (green lines) length and spacing are 20 km and 2 km respectively. This model has 5 arc-normal faults.

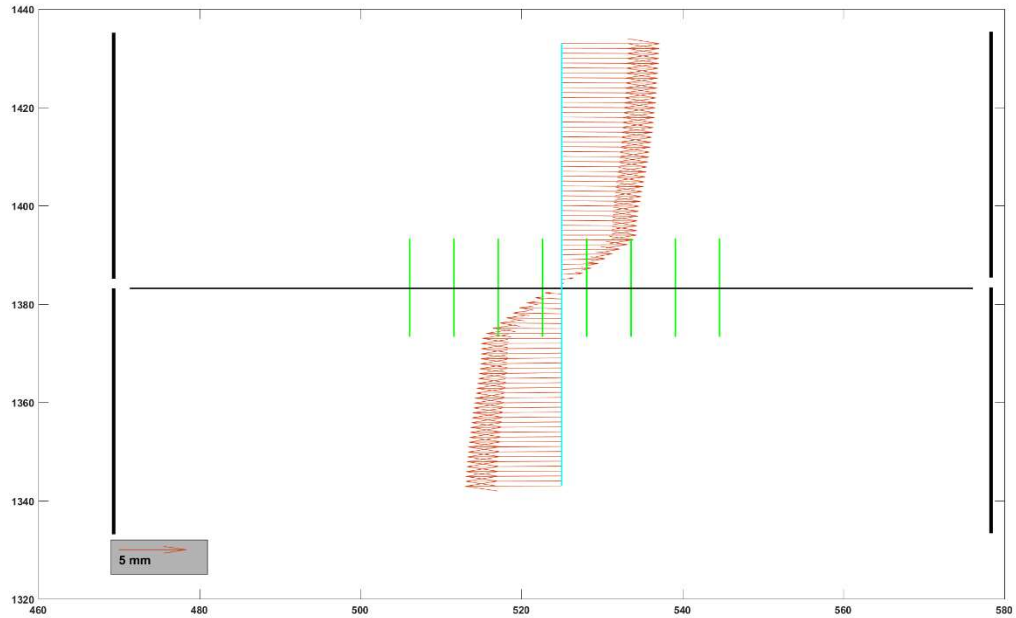

Figure **B-62**: Model D8: surface displacements (red vectors) along-profile line (cyan line). Arc-normal faults' (green lines) length and spacing are 20 km and 5 km respectively. This model has 4 arc-normal faults.

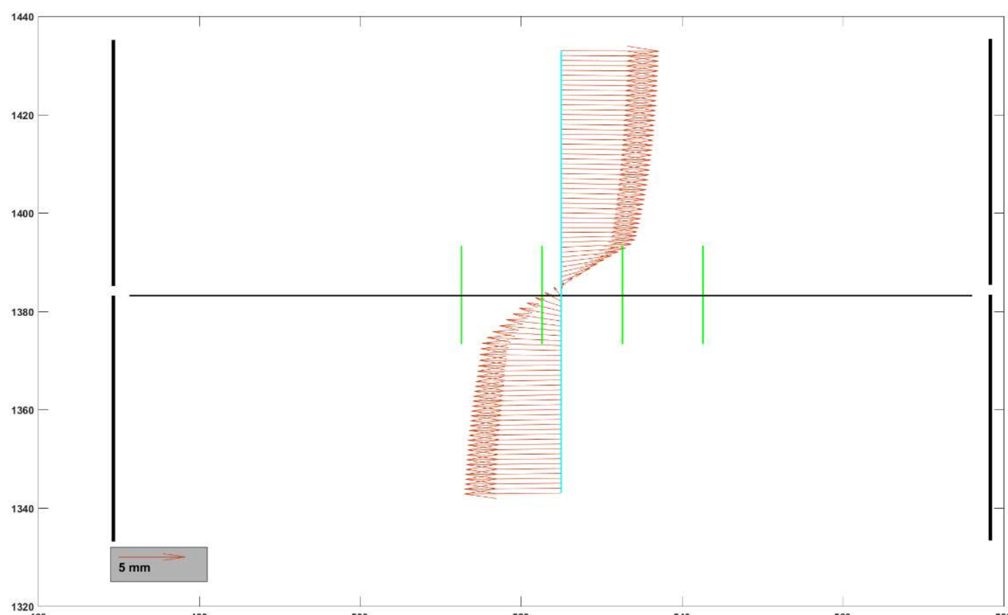

Figure **B-63**: Model D9: surface displacements (red vectors) along-profile line (cyan line). Arc-normal faults' (green lines) length and spacing are 20 km and 10 km respectively. This model has 4 arc-normal faults.

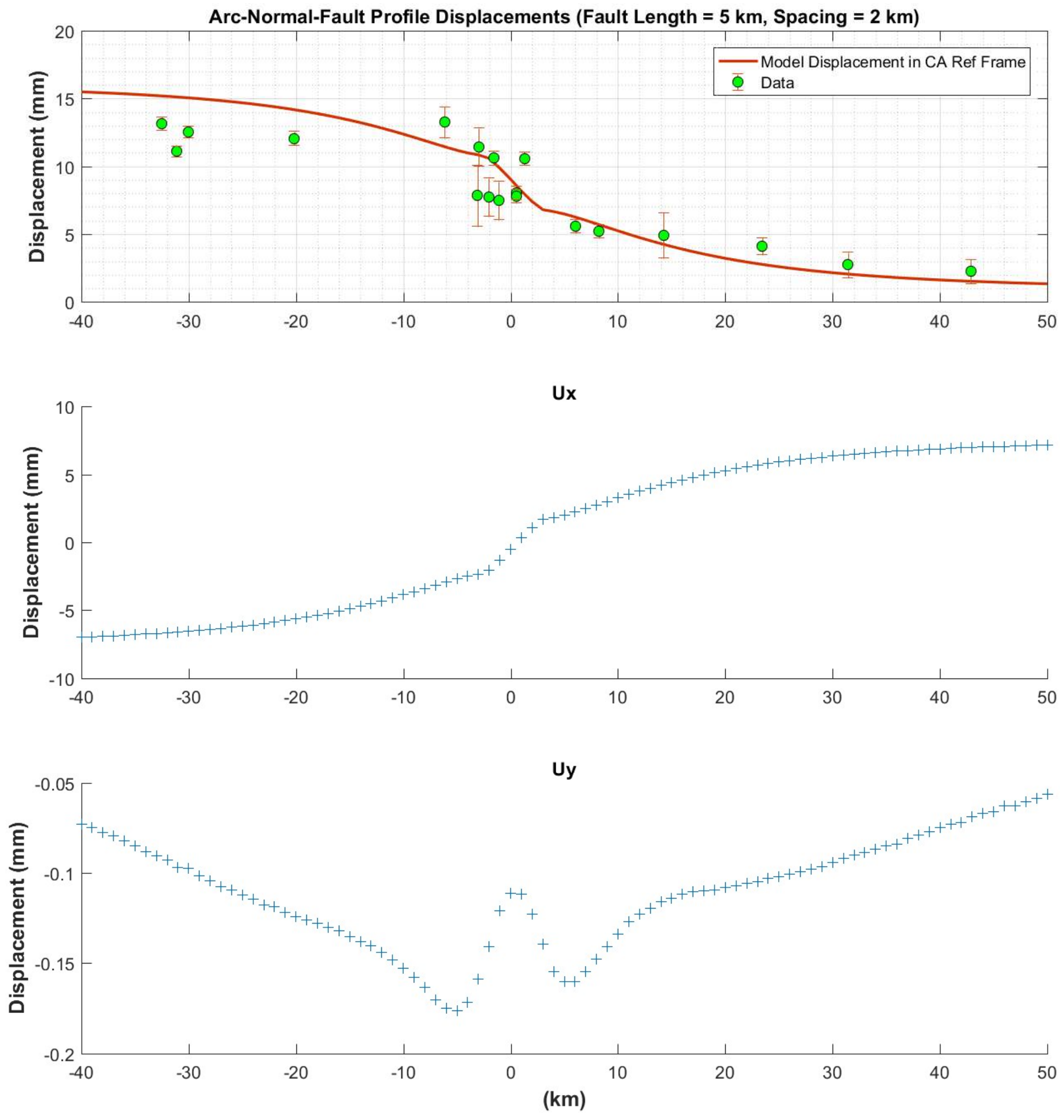

Figure **B-64**: Model D1: displacements along-profile. Arc-normal faults' length and spacing are 5 km and 2 km respectively. Top panel – profile displacements projected into horizontal line (azimuth = 270°). Middle panel – profile displacements in the x-direction. Bottom panel – profile displacements in the y-direction. 'Model Displacement in CA' data sets was created by adding an offset of 7 mm to the model displacements.

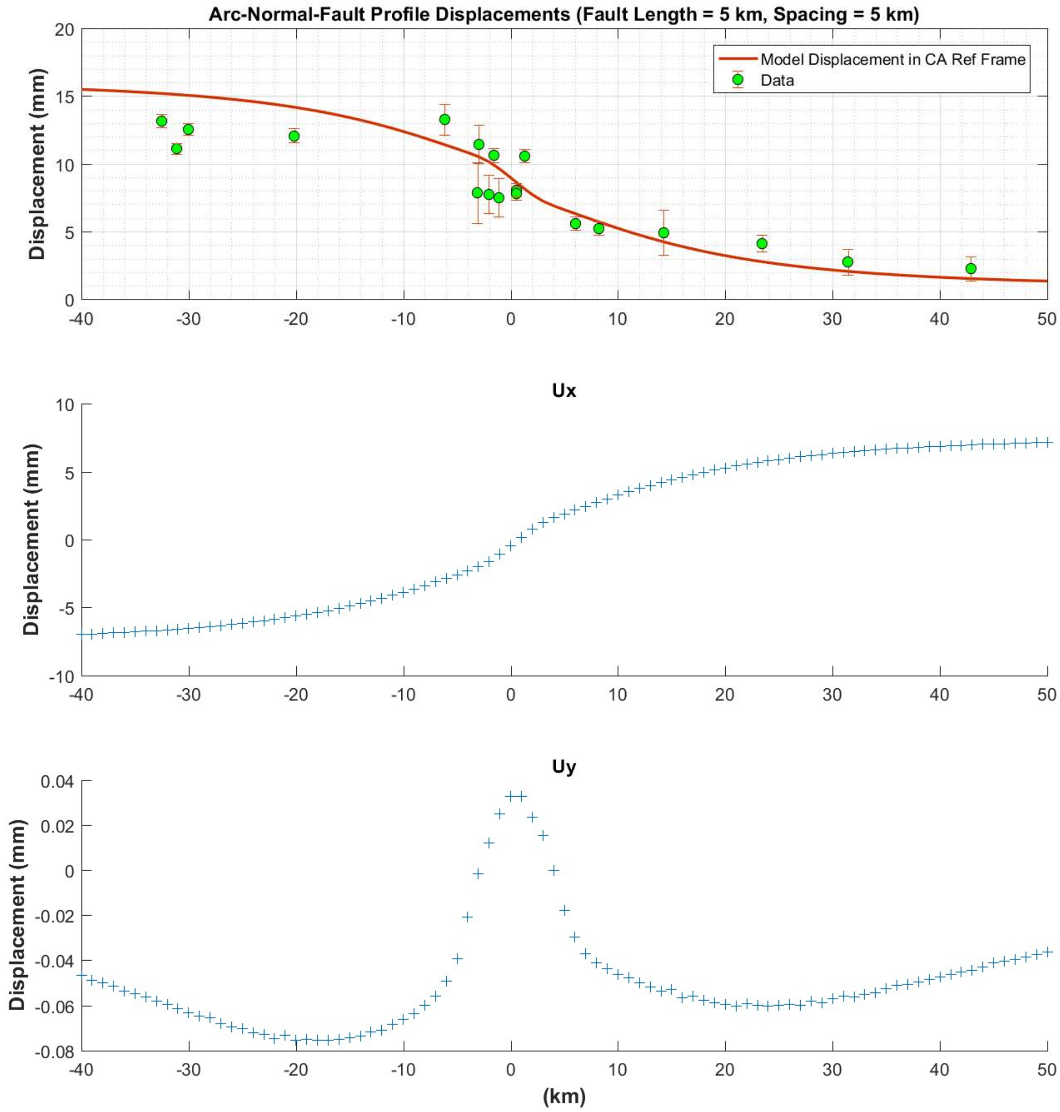

Figure **B-65**: Model D2: displacements along-profile. Arc-normal faults' length and spacing are 5 km and 5 km respectively. Top panel – profile displacements projected into horizontal line (azimuth = 270°). Middle panel – profile displacements in the x-direction. Bottom panel – profile displacements in the y-direction. 'Model Displacement in CA' data sets was created by adding an offset of 7 mm to the model displacements.

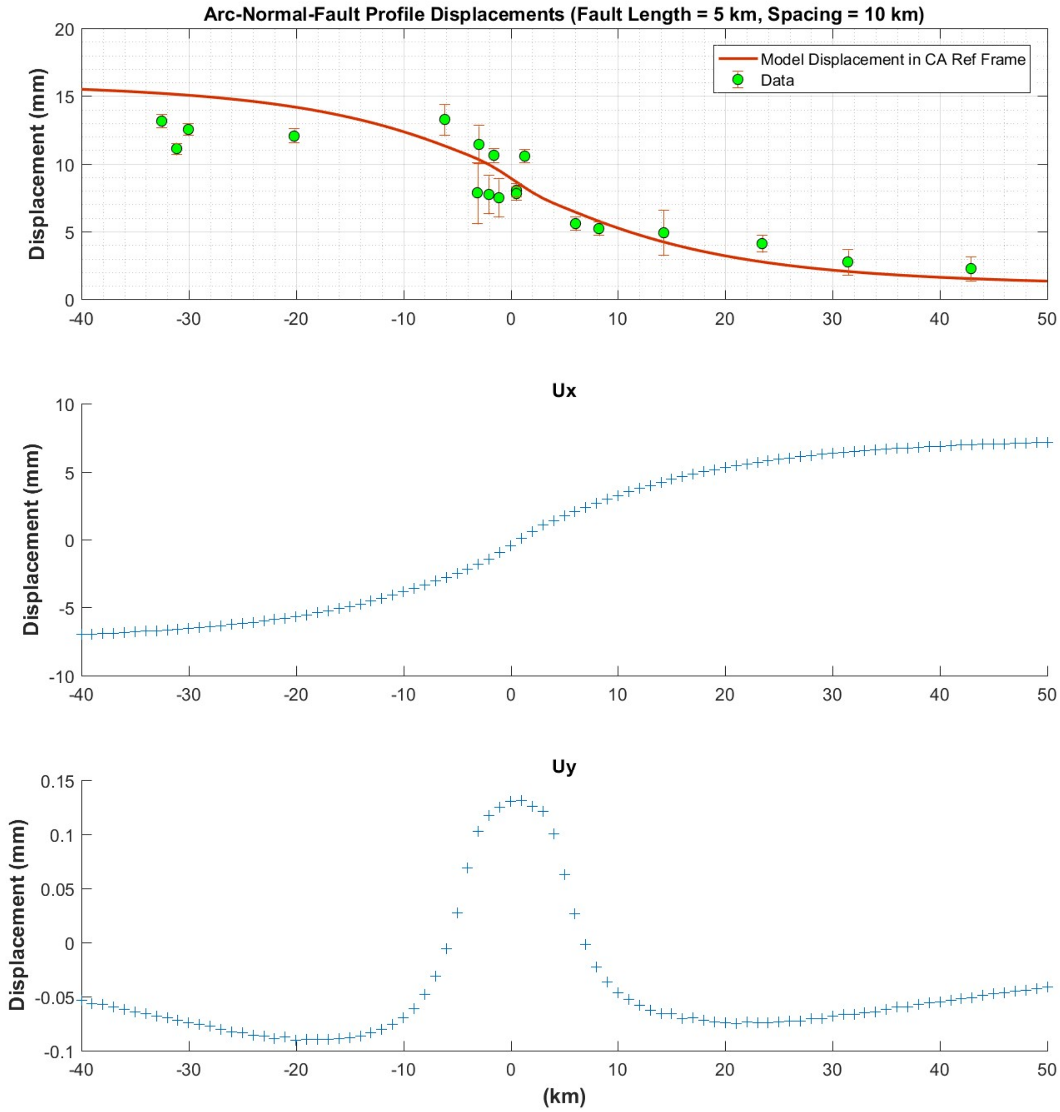

Figure **B-66**: Model D3: displacements along-profile. Arc-normal faults' length and spacing are 5 km and 10 km respectively. Top panel – profile displacements projected into horizontal line (azimuth = 270°). Middle panel – profile displacements in the x-direction. Bottom panel – profile displacements in the y-direction. 'Model Displacement in CA' data sets was created by adding an offset of 7 mm to the model displacements.

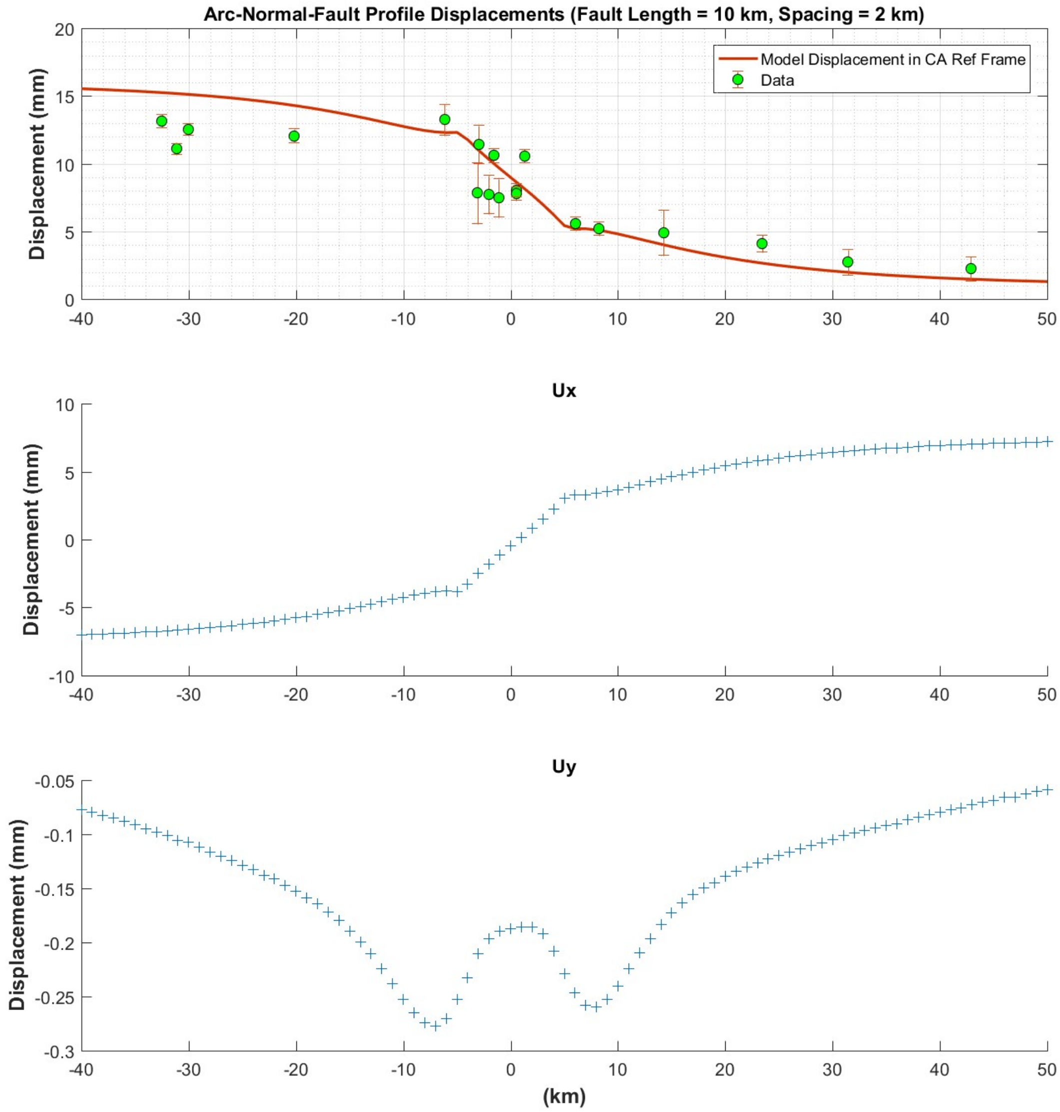

Figure **B-67**: Model D4: displacements along-profile. Arc-normal faults' length and spacing are 10 km and 2 km respectively. Top panel – profile displacements projected into horizontal line (azimuth = 270°). Middle panel – profile displacements in the x-direction. Bottom panel – profile displacements in the y-direction. 'Model Displacement in CA' data sets was created by adding an offset of 7 mm to the model displacements.

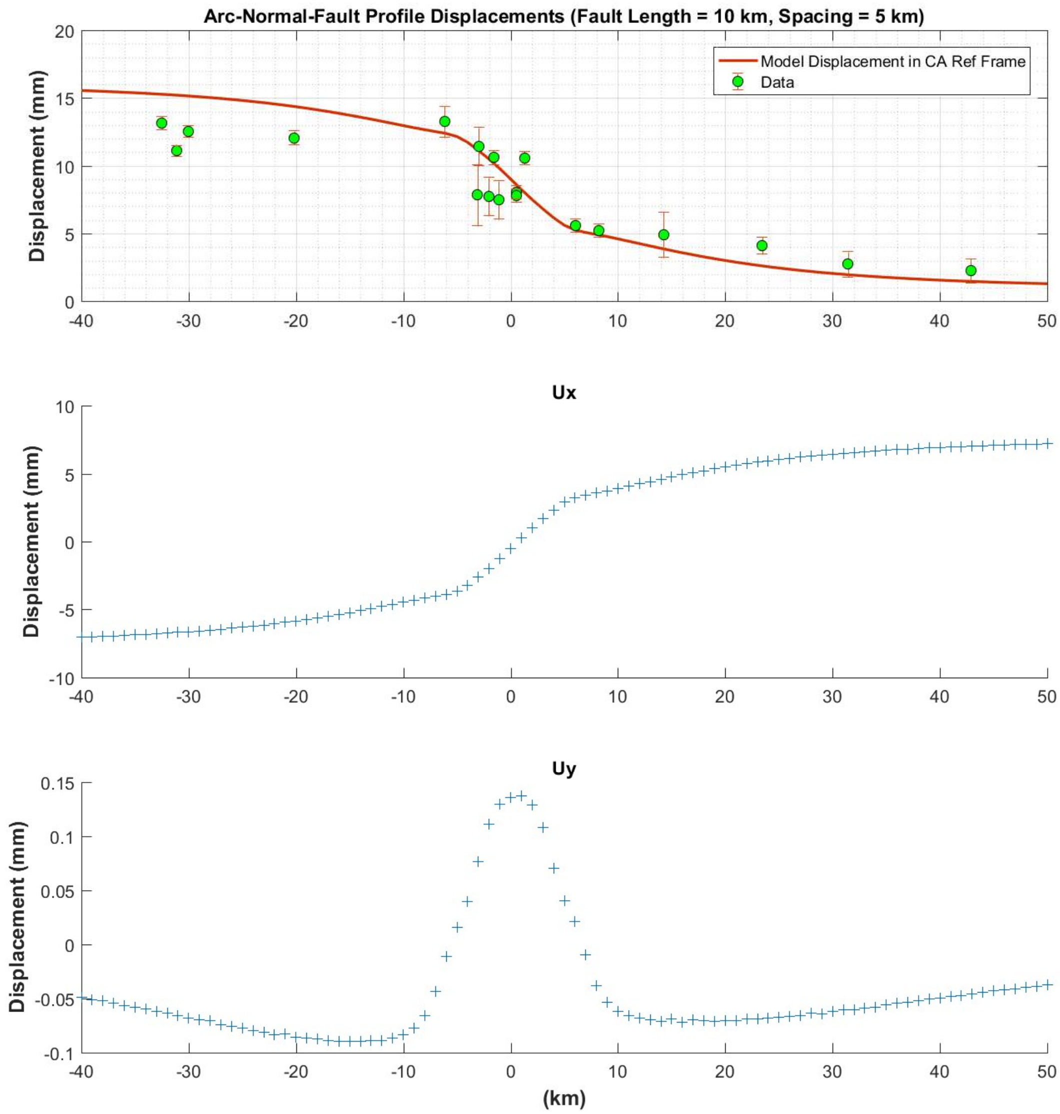

Figure **B-68**: Model D5: displacements along-profile. Arc-normal faults' length and spacing are 10 km and 5 km respectively. Top panel – profile displacements projected into horizontal line (azimuth = 270°). Middle panel – profile displacements in the x-direction. Bottom panel – profile displacements in the y-direction. 'Model Displacement in CA' data sets was created by adding an offset of 7 mm to the model displacements.

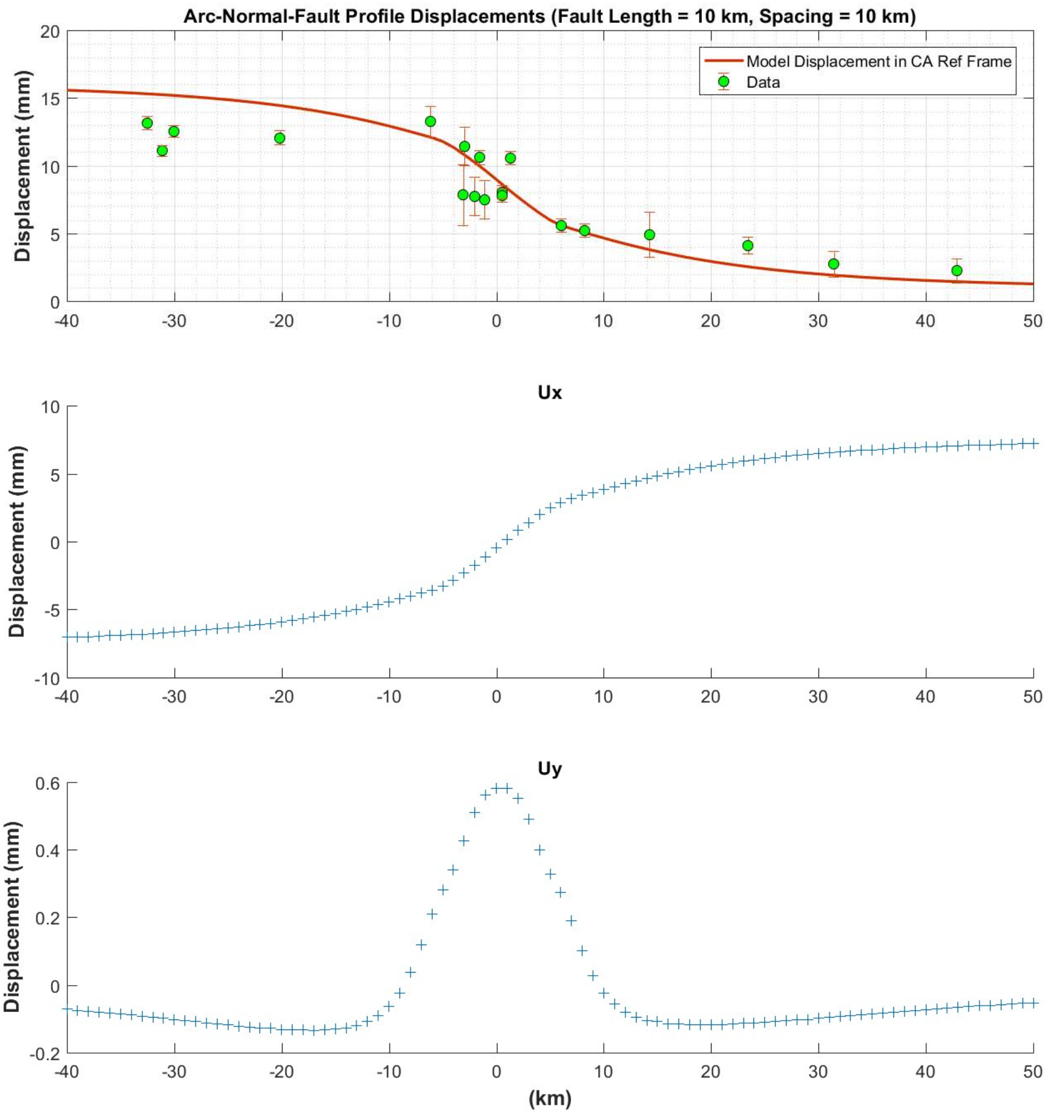

Figure **B-69**: Model D6: displacements along-profile. Arc-normal faults' length and spacing are 10 km and 10 km respectively. Top panel – profile displacements projected into horizontal line (azimuth = 270°). Middle panel – profile displacements in the x-direction. Bottom panel – profile displacements in the y-direction. 'Model Displacement in CA' data sets was created by adding an offset of 7 mm to the model displacements.

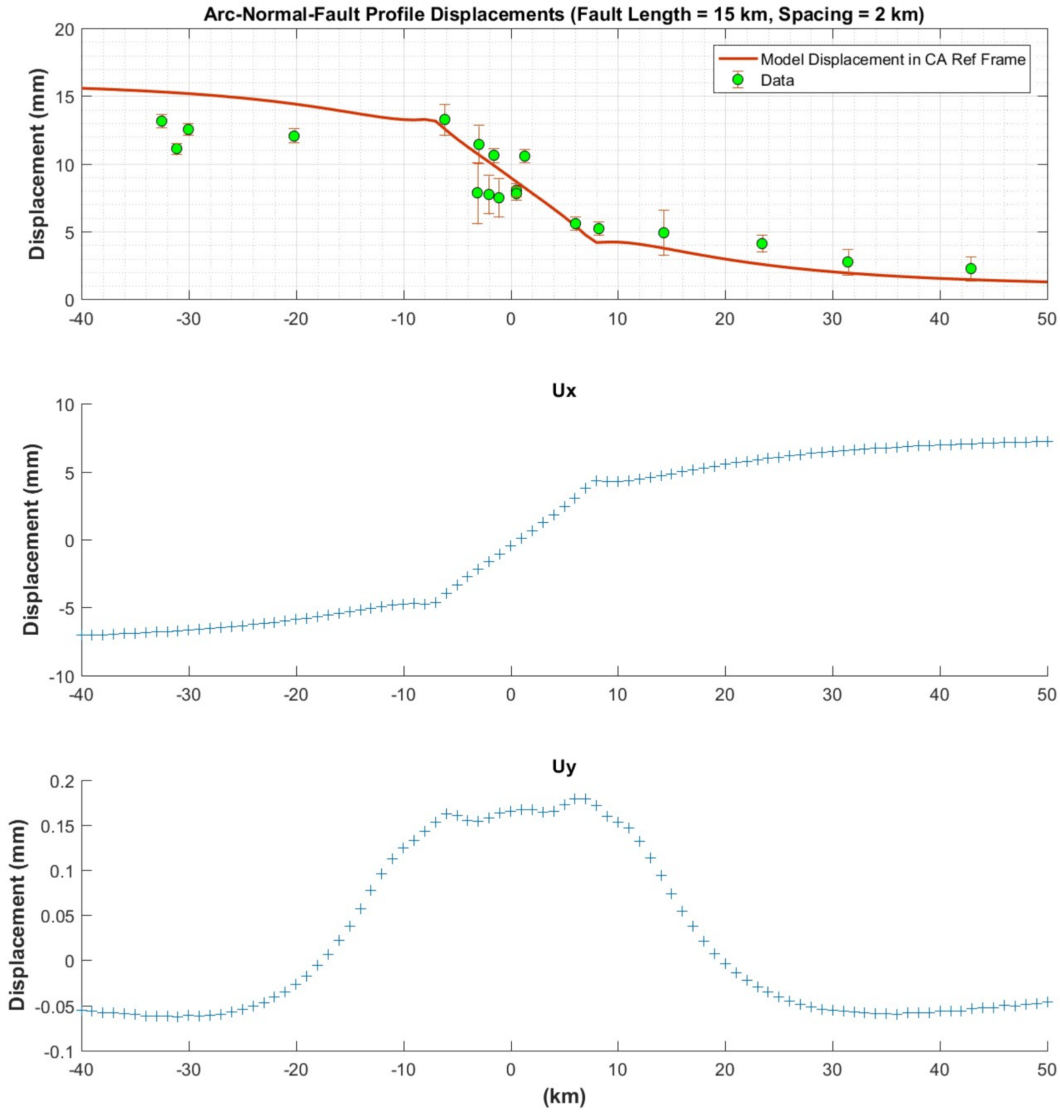

Figure **B-70**: Model D7: displacements along-profile. Arc-normal faults' length and spacing are 15 km and 2 km respectively. Top panel – profile displacements projected into horizontal line (azimuth = 270°). Middle panel – profile displacements in the x-direction. Bottom panel – profile displacements in the y-direction. 'Model Displacement in CA' data sets was created by adding an offset of 7 mm to the model displacements.

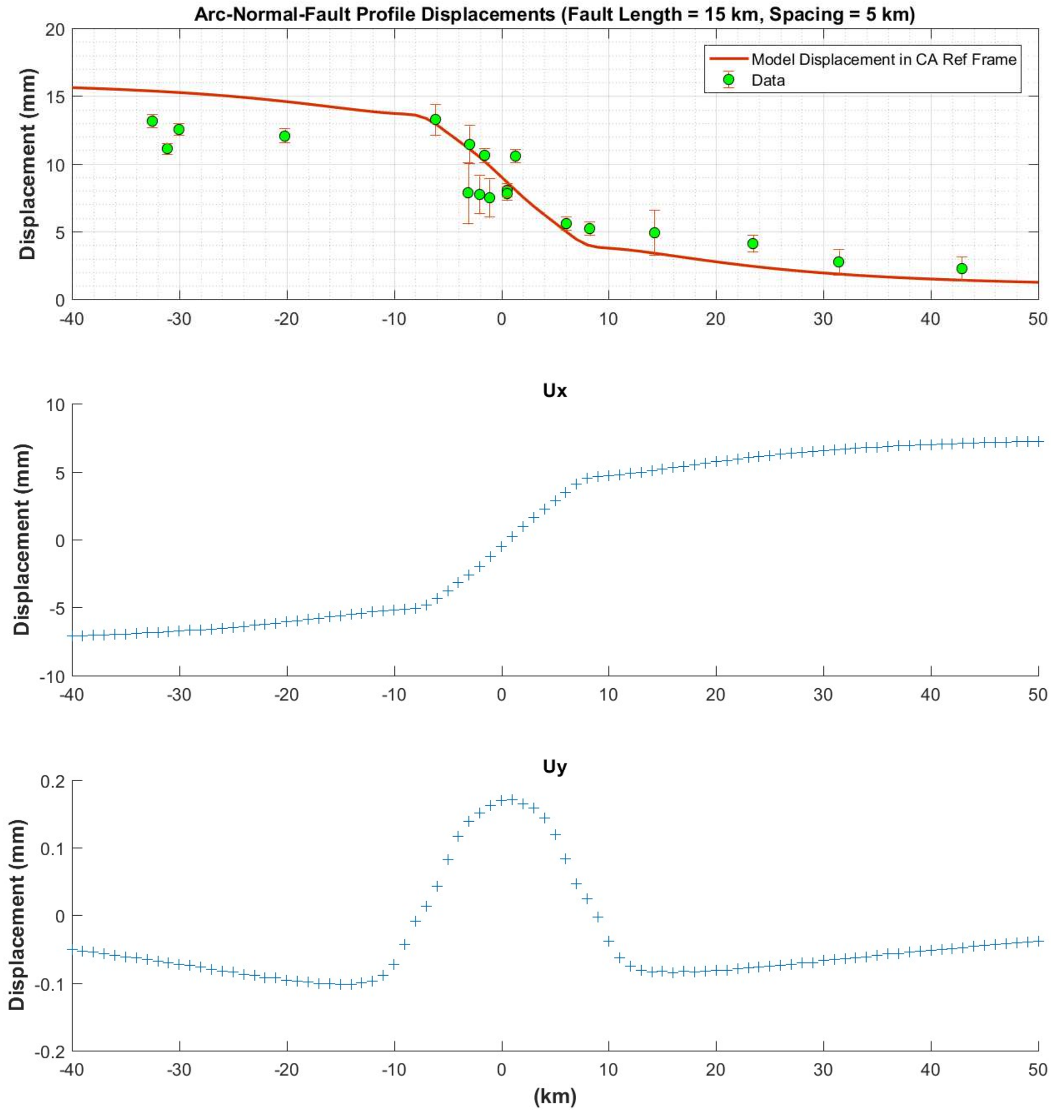

Figure **B-71**: Model D8: displacements along-profile. Arc-normal faults' length and spacing are 15 km and 5 km respectively. Top panel – profile displacements projected into horizontal line (azimuth = 270°). Middle panel – profile displacements in the x-direction. Bottom panel – profile displacements in the y-direction. 'Model Displacement in CA' data sets was created by adding an offset of 7 mm to the model displacements.

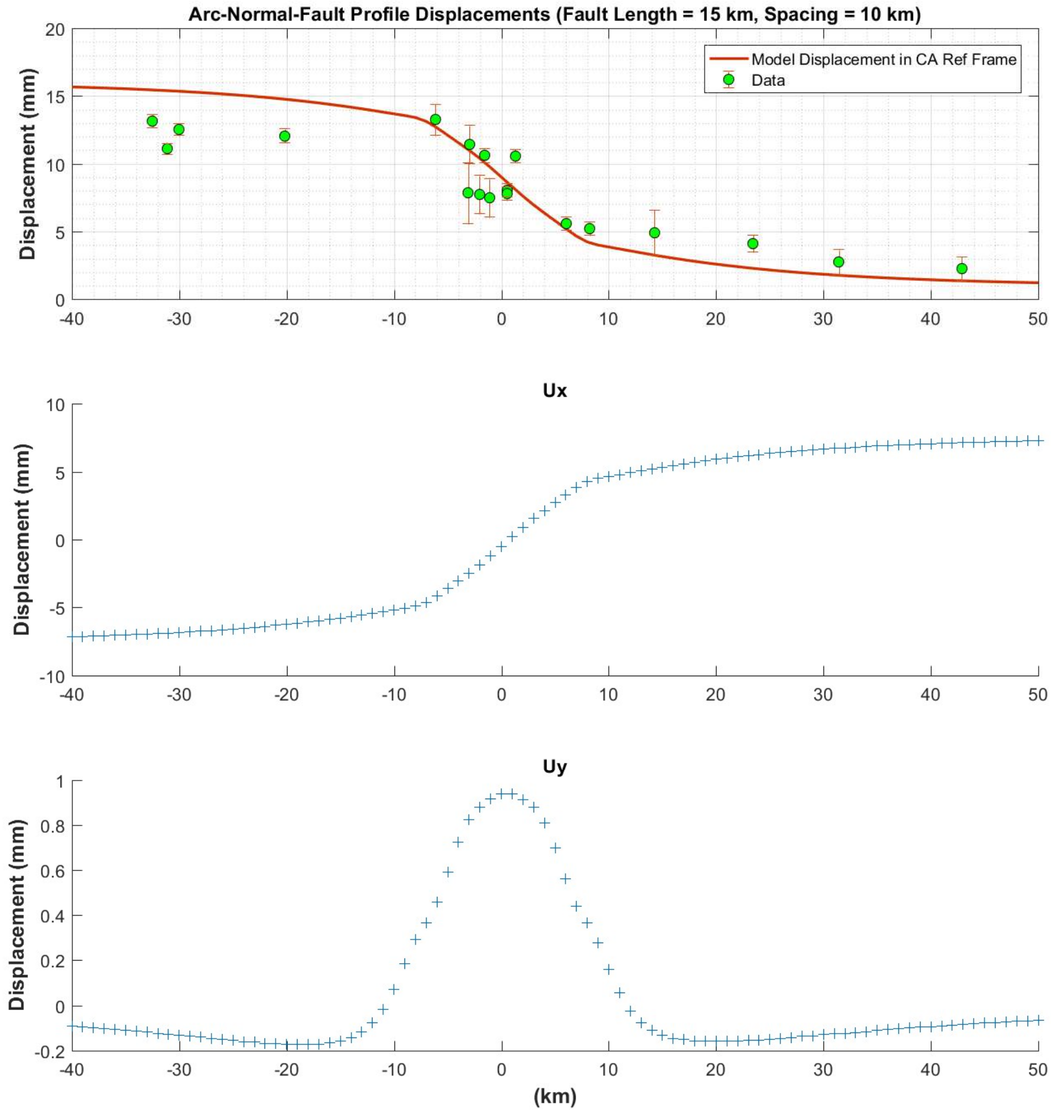

Figure **B-72**: Model D9: displacements along-profile. Arc-normal faults' length and spacing are 15 km and 10 km respectively. Top panel – profile displacements projected into horizontal line (azimuth = 270°). Middle panel – profile displacements in the x-direction. Bottom panel – profile displacements in the y-direction. 'Model Displacement in CA' data sets was created by adding an offset of 7 mm to the model displacements.

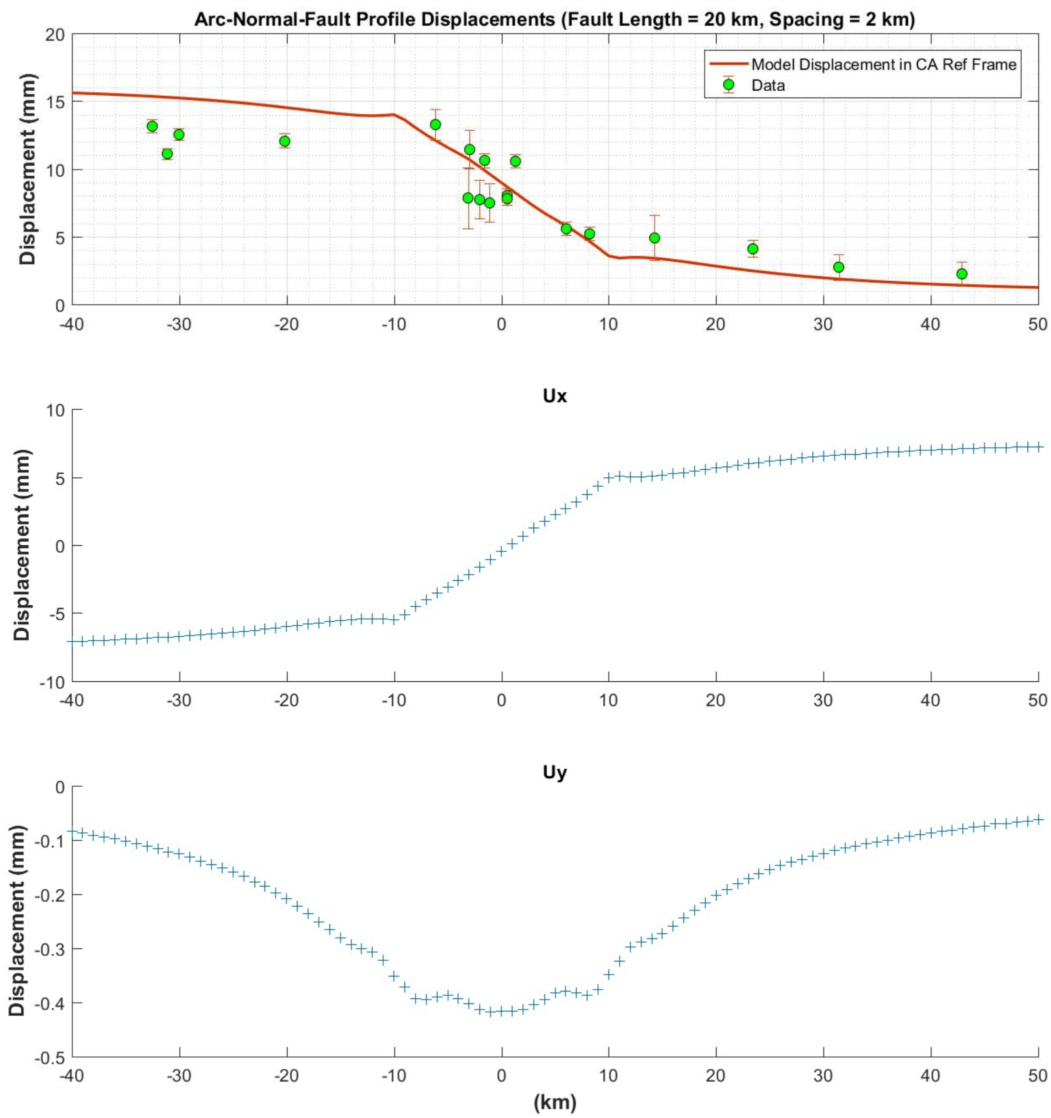

Figure **B-73**: Model D10: displacements along-profile. Arc-normal faults' length and spacing are 20 km and 2 km respectively. Top panel – profile displacements projected into horizontal line (azimuth = 270°). Middle panel – profile displacements in the x-direction. Bottom panel – profile displacements in the y-direction. 'Model Displacement in CA' data sets was created by adding an offset of 7 mm to the model displacements.

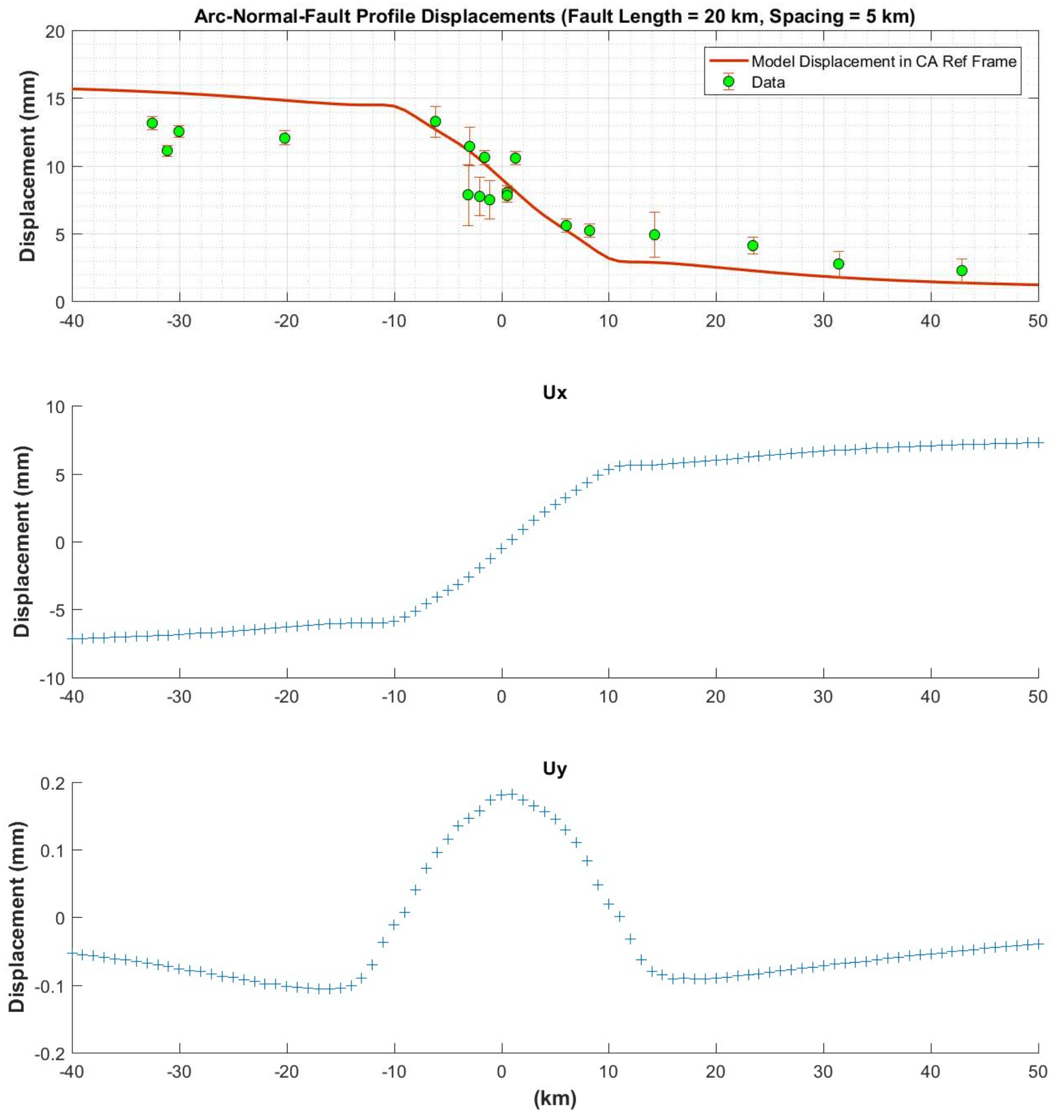

Figure **B-74**: Model D11: displacements along-profile. Arc-normal faults' length and spacing are 20 km and 5 km respectively. Top panel – profile displacements projected into horizontal line (azimuth = 270°). Middle panel – profile displacements in the x-direction. Bottom panel – profile displacements in the y-direction. 'Model Displacement in CA' data sets was created by adding an offset of 7 mm to the model displacements.

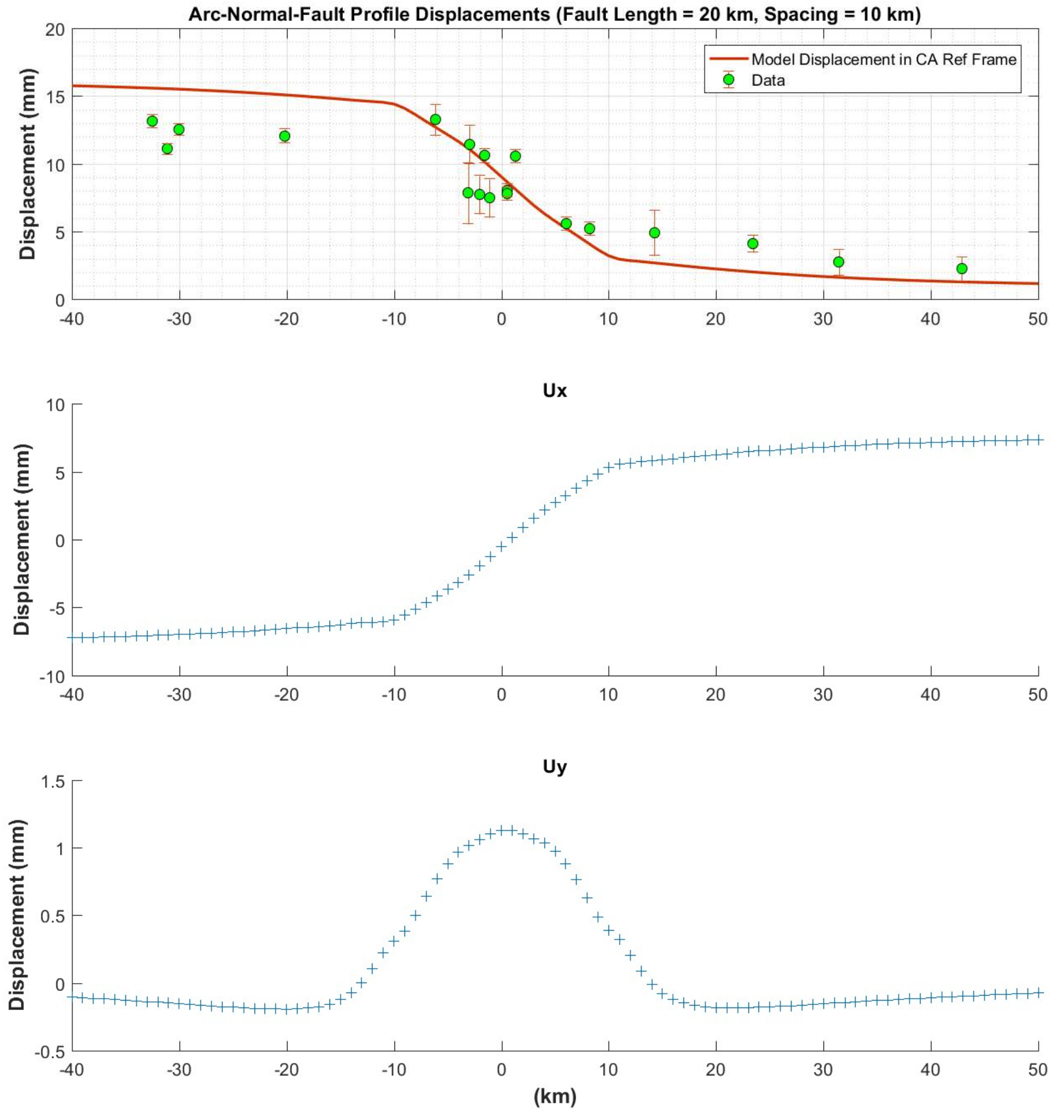

Figure **B-75**: Model D12: displacements along-profile. Arc-normal faults' length and spacing are 20 km and 10 km respectively. Top panel – profile displacements projected into horizontal line (azimuth = 270°). Middle panel – profile displacements in the x-direction. Bottom panel – profile displacements in the y-direction. 'Model Displacement in CA' data sets was created by adding an offset of 7 mm to the model displacements.

B.3 Model Set E Plots

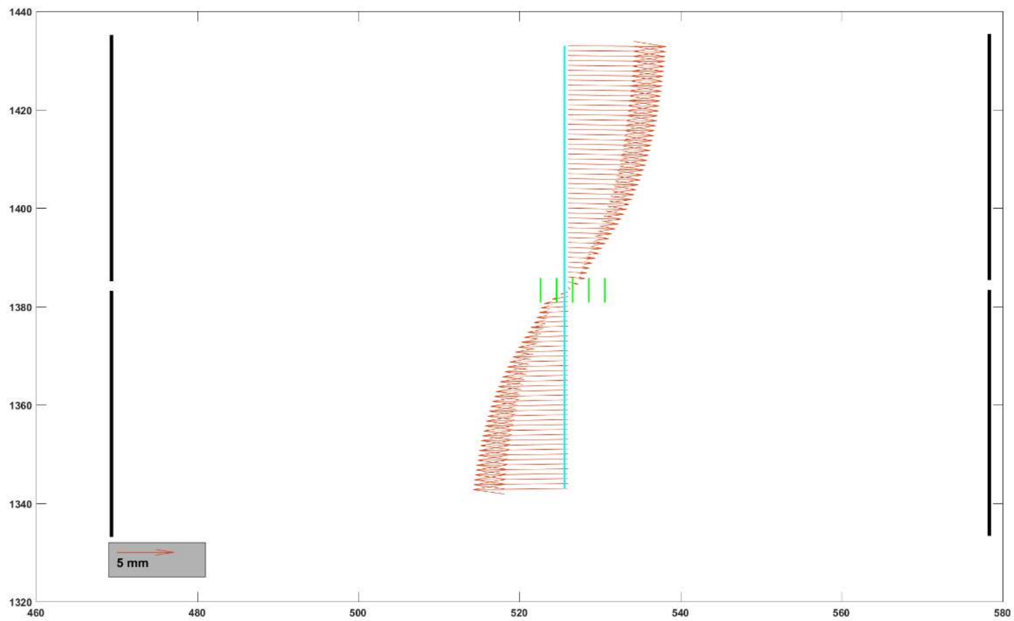

Figure **B-76**: Model E1: surface displacements (red vectors) along-profile line (cyan line). Arc-normal faults' (green lines) length and spacing are 5 km and 2 km respectively. This model has 5 arc-normal faults.

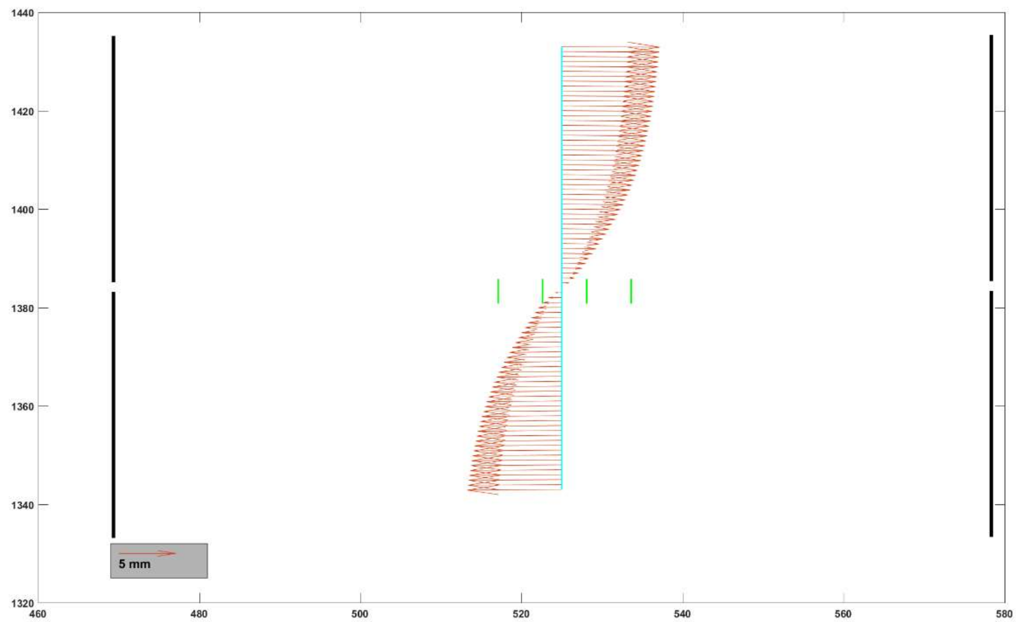

Figure **B-77**: Model E2: surface displacements (red vectors) along-profile line (cyan line). Arc-normal faults' (green lines) length and spacing are 5 km and 5 km respectively. This model has 4 arc-normal faults.

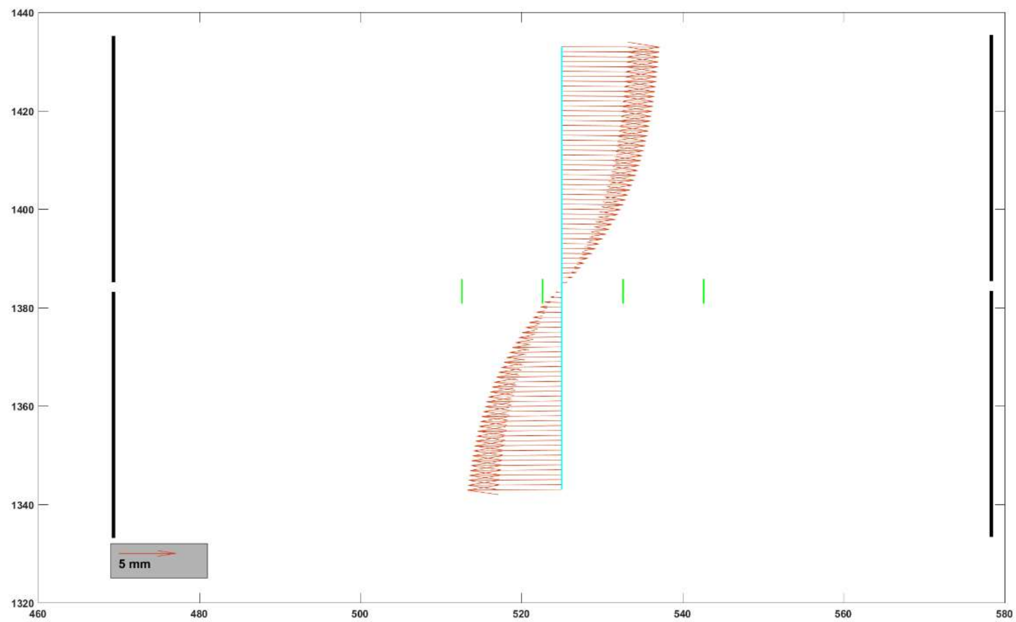

Figure **B-78**: Model E3: surface displacements (red vectors) along-profile line (cyan line). Arc-normal faults' (green lines) length and spacing are 5 km and 10 km respectively. This model has 4 arc-normal faults.

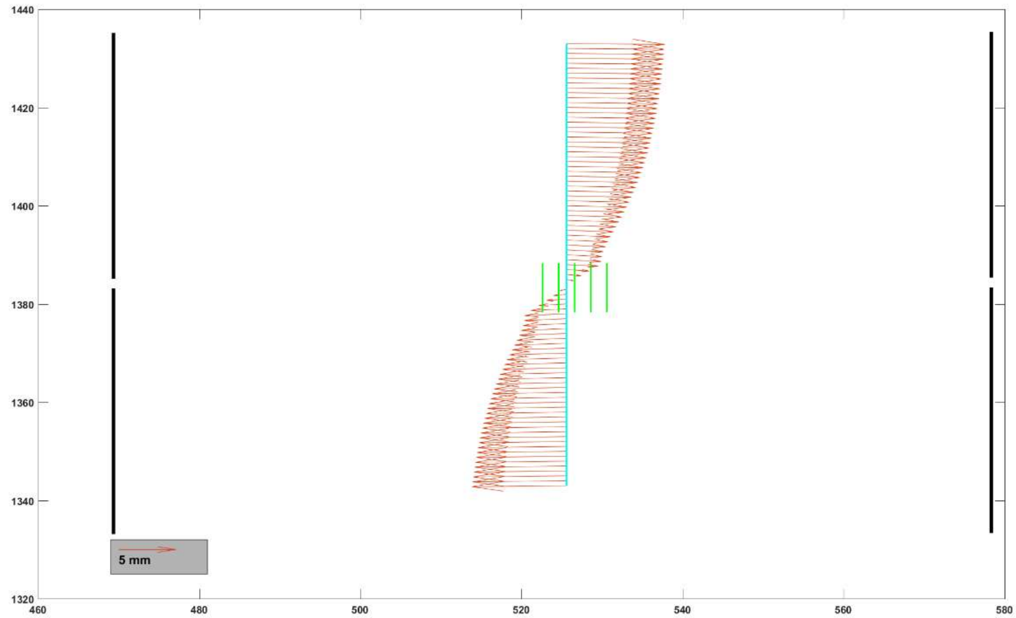

Figure **B-79**: Model E4: surface displacements (red vectors) along-profile line (cyan line). Arc-normal faults' (green lines) length and spacing are 10 km and 2 km respectively. This model has 5 arc-normal faults.

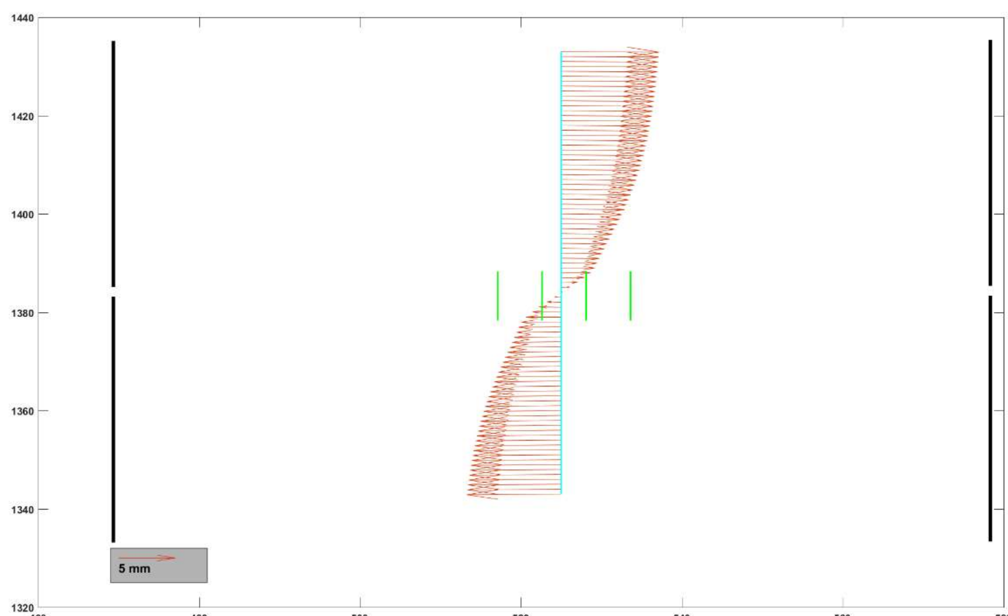

Figure **B-80**: Model E5: surface displacements (red vectors) along-profile line (cyan line). Arc-normal faults' (green lines) length and spacing are 10 km and 5 km respectively. This model has 4 arc-normal faults.

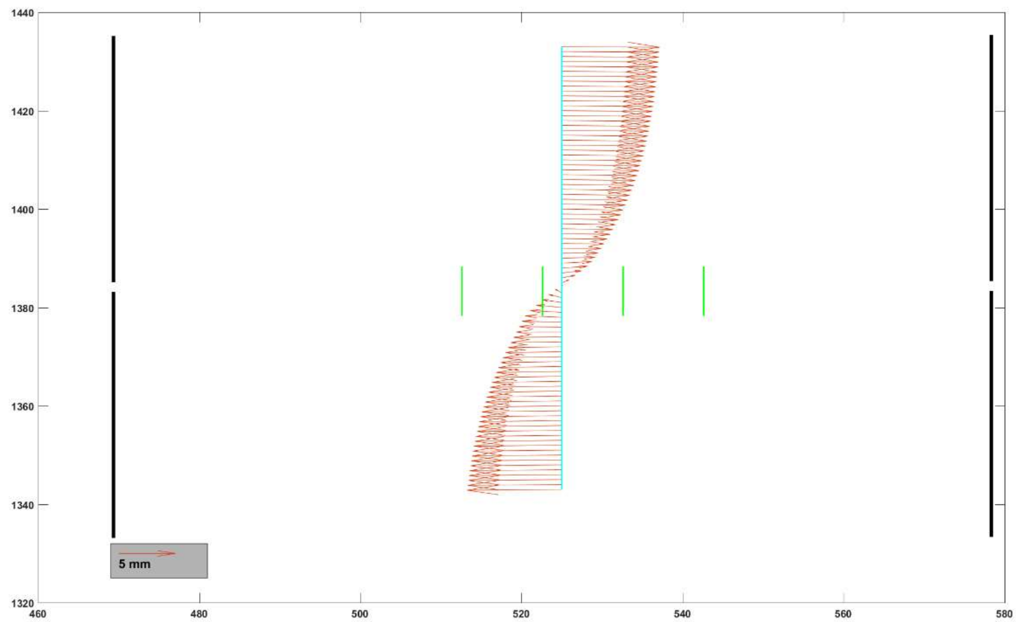

Figure **B-81**: Model E6: surface displacements (red vectors) along-profile line (cyan line). Arc-normal faults' (green lines) length and spacing are 10 km and 10 km respectively. This model has 4 arc-normal faults.

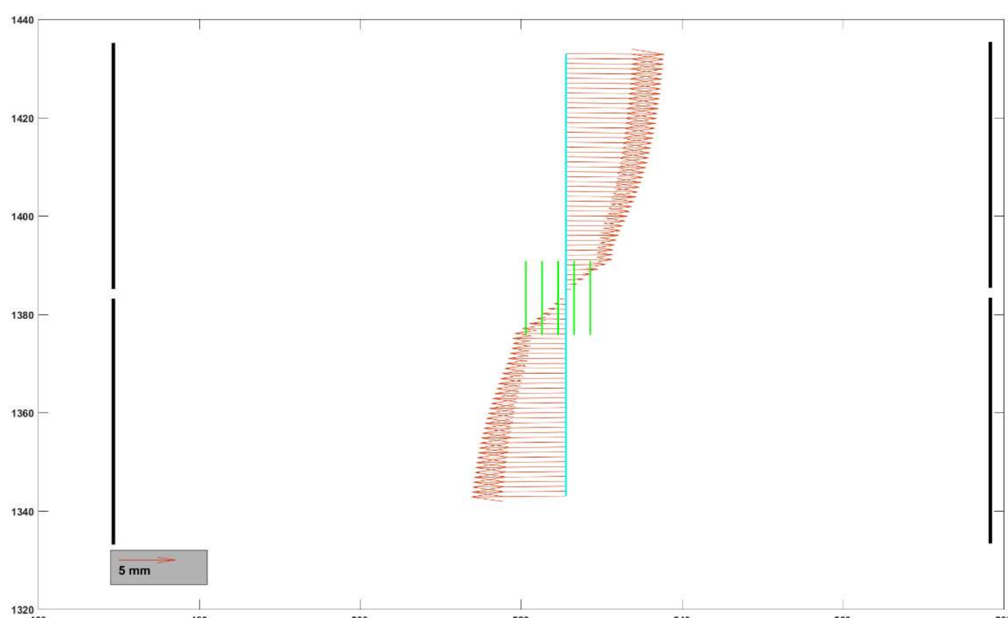

Figure **B-82**: Model E7: surface displacements (red vectors) along-profile line (cyan line). Arc-normal faults' (green lines) length and spacing are 15 km and 2 km respectively. This model has 5 arc-normal faults.

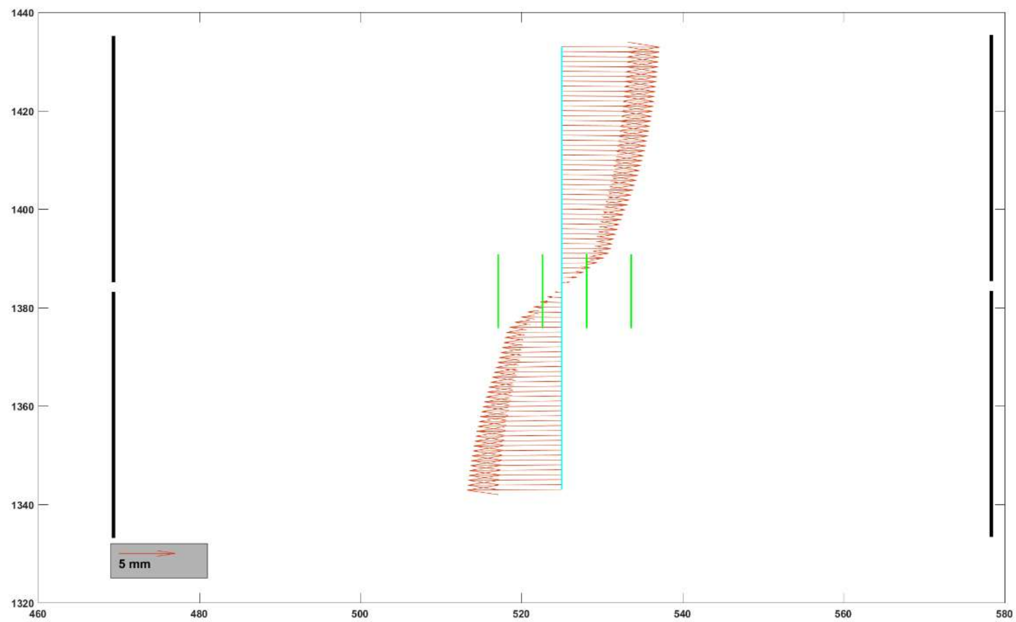

Figure **B-83**: Model E8: surface displacements (red vectors) along-profile line (cyan line). Arc-normal faults' (green lines) length and spacing are 15 km and 5 km respectively. This model has 4 arc-normal faults.

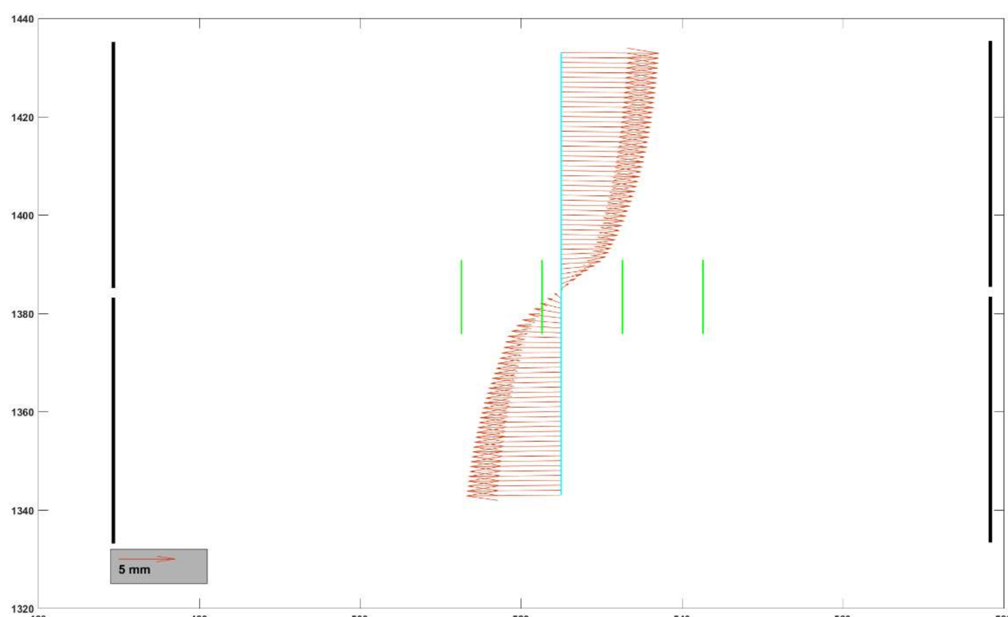

Figure **B-84**: Model E9: surface displacements (red vectors) along-profile line (cyan line). Arc-normal faults' (green lines) length and spacing are 15 km and 10 km respectively. This model has 4 arc-normal faults.

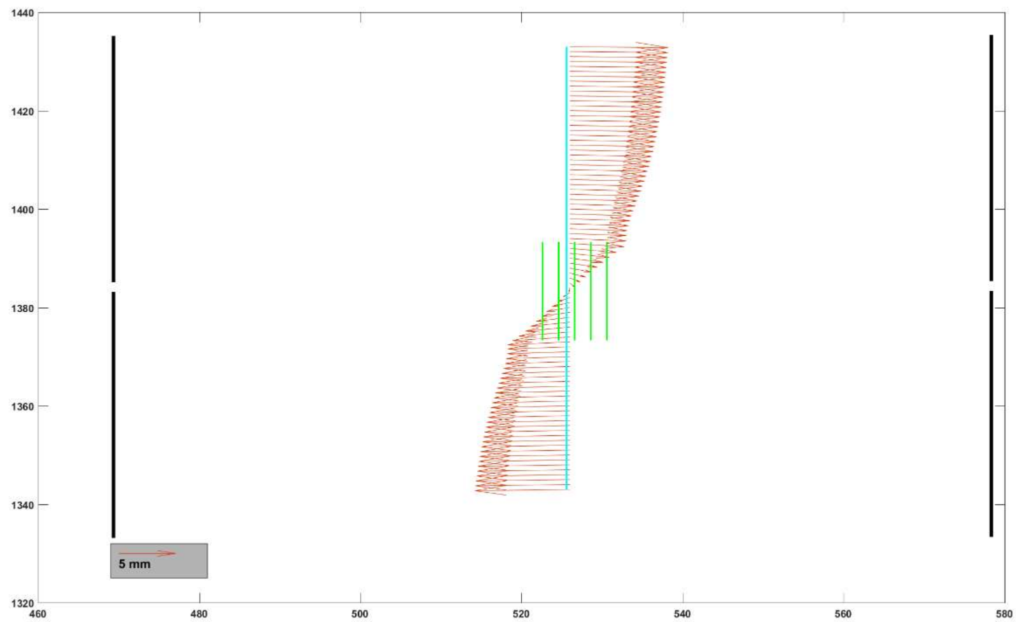

Figure **B-85**: Model E10: surface displacements (red vectors) along-profile line (cyan line). Arc-normal faults' (green lines) length and spacing are 20 km and 2 km respectively. This model has 5 arc-normal faults.

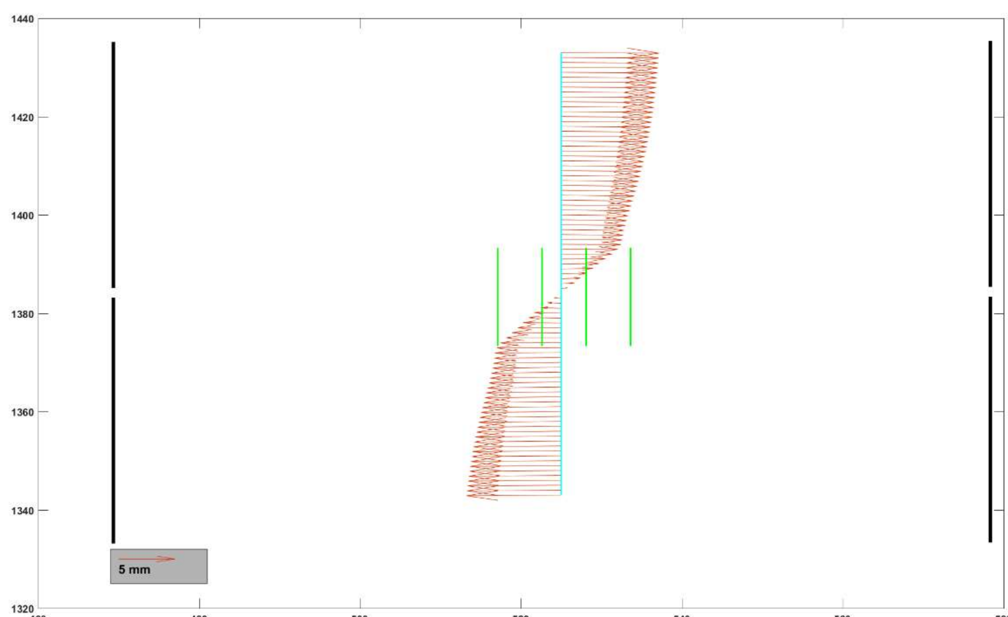

Figure **B-86**: Model E11: surface displacements (red vectors) along-profile line (cyan line). Arc-normal faults' (green lines) length and spacing are 20 km and 5 km respectively. This model has 4 arc-normal faults.

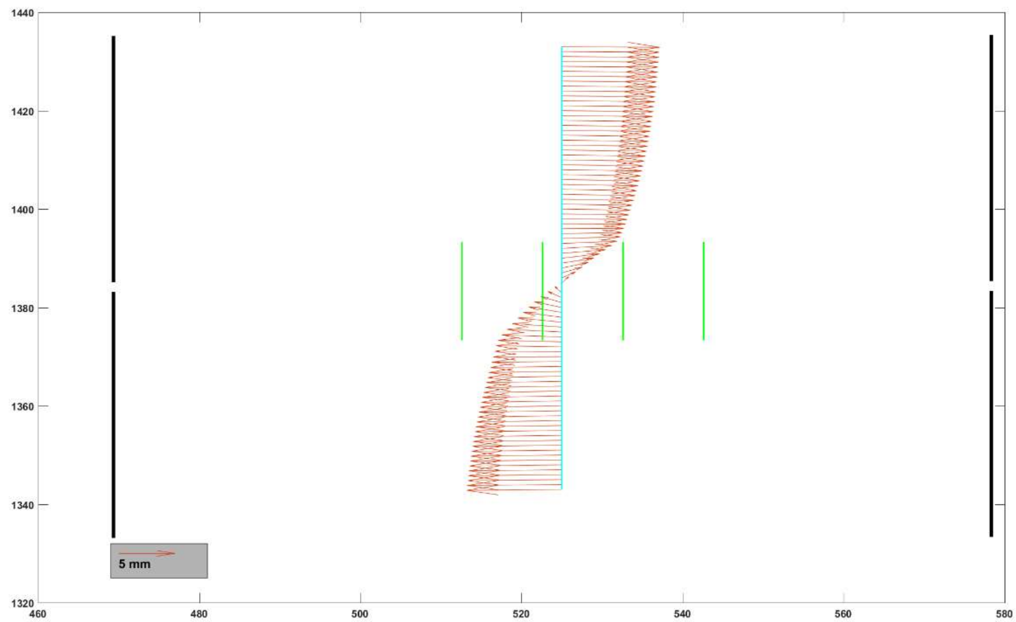

Figure **B-87**: Model E12: surface displacements (red vectors) along-profile line (cyan line). Arc-normal faults' (green lines) length and spacing are 20 km and 10 km respectively. This model has 4 arc-normal faults.

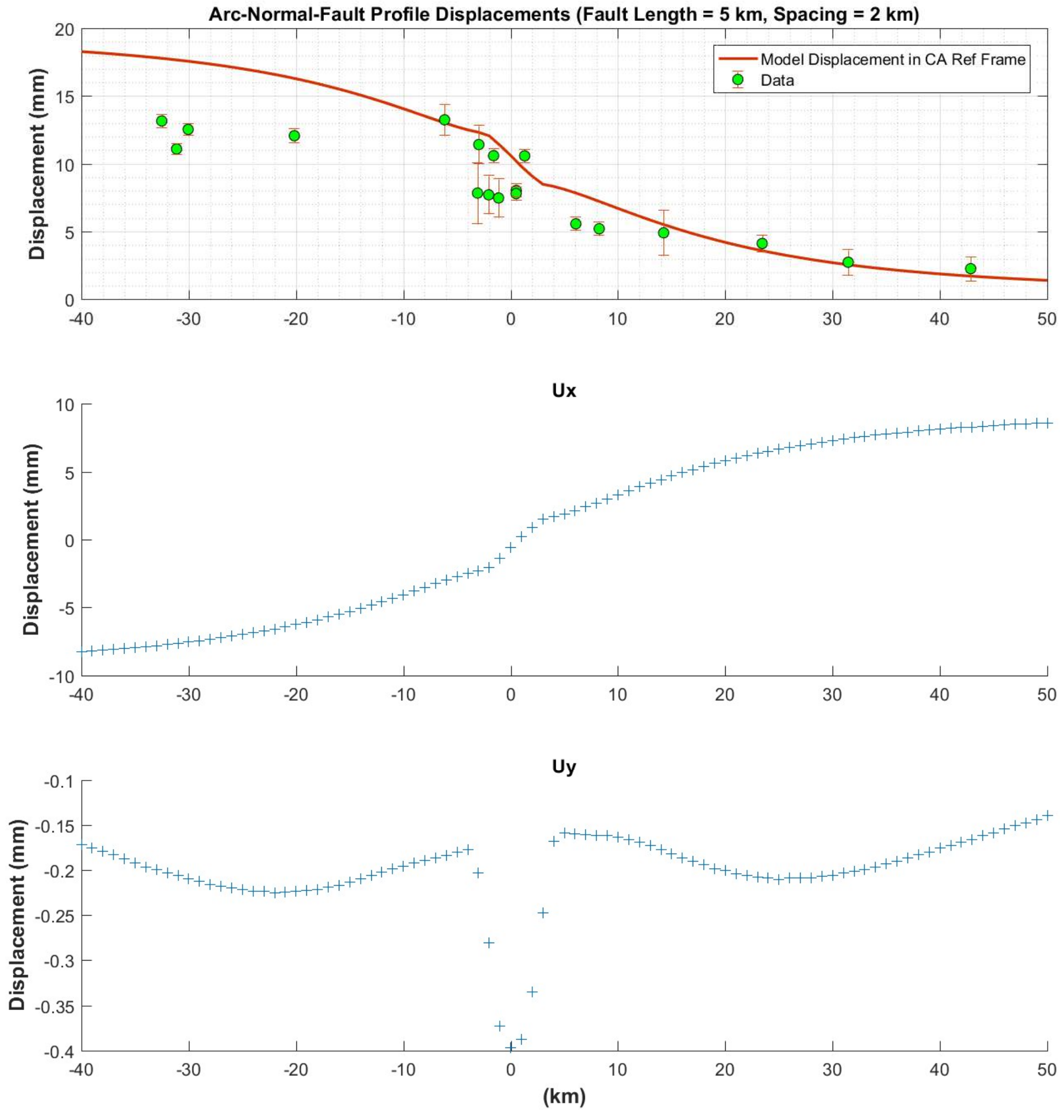

Figure **B-88**: Model E1: displacements along-profile. Arc-normal faults' length and spacing are 5 km and 2 km respectively. Top panel – profile displacements projected into horizontal line (azimuth = 270°). Middle panel – profile displacements in the x-direction. Bottom panel – profile displacements in the y-direction. 'Model Displacement in CA' data sets was created by adding an offset of 7 mm to the model displacements.

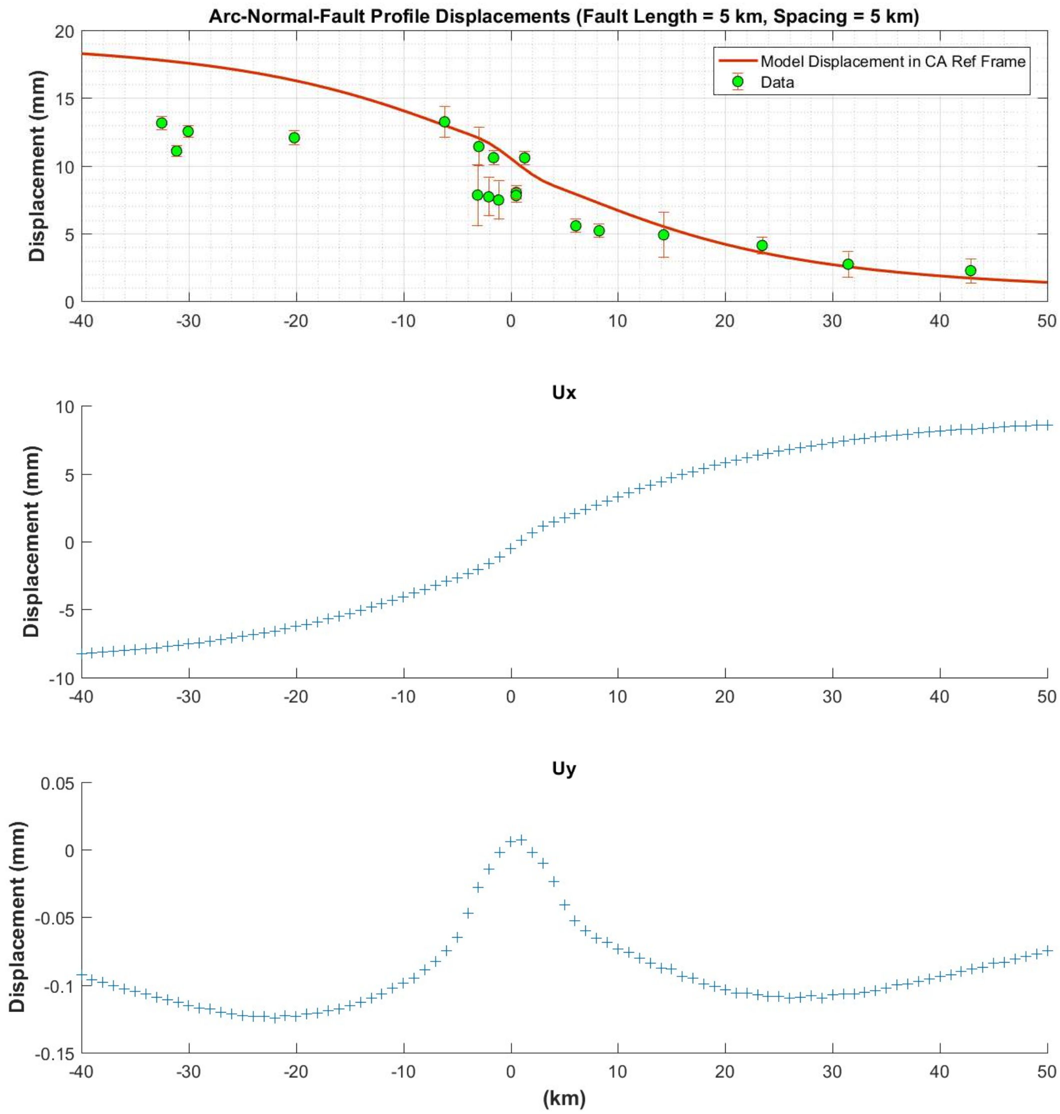

Figure **B-89**: Model E2: displacements along-profile. Arc-normal faults' length and spacing are 5 km and 5 km respectively. Top panel – profile displacements projected into horizontal line (azimuth = 270°). Middle panel – profile displacements in the x-direction. Bottom panel – profile displacements in the y-direction. 'Model Displacement in CA' data sets was created by adding an offset of 7 mm to the model displacements.

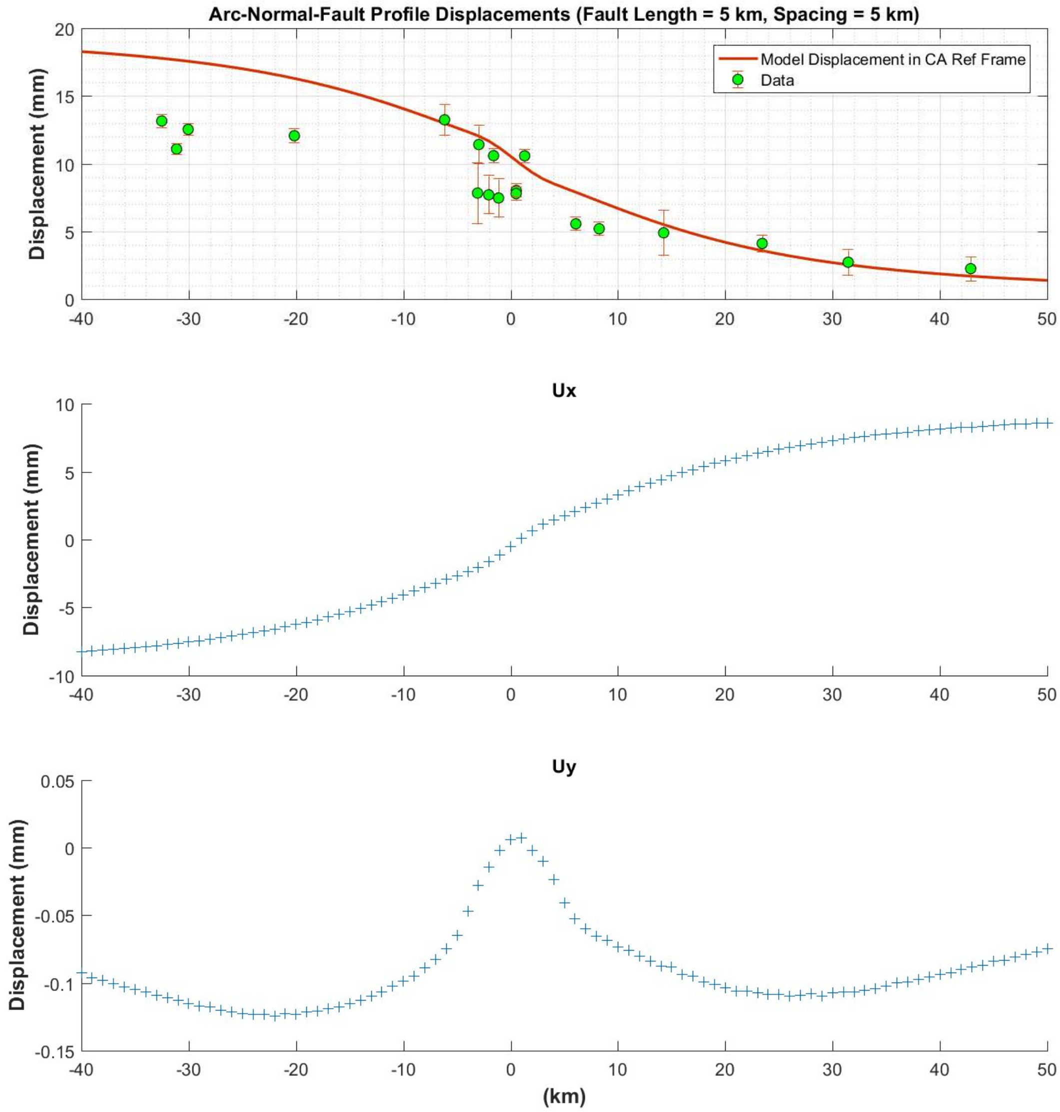

Figure **B-90**: Model E3: displacements along-profile. Arc-normal faults' length and spacing are 5 km and 10 km respectively. Top panel – profile displacements projected into horizontal line (azimuth = 270°). Middle panel – profile displacements in the x-direction. Bottom panel – profile displacements in the y-direction. 'Model Displacement in CA' data sets was created by adding an offset of 7 mm to the model displacements.

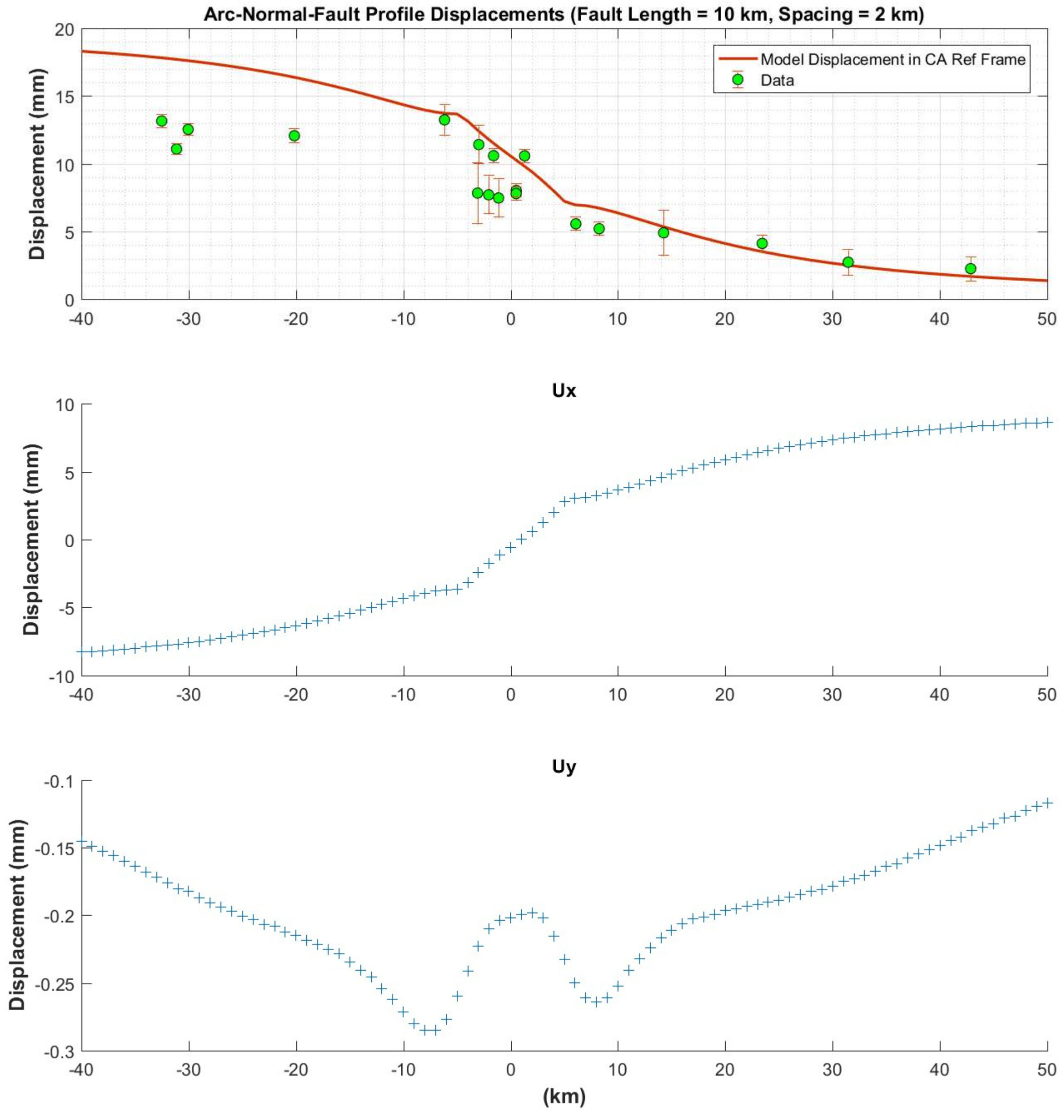

Figure **B-91**: Model E4: displacements along-profile. Arc-normal faults' length and spacing are 10 km and 2 km respectively. Top panel – profile displacements projected into horizontal line (azimuth = 270°). Middle panel – profile displacements in the x-direction. Bottom panel – profile displacements in the y-direction. 'Model Displacement in CA' data sets was created by adding an offset of 7 mm to the model displacements.

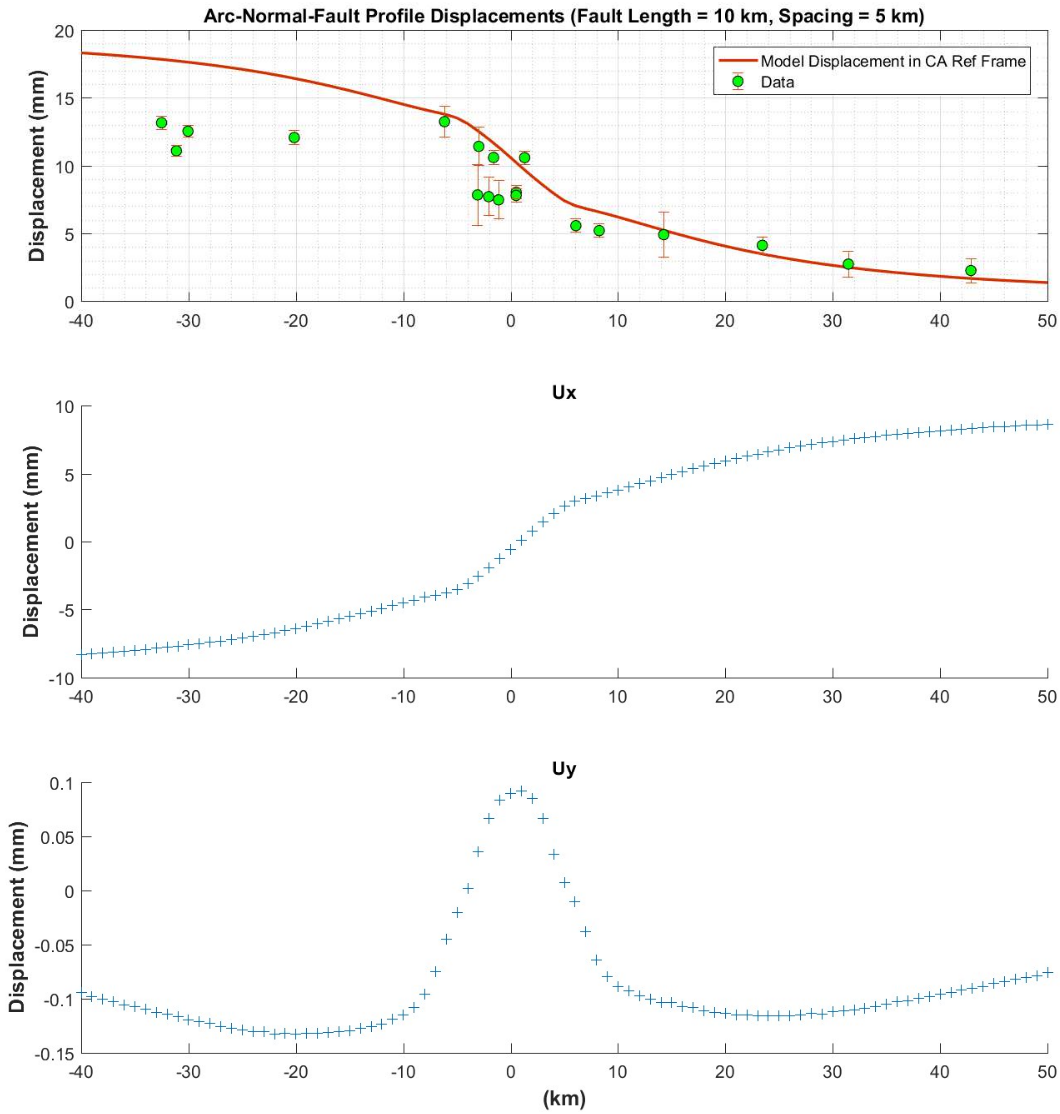

Figure **B-92**: Model E5: displacements along-profile. Arc-normal faults' length and spacing are 10 km and 5 km respectively. Top panel – profile displacements projected into horizontal line (azimuth = 270°). Middle panel – profile displacements in the x-direction. Bottom panel – profile displacements in the y-direction. 'Model Displacement in CA' data sets was created by adding an offset of 7 mm to the model displacements.

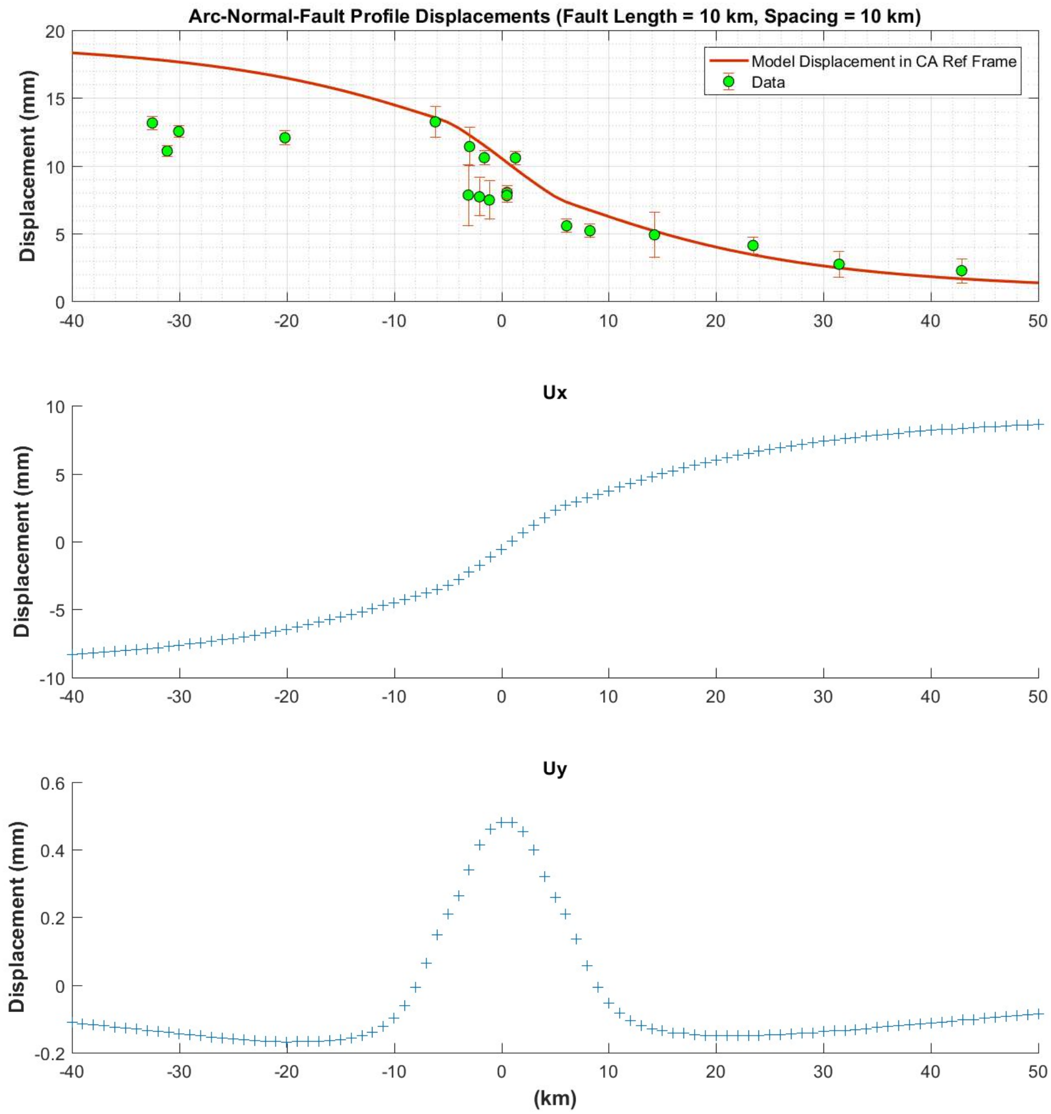

Figure **B-93**: Model E6: displacements along-profile. Arc-normal faults' length and spacing are 10 km and 10 km respectively. Top panel – profile displacements projected into horizontal line (azimuth = 270°). Middle panel – profile displacements in the x-direction. Bottom panel – profile displacements in the y-direction. 'Model Displacement in CA' data sets was created by adding an offset of 7 mm to the model displacements.

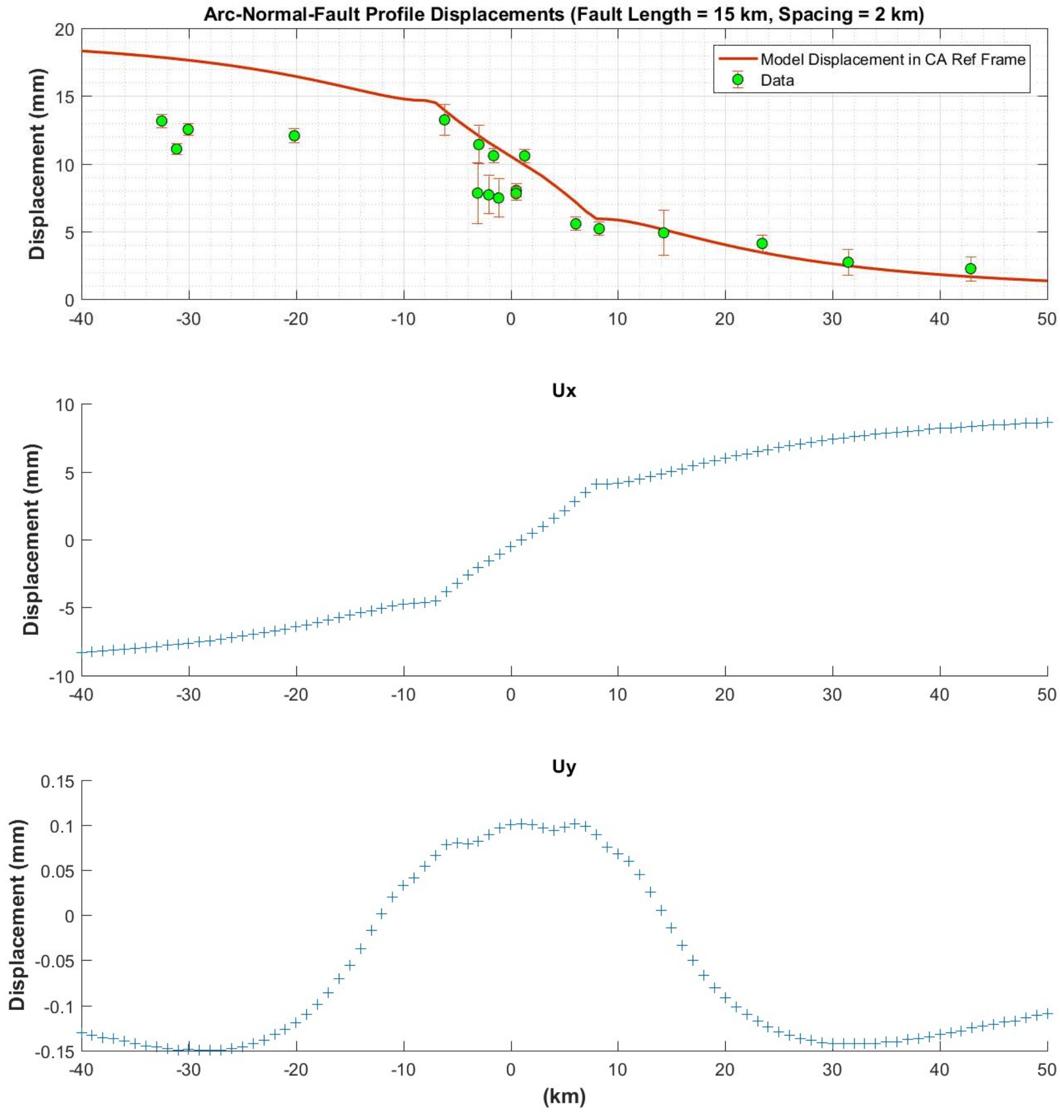

Figure **B-94**: Model E7: displacements along-profile. Arc-normal faults' length and spacing are 15 km and 2 km respectively. Top panel – profile displacements projected into horizontal line (azimuth = 270°). Middle panel – profile displacements in the x-direction. Bottom panel – profile displacements in the y-direction. 'Model Displacement in CA' data sets was created by adding an offset of 7 mm to the modeled displacement.

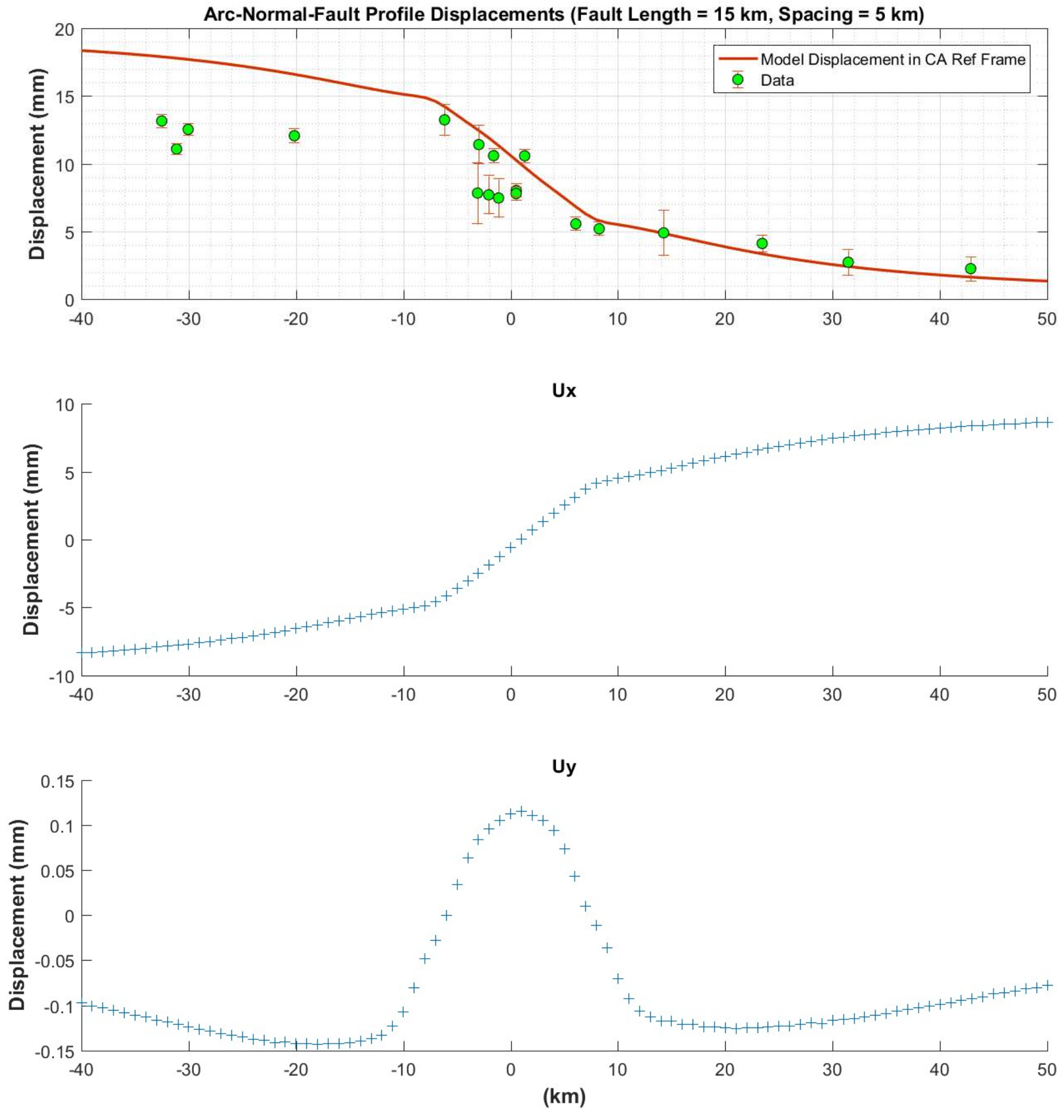

Figure **B-95**: Model E8: displacements along-profile. Arc-normal faults' length and spacing are 15 km and 5 km respectively. Top panel – profile displacements projected into horizontal line (azimuth = 270°). Middle panel – profile displacements in the x-direction. Bottom panel – profile displacements in the y-direction. 'Model Displacement in CA' data sets was created by adding an offset of 7 mm to the modeled displacement.

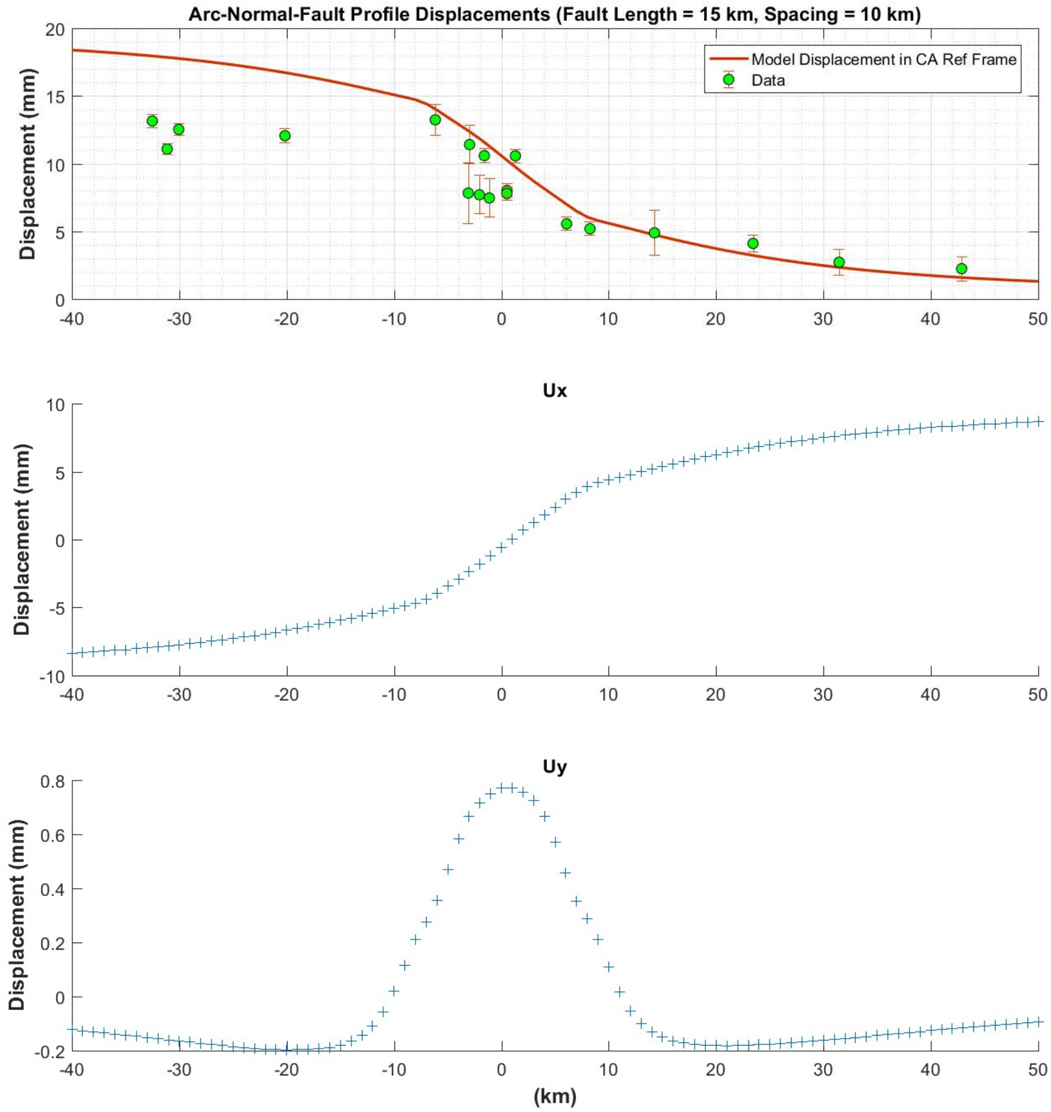

Figure **B-96**: Model E9: displacements along-profile. Arc-normal faults' length and spacing are 15 km and 10 km respectively. Top panel – profile displacements projected into horizontal line (azimuth = 270°). Middle panel – profile displacements in the x-direction. Bottom panel – profile displacements in the y-direction. 'Model Displacement in CA' data sets was created by adding an offset of 7 mm to the modeled displacement.

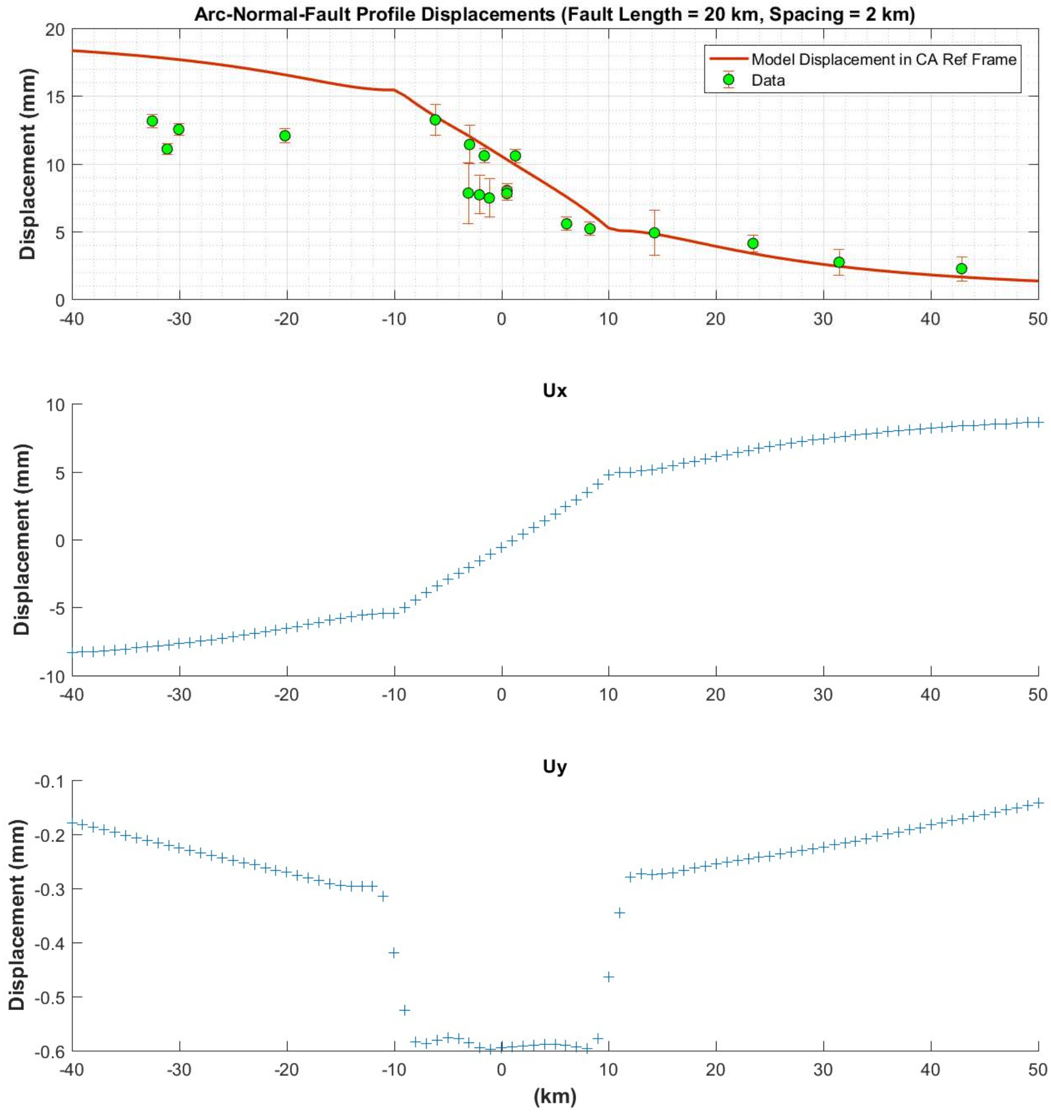

Figure **B-97**: Model E10: displacements along-profile. Arc-normal faults' length and spacing are 20 km and 2 km respectively. Top panel – profile displacements projected into horizontal line (azimuth = 270°). Middle panel – profile displacements in the x-direction. Bottom panel – profile displacements in the y-direction. 'Model Displacement in CA' data sets was created by adding an offset of 7 mm to the model displacements.

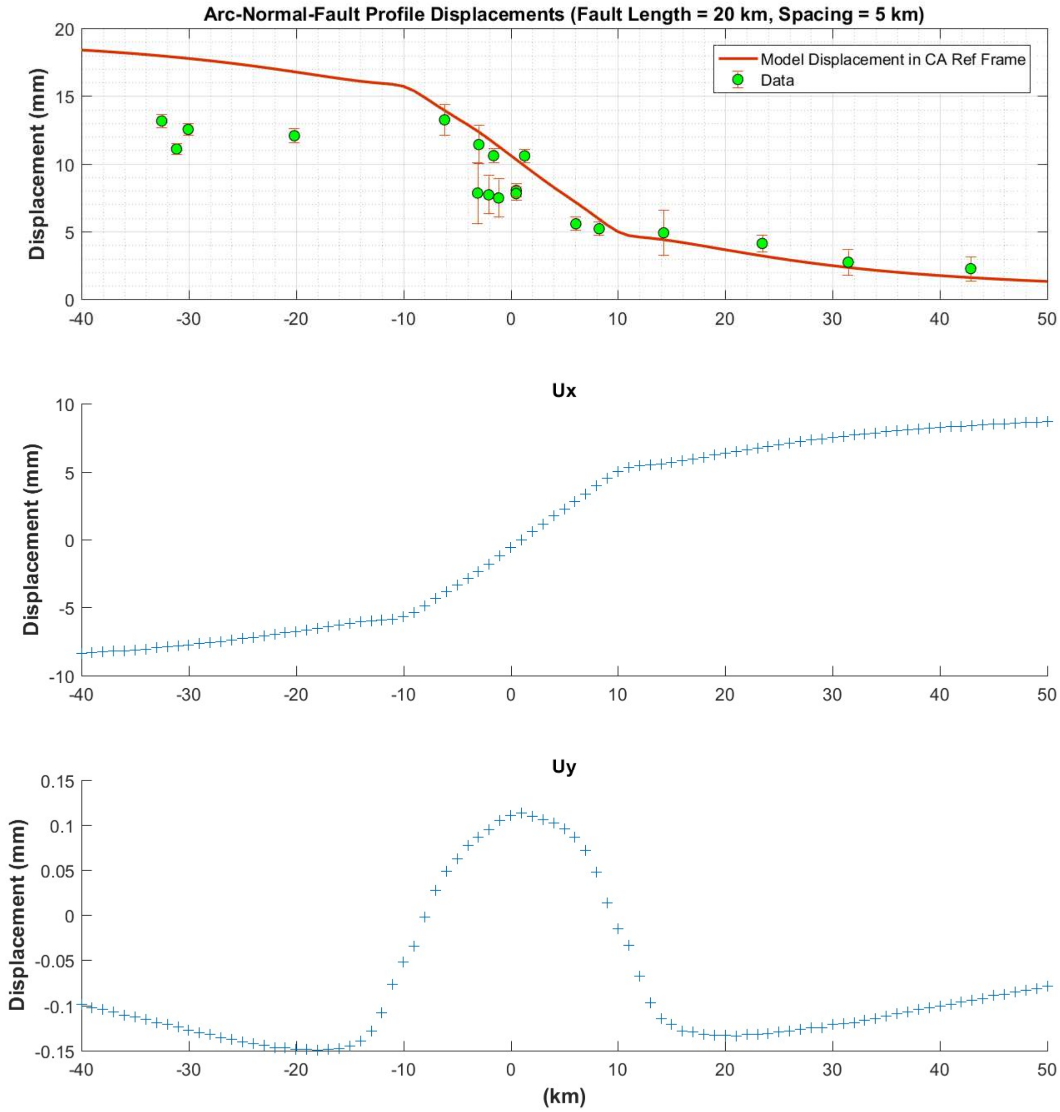

Figure **B-98**: Model E11: displacements along-profile. Arc-normal faults' length and spacing are 20 km and 5 km respectively. Top panel – profile displacements projected into horizontal line (azimuth = 270°). Middle panel – profile displacements in the x-direction. Bottom panel – profile displacements in the y-direction. 'Model Displacement in CA' data sets was created by adding an offset of 7 mm to the model displacements.

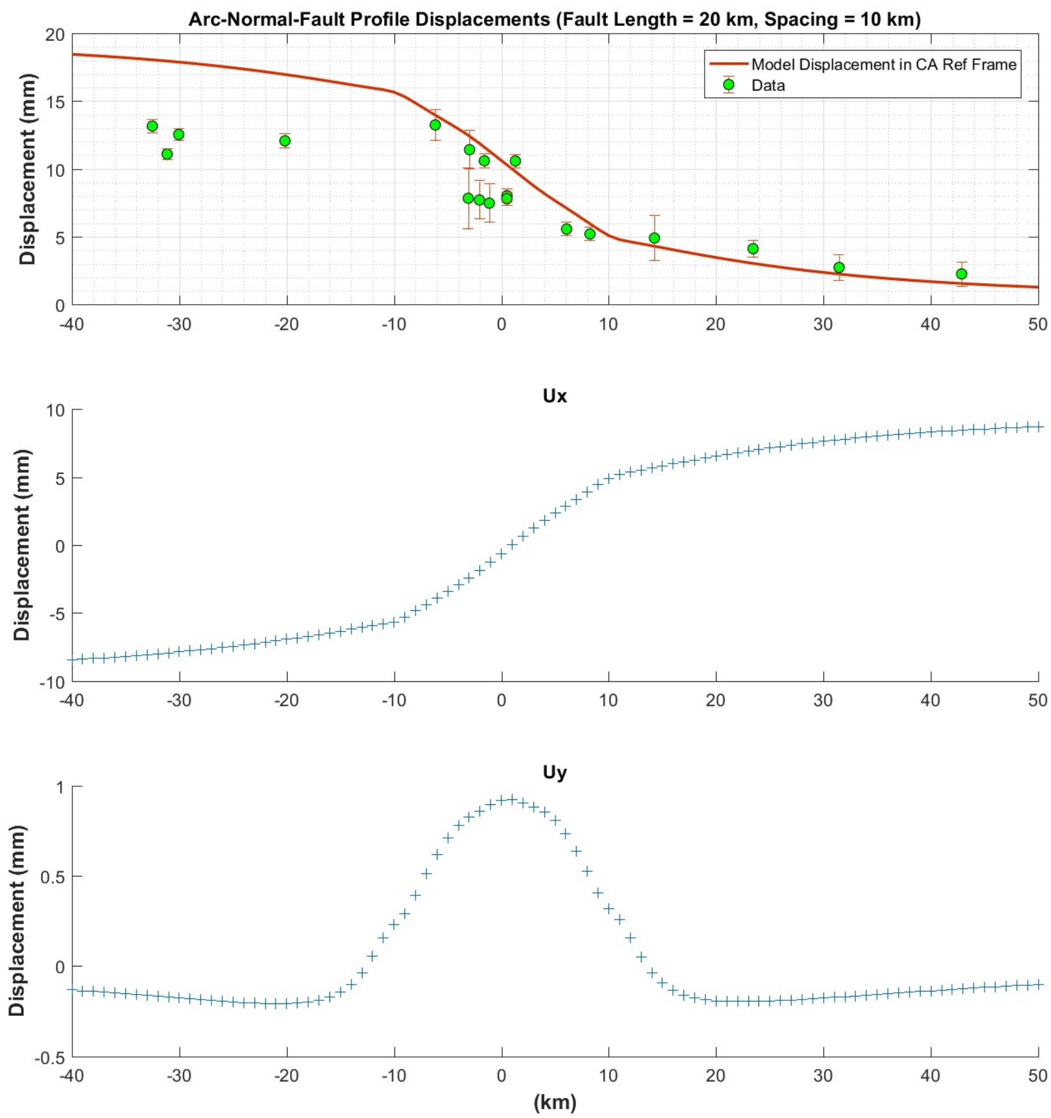

Figure **B-99**: Model E12: displacements along-profile. Arc-normal faults' length and spacing are 20 km and 10 km respectively. Top panel – profile displacements projected into horizontal line (azimuth = 270°). Middle panel – profile displacements in the x-direction. Bottom panel – profile displacements in the y-direction. 'Model Displacement in CA' data sets was created by adding an offset of 7 mm to the model displacements.

B.3 Model Set F Plots

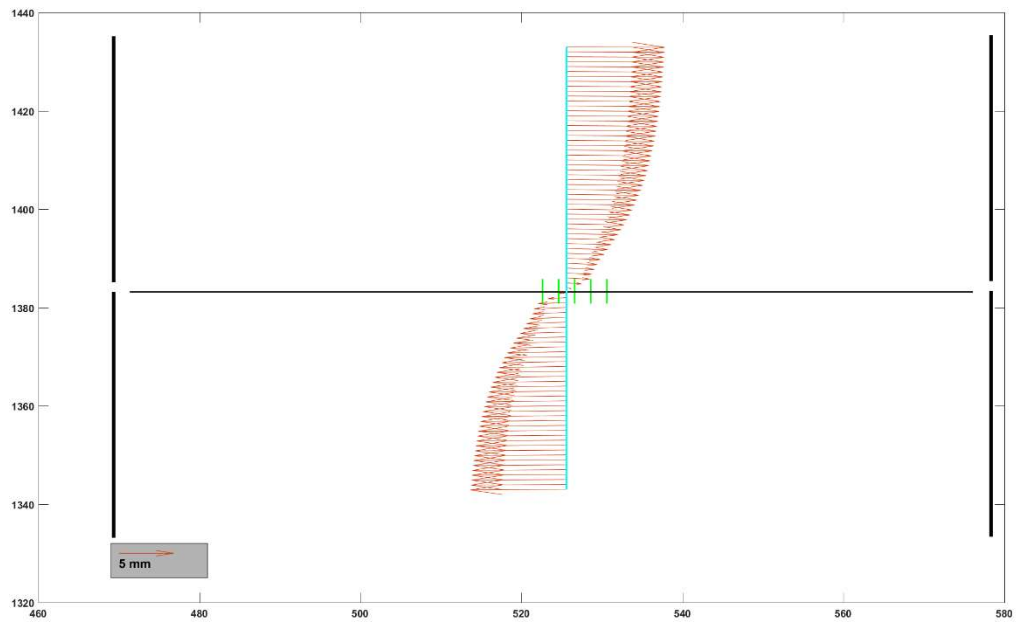

Figure **B-100**: Model F1: surface displacements (red vectors) along-profile line (cyan line). Arc-normal faults' (green lines) length and spacing are 5 km and 2 km respectively. This model has 5 arc-normal faults.

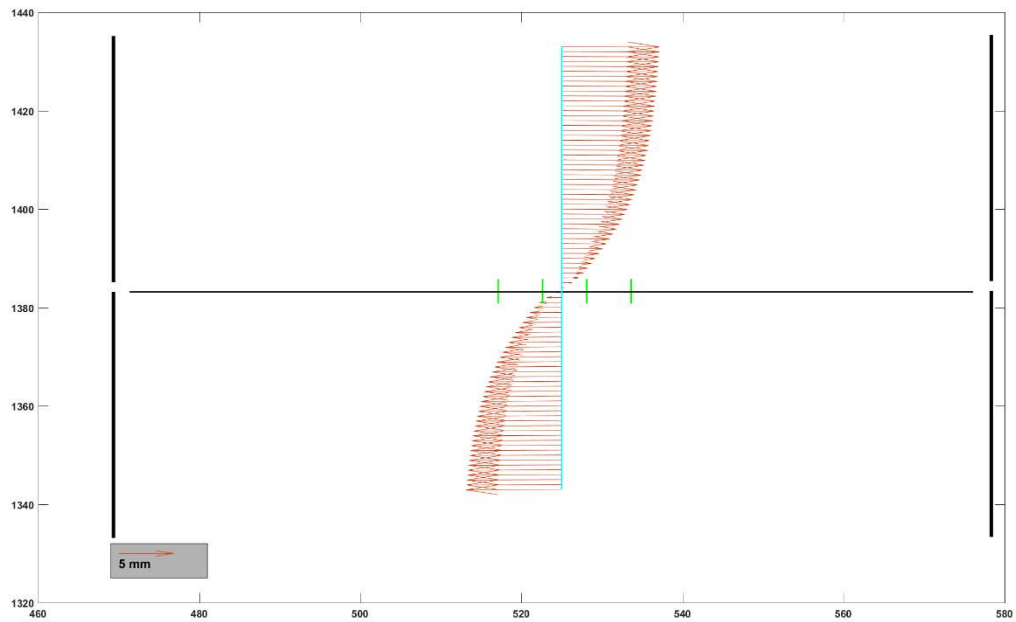

Figure **B-101**: Model F2: surface displacements (red vectors) along-profile line (cyan line). Arc-normal faults' (green lines) length and spacing are 5 km and 5 km respectively. This model has 4 arc-normal faults.

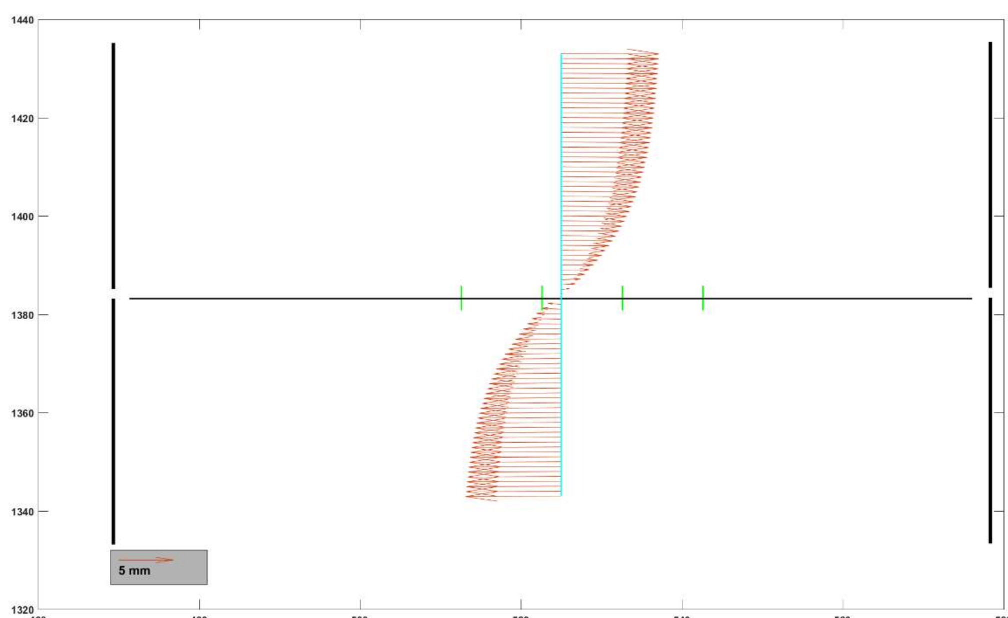

Figure **B-102**: Model F3: surface displacements (red vectors) along-profile line (cyan line). Arc-normal faults' (green lines) length and spacing are 5 km and 10 km respectively. This model has 4 arc-normal faults.

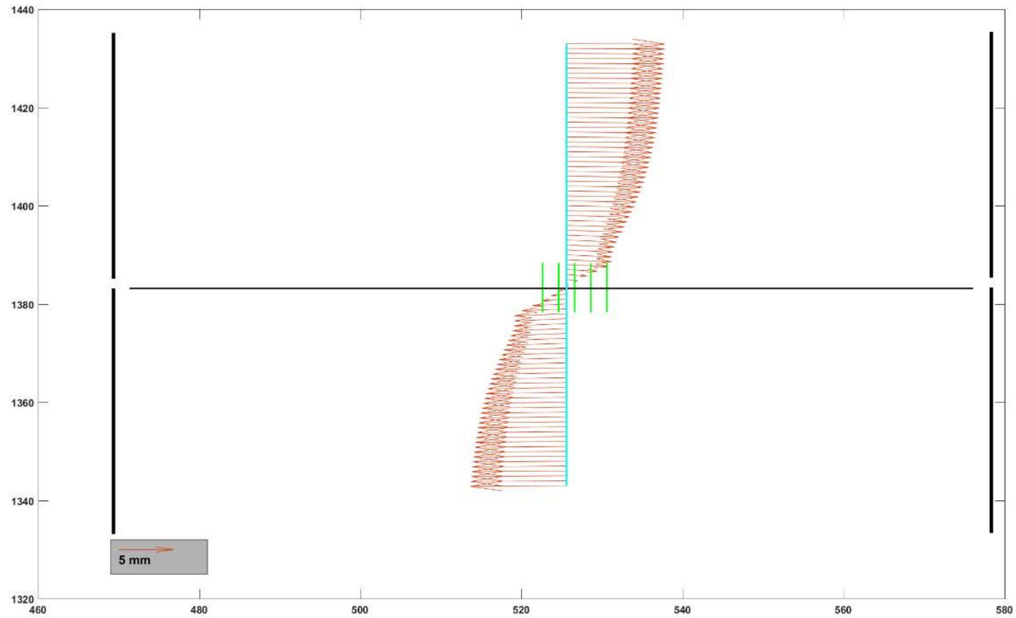

Figure **B-103**: Model F4: surface displacements (red vectors) along-profile line (cyan line). Arc-normal faults' (green lines) length and spacing are 10 km and 2 km respectively. This model has 5 arc-normal faults.

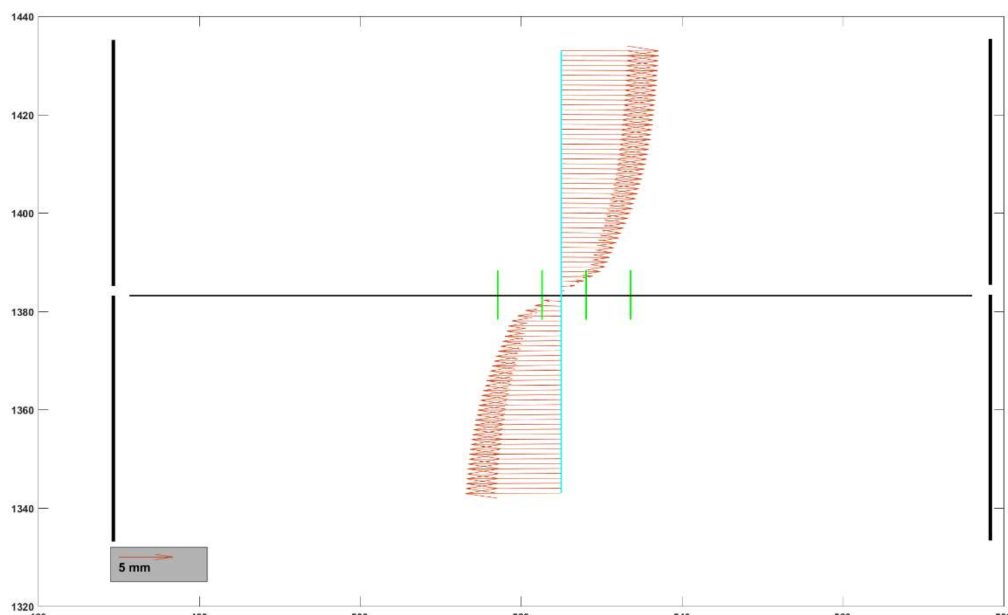

Figure **B-104**: Model F5: surface displacements (red vectors) along-profile line (cyan line). Arc-normal faults' (green lines) length and spacing are 10 km and 5 km respectively. This model has 4 arc-normal faults.

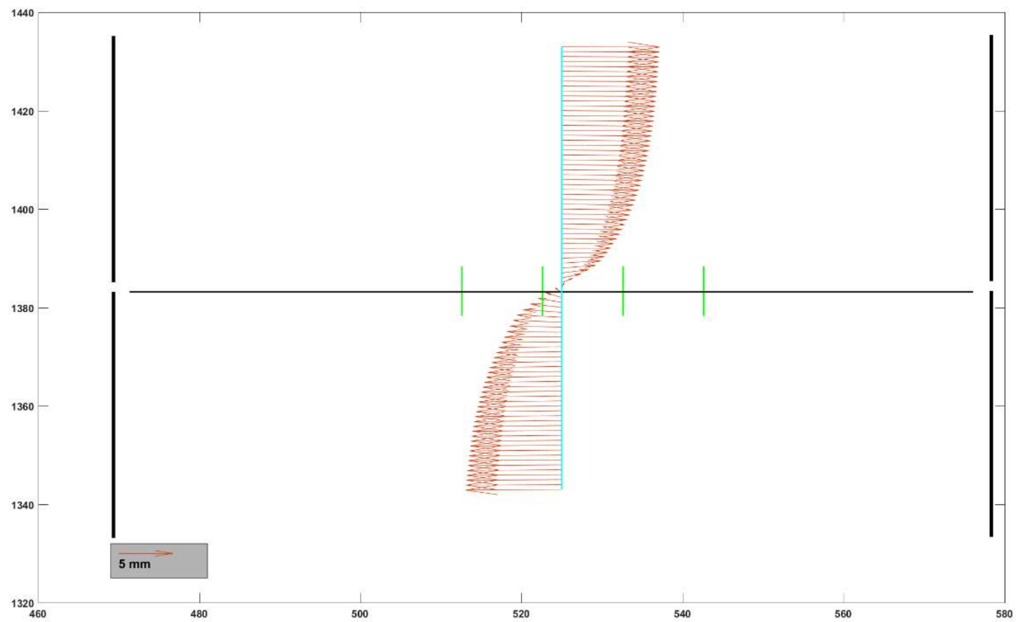

Figure **B-105**: Model F6: surface displacements (red vectors) along-profile line (cyan line). Arc-normal faults' (green lines) length and spacing are 10 km and 10 km respectively. This model has 4 arc-normal faults.

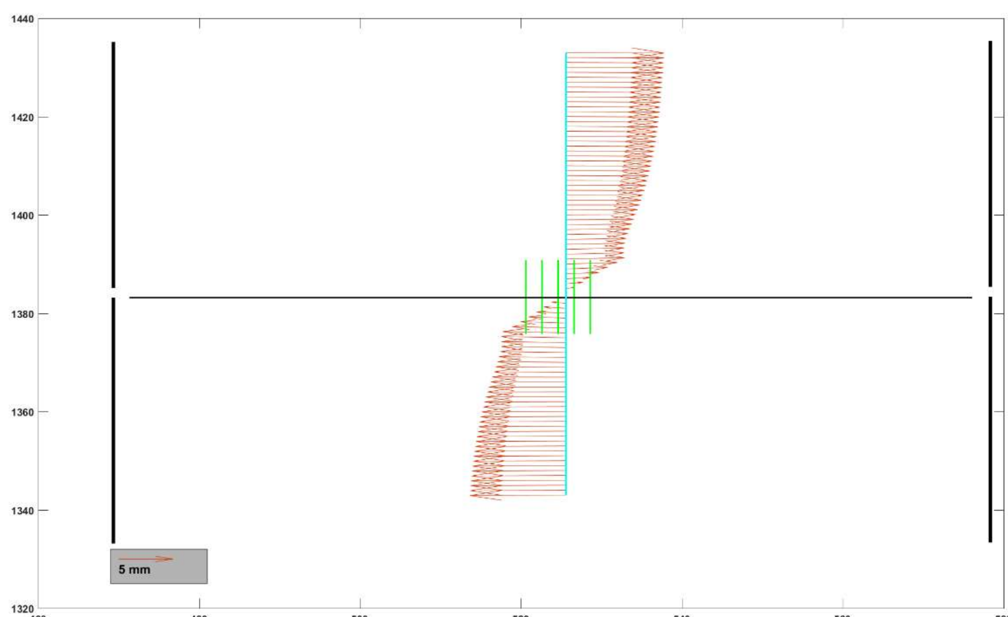

Figure **B-106**: Model F7: surface displacements (red vectors) along-profile line (cyan line). Arc-normal faults' (green lines) length and spacing are 15 km and 2 km respectively. This model has 4 arc-normal faults.

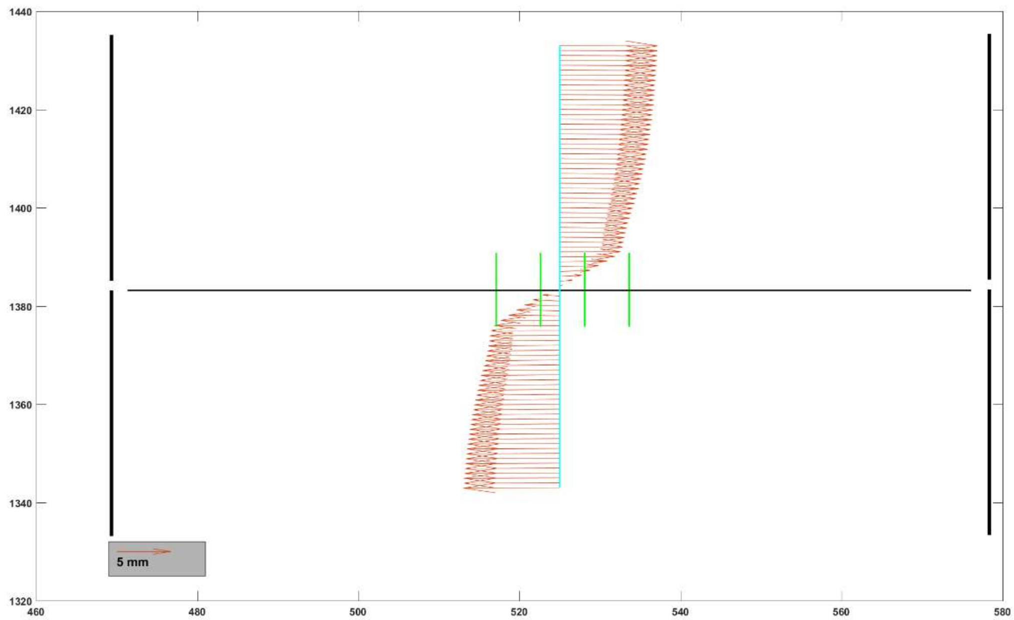

Figure **B-107**: Model F7: surface displacements (red vectors) along-profile line (cyan line). Arc-normal faults' (green lines) length and spacing are 15 km and 5 km respectively. This model has 4 arc-normal faults.

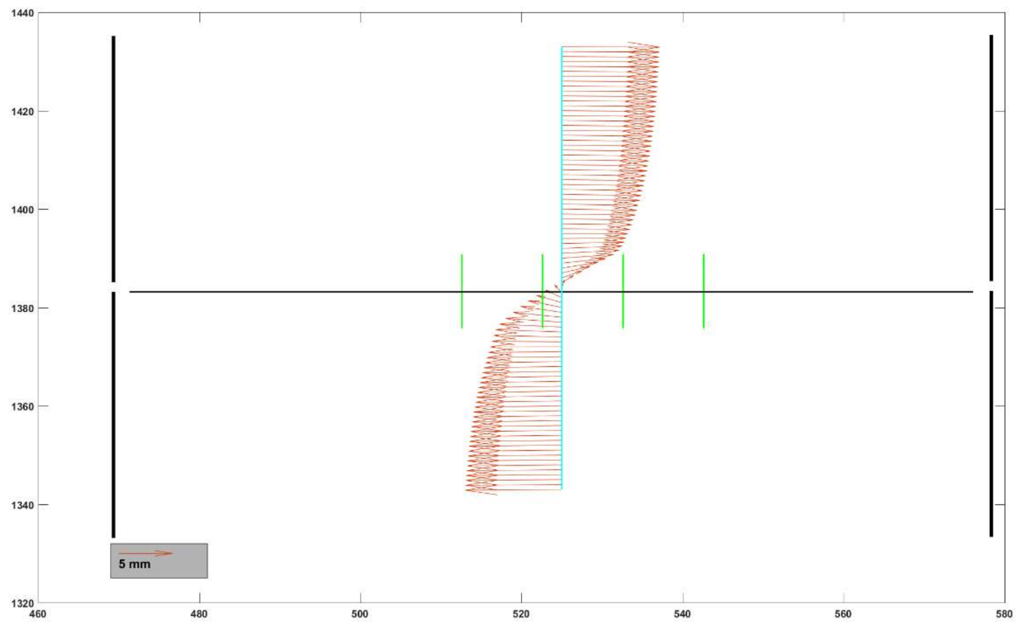

Figure **B-108**: Model F6: surface displacements (red vectors) along-profile line (cyan line). Arc-normal faults' (green lines) length and spacing are 15 km and 10 km respectively. This model has 4 arc-normal faults.

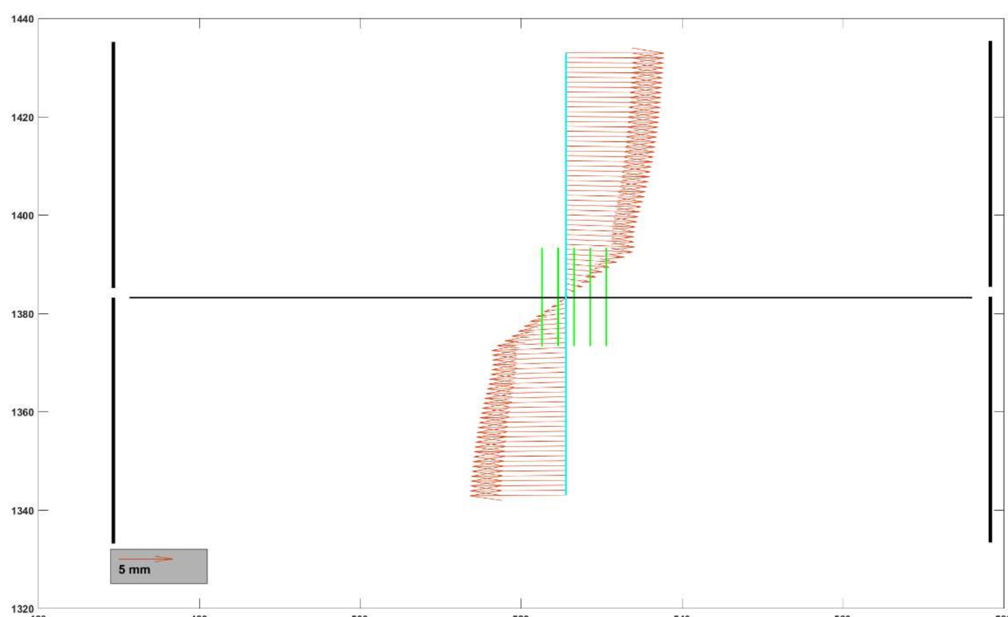

Figure **B-109**: Model F7: surface displacements (red vectors) along-profile line (cyan line). Arc-normal faults' (green lines) length and spacing are 20 km and 2 km respectively. This model has 5 arc-normal faults.

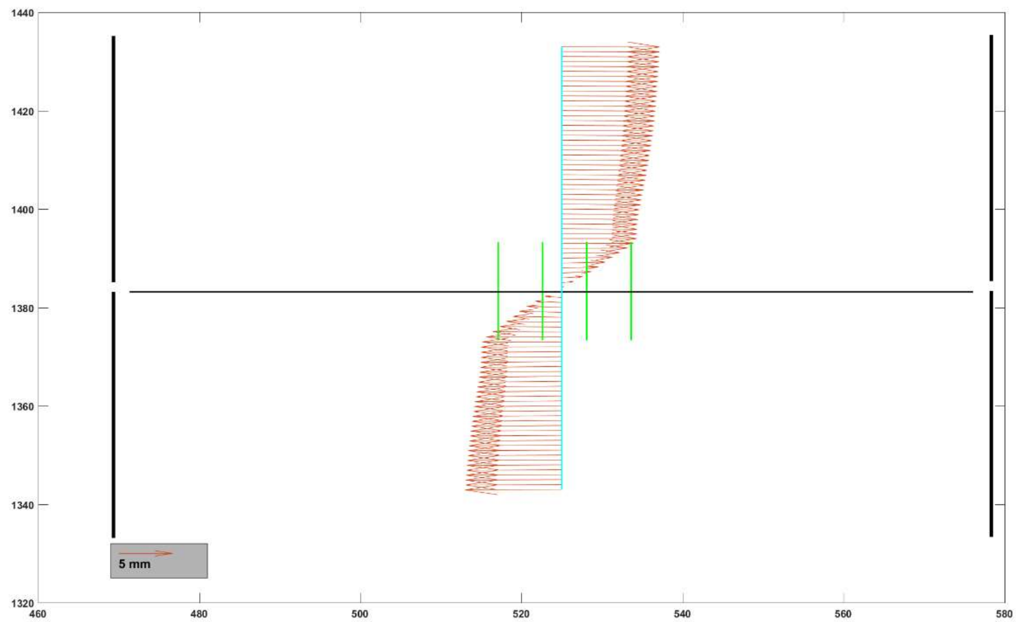

Figure **B-110**: Model F8: surface displacements (red vectors) along-profile line (cyan line). Arc-normal faults' (green lines) length and spacing are 20 km and 5 km respectively. This model has 4 arc-normal faults.

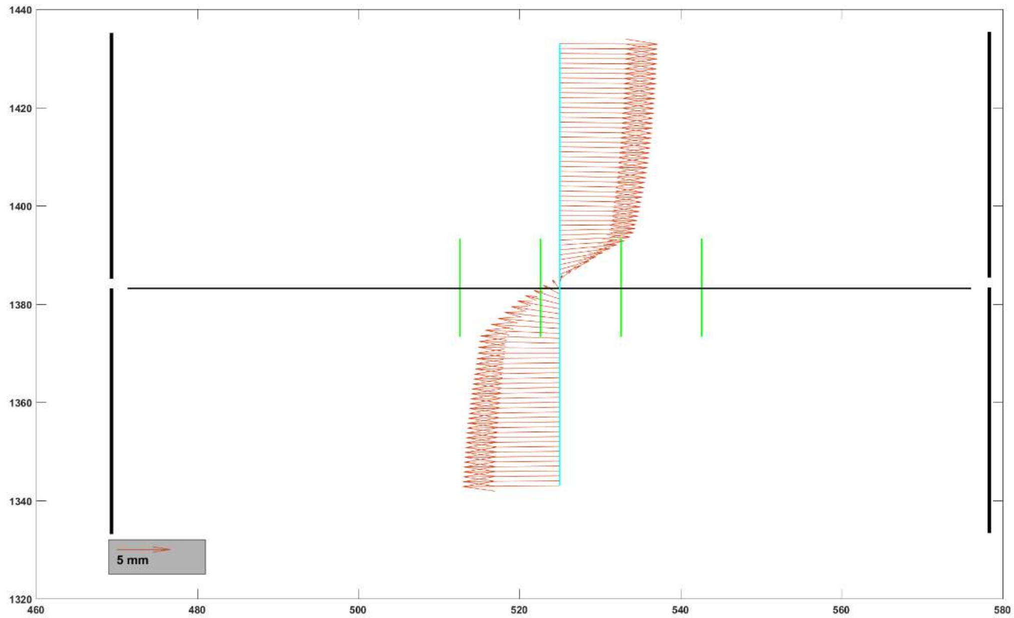

Figure **B-111**: Model F9: surface displacements (red vectors) along-profile line (cyan line). Arc-normal faults' (green lines) length and spacing are 20 km and 10 km respectively. This model has 4 arc-normal faults.

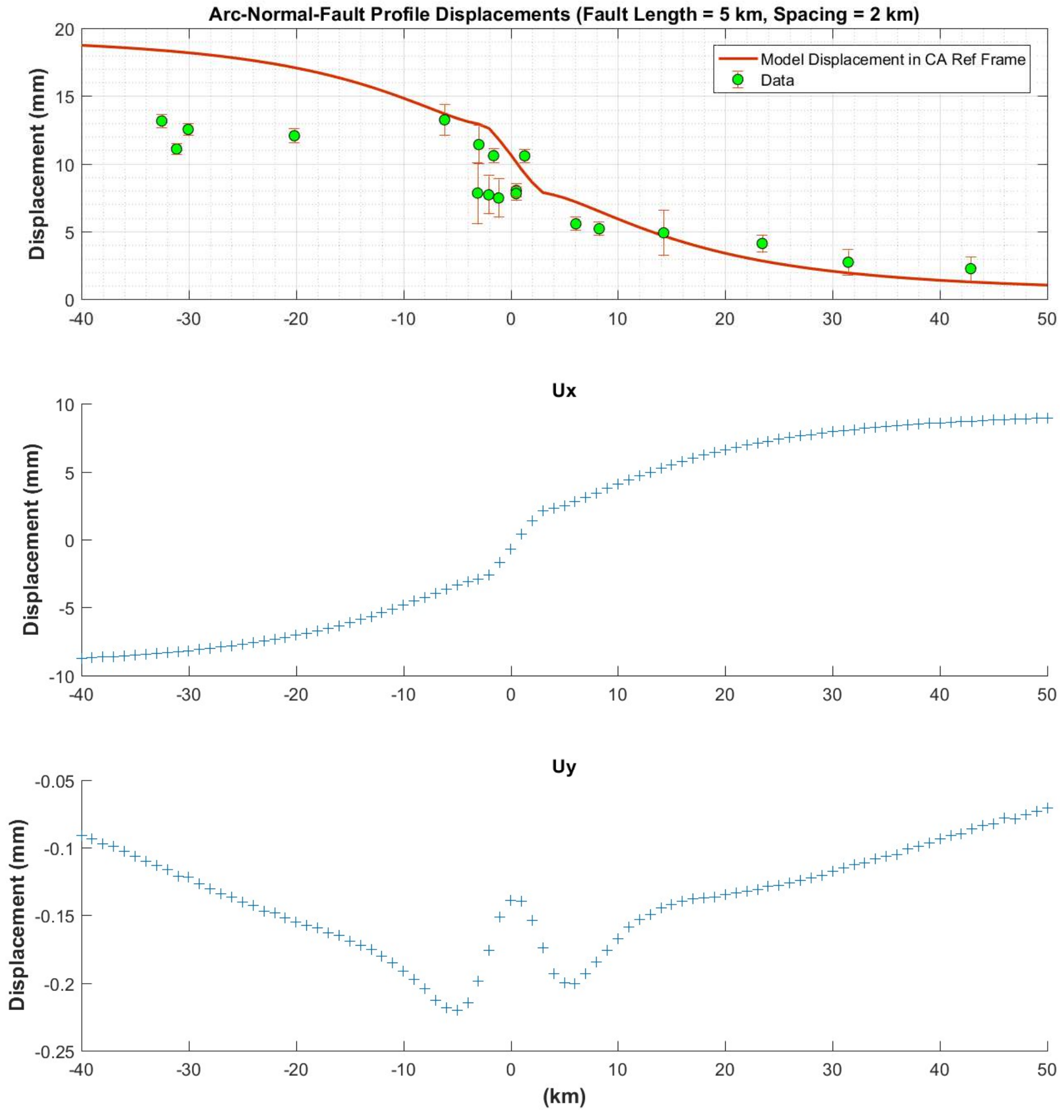

Figure **B-112**: Model F1: displacements along-profile. Arc-normal faults' length and spacing are 5 km and 2 km respectively. Top panel – profile displacements projected into horizontal line (azimuth = 270°). Middle panel – profile displacements in the x-direction. Bottom panel – profile displacements in the y-direction. 'Model Displacement in CA' data sets was created by adding an offset of 7 mm to the model displacements.

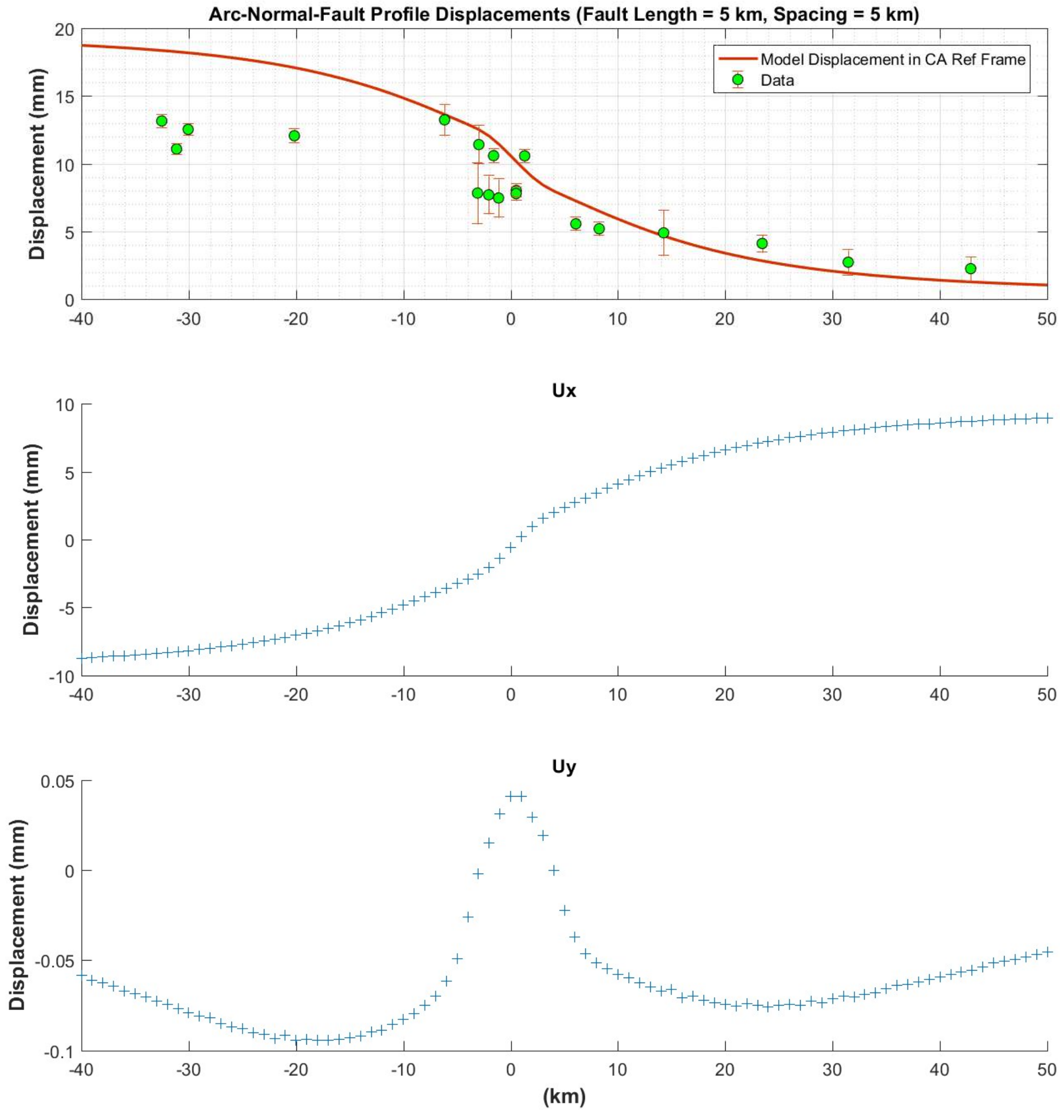

Figure **B-113**: Model F2: displacements along-profile. Arc-normal faults' length and spacing are 5 km and 5 km respectively. Top panel – profile displacements projected into horizontal line (azimuth = 270°). Middle panel – profile displacements in the x-direction. Bottom panel – profile displacements in the y-direction. 'Model Displacement in CA' data sets was created by adding an offset of 7 mm to the model displacements.

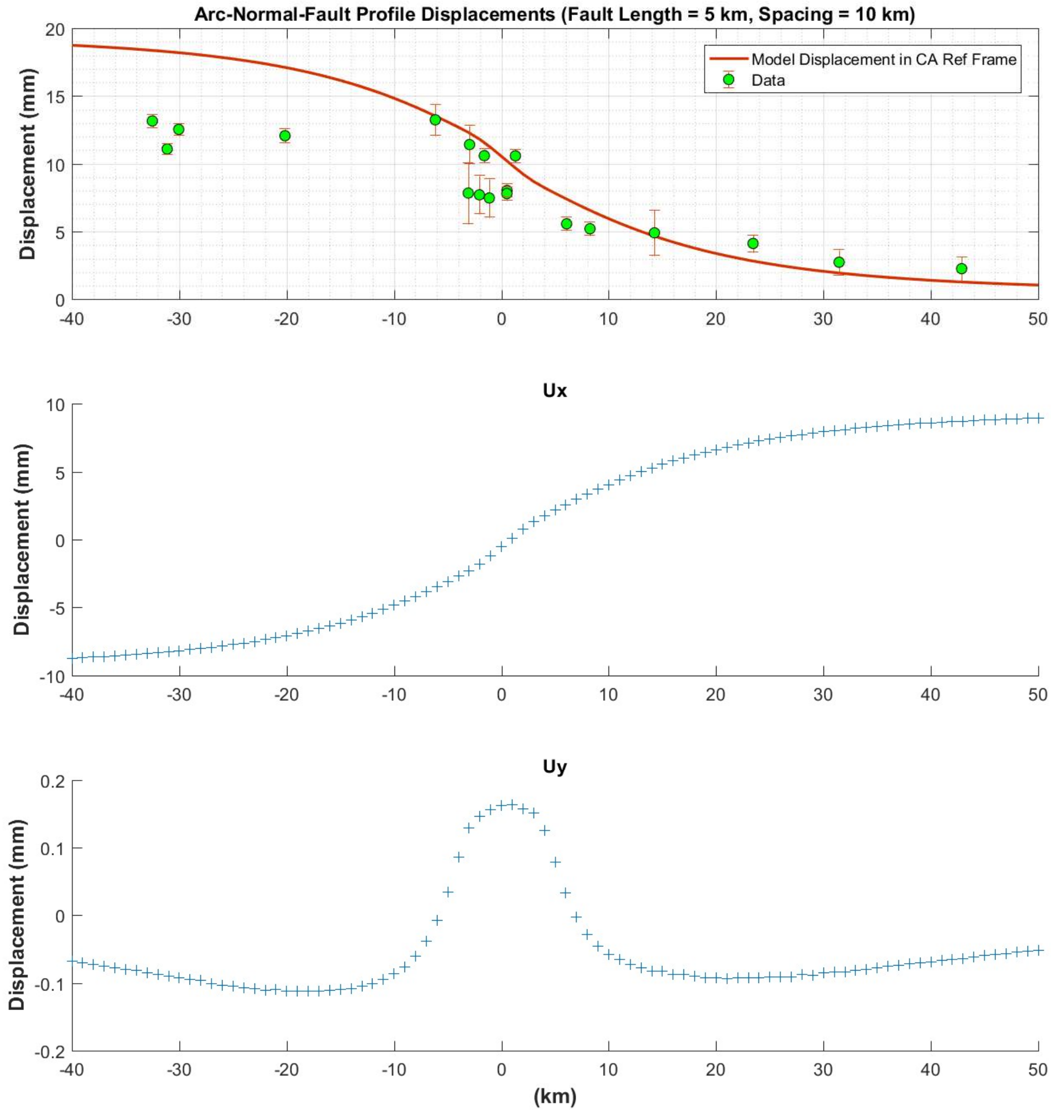

Figure **B-114**: Model F3: displacements along-profile. Arc-normal faults' length and spacing are 5 km and 10 km respectively. Top panel – profile displacements projected into horizontal line (azimuth = 270°). Middle panel – profile displacements in the x-direction. Bottom panel – profile displacements in the y-direction. 'Model Displacement in CA' data sets was created by adding an offset of 7 mm to the model displacements.

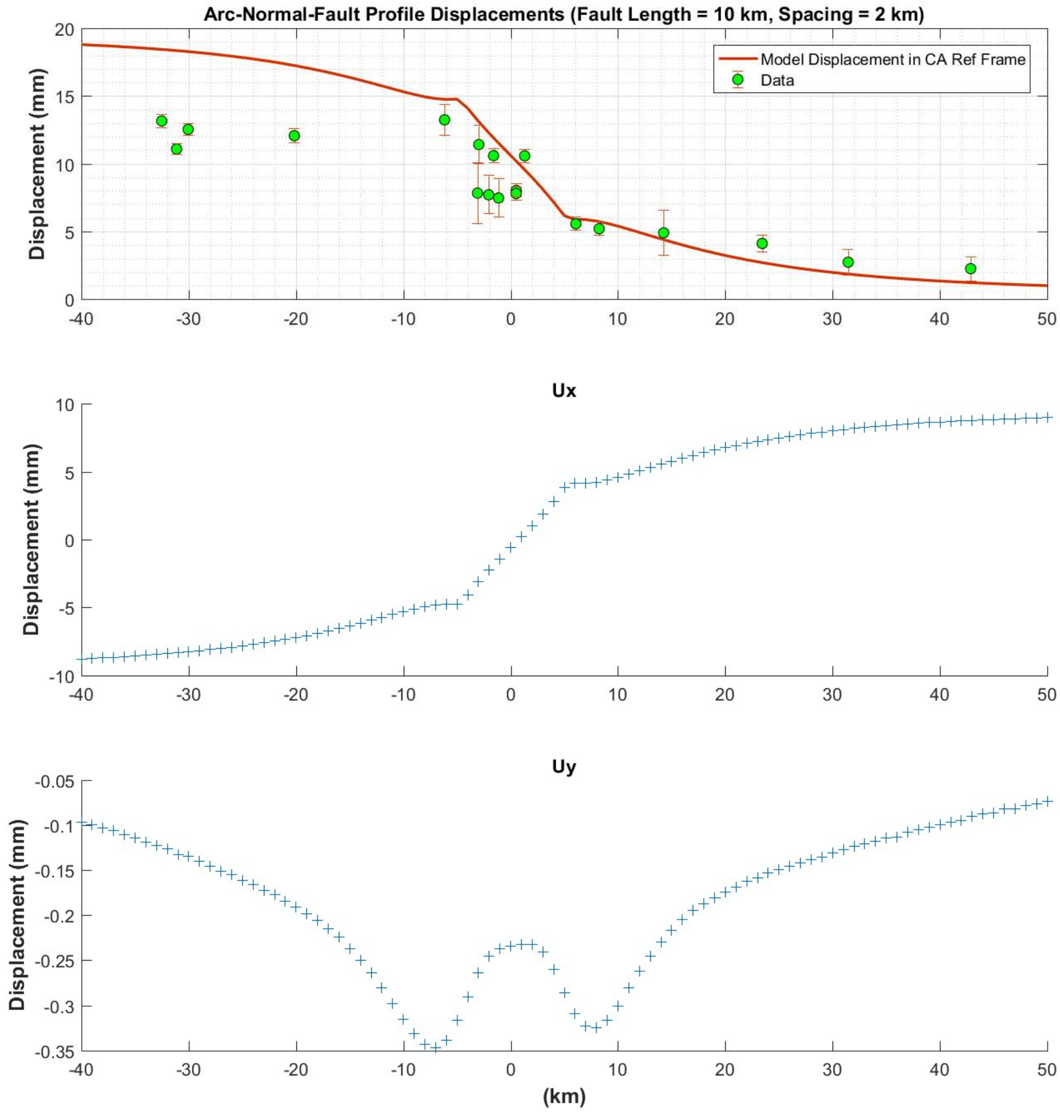

Figure **B-115**: Model F4: displacements along-profile. Arc-normal faults' length and spacing are 10 km and 2 km respectively. Top panel – profile displacements projected into horizontal line (azimuth = 270°). Middle panel – profile displacements in the x-direction. Bottom panel – profile displacements in the y-direction. 'Model Displacement in CA' data sets was created by adding an offset of 7 mm to the model displacements.

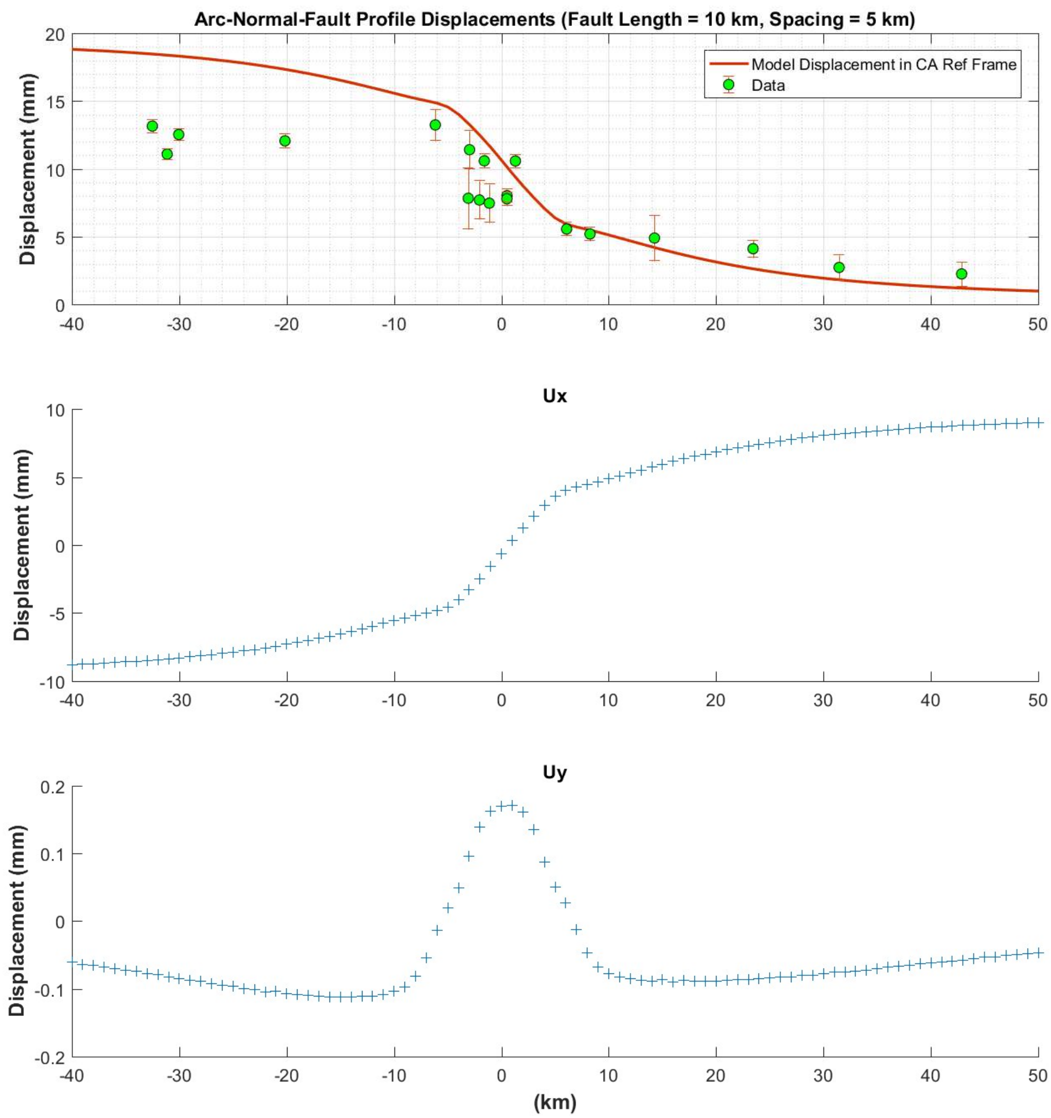

Figure **B-116**: Model F5: displacements along-profile. Arc-normal faults' length and spacing are 10 km and 5 km respectively. Top panel – profile displacements projected into horizontal line (azimuth = 270°). Middle panel – profile displacements in the x-direction. Bottom panel – profile displacements in the y-direction. 'Model Displacement in CA' data sets was created by adding an offset of 7 mm to the model displacements.

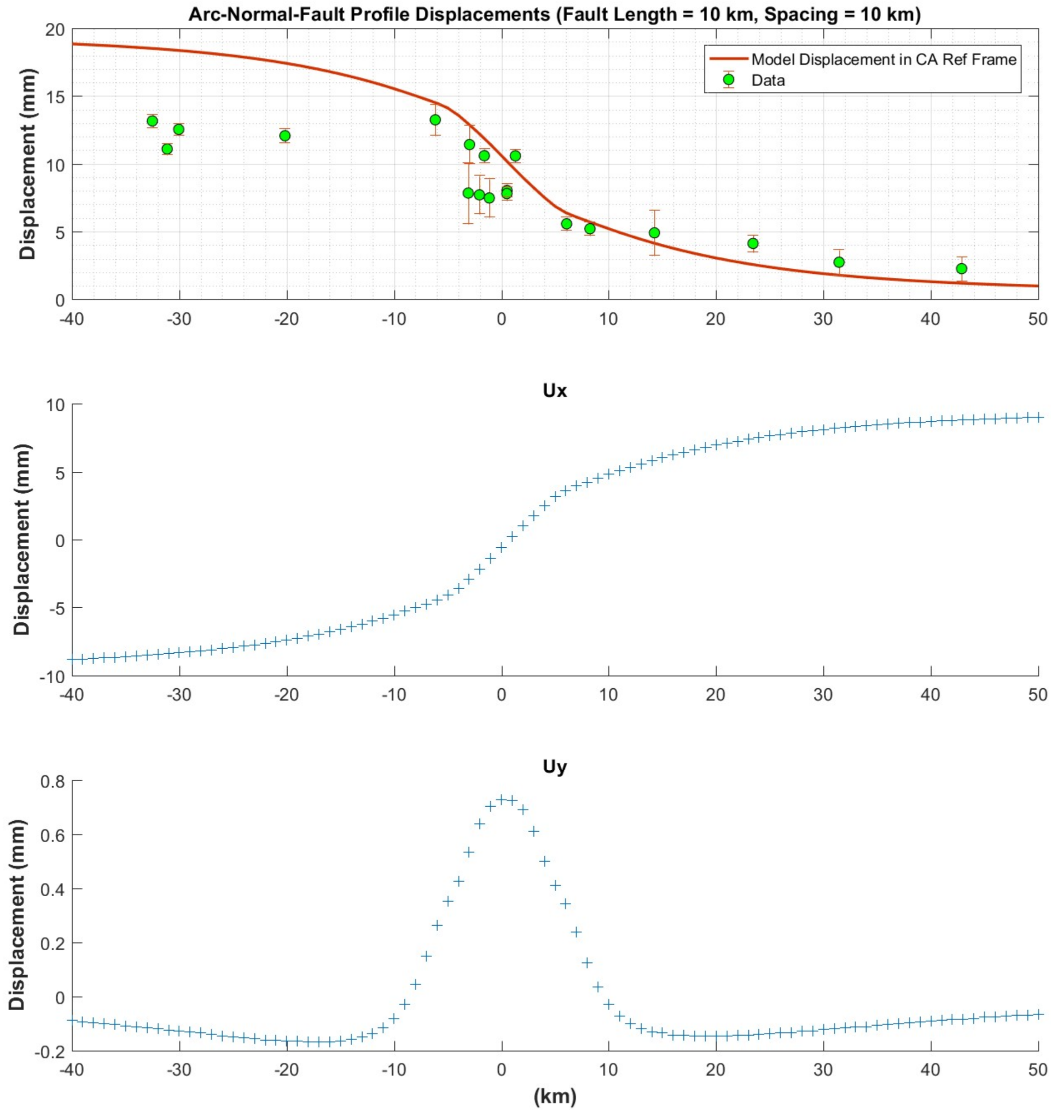

Figure **B-117**: Model F6: displacements along-profile. Arc-normal faults' length and spacing are 10 km and 10 km respectively. Top panel – profile displacements projected into horizontal line (azimuth = 270°). Middle panel – profile displacements in the x-direction. Bottom panel – profile displacements in the y-direction. 'Model Displacement in CA' data sets was created by adding an offset of 7 mm to the model displacements.

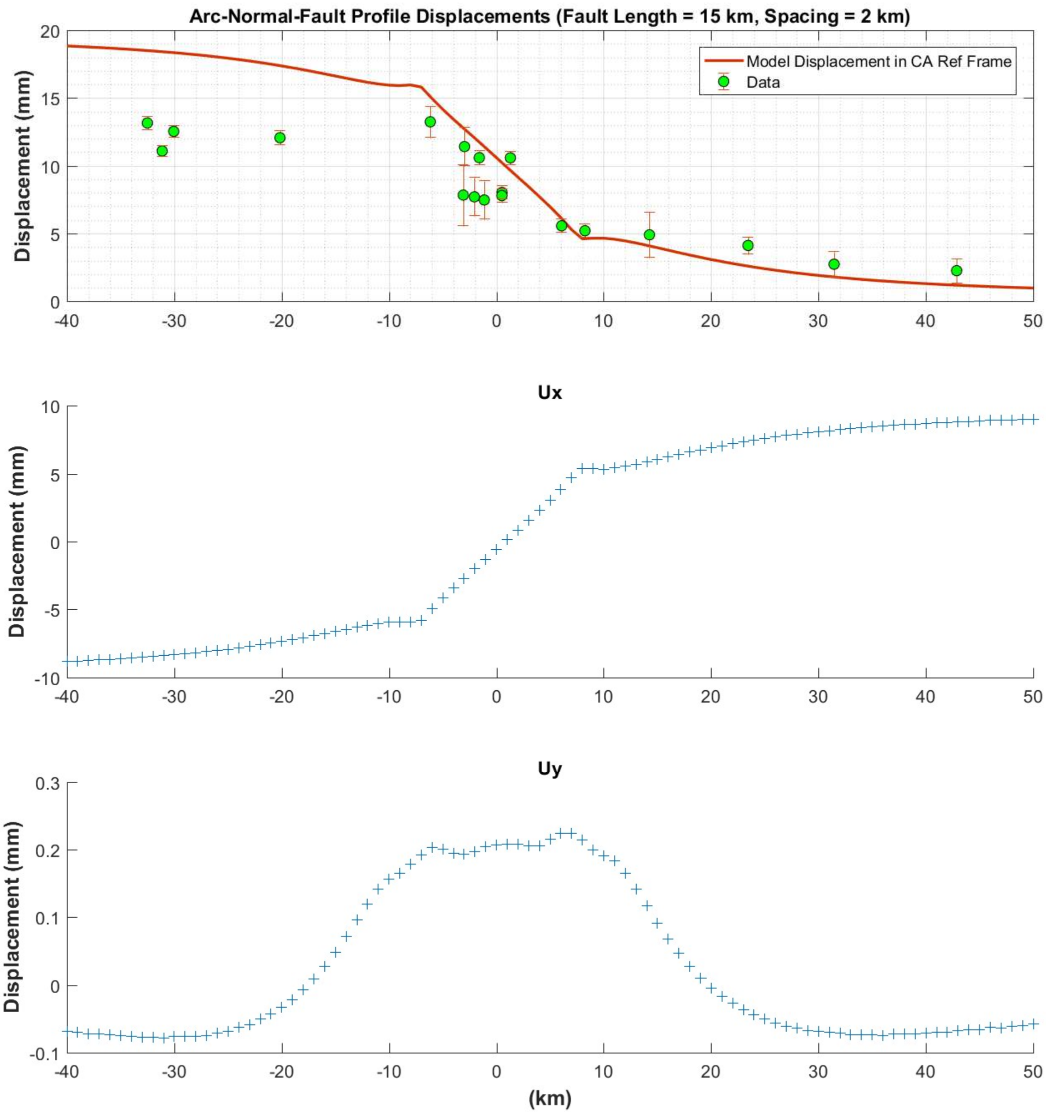

Figure **B-118**: Model F7: displacements along-profile. Arc-normal faults' length and spacing are 15 km and 2 km respectively. Top panel – profile displacements projected into horizontal line (azimuth = 270°). Middle panel – profile displacements in the x-direction. Bottom panel – profile displacements in the y-direction. 'Model Displacement in CA' data sets was created by adding an offset of 7 mm to the model displacements.

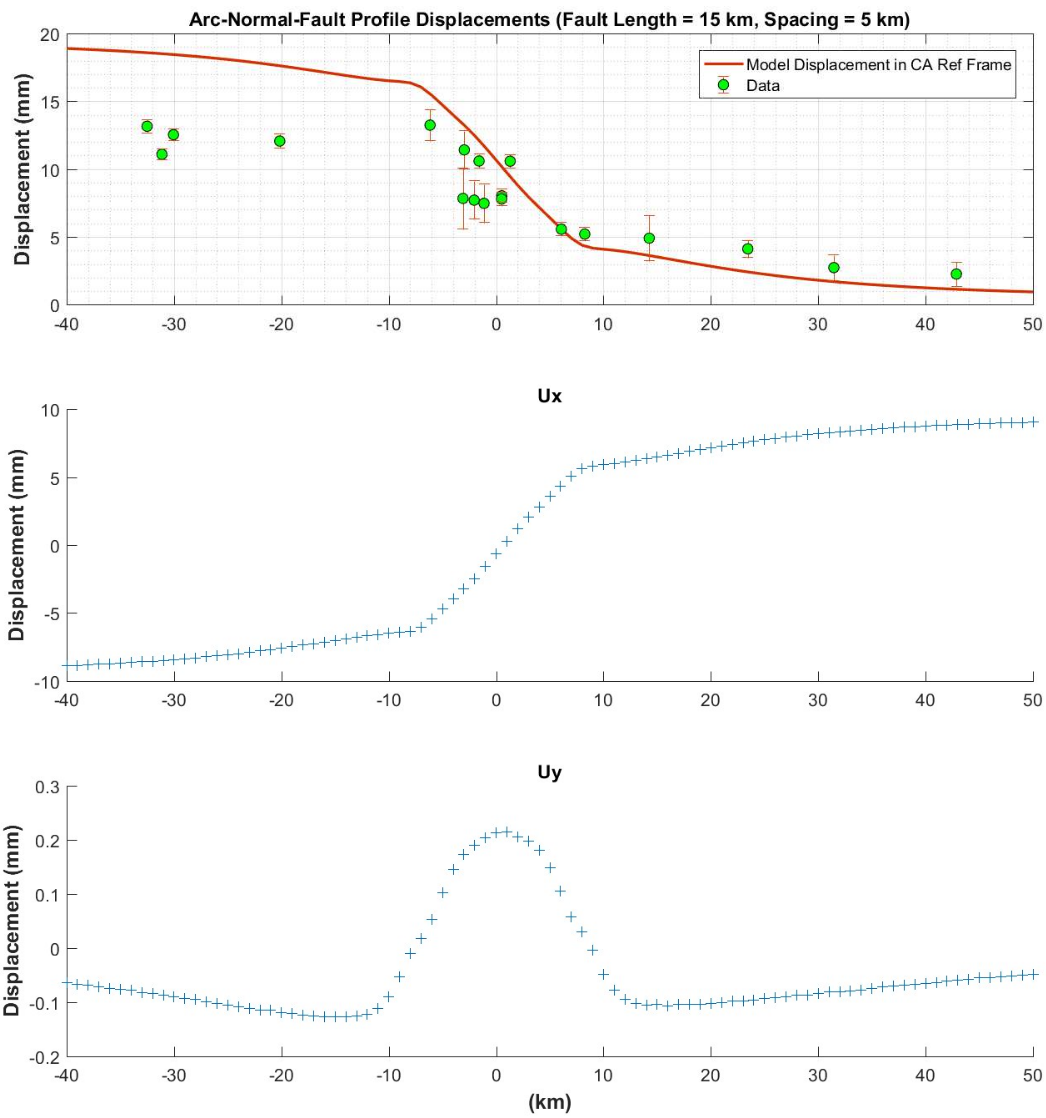

Figure **B-119**: Model F8: displacements along-profile. Arc-normal faults' length and spacing are 15 km and 5 km respectively. Top panel – profile displacements projected into horizontal line (azimuth = 270°). Middle panel – profile displacements in the x-direction. Bottom panel – profile displacements in the y-direction. 'Model Displacement in CA' data sets was created by adding an offset of 7 mm to the model displacements.

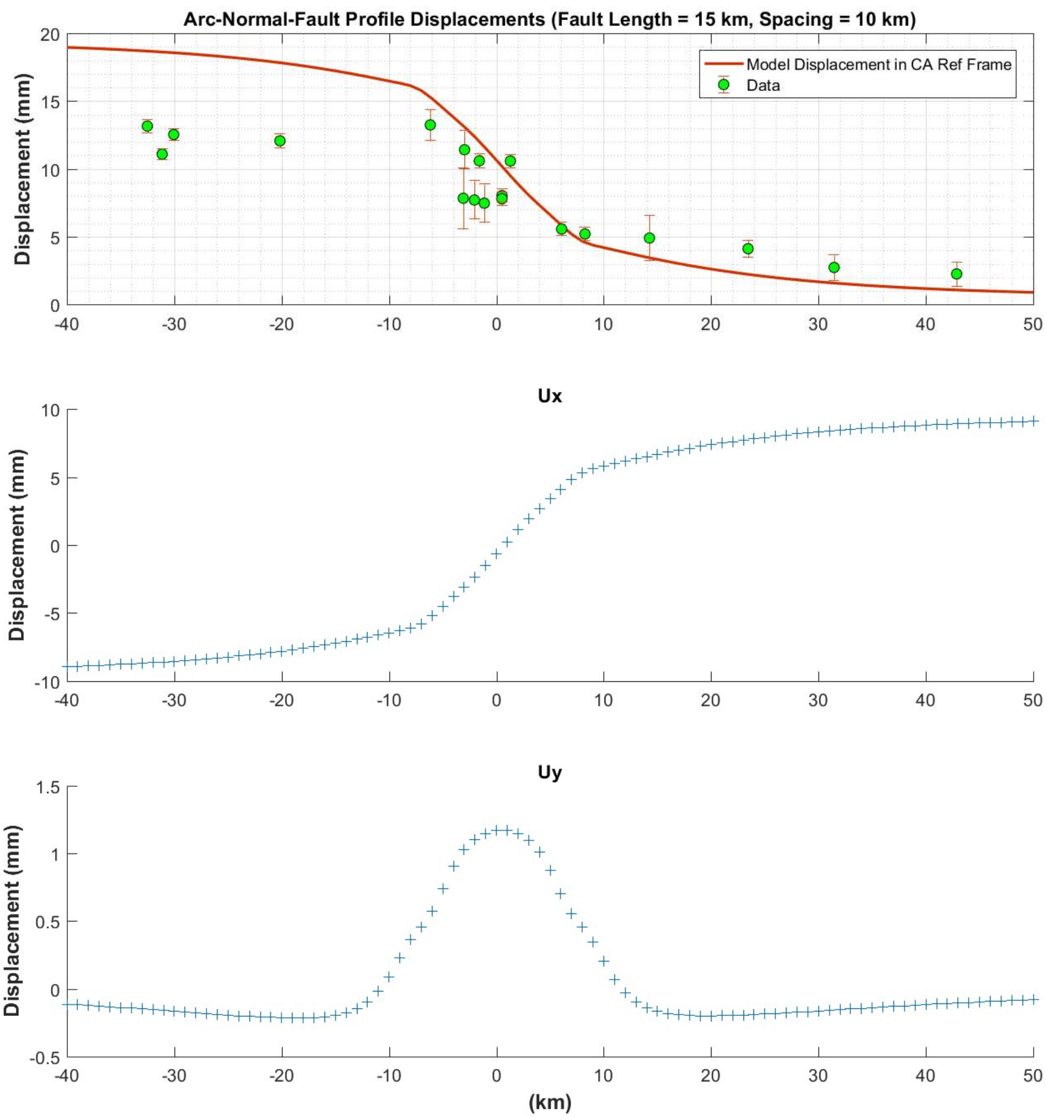

Figure **B-120**: Model F9: displacements along-profile. Arc-normal faults' length and spacing are 15 km and 10 km respectively. Top panel – profile displacements projected into horizontal line (azimuth = 270°). Middle panel – profile displacements in the x-direction. Bottom panel – profile displacements in the y-direction. 'Model Displacement in CA' data sets was created by adding an offset of 7 mm to the model displacements.

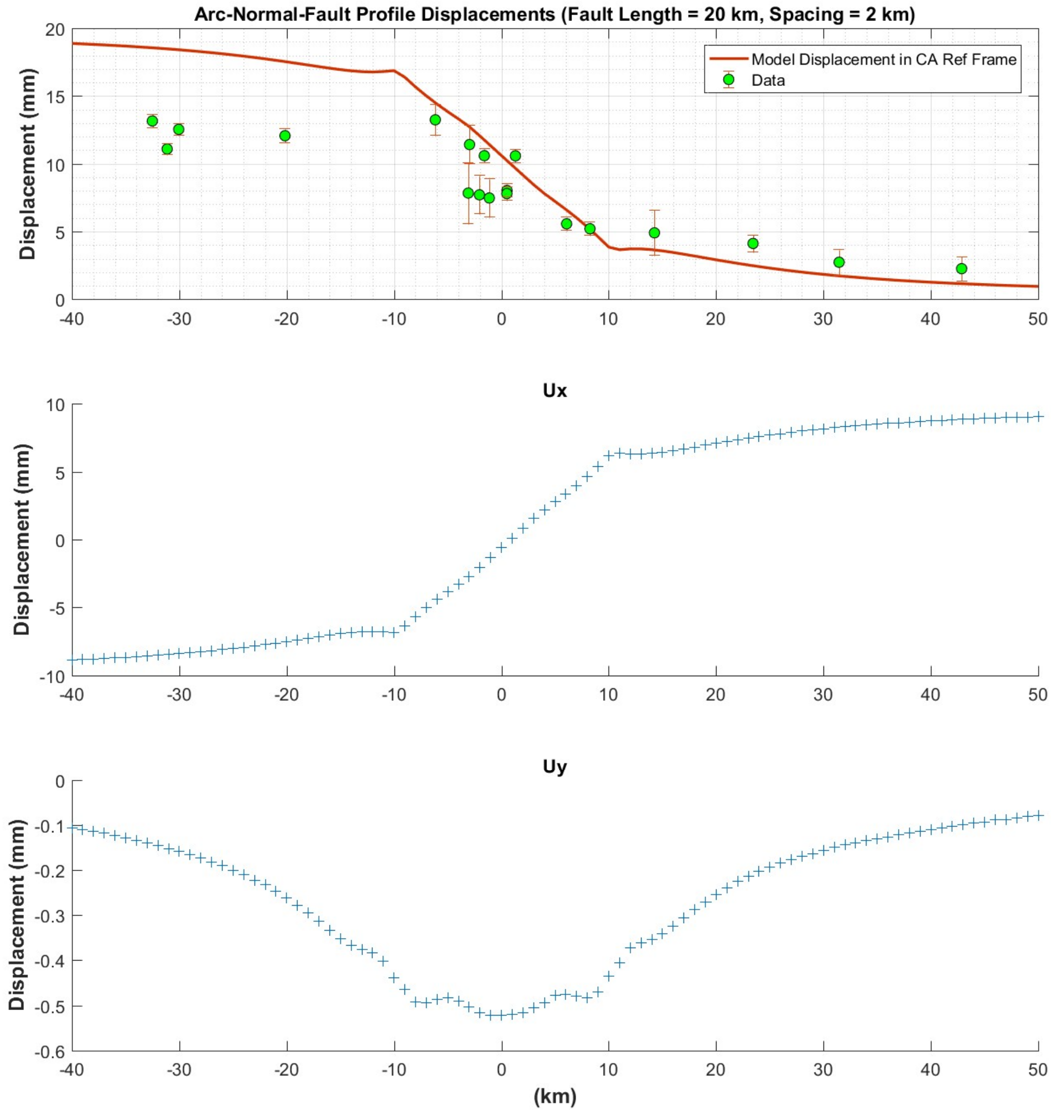

Figure **B-121**: Model F10: displacements along-profile. Arc-normal faults' length and spacing are 20 km and 2 km respectively. Top panel – profile displacements projected into horizontal line (azimuth = 270°). Middle panel – profile displacements in the x-direction. Bottom panel – profile displacements in the y-direction. 'Model Displacement in CA' data sets was created by adding an offset of 7 mm to the model displacements.

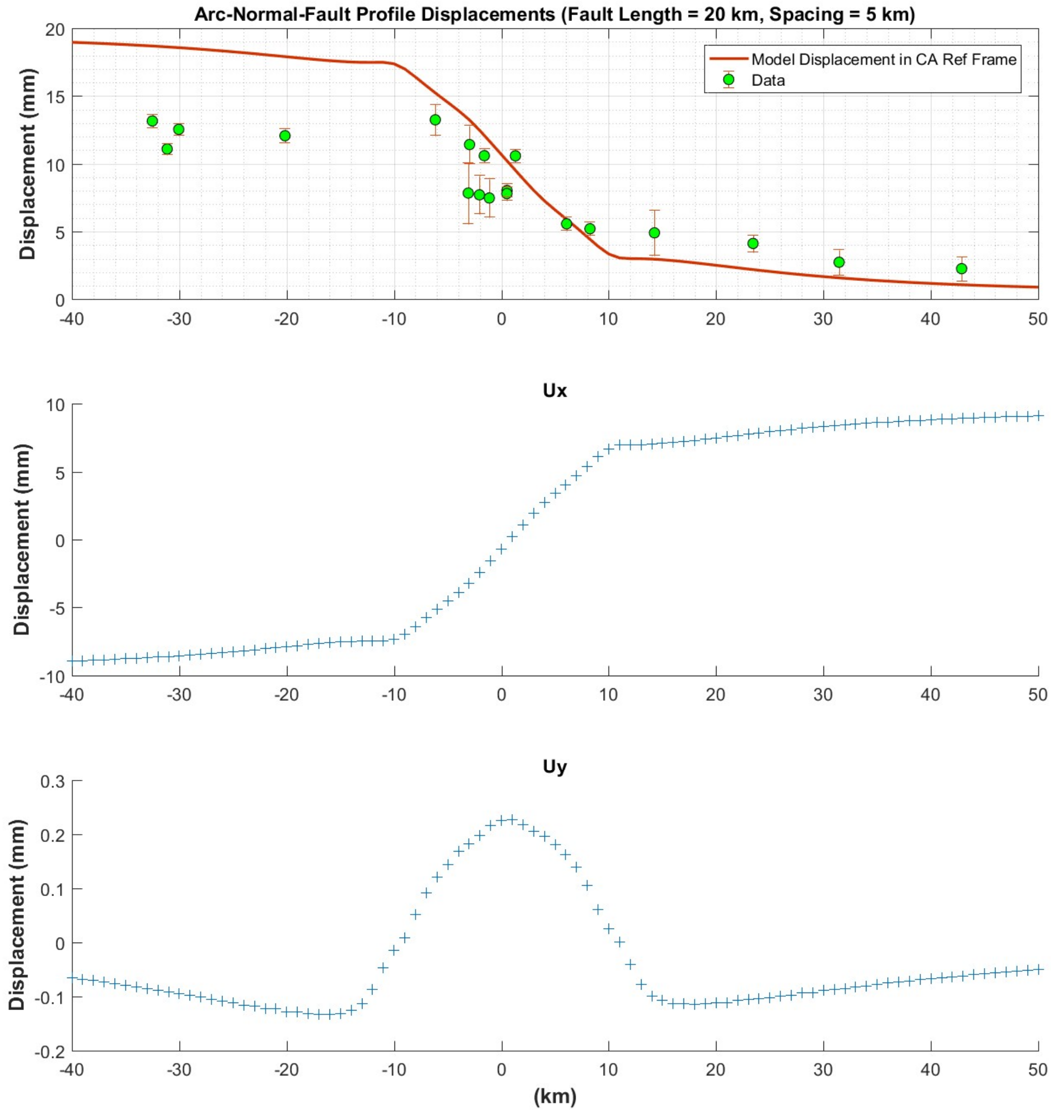

Figure **B-122**: Model F11: displacements along-profile. Arc-normal faults' length and spacing are 20 km and 5 km respectively. Top panel – profile displacements projected into horizontal line (azimuth = 270°). Middle panel – profile displacements in the x-direction. Bottom panel – profile displacements in the y-direction. 'Model Displacement in CA' data sets was created by adding an offset of 7 mm to the model displacements.

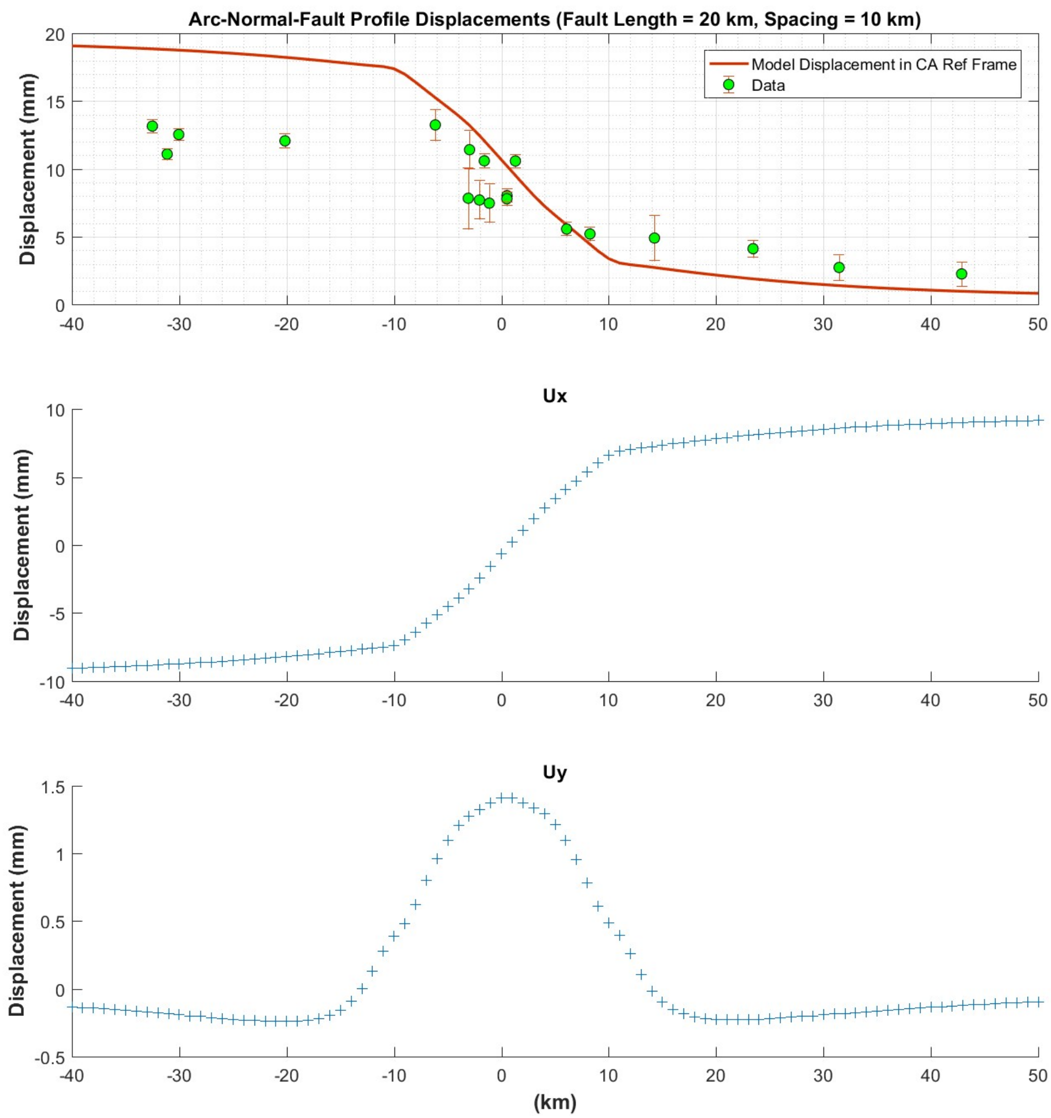

Figure **B-123**: Model F12: displacements along-profile. Arc-normal faults' length and spacing are 20 km and 10 km respectively. Top panel – profile displacements projected into horizontal line (azimuth = 270°). Middle panel – profile displacements in the x-direction. Bottom panel – profile displacements in the y-direction. 'Model Displacement in CA' data sets was created by adding an offset of 7 mm to the model displacements.

B.3 Model Set G Plots

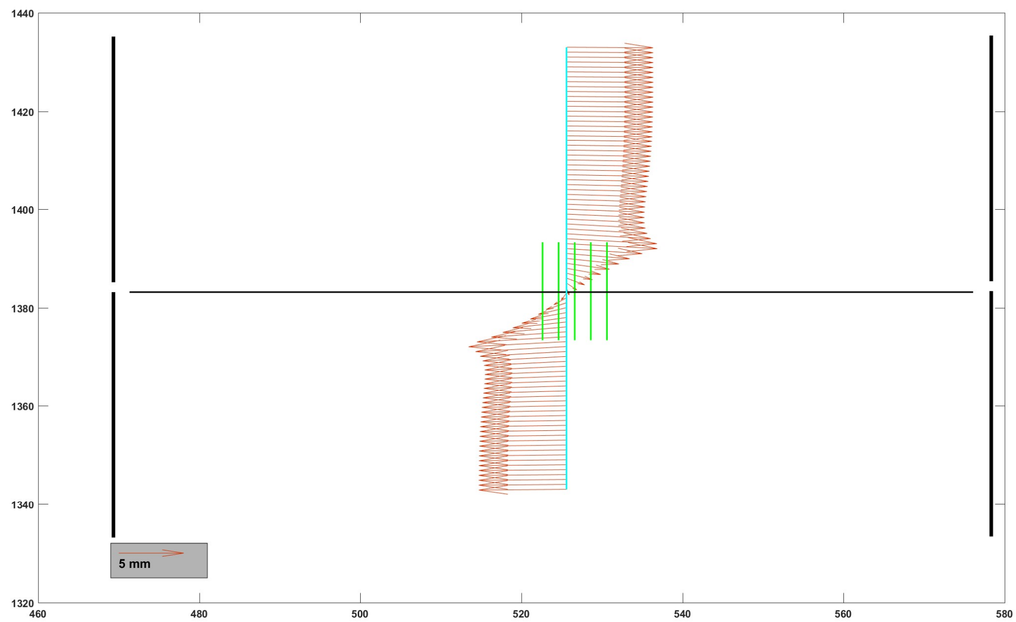

Figure **B-124**: Model G1: surface displacements (red vectors) along-profile line (cyan line). Arc-normal faults' (green lines) length and spacing are 20 km and 2 km respectively and had 1.4 mm of slip imposed on them. This model has 5 arc-normal faults.

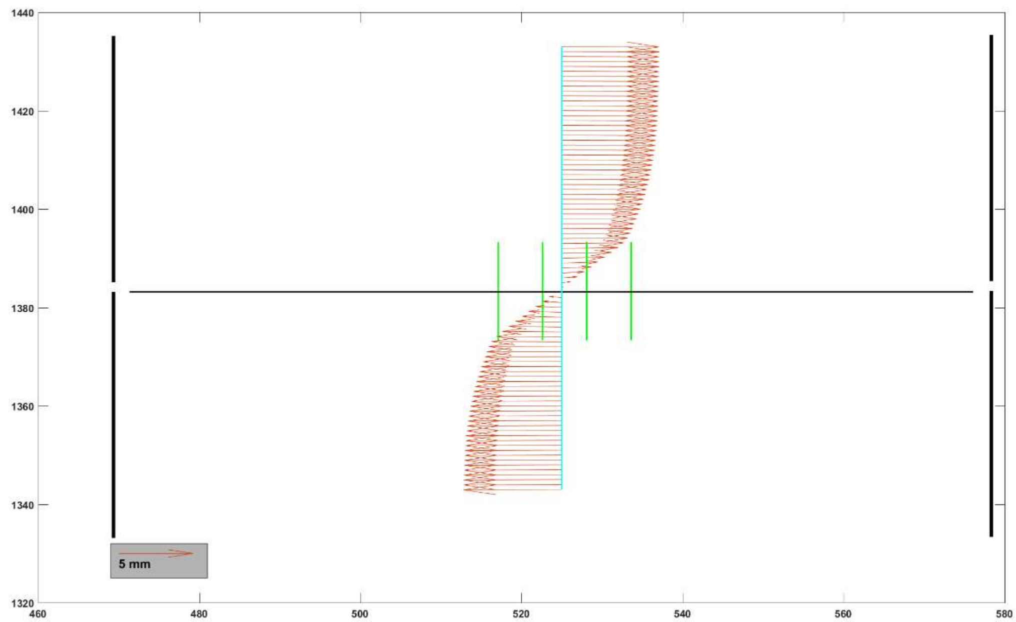

Figure **B-125**: Model G2: surface displacements (red vectors) along-profile line (cyan line). Arc-normal faults' (green lines) length and spacing are 20 km and 5 km respectively and had 3.8 mm of slip imposed on them. This model has 4 arc-normal faults.

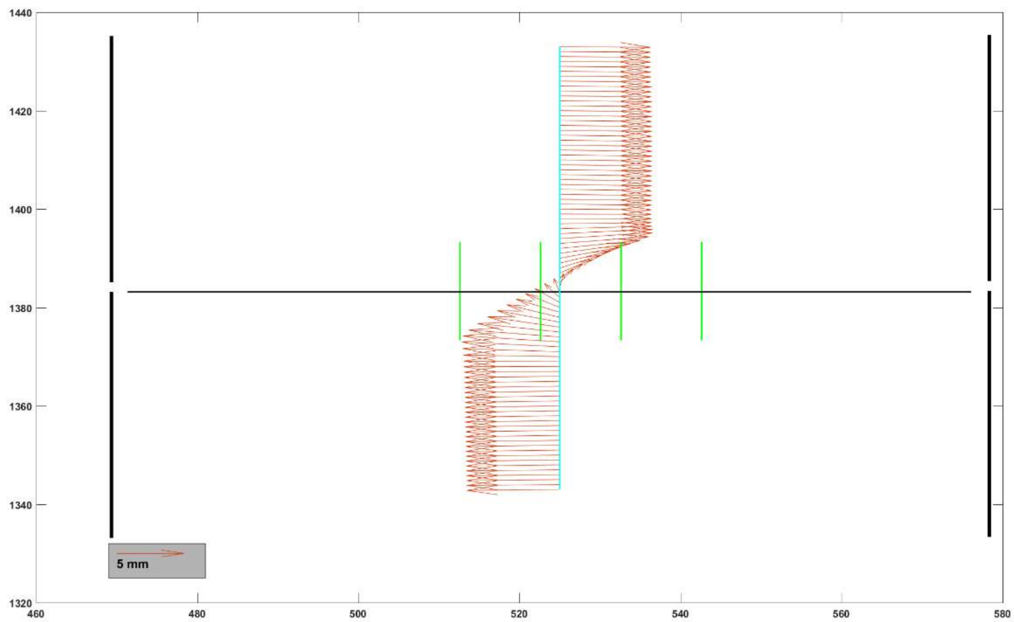

Figure **B-126**: Model G3: surface displacements (red vectors) along-profile line (cyan line). Arc-normal faults' (green lines) length and spacing are 20 km and 10 km respectively and had 7 mm of slip imposed on them. This model has 4 arc-normal faults.

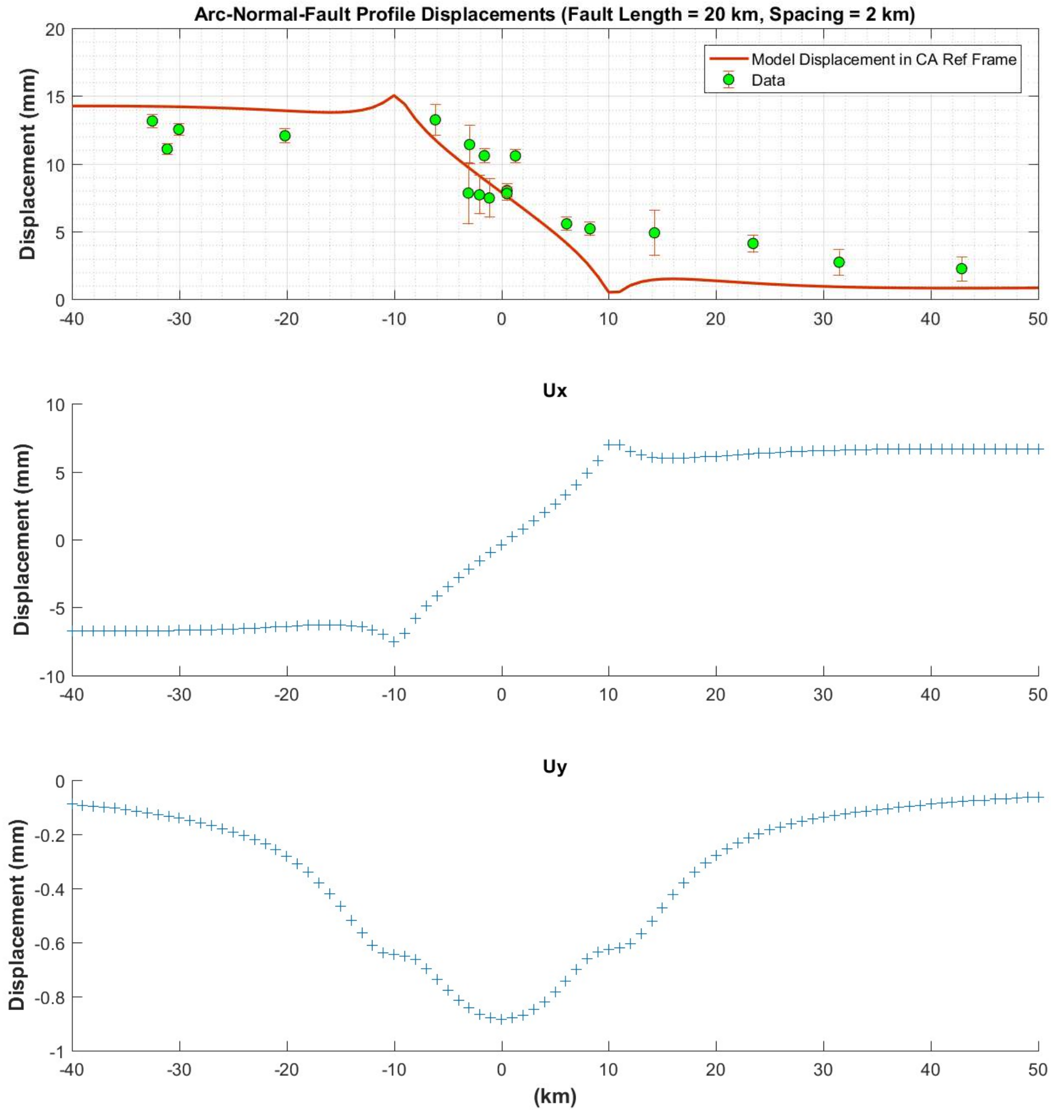

Figure **B-127**: Model G1: displacements along-profile. Arc-normal faults' length and spacing are 20 km and 2 km respectively and had 1.4 mm of slip imposed on them. Top panel – profile displacements projected into horizontal line (azimuth = 270°). Middle panel – profile displacements in the x-direction. Bottom panel – profile displacements in the y-direction. 'Model Displacement in CA' data sets was created by adding an offset of 7 mm to the model displacements.

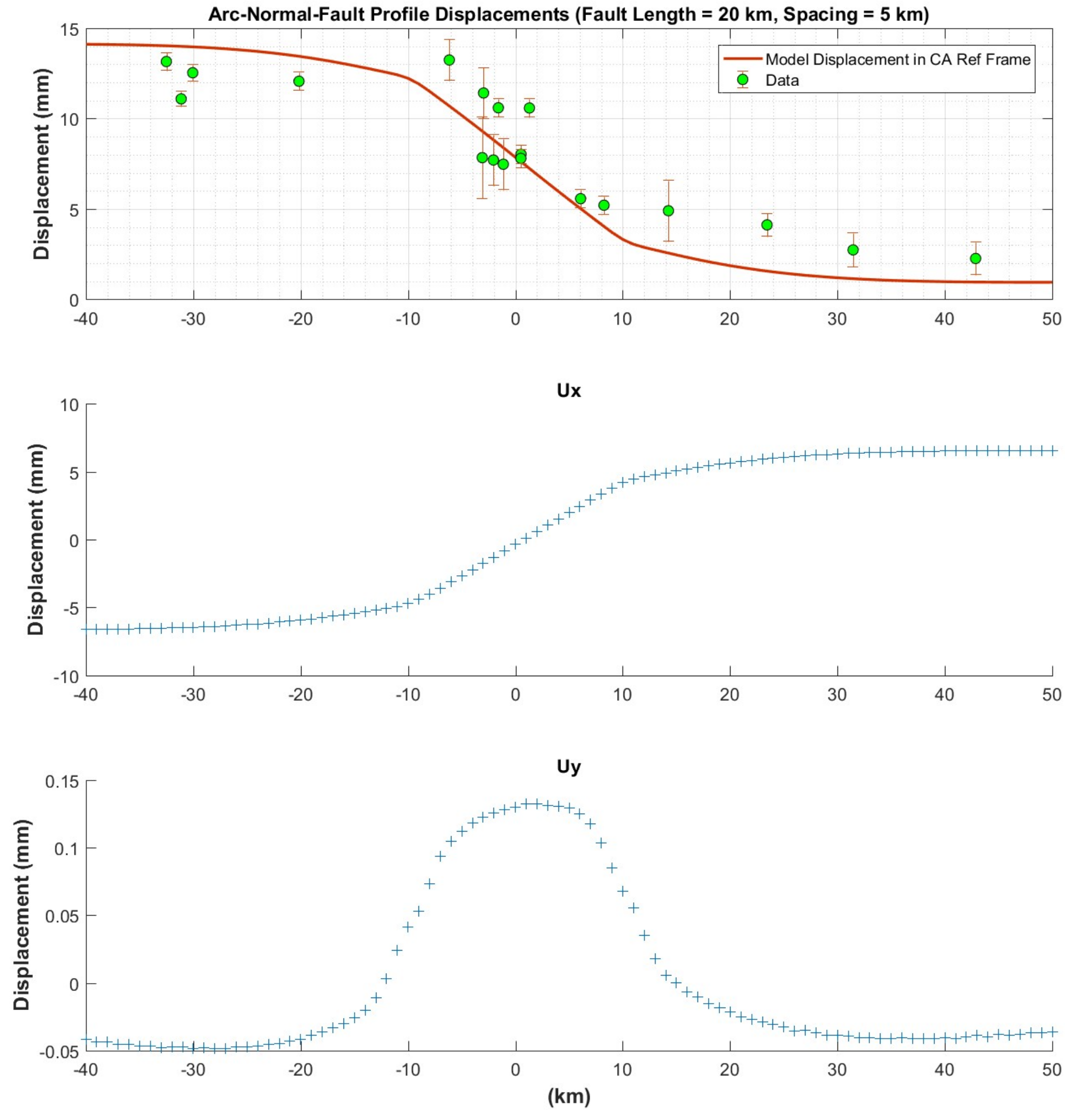

Figure **B-128**: Model G2: displacements along-profile. Arc-normal faults' length and spacing are 20 km and 5 km respectively and had 3.8 mm of slip imposed on them. Top panel – profile displacements projected into horizontal line (azimuth = 270°). Middle panel – profile displacements in the x-direction. Bottom panel – profile displacements in the y-direction. 'Model Displacement in CA' data sets was created by adding an offset of 7 mm to the model displacements.

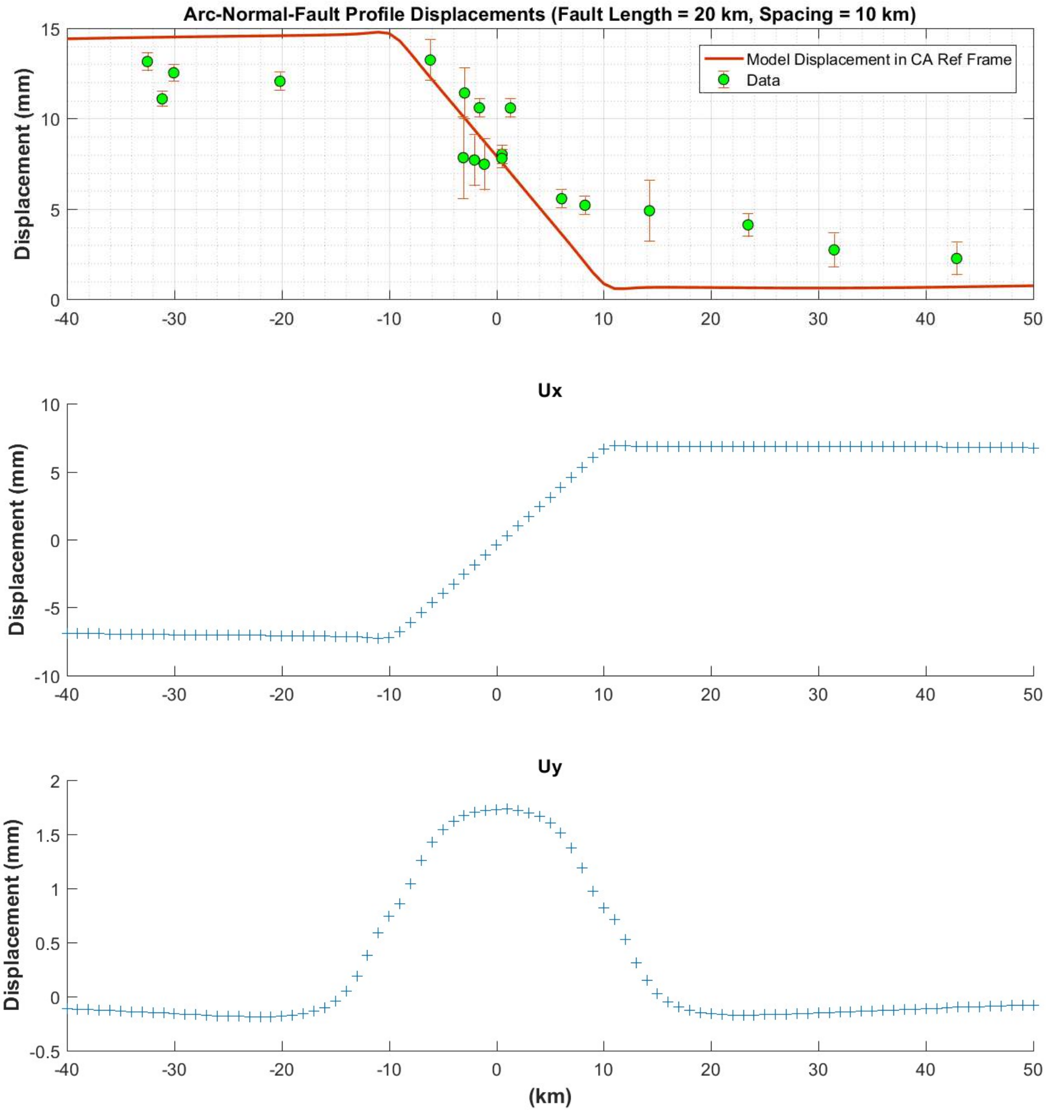

Figure **B-129**: Model G3: displacements along-profile. Arc-normal faults' length and spacing are 20 km and 10 km respectively and had 7 mm of slip imposed on them. Top panel – profile displacements projected into horizontal line (azimuth = 270°). Middle panel – profile displacements in the x-direction. Bottom panel – profile displacements in the y-direction. 'Model Displacement in CA' data sets was created by adding an offset of 7 mm to the model displacements.

B.4 Model Set H Plots

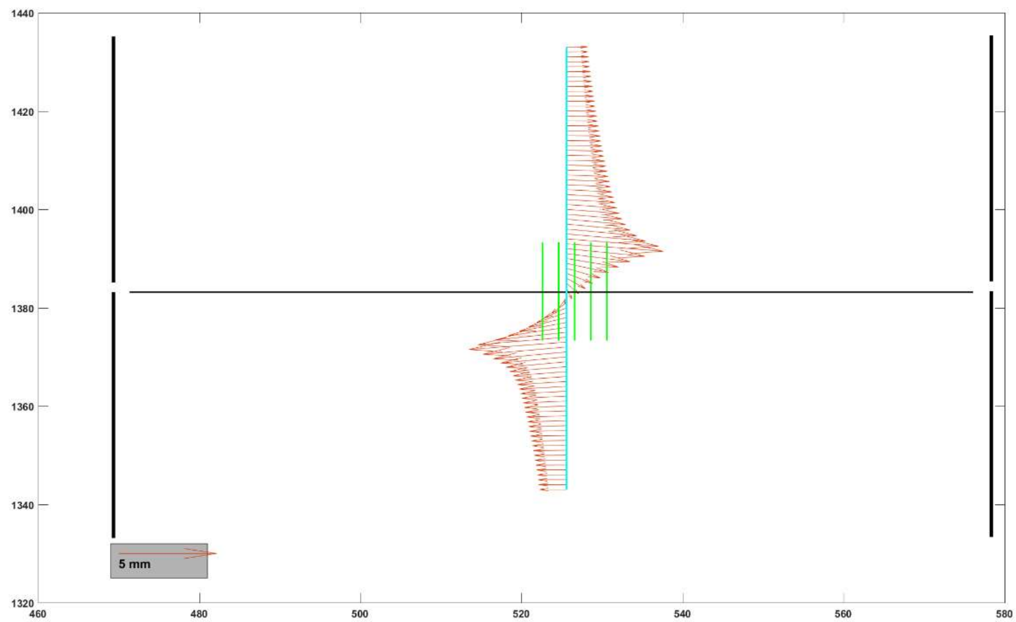

Figure **B-130**: Model H1: surface displacements (red vectors) along-profile line (cyan line). Arc-normal faults' (green lines) length and spacing are 20 km and 2 km respectively. This model has 5 arc-normal faults.

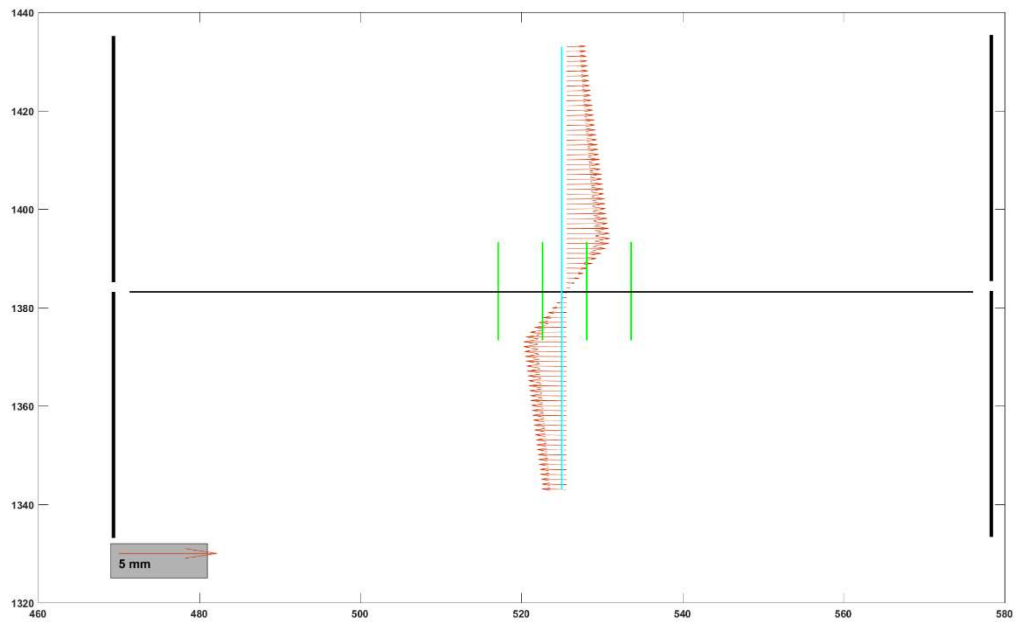

Figure **B-131**: Model H2: surface displacements (red vectors) along-profile line (cyan line). Arc-normal faults' (green lines) length and spacing are 20 km and 5 km respectively. This model has 4 arc-normal faults.

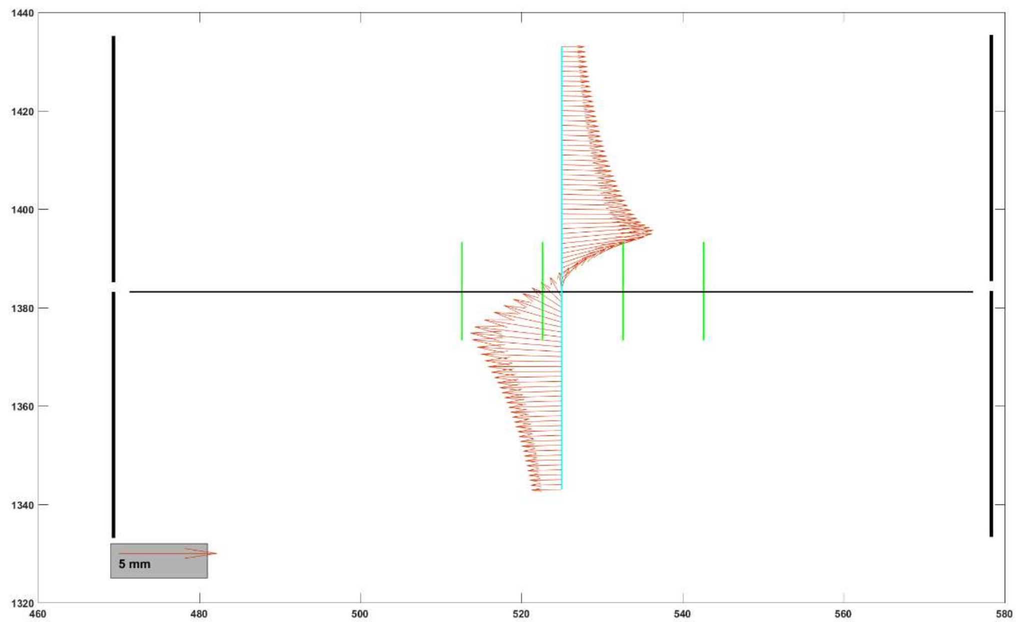

Figure **B-132**: Model H3: surface displacements (red vectors) along-profile line (cyan line). Arc-normal faults' (green lines) length and spacing are 20 km and 10 km respectively. This model has 4 arc-normal faults.

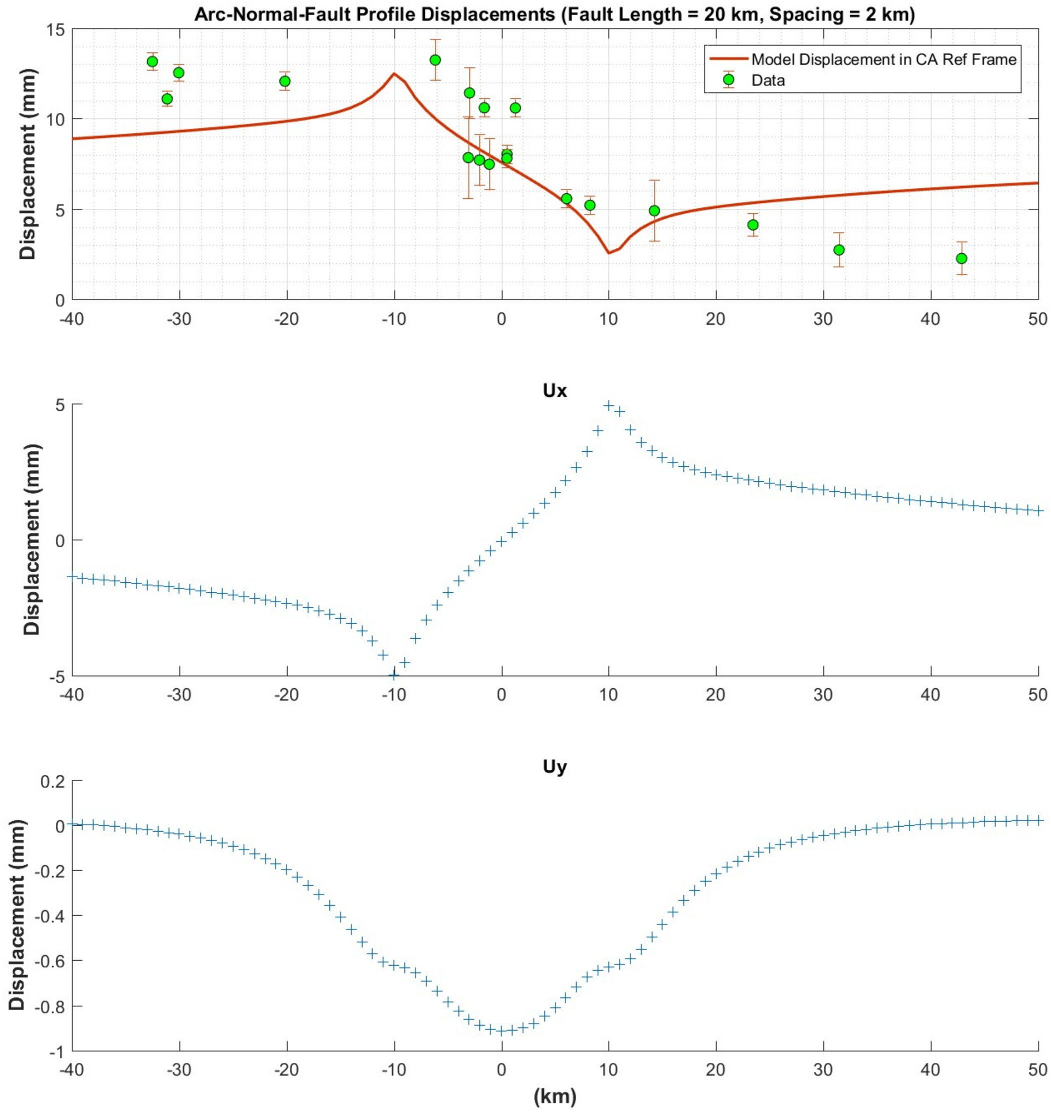

Figure **B-133**: Model H1: displacements along-profile. Arc-normal faults' length and spacing are 20 km and 2 km respectively. Top panel – profile displacements projected into horizontal line (azimuth = 270°). Middle panel – profile displacements in the x-direction. Bottom panel – profile displacements in the y-direction. 'Model Displacement in CA' data sets was created by adding an offset of 7 mm to the model displacements.

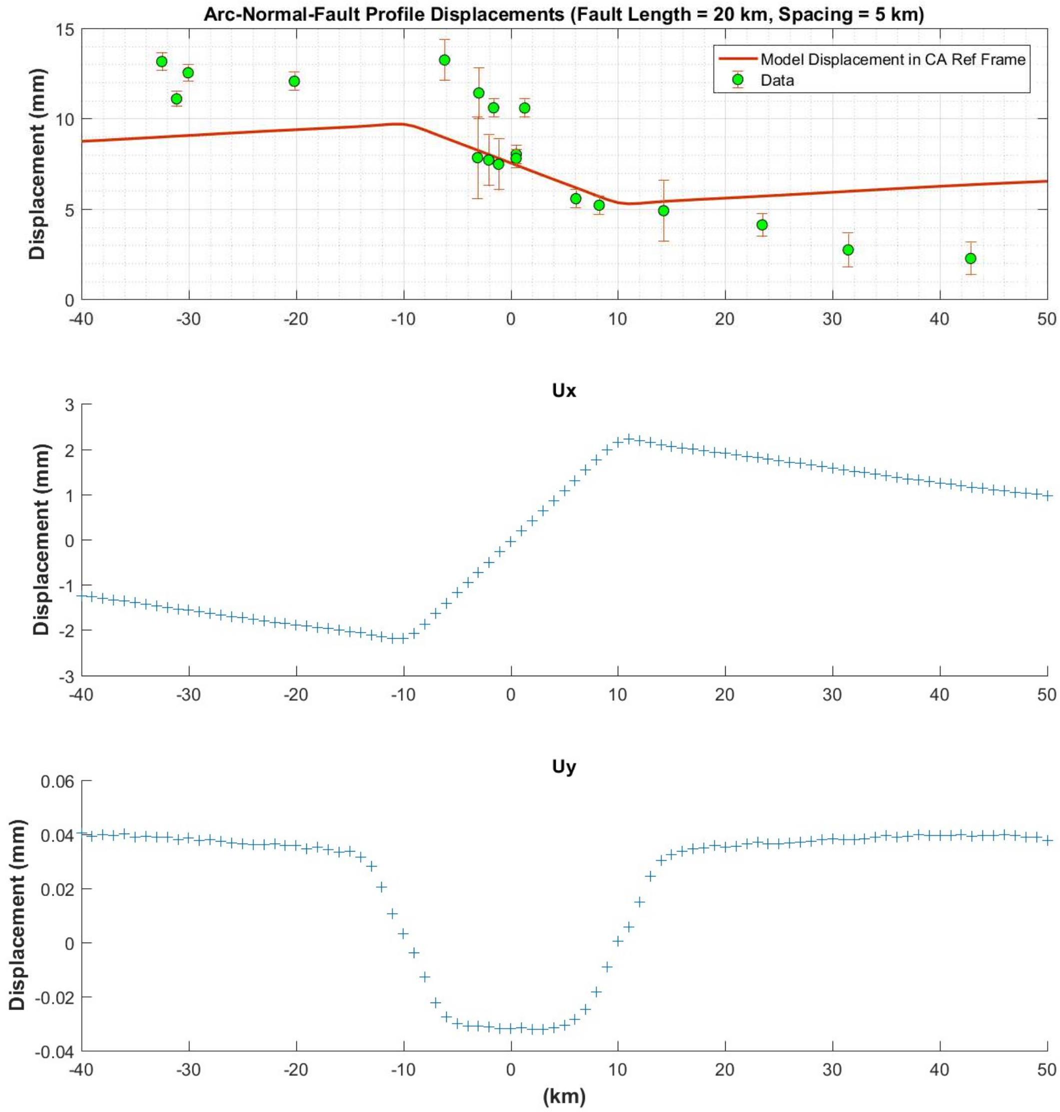

Figure **B-134**: Model H2: displacements along-profile. Arc-normal faults' length and spacing are 20 km and 5 km respectively. Top panel – profile displacements projected into horizontal line (azimuth = 270°). Middle panel – profile displacements in the x-direction. Bottom panel – profile displacements in the y-direction. 'Model Displacement in CA' data sets was created by adding an offset of 7 mm to the model displacements.

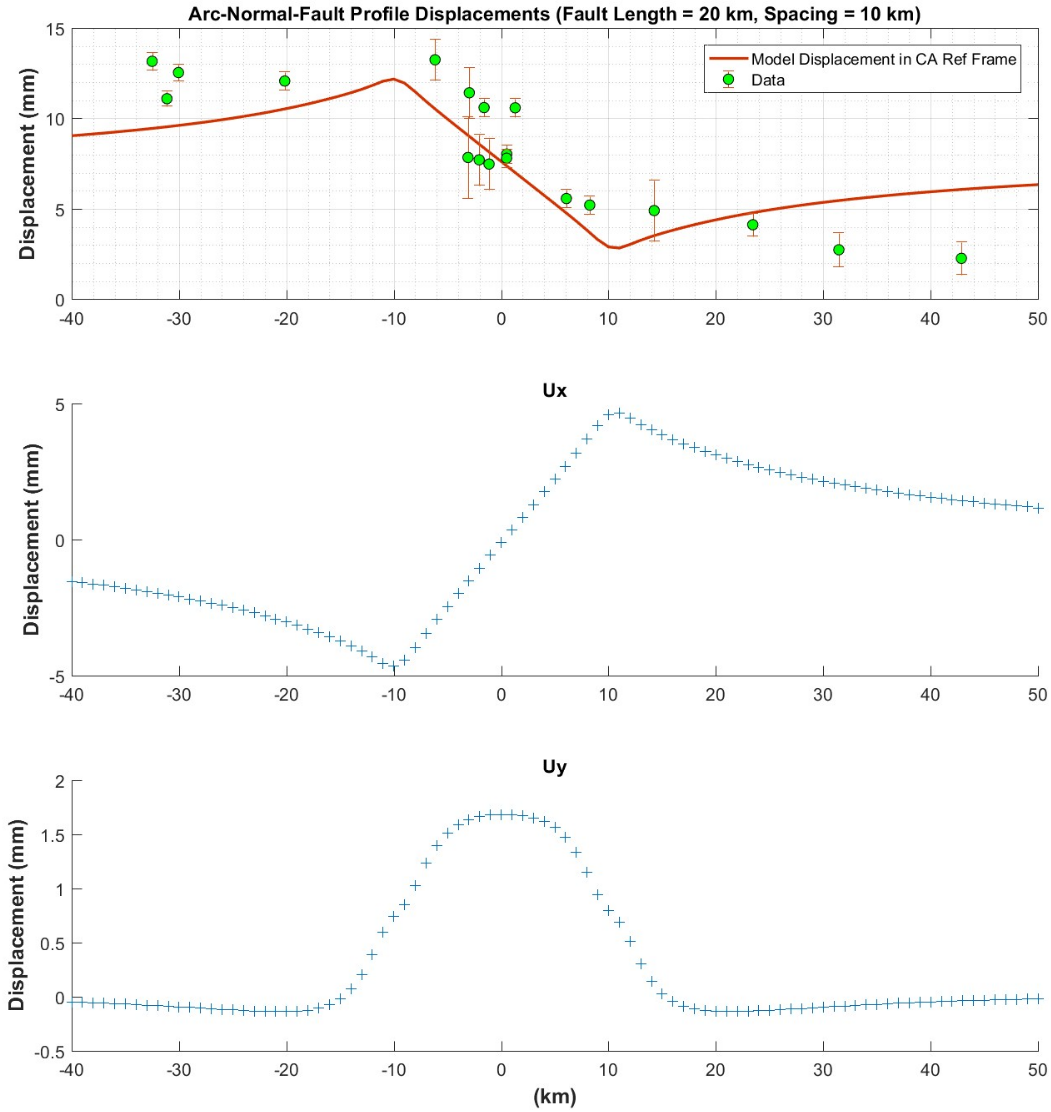

Figure **B-135**: Model H3: displacements along-profile. Arc-normal faults' length and spacing are 20 km and 10 km respectively. Top panel – profile displacements projected into horizontal line (azimuth = 270°). Middle panel – profile displacements in the x-direction. Bottom panel – profile displacements in the y-direction. 'Model Displacement in CA' data sets was created by adding an offset of 7 mm to the model displacements.

B.5 Model Set I Plots

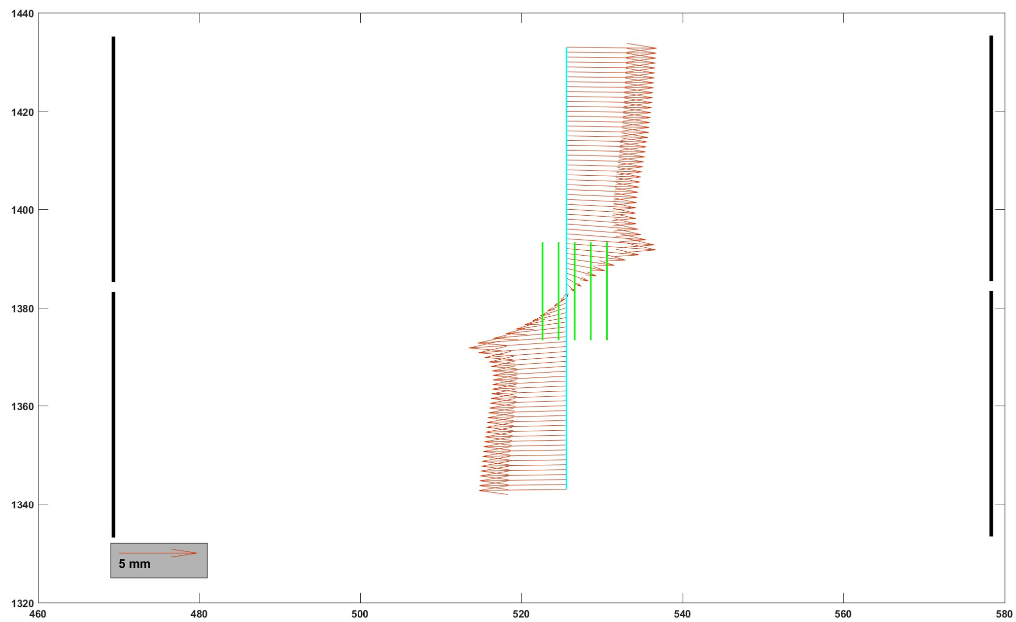

Figure **B-136**: Model I1: surface displacements (red vectors) along-profile line (cyan line). Arc-normal faults' (green lines) length and spacing are 20 km and 2 km respectively. This model has 5 arc-normal faults.

B.6 Model Set J Plots

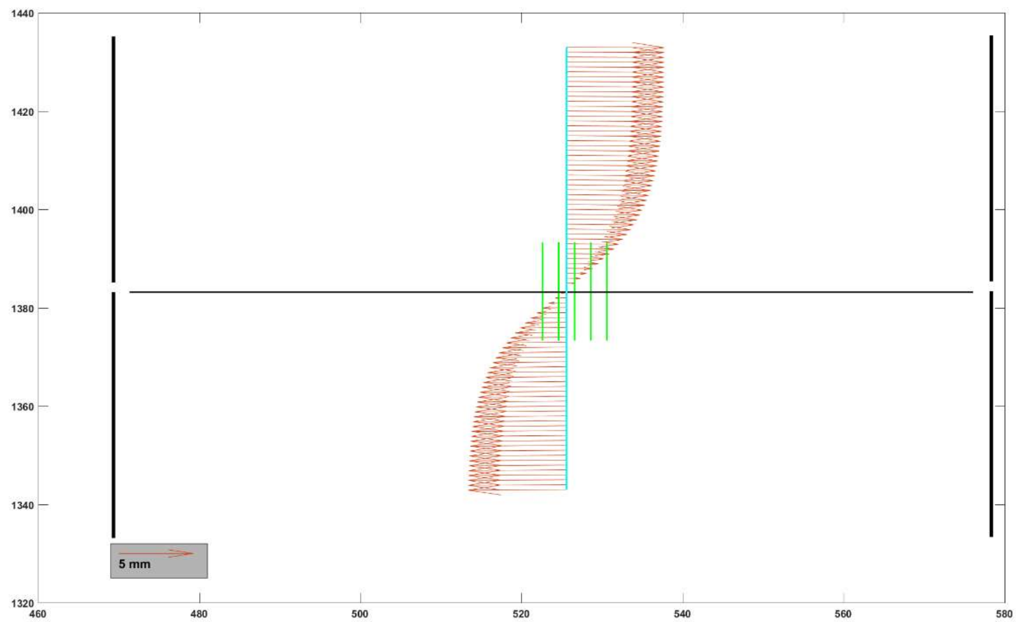

Figure **B-137**: Model J1: surface displacements (red vectors) along-profile line (cyan line). Arc-normal faults' (green lines) length and spacing are 20 km and 2 km respectively and had 1.4 mm of slip imposed on them. This model has 5 arc-normal faults.

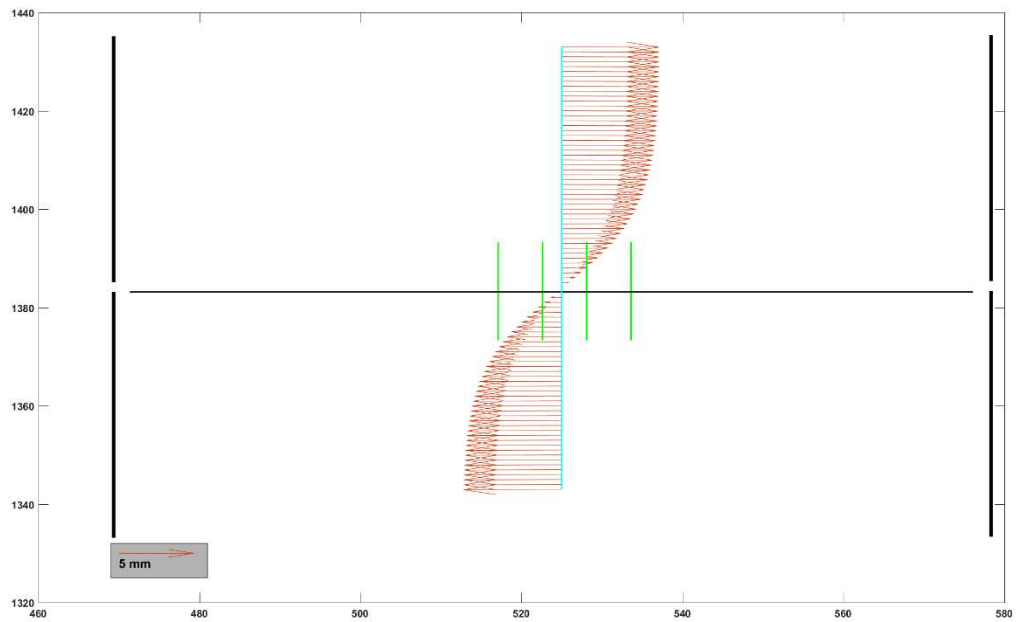

Figure **B-138**: Model J2: surface displacements (red vectors) along-profile line (cyan line). Arc-normal faults' (green lines) length and spacing are 20 km and 5 km respectively and had 3.8 mm of slip imposed on them. This model has 4 arc-normal faults.

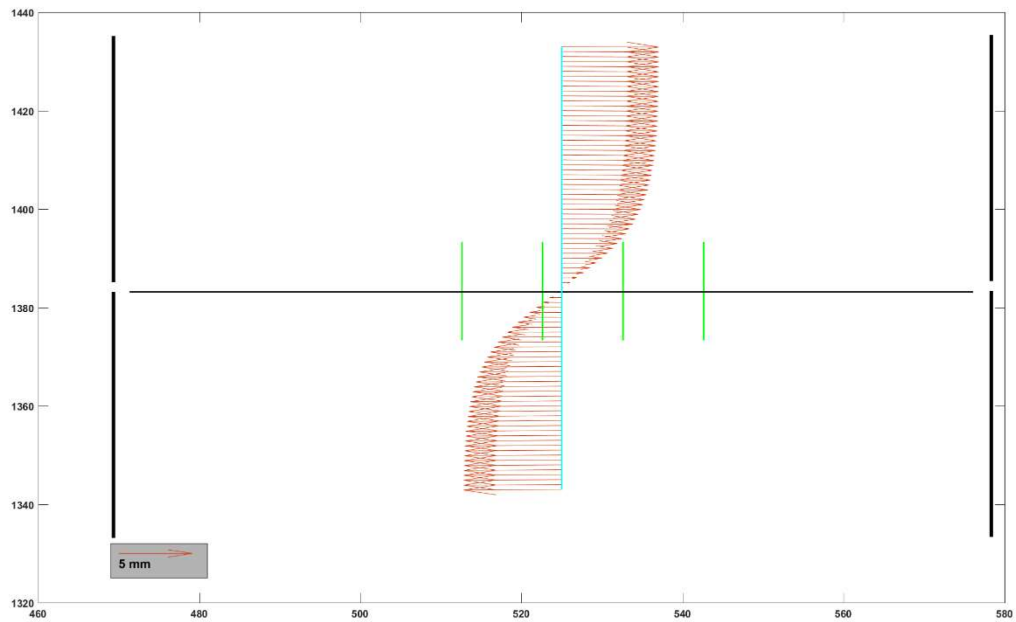

Figure **B-139**: Model J3: surface displacements (red vectors) along-profile line (cyan line). Arc-normal faults' (green lines) length and spacing are 20 km and 10 km respectively and had 7 mm of slip imposed on them. This model has 4 arc-normal faults.

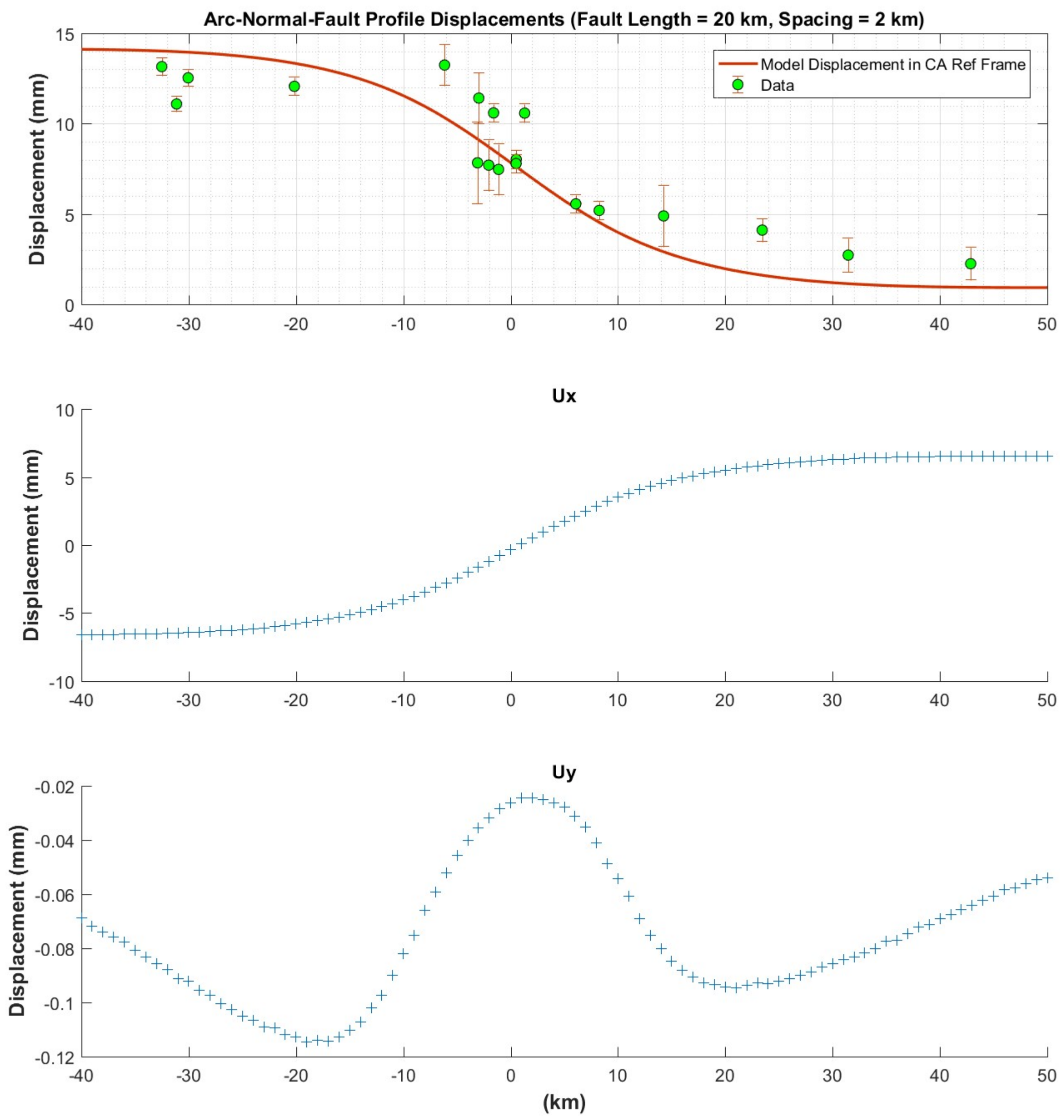

Figure **B-140**: Model J1: displacements along-profile. Arc-normal faults' length and spacing are 20 km and 2 km respectively and had 1.4 mm of slip imposed on them. Top panel – profile displacements projected into horizontal line (azimuth = 270°). Middle panel – profile displacements in the x-direction. Bottom panel – profile displacements in the y-direction. 'Model Displacement in CA' data sets was created by adding an offset of 7 mm to the model displacements.

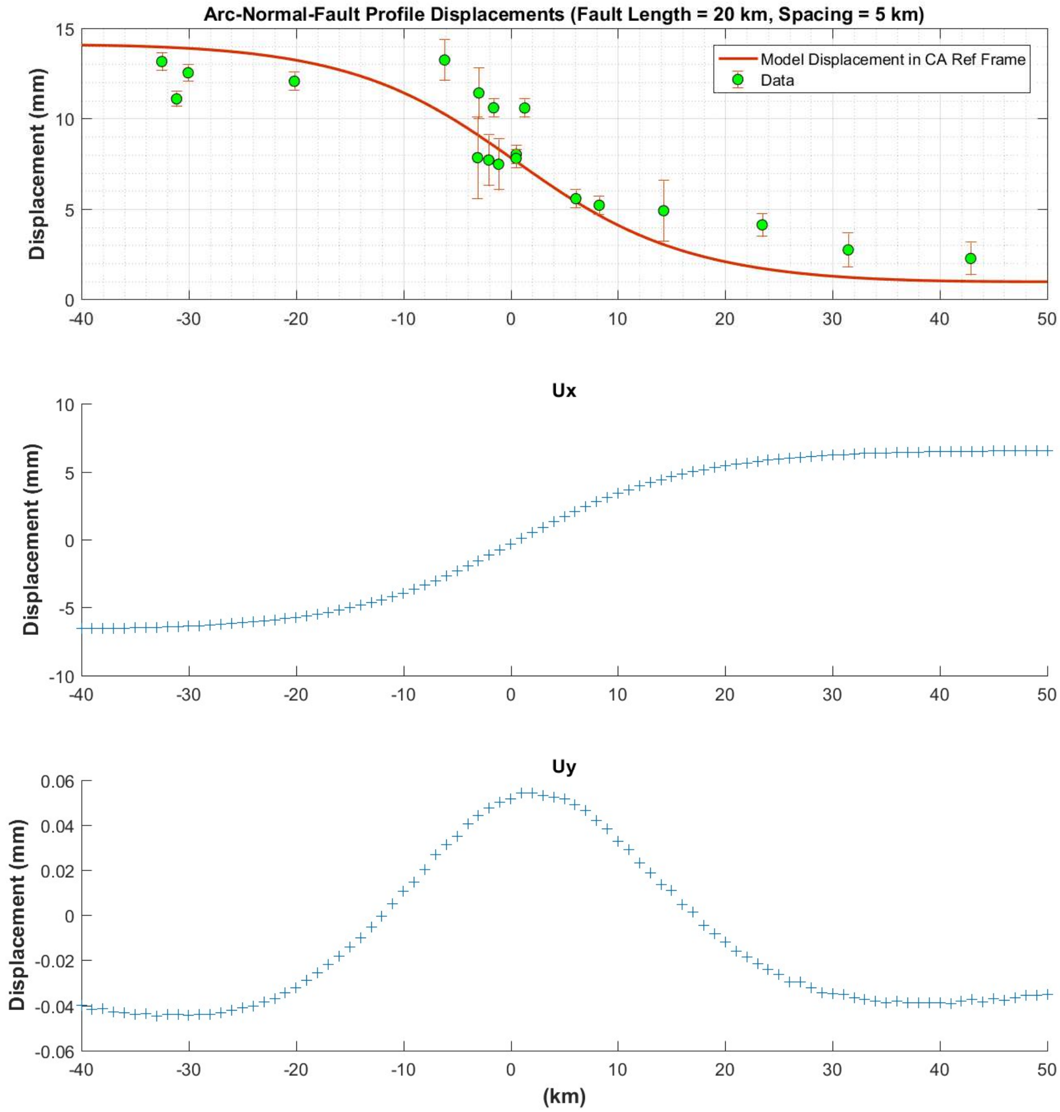

Figure **B-141:** Model J2: displacements along-profile. Arc-normal faults' length and spacing are 20 km and 5 km respectively and had 3.8 mm of slip imposed on them. Top panel – profile displacements projected into horizontal line (azimuth = 270°). Middle panel – profile displacements in the x-direction. Bottom panel – profile displacements in the y-direction. 'Model Displacement in CA' data sets was created by adding an offset of 7 mm to the model displacements.

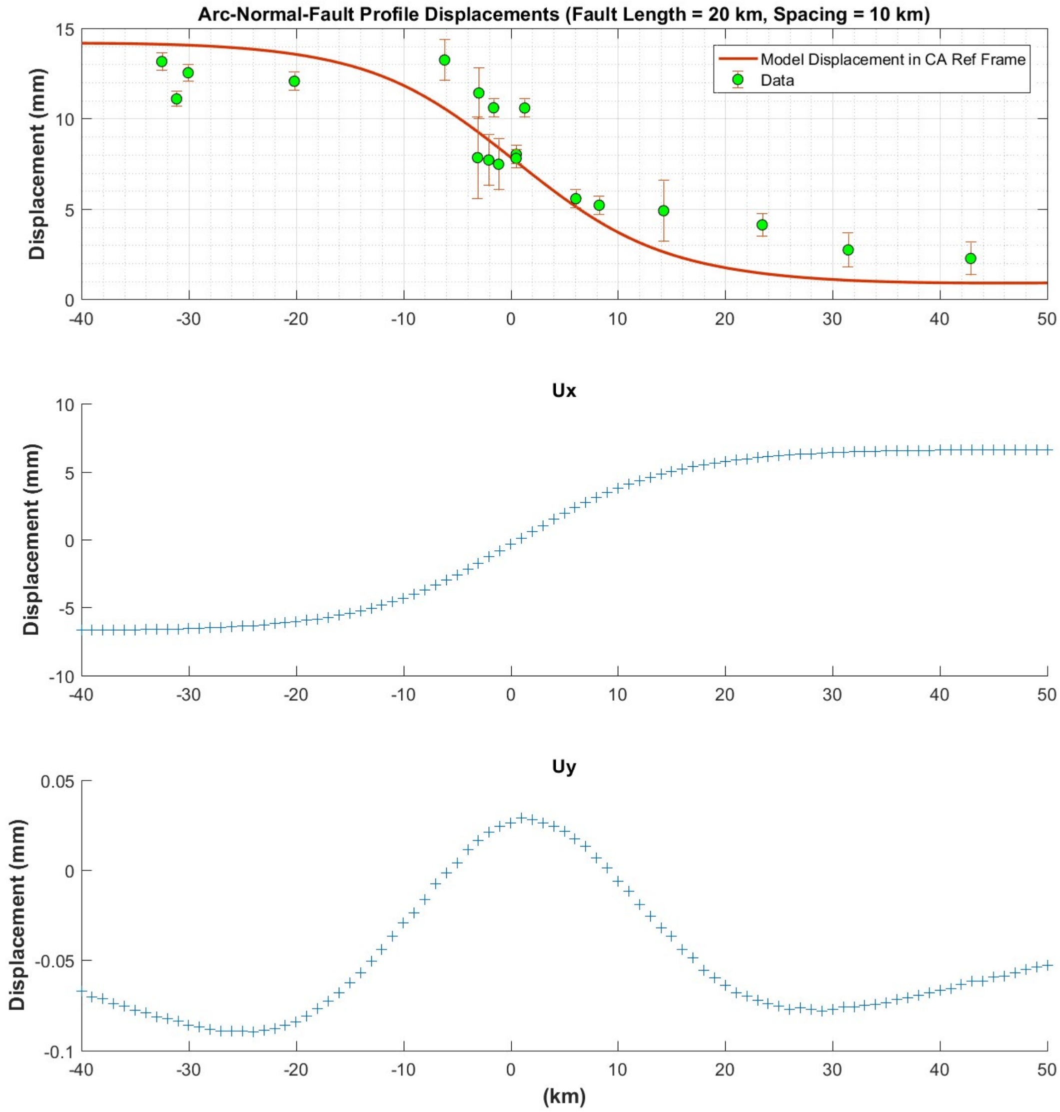

Figure **B-142**: Model J3: displacements along-profile. Arc-normal faults' length and spacing are 20 km and 10 km respectively and had 7 mm of slip imposed on them. Top panel – profile displacements projected into horizontal line (azimuth = 270°). Middle panel – profile displacements in the x-direction. Bottom panel – profile displacements in the y-direction. 'Model Displacement in CA' data sets was created by adding an offset of 7 mm to the model displacements.

B.6 Model Set K Plots

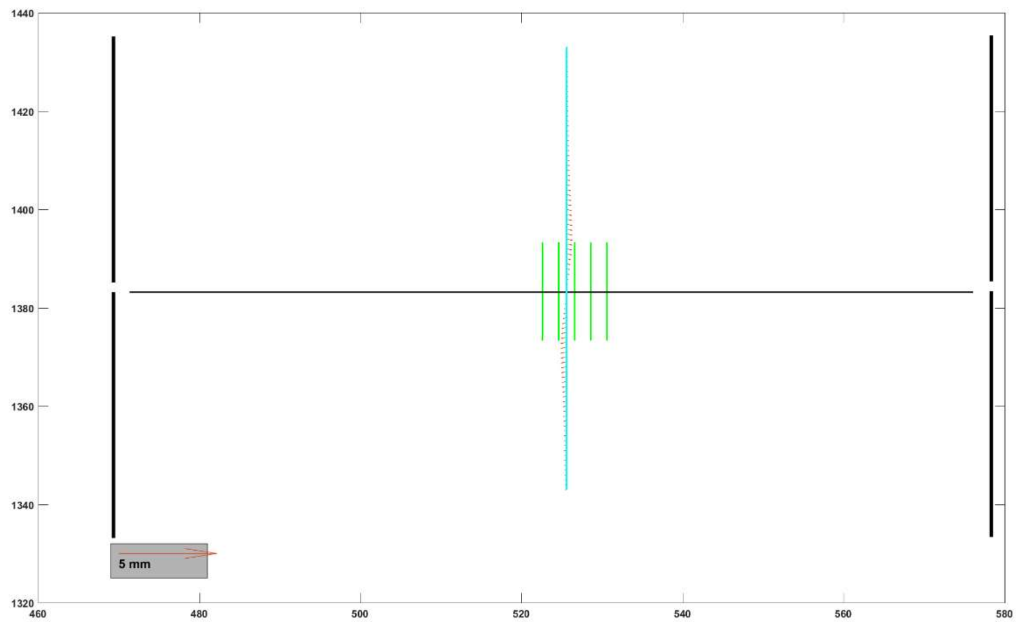

Figure **B-143**: Model K1: surface displacements (red vectors) along-profile line (cyan line). Arc-normal faults' (green lines) length and spacing are 20 km and 2 km respectively and had 1.4 mm of slip imposed on them. This model has 5 arc-normal faults.

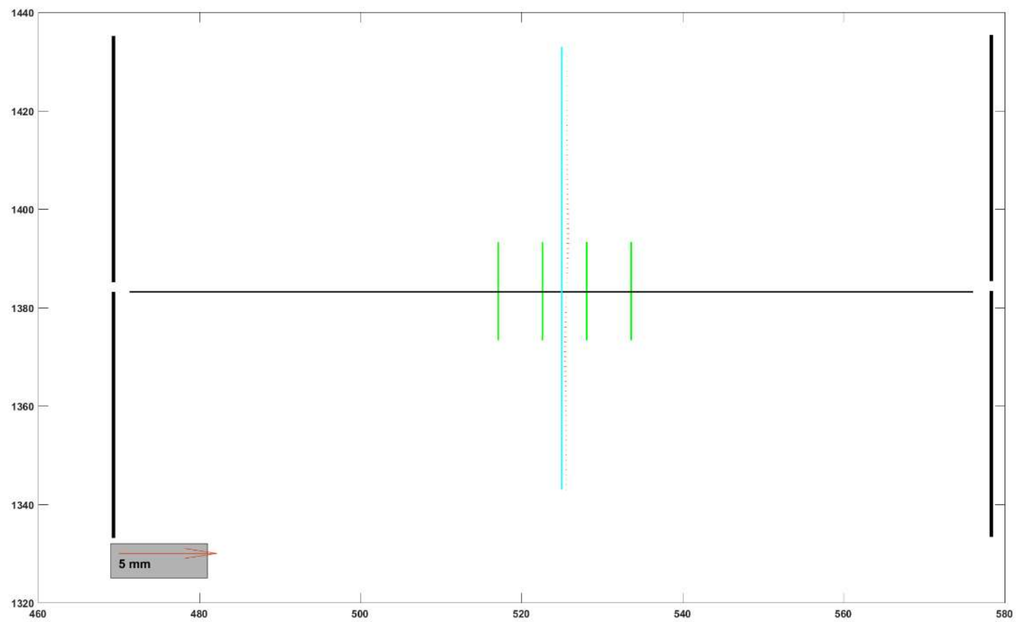

Figure **B-144**: Model K2: surface displacements (red vectors) along-profile line (cyan line). Arc-normal faults' (green lines) length and spacing are 20 km and 5 km respectively and had 3.8 mm of slip imposed on them. This model has 4 arc-normal faults.

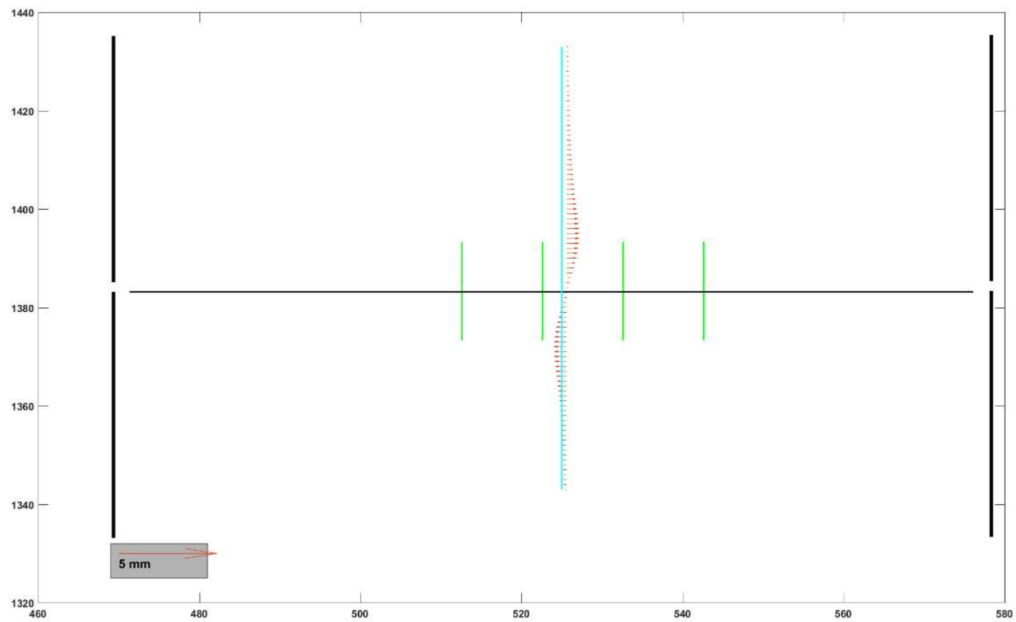

Figure **B-145**: Model K3: surface displacements (red vectors) along-profile line (cyan line). Arc-normal faults' (green lines) length and spacing are 20 km and 10 km respectively and had 7 mm of slip imposed on them. This model has 4 arc-normal faults.

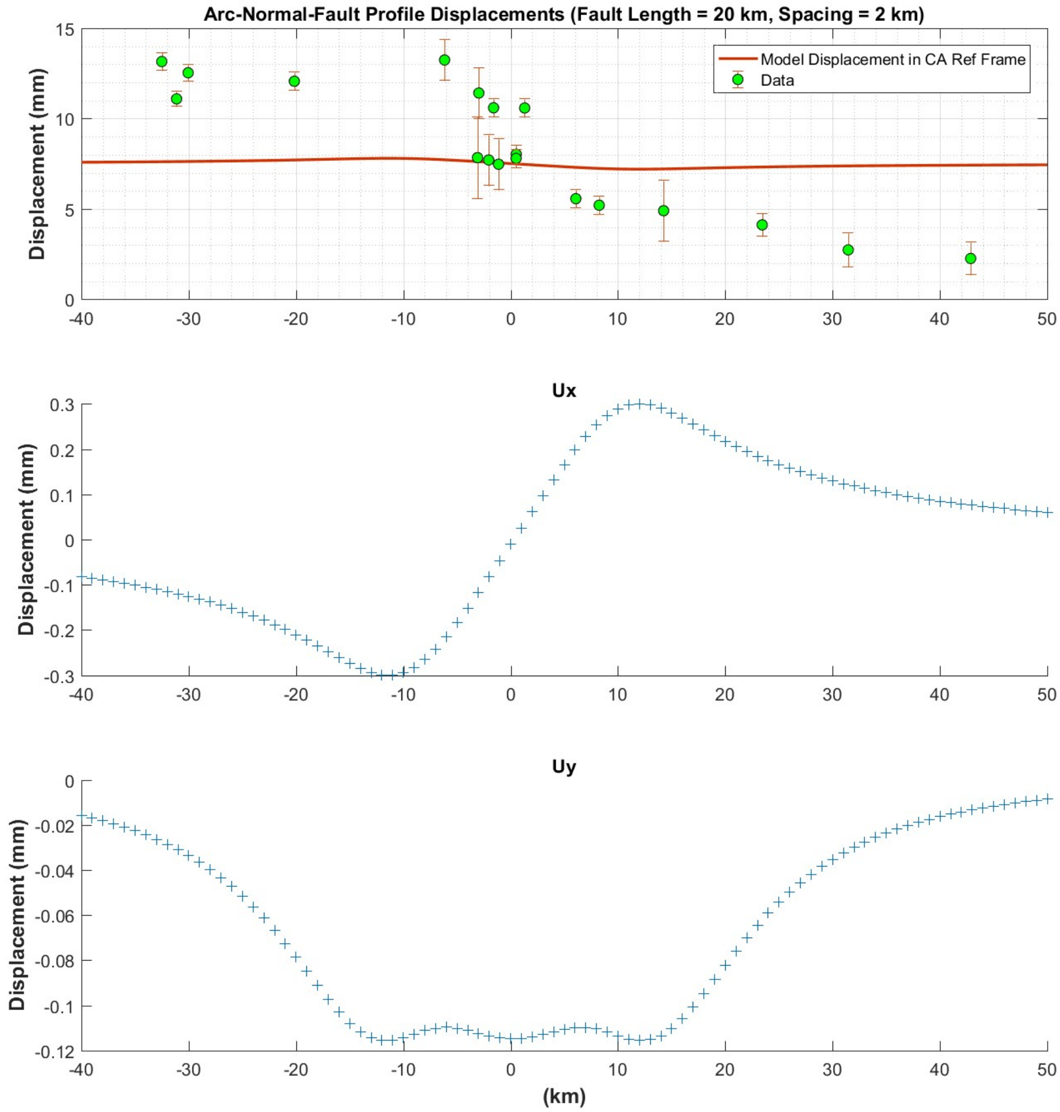

Figure **B-146**: Model K1: displacements along-profile. Arc-normal faults' length and spacing are 20 km and 2 km respectively and had 1.4 mm of slip imposed on them. Top panel – profile displacements projected into horizontal line (azimuth = 270°). Middle panel – profile displacements in the x-direction. Bottom panel – profile displacements in the y-direction. 'Model Displacement in CA' data sets was created by adding an offset of 7 mm to the model displacements.

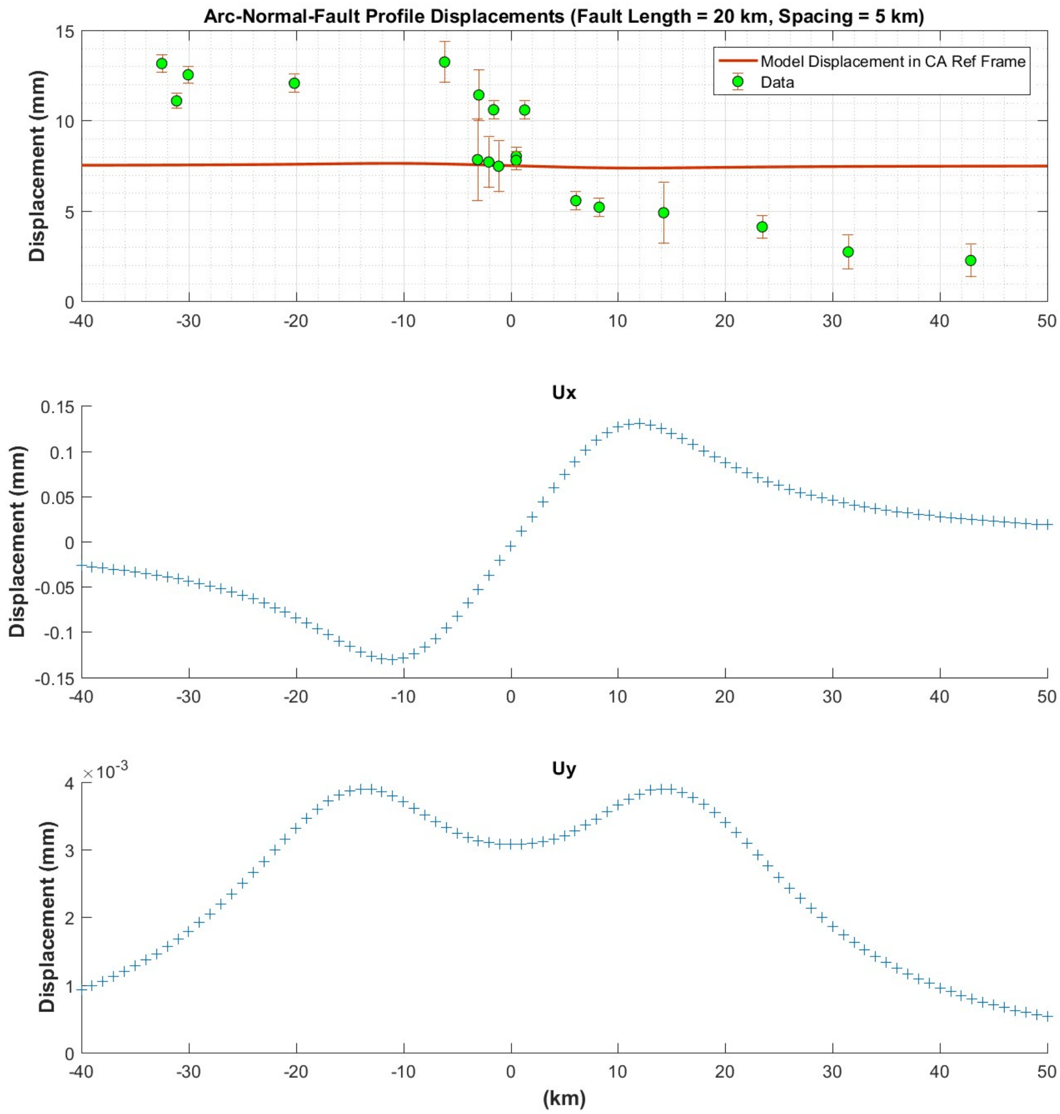

Figure **B-147**: Model K2: displacements along-profile. Arc-normal faults' length and spacing are 20 km and 5 km respectively and had 3.8 mm of slip imposed on them. Top panel – profile displacements projected into horizontal line (azimuth = 270°). Middle panel – profile displacements in the x-direction. Bottom panel – profile displacements in the y-direction. 'Model Displacement in CA' data sets was created by adding an offset of 7 mm to the model displacements.

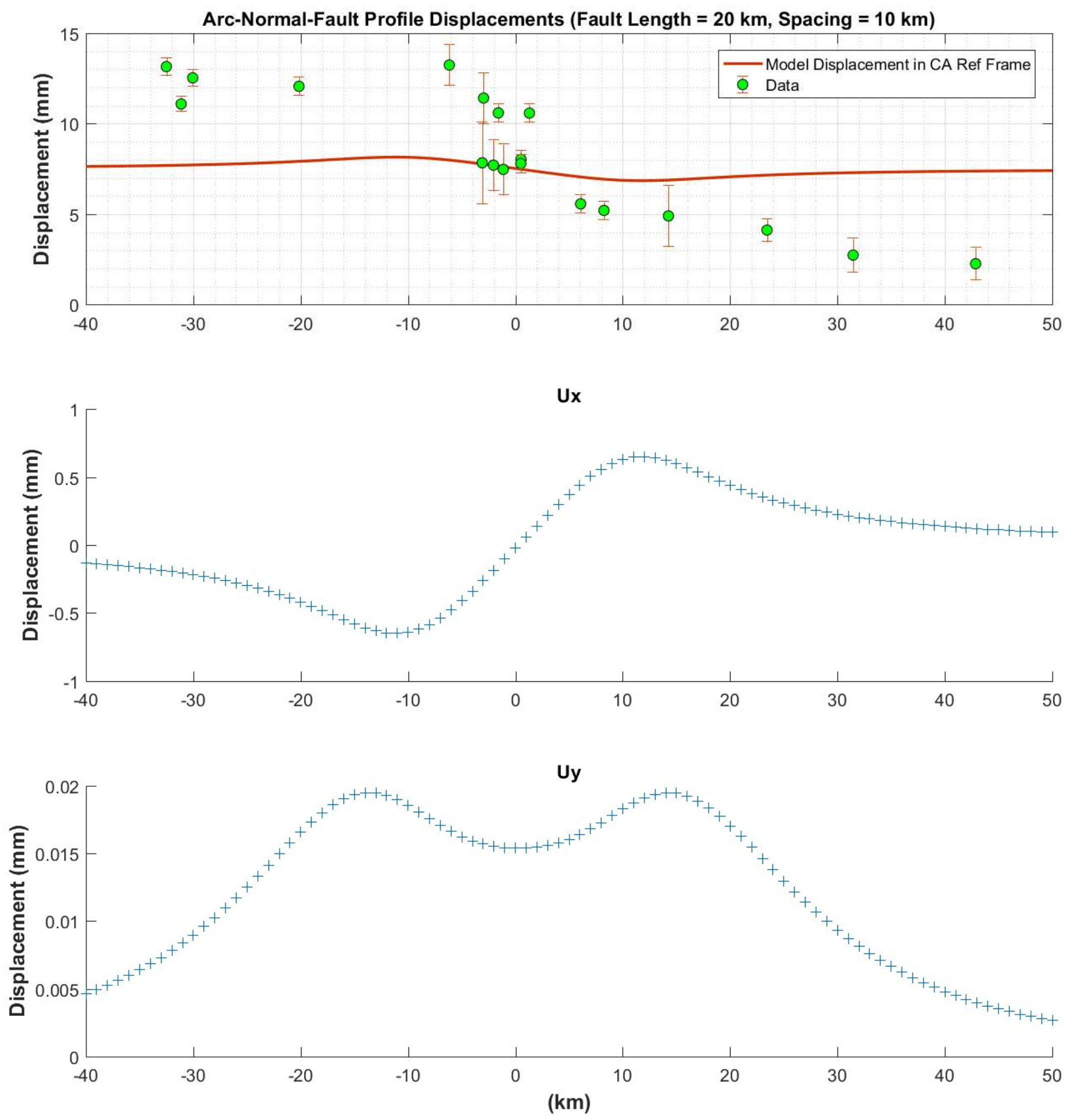

Figure **B-148**: Model K3: displacements along-profile. Arc-normal faults' length and spacing are 20 km and 10 km respectively and had 7 mm of slip imposed on them. Top panel – profile displacements projected into horizontal line (azimuth = 270°). Middle panel – profile displacements in the x-direction. Bottom panel – profile displacements in the y-direction. 'Model Displacement in CA' data sets was created by adding an offset of 7 mm to the model displacements.

B.7 Model Set L Plots

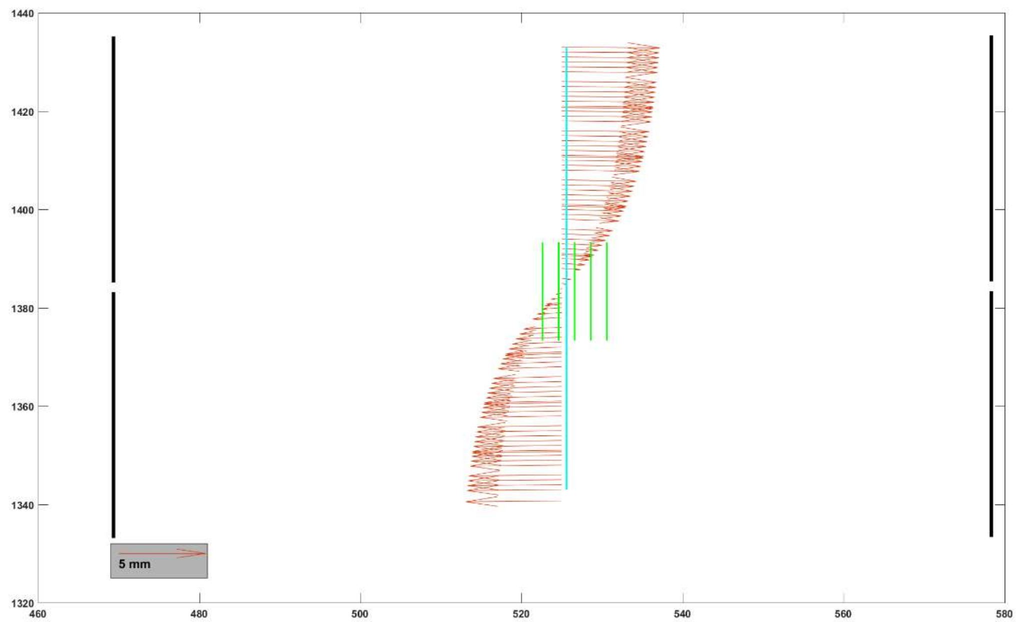

Figure **B-149**: Model L1: surface displacements (red vectors) along-profile line (cyan line). Arc-normal faults' (green lines) length and spacing are 20 km and 2 km respectively and had 1.4 mm of slip imposed on them. This model has 5 arc-normal faults.

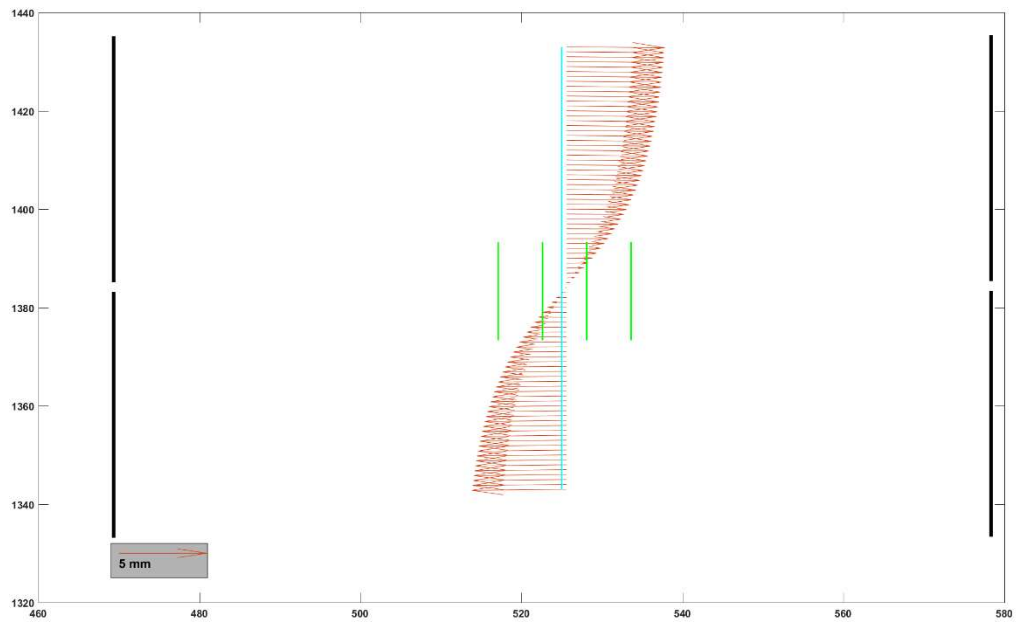

Figure **B-150**: Model L2: surface displacements (red vectors) along-profile line (cyan line). Arc-normal faults' (green lines) length and spacing are 20 km and 5 km respectively and had 3.8 mm of slip imposed on them. This model has 4 arc-normal faults.

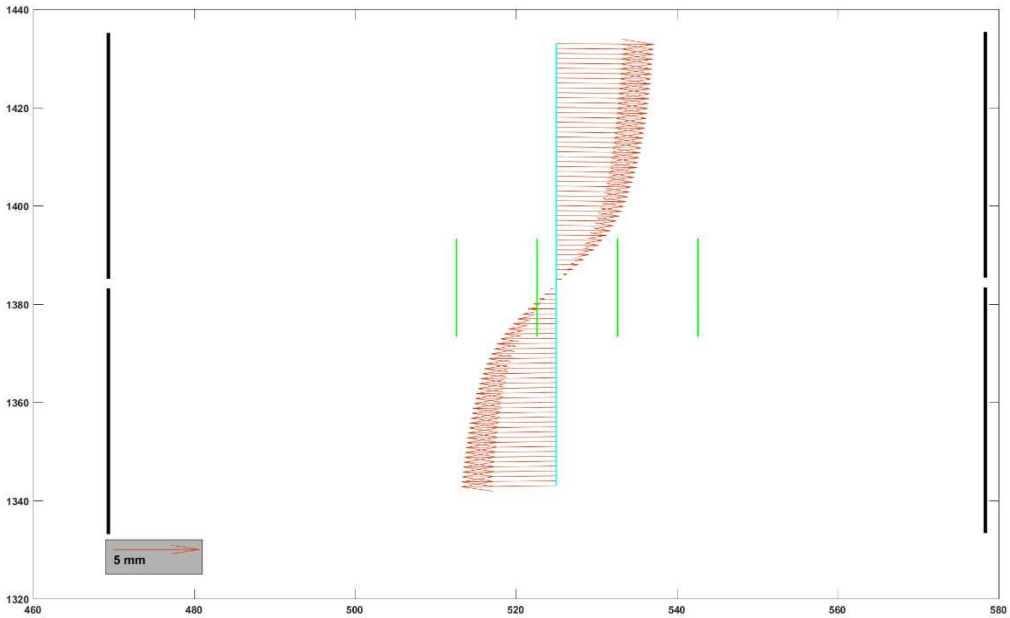

Figure **B-151**: Model L3: surface displacements (red vectors) along-profile line (cyan line). Arc-normal faults' (green lines) length and spacing are 20 km and 10 km respectively and had 7 mm of slip imposed on them. This model has 4 arc-normal faults.

B.8 Model Set M Plots

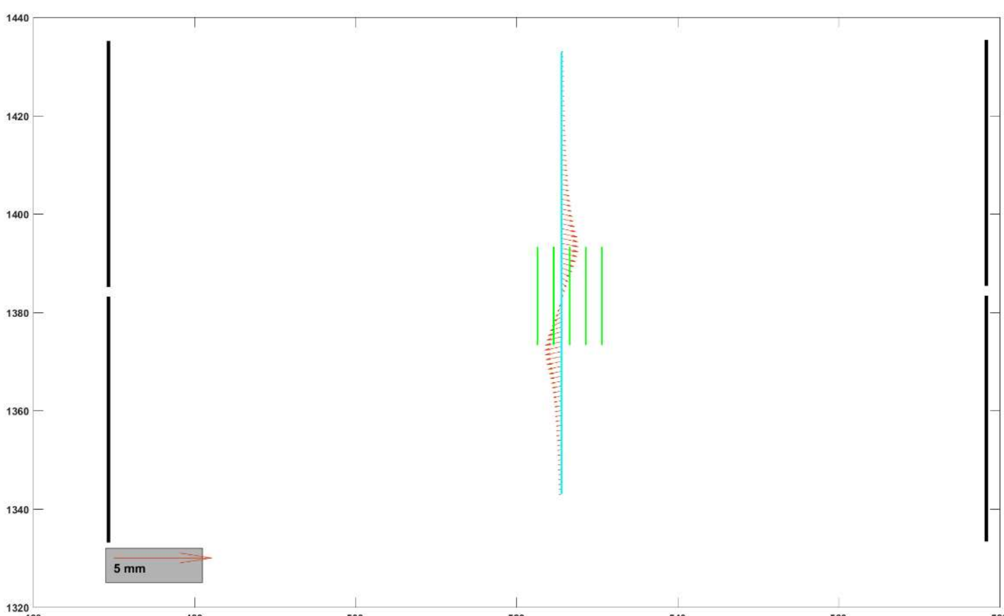

Figure **B-152**: Model M1: surface displacements (red vectors) along-profile line (cyan line). Arc-normal faults' (green lines) length and spacing are 20 km and 2 km respectively and had 1.4 mm of slip imposed on them. This model has 5 arc-normal faults.

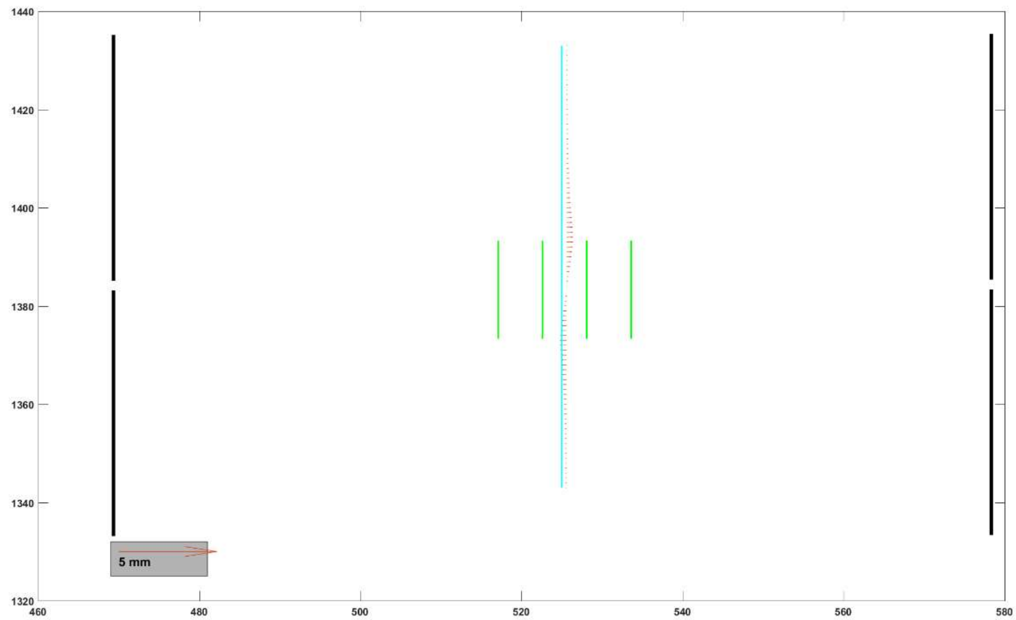

Figure **B-153**: Model M2: surface displacements (red vectors) along-profile line (cyan line). Arc-normal faults' (green lines) length and spacing are 20 km and 5 km respectively and had 3.8 mm of slip imposed on them. This model has 4 arc-normal faults.

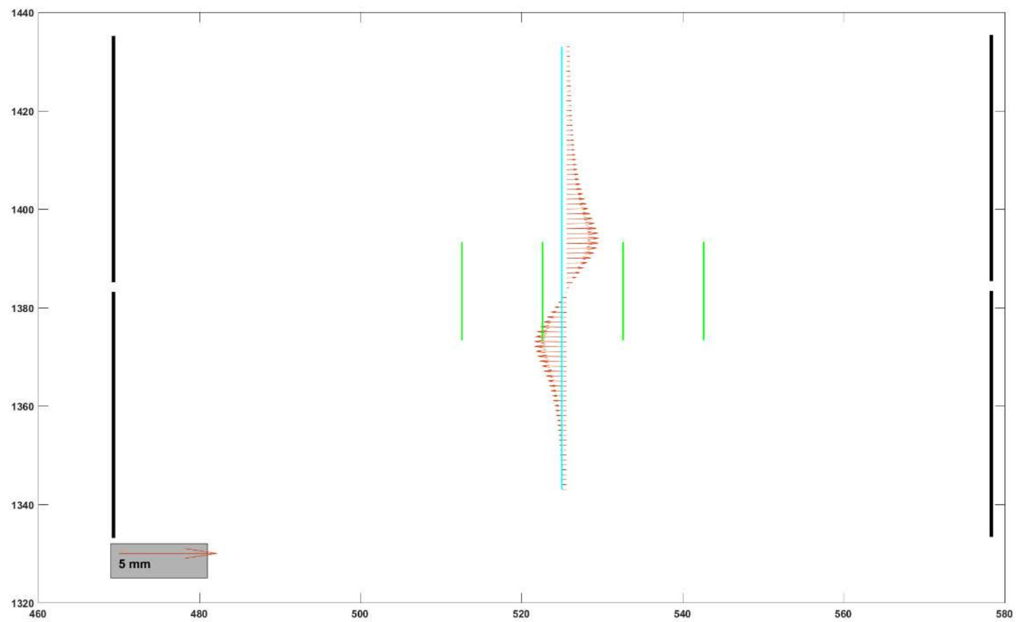

Figure **B-154**: Model M3: surface displacements (red vectors) along-profile line (cyan line). Arc-normal faults' (green lines) length and spacing are 20 km and 10 km respectively and had 7 mm of slip imposed on them. This model has 4 arc-normal faults.

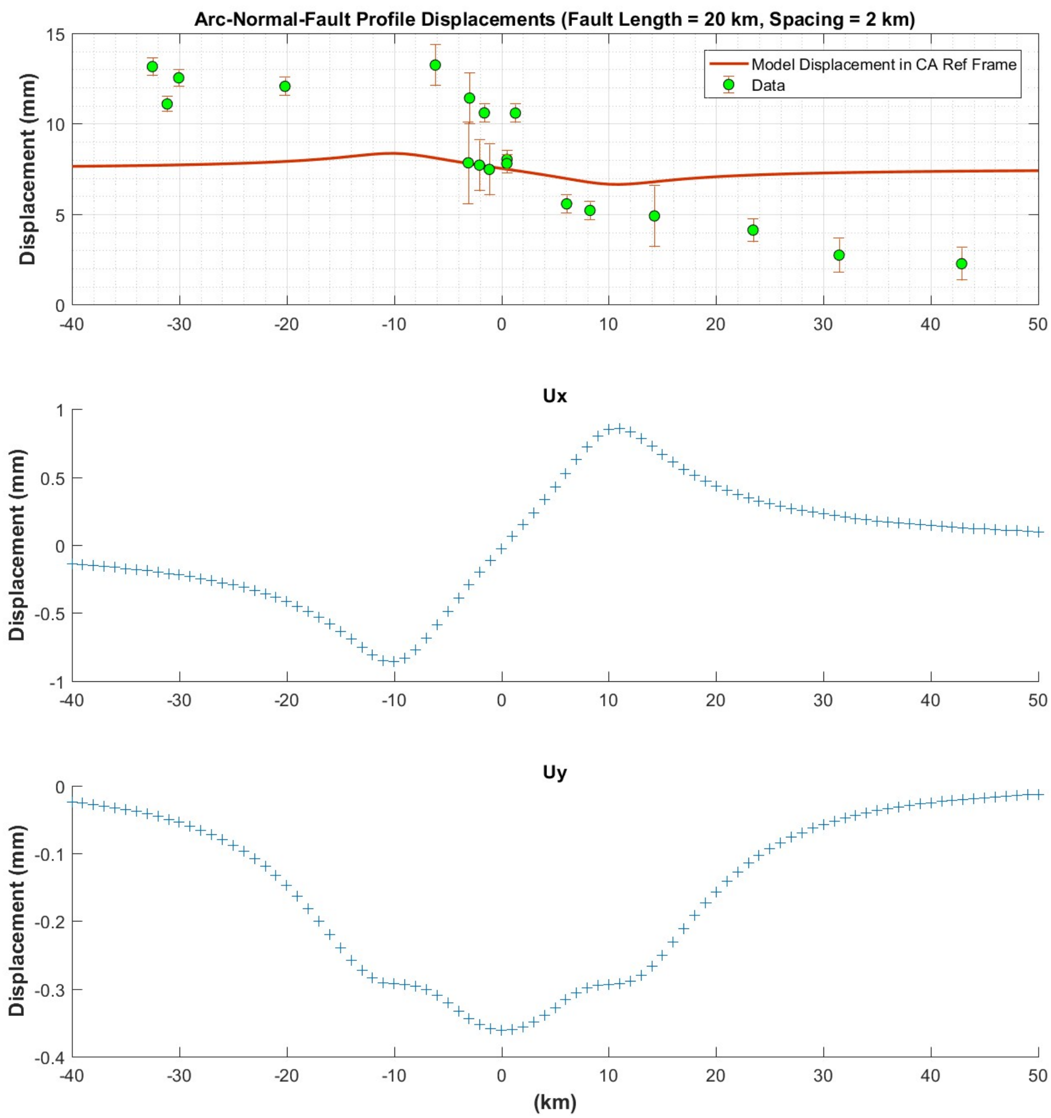

Figure **B-155**: Model M1: displacements along-profile. Arc-normal faults' length and spacing are 20 km and 2 km respectively and had 1.4 mm of slip imposed on them. Top panel – profile displacements projected into horizontal line (azimuth = 270°). Middle panel – profile displacements in the x-direction. Bottom panel – profile displacements in the y-direction. 'Model Displacement in CA' data sets was created by adding an offset of 7 mm to the model displacements.

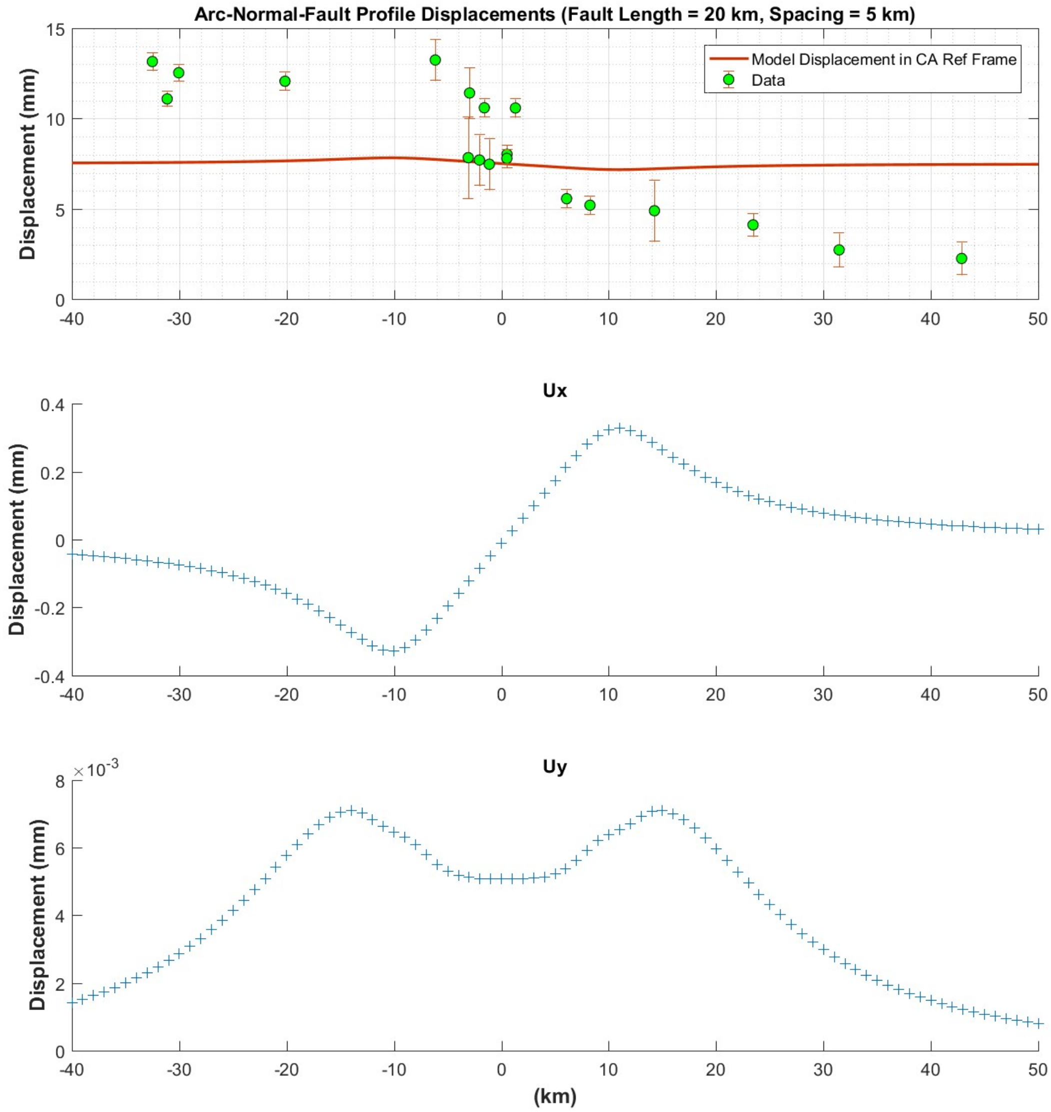

Figure **B-156**: Model M2: displacements along-profile. Arc-normal faults' length and spacing are 20 km and 5 km respectively and had 3.8 mm of slip imposed on them. Top panel – profile displacements projected into horizontal line (azimuth = 270°). Middle panel – profile displacements in the x-direction. Bottom panel – profile displacements in the y-direction. 'Model Displacement in CA' data sets was created by adding an offset of 7 mm to the model displacements.

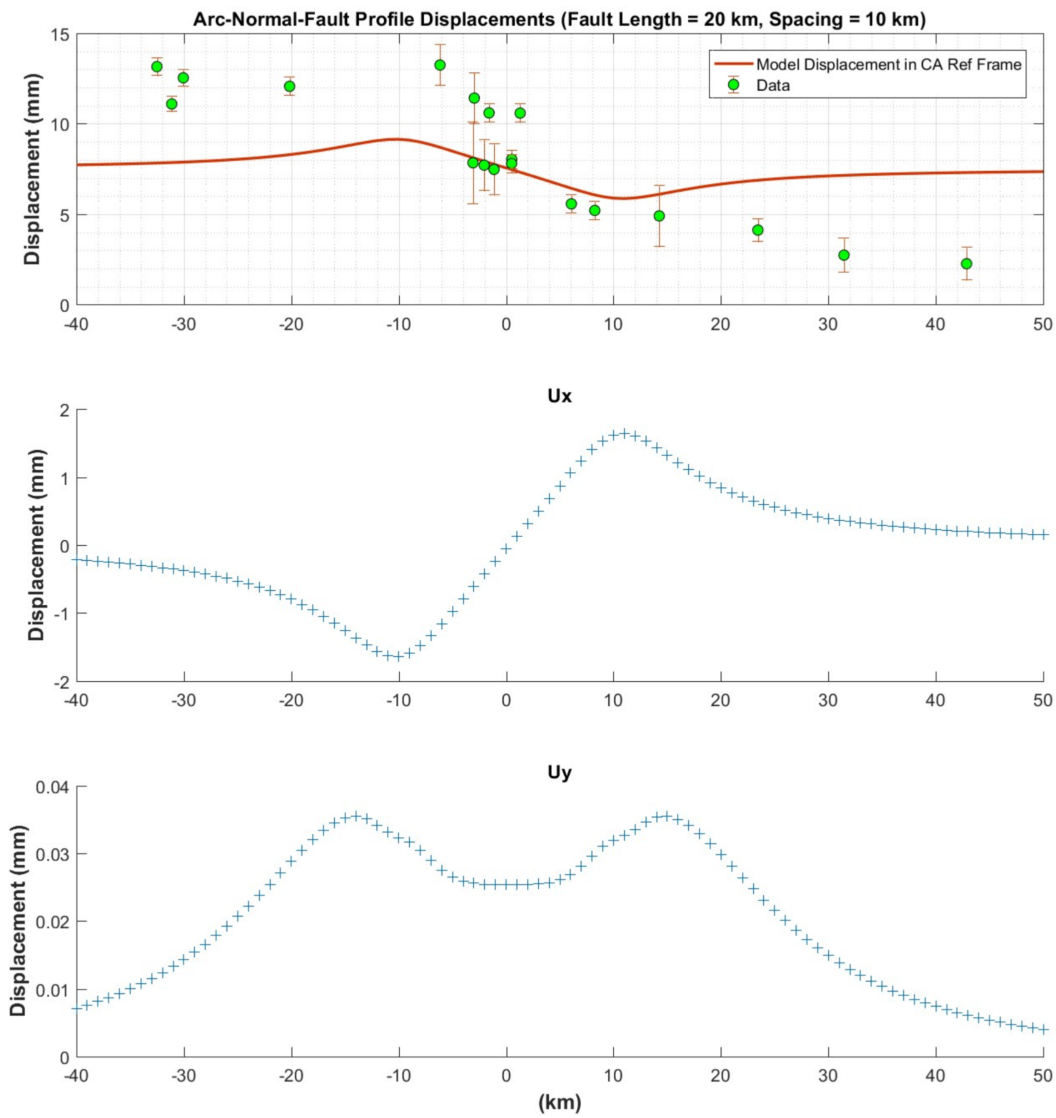

Figure **B-157**: Model M3: displacements along-profile. Arc-normal faults' length and spacing are 20 km and 10 km respectively and had 7 mm of slip imposed on them. Top panel – profile displacements projected into horizontal line (azimuth = 270°). Middle panel – profile displacements in the x-direction. Bottom panel – profile displacements in the y-direction. 'Model Displacement in CA' data sets was created by adding an offset of 7 mm to the model displacements.

B.9 Model Set N Plots

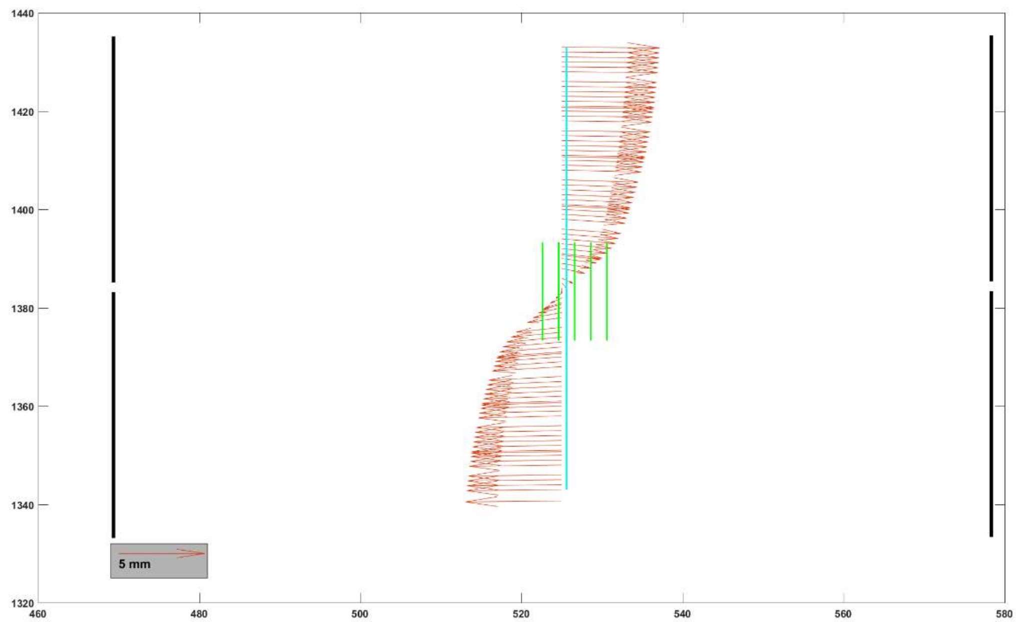

Figure **B-158**: Model N1: surface displacements (red vectors) along-profile line (cyan line). Arc-normal faults' (green lines) length and spacing are 20 km and 2 km respectively and had 1.4 mm of slip imposed on them. This model has 5 arc-normal faults.

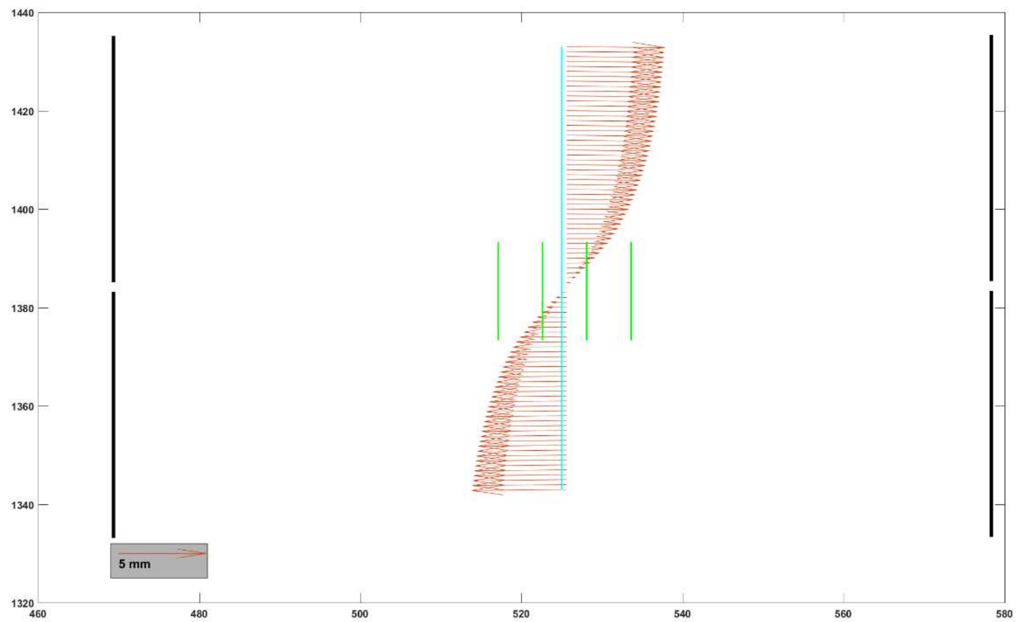

Figure **B-159**: Model N2: surface displacements (red vectors) along-profile line (cyan line). Arc-normal faults' (green lines) length and spacing are 20 km and 5 km respectively and had 3.8 mm of slip imposed on them. This model has 4 arc-normal faults.

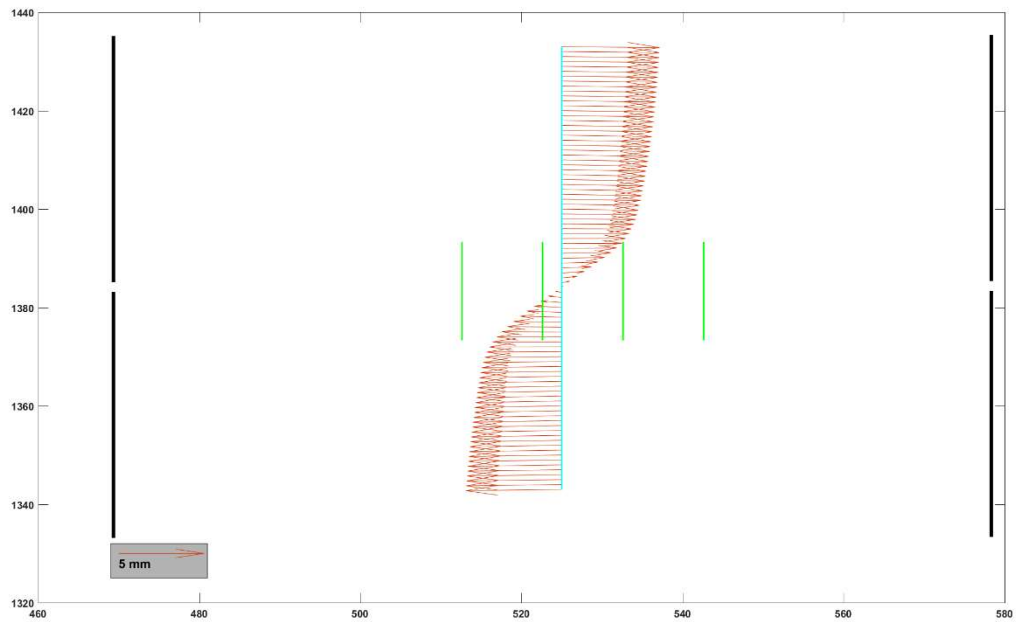

Figure **B-160**: Model N3: surface displacements (red vectors) along-profile line (cyan line). Arc-normal faults' (green lines) length and spacing are 20 km and 10 km respectively and had 7 mm of slip imposed on them. This model has 4 arc-normal faults.

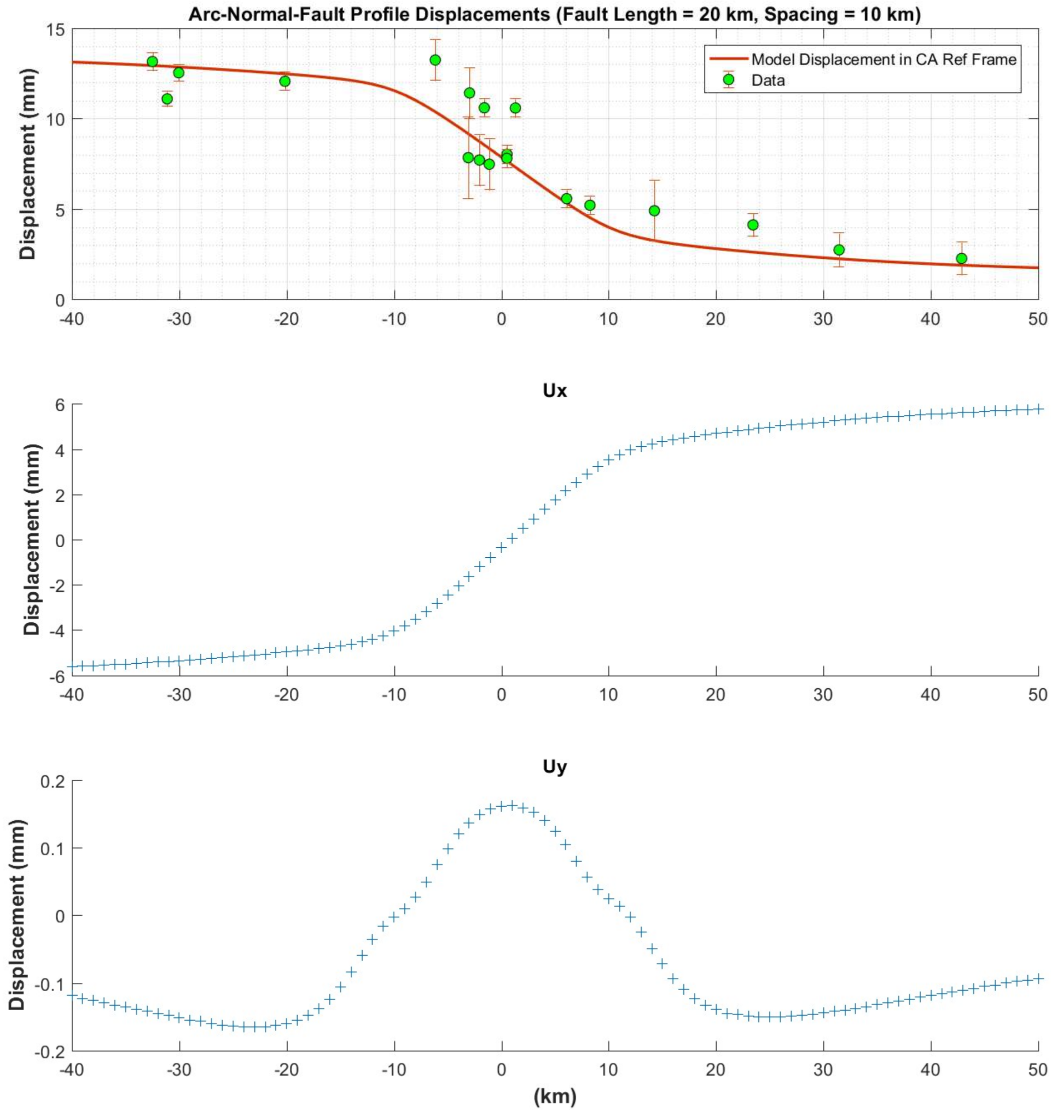

Figure **B-161**: Model N3: displacements along-profile. Arc-normal faults' length and spacing are 20 km and 10 km respectively and had 7 mm of slip imposed on them. Top panel – profile displacements projected into horizontal line (azimuth = 270°). Middle panel – profile displacements in the x-direction. Bottom panel – profile displacements in the y-direction. 'Model Displacement in CA' data sets was created by adding an offset of 7 mm to the model displacements.

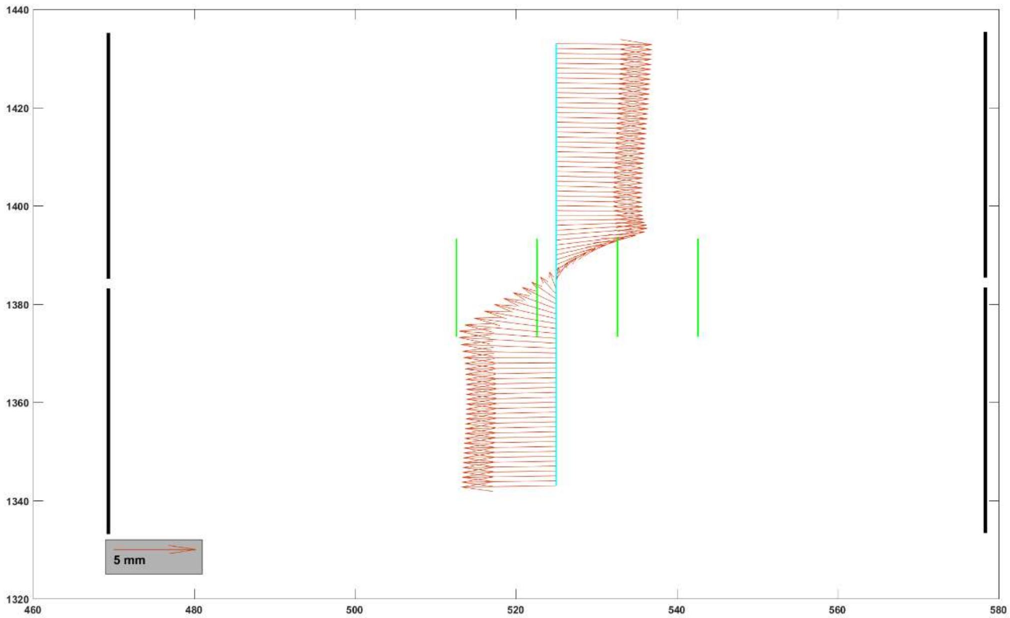

Figure **B-162**: Model I3: surface displacements (red vectors) along-profile line (cyan line). Arc-normal faults' (green lines) length and spacing are 20 km and 10 km respectively. This model has 4 arc-normal faults.

B.10 Model Set O Plots

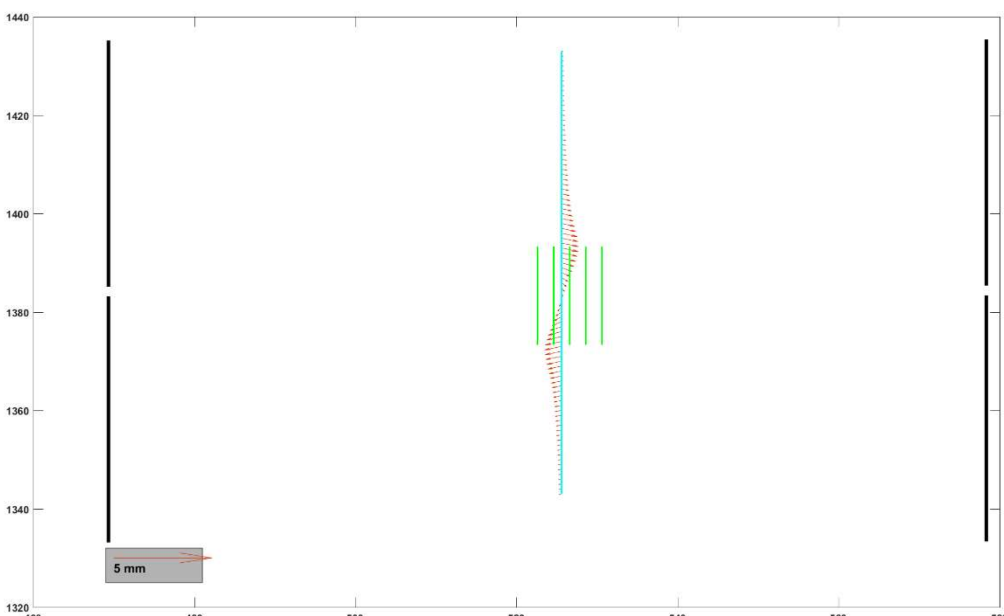

Figure **B-163**: Model O1: surface displacements (red vectors) along-profile line (cyan line). Arc-normal faults' (green lines) length and spacing are 20 km and 2 km respectively and had 10 mm of slip imposed on them. This model has 5 arc-normal faults.

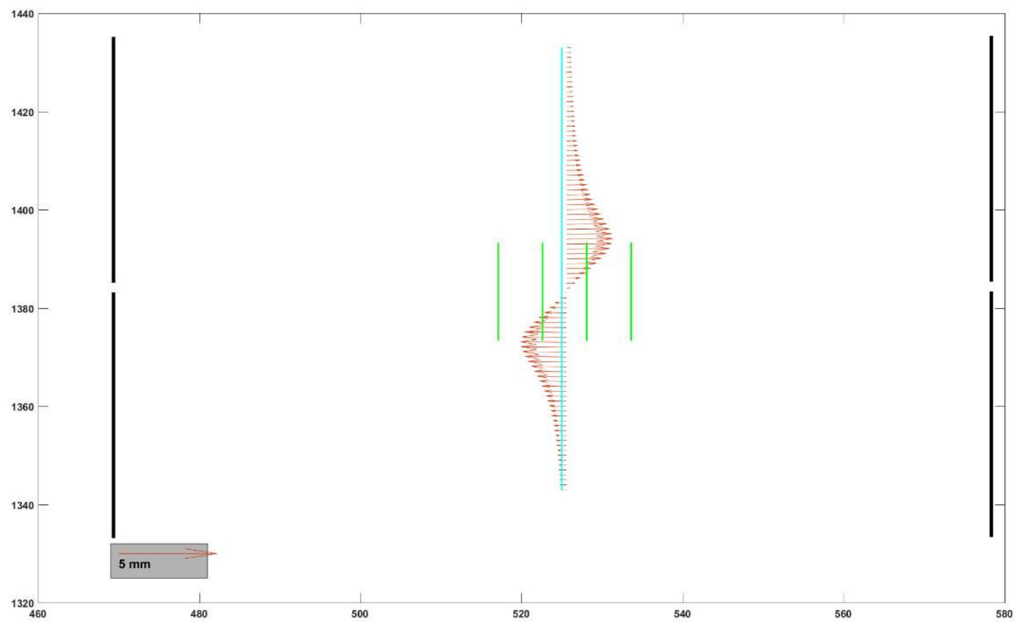

Figure **B-164**: Model O2: surface displacements (red vectors) along-profile line (cyan line). Arc-normal faults' (green lines) length and spacing are 20 km and 5 km respectively and had 10 mm of slip imposed on them. This model has 4 arc-normal faults.

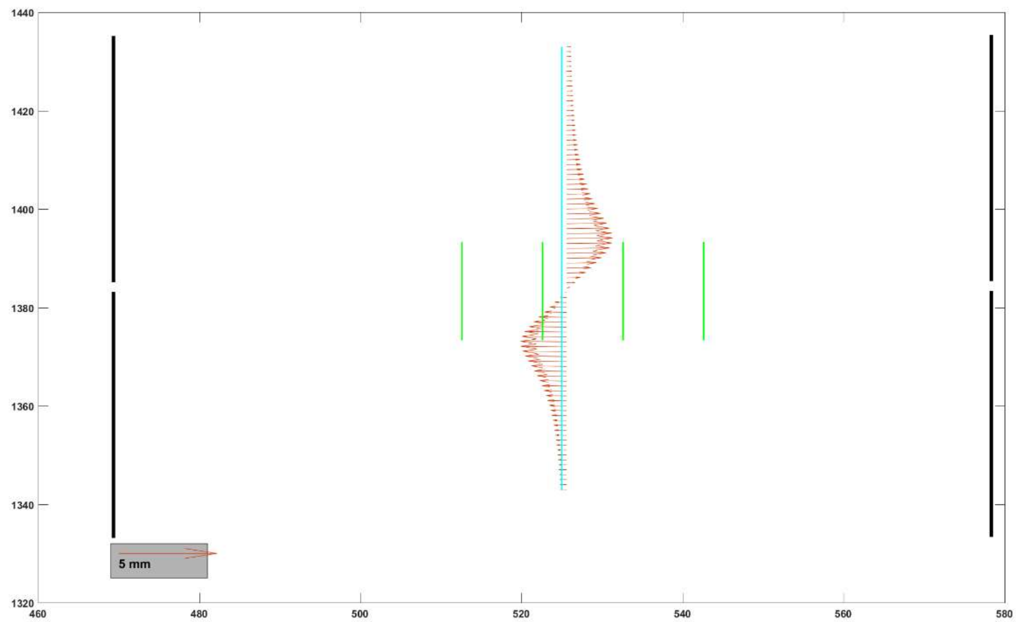

Figure **B-165**: Model O3: surface displacements (red vectors) along-profile line (cyan line). Arc-normal faults' (green lines) length and spacing are 20 km and 10 km respectively and had 10 mm of slip imposed on them. This model has 4 arc-normal faults.

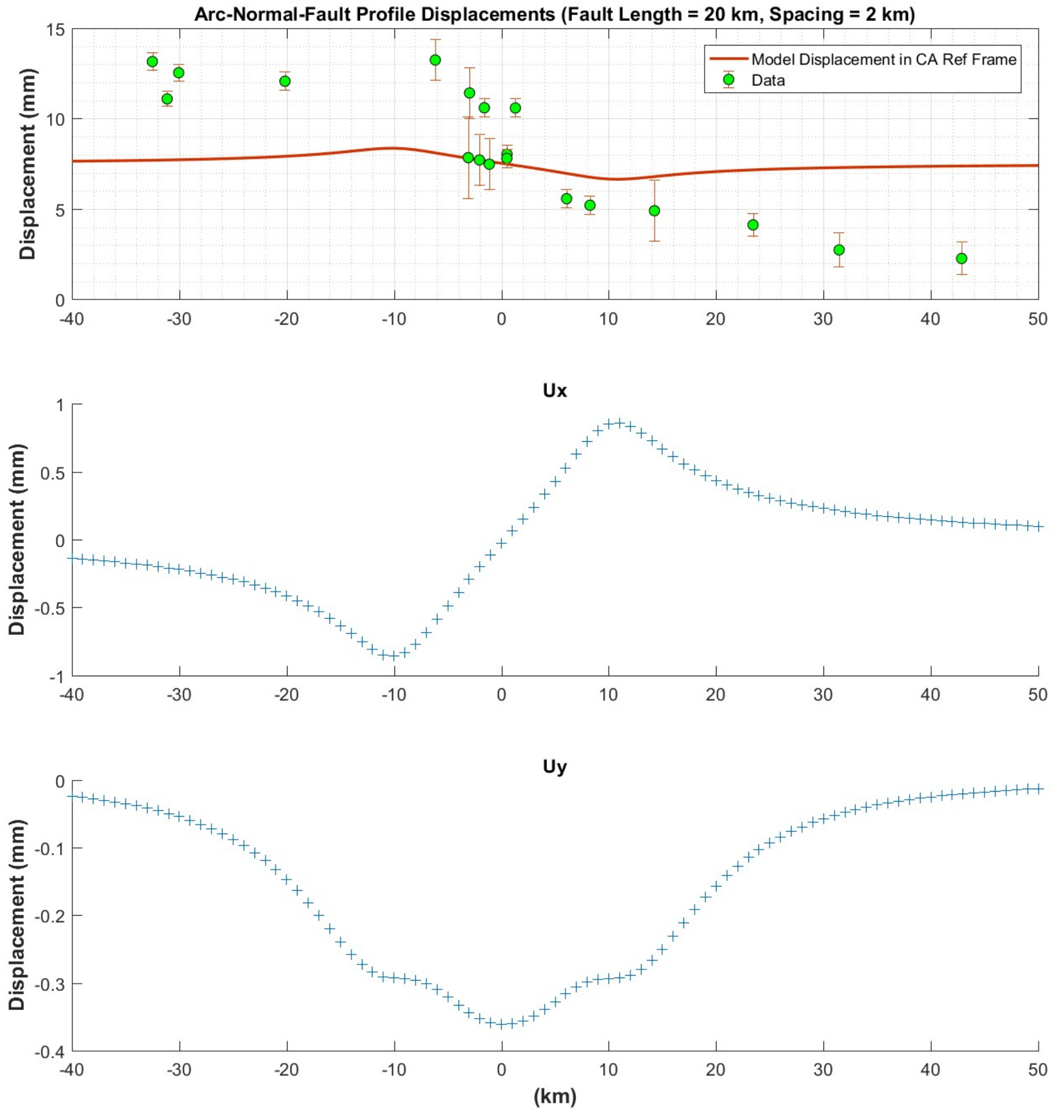

Figure **B-166**: Model O1: displacements along-profile. Arc-normal faults' length and spacing are 20 km and 2 km respectively and had 10 mm of slip imposed on them. Top panel – profile displacements projected into horizontal line (azimuth = 270°). Middle panel – profile displacements in the x-direction. Bottom panel – profile displacements in the y-direction. 'Model Displacement in CA' data sets was created by adding an offset of 7 mm to the model displacements.

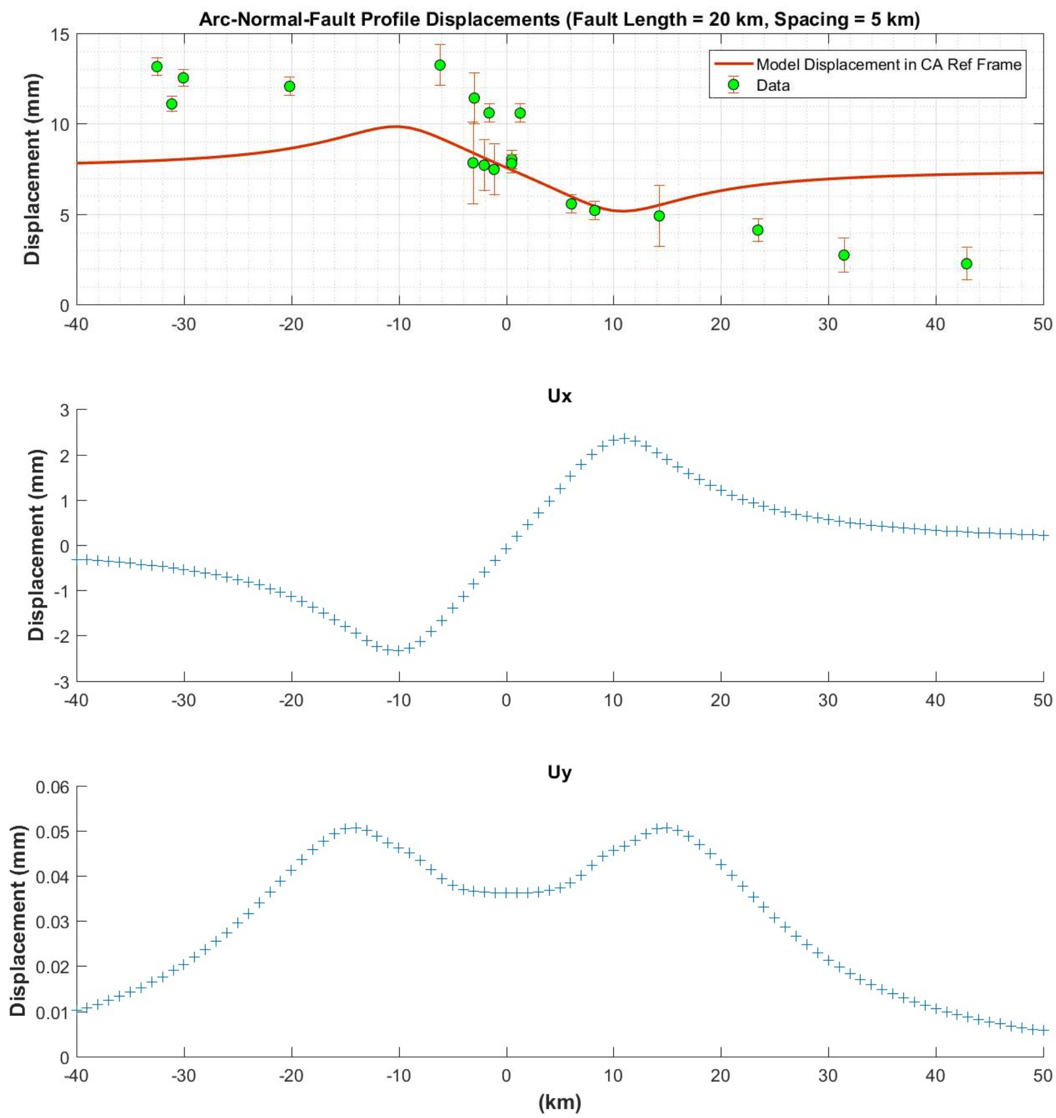

Figure **B-167**: Model O2: displacements along-profile. Arc-normal faults' length and spacing are 20 km and 5 km respectively and had 10 mm of slip imposed on them. Top panel – profile displacements projected into horizontal line (azimuth = 270°). Middle panel – profile displacements in the x-direction. Bottom panel – profile displacements in the y-direction. 'Model Displacement in CA' data sets was created by adding an offset of 7 mm to the model displacements.

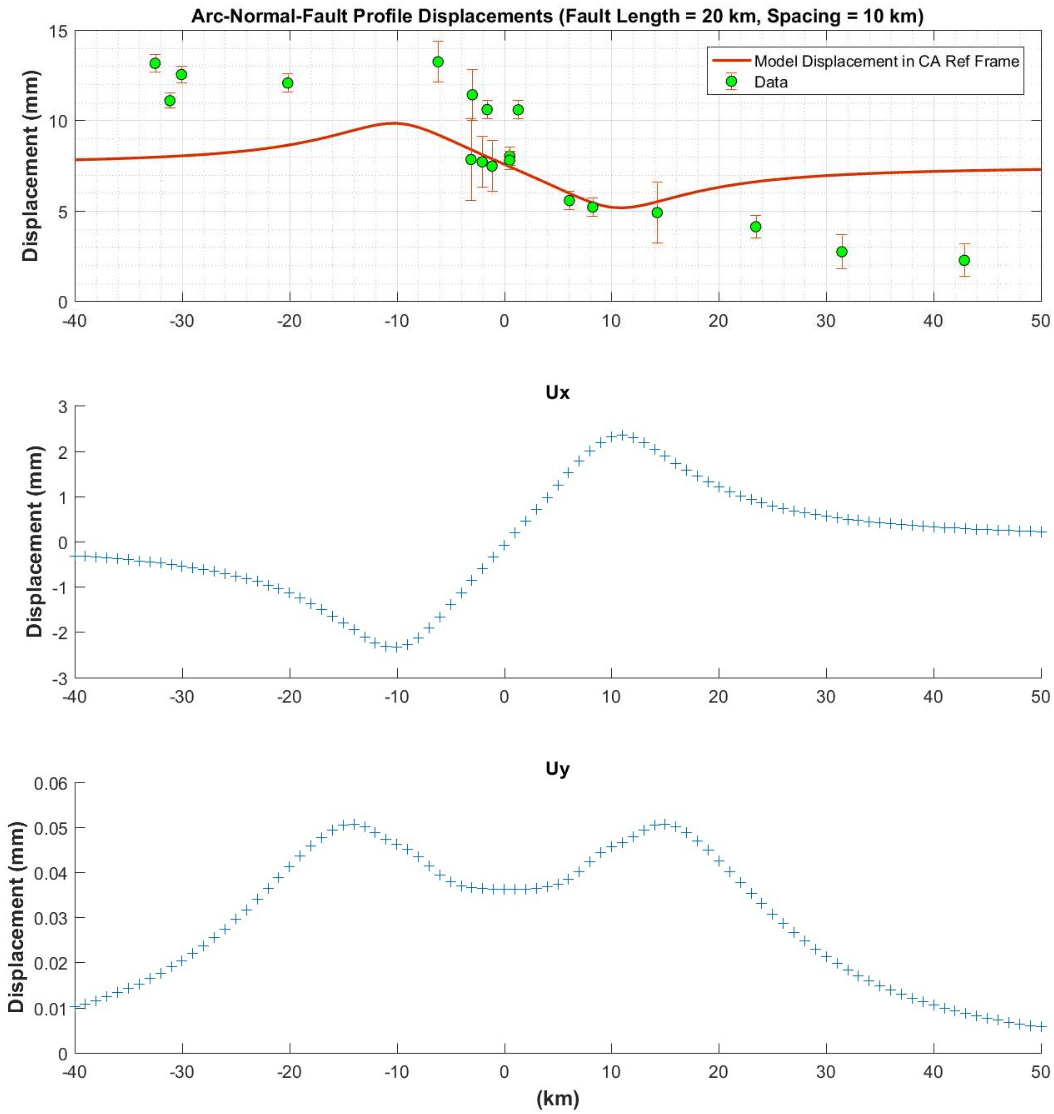

Figure **B-168**: Model O3: displacements along-profile. Arc-normal faults' length and spacing are 20 km and 10 km respectively and had 10 mm of slip imposed on them. Top panel – profile displacements projected into horizontal line (azimuth = 270°). Middle panel – profile displacements in the x-direction. Bottom panel – profile displacements in the y-direction. 'Model Displacement in CA' data sets was created by adding an offset of 7 mm to the model displacements.

B.11 Model Set P Plots

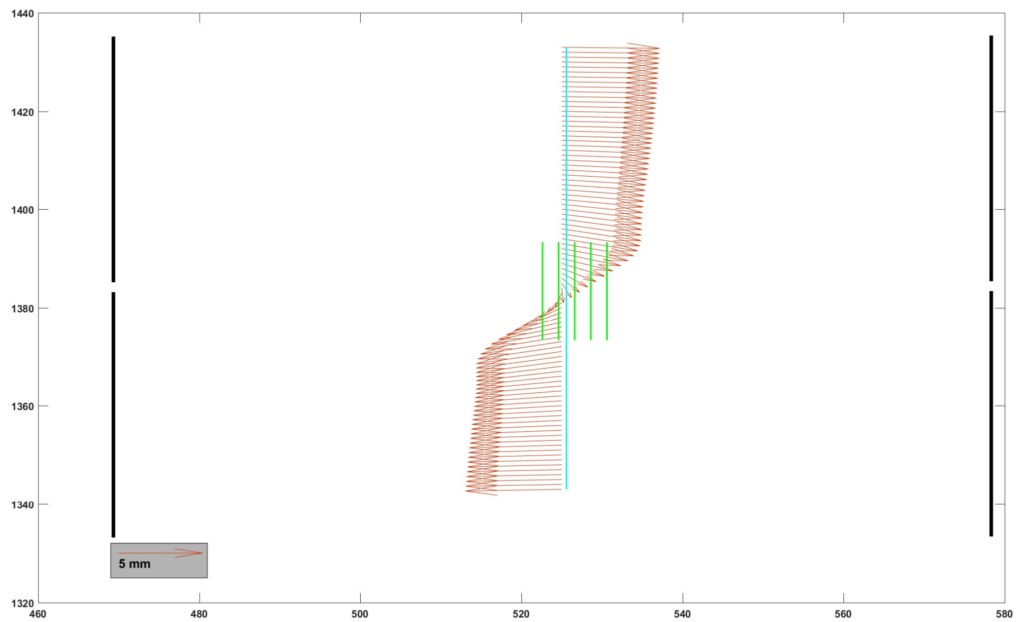

Figure **B-169**: Model P1: surface displacements (red vectors) along-profile line (cyan line). Arc-normal faults' (green lines) length and spacing are 20 km and 2 km respectively and had 10 mm of slip imposed on them. This model has 5 arc-normal faults.

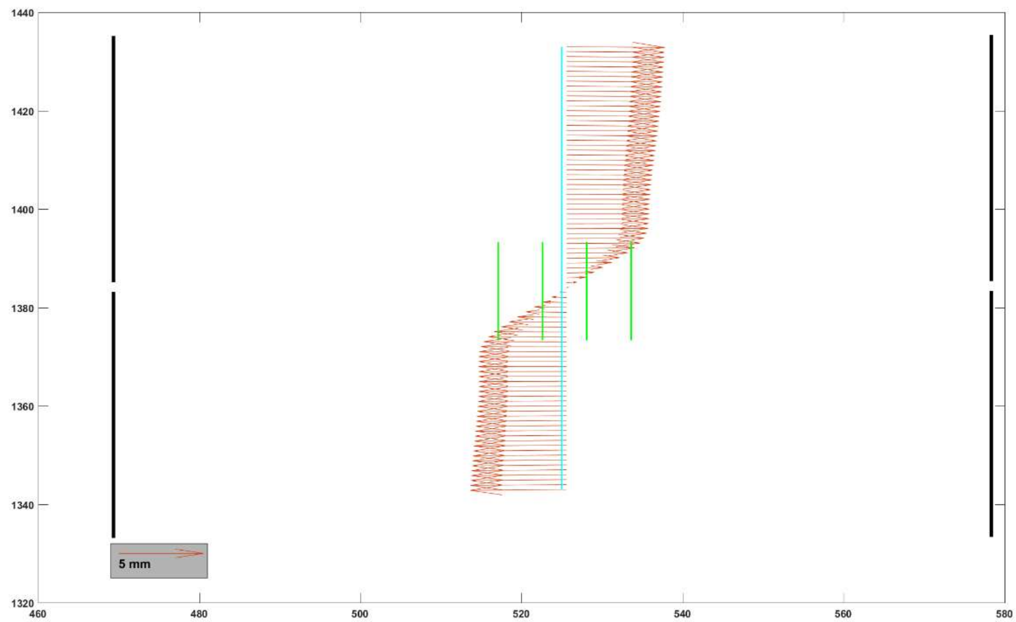

Figure **B-170**: Model P2: surface displacements (red vectors) along-profile line (cyan line). Arc-normal faults' (green lines) length and spacing are 20 km and 5 km respectively and had 10 mm of slip imposed on them. This model has 4 arc-normal faults.

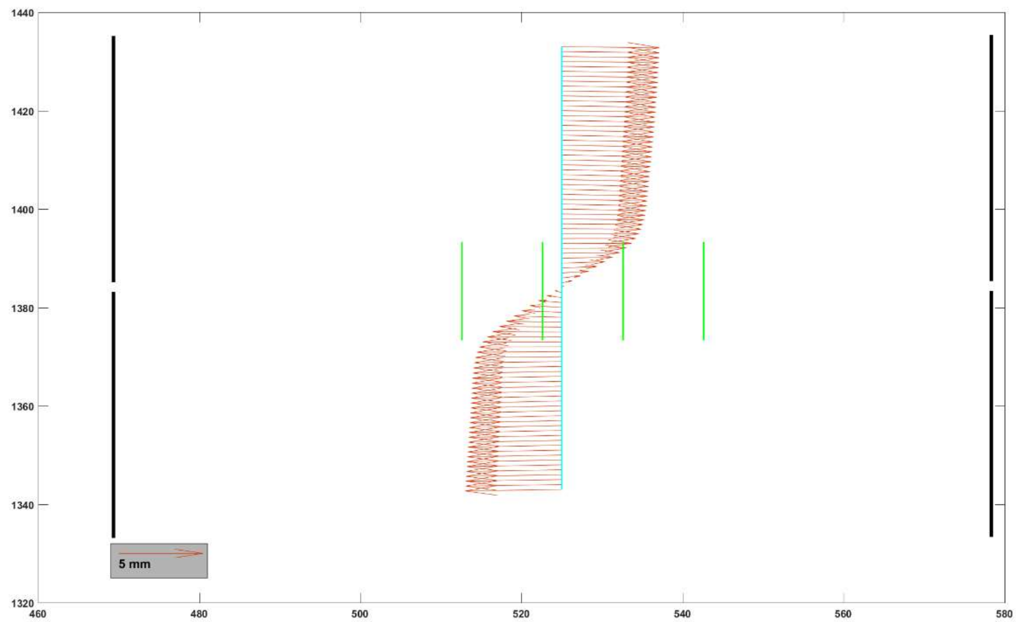

Figure **B-171**: Model P3: surface displacements (red vectors) along-profile line (cyan line). Arc-normal faults' (green lines) length and spacing are 20 km and 10 km respectively and had 10 mm of slip imposed on them. This model has 4 arc-normal faults.

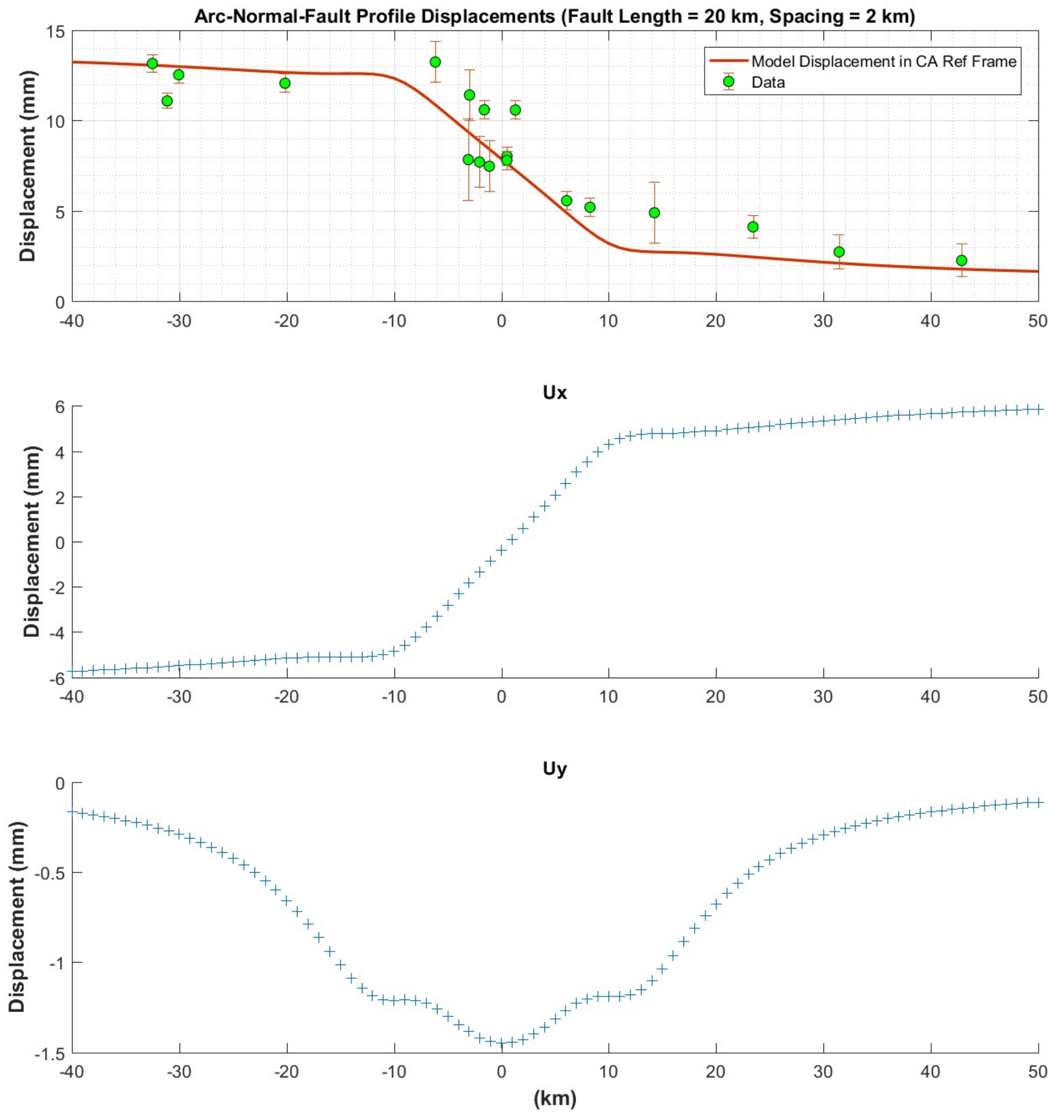

Figure **B-172**: Model P1: displacements along-profile. Arc-normal faults' length and spacing are 20 km and 2 km respectively and had 10 mm of slip imposed on them. Top panel – profile displacements projected into horizontal line (azimuth = 270°). Middle panel – profile displacements in the x-direction. Bottom panel – profile displacements in the y-direction. 'Model Displacement in CA' data sets was created by adding an offset of 7 mm to the model displacements.

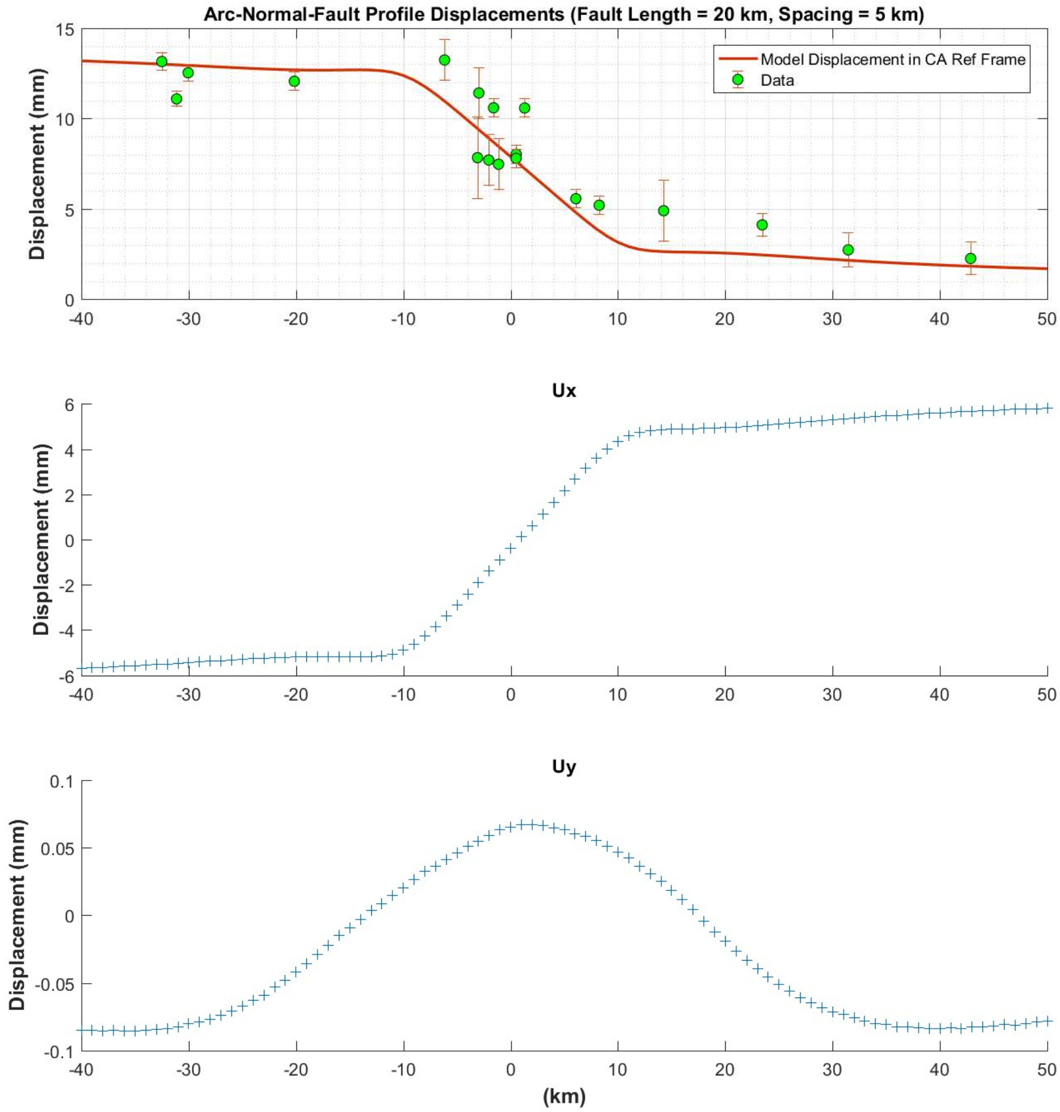

Figure **B-173**: Model P2: displacements along-profile. Arc-normal faults' length and spacing are 20 km and 5 km respectively and had 10 mm of slip imposed on them. Top panel – profile displacements projected into horizontal line (azimuth = 270°). Middle panel – profile displacements in the x-direction. Bottom panel – profile displacements in the y-direction. 'Model Displacement in CA' data sets was created by adding an offset of 7 mm to the model displacements.

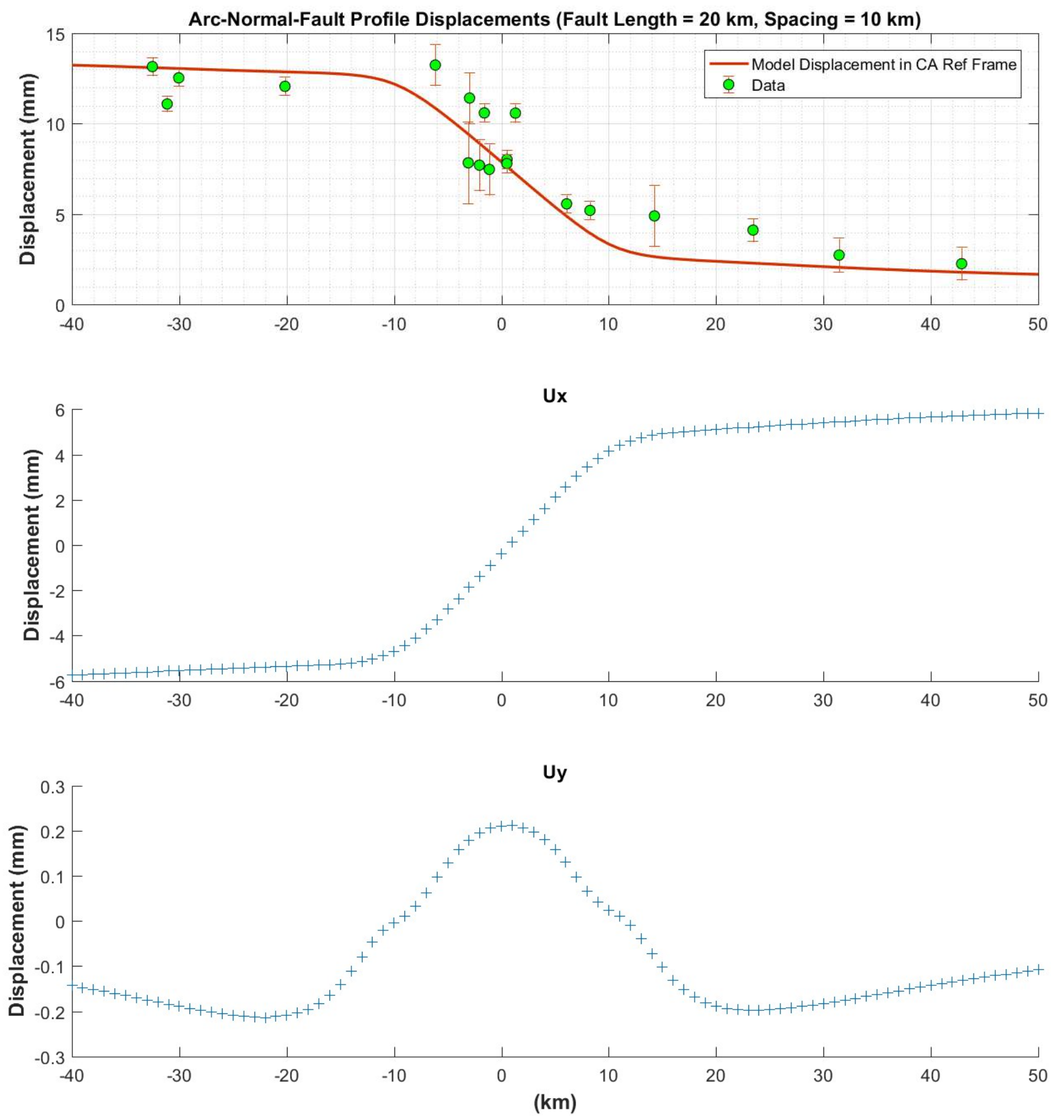

Figure **B-174**: Model P3: displacements along-profile. Arc-normal faults' length and spacing are 20 km and 10 km respectively and had 10 mm of slip imposed on them. Top panel – profile displacements projected into horizontal line (azimuth = 270°). Middle panel – profile displacements in the x-direction. Bottom panel – profile displacements in the y-direction. 'Model Displacement in CA' data sets was created by adding an offset of 7 mm to the model displacements.

B.12 Model Set Q Plots

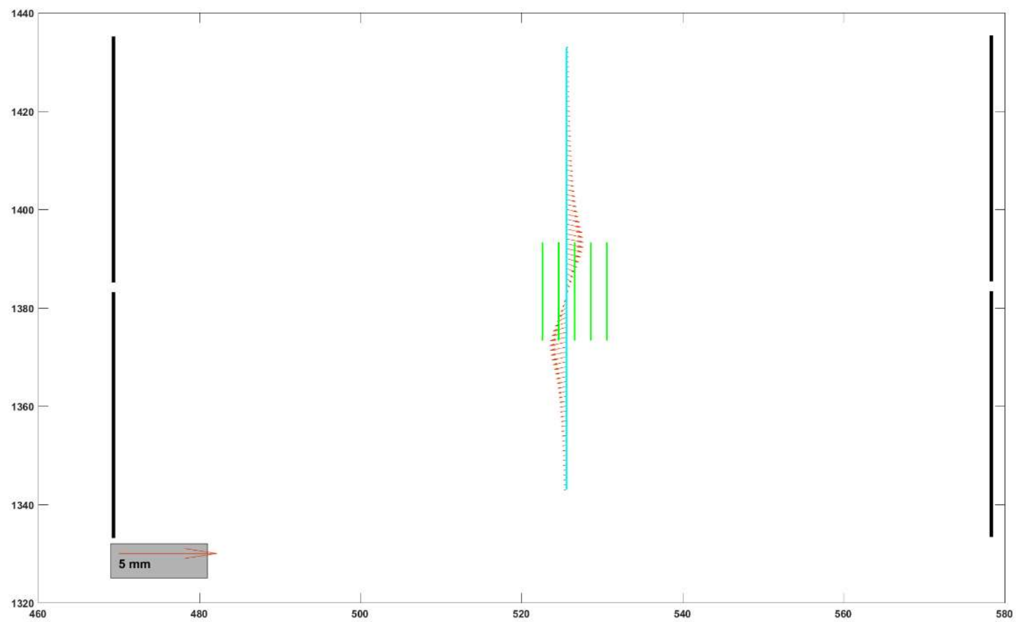

Figure **B-175**: Model Q1: surface displacements (red vectors) along-profile line (cyan line). Arc-normal faults' (green lines) length and spacing are 20 km and 2 km respectively and had 14 mm of slip imposed on them. This model has 5 arc-normal faults.

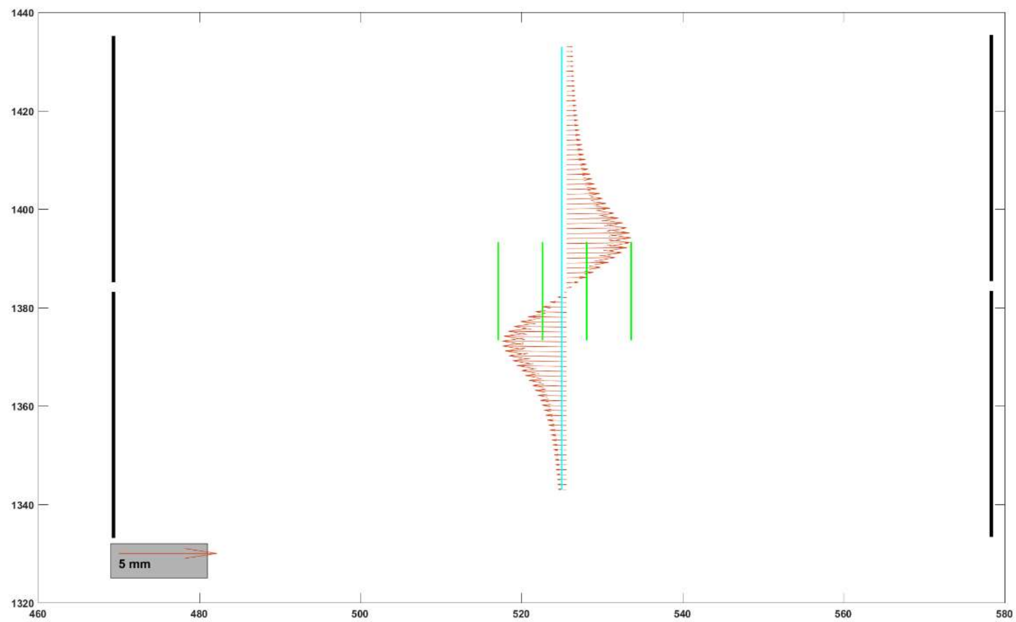

Figure **B-176**: Model Q2: surface displacements (red vectors) along-profile line (cyan line). Arc-normal faults' (green lines) length and spacing are 20 km and 5 km respectively and had 14 mm of slip imposed on them. This model has 4 arc-normal faults.

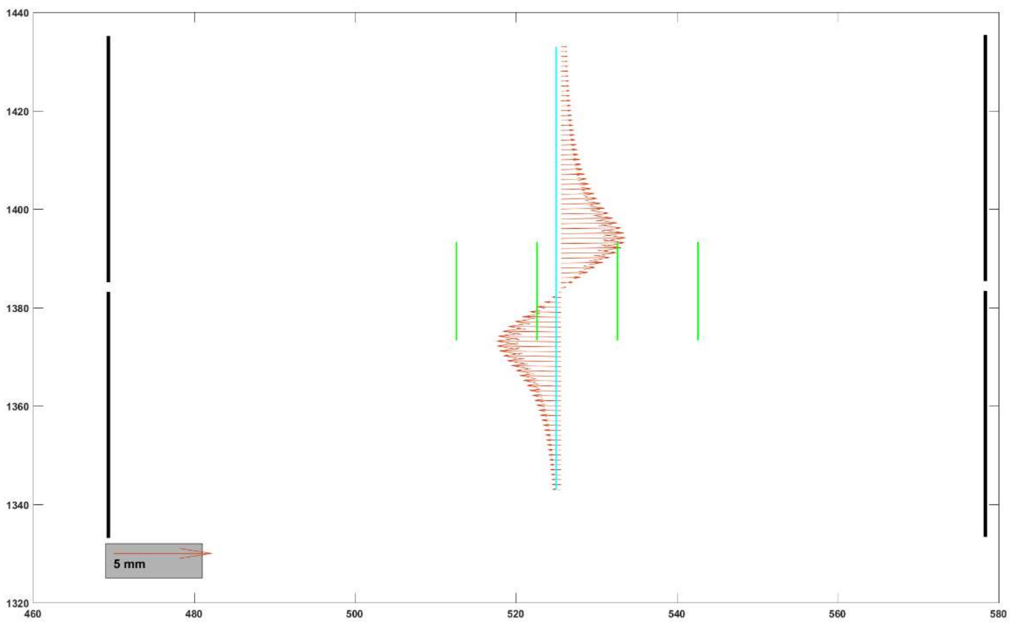

Figure **B-177**: Model Q3: surface displacements (red vectors) along-profile line (cyan line). Arc-normal faults' (green lines) length and spacing are 20 km and 10 km respectively and had 14 mm of slip imposed on them. This model has 4 arc-normal faults.

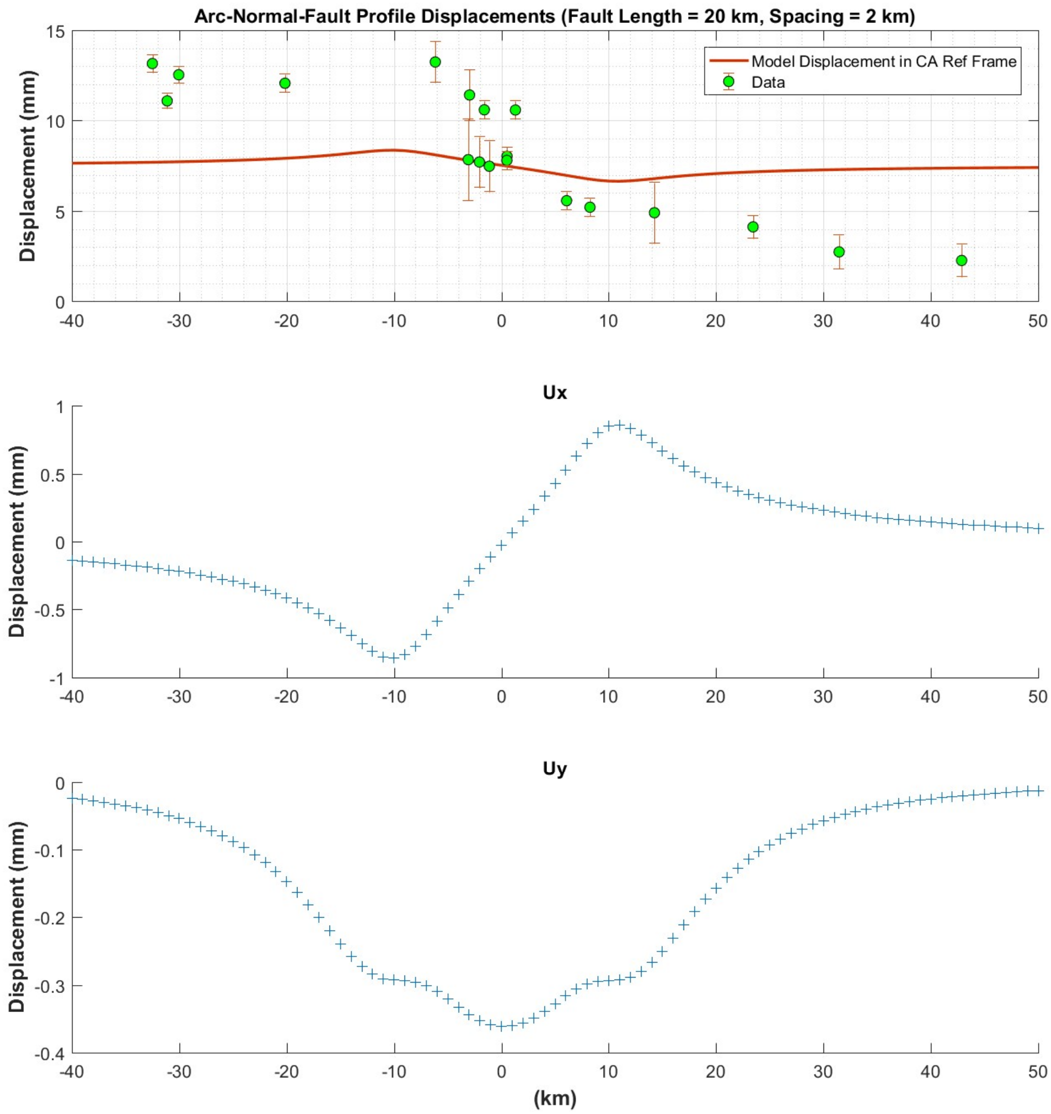

Figure **B-178**: Model Q1: displacements along-profile. Arc-normal faults' length and spacing are 20 km and 2 km respectively and had 14 mm of slip imposed on them. Top panel – profile displacements projected into horizontal line (azimuth = 270°). Middle panel – profile displacements in the x-direction. Bottom panel – profile displacements in the y-direction. 'Model Displacement in CA' data sets was created by adding an offset of 7 mm to the model displacements.

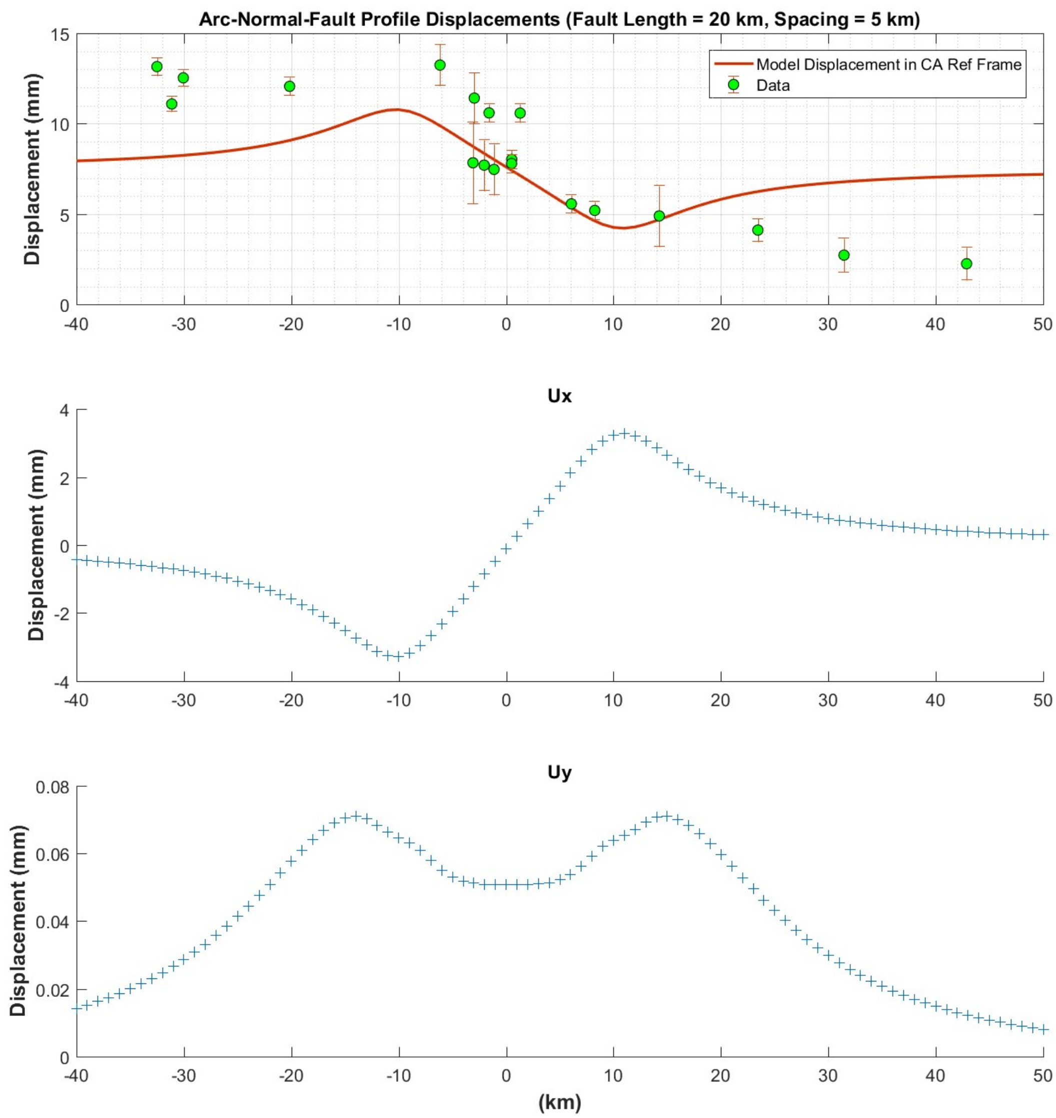

Figure **B-179**: Model Q2: displacements along-profile. Arc-normal faults' length and spacing are 20 km and 5 km respectively and had 14 mm of slip imposed on them. Top panel – profile displacements projected into horizontal line (azimuth = 270°). Middle panel – profile displacements in the x-direction. Bottom panel – profile displacements in the y-direction. 'Model Displacement in CA' data sets was created by adding an offset of 7 mm to the model displacements.

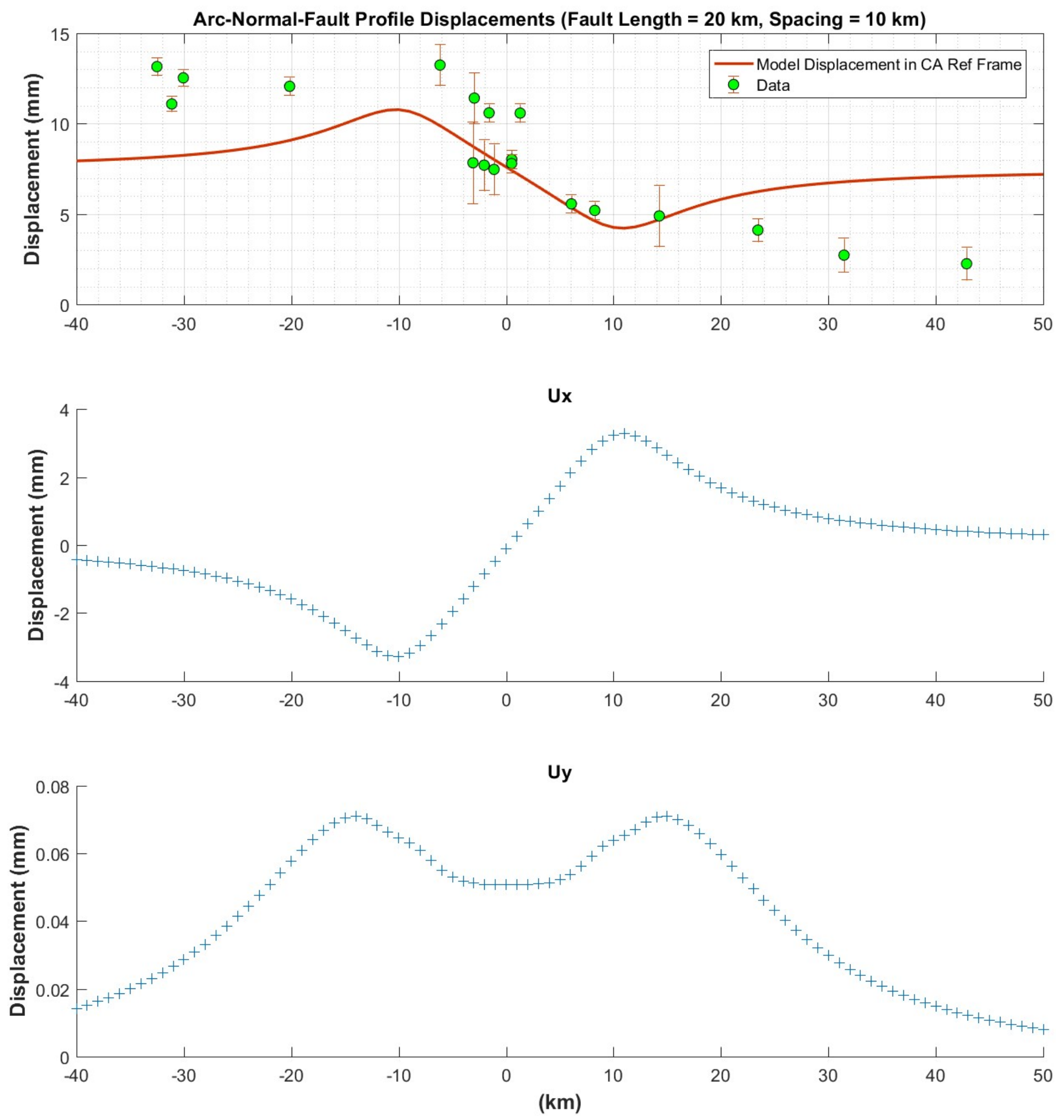

Figure **B-180**: Model Q3: displacements along-profile. Arc-normal faults' length and spacing are 20 km and 10 km respectively and had 14 mm of slip imposed on them. Top panel – profile displacements projected into horizontal line (azimuth = 270°). Middle panel – profile displacements in the x-direction. Bottom panel – profile displacements in the y-direction. 'Model Displacement in CA' data sets was created by adding an offset of 7 mm to the model displacements.

B.13 Model Set R Plots

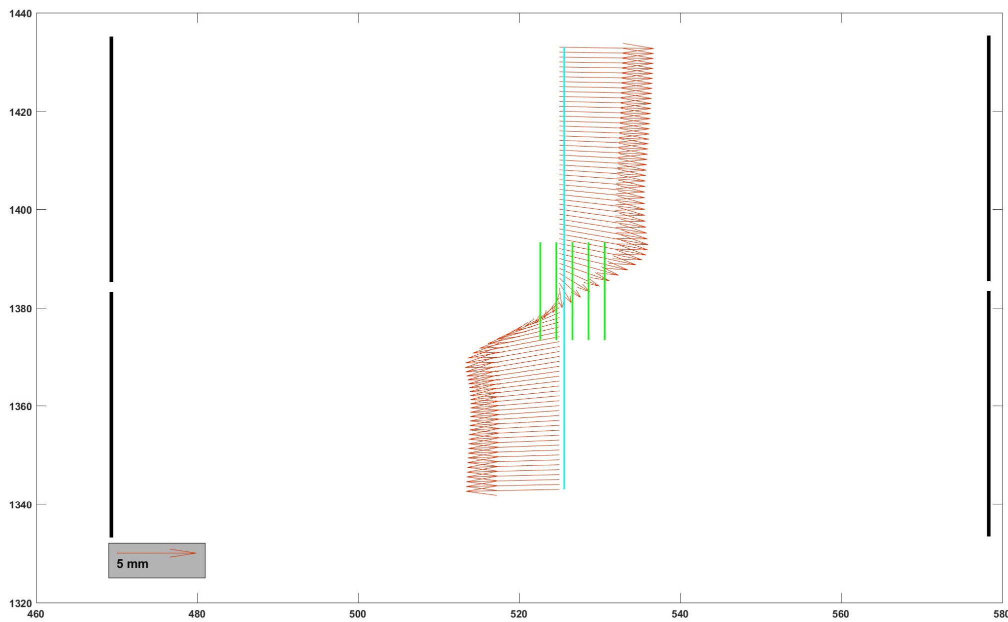

Figure **B-181**: Model R1: surface displacements (red vectors) along-profile line (cyan line). Arc-normal faults' (green lines) length and spacing are 20 km and 2 km respectively and had 14 mm of slip imposed on them. This model has 5 arc-normal faults.

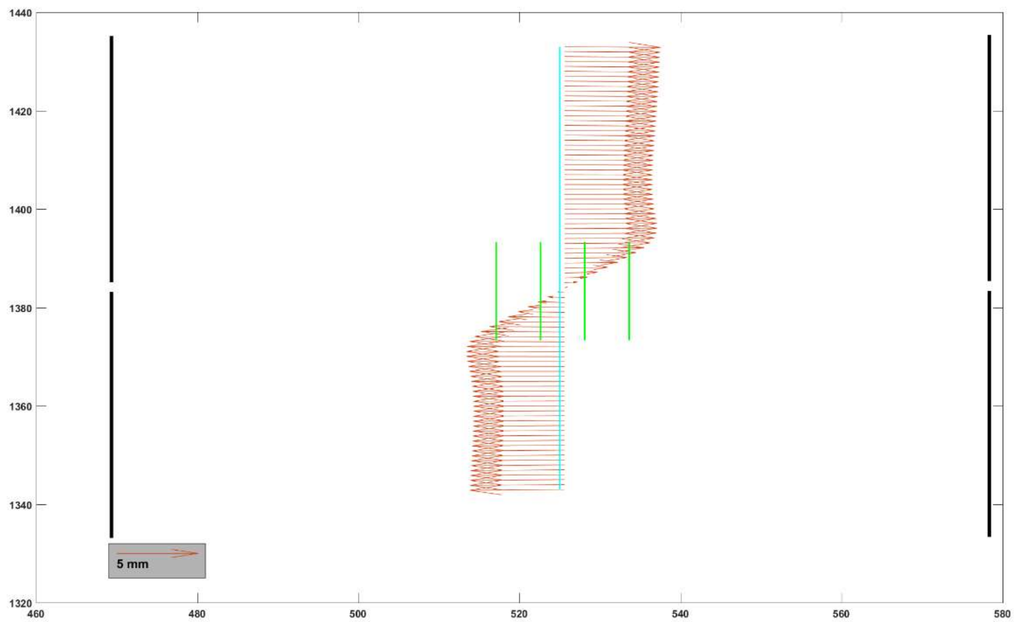

Figure **B-182**: Model R2: surface displacements (red vectors) along-profile line (cyan line). Arc-normal faults' (green lines) length and spacing are 20 km and 5 km respectively and had 14 mm of slip imposed on them. This model has 4 arc-normal faults.

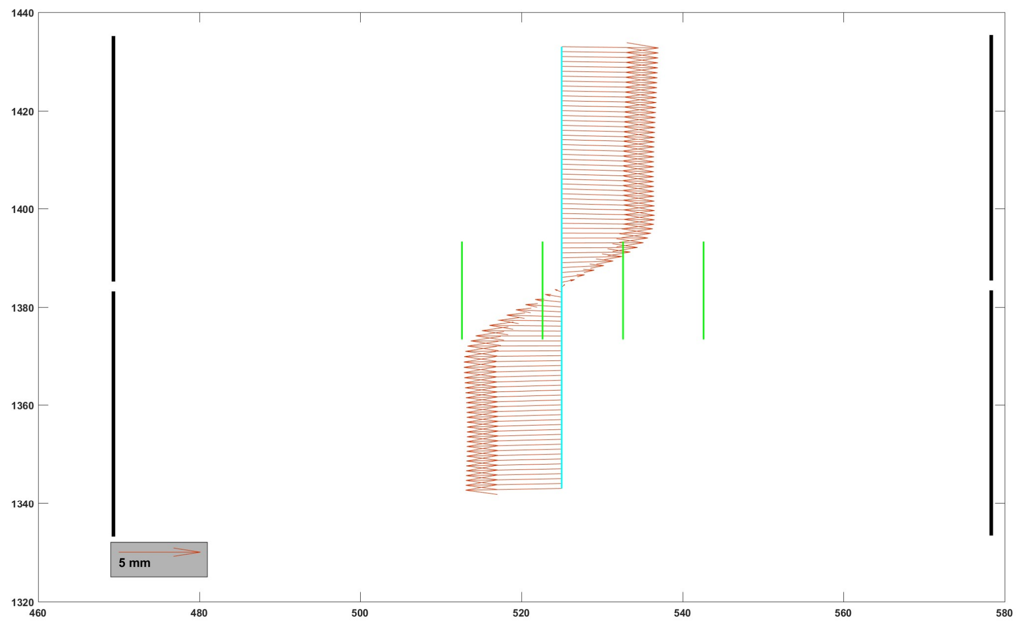

Figure **B-183**: Model R3: surface displacements (red vectors) along-profile line (cyan line). Arc-normal faults' (green lines) length and spacing are 20 km and 10 km respectively and had 14 mm of slip imposed on them. This model has 4 arc-normal faults.

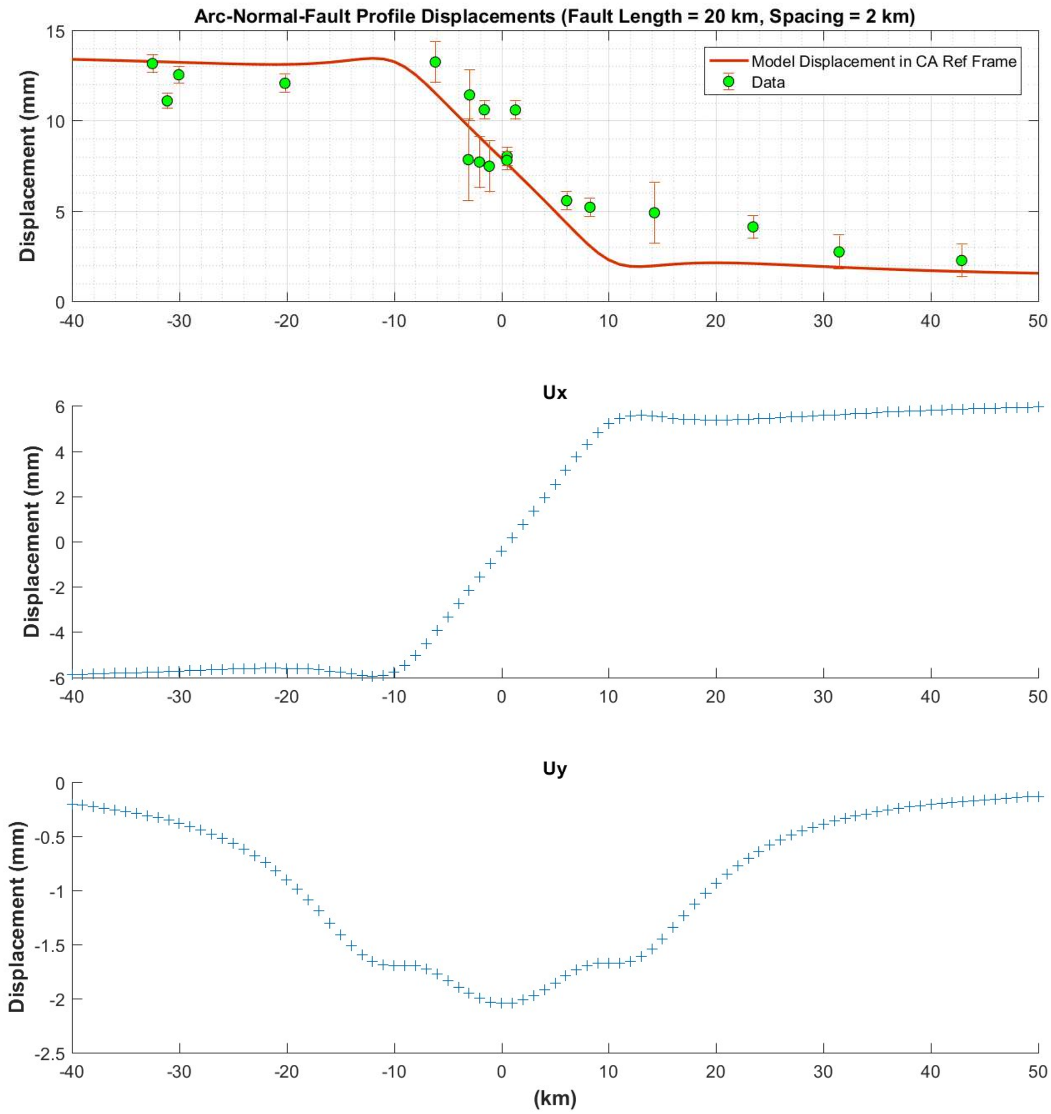

Figure **B-184**: Model R1: displacements along-profile. Arc-normal faults' length and spacing are 20 km and 2 km respectively and had 14 mm of slip imposed on them. Top panel – profile displacements projected into horizontal line (azimuth = 270°). Middle panel – profile displacements in the x-direction. Bottom panel – profile displacements in the y-direction. 'Model Displacement in CA' data sets was created by adding an offset of 7 mm to the model displacements.

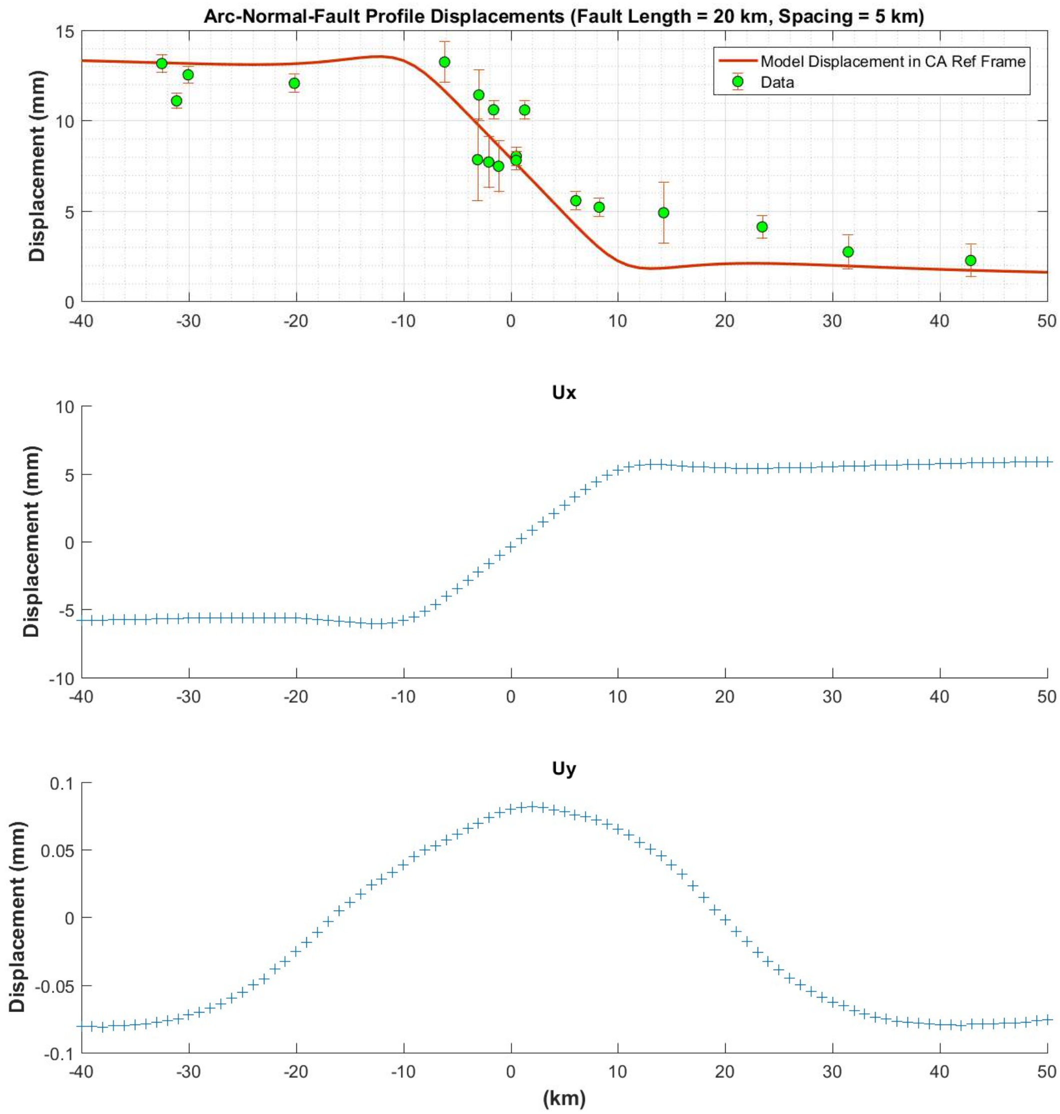

Figure **B-185**: Model R2: displacements along-profile. Arc-normal faults' length and spacing are 20 km and 5 km respectively and had 14 mm of slip imposed on them. Top panel – profile displacements projected into horizontal line (azimuth = 270°). Middle panel – profile displacements in the x-direction. Bottom panel – profile displacements in the y-direction. 'Model Displacement in CA' data sets was created by adding an offset of 7 mm to the model displacements.

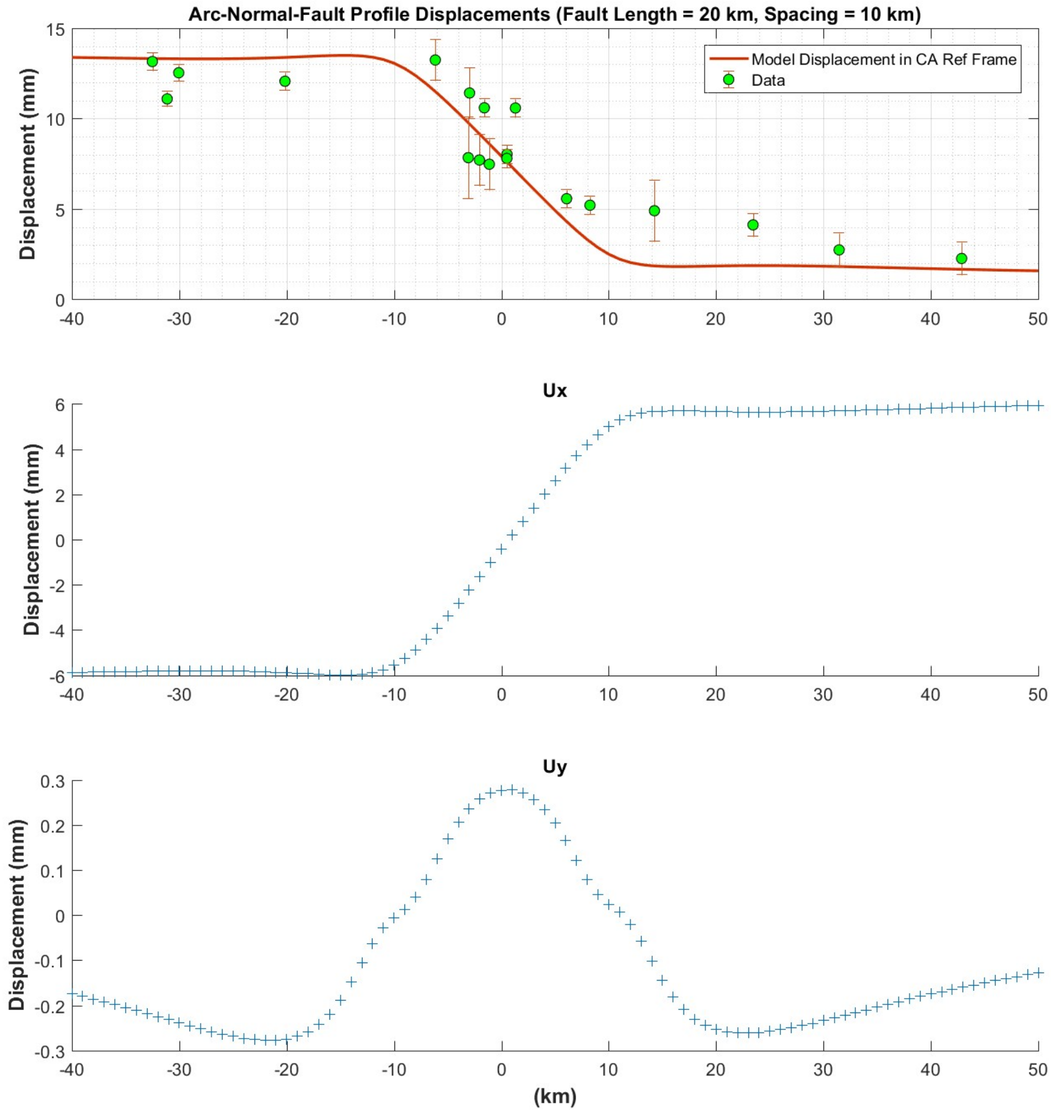

Figure **B-186**: Model R3: displacements along-profile. Arc-normal faults' length and spacing are 20 km and 10 km respectively and had 14 mm of slip imposed on them. Top panel – profile displacements projected into horizontal line (azimuth = 270°). Middle panel – profile displacements in the x-direction. Bottom panel – profile displacements in the y-direction. 'Model Displacement in CA' data sets was created by adding an offset of 7 mm to the model displacements.

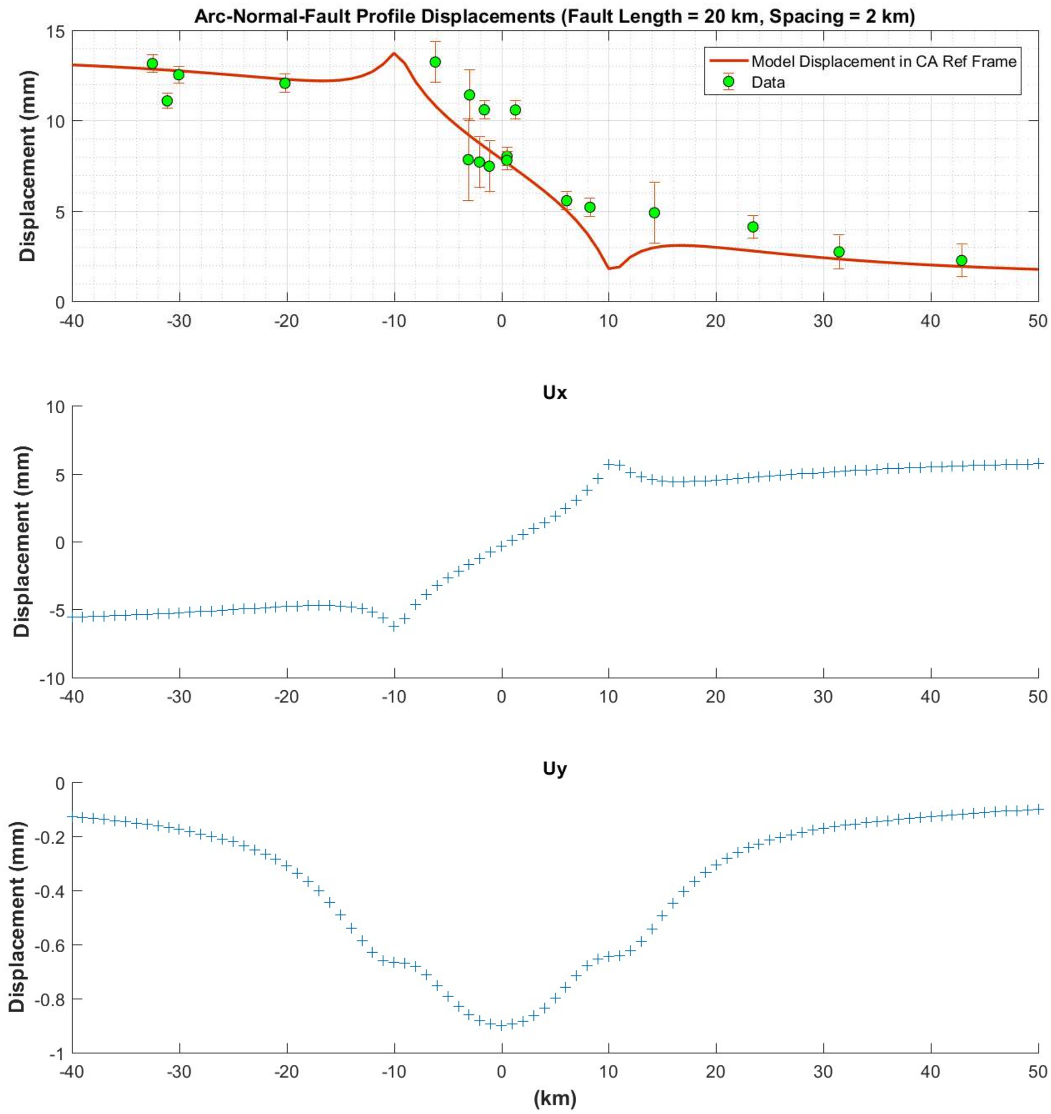

Figure **B-187**: Model I1: displacements along-profile. Arc-normal faults' length and spacing are 20 km and 2 km respectively. Top panel – profile displacements projected into horizontal line (azimuth = 270°). Middle panel – profile displacements in the x-direction. Bottom panel – profile displacements in the y-direction. 'Model Displacement in CA' data sets was created by adding an offset of 7 mm to the model displacements.

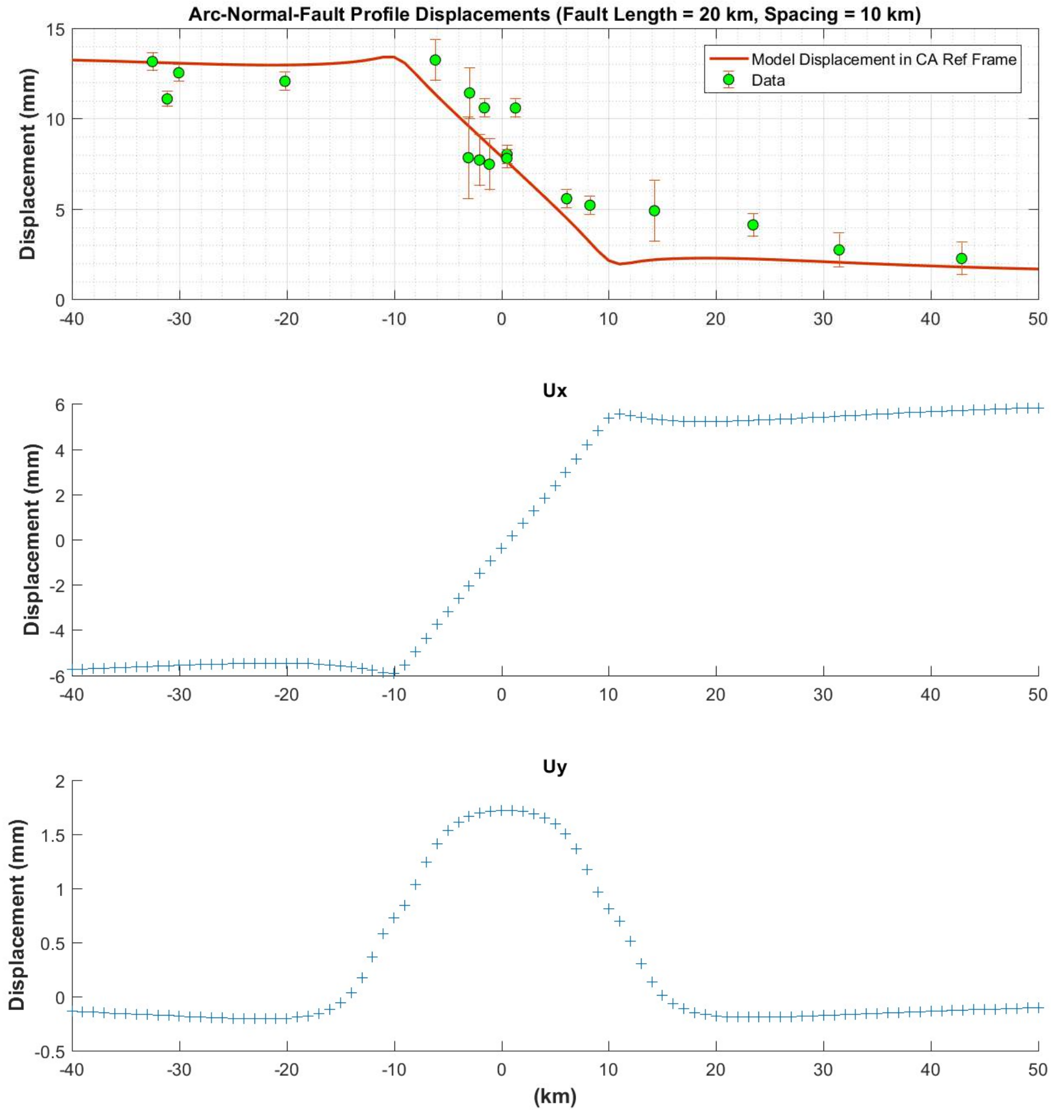

Figure **B-188**: Model I3: displacements along-profile. Arc-normal faults' length and spacing are 20 km and 10 km respectively. Top panel – profile displacements projected into horizontal line (azimuth = 270°). Middle panel – profile displacements in the x-direction. Bottom panel – profile displacements in the y-direction. 'Model Displacement in CA' data sets was created by adding an offset of 7 mm to the model displacements.

Appendix C
GPS Displacements from Daily Positions

Table **C-1**: Displacements for the M_w 5.3 June 26th earthquake from GPS daily static positions.

Station	Longitude	Latitude	Easting (mm)	Northing (mm)	Vertical (mm)	σ_E (mm)	σ_N (mm)	σ_V (mm)
GV01	-91.1134	-0.7824	174.7	915.6	583	-72.7	-130.5	-787.6
GV03	-91.1329	-0.7978	-1051.8	3462.4	2919.4	-72.9	-405.5	-1053.3
GV04	-91.1381	-0.8115	-1463.7	1890.8	6281.4	-140.1	-261	-2176.8
GV05	-91.1212	-0.8049	940.9	2241.5	5665.8	-227.4	-284.5	-1245.5
GV06	-91.1281	-0.8343	985.4	-4062.8	3563.6	-187.1	-381	-887.3
GV08	-91.1344	-0.8420	178.1	-2198.3	1510.6	-38.4	-205.2	-186.6
GV09	-91.1474	-0.8373	-710.7	-3459.8	1057.2	-96.2	-320.3	-1115.7
GV10	-91.1511	-0.8493	-277.5	-994.1	607.2	-24.5	-83.6	-165.7

Table **C-2**: Displacements for the M_l 4.9 July 5th earthquake from GPS daily static positions.

Station	Longitude	Latitude	Easting (mm)	Northing (mm)	Vertical (mm)	σ_E (mm)	σ_N (mm)	σ_V (mm)
GV01	-91.1134	-0.7824	178.2	923.2	589.4	-69.7	-122.2	-788.7
GV03	-91.1329	-0.7978	-1051.6	3467	2942.9	-90.9	-436.9	-1026.4
GV04	-91.1381	-0.8115	-1467.9	1903.3	6348.3	-151.9	-252.5	-2100.6
GV05	-91.1212	-0.8049	952.4	2245.8	5698.7	-213.2	-301.5	-1206.5
GV06	-91.1281	-0.8343	996.5	-4016	3608.2	-155.8	-580.7	-779.6
GV08	-91.1344	-0.8420	175.2	-2167.2	1496.2	-44.6	-334	-229.7
GV09	-91.1474	-0.8373	-718	-3426.8	1103	-67.5	-472.8	-1093.2
GV10	-91.1511	-0.8493	-275.8	-985.3	605.4	-33.5	-127.7	-182

Table **C-1**: Displacements for the M_l 4.8 July 5th earthquake from GPS daily static positions.

Station	**Longitude**	**Latitude**	**Easting (mm)**	**Northing (mm)**	**Vertical (mm)**	**σ_E (mm)**	**σ_N (mm)**	**σ_V (mm)**
GV01	-91.1134	-0.7824	179.2	921	591.1	-70.7	-151.3	-795.3
GV03	-91.1329	-0.7978	-1039.5	3432.5	2941.2	-157.7	-611.7	-1012
GV04	-91.1381	-0.8115	-1455.4	1894	6341.1	-225.9	-323.5	-2095.7
GV05	-91.1212	-0.8049	951.4	2216.3	5653.8	-234.9	-428	-1331.4
GV06	-91.1281	-0.8343	973.2	-3875.2	3522.9	-217.2	-937.9	-898.7
GV08	-91.1344	-0.8420	166.9	-2090.6	1450.1	-57.6	-520.8	-336
GV09	-91.1474	-0.8373	-702.9	-3311.5	1109.7	-126.3	-779.2	-1043.8
GV10	-91.1511	-0.8493	-268.8	-955.1	591.6	-55.4	-213.5	-229.9

Machel H. Higgins

EDUCATION

Ph.D. — The Pennsylvania State University, University Park, PA, 16803 — *2016 – 2021(exp)*
Thesis: Geodetic Exploration of the Kinematics and Fault Slip Rates of the Southeastern and Western Caribbean Plate Boundaries and the Caldera Dynamics of the Sierra Negra Volcano

MPhil, Computer Science\Seismology — The University of the West Indies, St. Augustine, Trinidad and Tobago, W.I. — *2011- 2013*
Thesis: Using Self-Organizing Maps to determine an Optimal Seismic Network Configuration

B. A. — Gettysburg College, Gettysburg, PA — *2000- 2004*

Majors: Physics, Computer Science

EXPERIENCE

2016 -	Research Assistant, Geodetic, Tectonics and Volcanology Lab, Dept of Geoscience, The Pennsylvania State University, State College, PA
2008 - 2016	Scientific Software Engineer - Seismic Research Centre, UWI, St. Augustine, Trinidad and Tobago, W.I.
2006 - 2008	Scientific Software Engineer - Montserrat Volcano Observatory, Flemmings, Montserrat
2004 - 2006	Software Engineer - Signature Domains Inc. Miami, FL, USA

PUBLICATIONS

Higgins, M., La Femina, P., Weber, J., Geirsson, H., Ryan, G. A., (2021). Strain Partitioning and Interseismic Fault Behaviour Along the Caribbean-South Transform American Transform Plate Boundary, *Tectonics* (in press).

Bell, A., La Femina, P.C., Ruiz, M., Amelung, F., Bagnardi, M., Bean, C., Bernard, B., Ebinger, C., Gleeson, M., Grannell, J., Hernandez, S., **Higgins, M**., Liorzou, C., Lundgren, P., Meier, N., Möllhoff, M., Oliva, S.J., Ruiz, A., and Stock, M., (2021). Trapdoor Faulting and Resurgence during the Inflation-Deflation Cycle of the 2018 Eruption of Sierra Negra Volcano, Galápagos Islands*, Nature Communications (*Paper #NCOMMS-20-29059C*)*.

Weber, J., Geirsson, H., La Femina, P., Robertson, R., Churches, C., Shaw, K., **Higgins, M**., Miller, K., (2020). Fault creep and strain partitioning in Trinidad-Tobago: Geodetic measurements, models, and origin of creep. *Tectonics*, *39*(1).

Stephens, K., Wauthier, C., Bussard, R., **Higgins, M**., La Femina, P.C., (2020). Assessment of Mitigation Strategies for Tropospheric Phase Contributions to InSAR Time-Series Datasets over Two Nicaraguan Volcanoes. *Remote Sensing* 12 (782).

Sun, J., Wauthier, C., Stephens, K., Gervais, M., Cervone, G., La Femina, P. C., & **Higgins, M.** (2020). Automatic detection of volcanic surface deformation using deep learning. *Journal of Geophysical Research - Solid Earth*, http://dx.doi.org/10.1029/2020JB019840.

Roman, Diana C., LaFemina, P.C., Bussard, R., Stephens, K., Wauthier, C., **Higgins, M**., Feineman, M., et al., (2019). Mechanisms of Unrest and Eruption at Persistently Restless Volcanoes: Insights From the 2015 Eruption of Telica Volcano, Nicaragua. *Geochemistry, Geophysics, Geosystems* 20 (8): 4162–83.

Weber, J., Geirsson, H., Latchman J., Shaw K., La Femina P., Wdowinski S., **Higgins M.**, Churches C., Norabuena E., (2015). Tectonic inversion in the Caribbean-South American plate boundary: GPS Geodesy, Seismology, and Tectonics of the Mw 6.7 April 22, 1997, Tobago earthquake, *Tectonics* 34 (6).

Symithe S., Calais E., de Chabalier J.B., **Higgins M.**, Robertson R., (2015). Current Block Motions and Strain Accumulation on Active Faults in the Caribbean, *Journal of Geophysical Research: Solid Earth*, 120, doi:10.1002/2014JB011779.